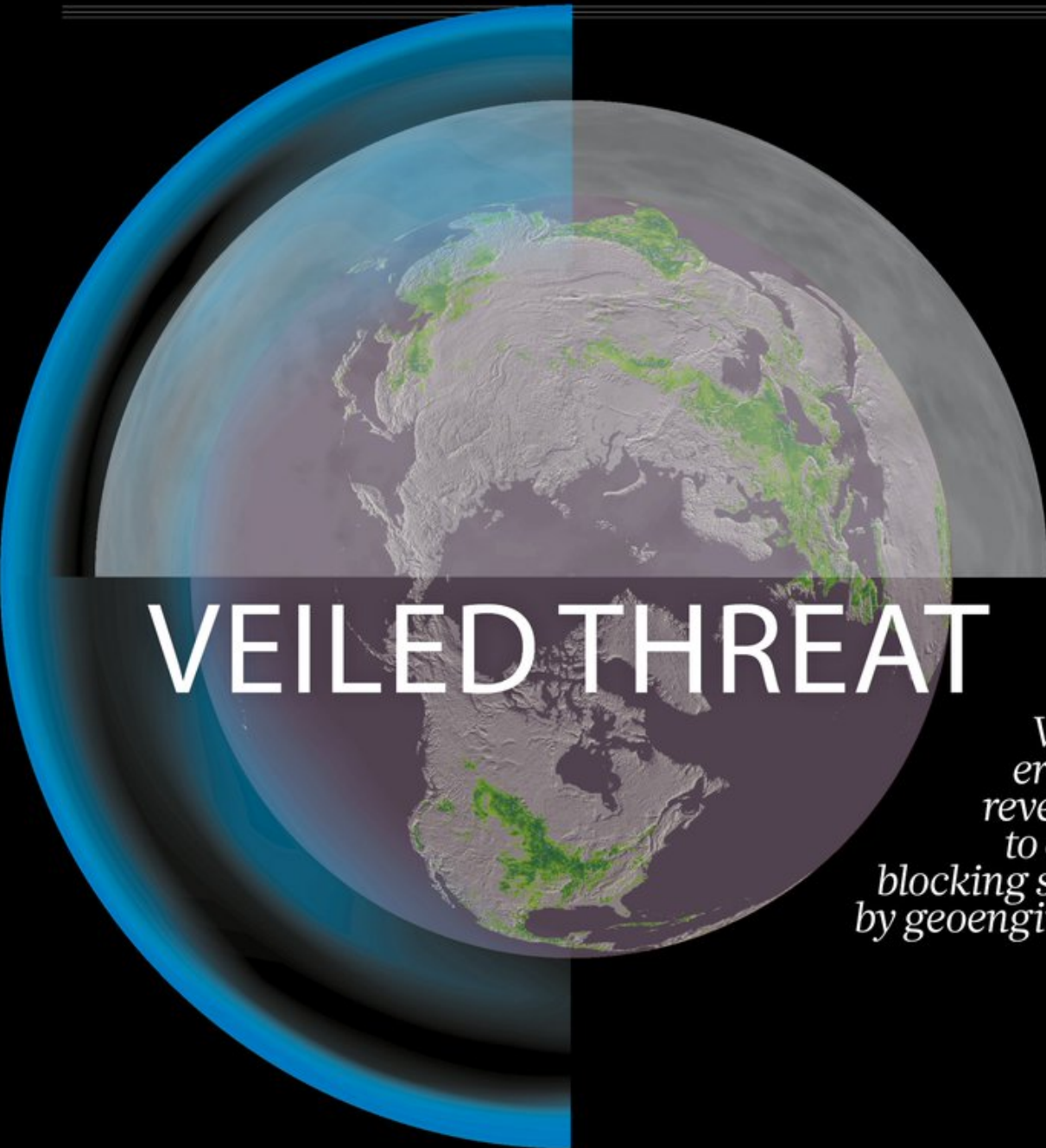


nature

THE INTERNATIONAL WEEKLY JOURNAL OF SCIENCE

VEILED THREAT

Volcanic eruptions reveal risks to crops of blocking sunlight by geoengineering
PAGE 480



CONSERVATION

SPLIT INTO Factions

Divisions mire international biodiversity assessment

PAGE 423

QUANTUM PHYSICS

PRECIOUS MOMENTS

Quantum magnet simulated by programmable qubit lattice

PAGES 438 & 456

BIOLOGICAL TECHNIQUES

EXPRESSION DYNAMICS

Velocity of RNA predicts destiny of individual cells

PAGES 434 & 494

NATURE.COM/NATURE

23 August 2018

Vol. 560, No. 7719

THIS WEEK

EDITORIALS

WORLD VIEW Online technology can solve replication problems p.411

OPIOIDS Drug tweaks offer a step towards safer painkillers p.412

Pretty Bird Ancient Americans farmed giant parrot p.412



Biodiversity needs more voices

The global body for biodiversity science and policy must embrace its inclusive approach and heal a damaging rift with its critics over how to value the natural world.

Most scientists and conservationists agree the planet is on the edge of an extinction crisis. But the best way to address that crisis is still the subject of some debate. A new international body was set up to help, by offering scientific advice to policymakers. But a dispute over how to value the natural world threatens to undermine its efforts. Both sides in the debate must remember what really matters here: securing a sustainable future for the planet.

The international body is the Intergovernmental Science-Policy Platform on Biodiversity and Ecosystem Services (IPBES). It is set to release a landmark report that scientists hope will accelerate global political efforts to address declining biodiversity — in the same way that work on global warming has been focused and energized by the Intergovernmental Panel on Climate Change (IPCC). IPBES has taken a more inclusive approach than the IPCC did, and it leans more heavily on researchers and scholars from science and the humanities, citizen scientists and representatives of indigenous peoples.

As we report in a News Feature on page 423, this level of inclusion presents a challenge: the different perspectives are making it difficult for the organization to present consensus, particularly on the relative importance of ecosystem services. To many of the organization's representatives from the developing world, a focus on ecosystem services — which includes placing a monetary value on aspects of biodiversity as a way to include them in political processes driven by economics — is unacceptable. This is frustrating for many in that field, whose influential names and research have no doubt helped to persuade countries to collectively protect nearly 15% of land and 10% of territorial waters. These specialists are used to driving policy initiatives such as IPBES, and they are concerned that their influence in the organization is weakening. An unfortunate outcome of the division could be a final IPBES report that these experienced experts do not support, which in turn could mean that the report is less likely to have the desired political impact.

From a historical perspective, their frustration is understandable: these scientists have struggled for 30 years to convince sceptical academics, conservationists and policymakers that environmental costs can be valued as actual monetary costs, which present and future generations will have to pay. But those who espouse ecosystem services need to make room for other types of expertise and ways of valuing biodiversity. It is always hard for a community that has historically had to fight to be taken seriously to then step up and take on the mantle of authority, but the leaders of ecosystem services have done this, and must now encourage those who take opposing views to do the same.

At the moment, the two sides are trading claim and counter-claim. But this public debate threatens to lose sight of both groups' shared goal: protecting biodiversity.

If the IPBES leadership ends up continuing without the endorsement of the ecosystem-services community, this will not go

unnoticed among the funders and policymakers it is trying to influence. Policymakers who rely on scientific knowledge are highly sensitive to internal disagreements; the IPCC was able to exercise genuine influence only once the internal scientific debate over anthropogenic climate change was settled, after 1996. Economic

"Economic arguments have become extremely persuasive with many policymakers."

arguments have become extremely persuasive with many policymakers, so it is important that future IPBES assessments include them prominently alongside other analyses.

The real battle is to slow down and eventually halt the loss of biodiversity. But it won't be won if discord continues among the members of what should be a winning team for the planet.

IPBES should acknowledge the expertise of colleagues from the ecosystem-services community in presenting ideas in a way that engages policymakers. And that community, in turn, needs to accept that there is virtue in being first among equals. ■

Referees' rights

Peer reviewers should not feel pressured to produce a report if key data are missing.

At *Nature*, we recognize that our peer reviewers have certain 'rights'. One of the most well known is the right to anonymity. Less widely known is that referees have the right to view the data and code that underlie a work if it would help in the evaluation, even if these have not been provided with the submission. Yet few referees exercise this right. They should do so.

Editors try to ensure that a manuscript contains sufficient detail and supporting data to allow a rigorous evaluation, while recognizing that access to some data may be restricted because of privacy concerns. We urge referees to check whether they have all the data and code they need before drafting their review. They should never feel pressured to supply a report if key information is lacking, and should feel free to contact *Nature* to request access. Some *Nature Research* journals go further: *Scientific Data* requires all data to be hosted in a trusted and accessible repository before a paper is submitted. And *Nature Methods*, *Nature Biotechnology* and *Nature Machine Intelligence* have this month begun to trial tools to enhance peer review of code.

Such practices obviously improve the review process and thus, ultimately, the paper itself. And requests to authors to supply data provide an important feedback mechanism, helping to encourage data and code sharing in the research communities. ■



No more excuses for non-reproducible methods

Online technologies make it easy to share precise experimental protocols — and doing so is essential to modern science, says Lenny Teytelman.

Here's a one-two punch to spark camaraderie among scientists: First, ask: "How long did it take to get your PhD?" Then follow up with: "How long would it have taken if all your experiments had worked the first or second time?"

Part of the probable time difference is due to inexperience, but not all of it. News last month brought a powerful reminder that access to detailed methods can be essential for getting experiments to work. In 2013, the US\$1.6-million Reproducibility Project: Cancer Biology set out to repeat key experiments from 50 high-profile cancer papers, and so assess the extent to which published results can be replicated. Instead, the project has decided to stop at 18 papers. One big reason for this was the difficulty of working out what exactly was done in the original experiments. Protocols — precise step-by-step recipes for repeating experiments — are missing from published research more often than not, and even the original researchers can have trouble pinpointing particulars years later.

I sympathize with those who struggle to chase down these details, but I am glad that their efforts have generated such a buzz. It will accelerate a shift towards better reporting.

Now should be springtime for methods sharing. Mobile-friendly, web-based technologies are maturing just as the need to improve reproducibility has gained widespread attention. A new era of more-efficient, more-confident science is ours to lose.

My own obsession with sharing methods started with an all-too-common frustration. I spent the first year and a half of my postdoc working out a protocol for single-cell microscopy. Assiduous tinkering showed that subtle changes to sample preparation were crucial. Instead of 1 microlitre of a chemical, I needed 5. Instead of a 15-minute incubation, I needed an hour. Alas, the general technique had already been published, so I got no credit for the work. Anyone else using the published recipe would have been either getting misleading results, or sharing my frustration at having had to waste time discovering the necessary adjustments for themselves — hence my enthusiasm for a central place to update protocols and share tips.

In 2012, two colleagues and I decided to launch exactly this kind of resource. It turns out that we were far from the first to recognize this need. When my PhD co-adviser realized I was serious about leaving my postdoc to pursue such a project, he connected me with a researcher who had tried something similar a dozen years earlier. That project, BioProtocol.com, raised a million dollars of venture capital to build a protocol repository. This was in the era of flip phones with green-and-black screens, and before online tools and ideals of sharing had surged. The company shut down during the dotcom bust, but the entrepreneurs retained a wealth of experience and insight, which they generously shared. Another venture, Protocol Online, was launched around the same time to organize disparate life-science protocols in a

central database. Later efforts include OpenWetWare (a wikipedia-like site for sharing step-by-step protocols) and Protocol Exchange (a preprint server for protocols, hosted by the publisher of *Nature*).

We launched protocols.io (a company in which I own equity) in 2014. This open-access repository of science methods lets researchers create and modify protocols, update versions and share them, either with select collaborators or with everyone. The protocols are dynamic and interactive, rather than static PDFs, so researchers can take notes and track time on smartphones as they perform experiments. When they publish papers, they can get a persistent identifier (in the form of a digital object identifier, or DOI) for their protocol and add it to the methods section. More than 10,000 protocols have now been uploaded, attracting 100,000 views every month. We and the authors frequently receive e-mails from researchers thanking us for saving them time.

One reason these efforts have taken off is that increased attention to problems with reproducibility has spurred initiatives with publishers, vendors, funders, and individual laboratories. Some 200 journals now instruct authors to link to protocols.io or a similar repository; reviewers have also started to push for this. And funders including the US-based Gordon and Betty Moore Foundation, Chan Zuckerberg Initiative and childhood-cancer charity Alex's Lemonade Stand Foundation either state explicitly in their guidelines, or plan to state, that methodological resources are to be shared in a public repository.

But the gap between meticulous methods and adequate description remains. To fill it, efforts must start at the bench, well before results are ready to be written up. Lab members and lab heads should be on the lookout for tools that facilitate tracking, and be willing to give them a try. And decisions about how to document and share methods should be made when researchers are designing their experiments, not when they are writing their manuscripts.

Of course, fully described, shared protocols will not fix everything in science. Knowing how much to document is a judgement call; some conditions will necessarily vary between labs. And even a detailed method will not produce reliable results if an experiment is vulnerable to artefacts, or if assays have not been thoroughly validated.

Still, skimpy protocols stall science, and the scientific community must mobilize itself to do more. Writing "we used a slightly modified version of the protocol from PaperZ", whether or not the full protocol can be found there, is clearly easier than spelling out all the steps — but it's not good enough. One day soon, publishing a paper without a link to a useful protocol in a methods repository will seem as outdated as using a mobile phone that can't connect to the Internet. ■

**A NEW ERA
OF
MORE-EFFICIENT,
MORE-CONFIDENT
SCIENCE
IS OURS
TO LOSE.**

Lenny Teytelman is co-founder and chief executive of protocols.io, a methods-sharing and documenting start-up in Berkeley, California. email: lenny@protocols.io

SEVEN DAYS

The news in brief

EVENTS

Salk lawsuit

Lawyers for the Salk Institute for Biological Studies went to court on 17 August in San Diego, California, asking a judge to narrow the scope of a gender-discrimination lawsuit filed by molecular biologist Beverly Emerson. Emerson alleges that systemic bias at the institute, in La Jolla, California, limited her pay and access to resources. The scientist, who filed suit in July 2017, also alleges that Salk's decision to let her contract expire in December 2017 constituted retaliation. Salk, which disputes the allegations, settled two other gender-discrimination lawsuits earlier this month. The judge overseeing Emerson's case will decide later this month which of the scientist's claims will go to trial.

PhD protections

Doctoral researchers at Germany's Max Planck Society have issued a set of recommendations to tackle issues that they say make them vulnerable to abuses of power, such as steep management hierarchies and pressure to publish. PhDnet, a group that represents the society's more than 5,000 doctoral researchers, published a document on 15 August detailing steps for preventing conflicts with supervisors, protecting early-career researchers, arbitrating problems and implementing consequences for offenders. Jana Lasser, a doctoral researcher at the Max Planck Institute for Dynamics and Self-Organization in Göttingen, Germany, and spokesperson for PhDnet, says that the group had been crafting recommendations for the treatment of PhD researchers, but work intensified after press reports earlier this year



PALLAVA BAGLA/CORBIS/GETTY

India's Moon mission hits further delay

The launch of India's second spacecraft to the Moon has been delayed for the second time this year. Kailasavadivoo Sivan, chair of the Indian Space Research Organisation in Bangalore, told reporters on 12 August that the agency is aiming to launch Chandrayaan-2 on 3 January next year — although the mission has a lift-off window of any time between January and March. The original launch date was April this year, and had already been

pushed back to October. Chandrayaan-2 will carry an orbiter that will travel around the Moon; a lander that will attempt India's first controlled, or soft, landing; and a rover. Sivan said that there were several reasons for the latest delay, including changes to design of the lander. He said these changes had increased the weight of the spacecraft and therefore the amount of fuel needed to complete the mission, further adding to the delays.

detailed allegations of bullying against a Max Planck institute director. Lasser says that under the society's rules, PhD supervisors are often solely responsible for deciding a doctoral candidate's contract duration, pay and publication activity, and this creates an imbalance of power.

POLICY

No extra oversight

The US government plans to remove 40-year-old regulations mandating extra reviews of gene-therapy research conducted under the auspices of the National

Institutes of Health (NIH). In a 16 August article in *The New England Journal of Medicine*, the directors of the NIH and the Food and Drug Administration (FDA) wrote that improved understanding of diseases, gene-delivery methods and safety risks mean that the FDA should be able to regulate gene therapies as they would any other treatment. The move follows a 2014 Institute of Medicine committee recommendation that only "exceptional" gene-therapy products need an extra review and approval by an NIH advisory committee. That advisory panel was originally

chartered in 1974 to advise the NIH director on emerging biotechnologies.

SPACE

Asteroid hunters

A NASA-funded telescope network devoted to detecting space rocks that could crash into Earth will expand into the Southern Hemisphere, which lacks a large-scale asteroid-surveillance effort. The agency confirmed on 13 August that it will provide US\$3.8 million over the next 4 years to support the construction and operation of two observatories south of the Equator. Researchers plan to

UKZN build one observatory in South Africa, but are still deciding on a location for the second outpost. The facilities will join two existing telescopes, on the islands of Maui and Hawaii, as part of the Asteroid Terrestrial-impact Last Alert System (ATLAS), run by the University of Hawaii. The planned observatories will also detect comets, supernovae and other benign celestial objects.

FACILITIES

Africa radio array

South Africa has given the green light to a 70-million-rand (US\$4.8-million) radio-telescope project that will study two cosmic mysteries: ultra-powerful events of unknown cause called fast radio bursts, and dark energy, a force that is accelerating the Universe's expansion. Construction on the Hydrogen Intensity and Real-time Analysis eXperiment (HIRAX) will begin next year in the Karoo desert. The region already hosts the 64-dish MeerKAT array. HIRAX will initially comprise 128 dish-like elements (**pictured**, the first few dishes), which together act as a single radio telescope. It will probe the characteristics of the Universe's dark energy 7 billion to 11 billion years



ago, and researchers hope that it will also locate fast radio bursts in their host galaxies for the first time. The telescope will be a Southern Hemisphere counterpart to the Canadian Hydrogen Intensity Mapping Experiment, which detected its first fast radio burst last month. HIRAX, funded by South Africa's National Research Foundation and the University of KwaZulu-Natal in Durban, will be expanded to 1,024 dishes by 2020.

PEOPLE

Brain-project chief

The executive director of the European Union's ambitious — but contentious — Human Brain Project (HBP) has left his post after a disagreement

with the institution that coordinates the initiative. The 10-year, €1-billion (US\$1.1-billion) project aims to simulate the human brain using computers, and is a flagship science initiative of the EU. In a joint statement on 16 August, Chris Ebell and the HBP's coordinating institution, the Swiss Federal Institute of Technology in Lausanne, said that they had decided to "separate by common agreement" following "differences of opinion on governance and on strategic orientations". Ebell became director of the project in 2015, after the HBP disbanded its small executive committee in favour of a 22-member governing board. The HBP, which involves more than 100 partner

institutions, had been criticized since its inception in 2013 by some neuroscientists for its scientific direction, its complicated structure and the lack of transparency surrounding its funding decisions.

Drug official sacked

The former head of China's drug regulator has been forced to resign from his current position, in the wake of a major vaccine scandal last month. The government announced on 16 August that Bi Jingquan, vice-director of the State Administration for Market Regulation (SAMR), had been dismissed, along with three other officials linked to the scandal. Last month, it was revealed that vaccine maker Changchun Changsheng Biotechnology, in Jilin province, had faked production data for several batches of rabies vaccine; it had also violated standards in making about 250,000 doses of a vaccine that protects against diphtheria, tetanus and whooping cough, potentially making the doses ineffective. Bi was head of the China Food and Drug Administration, from 2015 until the agency was merged into the SAMR in March. One of the agency's responsibilities was to ensure safe vaccine production.

TREND WATCH

The rate at which the US government grants visas to prospective students from Iran has declined dramatically during President Donald Trump's time in office, according to government data. And the visas that are granted take more time to arrive, according to a group of Iranian students that is petitioning the Trump administration to speed up the process.

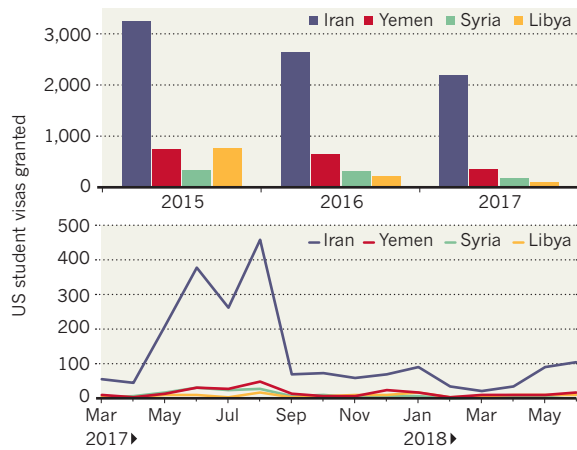
"We decided to come to the U.S. to do science with hopes of having equal rights to access information and education, regardless of race, color, and gender, even if that is just for a little while," the students wrote

in their petition to the homeland security and state departments, which has garnered more than 800 signatures since it was posted online in July 2018. "We have been feeling discriminated for a long time now."

Data from the US Department of State show that the number of visa approvals issued to Iranian students between March and June 2018 fell by 64% compared with the equivalent period last year. They also reveal that 687 Iranians received student visas between March and June of 2017, but only 249 were granted visas during the same period this year.

TRAVEL TROUBLES

Data from the US state department show a decline in the number of visas it has granted to citizens of Iran over the past several years. People from Iran, along with Libya, Syria and Yemen, are among those whose travel to the United States has been limited by President Donald Trump's immigration policies.



NEWS IN FOCUS

POLITICS What Pakistan's new government means for science p.419

FUNDING Wellcome Trust pulls grant following bullying allegations p.420

PUERTO RICO Hurricane Maria leaves clues to coral reefs' future p.421

BIODIVERSITY Disputes threaten global effort to protect species p.423



CHRISTOPHER RYNN/UNIV. DUNDEE



Denny inherited one set of chromosomes from her Neanderthal ancestors, depicted in this model.

EVOLUTION

First ancient-human hybrid

A direct descendant of two different groups of early humans has been found in Russia.

BY MATTHEW WARREN

A female who died around 90,000 years ago was half Neanderthal and half Denisovan, according to genome analysis of a bone discovered in a Siberian cave. This is the first time that scientists have identified an ancient individual whose parents belonged to distinct human groups. The findings were published on 22 August in *Nature*¹.

"To find a first-generation person of mixed ancestry from these groups is absolutely extraordinary," says population geneticist Pontus Skoglund at the Francis Crick Institute in London. "It's really great science

coupled with a little bit of luck."

The team, led by palaeogeneticists Viviane Slon and Svante Pääbo of the Max Planck Institute for Evolutionary Anthropology in Leipzig, Germany, conducted the genome analysis on a single bone fragment recovered from Denisova Cave in the Altai Mountains of Russia. This cave lends its name to the 'Denisovans', a group of extinct humans first identified on the basis of DNA sequences from the tip of a finger bone discovered² there in 2008. The Altai region, and the cave specifically, were also home to Neanderthals.

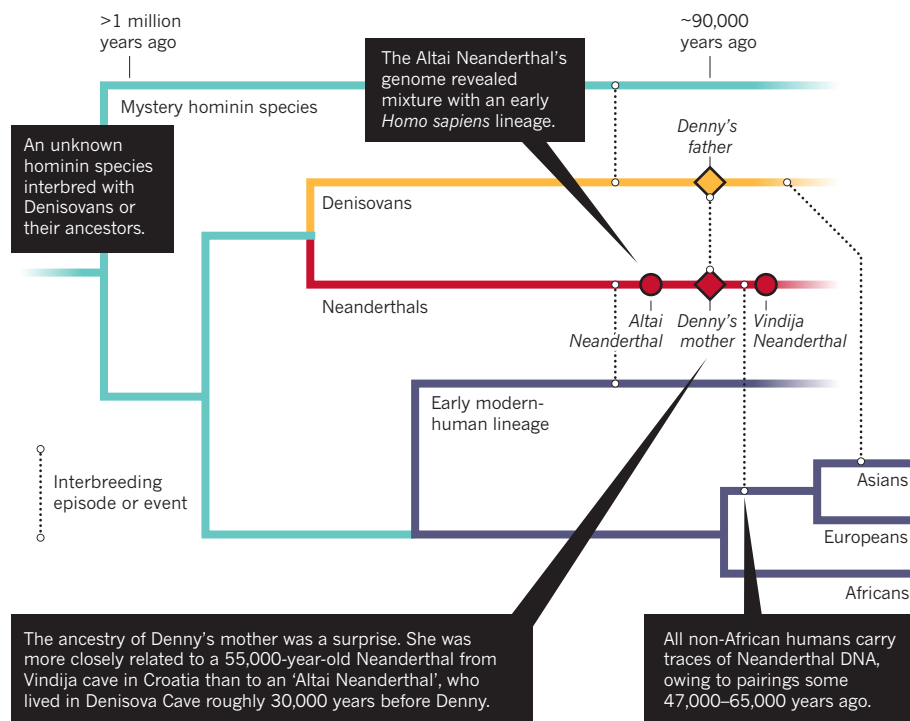
Given the patterns of genetic variation in ancient and modern humans, scientists

already knew that Denisovans and Neanderthals must have bred with each other — and with *Homo sapiens* (See 'Tangled tree'). But no one had previously found the first-generation offspring from such pairings, and Pääbo says that he questioned the data when his colleagues first shared them. "I thought they must have screwed up something," he says. Before the discovery of the Neanderthal-Denisovan individual, whom the team has affectionately named Denny, the best evidence for so close an association was found in the DNA of a *Homo sapiens* specimen who had a Neanderthal ancestor within the previous 4–6 generations³.

Pääbo's team first uncovered Denny's ▶

TANGLED TREE

A female born to a Neanderthal mother and Denisovan father roughly 90,000 years ago — nicknamed Denny — is one of many examples of interbreeding between ancient human groups.



The ancestry of Denny's mother was a surprise. She was more closely related to a 55,000-year-old Neanderthal from Vindija cave in Croatia than to an 'Altai Neanderthal', who lived in Denisova Cave roughly 30,000 years before Denny.

► remains several years ago, by looking through a collection of more than 2,000 unidentified bone fragments for signs of human proteins. In a 2016 paper⁴, they used radiocarbon dating to determine that the bone belonged to a hominin who lived more than 50,000 years ago (the upper limit of the dating technique; subsequent genetic analysis has put the specimen at around 90,000 years old, according to Pääbo). They then sequenced the specimen's mitochondrial DNA — the DNA found inside cells' energy converters — and compared that data to sequences from other ancient humans. This analysis showed that the specimen's mitochondrial DNA came from a Neanderthal.

But that was only half of the picture. Mitochondrial DNA is inherited from the mother and represents just a single line of inheritance, leaving the identity of the father and the individual's broader ancestry unknown.

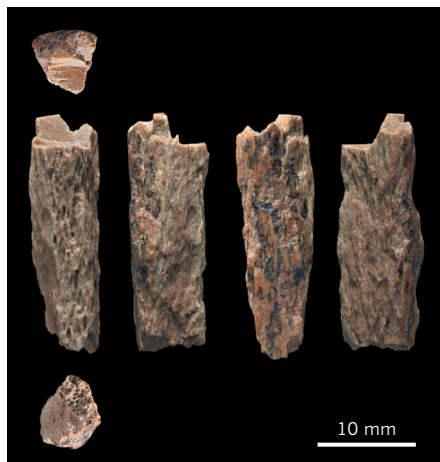
In the latest study, the team sought to get a clearer understanding of the specimen's ancestry by sequencing its genome and comparing the variation in its DNA to that of three other hominins — a Neanderthal and a Denisovan, both found in Denisova Cave, and a modern-day human from Africa. Around 40% of DNA fragments from the specimen matched Neanderthal DNA — but another 40% matched the Denisovan. By sequencing the sex chromosomes, the researchers also determined that the fragment came from a female, and the thickness of the bone suggested that she was at least 13 years old.

With equal amounts of Denisovan and Neanderthal DNA, the specimen seemed to

have one parent from each hominin group. But there was another possibility: Denny's parents could have belonged to a population of Denisovan–Neanderthal hybrids.

A FASCINATING GENOME

To work out which of these options was more likely, the researchers examined sites in the genome where Neanderthal and Denisovan genetics differ. At each of these locations, they compared fragments of Denny's DNA to the genomes of the two ancient hominins. In more than 40% of cases, one of the DNA fragments matched the Neanderthal genome, whereas the other matched that of a Denisovan, suggesting that she had acquired one set of chromosomes from a Neanderthal and the other from a Denisovan. That made it clear that Denny was



A bone fragment was sequenced for its genome.

the direct offspring of two distinct humans, says Pääbo. "We'd almost caught these people in the act."

The results convincingly demonstrate that the specimen is indeed a first-generation hybrid, says Kelley Harris, a population geneticist at the University of Washington in Seattle. Skoglund agrees: "It's a really clear-cut case," he says. "I think it's going to go into the textbooks right away."

Harris says that sexual encounters between Neanderthals and Denisovans might have been quite common. "The number of pure Denisovan bones that have been found I can count on one hand," she says — so the fact that a hybrid has already been discovered suggests that such offspring could have been widespread. This raises another interesting question: if Neanderthals and Denisovans mated frequently, why did the two hominin populations remain genetically distinct for several hundred-thousand years? Harris suggests that Neanderthal-Denisovan offspring could have been infertile or otherwise biologically unfit, preventing the two species from merging.

Neanderthal-Denisovan pairings could also have had some advantages, even if there were other costs, says Chris Stringer, a palaeoanthropologist at the Natural History Museum in London. Neanderthals and Denisovans were less genetically diverse than modern humans, and so interbreeding might have provided a way of "topping up" their genomes with a bit of extra genetic variation, he says.

Pääbo agrees that Neanderthals and Denisovans would have readily bred with each other when they met — but he thinks that those encounters were rare. Most Neanderthal remains have been found across western Eurasia, whereas Denisovans have so far been discovered only in their eponymous Siberian cave. Although the two groups' home turf overlapped in the Altai Mountains, and possibly elsewhere, these areas would have been sparsely populated.

With a Neanderthal mother and a Denisovan father, what should the new specimen be called? "We shy away a little from the word 'hybrid,'" says Pääbo. The term implies that the two groups are discrete species of human, whereas in reality the boundaries between them are blurry — as the new study shows. Defining a species in the natural world is not always clear-cut, says Harris, and it's interesting to see that long-running debates about how to categorize organisms are starting to be applied to humans.

Whatever scientists decide to call Denny, Skoglund says he would have loved to be able to meet her. "It's probably the most fascinating person who's ever had their genome sequenced." ■

1. Slon, V. et al. *Nature* <https://doi.org/10.1038/s41586-018-0455-x> (2018).

2. Krause, J. et al. *Nature* **464**, 894–897 (2010).

3. Fu, Q. et al. *Nature* **524**, 216–219 (2015).

4. Brown, S. et al. *Sci. Rep.* **6**, 23559 (2016).

POLITICS

Pakistani science in flux

New government promises to value education, but an economic crisis threatens research.

BY EHSAN MASOOD

Pakistan is reeling from a political earthquake — and researchers are both nervous and excited. On 18 August, the former cricket superstar Imran Khan was sworn in as prime minister. Khan's win has come as a shock because few expected that his party, Pakistan Tehreek-e-Insaf (Movement for Justice, or PTI), would defeat the country's former ruling party and the main opposition.

Khan arrives at a time when Pakistan's research community faces big challenges, from an economic crisis that is strangling labs to a chronic shortage of research and teaching positions for its PhD holders. Although research policy featured little in the bitterly fought election campaign, Khan has a track record of using science and education to alleviate poverty: he has founded a cancer hospital and a technical college. Many researchers are now excited about what he can achieve on a national stage.

"Imran is like our Kennedy. He can lead and he can inspire," says scientist-entrepreneur Faisal Khan, a synthetic biologist at Cecos University in the northern city of Peshawar.

Pakistan has a shortage of internationally competitive public universities. Furthermore, there is no clear path to a research career in the country's institutions, which have weak links to industry and face political interference in senior appointments.

Yet there is cross-party consensus that universities and research are important, says Athar Osama, a member of the Planning Commission, the government body that vets big research proposals. Pakistan has 192 universities, but their funding and regulatory body is in a constant battle to maintain quality in research and teaching. It is continually uncovering academics involved in plagiarism. Two years ago, it shut down 57 PhD and master's programmes because of concerns over quality.

Added to this, years of military rule have given officers an oversized say in the nation's affairs. Two of Pakistan's universities are in the top 500 of the latest QS World University Rankings; one is the National University of Sciences and Technology in Islamabad, which formed when a number of military training colleges amalgamated, and is run by a retired general. The other is the Pakistan Institute of Engineering and Applied Sciences, near Islamabad; it is a spin-off from the Atomic Energy Commission, which runs the country's nuclear programme.

It is difficult for civilian administrations to refuse, or carry out due diligence on, funding requests backed by military or industrial



Imran Khan was sworn in as prime minister of Pakistan this month.

ATHIT PERAWONGMETHA/REUTERS

interests. But former science minister Atta-ur-Rahman is sure that change is coming. He says Khan will protect the independence of institutions. Atta-ur-Rahman was science minister from 2000 to 2002 and universities minister from 2002 to 2008, under the most recent military government. He is now close to the PTI.

In Pakistan, vice-chancellor appointments at public universities must be approved by politicians, which can lead to nepotism. Over the past five years, Atta-ur-Rahman has chaired an independent committee established by the PTI to vet such appointments in the province of Khyber Pakhtunkhwa, which the PTI governs. There have been attempts at interference, he says, but Khan has backed the committee.

Atta-ur-Rahman is hoping to have a role in science policy in the new government. He is lobbying to revive a policy from his time as universities minister, in which the state paid for 2,000 students per year to enrol in PhDs at universities abroad. He's also calling on international universities to partner with Pakistani ones to improve local university quality and conduct joint research. Atta-ur-Rahman established the Pak-Austria Institute of Applied Sciences and Technology, north of Islamabad — a joint venture with Austria's network of Fachhochschule technology institutes.

But Faisal Khan urges the government to proceed with caution. He is a beneficiary of the policy to send PhD students abroad — he

returned from the University of Oxford, UK, in 2013 — and he says that it has created a small army of young people who returned home with no offers of a job. They have established the PhD Doctors' Association. In June, they organized a demonstration in Islamabad, complaining that the government has abandoned them.

Faisal Khan co-founded an incubator for start-up companies called Peshawar 2.0, and set up a lab at his university, using synthetic biology to manufacture enzymes for food processing. "I have 200 PhD-level CVs on my desk and no jobs to give them," he says.

Atta-ur-Rahman says that, after he left office, subsequent governments ignored his plans to provide grants for postdoctoral research and establish a tenure-track system for researchers.

Right now, scientists face a pressing challenge. Decades of corruption have brought the economy and the health system to its knees, says former public-health minister Sania Nishtar. Days before the country went to the polls on 25 July, the central bank stopped international foreign-currency transactions because of a shortage of reserves. This means researchers now need to obtain extra permissions to buy equipment from other countries. If researchers cannot instantly order supplies, this could bring academia to a halt, says Sabieh Anwar, a physicist at the Lahore University of Management Sciences. "The fallout on our capacity to do research will be immense and irreversible." ■

FUNDING

Wellcome pulls grant

Anti-bullying policy applied.

BY HOLLY ELSE

The Wellcome Trust has revoked a £3.5-million (US\$4.5-million) grant awarded to a top cancer geneticist, Nazneen Rahman, following allegations that she bullied people when she worked at the Institute of Cancer Research (ICR) in London.

The decision represents the first implementation of a pioneering anti-bullying and anti-harassment policy that Wellcome, a London-based charity, introduced in June. In addition, for two years, Rahman will not be able to apply for funding from Wellcome or sit on any of its advisory committees or boards.

The charity says that it learnt from the ICR in July that an independent investigation had deemed some of the allegations serious enough to warrant consideration at a disciplinary hearing. But Rahman resigned and the hearing did not take place.

"My team and I will complete our Wellcome-funded research prior to my leaving ICR in October," Rahman told *Nature*. "We are working with ICR and Wellcome to ensure science and patients can benefit from our work." She made no further comments about the allegations or the investigation.

The ICR has not made public its investigational report, which it says contains highly confidential information. But Wellcome says it had enough information to act.

Wellcome was the first major UK research funder to institute an anti-bullying and anti-harassment policy; the US National Science Foundation introduced similar rules a few months earlier. Scientists welcomed the policies at the time, but some expressed concerns that they did not go far enough.

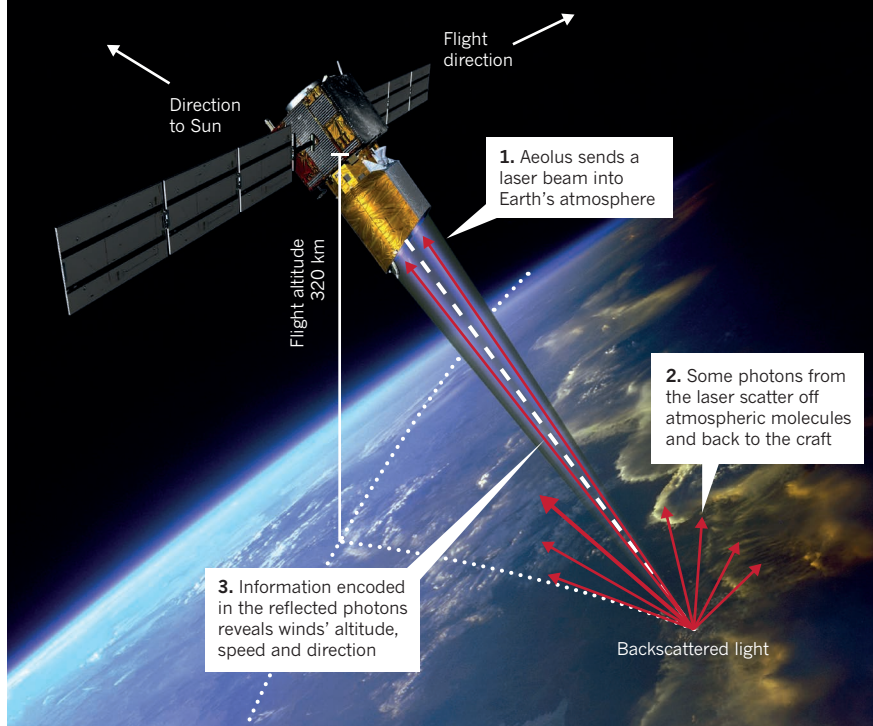
The Wellcome Trust says that it will update its policy in the wake of the ICR case. It will now require institutions to inform it of allegations when they decide to investigate, rather than when allegations are upheld. And it will prevent institutions from making secretive arrangements that keep them from sharing findings or otherwise applying the policy.

The ICR recognizes that it "could have done more to support those who came to us with concerns", and says it is "absolutely committed to learning the lessons". The institute says it is now working with Rahman and Wellcome to "complete and transition her research", and that it welcomes the efforts being made by the charity and others to improve the culture of the scientific community. ■

ESA

WORLD'S FIRST WIND-MAPPER

The European Space Agency's Aeolus satellite will be the first to map Earth's winds comprehensively from space. As the craft moves around the globe, it will build up a picture of air movement, helping to fill gaps in forecasting data.



METEOROLOGY

Spacecraft will map world's wind

Europe's long-awaited Aeolus mission will be the first satellite to monitor winds at a global level.

BY ALEXANDRA WITZE

After a two-decade wait, data from a pioneering wind-monitoring satellite are finally in meteorologists' sights. As *Nature* went to press, the European Space Agency's (ESA's) Aeolus mission — set to be the first to comprehensively monitor wind around the globe — was readying for launch from Kourou, French Guiana, on 22 August. Researchers think that the satellite's data will significantly improve weather forecasts, because the lack of detailed wind measurements is one of the biggest gaps in the global Earth-observing system¹.

Aeolus, a three-year, €480-million (US\$550-million) mission, will use ultraviolet lasers to track wind speed and

direction in the lowermost 30 kilometres of the atmosphere². Researchers have used similar lasers on aeroplanes to study winds in particular regions, but this will be the first wind-mapping mission to cover the entire globe. If Aeolus works as planned, forecasts will be improved substantially in tropical regions, and by a few per cent in Earth's mid- and high latitudes. "You may think that does not sound like very much, but if we improve forecasts by 2%, the value for society is many billions of dollars," says Lars Isaksen, a meteorologist at the European Centre for Medium-Range Weather Forecasts (ECMWF) in Reading, UK.

Until now, meteorologists have pieced together information on winds from a patchwork of sources, including weather

balloons and aeroplane flights. No satellite has directly measured winds, although scientists can infer wind speed and direction from satellite measurements of cloud movement, for instance.

CHALLENGES

ESA selected the mission in 1999. It is reaching the launch pad only now because of the difficulties of building a powerful enough laser. Fifty times each second, the satellite's laser will zap Earth's atmosphere with a beam of billions of ultraviolet photons (see 'World's first wind-mapper'). A few hundred of those photons will bounce off air molecules and particles and reflect back to the spacecraft's 1.5-metre primary telescope. Aeolus will measure not only the distance to the reflection — giving the altitude of the winds — but also the tiny change in wavelength created as the molecules move back and forth.

That 'Doppler shift' allows scientists to calculate the winds' speed and direction. "It's much more challenging than just measuring the signal coming back," says Oliver Reitebuch, an atmospheric physicist at the German Aerospace Center in Oberpfaffenhofen, who led aeroplane flights to test the satellite's technology. The information will, for instance, allow scientists to track winds of different velocities and at different altitudes in the atmosphere — information that is important for understanding developing storms, but that cannot be obtained globally in any other way.

The data from Aeolus will feed into numerical weather predictions, in which national weather services incorporate atmospheric conditions such as temperature, pressure and humidity to generate forecasts for the coming days³. Not incorporating winds can lead to errors: in one study, the ECMWF analysed a rainstorm in Europe in March 2014, and found that better data on winds above the Pacific Ocean in the days before the storm would have allowed a more accurate prediction of the heavy rains to come⁴.

If Aeolus launches successfully, mission controllers plan to switch on the laser system in September, with initial data arriving by the end of January 2019 and inserted into forecasting systems by April. And if the technology proves solid, it could help pave the way for future wind-mapping satellites, says Lars Peter Riishojaard, head of the World Meteorological Organization's Integrated Global Observing System in Geneva, Switzerland. ■

1. Baker, W. E. et al. *Bull. Am. Meteorol. Soc.* **95**, 543–564 (2014).
2. Stoffelen, A. et al. *Bull. Am. Meteorol. Soc.* **86**, 73–87 (2005).
3. Horányi, A., Cardinali, C., Rennie, M. & Isaksen, L. Q. J. R. Meteorol. Soc. **141**, 1223–1232 (2015).
4. Magnusson, L. Q. J. R. Meteorol. Soc. **143**, 2129–2142 (2017).

ECOLOGY

Hurricane Maria's coral-reef clues

Scientists struggle to predict future of deep-water reefs.

BY SARA REARDON IN LA PARGUERA,
PUERTO RICO

Dark skies hint at the hurricane that is moving quickly across the Caribbean on this early July morning, but the sea off Puerto Rico's southwest coast is glassy. Marine scientists Ernesto Weil and Juan Cruz Motta of the University of Puerto Rico–Mayagüez (UPRM) swim along the La Parguera reef, stopping to examine a fan coral marred by black patches of disease and a staghorn coral bleached white.

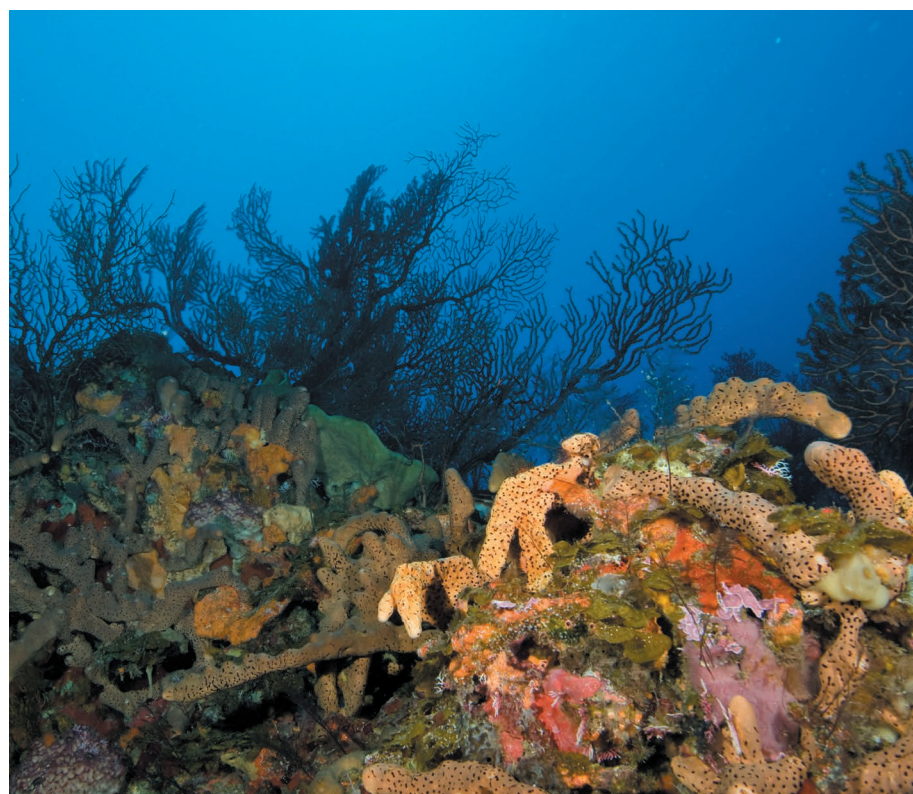
For decades, ecologists had thought that La Parguera and other reefs in the dimly lit 'mesophotic zone', 30–150 metres below the ocean surface, were sheltered from storms and temperature fluctuations — unlike corals in shallow waters. But several recent studies suggest that deep-water reefs are susceptible to the increasingly powerful hurricanes and ocean warming caused by climate change. And that casts doubt on the long-standing idea that deep-water corals could serve as refuges

for marine life displaced from increasingly vulnerable shallow reefs.

In Puerto Rico, such questions are more than academic. In September 2017, Hurricane Maria — a deadly category-4 storm — devastated the island and many of its surrounding reefs. Weil, Cruz Motta and their colleagues are tracking the health of deep-water corals at La Parguera, which escaped significant damage, and that of deep reefs that were directly in the storm's path. This natural experiment could help to reveal the extent to which turbulence from the more frequent and extreme hurricanes predicted by climate models could endanger deep reefs in the coming decades.

"If we're going to have one of these or two of these per year, it's going to be very hard for reefs and other coastal communities to recover," Weil says.

The UPRM researchers expected to see devastation at offshore reefs after Maria hit. "We pretty much thought it was the end of the world," says Nikolaos Schizas, a marine biologist at the university. But when the ▶



Hurricanes and ocean warming are thought to present a growing threat to deep coral reefs.

► team ventured out to La Parguera reef a few months after the storm, its deep-water corals seemed surprisingly healthy. Schizas suspects that this is because Maria travelled east to west across Puerto Rico, and lost strength over land.

TWILIGHT ZONE

The scientists are now analysing data collected by sensors that they studded on the reef's 80-metre-tall face before the hurricane. These continuously record information on water temperature, turbidity and other factors at various depths. The team's preliminary analysis suggests that Hurricane Maria sent waves crashing into the reef with unusual frequency and pushed a swell of cold water from the ocean bottom up to the reef.

It could take years to understand whether the changes observed during Maria affected the La Parguera reef ecosystem. But the data are intriguing because most previous measurements of hurricanes' hydrological impacts have come from continents, not islands, says Curt Storlazzi, an oceanographer at the US Geological Survey in Santa Cruz, California, who analysed the UPRM data.

Now the UPRM team is gearing up to visit a reef near Vieques, an island 13 kilometres off Puerto Rico's eastern coast that suffered severe storm damage. The researchers plan to survey

corals at depths of 30 metres or more, and to compare their data with photos and samples collected before the storm.

That contrast may reveal the hurricane's impact on shallow and deep-water corals. Reefs evolved to adapt to storms — even the occasional monster hurricane. But today, many corals face a variety of other threats, including ocean acidification and invasive sargassum algae. And warming waters have created a more

"We pretty much thought it was the end of the world."

hospitable environment for pathogens.

The UPRM team's surveys might also help researchers to understand whether deep-water reefs

could serve as a refuge for species fleeing damaged or destroyed corals in shallow waters. A study published last month in *Science* has cast doubt on that idea: survey data from four reefs in the Atlantic and Pacific oceans revealed little overlap between the species found on shallow and deep reefs (L. A. Rocha *et al.* *Science* **361**, 281–284; 2018). That makes it unlikely that residents of one type of reef could 'reseed' the other. The study also reported evidence of storm damage to some of the deep-water reefs, parts of which seem to have been buried by sediment stirred up by hurricanes.

And research by Tyler Smith, a coral-reef biologist at the University of the Virgin Islands in St Thomas, has found that hurricanes can scramble ocean temperature gradients, which could make deep-water reefs inhospitable to native species (T. B. Smith *et al.* *Glob. Change Biol.* **22**, 2756–2765; 2016).

Smith says that scientists will need more data to verify, or discard, the deep-refuge-reef idea. He and his colleagues are surveying reefs around the Virgin Islands that were hit by Hurricane Maria. Their early data suggest that visible hurricane damage stopped about 10 metres below the ocean surface.

But reefs' luck may not hold. More-frequent major storms and other threats could wear these ecosystems down over time. "To lose structural complexity here would be unbelievable," Schizas says. "But it's a little by little process." ■

CORRECTION

The News story 'Trove of exotic matter thrills physicists' (*Nature* **560**, 151–152; 2018) stated that the properties of a topological insulator were first seen experimentally in bismuth antimony in 2008. In fact, the property was first observed in mercury telluride in 2007.



BATTLE OVER BIODIVERSITY

An ideological clash could undermine a crucial assessment of the world's disappearing plant and animal life.

It's a hot and humid afternoon in the suburbs of Washington DC, and Bob Watson is looking worried. The renowned atmospheric chemist sits back on a bench in his yard, hemmed in by piles of paperwork. He speaks with his characteristic rapid-fire delivery as he explains the tensions surrounding the international committee he helms. The panel is supposed to provide scientific advice on one of the world's most intractable problems — the rapidly accelerating loss of plants and animals. But a rift in the research community risks diminishing the whole effort. In a few days' time, Watson will fly to England to mark his seventieth birthday, but right now he is not in a celebratory mood.

Watson is talking about a conflict infecting the Intergovernmental Science-Policy Platform on Biodiversity and Ecosystem Services (IPBES), a younger sibling to the Nobel-prizewinning Intergovernmental Panel on Climate Change (IPCC). Both have immense tasks. The IPCC provides timely, expert information on climate change, and it helped to lay the groundwork for international treaties aimed at slowing global warming, such as the 2015 Paris climate accord. The biodiversity panel

BY EHSAN MASOOD

has been tasked to focus on the epic disappearance of plant and animal populations.

As with climate change, humans are the main culprit in biodiversity loss. People have converted somewhere in the region of 50% of Earth's surface for human activities, and researchers warn that the resulting loss of animal and plant species is leading towards a mass extinction.

But whereas the elder IPCC has largely unified the scientific community and has had considerable international policy success, the six-year-old biodiversity panel has not yet been able to exert anything like the same degree of influence. Moreover, the scientific community it represents is a house divided. The world of biodiversity research is like an extended family that has split into feuding factions. Scientists from less-prosperous southern countries have squared off against colleagues from the wealthier north, and researchers from more empirical disciplines are arguing with those from humanities and the social sciences.

The issues underlying the rift reflect broader debates in science about traditional power structures and increasing access for underrepresented groups, as well as opposition to dominant economic systems. Until now,

ILLUSTRATION BY DAVID PARKINS

scientists and conservationists from developed countries have largely led efforts to study and assess species decline. But the decision-making levers within IPBES are now in the hands of scientists who say that conservation efforts need more input from developing countries, from researchers in the humanities and other non-empirical disciplines, and also from non-academics — such as farmers, citizen scientists and indigenous peoples.

"Ten years ago you had mostly ecologists and some economists. Now many more research and societal actors want to sit at the table," says Sandra Díaz, who is a co-leader of IPBES's upcoming global assessment of biodiversity, which will be the panel's signature accomplishment when it is published next May. "This is likely to create a richer fabric of knowledge," says Díaz, who is also an ecologist at the National University of Córdoba in Argentina.

But those on the opposite side of the rift, who give more weight to an empiricist approach and include some of the biggest names in biodiversity science, say that they have been sidelined. "I am bewildered by this controversy," says Pavan Sukhdev, an economist and president of the conservation group WWF. He leads a smaller and to some extent competing study for the United Nations called The Economics of Ecosystems and Biodiversity.

The feud comes at a crucial time for IPBES as it prepares its global biodiversity report, the most comprehensive assessment on this topic in 14 years. Watson is worried that a public falling out risks diluting the influence that the assessment will have with governments — and the chances for meaningful action to protect biodiversity. "There is no need to have this fracture," he says.

THE SEARCH FOR CONSENSUS

In some ways, the climate and biodiversity panels are relics from the twentieth century, an era when mostly male scientists — largely from developed countries — offered policy guidance to governments and the UN from a position of relatively unchallenged authority.

In 1985, an international science panel co-chaired by Watson established that industrial chemicals were degrading the ozone layer. That panel's reports¹ led to a legally binding treaty, the 1987 Montreal Protocol, which phased out those compounds. Similarly, in 1995, the IPCC provided the scientific consensus that humans were changing the climate². This paved the way for the 1997 Kyoto Protocol, which set limits on greenhouse-gas emissions from developed nations.

But biodiversity has always been the exception. Of the many global agreements in this area, none came about as the result of an IPCC-like process, in which a scientific consensus led to action. In fact, the biodiversity panel was only formed in 2012, a full two decades after international leaders signed the UN Convention on Biological Diversity at the famous Earth Summit in Rio de Janeiro, Brazil, in 1992.

There are many reasons why biodiversity scientists have been unable to exercise collective policy influence in the same way as their colleagues in climate research. "Biodiversity is not the same as greenhouse gases," says Sukhdev. An intergovernmental science team assessing greenhouse gases makes sense because climate change affects everyone, he says. But biodiversity is the responsibility of individual nation states, which makes the reasons for a world scientific panel less obvious. "Why should China be interested in [conserving India's] Royal Bengal tiger," he asks, "or for that matter, why should India be interested in the Chinese panda?"

North–South politics has also played a part. There was concern, for example, that a network of experts dominated by richer countries would slow down or weaken international agreements on regulating genetically modified organisms or sharing the benefits from biodiversity because of the strength of the agribusiness lobby in these countries.

Although those concerns remain strong, France and other European nations in 2005 pushed for establishing a strong international panel and provided key funding. Although their effort eventually fizzled, UN Environment resurrected a version of it³ and brought IPBES to life in 2012. The new panel, which has cost US\$31 million so far, comprises representatives from 129 member governments and is charged with, among other tasks, conducting periodic policy-relevant assessments

and providing training, especially in less-developed states.

The breakthrough happened partly because its founders realized it would work only if natural scientists, especially those from richer countries, agreed to be on an equal footing with social scientists, humanities researchers and experts in indigenous knowledge. Also crucial was a close partnership between IPBES's first two chairs: Zakri Abdul Hamid, former chief science adviser to Malaysia's prime minister, and Bob Watson, who had worked together previously bridging North–South divides.

Since its creation, IPBES has not been idle. Earlier this year it published assessments of biodiversity in different regions and a report on the state of land degradation, which concluded that such damaged environments threaten the well-being of 3.2 billion people⁴.

This month, IPBES research teams embarked on a widely anticipated assessment of the different ways in which species and ecosystems can be valued. That is one of the key sticking points between the different factions of the biodiversity community.

Although the current controversy has roots that reach back decades, it has heated up since 2016, when IPBES published an 800-page assessment on pollination⁵. This helped to focus attention on the fact that pesticide use has contributed to falling bee populations at a time when the global volume of pollinator-dependent crops has been increasing.

The report says that crops with a market value of up to \$577 billion (in 2015 prices) rely on animal pollination, and it includes a chapter on the economics of pollination. However, economic information is largely omitted from the report's summary, even though this is the section that most policymakers would read. Sukhdev and other scientists argue for greater prominence for such economic analysis as a way of quantifying the importance of species such as pollinators. But for the IPBES leadership, doing so would privilege one branch of economics above other disciplines and neglect non-monetary ways to value species.

Many in developing countries see monetary valuation as a 'Western' view of nature, says Unai Pascual, an ecological economist at the Basque

"THE WORLD BENEFITS FROM HAVING MORE OPEN CONVERSATIONS ACROSS THE SCIENCES AND ACROSS CULTURES."

Centre for Climate Change near Bilbao in Spain who is jointly leading the IPBES study on valuing biodiversity. "It is a product of a particular culture and world view and a particular economic system," he says.

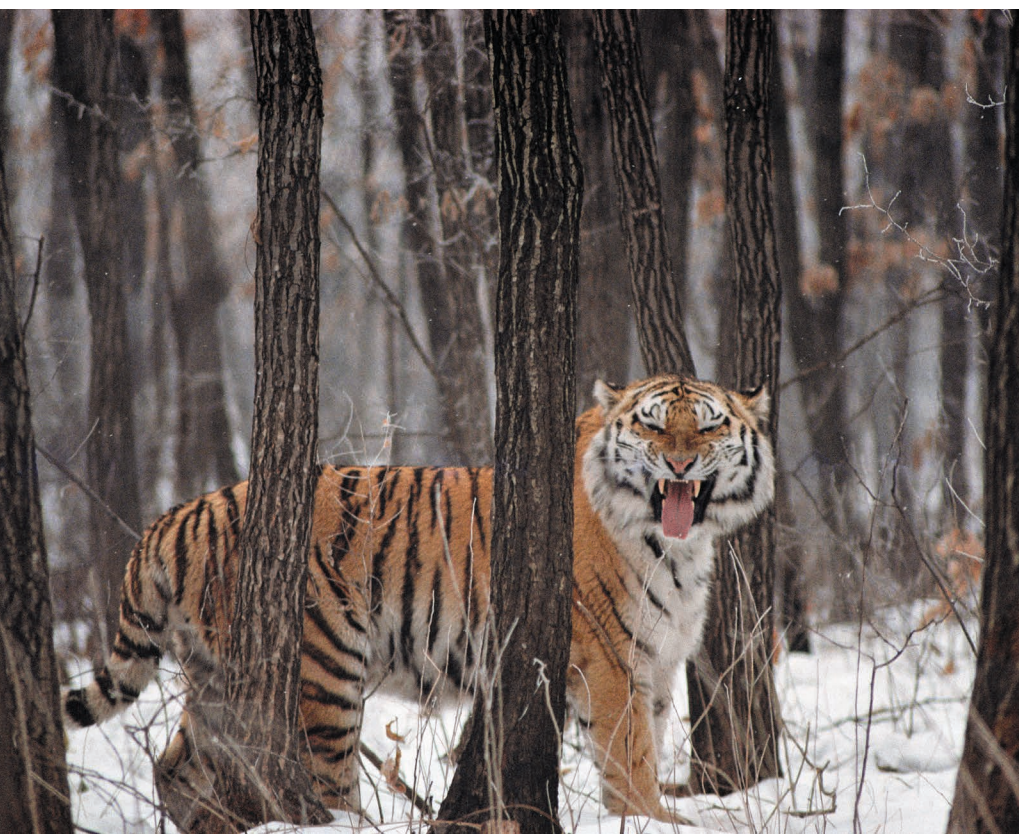
AT WHAT COST

These arguments have played out among members of the biodiversity family, but lately the critics of IPBES have sought a broader audience via the letters pages of *Science*, in which they called aspects of the process overly political and accused IPBES of excluding important science⁶.

One of the main points of contention is the concept of 'ecosystem services', an idea that gained prominence in 2001 at the start of the last big international assessment of biodiversity, the Millennium Assessment. Ecosystem services are those ecological characteristics, functions or processes that directly or indirectly contribute to human well-being⁷.

Ecologists consciously adopted economic language because it was a way to speak to politicians and other policymakers in familiar terms, says Watson, who also chaired that exercise. "We wanted to attract the full range of political actors," he adds.

But although ecosystem services has enjoyed some policy success, researchers who study ecology through this lens say that they have been pushed aside by the IPBES process. "There's too much confusion and negative energy," says Dolf de Groot, a professor of environmental sciences at Wageningen University in the Netherlands who chairs the Ecosystem Services Partnership, a network of some 3,000 scientists



MARC MORITSCH/NGC

working in that field. There is a perception among the network's members that they are being banned, he says.

"There is absolutely no ban" of ecosystem services, counters Díaz. "We are not planning to abolish it, erase it, or replace it."

But she adds that scientists working in ecosystem services and those who favour including economic analysis in biodiversity studies must be willing to work with researchers and non-scientists who disagree with such approaches. There is notable scepticism, she says, about the concept of ecosystem services among researchers and governments in developing countries.

Díaz and her colleagues have persuaded IPBES member governments to adopt an alternative assessment framework that they call Nature's Contribution to People. The newer concept, Díaz says, is more appropriate to an assessment of biodiversity because it will include the knowledge of indigenous communities, as well as researchers from developing countries. Many non-Western approaches to biodiversity are less reductive and more holistic, says Sebsebe Demissew, who heads the Gullele Botanic Garden in Addis Ababa and was a former member of IPBES's expert scientific panel. "In such cultures, it makes no sense to place a monetary value on a forest or a river because they are part of the whole body. It's like saying to a human: 'what price, your limb? Or what price, your kidney?'"

For de Groot, however, it is "simply wrong to say that ecosystem services is 'Western' science". He and his allies contend that the language of economic estimates is valuable because it attracts the attention of policymakers. "You are not going to stop the Trump government putting pipelines in nature reserves by emphasizing Nature's Contribution to People," de Groot says.

A HOUSE DIVIDED

One of Watson's biggest concerns is that policymakers will stop paying attention at the first sight of squabbling scientists. So in the first week of June, he convened a meeting of IPBES's scientists and government representatives in Bonn, Germany, to encourage them to green light the more-holistic approach of Nature's Contribution to People. Governments and UN agencies want the fledgling body to succeed in its ambition to be more inclusive, and they endorsed the new model.

Colombia's delegate to IPBES, Ana María Hernández, was at the Bonn meeting. She accepts that IPBES's assessments will challenge the way that scientists and policymakers think about issues. "The science community has one vision," she says. "But not everyone who knows about biodiversity or is a custodian of biodiversity is a scientist. We need to learn to listen to people even if they don't have a PhD," says Hernández, who is head of policy at the Alexander von Humboldt Biological Resources Research Institute in Bogotá.

Christiana Figueres, who successfully steered the Paris climate agreement as the former executive secretary of the UN Framework Convention on Climate Change, is also excited by the IPBES panel's more-inclusive approach. "The world benefits from having more open conversations across the sciences and across cultures. I really applaud and support what they're doing and I hope they succeed," she says.

But others worry about the schism rocking the biodiversity community and IPBES. And the two sides are not getting closer. In fact, the June IPBES meeting left out the Ecosystem Services Partnership, according to de Groot. "We were not invited to any meetings." In response, Watson says that the meeting was restricted to representatives of the 129 IPBES member governments, and the 49 that attended supported the shift away from ecosystem services.

Yet its critics argue that IPBES has become a vehicle for what its member researchers want, rather than offering up practical science that can spur and inform upcoming decisions — such as setting new targets to stem biodiversity loss. These are currently being discussed separately as part of the UN Convention on Biological Diversity.

The Amur or Siberian tiger is an endangered subspecies.

For IPBES to have the desired impact, it will have to move beyond this divide, says Maria Ivanova of the University of Massachusetts in Boston, who is writing a history of UN Environment. She recommends that Watson and the IPBES leadership extend an olive branch to their critics. "They should at least be having a more constructive dialogue than firing off letters to each other through the pages of academic journals," she says.

Watson seems to concur. The veteran of earlier North-South debates, and of many previous global scientific assessments, knows that the IPCC's early years were also dogged by intra-community skirmishes, in part over the evidence that humans were causing climate change. He also understands that the climate panel's influence would have been much reduced without the community uniting around a scientific consensus.

IPBES is also undergoing an external assessment that is due to report by May next year. The reviewers are well aware of the rift and the risk it poses to IPBES's ambitions for persuading policymakers to take steps that will reduce the loss of biodiversity. If IPBES is to succeed, Watson warns, "We must not, under any circumstances, split the academic community or governments." ■

Ehsan Masood writes about science and policy from London.

1. World Meteorological Organization. *Atmospheric Ozone 1985 Volume III* (WMO, 1985).
2. Intergovernmental Panel on Climate Change. *IPCC Second Assessment: Climate Change 1995* (IPCC, 1995).
3. Granjou, C., Mauz, I., Louvel, S. & Tournay, V. *Sci. Technol. Soc.* **18**, 9–27 (2013).
4. Intergovernmental Science-Policy Platform on Biodiversity and Ecosystem Services. *The Assessment Report on Land Degradation and Restoration* (IPBES, 2018).
5. Intergovernmental Science-Policy Platform on Biodiversity and Ecosystem Services. *Thematic Assessment on Pollinators, Pollination and Food Production* (IPBES, 2016).
6. Díaz, S. et al. *Science* **359**, 270–272 (2018).
7. Costanza, R. et al. *Ecosyst. Serv.* **28**, 1–16 (2017).

COMMENT

HISTORY OF MEDICINE Galen's modern approach to ageing in ancient Greece p.430

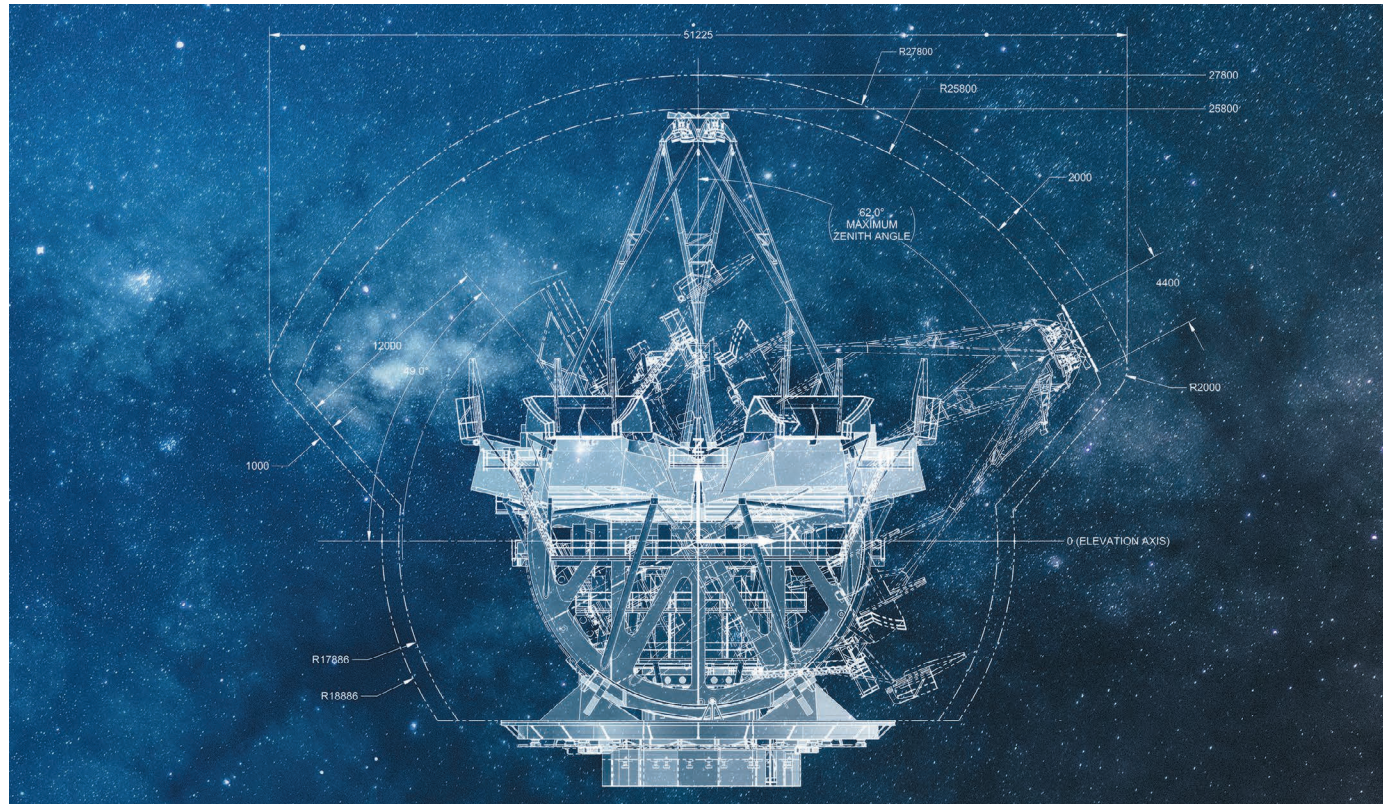


CONSERVATION Songbirds threatened by trapping in Spain p.431

MEDICAL RESEARCH Japanese trial of stem-cell therapy needs tightening up p.431

OBITUARY David Pines, physicist who described how electrons interact p.432

GIANT MAGELLAN TELESCOPE/GMTO CORPORATION



Blueprint of the Giant Magellan Telescope, a 25-metre-mirror telescope being built in Chile. It is run by an international consortium that includes US universities.

US astronomers face hard decisions

Building billion-dollar facilities in the 2020s and beyond will be impossible with the current model for funding and collaboration, warn **Matt Mountain** and **Adam Cohen**.

Every ten years, US astronomers set research priorities for the following decade. The latest cycle to pick projects for the 2020s has just started. In July, the US National Academy of Sciences launched the seventh Astronomical Decadal Survey (Astro2020) with a call for proposals for future telescopes and space missions. Over the coming year, these will be collected, assessed and discussed in open meetings. A ranked list of priority projects will be released in 2021. Funding permitting, those

at the top will be built over the next decades.

The two-year process is widely viewed as a gold standard for building consensus — many other fields have adopted it, from Earth sciences to solid-state physics¹. It carries weight with policymakers and funders. But as astronomy firmly enters the ‘big science’ era, we think that the decades-old system for funding federal astronomy needs debating and updating.

The science has never been so exciting. Earth-like planets have been found orbiting

other stars². Cosmologists are quantifying mysterious forces of ‘dark matter’ and ‘dark energy’³. Completely new windows have been opened onto the cosmos thanks to facilities such as the Atacama Large Millimeter/submillimeter Array (ALMA) in Chile and the Laser Interferometer Gravitational-Wave Observatory (LIGO), in the states of Washington and Louisiana.

But large facilities that can explore these frontiers cost billions of dollars and take decades to design, build and operate. ▶

► ALMA was proposed in 1990 and became operational in 2013. The James Webb Space Telescope (JWST) was approved in 2000 and will be launched in 2021. The Large Synoptic Survey Telescope, recommended in 2010 and under construction in Chile, will begin to map the sky in 2023. The fruits of the 2020 Decadal Survey won't see light until the 2030s.

The US community faces a daunting task. Each generation of facilities is getting more expensive and harder to build. Operational costs are mounting. Meanwhile, the research budgets of the US National Science Foundation (NSF) and NASA have remained more or less flat since the 1990s (see 'Astronomical costs'). Hard decisions have been made to close old but still-productive telescopes, which has proved insufficient to pay for new ones. And these pressures will only get worse as more big projects come online.

International competition is growing. The European Space Agency has picked its key projects as far ahead as 2044, including an advanced X-ray space observatory. The European Southern Observatory has fully funded its Extremely Large Telescope (ELT) in Chile. From the mid-2020s, its 39-metre-diameter mirror will collect more than ten times as much light as the largest optical telescopes today. China opened the world's biggest radio telescope in Guizhou province in 2016, and plans to launch a competitor to the Hubble Space Telescope⁴.

Without a concerted effort, a US scientist in the 2030s will be left without similarly capable facilities. We will face an unacceptable dilemma: support existing grants and cede US leadership, or abandon funding for key areas of research to support a few world-leading facilities.

As the presidents of organizations that build and operate major US publicly funded telescopes on behalf of the NSF and NASA, here we set out how entrenched assumptions and patterns of funding, development and collaboration must be reassessed.

FEDERAL SUPPORT ESSENTIAL

The United States has historically built its strength in astronomy on an eclectic mix of private and public observatories. Early telescopes such as those at the Mount Wilson, Griffith and Lick observatories in California were funded by foundations and run by universities. Edwin Hubble discovered the expansion of the Universe at Mount Wilson in the 1920s, for example. Until 2009, the United States hosted the world's largest telescopes: the twin W. M. Keck telescopes in Hawaii each have mirrors 10 m across and were paid for largely by philanthropy. (That accolade is now held by the 10.4-m Gran Telescopio Canarias in the Canary Islands, Spain.)

After the Second World War, the US federal government set up national observatories for radio and optical astronomy. The rationale was to boost national and economic security

by investing in basic science. On the ground, this has led the NSF to establish major facilities such as the Very Large Array in New Mexico, the Gemini Telescopes in Hawaii and Chile, and, most recently, ALMA. In space,

Financial pressure will only worsen in the 2020s.

NASA runs iconic observatories such as the Hubble and Spitzer space telescopes and the Chandra X-Ray telescope. US astronomers from any institution compete through a peer-review process for time on telescopes.

This mixed system has worked well for decades. But the next generation of ground-based telescopes has become so expensive that even consortia of universities and institutes are struggling, despite hefty contributions from billionaires, state governments and international partners.

US-led efforts to construct giant telescopes to match the European ELT plans have stalled. Both the Giant Magellan Telescope (GMT), a 25-metre-mirror telescope under construction in Chile, and the Thirty Meter Telescope (TMT), which it is hoped will be built on Mauna Kea in Hawaii, have been unable to find the billion dollars or more that each will need. In May, the two teams joined forces and announced they would seek extra NSF funding through the Decadal Survey⁵. In return, they will enable broad US community access to the two telescopes, providing coverage of both hemispheres of the night sky.

BIG SCIENCE PERCEPTIONS

Space astronomy has always been federally supported, and is expensive. The total bill of the JWST has mounted to more than US\$9 billion, not helped by a series of delays. The proposed Wide-Field Infrared Survey Telescope (WFIRST), which will examine exoplanets and dark energy should it launch in the late 2020s, would cost at least \$3 billion.

Both projects have come under fire for their costs. In February, US President Donald Trump proposed cancelling WFIRST, although Congress subsequently approved funding for it. Incoming NASA administrator Jim Bridenstine has queried the need for any large science missions. He said in May⁶: "If we can do smaller missions with multiple satellites, then any one of them that runs over doesn't clobber the decadal [survey] not only for this decade but also the next decade".

Yet if inflation is taken into account, the cost of the JWST is comparable with that of the Hubble telescope: \$3 billion in 1990 translates to around \$9 billion today (see 'Astronomical costs', middle right panel). Even in its peak funding year (2014), the JWST consumed less than 4% of NASA's total budget of \$17.6 billion, or almost 13% of NASA's science budget that year.

Even so, the costs of major projects already under way are eating into existing budgets. This problem is particularly acute at the NSF,

where the capital and operational costs of ground-based facilities are funded from different accounts. Each time the NSF issues an award to build a new telescope, the running costs must be found from the same limited pot of money that supports existing facilities and research grants. Other NSF-funded fields, such as ecology, face the same challenge.

This NSF funding structure was predicated on the idea that old telescopes would be mothballed, and budgets would grow. Some facilities have been shut or divested. For example, the McMath Pierce Solar Telescope in southern Arizona is due to become part of the Kitt Peak Visitor Centre. The 44-year-old Blanco Telescope in Chile, which just discovered 12 new moons orbiting Jupiter, is now funded by the US Department of Energy and the NSF, together with funding agencies in the United Kingdom, Spain, Brazil and Germany, and contributions from institutions.

But this strategy has reached its limits. Big science facilities will always be much more expensive to run than older, simpler ones. They are technically more complicated, use more energy and need many highly trained personnel. For example, the NSF contributes about \$40 million a year to ALMA's annual running cost of \$120 million; international partners cover the rest⁷. The Blanco telescope, commissioned in 1974, requires only \$7 million a year to operate.

Financial pressure will only worsen in the 2020s if big facilities such as the GMT and the TMT come online. We can no longer assume that mothballing older facilities or taxing grants will magically work 20 years from now. There are not enough older telescopes in the NSF's portfolio to shut down to pay for even part of the operational costs of these two proposed facilities.

The choices for the community and agencies are stark⁸. Facilities will need to be funded appropriately from the start, and operations funds planned beyond the end dates of agencies' budgets. Without realism and a genuine commitment to the next generations of scientists, the United States will give up its lead in areas of astronomy where it has excelled for decades. And this at a time when the scientific frontier of astronomy and astrophysics beckons more powerfully than at any other point since Galileo lifted his telescope to the night sky more than 400 years ago.

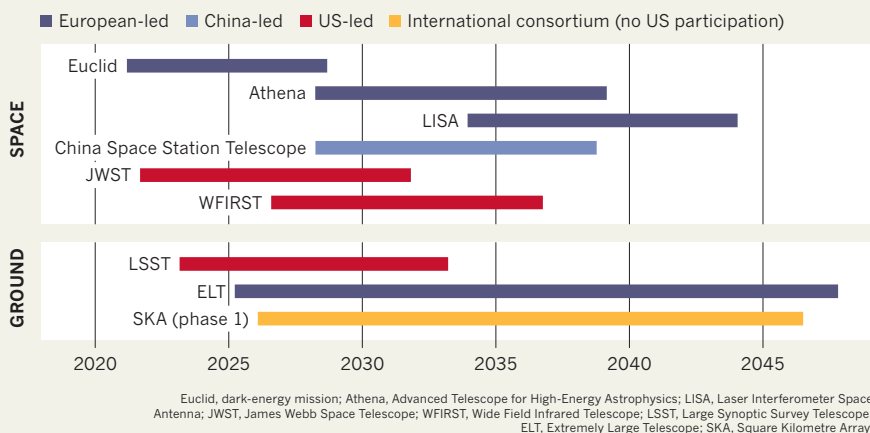
REDRAW THE LANDSCAPE

Astronomers need to keep the following three points in mind while they discuss options for the 2020s and beyond.

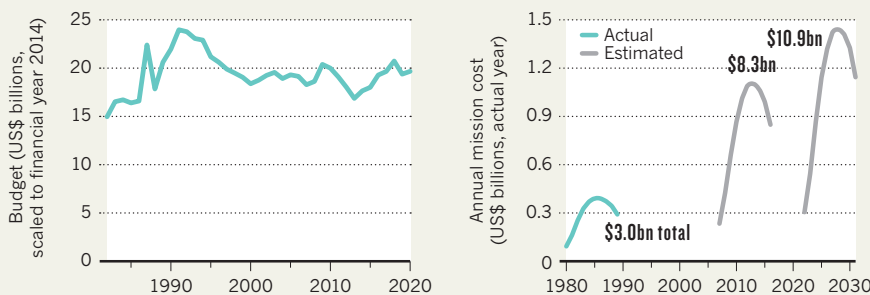
Recognize that size matters. Funding agencies and the community must accept that ever-larger facilities are inevitable if we are to explore frontiers. Astronomers are often asked whether they can get around the inexorable demand for larger telescopes by being more innovative. Can we do the same science

ASTRONOMICAL COSTS

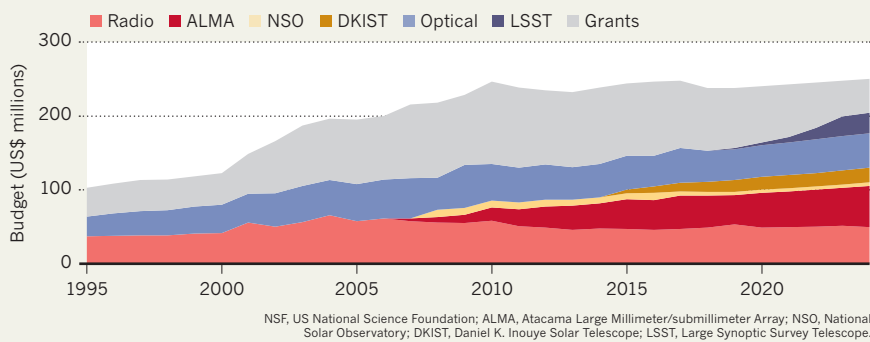
International astronomy projects are under way or planned, irrespective of the US Decadal Survey. US astronomers must decide in 2019 what competitive capabilities they need in the 2030s and beyond.



NASA's budget has changed little since the 1980s (left), but inflation has boosted mission costs (right), approximate cost of a Hubble Space Telescope if construction began in 2007 or 2022 rather than 1980.



The operating costs of observatories account for an increasing proportion of the NSF's Astronomy Division budget. This has put further pressure on grant funding since 2010 because of flat budgets.



with lots of small missions, for example? In many areas we cannot, at least with today's engineering options. Physics is unforgiving if you are trying to detect the earliest galaxies some 13.5 billion light-years away, or an Earth-like planet around another star 30 light years away. Larger optical telescope mirrors, a bigger array of radio antennas and more-powerful computers are necessary to catch and process more photons. Other countries already recognize that 20–40-m telescopes are inevitably the next step for optical astronomy on the ground, for example.

Plan internationally. Future big science facilities must be multinational, if they are

to be fully funded given the constraints and priorities for US federal funding. International planning and collaborations must be integrated into US plans. For example, the scientific potential, challenges and \$1.3-billion price tag of building ALMA at high altitude in Chile resulted in a partnership between the United States, Canada, Europe, Japan, South Korea, Taiwan and Chile. The JWST would not get off the ground without the 15% contribution from the European Space Agency and a 5% contribution from the Canadian Space Agency.

US researchers can no longer draw up their plans in splendid isolation, but must work alongside other nations' schedules. These

collaborations necessitate sharing of valuable telescope time and data with international partners, but also yield richer science that benefits the entire community.

Think long-term. The ten-year window of traditional decadal surveys is now insufficient to lay out a compelling, globally relevant science programme. Astronomers need to lay out the scientific narrative for at least the next 20 years. Each subsequent survey can always apply course corrections on a decadal cadence in response to a changing scientific landscape.

In this context, the impact of inflation needs to be recognized. Economic factors alone increase the costs of large projects whose development spans decades. Long-term projects resulting from the upcoming Decadal Survey have to be seen in this context. Facilities such as the JWST cannot be viewed as one-off burdens, but as long-term investments. Without this vision we would never have had the Hubble Space Telescope, ALMA or LIGO. We need to recognize the real impact of indexing the funding for our long-term big projects with inflation, and not just try to count the cost in today's dollars — or worse, yesterday's. We can no longer build a Hubble Space Telescope for \$3 billion.

It will be tough to create an ambitious future for US astronomy 20 years from now. The Decadal Survey needs to be far-sighted, strategic and responsive. Science, not economics, must come first. And the outcomes must meet the needs of future researchers: today's postdocs and PhD students, not just those sitting at National Academy tables. To quote Michelangelo, "The greater danger for most of us lies not in setting our aim too high and falling short; but in setting our aim too low, and achieving our mark." ■

Matt Mountain is president of the Association of Universities for Research in Astronomy (AURA), Washington DC, USA. **Adam Cohen** is president and chief executive of Associated Universities, Inc. (AUI), Washington DC, USA.
e-mails: mmountain@aura-astronomy.org; acohen@aui.edu

1. National Academies. *The Space Science Decadal Surveys: Lessons Learned and Best Practices* (National Academies Press, 2015).
2. Borucki, W. J. et al. *Astrophys. J.* **736**, 19 (2011).
3. Riess, A. G. et al. *Astrophys. J.* **855**, 136 (2018).
4. Zhan, H. A *Chinese Roadmap of Space Astronomy & the Chinese Space Station Optical Survey*. Kavli IAU Workshop on Global Coordination of Ground and Space Astrophysics, Leiden, 17–19 July 2017.
5. Overbye, D. 'Extremely Large, Extremely Expensive: The Race for the Next Giant Telescopes' *The New York Times* (11 June 2018).
6. Foust, J. 'Bridenstine optimistic WFIRST will avoid cancellation' *Space News* (17 May 2018).
7. National Science Board. *Study of Operations and Maintenance Costs for NSF Facilities* (NSF, 2018).
8. National Academies. *Powering Science: NASA's Large Strategic Science Missions* (National Academies Press, 2017).

GERONTOLOGY

A 2,000-year-old view of old age

Stanley M. Burstein and **Caleb E. Finch** reveal how a classic work by Greek physician Galen pioneered the idea of the ‘healthspan’.

How did the ancients see ageing? Many in the classical West saw old age as a disease. The prodigious Greek physician Galen thought otherwise. His treatise *Hygiene*, written around AD 175 and featuring the only surviving classical study of gerontology, framed ageing as a natural process that can be eased or even delayed through preventive measures such as diet. Thus the work, also known as *De sanitate tuenda* ('On the preservation of health'), resonates to a startling degree with ideas today, both on care of the elderly (*gerokomica* in ancient Greek) and on models of ageing.

Ian Johnston's excellent translation of *Hygiene* is the best appreciation yet of the classic — with the added benefit of a medically informed introduction (Johnston is a former neurosurgeon). It joins the extraordinary archive of Galen's medical writing, which comprises around 10% of extant ancient Greek literature.

As Johnston clarifies, Galen thought of ageing holistically, as a lifelong process with a number of stages, of which three were crucial: the first seven years of life, maturity and old age proper. He recognized that a person's ageing 'path' is highly individual, with a wide range of possible health outcomes at each stage. And he realized the importance of a healthy youth as the basis for a robust old age.

Galen's originality and insight were hard-won, as historian Susan Mattern has described in her 2013 biography *The Prince of Medicine*. He wrote *Hygiene* at the peak of his career, as physician to the Roman emperor Marcus Aurelius. His path to that exalted position took him from the Greek city of Pergamon (in what is now Turkey) to Alexandria, Egypt, where he mastered the work of predecessors such as Hippocrates and Herophilus. Becoming renowned as a physician and philosopher, he was called to Rome.

Galen adhered to many prevalent medical theories, including the concept of humours — based on bodily fluids such as blood — and the curative properties of 'divinely' inspired dreams. But he also pioneered the empirical study of human functions and diseases.

He developed treatments based on herbs and spices, which he administered to fellow doctors for verification. At a time when religious taboo forbade dissection of corpses, he found ingenious ways to investigate anatomy. He studied skeletons exposed in flooded cemeteries and, while treating the horrific wounds of gladiators, examined their exposed



An eighteenth-century mezzotint of a bust of Galen.

muscles and blood vessels. An ambitious self-promoter, he revelled in anatomical demonstrations on animals, including gruesome public vivisections of live Barbary macaques to demonstrate the function of nerves.

Given that breadth and depth, it's not surprising that the six books of *Hygiene* read like a lecture series for advanced medical students. Galen assumes his readers know the range of existing treatises. But what surprises is how far Galen has broken with earlier thinkers on lifespan and ageing. In the sixth century BC, Athenian statesman Solon saw old age reductively, as the last of ten life stages, each seven years long. Galen's more nuanced concept subdivided the final stage of his lifespan model into three phases of unspecified length, from active old age to senility. And he argued that the "causes of destruction" are present "innately from the beginning".

Galen saw elder care as integral to the work of an educated doctor, and believed it should emphasize prevention. He noted that many ills of ageing — such as dizziness, eye inflammation and ear pain — can be delayed or managed to maximize quality of life.

Galen's 'anti-ageing' regime might be prescribed today: he advocated walking and moderate running, and noted the health benefits of a simple diet involving gruel, raw honey, vegetables and fowl. (Amusingly, he exhaustively details wines suitable for the elderly, advising them to stick to "yellow" wines, and to "always choose the thinnest

Hygiene, Volumes I & II (Loeb Classical Library)
GALEN (TRANSLATED BY IAN JOHNSTON)
Loeb (2018)

in consistency".) He emphasized moderate treatments, avoiding strong purges and bloodletting but allowing gentle massage for kidney and bladder problems. *Hygiene* does not specifically discuss diseases of ageing, but in other books, such as *To Thrasylous*, Galen noted remarkably advanced treatments, such as surgical procedures for cataracts.

He mercilessly ridiculed an unnamed philosopher who claimed he could prolong life indefinitely — an ambition with echoes in our own era (see M. Baker *Nature* 517, 436–437; 2015). Death, Galen stressed, is inevitable as "the body deteriorates of itself". But life could be prolonged. At a time when many died long before 70, he cites two cases of extreme age: Antiochus, a doctor still practising in his eighties, and the grammarian Telephus, who lived to nearly 100 with his faculties intact. Galen notes that their achievement exemplified the success of principles laid out in *Hygiene*; he believed that the techniques contributed to his own longevity (he purportedly lived to 80).

The trailblazing insights in *Hygiene* suffered a mixed fate after Galen's death around AD 210. The treatise had become part of the Western medical curriculum by AD 500, and was translated into Arabic in the ninth century by Hunayn ibn Ishaq. However, Galen's key principles on elder care were omitted in the brief summary of *Hygiene* in the 1025 *The Canon of Medicine* by Persian polymath Avicenna (Ibn Sina), and in successors such as John Floyer's 1724 *Medicina Geronomica, or, The Galenic Art of Preserving Old Men's Healths*. It is only relatively recently that Galen's holistic approach to *gerokomica* as a road to optimizing the 'healthspan' — the length of time a person enjoys optimal health — has been rediscovered. ■

Stanley M. Burstein is Professor Emeritus of History at California State University, Los Angeles. His most recent book is *The World from 1000 BCE to 300 CE* (2017). **Caleb E. Finch** is ARCO Professor of Gerontology and Biological Sciences at the University of Southern California in Los Angeles. He is the author of *The Role of Global Air Pollution in Aging and Disease* (2018).
e-mails: sburste@calstatela.edu; cefinch@usc.edu

PETER PAUL RUBENS/WELLCOME/CC BY

Correspondence

Stop illegal trapping of Spain's songbirds

The European Union's Birds Directive protects 500 or so wild bird species (see go.nature.com/2m1pcgv). Yet illegal activities such as killing, trapping (**pictured**) and trading of songbirds continue (see go.nature.com/2oxjtxu). Malta was convicted in June by the European Court of Justice for allowing trapping. Italy fell into line in 2015, after warnings from the European Commission. Now, the battleground is Spain.

The Spanish government authorized the capture of 1,731,861 finches in 2013–18, presumably to provide a stock of captive-bred birds in case the ban on trapping was ever enforced (see go.nature.com/2mcg78z; in Spanish). In May, the European Commission gave Spain a two-month deadline to stop finch trapping altogether. As of 1 June, just 8 of Spain's 17 autonomous regions had suspended the trapping of goldfinches (*Carduelis carduelis*), greenfinches (*Carduelis chloris*), linnets (*Carduelis cannabina*), serins (*Serinus serinus*) and chaffinches (*Fringilla coelebs*). If the other regions fail to do the same, Spain could risk fines amounting to millions of euros.

We urge the new Spanish government to take prompt action to save wild songbirds.
Jorge S. Gutiérrez CESAM-University of Lisbon, Portugal.
José A. Masero University of Extremadura, Badajoz, Spain.
jorgesgutierrez@unex.es

Don't mix science and beliefs

I was intrigued by Alberto Kornblith's premise of using science to explain how facts can influence beliefs (*Nature* 559, 303; 2018). I agree that, as scientists, we should inform people about the complexity of reality, but we must be careful not to impose our own beliefs in doing so.



Scientists have the right to be passionate about their interpretations and convictions — but only as far as their bias is fully disclosed, as Kornblith respects. In my view, however, his analogy between an embryo and a mother's organ falls short. In advocating that women seeking abortion should not be held hostage by an organ, he mixes up two separate planes: useful information on embryo development and a moral interpretation that goes well beyond the information provided.

In political discussions, the value of science lies in its ability to provide models. These are our least-subjective interpretations of reality, yet we need to remind ourselves and instil in politicians that they are nevertheless not reality — they are simply useful tools for improving our awareness.

Silvo Conticello Institute for Study, Prevention and Cancer Network (ISPRO), Florence, Italy.
s.conticello@ispro.toscana.it

Tighten up clinical trial of stem cells

A task force in Japan's health ministry has conditionally approved the world's first clinical trial to treat patients with heart failure, using sheets of heart-muscle cells derived from 'reprogrammed' adult stem cells

(*Nature* 557, 619–620; 2018). In our view, two aspects of the trial protocol need to be addressed before it can be fast-tracked (see also *Nature* 557, 611–612; 2018 and Y. Yui *npj Regen. Med.* 3, 7; 2018).

First, we question the trial's use of allogeneic induced pluripotent stem (iPS) cells, called iPS stock cells and prepared by Kyoto University's Center for iPS Cell Research and Application. This use of heart-muscle cells from different donors could trigger transplant rejection by the patient. And using immunosuppressants to prevent rejection can cause unpleasant side effects, including a risk of promoting tumour development. We suggest that such risks be minimized by using autologous (that is, the patient's own) iPS cells in the trial instead.

Second, the task force has specified that the trial should involve three participants with "more serious" heart failure than was proposed in the submitted trial protocol. In our view, it would be better to recruit people who are less severely affected, given that the trial's main goal is to establish the procedure's safety. The intervention involves open heart surgery and is medically intensive, so by itself could kill those who are more vulnerable. This would also prevent proper evaluation of the stem-cell treatment.

Addressing these scientific and ethical concerns will ensure that the clinical trial amounts to more than a compassionate rescue attempt.

Akira Akabayashi, Eisuke Nakazawa University of Tokyo, Japan.

Nancy S. Jecker University of Washington School of Medicine, Seattle, Washington, USA.
akirasan-tky@umin.ac.jp

Pakistan needs more reservoirs, and fast

Political indecision is paving the way for a water crisis in Pakistan — and on a scale that affects the whole country, not just a metropolis (see M. Muller *Nature* 559, 174–176; 2018). We urge the incoming Pakistani government to break with a history of procrastination and provide more reservoirs with adequate capacity before it is too late.

Per person, Pakistan has the lowest dam storage capacity in the world (see go.nature.com/2nfjox7). Since identifying potential sites about 40 years ago, successive governments have continued to shy away from constructing new dams because of financial factors and political differences. The country has yet to build a dam large enough to meet its burgeoning water demand.

As Pakistan's partner in the 'Belt and Road' initiative, China can provide lessons on the effective management of water supplies (see, for example, J. Huang and G. Yang *Glob. Food Secur.* 12, 119–126; 2017).

Bold decisions, backed by political, economic and environmental viability, are needed to safeguard the world's sixth-largest population from increasingly severe droughts linked to future climate change.

Tariq Ali Center for Chinese Agricultural Policy, Chinese Academy of Sciences, Beijing, China.
Wei Xie Peking University, Beijing, China.
xiewei.ccap@pku.edu.cn

David Pines

(1924–2018)

Physicist who described how electrons interact.

David Pines is best known for his path-forging theory of the collective motion of electrons in metals. He also applied the theory to superconductors, atomic nuclei and neutron stars.

Pines developed this theory with David Bohm at Princeton University in New Jersey in the late 1940s. Their work solved a major puzzle in quantum mechanics, in which electrons are described as waves. Early quantum theory predicted the behaviour of electrons in metals, despite not taking into account the repulsion between electrons.

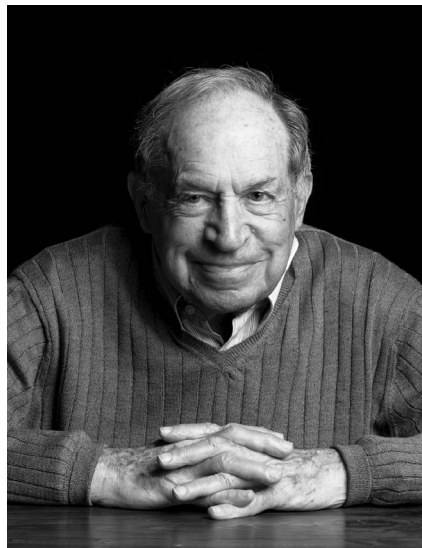
Pines and Bohm looked at electrons differently — as quantum plasma, analogous to a gas consisting of charged particles. They realized that electrons move as a group within a metal. Together, the electrons flow back and forth, alternately attracted to the positive ions that make up the crystal lattice and repelled by each other when they get too close to each other. Pines and Bohm showed that these oscillations in the density of electrons are quantized and exist only with a set of allowable energies; they called the oscillations plasmons. Plasmons soften the repulsive forces between individual electrons, thus explaining why the quantum theory worked.

Pines and Bohm's seminal papers launched the field of quantum materials. Their collective approach is still used to understand all forms of quantum matter.

Pines died on 3 May, aged 93. Born in Kansas City, Missouri, he spent much of his late childhood in Dallas, Texas. After being drafted into the US Navy during the last two years of the Second World War, he returned to his physics studies at the University of California, Berkeley, where he met his wife, Suzy.

Pines hoped to work on his PhD with J. Robert Oppenheimer, wartime leader of the Manhattan Project. When Oppenheimer moved to Princeton to become director of the Institute for Advanced Study (IAS), Pines followed him, to Princeton University. But Oppenheimer could not take him on, so Pines asked one of Oppenheimer's former students, Bohm, to be his adviser.

It was a difficult time for Bohm, who was arrested in 1950 for refusing to testify to a federal committee about his links to communist groups. He was acquitted in 1951 but, at a low point for US academia, lost his job. During this bleak period, Bohm lived as a lodger at Pines's house. Pines often reflected on how things might have turned out had Bohm accepted Pines's recommendation to use a Washington DC lawyer he knew.



In 1952, Pines moved to the University of Illinois at Urbana–Champaign (UIUC) to work with physicist John Bardeen. Pines spent most of his remaining career there. In 1954, Pines and Bardeen showed that scattered electrons in a crystal lattice can be attracted to each other (J. Bardeen and D. Pines *Phys. Rev.* **99**, 1140–1150; 1955). This interaction was a key element in the Bardeen–Cooper–Schrieffer (BCS) theory of superconductivity, developed in 1957. That summer, working with Aage Bohr and Ben Mottelson at the Neils Bohr Institute in Copenhagen, Pines extended BCS theory to nuclear physics. This accounted for the difference in the stability of isotopes with even and odd numbers of nucleons, such as uranium-238 and uranium-235.

Pines also worked on quantum liquids and superfluids — liquids that flow without losing energy. He applied superfluid theory to neutron stars, explaining the sudden glitches in the speed at which a pulsar rotates (D. Pines *et al. Prog. Theor. Phys.* **69**, 376–396; 1980). He contributed to 'many-body theory', the study of the collective behaviour of many interacting particles, and to high-temperature superconductivity, after it was discovered in 1987.

Pines was fascinated by 'emergence' — the large-scale behaviour of complex systems that arises from the microscopic properties of system constituents. For example, in superconductors, the pairing of electrons causes electricity to flow without resistance at low temperatures. Pines contributed to many influential articles, including 'The middle way' (R. B. Laughlin *et al. Proc. Natl Acad. Sci USA* **97**, 32–37; 2000), which calls

for researchers to seek emergent behaviour across quantum, soft and biological physics.

Indeed, Pines was a master of convening diverse people to pursue new directions. At the UIUC, he set up the Center for Advanced Study, which encompasses science, fine arts and agriculture. He was one of the first condensed-matter physicists active at the Aspen Center for Physics in Colorado, of which he was vice-president from 1968 to 1972. He co-founded the Santa Fe Institute (SFI) in New Mexico, and the Institute for Complex Adaptive Matter (ICAM-I2CAM), an international collective of scientists studying emergent phenomena. Young scientists and education were at the heart of all these endeavours.

Pines excelled at scientific diplomacy. During the cold war, he established the US–USSR Cooperative Program in Physics between 1968 and 1989, which promoted the exchange of ideas between the two communities. David and Suzy visited the USSR regularly and befriended Soviet scientists. In 1978, they travelled on the trans-Siberian railroad to a joint Soviet–American meeting in Moscow, only to discover that other members of the US delegation had cancelled, in protest against the harsh sentence given to a dissident scientist. Pines stayed on, hoping to diffuse the tension; he saved the commission, which operated until the end of the cold war. After the war, Pines organized a visiting programme for former Soviet physicists at the UIUC.

David will be remembered for his boundless energy and enthusiasm. No doubt born a genius, he never stopped growing in his science and life. He was always pushing the boundaries — even publishing several papers this year. He had a zest for life that continued into his 90s. Three years ago, proudly recounting that he had just driven himself from Santa Fe to Aspen — 480 kilometres through mountains — in 6 hours, he joked that the great thing about getting old is that "you get to drive your age". David treated a 90-mile-an-hour drive like a gentle walk in the park. ■

Piers Coleman is director of the Rutgers Center for Materials Theory, Rutgers, the State University of New Jersey in New Brunswick. He succeeded Pines as co-director of ICAM-I2CAM, at the University of California, Davis. **Laura Greene** is chief scientist at the National High Magnetic Field Laboratory, and professor at Florida State University in Tallahassee. She collaborated with Pines from the 1990s. e-mail: lhgreene@magnet.fsu.edu

BIOLOGICAL TECHNIQUES

Gene dynamics in single cells

A method has been developed to infer whether the expression of each gene in a single cell is increasing or decreasing, and at what rate, using RNA-sequencing data. This tool has many potential applications. SEE LETTER P.494

ALLON M. KLEIN

To understand and control complex systems, we must be able to measure the dynamics of their constituent parts. In biology, gene expression is probably the ultimate example of a complex system, with more than 20,000 genes orchestrating the functions of human tissues. However, we lack the tools to measure how genes vary in expression in individual cells over time. In a paper in *Nature*, La Manno *et al.*¹ describe a powerful method that enables the level and rate of change of expression to be estimated simultaneously for each gene in a single cell. The approach has considerable implications for studying cellular dynamics, particularly in disease progression and in complex processes such as embryonic development.

Biologists face an operational problem when trying to understand the dynamic changes in gene expression that occur as cells age, differentiate or become diseased. On the one hand, techniques that enable researchers to broadly measure the expression of all genes in a given cell involve destroying the cell of interest. This prohibits analysis over time and so provides only a snapshot of gene expression. On the other hand, techniques that enable the long-term measurement of gene expression in living cells can be used to track only a limited number of genes².

My group and many others previously attempted to infer the expression dynamics of all genes in a cell from destructive measurements of single cells, by organizing snapshot measurements into continuous ‘trajectories’ that approximate expression dynamics. But, because various gene-expression dynamics could give rise to the same snapshots, even the most sophisticated algorithms can produce incorrect results³.

La Manno *et al.* partially overcame this operational problem by realizing that existing snapshots of gene expression can, in fact, provide bona fide dynamic information. The authors analysed data that were generated by single-cell RNA sequencing. This approach is used typically to measure the abundance of messenger RNA transcripts for each gene in every cell of a sample. But the researchers showed that these RNA sequences also provided information on whether the expression of each gene

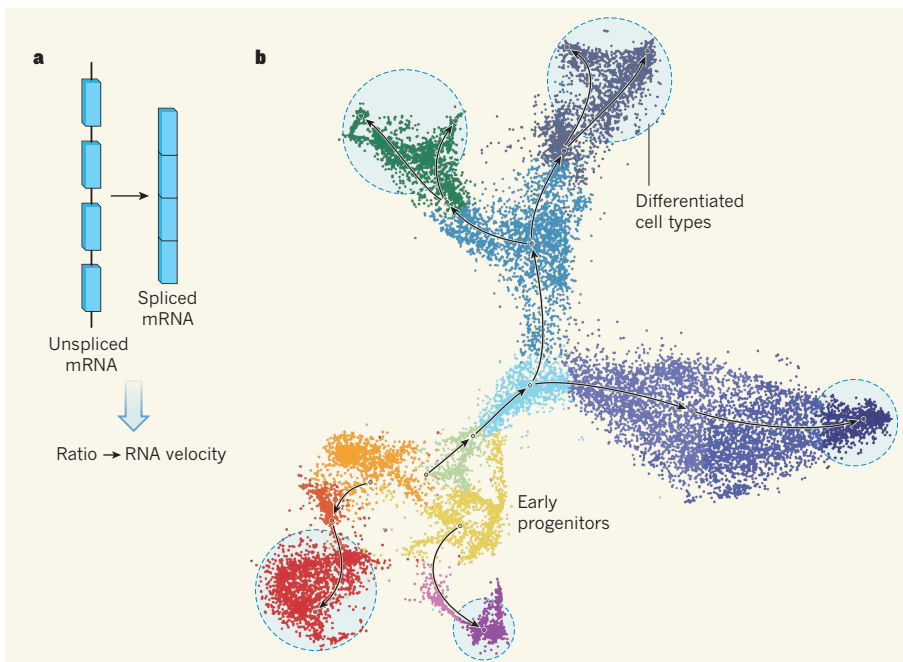


Figure 1 | Measuring dynamic changes in gene expression across complex tissues. **a**, As messenger RNA matures, sections of the immature transcript are removed — a process called splicing. When the expression of a gene increases, a transient increase in the proportion of immature, unspliced transcripts compared with that of mature, spliced transcripts is observed in the cell. By contrast, a higher proportion of spliced transcripts is seen for a short time when expression of the gene decreases (not shown). La Manno *et al.*¹ measured the ratio of unspliced to spliced transcripts for each gene in a single cell to calculate a quantity called the RNA velocity, which reveals how gene expression is changing. **b**, By measuring RNA velocity in thousands of cells in a tissue (here, in neurons in the developing mouse brain), the authors could generate maps that show not only how closely related cells are to one another (with closeness indicated by similar colours), but also which cells they will become similar to in the future (indicated by arrows), according to the gene-expression changes they are undergoing. RNA velocity successfully tracks early progenitors (orange and yellow) that eventually give rise to a range of differentiated cell types (blue dashed circles). (**b** adapted from Fig. 3c of ref. 1.)

was increasing or decreasing at the moment when the measurement was taken.

La Manno *et al.* exploited the fact that freshly transcribed mRNA contains segments that are later cut out (spliced) during the formation of mature mRNA. For a gene that is stably expressed, a small fraction of its mRNA will always be found in the immature, unspliced form, because older transcripts are replaced continuously with new ones. When a gene has just been activated, for a short time there will be a much higher proportion of immature transcripts. Conversely, when the expression of a gene is repressed, the proportion of short-lived, unspliced transcripts will drop before the longer-lived mature mRNA

transcripts decay. Therefore, for each gene in a cell, the ratio of unspliced mRNA to spliced mRNA can be used to directly infer instantaneous expression dynamics — that is, the ‘RNA velocity’ of each gene, which can then be used to deduce the cellular changes that are taking place in a tissue (Fig. 1).

This approach has already been used on bulk RNA-sequencing data sets^{4,5}. La Manno *et al.* realized that the method can be applied to single-cell data, for which it is considerably more useful. These data provide a much higher-resolution picture of dynamic processes — particularly in complex tissues, which contain many cell types with varied gene-expression patterns that are amalgamated in bulk

analyses. The authors found that existing algorithms for the analysis of data from single-cell RNA sequencing routinely discard information about immature, unspliced mRNA. By completely reworking their computational pipelines to salvage these data, they could recover information about both spliced and unspliced forms of each transcript, and therefore predict RNA velocity.

As is often the case, much effort and technical ingenuity were required for La Manno *et al.* to translate their initial idea into a robust set of working algorithms. Among the challenges that they had to overcome was the fact that measuring gene expression in single cells can be noisy. This is because most of the mRNA molecules in each cell are lost in the attempt to sequence them, leaving researchers with only a patchy picture of gene expression. Another challenge was determining how to infer the baseline ratio of spliced to unspliced transcripts for each gene when it is undergoing stable transcription. The authors needed to apply cutting-edge approaches in statistics and machine learning to solve these problems.

La Manno and co-workers beautifully demonstrate the usefulness of their approach using both published and newly collected data sets. For instance, they showed that RNA velocity could accurately detect the increases and decreases in gene expression that cells in the embryo are known to undergo as they differentiate from a cell type called a neural crest cell into chromaffin cells of the adrenal glands. The authors also used RNA velocity to investigate gene-expression dynamics in the developing hippocampus of the mouse brain, during intestinal stem-cell differentiation and more. This array of examples suggests that the method will have wide value. Among the group's most important achievements was the analysis of human embryonic tissue, in which other forms of dynamic measurement would be very difficult, or even impossible, to carry out because of the technical and ethical issues that are associated with studying living human embryos.

Developing an analysis of RNA velocity for single cells is a major breakthrough. But, of course, it has limitations. By its nature, RNA velocity cannot actually track a given cell over time, it is limited to the study of mRNA, and it does not provide information about the spatial organization of cells. These limitations could be restrictive when exploring phenomena in stem-cell biology, embryonic development or the onset of disease, which are likely to depend on the lineage and arrangement of cells, and which can be driven by mechanisms other than transcription, including protein phosphorylation. The method gives only a probabilistic description of cell dynamics, which is pieced together from instantaneous velocities. As a result of these limitations, there is little doubt that the spatio-temporal expression dynamics of genes will continue to be studied using complementary methods such

as live imaging.

Nonetheless, the ability to infer true, instantaneous RNA velocities in single cells is a leap forward for studies of gene-expression dynamics on the whole-genome scale. Indeed, the authors' approach has already been applied by other researchers⁶. In the immediate future, I can foresee RNA velocity easily becoming an essential tool for single-cell analysts. ■

Allon M. Klein is in the Department of Systems Biology, Harvard Medical School,

Boston, Massachusetts 02115, USA.
e-mail: allon_klein@hms.harvard.edu

1. La Manno, G. *et al.* *Nature* **560**, 494–498 (2018).
2. Specht, E. A., Braselmann, E. & Palmer, A. E. *Annu. Rev. Physiol.* **79**, 93–117 (2017).
3. Weinreb, C., Wolock, S., Tusi, B. K., Socolovsky, M. & Klein, A. M. *Proc. Natl. Acad. Sci. USA* **115**, E2467–E2476 (2018).
4. Zeisel, A. *et al.* *Mol. Syst. Biol.* **7**, 529 (2011).
5. Gray, J. M. *et al.* *PLoS ONE* **9**, e89673 (2014).
6. Plass, M. *et al.* *Science* **360**, eaao1723 (2018).

This article was published online on 8 August 2018.

CONDENSED-MATTER PHYSICS

Electric and magnetic domains inverted

Certain materials contain both electric dipoles and magnetic moments. An experiment demonstrates that these properties can be coupled in previously unrecognized ways, leading to advanced functionality. [SEE LETTER P.466](#)

JOHN T. HERON & JULIA A. MUNDY

The ability to use an electric or magnetic field to manipulate the orientation of electric dipoles or magnetic moments associated with atoms, ions or molecules in a material provides a vast array of functions. In rare materials called magnetoelectric multiferroics, the dipoles are intimately coupled to the moments, and a single field can control both¹. After the field is applied, however, the dipoles and moments typically all have the same orientation, and the original pattern that they formed is lost. On page 466, Leo *et al.*² show that, in two particular materials, a magnetic field can flip each of the dipoles or moments while preserving the structure of the original pattern. The work illustrates how the

complex coupling in these materials could be used to uncover other, previously unobserved electric and magnetic effects.

When most materials are placed in an electric field, their positive and negative charges shift by a tiny amount (less than 0.1 nanometres, which is about the radius of an atom). This microscopic movement leads to a macroscopic, measurable response: an electric polarization. In ferroelectric materials, however, clusters of ions assemble in a way that results in electric dipoles and a macroscopic polarization, even in the absence of an electric field.

Ferroelectrics are typically composed of domains — mesoscopic regions, often 100 nm to several micrometres in size, in which dipoles are aligned. Applying a strong electric field to a ferroelectric material causes all of the dipoles

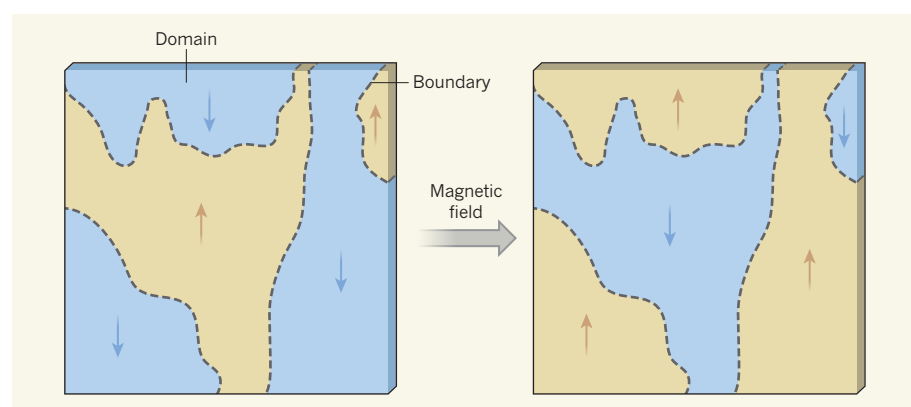


Figure 1 | Domain inversion. Certain materials are composed of regions of aligned electric dipoles or magnetic moments, known as domains. The arrows indicate the direction of the dipoles or moments in each domain. Leo *et al.*² show that, in two fundamentally different materials, a uniform magnetic field can reverse these directions, without changing the boundaries between the domains — rather than causing all the dipoles or moments to point in the same direction.

to point in a single direction, erasing both the original domain pattern and any engineered functions of the domain structure or of the boundaries between domains³.

There is a magnetic analogue to this phenomenon. A ferromagnetic material contains concerted arrangements of electron magnetic moments, which are located on specific sites of the material's atomic lattice. These moments generate a macroscopic magnetization that can be controlled using a magnetic field. Most ferromagnetic materials are also composed of mesoscopic domains.

Despite the apparent macroscopic similarities between ferroelectricity and ferromagnetism, materials that exhibit both phenomena, known as multiferroics, are exceedingly rare⁴. Magnetoelectric materials — those in which electric and magnetic properties are coupled, but that do not necessarily possess ferroelectric or ferromagnetic order — are also uncommon. Most exotic are magnetoelectric multiferroics, in which ferroelectricity and ferromagnetism are intrinsically coupled. This coupling holds great potential for next-generation devices, such as data-storage units that run on ultra-low power, highly sensitive magnetic-field detectors⁵ and energy-efficient nanoscale motors⁶. Much of the research focus on magnetoelectric multiferroics so far has centred on the control of magnetism using electric fields of ever-decreasing strength⁷.

Identifying multiferroics is a great challenge. In the current work, however, Leo and colleagues recognize that once such a material is identified, the complex parameters that give rise to this state of matter can be combined or manipulated in completely distinct ways. They illustrate this new way of thinking about multifunctional materials by considering the intertwined electric and magnetic properties of two such materials, imaging the domain structure while applying an external magnetic field.

The authors observed domains in the materials using a technique called optical second-harmonic generation. In this approach, two photons interact with a material to produce a single photon that has twice the frequency of the incident photons. The technique is sensitive to the spatial and magnetic (point-group) symmetry of the material's lattice, making it a powerful probe of structural, electronic and magnetic order. Of particular relevance to the authors' work is that second-harmonic generation is sensitive to magnetism even when the magnitude of the magnetic moments in the material is 1,000 times smaller than that of the moments in a typical ferromagnet^{1,8} — a sensitivity that can be matched by few complementary techniques.

Leo *et al.* studied ferromagnetic domains in one of the materials as a perpendicular magnetic field was swept across the material, and ferroelectric domains in the other material during application of a parallel magnetic field. They found that when the field was gradually changed from one direction to the opposite

direction, the boundaries between the domains moved. But, remarkably, when this process was complete, the polarization or magnetization of each domain was reversed and the original domain pattern was recovered (Fig. 1).

Such an effect is similar to switching the black and white squares of a chessboard, without changing the boundaries between the squares. It is in sharp contrast to what is usually observed when a uniform field is applied to a material: an alignment of all the electric dipoles or magnetic moments, or in the chess analogy, a conversion of all the squares to a single colour.

The authors explain the inversion effect as being due to the coupling of three order parameters — variables that describe the alignment of dipoles or moments in a material. The first parameter represents the observed domain distribution. The second parameter, which is unaffected by the applied magnetic field, imprints the original domain pattern onto the first parameter. Finally, the third parameter, which is directly controlled by the field, causes the observed domain distribution to be inverted.

Leo and colleagues' results suggest that the coupling of multiple order parameters is generic, but it remains to be seen how frequently it manifests in other materials. Perhaps more importantly, however, the study shows how multiple order parameters in certain materials

can be exploited. Although magnetoelectric multiferroics have garnered much interest because of their strongly coupled magnetization and ferroelectric polarization, future work might find ways to combine the many order parameters in these materials to derive new functions. Precisely what other relationships might be lurking between these parameters is uncertain. Nevertheless, the authors' demonstration of domain-pattern inversion resulting from the coupling of three order parameters is a big step forward in our understanding of complex coupling in multiferroic materials. ■

John T. Heron is in the Department of Materials Science and Engineering, University of Michigan, Ann Arbor, Michigan 48109, USA. **Julia A. Mundy** is in the Department of Physics, Harvard University, Cambridge, Massachusetts 02138, USA.
e-mails: jtheron@umich.edu; mundy@fas.harvard.edu

1. Fiebig, M., Lottermoser, T., Meier, D. & Trassin, M. *Nature Rev. Mater.* **1**, 16046 (2016).
2. Leo, N. *et al.* *Nature* **560**, 466–470 (2018).
3. Catalan, G., Seidel, J., Ramesh, R. & Scott, J. F. *Rev. Mod. Phys.* **84**, 119–156 (2012).
4. Hill, N. A. J. *Phys. Chem. B* **104**, 6694–6709 (2000).
5. Li, M. *et al.* *Appl. Phys. Lett.* **110**, 143510 (2017).
6. Sohn, H. *et al.* *ACS Nano* **9**, 4814–4826 (2015).
7. Meisenheimer, P. B., Novakov, S., Vu, N. M. & Heron, J. T. J. *Appl. Phys.* **123**, 240901 (2018).
8. Fiebig, M. *et al.* *Phys. Rev. Lett.* **84**, 5620–5623 (2000).

MICROBIOLOGY

Checkpoint for gut microbes after birth

The route to the establishment of a beneficial microbial community in the gut after birth is not fully understood. It now emerges that a gut-cell protein in newborn mice shapes the long-term composition of this community. SEE LETTER P.489

**ANDREW J. MACPHERSON
& STEPHANIE C. GANAL-VONARBURG**

Although people think of divorce, bereavement and job loss as major life events, perhaps no change in a person's life is quite as dramatic as the moment of their birth. As a baby exits the birth canal, the newborn infant loses placental support, and the respiratory system and gut must start to function. Moreover, both beneficial and pathogenic microorganisms will be encountered, and will compete to colonize the baby's body. Writing in *Nature*, Fulde *et al.*¹ report that the intestinal receptor protein TLR5 is involved in actively shaping the long-term composition of the gut microbial community, termed the microbiota, in newborn mice.

The bacterial colonization of the gut normally starts in the birth canal². Then,

successive waves of increases and decreases in microbial species occur during a period of microbial change, which lasts approximately 18 months in humans³. Nutritional conditions and immune-system development in early life both affect gut colonization, with far-reaching consequences for later growth and health. Tragically, more than 15 million children around the globe under the age of 5 years suffer from malnutrition and severe wasting (go.nature.com/2n3rxob). This is caused by a combination of insufficient calorie intake and a type of immune dysfunction that is linked to abnormal bacterial colonization in the gut, called environmental enteropathy. The correct functioning of immune cells called B cells and T cells is partly determined by exposure during their early development to non-pathogenic microbes, which can therefore have long-term consequences for the composition of microbial

species in the microbiota and subsequent resistance to pathogenic challenges⁴.

The immature, vulnerable immune system of a newborn can to some extent be shielded from pathogenic attack by the presence of antibodies from the infant's mother, transferred across the placenta or in breast milk — a particularly effective health-boosting measure. Breast-milk antibodies that remain in the gut can help to determine the composition of microbes that colonize the intestine, and thereby prevent excessive immune responses to non-pathogenic microbes^{5,6}. Yet despite this maternally provided immune protection, an infant still faces an extremely sensitive period in early life when the progressive microbial colonization of internal and external body surfaces occurs concurrently with the development and maturation of the immune system.

The cellular composition and function of almost every organ changes when a germ-free animal becomes colonized with a microbiota. Such changes are triggered by molecules from the microbes themselves, and the results can help to prevent inflammation as an animal adapts to the presence of microbes on its body surfaces.

It was previously thought that the adaptation of host tissues to accommodate the presence of intestinal microbes could occur equally effectively at any age, on the basis of experiments that introduced a microbiota into adult animals raised in germ-free conditions. Yet awareness is growing that, as a newborn animal develops, an ordered, age-dependent sequence of interrelated immune and microbial checkpoints is required for proper adaptation and to ensure a healthy microbial composition⁷. Examples of adaptations in the crucial early time window include regulation of the induction of different classes of antibody called isotypes and of the numbers of immune cells called natural killer T cells in the intestine^{7,8}. Microbial colonization of the newborn animal is not necessary for the innate branch of the immune system to develop, because molecules from maternal microbes delivered across the placenta and in milk can suffice to drive some of this process⁹.

Previous studies^{10–12} of mice that are deficient in TLR5, a receptor belonging to a family that is linked to microbial recognition, reported that gut microbes in such animals have defects that trigger metabolic abnormalities such as body-weight gain and fatty changes in the liver. To investigate how postnatal development affects the establishment of the gut microbial community, Fulde and co-workers compared gene expression in gut epithelial cells in three-day-old mice with that in adult mice, and found that the gene encoding TLR5 is highly expressed in the infant mice. The authors then investigated whether this protein has a role in early postnatal gut development.

Fulde and co-workers show that the expression of TLR5 in intestinal epithelial cells in early life is an example of a checkpoint in a

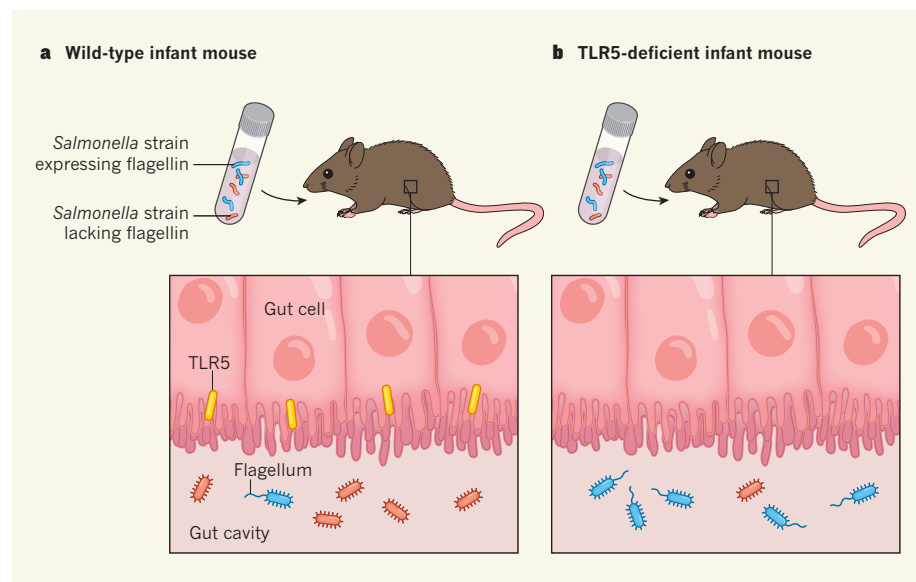


Figure 1 | A host protein affects the composition of the gut microbial community. Fulde *et al.*¹ report that the expression of the protein TLR5 in gut cells during a limited time window in early postnatal development in mice helps to reduce the presence of bacteria that express the protein flagellin. This protein is a component of a bacterial structure called a flagellum, and is a hallmark of pathogenic bacteria, although not all bacteria that express flagellin are pathogenic. **a, b**, When the authors gave wild-type or TLR5-deficient infant mice a bacterial sample that was an equal mixture of flagellar and non-flagellar strains of *Salmonella*, they found that a higher proportion of flagellin-expressing bacteria were present in the gut of the TLR5-deficient mice (**b**) than in the wild-type mice (**a**). Additional experiments revealed that early expression of TLR5 can help to shape the long-term composition of microbial species residing in the gut.

developmental process that is coordinated with microbial colonization to achieve healthy mutualism between the host and its microbiota. TLR5 can bind the bacterial protein flagellin, and the authors found that this drives secretion of the antimicrobial protein Reg3γ. Both TLR5 and Reg3γ help to limit early-life colonization by bacteria that express flagellin, which is a component of the flagellar structure that aids bacterial motility. Flagellin is found on some pathogenic bacteria, although not all bacteria that express flagellin are pathogenic. The authors determined when during development this TLR5-linked effect occurred by conducting colonization experiments in which infant mice (up to 10 days old) received an equal mixture of non-flagellated and flagellated strains of *Salmonella* bacteria. In wild-type mice, the intestinal colonization of the strain lacking flagellin was consistently higher than that of the strain that had flagellin. This difference was not seen in TLR5-deficient mice (Fig. 1).

In another experimental approach taken by Fulde and colleagues, germ-free, wild-type pups were intestinally colonized with either a 'healthy' microbiota derived from wild-type mice or a 'dysbiotic' microbiota from TLR5-deficient mice, which would be liable to trigger changes linked to metabolic disease^{10–12}. Fulde *et al.* found that wild-type pups could drive the species composition of the dysbiotic-microbiota gut residents towards that of the microbiota derived from wild-type mice. However, it seems that TLR5 is required to shape microbial composition only during a specific postnatal time frame,

because the authors found that the dysbiotic microbial composition was less effectively shaped if transferred into germ-free, TLR5-deficient pups or adult, germ-free, wild-type mice. Once the microbiota composition had been shaped, it persisted long into adult life (at least 42 days). The window of opportunity for this microbiota-shaping effect is restricted to early postnatal life by the downregulation of TLR5 expression in gut epithelial cells at weaning (approximately 21 days after birth).

The gut microbial composition for a given animal strain varies considerably with the different housing facilities used for laboratory animals and even between cages in a single facility, with the microbial composition changing gradually from generation to generation even in a continuously inbred colony. External influences, such as dietary changes or environmental cage-associated effects, might bring about changes that could confound experimental results. One way around this is to breed heterozygous animals (those that have a mutation in only one of the two copies of a gene of interest), and then to compare the gut microbes of littermates that are either deficient in the gene of interest or wild type. Yet, as others have reported¹³, with this kind of approach, differences in gut-microbe composition are dominated by the transmission of microbiota from parents to their offspring, rather than being mainly affected by whether the offspring are deficient for a certain gene, such as the gene that encodes TLR5.

Nevertheless, in the context of the gut microbes and the stage of postnatal

development that they studied, Fulde and colleagues show not only that TLR5-deficient animals develop an abnormal gut microbial community, but also that the presence of TLR5 in gut cells is sufficient to drive the community towards a more normal composition by limiting the presence of flagellated bacteria.

As with every major advance, questions remain. Determining the way in which different microbes associate and occupy niches in the gut in the presence or absence of TLR5 will require studies using mouse colonies in which the animals have a range of predefined, stable microbial compositions. This will allow researchers to discover how the presence or absence of microbial species affects the microbiota interaction with the host, and, by using a technique known as stable isotope tracing, to assess whether molecular crosstalk between

microbial species affects the overall assembly of the microbiota.

Fulde and colleagues' work provides two key messages. First, it shows that TLR5 expression in early life can have a lasting effect on the composition of the intestinal microbial community. And second, it supports the emerging idea of sequential milestones during the mutually connected postnatal development of a host and its associated microbes. ■

Andrew J. Macpherson and Stephanie C. Ganal-Vonarburg are in the University Clinic for Visceral Surgery and Medicine, Bern University Hospital, and in the Department for BioMedical Research, University of Bern, 3008 Bern, Switzerland.
e-mails: andrew.macpherson@insel.ch; stephanie.ganal@dbmr.unibe.ch

1. Fulde, M. et al. *Nature* **560**, 489–493 (2018).
2. Dominguez-Bello, M. G. et al. *Proc. Natl Acad. Sci. USA* **107**, 11971–11975 (2010).
3. Yatsunenko, T. et al. *Nature* **486**, 222–227 (2012).
4. Macpherson, A. J., Gomez de Agüero, M. & Ganal-Vonarburg, S. C. *Nature Rev. Immunol.* **17**, 508–517 (2017).
5. Rogier, E. W. et al. *Proc. Natl Acad. Sci. USA* **111**, 3074–3079 (2014).
6. Koch, M. A. et al. *Cell* **165**, 827–841 (2016).
7. Gensollen, T., Iyer, S. S., Kasper, D. L. & Blumberg, R. S. *Science* **352**, 539–544 (2016).
8. Olszak, T. et al. *Science* **336**, 489–493 (2012).
9. Gomez de Agüero, M. et al. *Science* **351**, 1296–1302 (2016).
10. Vijay-Kumar, M. et al. *Science* **328**, 228–231 (2010).
11. Chassaing, B., Ley, R. E. & Gewirtz, A. T. *Gastroenterology* **147**, 1363–1377 (2014).
12. Carvalho, F. A. et al. *Cell Host Microbe* **12**, 139–152 (2012).
13. Ubeda, C. et al. *J. Exp. Med.* **209**, 1445–1456 (2012).

This article was published online on 8 August 2018.

interaction between two qubits depends on the surrounding magnetic fields. The programmability of the authors' device comes from the fact that this magnetic environment can be changed by introducing additional magnetic fields through current-carrying loops adjacent to the qubits.

King and colleagues' device was originally designed to solve combinatorial optimization problems⁸, in which a set of variables each have to be assigned a value of either '0' or '1' with the goal of minimizing a particular function of these variables. Such problems can occur when, for example, deciding which manufacturing task to assign to which factory, finding the shortest route through a series of cities, and deciding in which assets to invest. These tasks all belong to a class of difficult computational problem for which no efficient classical algorithm exists.

It was therefore hoped that a quantum optimizer could help, by making use of quantum tunnelling to more efficiently explore the range of possible variable assignments. Experiments on previous generations

QUANTUM PHYSICS

Programmable quantum simulation

A programmable array of superconducting quantum bits can simulate phase transitions in quantum systems, a step towards the study of exotic physics that is difficult or inefficient to model using ordinary computers. SEE LETTER P.456

MATTHIAS TROYER

In a 1981 lecture, the physicist Richard Feynman discussed the challenge of simulating quantum systems on conventional computers¹. The memory required on such a computer to accurately store the state of a quantum system consisting of many particles increases exponentially with the number of particles. Feynman therefore proposed instead to build a quantum computer — a computer based on quantum-mechanical elements. Although large-scale quantum computers are yet to be developed, special-purpose quantum simulators for studying specific quantum models have been built^{2,3}. These simulators have been based on technologies such as ultracold atomic gases⁴, trapped ions⁵ and superconducting circuits⁶. On page 456, King *et al.*⁷ report a quantum simulator based on 1,800 superconducting quantum bits (qubits) that is programmable, adding another technology to our portfolio of quantum simulators.

The qubits used by King and colleagues are made from loops of superconducting niobium metal⁸. The loops are designed in such a way that, at low (millikelvin) temperatures, there are two energetically favourable states: one in which a persistent electric current circulates around the loop in an anticlockwise direction, and one in which such a current circulates in a clockwise direction. These states can be

associated with the '0' and '1' of an ordinary (classical) bit. Because of a phenomenon known as quantum tunnelling, a loop can exist in both states at the same time, turning the classical bit into a qubit.

An anticlockwise current produces a magnetic field that threads up through the loop, whereas a clockwise current generates a magnetic field in the opposite direction. Intrinsic interactions between these fields lead to interactions between the qubits. The strength of the

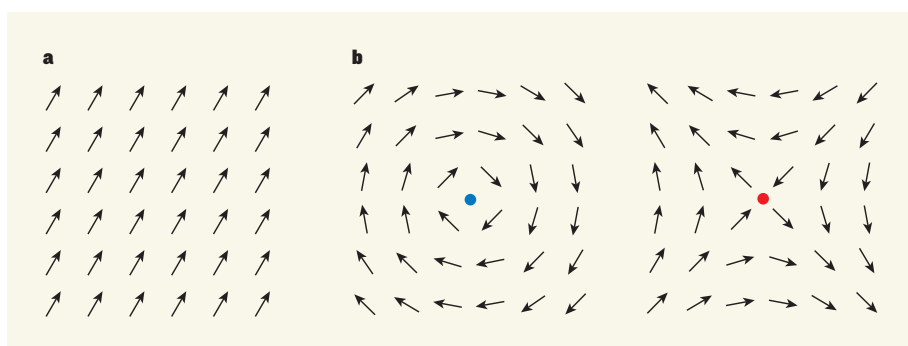


Figure 1 | Topological features in a quantum magnet. King *et al.*⁷ report a quantum simulation of a particular model of a quantum magnet. In the model, the magnetic moments (arrows) of electrons can point in any direction on a plane. **a**, At zero kelvin, all of the moments point in the same direction. **b**, At non-zero temperatures, topological features can emerge. Such features include vortices (blue) and antivortices (red) — points around which moments rotate clockwise or anticlockwise, respectively, when traversing a closed loop around the point in a clockwise direction. (Adapted from Extended Data Fig. 1 of ref. 7.)

of the authors' device have demonstrated that quantum effects can be used to find solutions to optimization problems⁸. However, these devices were not shown to have advantages over classical algorithms for real-world optimization problems⁹.

In the current paper, King *et al.* used their device not for optimization tasks, but for its more promising 'native' function of simulating quantum systems. In a model of a quantum magnet, the '0' and '1' states of a qubit in the device could correspond to the magnetic moment of a localized electron pointing up or down.

The authors simulated a particular quantum-magnet model in which competing interactions between magnetic moments give rise to a phase of matter that can be described by moments pointing in any direction on a plane. At zero kelvin, all of these moments are aligned (Fig. 1a). However, at non-zero temperatures, features known as topological defects emerge. Two such defects are vortices and antivortices — points around which moments rotate clockwise or anticlockwise, respectively, when circling the point in a clockwise direction (Fig. 1b).

At low temperatures, defects show up as tightly bound pairs of vortices and antivortices. As the temperature is increased, the system undergoes a phase transition in which these pairs of defects unbind to form isolated vortices and antivortices^{10,11}. Work on this transition resulted in the 2016 Nobel Prize in Physics (see go.nature.com/2napzlx). The phenomenon has been observed in liquid-helium films¹², layered magnets¹³ and ultracold atomic gases¹⁴. King *et al.* realized the transition in their quantum simulator, suggesting that such devices could be used to study this transition and others in a variety of models.

As interesting as the observed phase transition is, the main strength and impact of the paper is not in the specific model, but rather in the demonstration that reliable programmable quantum simulators that have more than 1,000 qubits can be built. Previous generations of King and colleagues' device had many defective qubits^{8,9}, but the current study required a perfect array of working qubits. This requirement was met thanks to improvements in the authors' fabrication technology over the past decade.

King and colleagues' observations are consistent with state-of-the-art classical simulations, showing that the results obtained by such quantum simulators can be trusted. This is an exciting development, as I have argued previously that the authors' device could have greater potential for quantum simulation than for optimization problems.

A limitation of the current device is that it can realize only what are known as stoquastic quantum models. These can be mapped to corresponding purely classical models and can, therefore, be simulated on

classical computers. Although this mapping allows experiments to be compared to classical simulations, it limits the usefulness of the quantum simulator. To go beyond what is tractable on classical computers, two avenues of further development could be explored.

The first is to carry out quantum simulations of dynamical non-equilibrium effects, such as the propagation of excitations that occurs after the system of qubits is perturbed. Such effects are difficult to simulate classically, even in the case of stoquastic models. However, in contrast to quantum simulators built from dilute ultracold atomic gases or trapped ions, solid-state devices such as that made by the authors are subject to substantial environmental noise from lattice vibrations, and from electric-charge and magnetic-field fluctuations. This noise destroys the purely quantum evolution of the qubits. The design of qubits that have low sensitivity to noise will therefore be crucial for the study of quantum dynamics using solid-state quantum simulators.

The second direction for future development is to introduce other types of programmable interaction between the qubits that would realize non-stoquastic models for which no efficient classical simulators exist. Such models include those of frustrated quantum magnets,

in which competing interactions give rise to unusual quantum phenomena, and to phases of matter that contain exotic types of excitation. A programmable quantum simulator for such models would open up entirely new approaches for studying complex quantum systems. ■

Matthias Troyer is at Microsoft Quantum, Redmond, Washington 98052, USA, and the Institute of Theoretical Physics, ETH Zurich, Zurich, Switzerland.
e-mail: mtroyer@microsoft.com

1. Feynman, R. P. *Int. J. Theor. Phys.* **21**, 467–488 (1982).
2. Cirac, J. I. & Zoller, P. *Nature Phys.* **8**, 264–266 (2012).
3. Georgescu, I. M., Ashhab, S. & Nori, F. *Rev. Mod. Phys.* **86**, 153–185 (2014).
4. Bloch, I., Dalibard, J. & Nascimbène, S. *Nature Phys.* **8**, 267–276 (2012).
5. Blatt, R. & Roos, C. F. *Nature Phys.* **8**, 277–284 (2012).
6. Houck, A. A., Türeci, H. E. & Koch, J. *Nature Phys.* **8**, 292–299 (2012).
7. King, A. D. *et al.* *Nature* **560**, 456–460 (2018).
8. Johnson, M. W. *et al.* *Nature* **473**, 194–198 (2011).
9. Rønnow, T. F. *et al.* *Science* **345**, 420–424 (2014).
10. Berezinskii, V. L. *Sov. Phys. J. Exp. Theor. Phys.* **32**, 493–500 (1970).
11. Kosterlitz, J. M. & Thouless, D. J. *J. Phys. C Solid State Phys.* **6**, 1181–1203 (1973).
12. Bishop, D. J. & Reppy, J. D. *Phys. Rev. Lett.* **40**, 1727–1730 (1978).
13. Dürr, W. *et al.* *Phys. Rev. Lett.* **62**, 206–209 (1989).
14. Hadzibabic, Z., Krüger, P., Cheneau, M., Battelier, B. & Dalibard, J. *Nature* **441**, 1118–1121 (2006).

MEDICAL RESEARCH

Diet boosts cancer-drug effectiveness

A drug that slows cancer growth has been found to elevate the level of the hormone insulin. This insulin rise lessens the drug's effectiveness, but a diet that lowers insulin can increase the benefits of the therapy in mice. SEE LETTER P.499

MICHAEL POLLAK

Most studies of the causes of resistance to cancer treatment focus on the tumour itself. However, some resistance mechanisms might involve alterations in the host rather than the cancer. A particularly conspicuous gap in our knowledge concerns the possibility that dietary factors influence the outcome of some cancer treatments. This has been widely assumed not to be the case, but writing in *Nature*, Hopkins *et al.*¹ show that cancer drugs that inhibit the signalling protein PI3K are considerably more effective in mice if the animals are on a specific diet. The authors provide a plausible mechanism for why this is so.

A person with cancer might wonder whether their diet could affect their prognosis. A wide range of dietary recommendations are available, both on the Internet and from

physicians and dieticians. Such advice is often conflicting. For example, a patient might read that extreme dietary calorie restriction helps to 'starve' a tumour in a clinically useful manner, but might also come across information suggesting that the opposite approach of maximizing calorie intake is beneficial, to avoid cancer-associated weight loss linked to later stages of the disease. Clinical data to support either of these approaches are not compelling. Physicians lack high-quality data on which to base dietary advice for people undergoing cancer treatment.

Hopkins and colleagues now provide evidence from mouse experiments that a diet that keeps levels of the hormone insulin low improves the effectiveness of cancer drugs that inhibit PI3K. There is great interest in trying to inhibit PI3K signalling in cancer cells, because mutations that cause

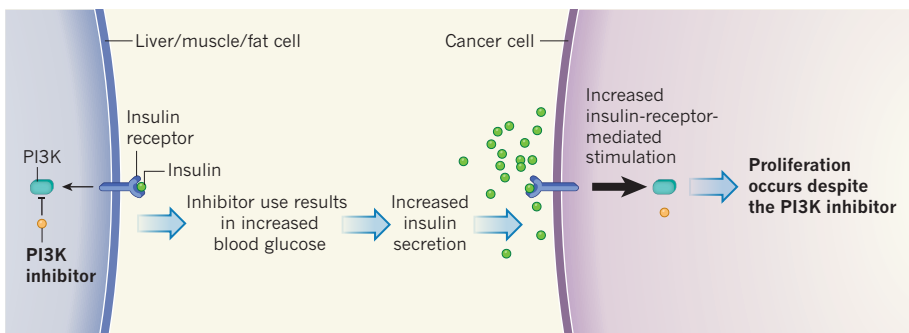


Figure 1 | Effectiveness of a cancer drug is linked to blood insulin levels. Activation of the PI3K signalling pathway can boost cancer-cell proliferation, yet the effectiveness of drugs that block PI3K to treat cancer is often disappointing. PI3K acts in the pathway regulated by the hormone insulin, which controls blood glucose levels. Insulin is released by the pancreas (not shown) in response to high blood glucose. When insulin binds to its receptor on liver, muscle or fat cells, PI3K signalling in these tissues is activated, which ultimately lowers glucose in the bloodstream. However, this process can be inhibited by drugs that target PI3K. Hopkins *et al.*¹ report that glucose and insulin levels increased in mice that received PI3K inhibitors compared with the levels in mice that did not receive the drug. The authors found that the inhibitor-driven rise in insulin levels can enable cancer cells that express insulin receptors to proliferate despite drug treatment. This might be because insulin-receptor signalling increases sufficiently in the cancer cells to overcome the inhibitor's ability to block PI3K action. The authors found that a diet that lowers insulin levels boosts the effectiveness of PI3K inhibitors in cancer treatment in mice.

excessive activation of this pathway are common in many kinds of cancer². The pharmaceutical industry has invested heavily in developing drugs that inhibit the PI3K signalling pathway, but most clinical trials of these agents have revealed only modest benefits.

The authors offer a fresh perspective on the effect of PI3K inhibition by taking into account the fact that these inhibitors not only target cancer cells, but also act on tissues that regulate blood glucose levels. In glucose regulation, insulin is secreted by the β -cells of the pancreas when blood glucose levels rise. Insulin binding to receptors on its target cells activates the PI3K signalling pathway in liver, muscle and fat, causing changes in glucose production and uptake that reduce the glucose concentration in the bloodstream.

Cancer cells commonly also express insulin receptors, and, as in normal cells, signalling through the insulin receptor activates the PI3K signalling pathway. However, in cancer cells, pathway activation causes an increase in cell proliferation and a reduction in cell death, rather than affecting blood-glucose regulation. This is in keeping with the observation that insulin-like hormones and the PI3K signalling pathway are both ancient in evolutionary terms^{3,4}, and their roles in stimulating cellular nutrient use and proliferation pre-date their function of blood-glucose regulation.

Hopkins and colleagues' results confirm previous reports^{5–7} that PI3K inhibitors raise blood glucose by blocking signalling downstream of the insulin receptor in tissues involved in blood-glucose regulation. The authors go on to show that this increase in blood glucose causes a substantial elevation in insulin levels in the bloodstream. This rise in insulin probably results from pancreatic β -cells responding to high blood glucose concentrations by secreting extra insulin

in an attempt to restore normal glucose levels. The authors make the key finding that, in cancer cells that express insulin receptors, this rise in insulin is sufficient to increase signalling downstream of the insulin receptor to activate PI3K and overcome the action of the PI3K inhibitor on the pathway (Fig. 1). This lessens the drug's therapeutic effect and enables cancer cells to proliferate despite drug treatment.

Furthermore, Hopkins *et al.* show that combining a PI3K inhibitor with a pharmaceutical or dietary intervention that lowers blood glucose reduces the drug-induced elevation in insulin, and that this increases the effectiveness of PI3K inhibitors in slowing cancer growth, compared with the effect of the

Differences in diet could contribute to variability in response to cancer treatments.”

drug in animals that do not receive a glucose-lowering intervention. The most effective intervention tested was a type of low-carbohydrate, high-fat diet termed a ketogenic diet, which improved the action of the PI3K inhibitor to a greater extent than was observed for the drug metformin, which reduces glucose output from the liver, or for the drug canagliflozin, which causes glucose loss in the urine. Notably, the authors found that a ketogenic diet in the absence of the inhibitor drug did not curb cancer growth in mice. Consistent with this, early-stage clinical trials have not shown that this diet alone improves cancer survival⁸.

Hopkins and colleagues' findings are important because they identify a mechanism of resistance to cancer therapy that is based on a hormonal response of the host, rather than on alterations in cancer cells. The key element of this response is a rise in insulin levels, but whether other hormones involved in

regulating glucose metabolism also contribute to the effect is not known. Previous research⁹ indicates that high insulin levels associated with obesity can increase the risk of cancer or worsen prognosis. The work by Hopkins *et al.* reveals an additional connection between insulin and cancer by illuminating a way in which this hormone can influence the usefulness of a cancer drug.

Certain PI3K-inhibitor drugs block only the δ version of the protein, which is found in blood cancers, but not in common solid tumours or in the organs that regulate blood glucose. These inhibitors presumably do not significantly elevate blood insulin levels, so the mechanism of resistance described by Hopkins *et al.* does not occur. If this is the case, it might help to explain why this particular type of PI3K inhibitor was the first to show sufficient activity in clinical trials to be approved for clinical use.

Hopkins *et al.* provide a firm basis for investigating dietary or pharmaceutical approaches to reduce insulin signalling in cancers to enhance the effectiveness of PI3K inhibitors. The authors' data indicate that previous attempts¹⁰ to predict whether this class of drug would be effective by examining tumour characteristics would have overlooked the part played by host insulin levels.

Substantial patient-to-patient variability in the response to anticancer drugs often occurs even among patients whose tumours show similar genetic abnormalities. Along with another paper¹¹, published last month, which demonstrates that a diet rich in the amino acid histidine can increase the effectiveness of the anticancer drug methotrexate, Hopkins and colleagues' study supports the idea that differences in diet could contribute to variability in response to cancer treatments. Excitingly and unexpectedly, we now have a rationale for clinical research to determine whether the efficiency of certain cancer drugs might be improved by pairing them with specific diets. ■

Michael Pollak is in the Department of Oncology and at the Segal and Goodman Cancer Centres of McGill University, Montreal, Quebec H3T 1E2, Canada.
e-mail: michael.pollak@mcgill.ca

1. Hopkins, B. D. *et al.* *Nature* **560**, 499–503 (2018).
2. Fruman, D. A. *et al.* *Cell* **170**, 605–635 (2017).
3. Philippon, H., Brochier-Armanet, C. & Perrière, G. *BMC Evol. Biol.* **15**, 226 (2015).
4. De Meyts, P. *BioEssays* **26**, 1351–1362 (2004).
5. Gallagher, E. J. *et al.* *Oncogene* **31**, 3213–3222 (2012).
6. Chi, M., Ye, Y., Zhang, X. D. & Chen, J. *Drug Design Dev. Ther.* **8**, 255–262 (2014).
7. Blouin, M. J., Zhao, Y., Birman, E. & Pollak, M. *Eur. J. Cancer* **48** (Suppl. 5), S151 (2012).
8. Erickson, N., Boscheri, A., Linke, B. & Huebner, J. *Med. Oncol.* **34**, 72 (2017).
9. Kilil-Drori, A. J., Azoulay, L. & Pollak, M. N. *Nature Rev. Clin. Oncol.* **14**, 85–99 (2017).
10. O'Brien, C. *et al.* *Clin. Cancer Res.* **16**, 3670–3683 (2010).
11. Kanarek, N. *et al.* *Nature* **559**, 632–636 (2018).

This article was published online on 6 August 2018.

Autism-like phenotype and risk gene mRNA deadenylation by CPEB4 mis-splicing

Alberto Parras^{1,2}, Héctor Anta^{3,4}, María Santos-Galindo^{1,2}, Vivek Swarup⁵, Ainara Elorza^{1,2}, José L. Nieto-González^{2,6}, Sara Picó^{1,2}, Ivó H. Hernández^{1,2,7}, Juan I. Díaz-Hernández^{1,2}, Eulàlia Belloch⁴, Annie Rodolosse⁴, Neelroop N. Parikshak⁵, Olga Peñagarikano^{5,8,9}, Rafael Fernández-Chacón^{2,6}, Manuel Irimia^{10,11}, Pilar Navarro³, Daniel H. Geschwind⁵, Raúl Méndez^{4,12*} & José J. Lucas^{1,2*}

Common genetic contributions to autism spectrum disorder (ASD) reside in risk gene variants that individually have minimal effect sizes. As environmental factors that perturb neurodevelopment also underlie idiopathic ASD, it is crucial to identify altered regulators that can orchestrate multiple ASD risk genes during neurodevelopment. Cytoplasmic polyadenylation element binding proteins 1–4 (CPEB1–4) regulate the translation of specific mRNAs by modulating their poly(A)-tails and thereby participate in embryonic development and synaptic plasticity. Here we find that CPEB4 binds transcripts of most high-confidence ASD risk genes. The brains of individuals with idiopathic ASD show imbalances in CPEB4 transcript isoforms that result from decreased inclusion of a neuron-specific microexon. In addition, 9% of the transcriptome shows reduced poly(A)-tail length. Notably, this percentage is much higher for high-confidence ASD risk genes, correlating with reduced expression of the protein products of ASD risk genes. An equivalent imbalance in CPEB4 transcript isoforms in mice mimics the changes in mRNA polyadenylation and protein expression of ASD risk genes and induces ASD-like neuroanatomical, electrophysiological and behavioural phenotypes. Together, these data identify CPEB4 as a regulator of ASD risk genes.

ASD is highly heritable¹. However, despite the importance of genetic determinants in ASD, environmental factors that perturb neurodevelopment also contribute to its development^{2–4}. A minority of ASD cases are syndromic forms caused by highly penetrant single-gene mutations or chromosomal abnormalities; these forms are often characterized by additional phenotypes, such as intellectual disability, epilepsy and craniofacial dysmorphology⁵. By contrast, most cases are idiopathic, with genetic causality residing in polygenic risk involving small effect-size variants in hundreds of genes^{5–8}. It is therefore important to investigate whether altered regulators in the brains of individuals with idiopathic ASD could orchestrate pathogenic changes in numerous ASD risk genes during neurodevelopment.

CPEB1–4 are RNA-binding proteins that repress or activate translation of mRNAs with CPE sequences in their 3' untranslated regions (UTRs) by inducing cytoplasmic shortening or elongation of their poly(A)-tails⁹. CPEBs were initially shown to regulate certain mRNAs in response to embryonic environmental clues, such as hormones^{9,10}; later, they were shown to be involved in learning and memory by modulating synaptic plasticity^{9,11,12}. As deletion of CPEB1 rescues the fragile X-like phenotype of FMRI knockout (KO) mice¹³, it has been suggested that manipulating CPEB1 might have therapeutic value for this monogenic X-linked intellectual disability syndrome, in which up to 50% of cases also show autistic features. However, whether CPEBs also contribute to the aetiology of a broader range of

neurodevelopmental disorders—including non-syndromic ASD—has not been studied.

ASD risk gene mRNAs bear CPEs and bind CPEB4

To investigate the CPEB-bound brain transcriptome in the context of a disease, we performed RNA immunoprecipitation (RIP) with CPEB1 and CPEB4 on striatal RNA from wild-type mice and from a mouse model of Huntington's disease in which altered CPEB1 and CPEB4 levels correlate with transcriptomic poly(A)-tail length changes (Extended Data Fig. 1a–c). Regardless of genotype, 7.9% of transcripts were bound only by CPEB4, 5.8% only by CPEB1 and 7.0% by both (Fig. 1a and Supplementary Table 1a). Enrichment of CPE sequences on the 3' UTRs of RIP-detected transcripts supported the specificity of this binding (Extended Data Fig. 1b). When we compared CPEB-specific targets with changes in polyadenylation associated with the Huntington's disease model, we found that CPEB4-specific mRNAs were enriched in deadenylated transcripts (Extended Data Fig. 1c). Notably, the largest fold change in this category was seen in *Auts2*, a gene linked to ASD¹⁴, and several high-confidence ASD risk genes (*Dyrk1a*, *Cul3*, and *Ptchd1*; categories 1–2 in the SFARI database of autism-associated genes (<https://gene.sfari.org/>)) were among the forty CPEB4 targets with the most prominent poly(A) shortening (fold change ≤ -3.0) (Extended Data Fig. 1d and Supplementary Table 1b). The enrichment of CPEB4-specific deadenylated mRNAs for SFARI

¹Centro de Biología Molecular 'Severo Ochoa' (CBMSO) CSIC/UAM, Madrid, Spain. ²Networking Research Center on Neurodegenerative Diseases (CIBERNED), Instituto de Salud Carlos III, Madrid, Spain. ³Cancer Research Program, Hospital del Mar Medical Research Institute (IMIM), Barcelona, Spain. ⁴Institute for Research in Biomedicine (IRB), Barcelona Institute of Science and Technology, Barcelona, Spain. ⁵Department of Neurology, Center for Autism Research and Treatment, Semel Institute, David Geffen School of Medicine, UCLA, Los Angeles, CA, USA. ⁶Instituto de Biomedicina de Sevilla (IBIS), Hospital Universitario Virgen del Rocío/CSIC/Universidad de Sevilla and Departamento de Fisiología Médica y Biofísica, Seville, Spain. ⁷Facultad de Ciencias, Departamento de Biología (Unidad Docente Fisiología Animal), Universidad Autónoma de Madrid, Madrid, Spain. ⁸Department of Pharmacology, School of Medicine, University of the Basque Country (UPV/EHU), Leioa, Spain. ⁹Centro de Investigación Biomédica en Red en Salud Mental (CIBERSAM), Madrid, Spain. ¹⁰Centre for Genomic Regulation (CRG), Barcelona Institute for Science and Technology, Barcelona, Spain. ¹¹Universitat Pompeu Fabra, Barcelona, Spain. ¹²Institució Catalana de Recerca i Estudis Avançats (ICREA), Barcelona, Spain. *e-mail: raul.mendez@irbbarcelona.org; jjlucas@cbm.csic.es

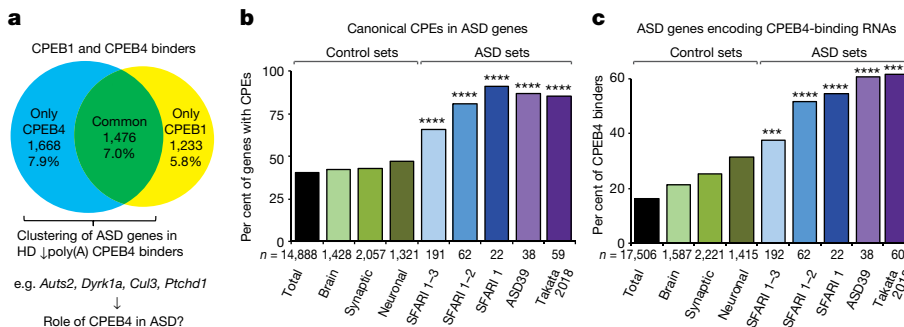


Fig. 1 | ASD risk gene mRNAs bear CPEs and bind CPEB4. **a**, Percentage of CPEB1- and/or CPEB4-binding transcripts in mouse striatum. HD, Huntington's disease. **b, c**, Percentage of transcripts with canonical CPEs (**b**) and bound by CPEB4 (**c**) in control gene sets and high-confidence ASD

genes (Extended Data Fig. 1e) led us to hypothesize that CPEB4 is involved in the expression of ASD risk genes.

We then analysed the incidence of CPEB4 binders in a compiled set of ASD genetic risk candidates from the SFARI database (Supplementary Table 2). CPEB4 binders were enriched in ASD risk genes and also in a smaller curated list of ASD-only genes, which cause ASD but not intellectual disability (Extended Data Fig. 1f; a weaker enrichment was also observed for CPEB1 target mRNAs). CPEB4 binders were also overrepresented within several functional co-expression modules that represent shared pathology in the ASD brain, as identified in previous microarray¹⁵ and RNA sequencing (RNA-seq)¹⁶ studies (Extended Data Fig. 1g).

Next, we found an increase in canonical CPEs in the 3' UTRs of mRNAs of ASD risk genes in the highest-confidence SFARI categories, in the 39 genes containing rare de novo protein-disrupting mutations identified in two whole-exome sequencing studies for simplex ASD^{17,18}, and in the equivalent 61 genes from a recent study¹⁹ ('ASD39' and 'Takata 2018' lists; Supplementary Table 2) when compared with multiple control gene sets (brain-, synapse- and neuron-enriched transcriptomes; Fig. 1b). This enrichment remained after all and brain-, neuron- and synapse-enriched genes were stratified with respect to the ASD genes for 5' UTR, coding sequence (CDS) or 3' UTR length, gene size, or ratio of neuronal-to-glial expression (Extended Data Fig. 1h and Supplementary Table 5). We then confirmed that most high-confidence ASD risk genes were CPEB4 targets (Fig. 1c). Together, these data show that mRNAs of the majority of high-confidence ASD risk genes contain CPEs and are bound by CPEB4.

CPEB4 alteration in idiopathic ASD

To assess whether CPEBs are altered in the brains of individuals with idiopathic ASD, we analysed transcript levels in RNA-seq data¹⁶ from post-mortem cortex (43 cases of idiopathic ASD, 63 neurotypical control individuals). We found no changes in mRNA expression for *CPEB1* or *CPEB2*, a slight decrease for *CPEB3* and a slight increase for *CPEB4* (Fig. 2a and Extended Data Fig. 2a). At the protein level, only CPEB4 was substantially altered in the brains of individuals with idiopathic ASD. More precisely, we found decreased levels of CPEB4 in young (35 years old or less) individuals with ASD (Fig. 2b and Extended Data Fig. 2b, c). This decrease, despite an increase in transcript levels, suggests disruption of the post-transcriptional autoamplification loop that regulates CPEB4 levels^{20,21} in line with the binding of CPEB4 to its own transcript (Supplementary Table 1a).

Splicing alterations^{15,22}, particularly of microexons²³, have been reported in ASD. We thus looked for potential splicing alterations in mRNAs of the different CPEBs in our published¹⁶ rMATS (replicate multivariate analysis of transcript splicing) analysis of cortical RNA-seq data. Only CPEB4 showed splicing alterations in ASD samples, involving different combinations of two consecutive alternatively spliced exons (Extended Data Fig. 2d); the 51-nucleotide exon 3 and the 24-nucleotide neuron-specific microexon (exon 4) (Fig. 2c).

risk genes (SFARI categories 1–3, ASD39 and Takata lists^{17–19}). **b, c**, One-sided Fisher's exact test, ***P < 0.05 compared to total, brain and synaptic transcriptomes, ****P < 0.05 compared to each control set.

To specifically investigate changes in the level of inclusion of these exons, we re-analysed the RNA-seq data using VAST-TOOLS (vertebrate alternative splicing and transcription tools)²⁴. This revealed less inclusion of exon 4 in the brains of individuals with ASD (change in per cent spliced in (ΔPSI) = -7.6, Extended Data Fig. 2e); as with the decrease in CPEB4 protein levels, this was stronger in individuals under 35 years old (ΔPSI = -8.8) (Fig. 2d). Notably, this microexon

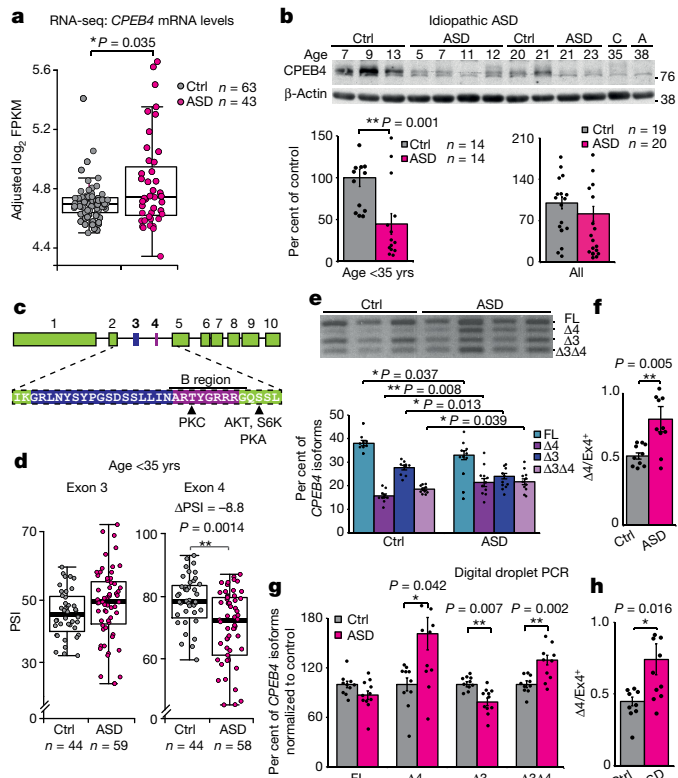


Fig. 2 | CPEB4 alterations in brains of individuals with idiopathic ASD. **a, b**, CPEB4 mRNA (**a**) and protein levels (**b**) in cortex. Ctrl, control. **c**, Alternatively spliced exons (3 and 4) of CPEB4. Arrowheads show putative phosphorylation sites. **d**, PSI for exons 3 and 4. **e–h**, RT-PCR in brain tissue from young (below 35 years old) controls (n = 10) and individuals with idiopathic ASD (n = 11). **e, f**, With external primers. **e**, Percentage of CPEB4 isoforms. **f**, Ratio of isoforms without exon 4 to those with exon 4 ($\Delta 4/\text{Ex}4^+$). **g, h**, Digital-droplet PCR. **g**, CPEB4 isoform percentage normalized to control. **h**, $\Delta 4/\text{Ex}4^+$ ratio. FL, full-length CPEB4. For gel source data, see Supplementary Fig. 1. **a, d, f, h**, Two-sided Mann-Whitney-Wilcoxon test. **b, e, g**, Two-sided unpaired t-test. Box plots: centre line shows median; box shows 25th and 75th percentiles; whiskers show minimum and maximum values. Bar graphs show mean \pm s.e.m.

encodes the 8-amino-acid B region²⁵, which adds potential motifs for post-translational modifications, such as phosphorylation by AKT, S6K, PKA or PKC (NETPHOS 2.0)²⁵ (Fig. 2c). By contrast, individuals under 35 years old with ASD showed a tendency to include more exon 3 (Fig. 2d).

We used isoform-specific exon-junction RNA-seq reads to estimate the relative abundance of the four possible isoforms resulting from alternative splicing of exons 3 and 4 (full-length CPEB4, CPEB4Δ3, CPEB4Δ4 and CPEB4Δ3Δ4). This revealed a significant ($P=0.013$) increase in the CPEB4Δ4 transcript in individuals with ASD (Extended Data Fig. 2f). PCR with reverse transcription (RT-PCR) using primers that simultaneously amplify the four isoforms confirmed the increase in Δ4 transcripts (CPEB4Δ4 and CPEB4Δ3Δ4) at the expense of isoforms containing exon 4 (Ex4⁺; full-length CPEB4 and CPEB4Δ3) in young individuals with ASD (Fig. 2e, f), a pattern that was further validated using conventional and digital-droplet absolute qRT-PCR (Fig. 2g, h and Extended Data Fig. 2g–i). Overall, these data demonstrate an increased Δ4/Ex4⁺ CPEB4 transcript ratio in individuals with ASD, together with slightly increased total RNA and decreased total protein levels.

Deadenylation of ASD gene mRNAs in ASD

We next investigated potential genome-wide changes in poly(A)-tail length in mRNA from post-mortem prefrontal cortex tissue from young control individuals and individuals with idiopathic ASD (Extended Data Fig. 3a). In ASD samples, 10.2% and 9.1% of transcripts showed poly(A)-tail lengthening and shortening, respectively (Fig. 3a ‘Total’ column and Supplementary Table 3). Notably, transcripts that were deadenylated in the brains of individuals with ASD were substantially enriched in CPEB4 binders (Extended Data Fig. 3b). Gene ontology analysis showed ‘oxytocin signalling pathway’—which has been implicated in social behaviour and proposed to be therapeutically relevant to ASD²⁶—as the most significantly enriched term (among deadenylated CPEB4-binding transcripts, Extended Data Fig. 3c). The SFARI ASD risk genes showed a global deadenylation signature (Fig. 3a and Extended Data Fig. 3d, e). Notably, the poly(A)-tail shortening of ASD genes was progressively exacerbated with increased confidence in causality, as defined by SFARI curated gene categories (Fig. 3a). This was not a by-product of enrichment of brain-, neuron- or synapse-specific transcripts, biased 5' UTR, CDS or 3' UTR lengths, gene sizes or the ratio of neuronal-to-glial expression (Extended Data Fig. 3f, g and Supplementary Table 5). As expected, CPEB4 binders were overrepresented among deadenylated SFARI category 1–3 genes (Fig. 3b), thus suggesting that CPEB4 is involved in the observed deadenylation of ASD genes.

We next analysed the protein levels of CPEB4-bound ASD risk genes in cortical tissue from young people with idiopathic ASD (Fig. 3c). The four studied SFARI category 1–2 genes (*PTEN*, *DYRK1A*, *FOXP1* and *WAC*) that showed poly(A) shortening (*PTEN* transcript deadenylation also validated by high-resolution poly(A) tail assay (Hire-PAT), Extended Data Fig. 3h) showed decreased protein levels in the brains of individuals with ASD despite unchanged transcript levels (Fig. 3d). A similar pattern was observed for tested SFARI category 3 genes that showed a trend towards deadenylation (*AUTS2*, *RBFOX1* and *ZBTB20*). Furthermore, *PCDH9*, a SFARI category 4 gene with one of the most prominent shortenings in poly(A)-tail length, also showed decreased protein levels despite increased transcript levels (Fig. 3c, d). Unaltered protein levels of neuron- and glia-specific genes such as *CALB1*, *DRD2*, *SNAP25*, *TUBB3* and *IBA1* (also known as *AIF1*), the poly(A) tails of which were not changed in ASD (Extended Data Fig. 3i), rule out an underlying non-specific decrease in protein translation in ASD. Together, these results are consistent with Δ4 CPEB4 isoforms favouring deadenylation (and concomitant decreased protein levels) of target transcripts, including CPEB4 itself, and multiple ASD risk genes.

These data indicate that ASD risk genes are enriched in CPEB4-containing and CPEB4-binding transcripts. Moreover, the brains of individuals with idiopathic ASD show (i) CPEB4 mis-splicing (exon 4

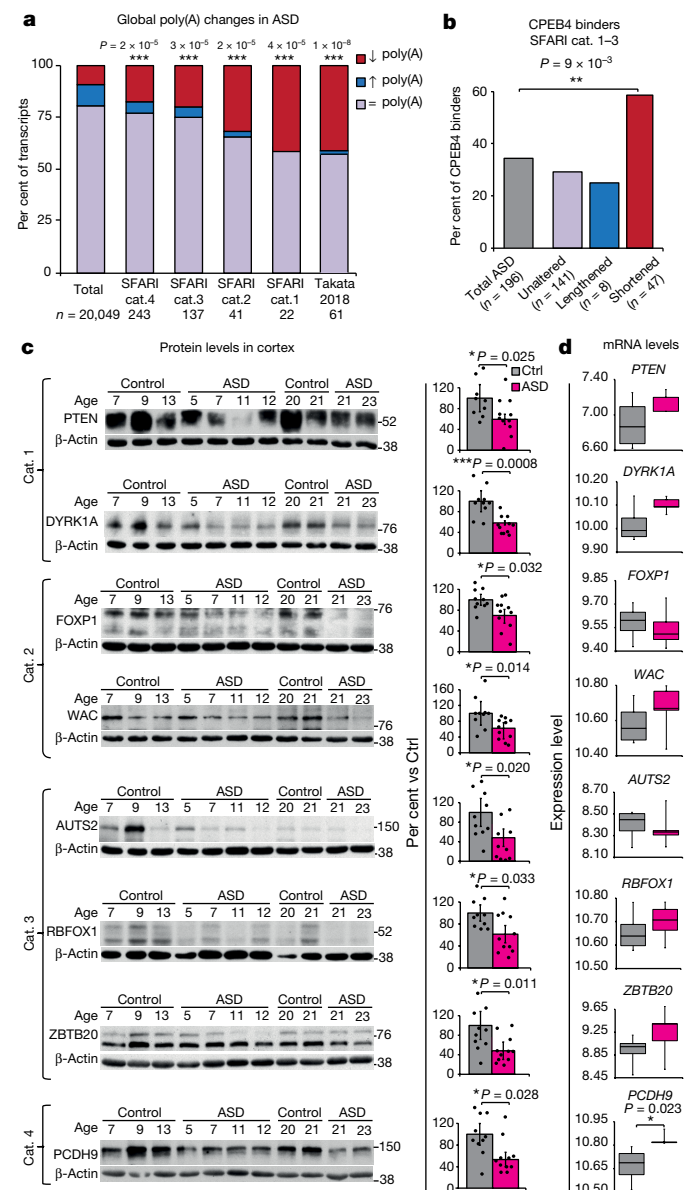


Fig. 3 | ASD risk gene mRNA deadenylation and decreased protein levels. **a**, Poly(A)-tail length changes in cortex from individuals with ASD cases ($n=6$) compared with control ($n=5$) in whole transcriptome (total) and in ASD gene lists. **b**, CPEB4 binders in ASD genes grouped according to poly(A)-tail change. **c**, Protein levels in cortex of individuals with idiopathic ASD ($n=11$) and control individuals ($n=10$) under 35 years old. **d**, mRNA levels in individuals with ASD ($n=6$) and control individuals ($n=5$). **a**, One-sided Fisher's exact test, P values for ASD deadenylated transcripts versus total. **b**, One-sided Fisher's exact test. **c, d**, Two-sided unpaired t -test. Box plots: centre line shows median; box shows 25th and 75th percentiles; whiskers show minimum and maximum values. Bar graphs show mean \pm s.e.m.

skipping) and reduced CPEB4 protein levels, (ii) a molecular signature of mRNA deadenylation that markedly affects high-confidence ASD risk genes and (iii) concomitant decreased protein levels of multiple CPEB4-target and deadenylated ASD risk gene products.

ASD-like poly(A) changes in TgCPEB4Δ4 mice

To determine whether changes in CPEB4 splicing and/or protein levels can cause the observed changes in polyadenylation and translation of ASD risk gene mRNAs, we used different mouse models to mimic the changes in CPEB4 observed in the brains of individuals with idiopathic ASD. First, we used two models to emulate the decreased CPEB4

protein levels: a heterozygous CPEB4 KO^{GT/+} model²⁷ that shows a partial reduction in CPEB4 protein with unaltered isoform ratios (Extended Data Fig. 4a); and a homozygous CPEB4 KO model²⁰ that shows full suppression of CPEB4 protein (Extended Data Fig. 4b). Both models showed similar changes in global transcript polyadenylation, but in the opposite direction to what was observed in ASD (Extended Data Fig. 4c–f and Supplementary Table 4). CPEB4-deficient mice showed prominent poly(A) lengthening in ASD risk genes (Extended Data Fig. 4c–h). Therefore, we concluded that the decreased polyadenylation of ASD risk gene mRNAs in the brains of individuals with ASD was not likely to be a consequence of their reduced CPEB4 levels—on the contrary, decreased CPEB4 by itself had the opposite effect.

To explore the effects of the increase in $\Delta 4$ CPEB4 transcript isoforms, we generated mice with conditional neuron-specific overexpression of the CPEB4 $\Delta 4$ transcript (TgCPEB4 $\Delta 4$ mice, which are double transgenic: CamKII-tTA + TetO- β Gal/CPEB4 $\Delta 4$; Fig. 4a and Extended Data Fig. 5a). TgCPEB4 $\Delta 4$ mice did not display perinatal lethality—based on live births—and were indistinguishable from their control (wild-type and single-transgenic) littermates from birth to weaning (Extended Data Fig. 5a). However, at weaning (3 weeks), up to 40% of TgCPEB4 $\Delta 4$ mice began to develop cranial dysmorphology suggestive of hydrocephalus. TgCPEB4 $\Delta 4$ mice with cranial dysmorphology died prematurely, with a peak of mortality at 7 weeks of age (Extended Data Fig. 5b). TgCPEB4 $\Delta 4$ mice with normal cranial morphology did not present any obvious abnormality nor die prematurely, but they were smaller than their control littermates starting at 3 weeks of age (Extended Data Fig. 5c). In the remaining study, analysis was restricted to TgCPEB4 $\Delta 4$ mice with normal cranial morphology. Transgene expression in TgCPEB4 $\Delta 4$ mice takes place in neurons of forebrain structures, such as the cortex and striatum (Extended Data Fig. 5d, e). Notably, overexpression of CPEB4 $\Delta 4$ transcript resulted in a $\Delta 4/Ex4^+$ transcript ratio (Fig. 4b, c) similar to that observed in brains of individuals with idiopathic ASD (Fig. 2h). Total CPEB4 protein levels in TgCPEB4 $\Delta 4$ mice were moderately increased in young adults (1.5 months), were not increased at 12 months and showed a tendency to decrease at 2 years, despite increased transcript levels at all ages (Extended Data Fig. 5f, g). Likewise, as in the brains of humans with ASD, the other CPEBs were essentially unaltered in TgCPEB4 $\Delta 4$ mice (Extended Data Fig. 5f, g). Notably, global poly(A)-tail length changes in TgCPEB4 $\Delta 4$ mice overlapped significantly ($P = 1 \times 10^{-110}$) with those observed in individuals with idiopathic ASD (Fig. 4d, Supplementary Table 4 and Extended Data Fig. 6a) and replicated the predominant deadenylation of ASD risk genes in a pattern that correlated with increasing ASD risk gene confidence (Fig. 4e). The latter result was robust to different stratification analyses (Extended Data Fig. 6b, c and Supplementary Table 5). Thus, a CPEB4 transcript isoform imbalance in mice that mimics the increase in $\Delta 4$ isoforms observed in individuals with ASD was sufficient to induce the ASD-associated poly(A) signature.

As in the brains of humans with ASD, the shortened poly(A) tail length of ASD risk gene transcripts correlated with the reduction in protein levels in the cortex and striatum of TgCPEB4 $\Delta 4$ mice (Fig. 4f and Extended Data Fig. 6d). *Zbtb20*, *Tnrc6b*, *Chd2*, *Foxp1*, *Wac*, *Auts2* and *Gpc6* were among the deadenylated SFARI category 1–4 genes (*Auts2* deadenylation was also validated by Hire-PAT, Extended Data Fig. 6e) whose transcripts are bound by CPEB4, and they all showed decreases in protein level without decreases in transcript level (Fig. 4f, g and Supplementary Table 4). It is worth noting that expression of RBFOX1 protein—one of the few splicing factors that enable microexon processing in neurons²⁸ and that is known to regulate alternative splicing of CPEB4²⁹—was also decreased in TgCPEB4 $\Delta 4$ mice (Fig. 4f) and that *Cpeb4* itself showed poly(A) tail shortening in TgCPEB4 $\Delta 4$ mice (Supplementary Table 4), which may explain why protein levels do not match the increased transcript levels. The lack of changes in protein levels of non-deadenylated neuron- and glia-specific genes rules out a non-specific decrease in protein translation efficiency in TgCPEB4 $\Delta 4$ mice (Extended Data Fig. 6f).

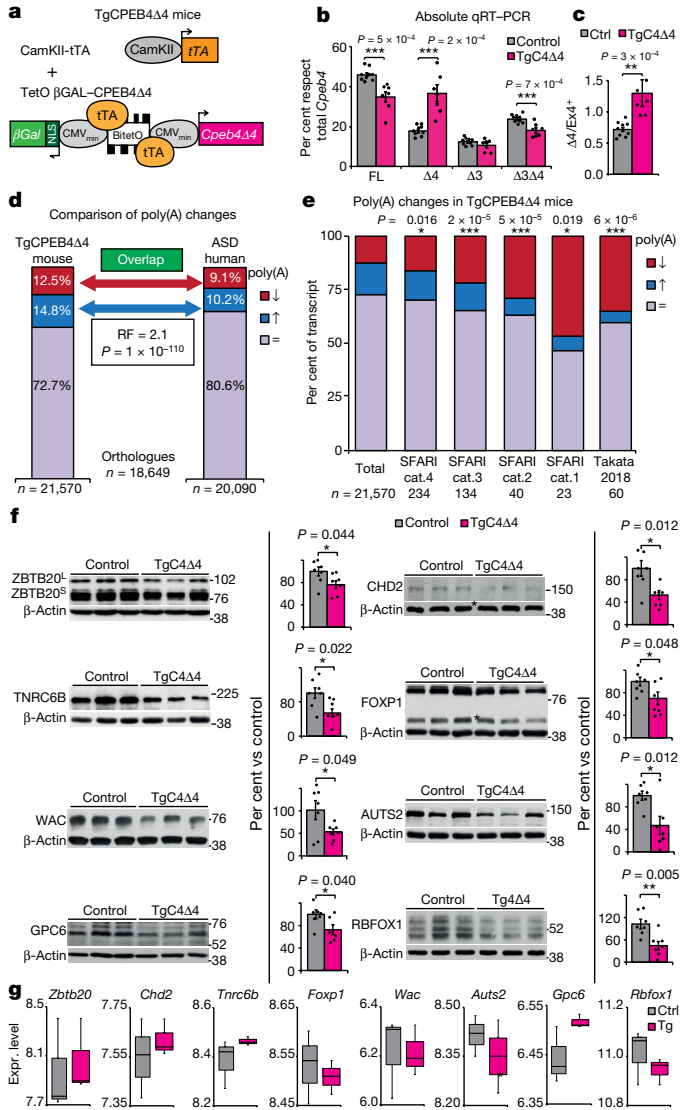


Fig. 4 | ASD-like poly(A) changes in TgCPEB4 $\Delta 4$ mice. **a**, Transgenesis construct design. **b, c**, Splicing isoform percentage (**b**) and $\Delta 4/Ex4^+$ ratio (**c**) of CPEB4 in striatum of 1.5-month-old control ($n = 9$) and TgCPEB4 $\Delta 4$ ($n = 7$) mice. **d**, Comparison of poly(A) changes in individuals with ASD and TgCPEB4 $\Delta 4$ mice; RF, representation factor. **e**, Transcripts with poly(A)-tail changes in cortex and striatum of control versus TgCPEB4 $\Delta 4$ mice ($n = 3$) in whole transcriptome and ASD gene lists. **f**, Protein levels in cortex of 1.5-month-old control and TgCPEB4 $\Delta 4$ mice ($n = 7$). **g**, mRNA levels in cortex of 1.5-month-old control and TgCPEB4 $\Delta 4$ mice ($n = 3$). **b, f, g**, Two-sided unpaired *t*-test. **c, f**, Two-sided Mann–Whitney–Wilcoxon test. **d**, Hypergeometric test. **e**, One-sided Fisher's exact test, *P* values for ASD deadenylated transcripts versus total. Box plots: centre line shows median; box shows 25th and 75th percentiles; whiskers show minimum and maximum values. Bar graphs show mean \pm s.e.m.

We also generated TgCPEB4 $\Delta 4$ mice in a CPEB4 knockout heterozygous background (Extended Data Fig. 7a). Notably, the CPEB4 transcript isoform imbalance persisted in TgCPEB4 $\Delta 4$ /CPEB4-KO^{GT/+} mice without increased CPEB4 protein levels (Extended Data Fig. 7b, c). ASD genes that showed decreased protein expression in TgCPEB4 $\Delta 4$ mice showed similar decreases in protein levels in TgCPEB4 $\Delta 4$ /CPEB4-KO^{GT/+} mice, whereas control neuronal and glial genes were unaltered (Extended Data Fig. 7d, e). These data strongly suggest that the observed effects are due to the transcript isoform imbalance rather than to increased CPEB4 protein levels. Consistent with this, we did not observe decreased protein levels of ASD risk genes in CPEB4-KO^{GT/+} mice, which only have decreased CPEB4 protein expression (Extended Data Fig. 7f).

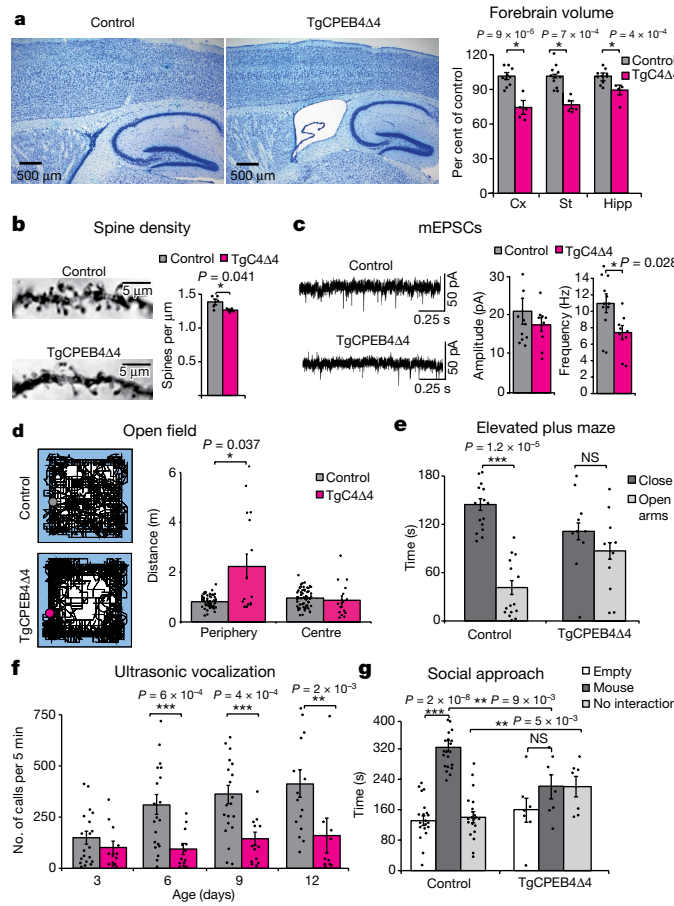


Fig. 5 | ASD-like phenotypes in TgCPEB4 $\Delta 4$ mice. **a**, Forebrain volume in control ($n=10$) and TgCPEB4 $\Delta 4$ ($n=5$) mice. Cx, cortex; St, striatum; Hipp, hippocampus. **b**, Spine density in layer 2/3 pyramidal neurons ($n=14$ cells from 5 controls, $n=12$ cells from 4 TgCPEB4 $\Delta 4$ mice). **c**, mEPSCs recorded from somatosensory cortical pyramidal neurons ($n=11$ cells from 5 controls, $n=9$ cells from 5 TgCPEB4 $\Delta 4$ mice). **d**, Distance travelled in open field by control ($n=60$) and TgCPEB4 $\Delta 4$ mice ($n=16$). **e**, Time spent in closed and open arms of elevated plus maze for control ($n=15$) and TgCPEB4 $\Delta 4$ mice ($n=10$). **f**, Ultrasonic calls made by control ($n=20$) and TgCPEB4 $\Delta 4$ mice ($n=13$) at postnatal day 3 (P3), P6, P9 and P12. **g**, Time spent interacting with empty cage and unfamiliar mouse in social approach test for control ($n=20$) and TgCPEB4 $\Delta 4$ mice ($n=7$). **a–c**, **f**, Two-sided unpaired *t*-test. **e**, Two-sided paired *t*-test. **g**, Two-sided Wilcoxon signed-rank test. NS, not significant. Data are mean \pm s.e.m.

ASD-related phenotypes of TgCPEB4 $\Delta 4$ mice

We then tested whether TgCPEB4 $\Delta 4$ mice showed potential ASD-related anatomical, electrophysiological and/or behavioural abnormalities. We observed reduced brain weight in TgCPEB4 $\Delta 4$ mice (Extended Data Fig. 8a) and in TgCPEB4 $\Delta 4$ /CPEB4-KO $^{GT/+}$ mice, but not in CPEB4-KO $^{GT/+}$ mice, with volume reductions in the cortex, striatum and hippocampus together with lateral ventricle enlargement (Fig. 5a). There was also a twofold increase in caspase-3-positive cells, without decreased neuronal density (Extended Data Fig. 8b, c). Dendritic spine dysgenesis is frequent in humans with ASD and in mouse models³⁰. We found a 9.2% decrease in total spine density in TgCPEB4 $\Delta 4$ mice (Fig. 5b) but not in CPEB4-KO $^{GT/+}$ mice (Extended Data Fig. 8d). Whole-cell recordings of miniature excitatory postsynaptic currents (mEPSCs) in layer V pyramidal neurons of somatosensory cortex revealed no differences in the mean amplitude but a 32% reduction in the mean frequency in TgCPEB4 $\Delta 4$ mice (Fig. 5c), resembling mice with neurexin dysfunction³¹. No such electrophysiological alterations were observed in CPEB4-KO $^{GT/+}$ mice (Extended Data Fig. 8e).

Together with the deficit in spine density, these findings are compatible with a presynaptic shortfall in neurotransmitter release and/or a reduction in the number of excitatory synapses.

We then assayed behaviour. In the open field test, TgCPEB4 $\Delta 4$ mice showed stereotypical running at the cage periphery (Fig. 5d); this was not due to anxiety-related behaviour because, in the elevated plus-maze test, TgCPEB4 $\Delta 4$ mice showed reduced levels of anxiety (Fig. 5e). In the ultrasonic vocalization test, TgCPEB4 $\Delta 4$ mice emitted substantially fewer ultrasonic vocalizations than control littermates (Fig. 5f). In the social approach test, TgCPEB4 $\Delta 4$ mice did not show a preference to interact with the cage containing a mouse over the empty one, indicating a dysfunction in sociability (Fig. 5g). TgCPEB4 $\Delta 4$ /CPEB4-KO $^{GT/+}$ mice, but not CPEB4-KO $^{GT/+}$ mice, mimicked these ASD-like behaviours (Extended Data Fig. 8f–h), demonstrating that the behavioural changes are due to the altered transcript isoform ratio and not to altered total CPEB4 protein levels. Notably, TgCPEB4 $\Delta 4$ mice treated with doxycycline to express the transgene only during embryonic and early postnatal life (ON/OFF-TgCPEB4 $\Delta 4$ mice) displayed stereotypic running in the open field test and the deficit in social approach, whereas TgCPEB4 $\Delta 4$ mice treated to express the transgene only after the age of 3 weeks (OFF/ON-TgCPEB4 $\Delta 4$ mice) did not (Extended Data Fig. 9), indicating that these ASD-like phenotypes in TgCPEB4 $\Delta 4$ mice originate during development. Together, the stereotypic running, the ultrasonic vocalization communication deficit and the diminished social interaction indicate that TgCPEB4 $\Delta 4$ mice display components of autistic-like behaviour that have been seen in multiple mouse models containing single ASD mutations.

Hundreds of minimally penetrant mutations have been implicated in ASD⁶, and only a few of these will coincide in a given individual. Accordingly, environment-triggered misexpression of multiple ASD-related genes may contribute to the development of ASD⁴, and CPEB4 is well positioned to act as one such regulator driven by perturbation of neurodevelopment. It is conceivable that development-modifying factors that have been proposed as non-genetic causes of ASD^{1,32} could modulate the developmental functions of CPEB4 by inducing its mis-splicing. Prenatal cytomegalovirus infection—which has been related to ASD³³—has been shown to remodel RNA splicing and polyadenylation in a CPEB1-dependent manner and to increase CPEB4 expression³⁴.

The molecular signature of transcript deadenylation in the brains of individuals with idiopathic ASD, combined with proteomics data and the identification of gene modules that are dysregulated in these brains, may identify additional risk genes or pathophysiological pathways. Finally, preclinical studies have mainly relied on mouse models of monogenic syndromic ASD. As CPEB4 mis-splicing orchestrates the expression of a plethora of ASD risk genes, preclinical testing in TgCPEB4 $\Delta 4$ mice might be relevant for a wide range of ASDs.

Online content

Any Methods, including any statements of data availability and Nature Research reporting summaries, along with any additional references and Source Data files, are available in the online version of the paper at <https://doi.org/10.1038/s41586-018-0423-5>.

Received: 12 May 2017; Accepted: 26 June 2018;

Published online 15 August 2018.

1. Hallmayer, J. et al. Genetic heritability and shared environmental factors among twin pairs with autism. *Arch. Gen. Psychiatry* **68**, 1095–1102 (2011).
2. Sandin, S. et al. The familial risk of autism. *J. Am. Med. Assoc.* **311**, 1770–1777 (2014).
3. De Rubeis, S. & Buxbaum, J. D. Genetics and genomics of autism spectrum disorder: embracing complexity. *Hum. Mol. Genet.* **24** (R1), R24–R31 (2015).
4. Kim, Y. S. & Leventhal, B. L. Genetic epidemiology and insights into interactive genetic and environmental effects in autism spectrum disorders. *Biol. Psychiatry* **77**, 66–74 (2015).
5. Szatmari, P. & Zoghbi, H. Y. Lessons learned from studying syndromic autism spectrum disorders. *Nat. Neurosci.* **19**, 1408–1417 (2016).
6. Gaugler, T. et al. Most genetic risk for autism resides with common variation. *Nat. Genet.* **46**, 881–885 (2014).

7. Geschwind, D. H. & State, M. W. Gene hunting in autism spectrum disorder: on the path to precision medicine. *Lancet* **14**, 1109–1120 (2015).
8. Willsey, A. J. & State, M. W. Autism spectrum disorders: from genes to neurobiology. *Curr. Opin. Neurobiol.* **30**, 92–99 (2015).
9. Ivshina, M., Lasko, P. & Richter, J. D. Cytoplasmic polyadenylation element binding proteins in development, health, and disease. *Annu. Rev. Cell Dev. Biol.* **30**, 393–415 (2014).
10. Sarkissian, M., Mendez, R. & Richter, J. D. Progesterone and insulin stimulation of CPEB-dependent polyadenylation is regulated by Aurora A and glycogen synthase kinase-3. *Genes Dev.* **18**, 48–61 (2004).
11. Si, K. et al. A neuronal isoform of CPEB regulates local protein synthesis and stabilizes synapse-specific long-term facilitation in aplysia. *Cell* **115**, 893–904 (2003).
12. Fioriti, L. et al. The persistence of hippocampal-based memory requires protein synthesis mediated by the prion-like protein CPEB3. *Neuron* **86**, 1433–1448 (2015).
13. Udagawa, T. et al. Genetic and acute CPEB1 depletion ameliorate fragile X pathophysiology. *Nat. Med.* **19**, 1473–1477 (2013).
14. Sultana, R. et al. Identification of a novel gene on chromosome 7q11.2 interrupted by a translocation breakpoint in a pair of autistic twins. *Genomics* **80**, 129–134 (2002).
15. Voineagu, I. et al. Transcriptomic analysis of autistic brain reveals convergent molecular pathology. *Nature* **474**, 380–384 (2011).
16. Parikshak, N. N. et al. Genome-wide changes in lncRNA, splicing, and regional gene expression patterns in autism. *Nature* **540**, 423–427 (2016).
17. Iossifov, I. et al. The contribution of *de novo* coding mutations to autism spectrum disorder. *Nature* **515**, 216–221 (2014).
18. De Rubeis, S. et al. Synaptic, transcriptional and chromatin genes disrupted in autism. *Nature* **515**, 209–215 (2014).
19. Takata, A. et al. Integrative analyses of *de novo* mutations provide deeper biological insights into autism spectrum disorder. *Cell Reports* **22**, 734–747 (2018).
20. Calderone, V. et al. Sequential functions of CPEB1 and CPEB4 regulate pathologic expression of vascular endothelial growth factor and angiogenesis in chronic liver disease. *Gastroenterology* **150**, 982–997 (2016).
21. Igéa, A. & Méndez, R. Meiosis requires a translational positive loop where CPEB1 ensures its replacement by CPEB4. *EMBO J.* **29**, 2182–2193 (2010).
22. Xiong, H.Y. et al. The human splicing code reveals new insights into the genetic determinants of disease. *Science* **347**, 1254806 (2015).
23. Irimia, M. et al. A highly conserved program of neuronal microexons is misregulated in autistic brains. *Cell* **159**, 1511–1523 (2014).
24. Tapial, J. et al. An atlas of alternative splicing profiles and functional associations reveals new regulatory programs and genes that simultaneously express multiple major isoforms. *Genome Res.* **27**, 1759–1768 (2017).
25. Theis, M., Si, K. & Kandel, E. R. Two previously undescribed members of the mouse CPEB family of genes and their inducible expression in the principal cell layers of the hippocampus. *Proc. Natl. Acad. Sci. USA* **100**, 9602–9607 (2003).
26. Yamasue, H. & Domes, G. Oxytocin and autism spectrum disorders. *Curr. Top. Behav. Neurosci.* **35**, 449–465 (2018).
27. Hu, W., Yuan, B. & Lodish, H. F. Cpeb4-mediated translational regulatory circuitry controls terminal erythroid differentiation. *Dev. Cell* **30**, 660–672 (2014).
28. Li, Y. I., Sanchez-Pulido, L., Haerty, W. & Ponting, C. P. RBFOX and PTBP1 proteins regulate the alternative splicing of micro-exons in human brain transcripts. *Genome Res.* **25**, 1–13 (2015).
29. Pedrotti, S. et al. The RNA-binding protein Rbfox1 regulates splicing required for skeletal muscle structure and function. *Hum. Mol. Genet.* **24**, 2360–2374 (2015).
30. Chen, J. A., Peñagarikano, O., Belgard, T. G., Swarup, V. & Geschwind, D. H. The emerging picture of autism spectrum disorder: genetics and pathology. *Annu. Rev. Pathol.* **10**, 111–144 (2015).
31. Rabaneda, L. G., Robles-Lanuza, E., Nieto-González, J. L. & Scholl, F. G. Neurexin dysfunction in adult neurons results in autistic-like behavior in mice. *Cell Reports* **8**, 338–346 (2014).
32. Kalkbrenner, A. E., Schmidt, R. J. & Penlesky, A. C. Environmental chemical exposures and autism spectrum disorders: a review of the epidemiological evidence. *Curr. Probl. Pediatr. Adolesc. Health Care* **44**, 277–318 (2014).
33. Maeyama, K. et al. Congenital cytomegalovirus infection in children with autism spectrum disorder: systematic review and meta-analysis. *J. Autism Dev. Disord.* **48**, 1483–1491 (2018).
34. Batra, R. et al. RNA-binding protein CPEB1 remodels host and viral RNA landscapes. *Nat. Struct. Mol. Biol.* **23**, 1101–1110 (2016).

Acknowledgements This work was supported by grants: ISCIII-CiberNed-PI2013/09 & -PI2015-2/06 (J.J.L., R.F.-C.), FEDER-PI14/00125 & -PI17/00199 (P.N.), MINECO-SAF2012-34177 & -SAF2015-65371-R (J.J.L.), FEDER-BFU2014-54122-P (R.M.), -BFU2014-55076-P (M.I.), -BFU2016-76050-P (R.F.-C.), -SEV-2012-0208 to CRG by European Union FEDER (M.I.); NIMH 5R37 MH060233, 5R01 MH09714 and 5R01 MH100027 (D.H.G.); Junta de Andalucía-P12-CTS-2232 & -CTS-600 (R.F.-C.); Generalitat de Catalunya-2014/SGR/143 (P.N.); ERC-StG-LS2-637591 (M.I.); and from Fundación Botín-Banco Santander/Santander Universities Global Division, Fundación BBVA, and Fundación Ramón Areces. A.P. was recipient of a MICINN FPI-fellowship; N.N.P. was supported by the NRSA F30 MH099886, UCLA Medical Scientist Training Program and V.S. by a Larry Hillblom Postdoctoral Fellowship. We thank the computing facilities of Extremadura Research Centre for Advanced Technologies (CETA-CIEMAT/Government of Spain), which is funded by ERDF. Tissue, biological specimens or data used in this research were obtained from the Autism BrainNet (formerly the Autism Tissue Program), which is sponsored by the Simons Foundation, and the University of Maryland Brain and Tissue Bank (a component of the NIH NeuroBioBank). We thank the patients and families who participated in the tissue donation programs; R. García-Escudero for bioinformatics advice; M. Lucas for technical assistance; and the following core facilities: CBMSO-Genomics & Massive Sequencing, CBMSO-Animal Facility, CBMSO-Confocal Microscopy, CBMSO-CNB Mouse Transgenesis, CNB-Proteomics, IRB-Functional Genomic and IRB-Bioinformatics/Biostatistics.

Reviewer information *Nature* thanks R. Kelleher, N. Sonnenberg and the other anonymous reviewer(s) for their contribution to the peer review of this work.

Author contributions A.P. contributed to study design and was involved in all assays and data collection. H.A. and E.B. contributed to RIP and PolyU chromatography experiments and analysed data from doxycycline-treated mice. M.S.-G., S.P. and I.H.H. performed western blotting and qRT-PCR analysis. J.L.N.-G. performed electrophysiological recordings. A.R. optimized microarray processing. V.S., A.E., J.I.D.-H., N.N.P. and M.I. performed bioinformatics analyses. R.F.-C., P.N., O.P., M.I., R.M. and D.H.G. made intellectual contributions to experimental design and discussion. D.H.G., R.M. and J.J.L. directed the study and designed experiments. J.J.L. wrote the paper with input from all authors.

Competing interests The authors declare no competing interests.

Additional information

Extended data is available for this paper at <https://doi.org/10.1038/s41586-018-0423-5>.

Supplementary information is available for this paper at <https://doi.org/10.1038/s41586-018-0423-5>.

Reprints and permissions information is available at <http://www.nature.com/reprints>.

Correspondence and requests for materials should be addressed to R.M. or J.J.L.

Publisher's note: Springer Nature remains neutral with regard to jurisdictional claims in published maps and institutional affiliations.

METHODS

Human brain tissue samples. Brain specimens from the frontal and temporal cortex of individuals with ASD and control individuals used in immunoblotting, RNA sequencing, absolute qRT-PCR, digital-droplet PCR and poly(U) chromatography were provided by University of Maryland Brain and Tissue Bank, the NIH NeuroBioBank (NBB) and the Autism Tissue Program (ATP) Brain Bank at The Harvard Brain and Tissue Bank. Written informed consent for brain removal after death for diagnostic and research purposes was obtained from brain donors and/or next of kin. Brain sample and donor metadata are available in Supplementary Table 6.

Animals. We used R6/1 mice transgenic for the human exon-1-Htt gene³⁵ as a mouse model of Huntington's disease because our unpublished results show that these mice have altered levels of CPEBs (specifically CPEB1 and CPEB4), which correlate with changes in the poly(A)-tail length of numerous mRNAs. R6/1 mice were in a B6CBAF1/J background. Heterozygous CPEB4 KO^{GT/+} mice²⁷ contain a gene trap between exons 1 and 2 that prevents formation of the full-length CPEB4 protein while allowing expression of the N-terminal low complexity domain (LCD)³⁶, thus resulting in a partial reduction in CPEB4 protein. CPEB4 KO mice²⁰ contain homozygous deletion of constitutive exon 2, resulting in a premature stop codon and full suppression of CPEB4 protein expression. CamkII-tTA (tTA)³⁷, CPEB4 KO^{GT/+} and CPEB4 KO mice were in a C57BL/6J background. Conditional mice expressing human CPEB4 lacking exon 4 (TgCPEB4Δ4) were generated (for details, see 'Generation of TgCPEB4Δ4 mice' below) for this study and used in a C57BL/6J background. All mice were housed in the CBMSO animal facility. Mice were housed four per cage with food and water available ad libitum and maintained in a temperature-controlled environment on a 12 h–12 h light–dark cycle with light onset at 08:00. Animal housing and maintenance protocols followed local authority guidelines. Animal experiments were performed under protocols (P15/P16/P18/P22) approved by the Centro de Biología Molecular Severo Ochoa Institutional Animal Care and Utilization Committee (Comité de Ética de Experimentación Animal del CBM, CEEA-CBM), and Comunidad de Madrid PROEX 293/15.

RIP. Four male wild-type and R6/1 mice (HD mice) were killed by cervical dislocation at the age of 7–8 months. Total striatum (St) was quickly dissected on an ice-cold plate and cut into pieces. The pool of the four wild-type or R6/1 striata was washed twice with phosphate buffer solution (PBS), crosslinked with 0.5% formaldehyde in PBS for 7 min at room temperature and treated with glycine 1 M for 5 min. After two washes with cold PBS, pooled samples were homogenized in lysis buffer (50 mM Tris, pH 8.0, 150 mM NaCl, 1% NP-40, 0.5% deoxycholate, 0.1% SDS, 1 mM EDTA, protease inhibitor (Complete, Roche, 11697498001), RNase inhibitor (Ribolock, Life Technologies, EO0381)) and centrifuged at 13,000g for 10 min at 4°C. Dynabeads protein A (Life Technologies, 10001D) were washed twice with PBS and incubated with anti-CPEB4 antibody (10 µg, Abcam, ab83009), anti-CPEB1 antibody (5 µg, Proteintech, 13274-1-AP) or rabbit IgG (5 µg, Sigma, I5006) for 2 h. Next, dynabeads were washed once with PBS and twice with triethanolamine 0.2 M pH 8.2, incubated with dimethyl pimelimidate 20 mM for 30 min, treated with Tris 50 mM pH 8.0 and washed twice with lysis buffer. Lysates were precleared with unconjugated dynabeads for 20 min at 4°C in a wheel, an aliquot was stored at -80°C (input) and the rest of the extract was immunoprecipitated with the antibody-conjugated dynabeads overnight at 4°C in a wheel. Immunoprecipitates were washed six times in cold lysis buffer.

For protein extraction, samples were incubated with Laemmli buffer (10% SDS, 0.325 M Tris HCl pH 7.5, glycerol 25%) for 20 min at 60°C. Dynabeads were removed with the help of a magnet and samples were boiled after adding DTT 0.1 M and bromophenol blue 0.1%.

For RNA extraction, immunoprecipitates were resuspended in 100 µl of proteinase K buffer (200 mM Tris pH 7.5, 100 mM NaCl, 10 mM EDTA, 1% SDS) containing 0.7 µg/µl of proteinase K (Roche, 03115852001) and incubated for 1 h at 42°C and 1 h at 65°C. RNA was extracted using the TRIzol reagent (Invitrogen, 15596018). In brief, samples were resuspended in 300 µl of TRIzol. Then, 20 µg of glycogen was added. Samples were vortexed, incubated for 5 min at room temperature and centrifuged at 14,000g for 15 min at 4°C. The aqueous phase was recovered, mixed with 1 volume of isopropanol, incubated for 5 min at room temperature and precipitated at 14,000g for 30 min at 4°C. The pellet was washed with 300 µl of ice-cold 75% ethanol and centrifuged at 14,000g for 10 min at 4°C. The pellets were resuspended in 100 µl of nuclease-free water. To ensure complete removal of the phenol, the RNA was precipitated again. To this end, 10 µl of sodium acetate 3 M pH 5.6 and 250 µl of 75% ethanol were added. Samples were vortexed and stored at -20°C for 1 h. Then, they were precipitated at 14,000g for 30 min at 4°C. The pellet was washed with 75% ethanol and centrifuged again at 14,000g for 10 min at 4°C. Pellets were air-dried for 5 min and resuspended in nuclease-free water.

RNA isolation, whole transcriptome amplification and microarray processing. Input and immunoprecipitated RNA were purified using Agencourt RNAClean

XP bead suspension (Beckman Coulter, A66514). Library preparation and amplification were performed following the distributor's (Sigma-Aldrich) recommendations for WTA2 from purified immunoprecipitated or diluted input RNA. SYBR green (Sigma-Aldrich, 163795-75-3) was added to the amplification reaction, which was performed in a CFX real-time instrument (Bio-Rad) to monitor amplification yield. When the SYBR green signal reached a plateau after 27 cycles, the reaction was stopped. Amplified cDNA was purified and quantified on a Nanodrop ND-1000 spectrophotometer (Thermo Fisher). Eight micrograms of cDNA was subsequently fragmented by DNaseI and biotinylated by terminal transferase obtained from GeneChip Mapping 250K Nsp Assay Kit (Affymetrix, 900753). After hybridization for 16 h at 45°C, washing and staining were performed in the Affymetrix GeneAtlas Fluidics Station. The arrays were scanned in the GeneAtlas Imaging Station. All processing was performed according to the manufacturer's recommendations. CEL files were generated from DAT files using Affymetrix Command Console software. To generate the log₂ expression estimates, overall array intensity was normalized between arrays and the probe intensity of all probes in a probe set summarized to a single value using the RMA (Robust Multichip Average) algorithm³⁸.

To compare samples from different conditions, fold changes (FCs) were computed after mean and variance normalization using a generalized additive model (GAM) on the M–A plot (M = log ratio, A = mean average) comparing mean intensity and FC for each probeset. An empirical Bayes partial density model was then used to compute the posterior probability of differential expression. Differentially expressed genes were defined as those with a maximum false discovery rate (FDR) of 5% and a log₂ FC threshold of 1.75. We calculated the input versus immunoprecipitated FC for CPEB1 and CPEB4 binders considering a transcript positive when at least one probe showed a FC above 1.75 in wild-type or HD mice.

Enrichment and co-expression network analysis of CPEB4 and CPEB1 binders. Enrichment analysis studies use a one-sided Fisher's exact test to evaluate whether a gene set, in this case CPEB4 or CPEB1 binders determined by RIP, is enriched over background, providing a P value and enrichment value. We used a curated ASD candidate gene list from the Simons Foundation Autism Research Initiative (SFARI) AutDB database, referred to as the ASD SFARI list and a more restrictive, smaller ASD-only gene list, where genes linked to intellectual disability were removed. The gene set (CPEB4 and CPEB1 binders) was also used to study enrichment in functional co-expression modules that represent shared pathology in ASD brain. These gene modules derived from previous unbiased weighted gene co-expression network analysis (WGCNA) obtained by gene array¹⁵ and by RNA-seq¹⁶ studies from ASD post-mortem samples.

Analysis of canonical and functional CPE sequences. 3' UTR sequences from selected gene sets were extracted from Ensembl (<http://www.ensembl.org/>)³⁹ and incidence of canonical and functional CPE (cytoplasmic polyadenylation element) sequences was detected using an algorithm as described⁴⁰ (<http://genome.crg.es/CPE/>). The list of brain genes was obtained from the human protein atlas (<http://proteinatlas.org/humanproteome/brain>), neuronal, astrocytic and oligodendrocyte-enriched genes from published data⁴¹, synaptic-enriched genes from published data⁴² and the ASD gene lists was obtained in July 2017 from the SFARI database (categories 1 to 4, https://gene.sfari.org/autdb/GS_Home.do). The ASD39 gene list consists of the 39 genes containing rare de novo protein disrupting mutations identified in the two largest whole-exome sequencing studies in simplex ASD^{17,18}. The Takata gene list consists of the 61 genes enriched for damaging de novo mutations in ASD identified by Takata et al.¹⁹. All lists of ASD-causing genes are shown in Supplementary Table 2.

Simulations. To compare feature enrichment in our subset of high-confidence ASD genes (SFARI cat. 1–2), we first selected several control gene groups: total genome, brain-enriched (from the human protein atlas), neuron-enriched⁴¹ and synapse-enriched⁴², and removed those genes previously linked to ASD (that is, any SFARI category). Then, for each simulation and control group, each ASD gene was matched randomly with a gene from the control group based on its 5' UTR (± 75 nt), 3' UTR (± 150 nt) or CDS length (± 200 nt), genomic size ($\pm 2,000$ bp) or ratio of neuronal-to-glial expression (± 0.1). For the latter, RNA-seq data for isolated populations of neurons, astrocytes, microglia, new oligodendrocytes and oligodendrocyte precursors was obtained⁴³ and expression values calculated using VAST-TOOLS²⁴. An average value for all glial cell types was calculated for each gene and the average ratio between the expression in neurons and that in glia (NvsG) used for stratification. Next, the percentage of CPEs, CPEB4 binders and genes with poly(A)-tail shortened or lengthened in ASD human samples or in TgCPEB4Δ4, CPEB4 KO^{GT/+} or CPEB4 KO mice were calculated in each control and stratified test subset. This process was repeated 10,000 times and P values were calculated as the number of times the stratified control showed the same or higher percentage (or lower, if testing for depletion) than the test set, divided by 10,000. All results are shown in Supplementary Table 5.

Quantification of CPEB gene expression in human post-mortem ASD samples. CPEB expression levels in post-mortem prefrontal (Ba9) and temporal (Ba41-42-22)

cortex samples from individuals with idiopathic ASD ($n=43$ samples from 26 individuals) and control individuals ($n=63$ samples from 33 individuals) were evaluated from RNA-seq data¹⁶. In brief, the paired-end raw reads were mapped to the human reference genome assembly GRCh37.73 using TopHat2⁴⁴, and the counts were quantified using HTSeq⁴⁵. Gene length, G+C content and library size were normalized (referred to as 'normalized FPKM') using the cqn package in R⁴⁶. Linear mixed effects were used, modelling to account for effects from biological covariates (condition, age, sex, brain region), technical variables related to sample processing (RIN, brain bank, sequencing batch), technical variables related to sequencing quality metrics and individual ID was set as a random effect accounting for the fact that multiple samples came from the same individual.

Quantification of CPEBs transcript splicing and differential splicing analysis. We used $n=81$ control and $n=82$ ASD cortical prefrontal and temporal samples from $n=47$ ASD and $n=44$ control individuals¹⁶. We computed per cent spliced in (PSI) values using: (1) VAST-TOOLS (<https://github.com/vastgroup/vast-tools>). This software consists of multiple utilities to align and process raw RNA-seq reads to derive PSIs for all types of alternative splicing²⁴. (2) Multivariate analysis of transcript splicing (MATS, v3.08), which utilizes TopHat2⁴⁷ aligned reads and a custom splice-junction library. In order to account for the effects of covariates, we used PSI values in the linear mixed effects model described below for differential splicing analysis: lme(PSI ~ diagnosis + age + sex + brain_region + sequencing_batch + brain_bank_batch + RIN + seqSV1 + seqSV2, rand = ~1|individualID), where two sequencing surrogate variables (seqSV1 and seqSV2) were used as covariates. **RNA extraction and cDNA synthesis.** Total tissue RNA was extracted from prefrontal cortex (Ba8/9) of control individuals ($n=15$) and individuals with idiopathic ASD ($n=16$) and striatum, cortex or forebrain from control, CPEB4 KO^{GT/+}, TgCPEB4Δ4, CPEB4 KO and TgCPEB4Δ4/CPEB4-KO^{GT/+} mice using the Maxwell 16 LEV simplyRNA Tissue Kit (Promega, AS1280). Quantification and quality determination of RNA was done on a Nanodrop ND-1000 spectrophotometer and Nanodrop 1000 v.3.7.1 (Thermo Scientific). Retrotranscription (RT) reactions were performed using the iScript cDNA Synthesis kit (Bio-Rad, PN170-8891) following the manufacturer's instructions. In brief, 1,000 ng of total RNA from each sample was combined with 10 µl of master mix (includes all necessary reagents along with a mixture of random primers and oligo-dT for priming). The reaction volume was completed up to 40 µl with DNase/RNase-free distilled water (Gibco, PN 10977). Thermal conditions consisted of the following steps: 5 min at 25 °C; 20 min at 46 °C and 1 min at 95 °C.

CPEB4 PCR flanking primers. Specific primers were designed in CPEB4 exon 2 (forward, 5'-ggacgtttgatcgactcac-3') and exon 5 (reverse, 5'-gagggttgcacccacggc-3') and we verified that they amplified the four CPEB4 splicing isoforms (full-length, Δ4, Δ3 and Δ3Δ4) in human and mouse brain cDNA. PCR amplification protocol used: 10 min at 94 °C + 33 cycles (30 s at 94 °C + 30 s at 58 °C + 2 min at 72 °C) + 10 min at 72 °C. PCR products according with the four CPEB4 isoforms were resolved on 2.2% agarose/gelgreen (Biotium, 41004) gels run at 125 V for 1.5 h. Images were scanned with densitometer (Bio-Rad, GS-900) and quantified with Image Laboratory 5.2 (Bio-Rad). Finally, the percentage of each CPEB4 isoform was calculated.

Digital-droplet PCR. mRNAs of each of the CPEB4 splicing isoforms were measured by digital-droplet PCR (ddPCR) in a BioRad QX200 Digital Droplet PCR system (Bio-Rad, 1864100). All PCR reactions were made in three replicates and assayed in 96-well plates. The PCR reaction volume was 22 µl using QX200 ddPCR Evagreen Supermix (Bio-Rad, 1864034). Each reaction included 11 µl of ddPCR Evagreen Supermix, forward and reverse primers at 0.9 µM each and 4 ng of template cDNA. The PCR reaction mixture was loaded into an 8-well DG8 Cartridge for QX200 (Bio-Rad, 1864008) and droplets with oil for EvaGreen (Bio-Rad, 1864005) were formed with the Bio-Rad QX200 Droplet Generator (Bio-Rad, 1864101), following the manufacturer's instructions. During emulsion, the QX200 droplet generator partitions the samples into 20,000 nanolitre-sized droplets. The droplets were then transferred to a 96-well plate and sealed with a Bio-Rad PX1 PCR Plate Sealer (Bio-Rad, 1814000). Optimal ddPCR annealing temperatures for the CPEB4 isoforms assays were determined by incorporating a temperature gradient from 55.6 °C to 66.6 °C. FL-CPEB4 and CPEB4Δ3 were amplified using the following cycling conditions: 95 °C for 5 min, 40 × (95 °C for 30 s and an annealing-extension step at 60 °C for 1 min) and 90 °C for 5 min. CPEB4Δ4 and CPEB4Δ3Δ4 were amplified using: 95 °C for 5 min, 40 × (95 °C for 30 s + 62 °C for 1 min) and 90 °C for 5 min. Finally, droplets were read on the QX200 Droplet Reader (Bio-Rad, 1864003) and data were analysed with Quantssoft Version 1.6.6.0320 (Bio-Rad). The primers used to amplify each CPEB4 isoform are detailed in Supplementary Table 7.

Real-time qRT-PCR. Quantification was performed by real-time PCR using a CFX 384 Real Time System C1000 Thermal Cycler (Bio-Rad) in combination with SsoFast Eva Green (Bio-Rad, CN 172-5204) and 0.25 µM of primer pair was used. Data were analysed by GenEx 5.3.7 software (Multid AnAlyses AB). The mRNA levels were normalized first relative to total RNA and then relative to the

18S ribosome subunit, ACTB, GAPDH and TUBB gene expression in each sample. Absolute quantitative PCR was performed to determine the percentage of each CPEB4 splicing isoform in both human and mouse species using specific primers (Supplementary Table 7). For every primer couple, specificity was tested and PCR assay conditions were adjusted to obtain a single amplicon that was analysed by both melting curve analysis and agarose gel electrophoresis. Amplicons of each CPEB4 isoform were serially diluted to generate a calibration curve. A duplication of this curve was made to give robustness. Next, total tissue RNA was extracted, and quantitative real-time RT-PCR was performed. Finally, the percentage of each CPEB4 isoform with respect to total CPEB4 copies was calculated.

Western blot. Samples from human brain were stored at -80 °C and were ground with a mortar in a frozen environment with liquid nitrogen to prevent thawing of the samples, resulting in tissue powder. For mouse, brains were quickly dissected on an ice-cold plate and the different structures stored at -80 °C. Human and mouse extracts were prepared by homogenizing the brain areas in ice-cold extraction buffer (20 mM HEPES pH 7.4, 100 mM NaCl, 20 mM NaF, 1% Triton X-100, 1 mM sodium orthovanadate, 1 µM okadaic acid, 5 mM sodium pyrophosphate, 30 mM β-glycerophosphate, 5 mM EDTA, protease inhibitors (Complete, Roche, Cat. No 11697498001)). Homogenates were centrifuged at 15,000g for 15 min at 4 °C. The resulting supernatant was collected, and protein content determined by Quick Start Bradford kit assay (Bio-Rad, 500-0203). Between 10 and 20 µg of total protein was electrophoresed on 10% SDS-polyacrylamide gel, transferred to a nitrocellulose blotting membrane (Amersham Protran 0.45 µm, GE Healthcare Life Sciences, 10600002) and blocked in TBS-T (150 mM NaCl, 20 mM Tris-HCl, pH 7.5, 0.1% Tween 20) supplemented with 5% non-fat dry milk. Membranes were incubated overnight at 4 °C with the primary antibody in TBS-T supplemented with 5% non-fat dry milk, washed with TBS-T and next incubated with secondary HRP-conjugated anti-mouse IgG (1:2,000, DAKO, P0447), anti-rabbit IgG (1:2,000, DAKO, P0448) or anti-rat IgG-Fc fragment (1:5,000, Bethyl, A110-136P) and developed using the ECL detection kit (Perkin Elmer, NEL105001EA). Images were scanned with densitometer (Bio-Rad, GS-900) and quantified with Image Laboratory 5.2 (Bio-Rad).

Antibodies. Rabbit CPEB1 (1:350, Santacruz, sc-33193); rabbit CPEB2 (1:1,000, Abcam, ab51069); rabbit CPEB3 (1:1,000, Abcam, ab10883); rabbit CPEB4 (1:1,000, Abcam, ab83009); rabbit PTEN (1:1,000, Cell Signaling, 9559S); mouse DYRK1A (1:1,000, Abnova, H00001859-M01); rabbit FOXP1 (1:2,000 for mouse and 1:500 for human samples, Abcam, ab16645); rabbit WAC (1:500, Merk Millipore, ABE471); rabbit AUTS2 (1:750, Sigma, HPA000390); mouse RBFOX1 (1:2,000 for mouse and 1:1,000 for human samples, Merk Millipore, MABE985), rabbit PCDH9 (1:500, Abcam, ab171166); rabbit ZBTB20 (1:300, SantaCruz, sc-99728); mouse CALB1 (1:1,000, Sigma, C9848); rabbit D2R (1:800, Calbiochem, 324396), rabbit SNAP25 (1:2,500, abcam, ab5666), mouse TUBB3 (1:2,500, Novus, NB120-11314), rabbit IBA1 (1:1,000, Wako, 019-19741), rabbit TNRC6B (1:500, Merk Millipore, AB9913); rat CHD2 (1:750, Merk Millipore, MABE873); rabbit GPC6 (1:1,000, Abcam, ab136295); mouse β-ACTIN (1:25,000, Sigma, A2228).

Poly(U) chromatography. Human samples. Brain specimens from prefrontal cortex (Ba8/9) of individuals with ASD ($n=6$) and control males ($n=5$) aged between 5 and 23 years. To verify RNA integrity and poly(A)-tail quality, we performed Hire-PAT of a typical normalizer gene (ACTB) and found any alterations in control or ASD brains.

Mouse samples. Wild-type, CPEB4 KO^{GT/+} and CPEB4 KO ($n=2$) and control versus TgCPEB4Δ4 mice ($n=3$) were killed by cervical dislocation at the age of 6 weeks. The cortex and striatum together were quickly dissected on an ice-cold plate.

Human and mouse samples were homogenized and total RNA was extracted using the Maxwell 16 LEV simplyRNA Tissue Kit (Promega, AS1280), and stored at -80 °C until use. The poly(A) RNA fraction was purified by poly(U) chromatography⁴⁸. Poly(U)-agarose (Sigma, p8563) was suspended in swelling buffer (0.05 M Tris-HCl, pH 7.5, 1 M NaCl) 35 ml/g, incubated overnight at room temperature and loaded into the chromatography column. An aliquot of total RNA was stored at -80 °C (input) and the rest was incubated with sample buffer (0.01 M Tris-HCl, pH 7.5, 1 mM EDTA, 1% SDS) for 5 min at 65 °C and chilled on ice. Binding buffer was added (0.05 M Tris-HCl, pH 7.5, 0.7 M NaCl, 10 mM EDTA, 25% [v/v] formamide) and then the sample was loaded into the poly(U)-agarose chromatography column (Mobitec, M1002 s) and incubated for 30 min at room temperature (25 °C) with agitation. Next, the column containing the sample was washed three times at 25 °C and six times at 55 °C with washing buffer (0.05 M Tris-HCl, pH 7.5, 0.1 M NaCl, 10 mM EDTA, 25% [v/v] formamide). The 55 °C washes were collected and stored at -80 °C (short poly(A)-tail fraction). The remaining poly(A) RNA (long poly(A)-tail fraction) was eluted with elution buffer (0.05 M HEPES, pH 7, 10 mM EDTA, 90% [v/v] formamide) at 55 °C and stored at -80 °C. The RNA of the two poly(A) fractions was precipitated by adding 1 volume of isopropanol, 1/10th volumes of sodium acetate 3 M pH 5.2 and 20 µg of glycogen (Sigma, G1767). The samples were incubated at -20 °C for 20 min and centrifuged for 15 min at 14,000g

at 4°C. The supernatant was removed and the pellet was washed with 750 µl of ethanol and centrifuged at 14,000g and 4°C for 5 min. The supernatant was removed and the pellet was air-dried for 5 min. The RNAs were resuspended in 300 µl of nuclease-free water and then 300 µl of acid phenol:chloroform (5:1) were added. Samples were vortexed and centrifuged for 10 min at 14,000g and 4°C. The aqueous phase was recovered, mixed with 1 volume of chloroform, vortexed and centrifuged again. The aqueous phase was recovered and precipitated again using the isopropanol precipitation. When setting up the method, we perform digestion of the non-poly(A) mRNA regions followed by end-labeling of the poly(A) for each eluted fraction and Urea-PAGE to confirm the average length in each fragment. We also compared poly(A)-tail by HIRE-PAT assay of control genes in input, washed and eluted fractions to verify that it worked properly.

Human PrimeView and GeneAtlas MG-430pm microarray analysis. cDNA library preparation and amplification were performed according to the manufacturer's instructions (Sigma-Aldrich) for the WTA2 kit from 25 ng starting material. The cDNA was amplified for 17 cycles and purified using PureLink Quick PCR Purification Kit (Invitrogen, K310001). Quantification of amplified cDNA was done on a Nanodrop ND-1000 spectrophotometer (Thermo Fisher Scientific). Eight and a half micrograms of the cDNA from each sample was fragmented and labelling with GeneChip Mapping 250K Nsp assay kit (Affymetrix, 900753) following the manufacturer's instructions.

Human. Samples ready to hybridize were denatured at 99°C for 2 min before incubation into the GeneChip Human PrimeView arrays (Affymetrix, 901838). Hybridization was performed for 16 h at 45°C and 60 rpm in the GeneChip Hybridization Oven 645 (Affymetrix, 00-0331). Washing and stain steps after hybridization were performed in the GeneChip Fluidics Station 450 (Affymetrix, 00-0079), following the specific script for PrimeView arrays. Finally, the arrays were scanned with GeneChip Scanner GCS3000 (Affymetrix) using default parameters, and the generation of CEL files for bioinformatics analysis was done with Command Console software (Affymetrix).

Mouse. Hybridization was performed using the GeneAtlas Hyb, Wash and Stain Kit for 3' IVT arrays. Samples ready to hybridize were denatured at 96°C for 10 min before incubation into Mouse MG-430pm Array Strip (Affymetrix, 901570), the hybridization was performed for 16 h at 45°C in the GeneAtlas Hybridization Oven (Affymetrix, 00-0331). Washing and stain steps after hybridization were performed in the GeneAtlas Fluidics Station (Affymetrix, 00-0079), following the specific script for Mouse MG-430pm arrays. Finally, the arrays were scanned with GeneAtlas Scanner (Affymetrix) using default parameters, and the generation of CEL files for bioinformatics analysis was done with GeneAtlas software (Affymetrix).

Processing of microarray samples was performed using R⁴⁹ and Bioconductor⁵⁰. Raw CEL files were normalized using RMA background correction and summarization⁵¹. Standard quality controls were performed in order to identify abnormal samples⁵² regarding: a) spatial artefacts in the hybridization process (scan images and pseudo-images from probe level models); b) intensity dependences of differences between chips (MvA plots); c) RNA quality (RNA digest plot); and d) global intensity levels (boxplot of perfect match log-intensity distributions before and after normalization and RLE plots). Probeset annotation was performed using the information available in Affymetrix web page (<https://www.affymetrix.com/analysis/index.affx>) using version na35.

Expression values were adjusted for technical biases as described⁵³ using a linear model and implemented with the R package 'limma'⁵⁴. For each biological replicate the log₂ FC was computed between WASH and ELUTED samples and used to find significant differences between wild-type and CPEB4 KO^{GT/+} or CPEB4 KO mice ($n=2$), control and TgCPEB4Δ4 mice ($n=3$) and human control ($n=5$) and ASD individuals ($n=6$). Differential expression was performed using a linear model with fluidics and amplification batch as covariates. P values were adjusted with the Benjamini and Hochberg correction. We considered one transcript is shortened when $P < 0.05$ and FC is negative and lengthened when $P < 0.05$ and FC is positive, in at least one probe. If the same transcript showed opposite results for different probes, it was considered as not changed.

Differential gene expression array. Individual probeset expression values for each selected gene were annotated with Annmap library R package version 1.22.0. (<https://bioconductor.org/packages/release/bioc/html/annmap.html>), using *Homo sapiens* v84 Primeview Human Gene Array and *Mus musculus* v84 Mouse Genome 430A 2.0 databases. Those probesets annotated as reliable were preferentially selected for analysis. For those genes lacking a reliable probeset, the whole group of probesets was taken for comparisons. Graph bars were plotted using the mean of RMA normalized expression values from the Primeview human gene array in case of human samples and mouse genome 430pm array in case of mice. The expression values were calculated using R⁴⁹ and BioConductor⁵⁰ packages.

HIRE-PAT assay. USB Poly(A) Tail-Length Assay Kit (Affymetrix, 76455) based on HIRE-PAT method, was used. Frontal cortex (Ba8/9) of individuals with ASD ($n=3$) and control individuals ($n=3$) and total striatal RNA from 1.5-month-

old control and TgCPEB4Δ4 mice ($n=3$) was extracted using the Maxwell 16 LEV simplyRNA Tissue Kit (Promega, AS1280) and stored at -80°C until use. G/I tailing (1 µg of total RNA) and reverse transcription were performed according to the manufacturer's instructions. Poly(A) size was determined by subtracting the PCR amplicon size obtained with the Universal primer and forward specific primers. To verify that the measured poly(A) tail corresponds to specific gene three different forward specific primers were tested (Supplementary Table 7). PCR products were resolved on 2.5% agarose with GelGreen (Biotium, 41004) gels run at 120V for 1.5h.

Gene ontology analysis. CPEB4 binders with poly(A)-tail changes in the pre-frontal cortex of individuals with ASD were analysed with DAVID Bioinformatics Resources 6.7, KEGG pathway annotation⁵⁵.

Human-mouse altered poly(A) tail length geneset comparison. To compare transcripts with altered poly(A) tail in individuals with ASD and CPEB4-modified mice, we first converted the gene set from mouse into their human orthologues (18,649 total orthologous genes) using Ensembl Genes 85 *Mus musculus* GRCh38p4 Biomart (<http://www.ensembl.org/biomart/>)³⁹. Then we calculated the statistical significance of the overlap between genes with poly(A) changes in human ASD and CPEB4-modified mice by hypergeometric distribution test. We considered overlapping when the representation factor was >1 and $P < 0.05$, and dissimilar when the representation factor was <1 and $P < 0.05$.

Generation of TgCPEB4Δ4 mice. Human CPEB4 cDNA lacking exon 4 (CPEB4Δ4) was cloned into a plasmid containing a bidirectional TetO sequence to also express a LacZ reporter with a nuclear localization signal (pBI-G, Clontech, 631004). The construct was microinjected into single-cell CBA × C57BL/6 embryos and resulting TetO βGAL/CPEB4Δ4 founder mice were backcrossed with wild-type C57BL/6J mice (TetO βGAL/CPEB4Δ4). TetO βGAL/CPEB4Δ4 mice were crossed with CamkII-tTA (tTA) mice³⁷ to obtain conditional double transgenic mice with forebrain neuron expression of CPEB4Δ4 (TgCPEB4Δ4 mice). There are different CamkII-tTA transgenic mouse lines³⁷ and, for this study, we chose one with expression starting at late embryonic age⁵⁶. Upon observation of premature death of the subset of TgCPEB4Δ4 mice showing cranial dysmorphology, these were systematically culled when found.

To generate TgCPEB4Δ4 mice with transgene expression starting after weaning (OFF/ON-TgCPEB4Δ4 mice) pregnant females were isolated and kept on doxycycline (Sigma, D9891, 0.5g/l) until weaning of the litter. After weaning, the progeny was switched to plain water to allow expression of the transgene.

To generate TgCPEB4Δ4 mice that expressed the transgene only during embryonic and early postnatal development (ON/OFF-TgCPEB4Δ4 mice) pregnant females were isolated and kept on plain water until birth of the litter, when water was replaced by doxycycline solution (Sigma, D9891, 2g/l) so doxycycline intake started in the pups through the milk. The progeny were kept on doxycycline throughout the rest of the experiment.

Immunohistochemistry. Mice were euthanized with CO₂. Brains were immediately removed and dissected on an ice-cold plate and left hemispheres, processed for histology, were placed in 4% paraformaldehyde in Sorenson's phosphate buffer overnight and then immersed in 30% sucrose in PBS for 72 h. Once cryoprotected, the samples were included in optimum cutting temperature (OCT) compound (Tissue-Tek, Sakura Finetek Europe, 4583), frozen and stored at -80°C until use. 30-µm sagittal sections were cut on a cryostat (Thermo Scientific), collected and stored free floating in glycol containing buffer (30% glycerol, 30% ethylene glycol in 0.02 M phosphate buffer) at -20°C. Before staining, sections were washed with PBS to eliminate the cryoprotective buffer and immersed in 0.3% H₂O₂ in PBS for 30 min to quench endogenous peroxidase activity. Sections were immersed for 1 h in blocking solution (PBS containing 0.5% fetal bovine serum, 0.3% Triton X-100 and 1% BSA) and incubated overnight at 4°C with the corresponding primary antibody diluted in blocking solution. After washing, brain sections were incubated first with biotinylated anti-rabbit or anti-mouse secondary antibody and then with avidin-biotin complex using the Elite Vectastain kit (Vector Laboratories, PK-6101-2). Chromogen reactions were performed with diaminobenzidine (SIGMAFAST™ DAB, Sigma, D4293) for 10 min. Sections were mounted on glass slides and coverslipped with Mowiol (Calbiochem, 475904). Images were captured using an Olympus BX41 microscope with an Olympus camera DP-70 and Olympus cellSens Entry v.1.7 (Olympus Denmark A/S)

Antibodies. Rabbit CPEB4 (1:1,000, Aviva, ARP41024_P050); rabbit β-GAL (1:2,000, Invitrogen, A-11132); rabbit cleaved CASP3, Asp175 (1:60, Cell Signaling, 9661)

Golgi spine analysis. Control ($n=5$) versus TgCPEB4Δ4 mice ($n=4$) three-month-old mice, and wild-type ($n=3$) versus CPEB4 KO^{GT/+} ($n=4$) fifteen-month-old mice were completely anaesthetized with an intraperitoneal pentobarbital injection (60 mg/kg Dolethal, Vetoquinol). The whole brain was extracted and immersed in Golgi-Cox staining solution (FD Rapid GolgiStain kit, FD Neurotechnologies, cat. PK401). One-hundred-and-fifty-micrometre sagittal sections were obtained in a Leica VT1200S vibratome and mounted on

gelatin-coated slides. Golgi staining was performed per the manufacturer's instructions. Afterwards, all sections were counterstained with toluidine blue pH 4.0 (1 g/l toluidine blue (Sigma, 198161), 0.8 M glacial acetic acid) and coverslipped with DePeX (Amsbio, 18243.02). Pyramidal neurons from layer II/III of the cortex were identified by their distance from the pia mater and their distinct morphologies. Secondary, tertiary and quaternary dendrites of these neurons were selected for analysis. Z-stacks of the entire apical dendritic tree of Golgi stained pyramidal neurons (up to 80 µm total on z-axis, optical section thickness = 0.5 µm) were taken at 40× magnification with 2× optical zoom on a vertical Zeiss Axio Imager.Z1 M and analysed by Laser Scanning Microscope LSM 510 v.4.2 SP1 (Carl Zeiss). Spine density, length and classification were performed as described⁵⁷, by researchers blinded to genotype.

Brain weight and volumetric analysis. One-and-a-half-month-old mice were completely anaesthetized with an intraperitoneal pentobarbital injection (60 mg/kg Dolethal, Vetoquinol). The whole brain was extracted and weighed in a precision scale (Metter Toledo, AB265-S). Left hemispheres were fixed in 4% paraformaldehyde, immersed in 30% sucrose, immersed in OCT compound (Tissue-Tek, Sakura Finetek Europe, 4583), frozen and stored at -80°C. Sagittal sections (30 µm thick) were cut on a cryostat and every sixth section was counterstained with toluidine blue pH 4.0 (1 g/l Toluidine Blue (Sigma, 198161), 0.8 M glacial acetic acid). Digital images were captured at a 2.5× magnification (Canon EOS 450D digital camera) and the hippocampal, striatal and motor and somatosensory cortical areas from 20–22 sections for each animal were calculated using ImageJ software⁵⁸. Considering a separation of 180 µm between each section, the total structure volume in each mouse was calculated.

Electrophysiology. For preparation of acute brain slices, we based our method on the N-methyl-D-glucamine (NMDG) protective recovery method^{59–61}. In brief, 5–6-week-old control versus TgCPEB4Δ4 ($n=5$) mice and wild-type versus CPEB4 KO^{GT/+} ($n=5$) mice of both sexes were anaesthetized with 2% tribromoethanol (0.15 ml/10 mg) and rapidly decapitated. The brains were dissected out and transferred to NMDG ice-cold artificial cerebrospinal fluid (ACSF) composed of (in mM): 93 NMDG, 2.5 KCl, 1.2 NaH₂PO₄, 30 NaHCO₃, 25 D-glucose, 20 HEPES, 5 Na-ascorbate, 2 thiourea, 3 Na-pyruvate, 10 MgSO₄, and 0.5 CaCl₂. The pH of the solution was titrated to pH 7.3–7.4 with concentrated HCl (osmolality 310–315 mOsmol/kg) and bubbled with carbogen (5% CO₂/95% O₂). 350-µm coronal slices were cut on a Vibratome VT1200S (Leica) and transferred for initial recovery to NMDG ACSF at 33 ± 1 °C. Finally, slices were placed in a holding chamber at room temperature with normal ACSF composed of (in mM): 126 NaCl, 2.5 KCl, 2 CaCl₂, 2 MgCl₂, 1.25 NaH₂PO₄, 26 NaHCO₃, and 10 D-glucose (osmolality 305–315 mOsmol/kg), pH 7.4, when bubbled with carbogen (5% CO₂/95% O₂). **Recordings.** For whole-cell patch-clamp recordings, slices were transferred into a recording chamber that was perfused with 33 ± 1 °C bubbled ACSF at 2–3 ml/min. Pyramidal neurons of the somatosensory cortex were visualized by a Nikon Eclipse FN1 microscope, a 40× water immersion objective (Nikon), and a USB 2.0 monochrome camera (DMK 31BU03.H, TheImagingSource). Whole-cell recordings were performed using a double patch clamp EPC10 plus amplifier (HEKA). Under voltage-clamp conditions, the patch-pipettes for excitatory postsynaptic currents recording contained (mM): 120 K-gluconate, 10 KCl, 10 phosphocreatine disodium salt, 2 MgATP, 0.3 NaGTP, 0.1 EGTA, 10 HEPES, pH 7.2 adjusted with KOH, osmolality 280–290 mOsmol/kg. Recording of mEPSCs were done in the presence of tetrodotoxin (1 µM) and picrotoxin (50 µM) to block sodium channels and GABA_A receptors, respectively. Cells were held in voltage-clamp mode at a holding potential (V_{hold}) of -70 mV, while resistance was compensated by 70% (lag 10 µs). Recordings were discontinued if series resistances increased by >50% or exceeded 15 MΩ.

Currents were low-pass filtered at 3 kHz, digitized at 20 kHz and acquired using PatchMaster software (HEKA). All miniature postsynaptic currents were analysed with the program Stimfit⁶². Recordings were first digitally filtered at 1 kHz. For each cell, all events were inspected to avoid false-positive events, and then an average of all events detected was made.

Cleaved caspase-3 quantification. One-and-a-half-month-old control and TgCPEB4Δ4 mice ($n=6$) were analysed. The total number of immunopositive cells with apoptotic shape was quantified in the cortex of three sections per animal using an Olympus BX41 microscope with an Olympus camera DP-70 (Olympus Denmark A/S). Means of the three sections were calculated.

Stereology. Sagittal sections (30-µm thick) counterstained with toluidine blue pH 4.0 (1 g/l toluidine blue (Sigma, 198161), 0.8 M glacial acetic acid) from the volumetric analysis were used. Sections containing striatum were selected and the 10 most central sections were analysed. One randomly selected 60 µm × 60 µm optical dissector at 60× magnification with an Olympus BX41 microscope with an Olympus camera DP-70 (Olympus Denmark A/S) was analysed in each section. Total neuronal cell number per dissector was assessed by a researcher blind to genotype. Striatal neuronal cell density was calculated and compared for control ($n=19$) and TgCPEB4Δ4 mice ($n=5$).

Behavioural testing. Open field. Locomotor activity was measured in 5-week-old mice in clear Plexiglas boxes measuring 27.5 cm × 27.5 cm, outfitted with photo-beam detectors for monitoring horizontal and vertical activity. Activity levels were recorded with a MED Associates' Activity Monitor and were analysed with the MED Associates' Activity Monitor Data Analysis v.5.93.773 software. Mice were placed in the centre of the open-field apparatus and left to move freely. Data were individually recorded for each animal for 15 min. Distance walked in the periphery (3.5 cm from the edges) and in the centre of the box was measured. **Ultrasonic vocalization.** Numbers of ultrasonic vocalizations (UsVs) were measured at the age of 3, 6, 9 and 12 postnatal days in mice. The dam was removed from a temperature-controlled home cage where the pups remained. Then, pups were removed individually and placed in a plate equipped to record UsV for 5 min (Avisoft Recorder). To avoid potential confounding effects due to temperature, the room was maintained at 21 °C and body temperature was measured with an axillary probe after the 5 min test. UsV was analysed with Avisoft SASLab Pro v.5.2.09 software.

Social approach. Social interaction was examined in 5-week-old mice. The first day (training), mice were allowed to explore an empty Plexiglas box measuring 45 cm × 45 cm for 10 min. The next day (test), mice were placed in the same box containing two wire cages placed in opposite corners, one empty and the other with an unknown (gender paired) mouse on it. Mice were recorded for 10 min and the time spent interacting with each cage was measured.

Elevated plus maze. Anxiety-like behaviour was examined in 5-week-old mice. Animals were tested in a 5 min single-trial elevated plus maze in which the mouse was allowed to move freely along the apparatus under a constant intense white light. Animal movement was recorded and the total time spent standing or walking on the open and closed arms was measured. The criterion was the head, forelimbs and hindlimbs being placed on open or closed arms. Maze consists of four arms (two open without walls and two enclosed by 15 cm high walls) 26 cm long and 5 cm wide, and it is elevated 40 cm off the floor.

Data analysis. Statistical analysis was performed with SPSS 21.0 (SPSS Statistic IBM). Data are represented as mean ± s.e.m. with 95% confidence intervals. In box plots, box segments show median, 25th and 75th percentiles, whiskers above and below show the locations of the minimum and maximum. Higher or lower points (outliers) are plotted individually or not plotted. The normality of the data was analysed by Shapiro-Wilk test ($n<50$) or Kolmogorov-Smirnov test ($n>50$). Homogeneity of variance was analysed by Levene's test. For comparison of two independent groups two-tail unpaired Student's *t*-test (data with normal distribution), Mann-Whitney-Wilcoxon or Kolmogorov-Smirnov tests (with non-normal distribution) were performed. To compare dependent measurements, we used a paired *t*-test (normal distribution) or Wilcoxon signed-rank tests (non-normal). For multiple comparisons, data with a normal distribution were analysed by one-way ANOVA followed by a Tukey's or a Games-Howell's post hoc test. Statistical significance of non-parametric data for multiple comparisons was determined by Kruskal-Wallis one-way ANOVA. Enrichment tests were carried out using one-sided Fisher's exact test. A critical value for significance of $P<0.05$ was used throughout the study.

Reporting summary. Further information on experimental design is available in the Nature Research Reporting Summary linked to this paper.

Data availability. The data that support the findings of this study are available from the corresponding authors upon reasonable request.

35. Mangiarini, L. et al. Exon 1 of the HD gene with an expanded CAG repeat is sufficient to cause a progressive neurological phenotype in transgenic mice. *Cell* **87**, 493–506 (1996).
36. Shin, J., Salameh, J. S. & Richter, J. D. Impaired neurodevelopment by the low complexity domain of CPEB4 reveals a convergent pathway with neurodegeneration. *Sci. Rep.* **6**, 29395 (2016).
37. Mayford, M., et al. Control of memory formation through regulated expression of a CAMKII transgene. *Science* **274**, 1678–1683 (1996).
38. Irizarry, R. A. et al. Summaries of Affymetrix GeneChip probe level data. *Nucleic Acids Res.* **31**, e15 (2003).
39. Yates, A. et al. Ensembl 2016. *Nucleic Acids Res.* **44**, D710–D716 (2016).
40. Piqué, M., López, J. M., Foissac, S., Guigó, R. & Méndez, R. A combinatorial code for CPE-mediated translational control. *Cell* **132**, 434–448 (2008).
41. Cahoy, J. D. et al. A transcriptome database for astrocytes, neurons, and oligodendrocytes: a new resource for understanding brain development and function. *J. Neurosci.* **28**, 264–278 (2008).
42. Cajigas, I. J. et al. The local transcriptome in the synaptic neuropil revealed by deep sequencing and high-resolution imaging. *Neuron* **74**, 453–466 (2012).
43. Zhang, Y. et al. An RNA-seqencing transcriptome and splicing database of glia, neurons, and vascular cells of the cerebral cortex. *J. Neurosci.* **34**, 11929–11947 (2014).
44. Kim, D. et al. TopHat2: accurate alignment of transcriptomes in the presence of insertions, deletions and gene fusions. *Genome Biol.* **14**, R36 (2013).
45. Anders, S., Pyl, P. T. & Huber, W. HTSeq—a Python framework to work with high-throughput sequencing data. *Bioinformatics* **31**, 166–169 (2015).

46. Hansen, K. D., Irizarry, R. A. & Wu, Z. Removing technical variability in RNA-seq data using conditional quantile normalization. *Biostatistics* **13**, 204–216 (2012).

47. Shen, S. et al. MATS: a Bayesian framework for flexible detection of differential alternative splicing from RNA-seq data. *Nucleic Acids Res.* **40**, e61 (2012).

48. Belloc, E. & Méndez, R. A deadenylation negative feedback mechanism governs meiotic metaphase arrest. *Nature* **452**, 1017–1021 (2008).

49. R Development Core Team. *R: A language and environment for statistical computing* (R Foundation for Statistical Computing, 2014).

50. Gentleman, R. C. et al. Bioconductor: open software development for computational biology and bioinformatics. *Genome Biol.* **5**, R80 (2004).

51. Irizarry, R. A. et al. Exploration, normalization, and summaries of high density oligonucleotide array probe level data. *Biostatistics* **4**, 249–264 (2003).

52. Gentleman, R. C., Carey, V. J., Huber, W., Irizarry, R. & Dudoit, S. *Bioinformatics and Computational Biology Solutions Using R and Bioconductor* (Springer, New York, 2005).

53. Eklund, A. C. & Szallasi, Z. Correction of technical bias in clinical microarray data improves concordance with known biological information. *Genome Biol.* **9**, R26 (2008).

54. Ritchie, M. E. et al. limma powers differential expression analyses for RNA-sequencing and microarray studies. *Nucleic Acids Res.* **43**, e47 (2015).

55. Huang, W., Sherman, B. T. & Lempicki, R. A. Systematic and integrative analysis of large gene lists using DAVID bioinformatics resources. *Nat. Protocols* **4**, 44–57 (2009).

56. Lucas, J. J. et al. Decreased nuclear β -catenin, tau hyperphosphorylation and neurodegeneration in GSK-3 β conditional transgenic mice. *EMBO J.* **20**, 27–39 (2001).

57. Risher, W. C., Ustunkaya, T., Singh Alvarado, J. & Eroglu, C. Rapid Golgi analysis method for efficient and unbiased classification of dendritic spines. *PLoS ONE* **9**, e107591 (2014).

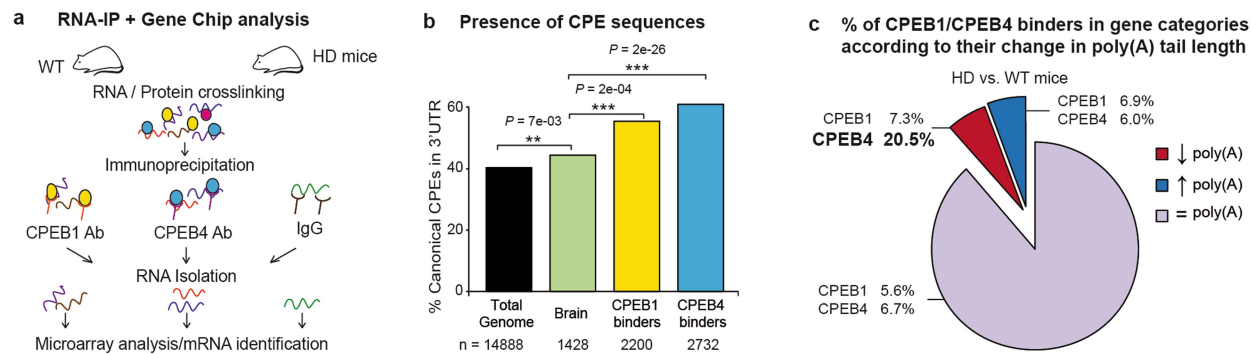
58. Schneider, C. A., Rasband, W. S. & Eliceiri, K. W. NIH Image to ImageJ: 25 years of image analysis. *Nat. Methods* **9**, 671–675 (2012).

59. Peça, J. et al. Shank3 mutant mice display autistic-like behaviours and striatal dysfunction. *Nature* **472**, 437–442 (2011).

60. Ting, J. T., Daigle, T. L., Chen, Q. & Feng, G. Acute brain slice methods for adult and aging animals: application of targeted patch clamp analysis and optogenetics. *Methods Mol. Biol.* **1183**, 221–242 (2014).

61. Zhao, S. et al. Cell type-specific channelrhodopsin-2 transgenic mice for optogenetic dissection of neural circuitry function. *Nat. Methods* **8**, 745–752 (2011).

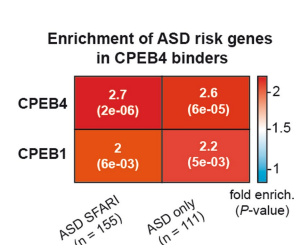
62. Guzman, S. J., Schlögl, A. & Schmidt-Hieber, C. Stimfit: quantifying electrophysiological data with Python. *Front. Neuroinform.* **8**, 16 (2014).

**d CPEB4 binders with shortened poly(A)-tail length (FC ≤ -3.0)**

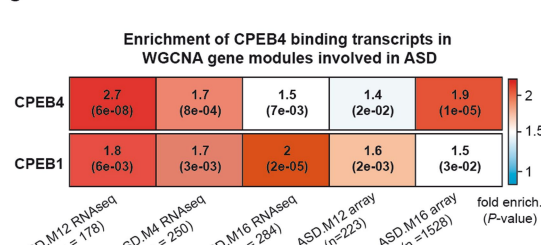
Nº	FC	Symbol	Gene Name	CPEB1-binding
1	-5.4	Auts2	Autism susceptibility candidate 2	Y
2	-5.3	Akap10	A kinase (PRKA) anchor protein 10	Y
3	-4.9	Rock1	Rho-associated coiled-coil containing protein kinase 1	Y
4	-4.5	Ktn1	Kinetin 1	Y
5	-3.9	Slik	STE20-like kinase	Y
6	-3.9	Kpnb1	Karyopherin (importin) beta 1	Y
7	-3.9	Ssr3	Signal sequence receptor, gamma	Y
8	-3.8	Rp2h	Retinitis pigmentosa 2 homolog (human)	N
9	-3.8	Bach2	BTB and CNC homology 2	Y
10	-3.7	Cpsf6	Cleavage and polyadenylation specific factor 6	N
11	-3.7	Pan3	PAN3 polyA specific ribonuclease subunit homolog	N
12	-3.6	Tmx3	Thioredoxin-related transmembrane protein 3	N
13	-3.6	Ube2d3	Ubiquitin-conjugating enzyme E2D 3	N
14	-3.6	Eph43	Eph receptor A3	N
15	-3.6	Zfx	Zinc finger protein X-linked	Y
16	-3.5	Crbn	Cereblon	Y
17	-3.4	Rnd3	Rho family GTPase 3	N
18	-3.4	Dyrk1a	Dual-specificity tyrosine-phosphorylation regulated kinase 1a	N
19	-3.4	Hey2	Hairy/enhancer-of-split related with YRPW motif 2	N
20	-3.4	Mynn	Myoneurin	N
21	-3.3	Cers6	Ceramide synthase 6	Y
22	-3.2	Klh28	Kelch-like 28	N
23	-3.2	Plagl1	Pleiomorphic adenoma gene-like 1	Y
24	-3.2	Dtw d2	DTW domain containing 2	N
25	-3.2	0630041G16Rik	RIKEN cDNA 0630041G16 gene	N
26	-3.2	Arl6ip6	ADP-ribosylation factor-like 6 interacting protein 6	N
27	-3.2	Ccdc88a	Coiled coil domain containing 88A	N
28	-3.2	Sp3	Trans-acting transcription factor 3	N
29	-3.2	Ctso	Cathepsin O	Y
30	-3.2	Cul3	Cullin 3	Y
31	-3.2	2810474O19Rik	RIKEN cDNA 2810474O19 gene	Y
32	-3.1	Tmc05	Transmembrane and coiled-coil domains 5	N
33	-3.1	Camk4	Calcium/calmodulin-dependent protein kinase IV	Y
34	-3.1	Zhx1	Zinc fingers and homeoboxes 1	Y
35	-3.1	Cep290	Centrosomal protein 290	N
36	-3.0	Eif4a2	Eukaryotic translation initiation factor 4A2	Y
37	-3.0	Wnt5a	Wingless-related MMTV integration site 5A	Y
38	-3.0	Metap2	Methionine aminopeptidase 2	N
39	-3.0	Ptchd1	Patched domain containing 1	N
40	-3.0	Birc6	Baculoviral IAP repeat-containing 6	Y

ASD causing genes

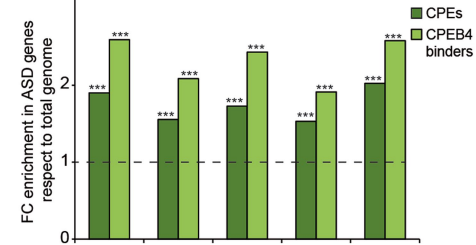
f



g



h



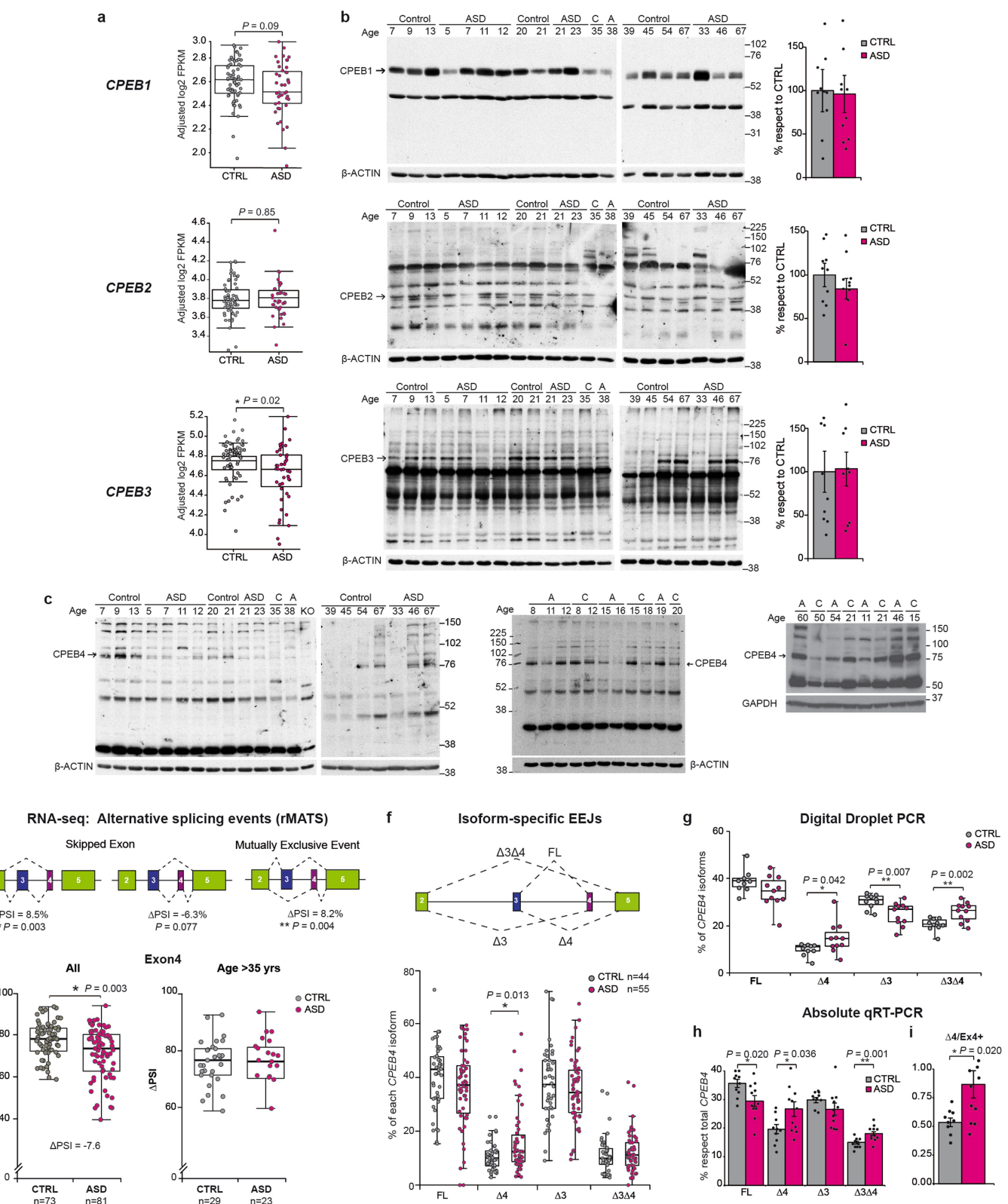
Extended Data Fig. 1 | Enrichment in ASD risk genes among CPEB1–4 binding transcripts whose poly(A)-tail was shortened in an HD mouse model with altered CPEBs. a, Experimental design of RIP from wild-type and HD mice (with altered CPEB1 and CPEB4, see Methods).

b, Percentage of CPE sequences in the 3' UTR of total genome, brain genes and CPEB1 and CPEB4 binders from the RIP experiment. c, Percentage of CPEB1- or CPEB4-only binders with shortened (red), lengthened (blue) or unaltered (purple) poly(A) tails. d, Symbol and gene names of CPEB4 binders in wild-type striatum with the most shortened poly(A)-tails ($FC \leq -3.0$) in HD mice. The last column indicates whether they are also CPEB1 binders (Y, yes; N, no). High-confidence ASD risk genes (SFARI categories 1–3) are highlighted in pink. e, FC enrichment of

high-confidence ASD genes (SFARI categories 1–3 and 1–2) in CPEB4 binders whose poly(A) tails were shortened in HD mice ($FC \leq -3.0$).

f, Heat maps of CPEB4/CPEB1 binders in SFARI ASD genes or with intellectual disability genes removed (ASD only). g, As in f, for weighted gene co-expression network analysis (WGCNA) modules involved in ASD.

h, FC enrichment of percentage of CPE sequences and CPEB4 binders of ASD genes (SFARI categories 1–2, $n = 63$) versus total genome stratified by 5' UTR, 3' UTR, CDS or gDNA length and ratio of neuronal-to-glial expression. b, e–g, One-sided Fisher's exact test. c, Pearson's chi-squared test. h, Statistical details for simulations in Methods section. ** $P < 0.01$, *** $P < 0.001$.

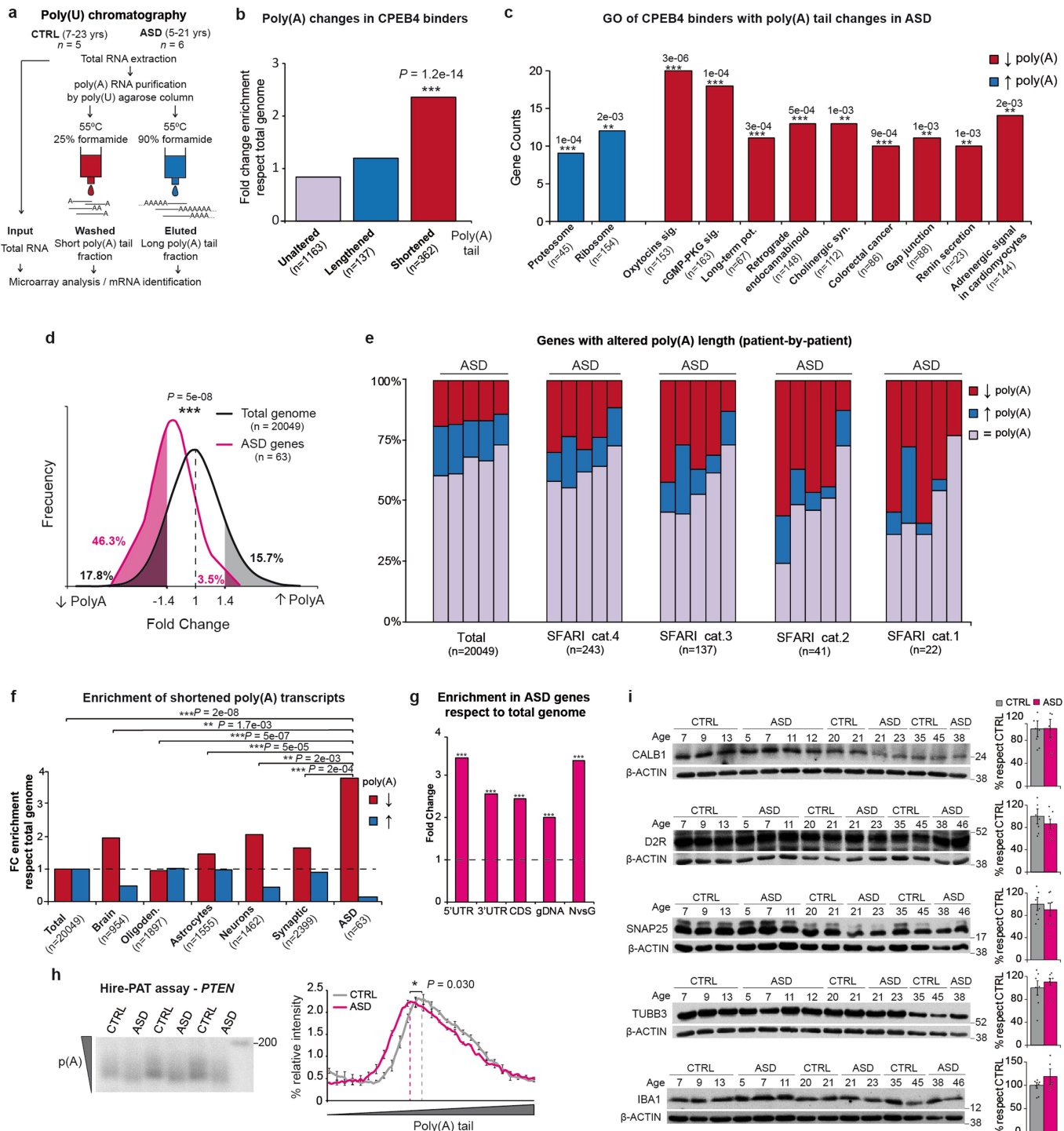


Extended Data Fig. 2 | mRNA and protein levels of CPEBs in cortex of individuals with idiopathic ASD and features of CPEB4 mis-splicing.

a, CPEB1–CPEB3 mRNA expression levels according to RNA-seq data ($n = 63$ for control, $n = 43$ for ASD). **b, c**, CPEB1–3 protein levels (**b**; $n = 10$) and CPEB4 protein levels (**c**; $n = 20$ for control and $n = 19$ for ASD). **d**, Diagram representing the alternative splicing of CPEB4 by rMATS. PSI is shown under each event ($n = 81$ for control and $n = 82$ ASD cortical prefrontal and temporal samples). **e**, CPEB4 exon 4 inclusion level (PSI) in all (left) and over-35-year-old (right) individuals. **f**, Percentage of each CPEB4 splicing isoform by VAST-TOOLS analysis of isoform-specific

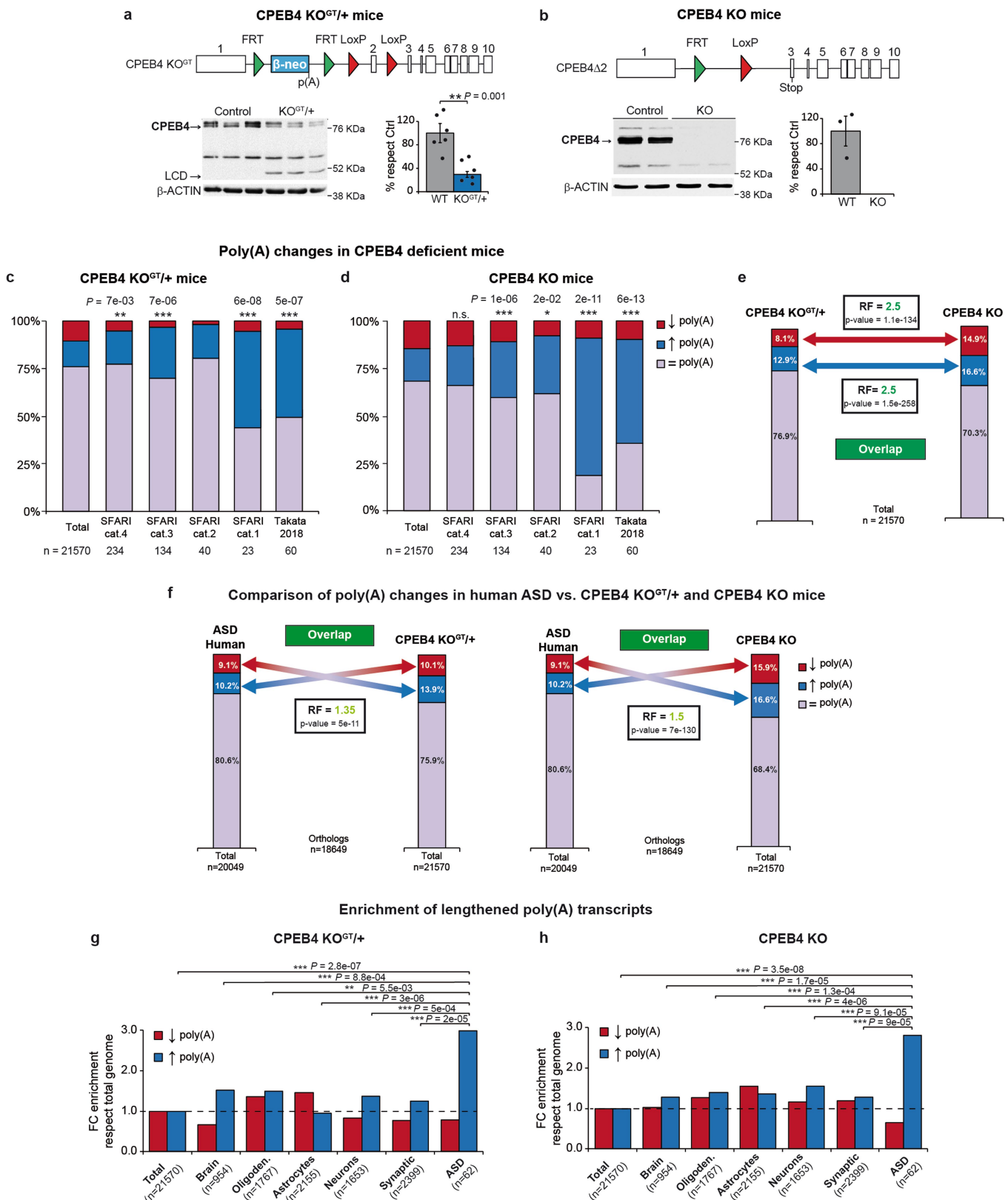
exon–exon junctions (EEJs). **g, h**, Percentage of each CPEB4 splicing isoform by digital-droplet PCR (**g**) and absolute qRT-PCR (**h**).

i, $\Delta 4/\text{Ex}4^+$ CPEB4 isoform ratio in cortex from individuals with idiopathic ASD ($n = 11$) and control individuals ($n = 10$) under 35 years old. For gel source data, see Supplementary Fig. 1. **a, d–g, i**, Two-sided Mann–Whitney–Wilcoxon test. **b, h**, Two-sided unpaired *t*-test. Box plots: centre line shows median; box shows 25th and 75th percentiles; whiskers show minimum and maximum values. Bar graphs show mean \pm s.e.m. $*P < 0.05$, $**P < 0.01$.



Extended Data Fig. 3 | Supplementary data for global poly(A)-alterations and protein levels in brains from individuals with idiopathic ASD. **a**, Experimental design. **b**, Poly(A) changes in CPEB4 binders. **c**, Gene counts histogram from GO analysis (KEGG pathways) of genes with poly(A) tail changes. **d**, Frequency distribution of FCs of poly(A) alteration of total genes (black) and ASD genes (SFARI categories 1–2, pink). **e**, Percentage of genes with shortened (red), lengthened (blue) or unaltered (purple) poly(A)-tail length in the whole transcriptome and ASD genes (SFARI categories 4–1) patient-by-patient. **f**, FC enrichment of brain-, oligodendrocytic-, astrocytic-, neuronal-, synaptic- and ASD-specific genes (SFARI categories 1–2) with shortened poly(A)-tails compared to total genome. **g**, FC enrichment of ASD (SFARI categories

1–2) genes shortened in ASD human versus total genome stratified by 5' UTR, 3' UTR, CDS and gDNA length and by ratio or neuronal-to-glial expression. **h**, Hire-PAT assay of PTEN poly(A)-tail in control and ASD cases ($n = 3$). **i**, Protein levels of neuronal and astrocytic specific genes in cortex from individuals with idiopathic ASD and control individuals ($n = 7$). For gel source data, see Supplementary Fig. 1. **b**, **f**, One-sided Fisher's exact test. **c**, FDR Benjamini–Hochberg. **d**, Two-sided Mann–Whitney–Wilcoxon test. **P** values of genes with shortened poly(A) in each group with respect to ASD genes. **g**, Statistical details in Methods. **h**, **i**, Two-sided unpaired *t*-test. Data are mean \pm s.e.m. * $P < 0.05$, ** $P < 0.01$, *** $P < 0.001$.

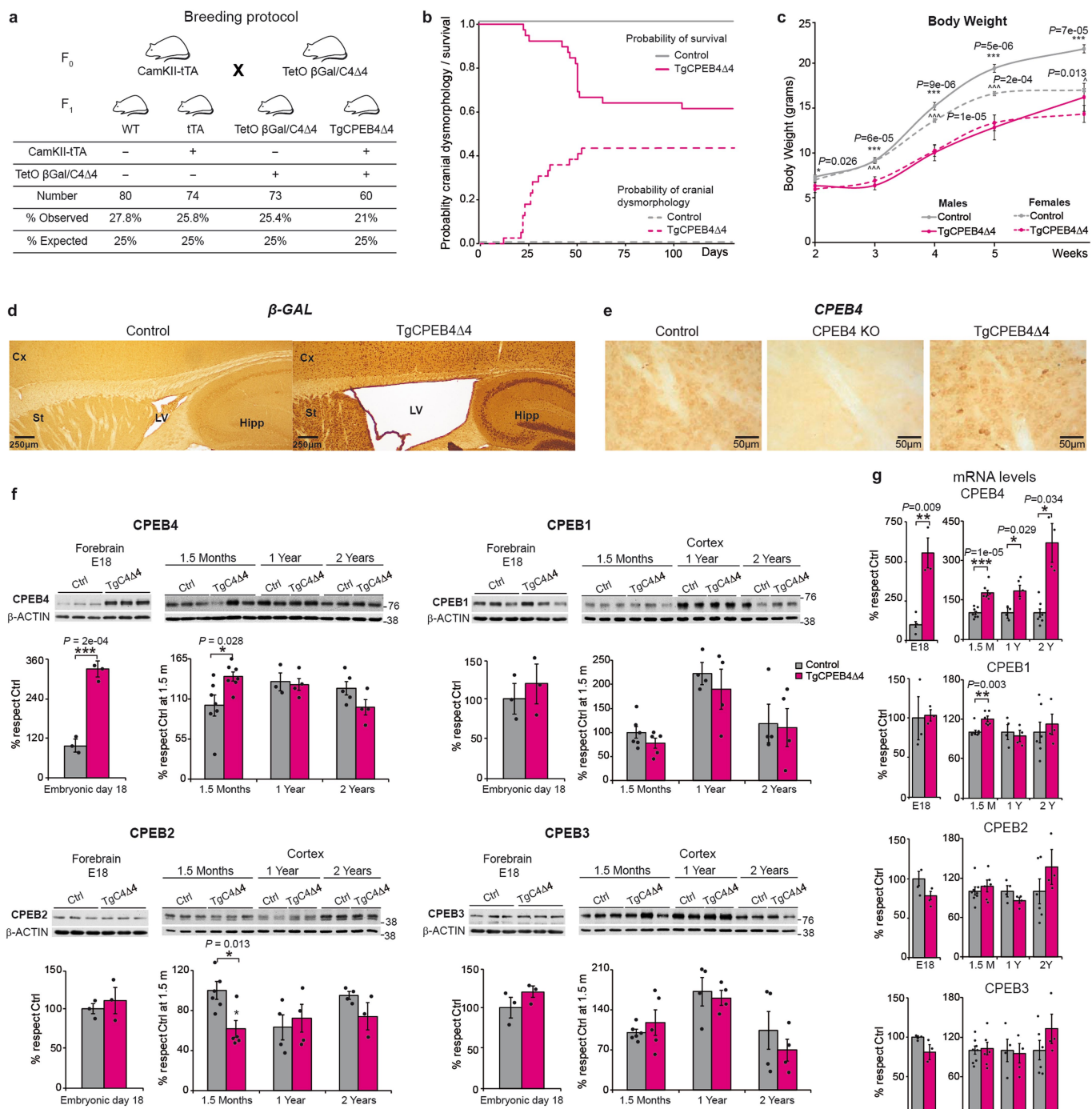


Extended Data Fig. 4 | Poly(A) changes in CPEB4-deficient mice.

a, b, Construct design and CPEB4 protein levels of CPEB4 KO^{GT/+} mice (**a**; $n = 7$) and CPEB4 KO mice (**b**; $n = 3$). LCD isoform. **c, d**, Percentage of transcripts with poly(A)-tail changes in CPEB4 KO^{GT/+} (**c**) and CPEB4 KO (**d**) cortex and striatal samples ($n = 2$), in whole transcriptome and in ASD gene lists. **e**, Comparison of genes with poly(A) changes between CPEB4 KO^{GT/+} and CPEB4 KO mice. **f**, Comparison of genes with poly(A) changes between ASD cases and CPEB4-deficient mice. **g, h**, FC enrichment of brain-, oligodendrocyte-, astrocyte-, neuron-, synapse- and

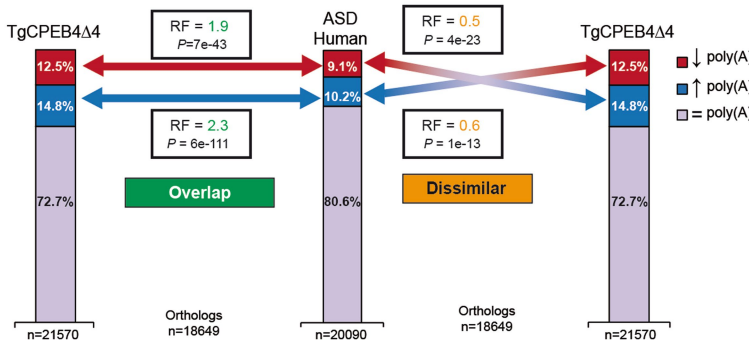
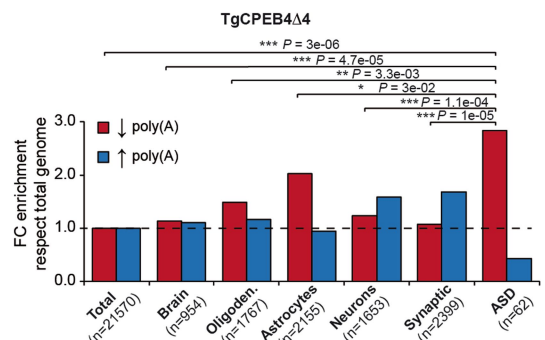
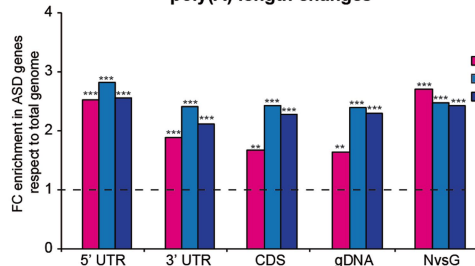
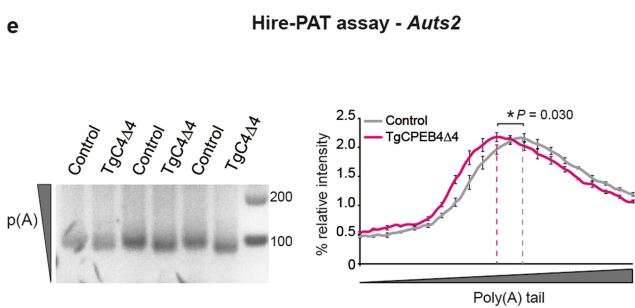
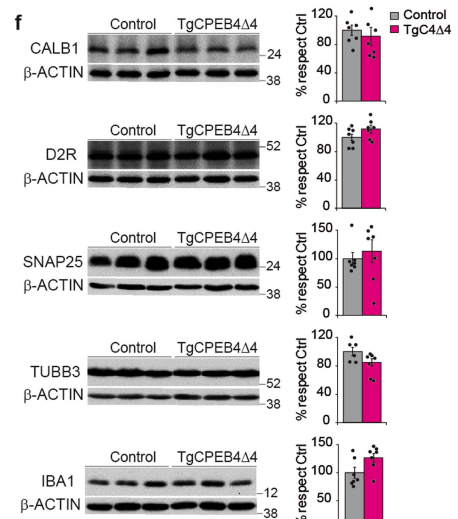
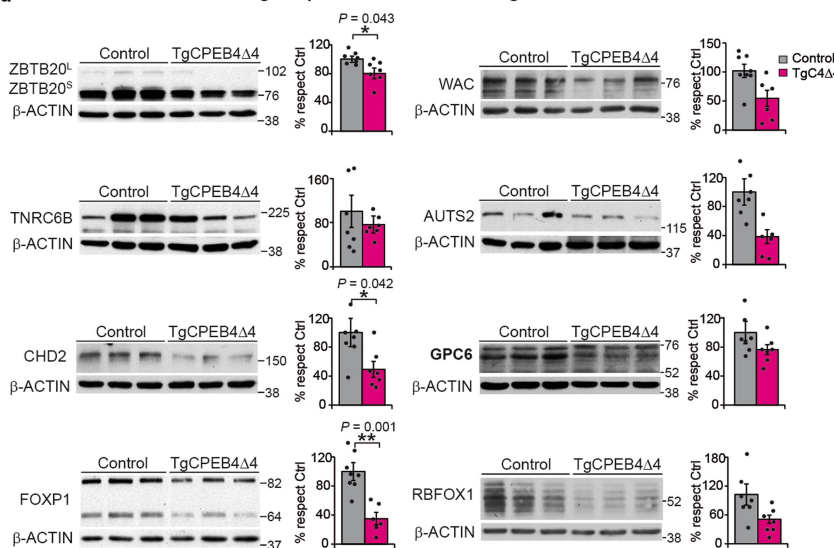
ASD-specific genes (SFARI categories 1–2) with lengthened poly(A)-tails with respect to total transcriptome in CPEB4 KO^{GT/+} mice (**g**) and CPEB4 KO mice (**h**). For gel source data, see Supplementary Fig. 1.

a, Two-sided unpaired *t*-test. **c, d**, One-sided Fisher's exact test, *P* values of ASD transcripts with lengthened poly(A) versus total. **e, f**, Hypergeometric test. **g, h**, One-sided Fisher's exact test, *P* values of genes with lengthened poly(A) in each group with respect to ASD genes. Data are mean \pm s.e.m. **P* < 0.05, ***P* < 0.01, ****P* < 0.001.



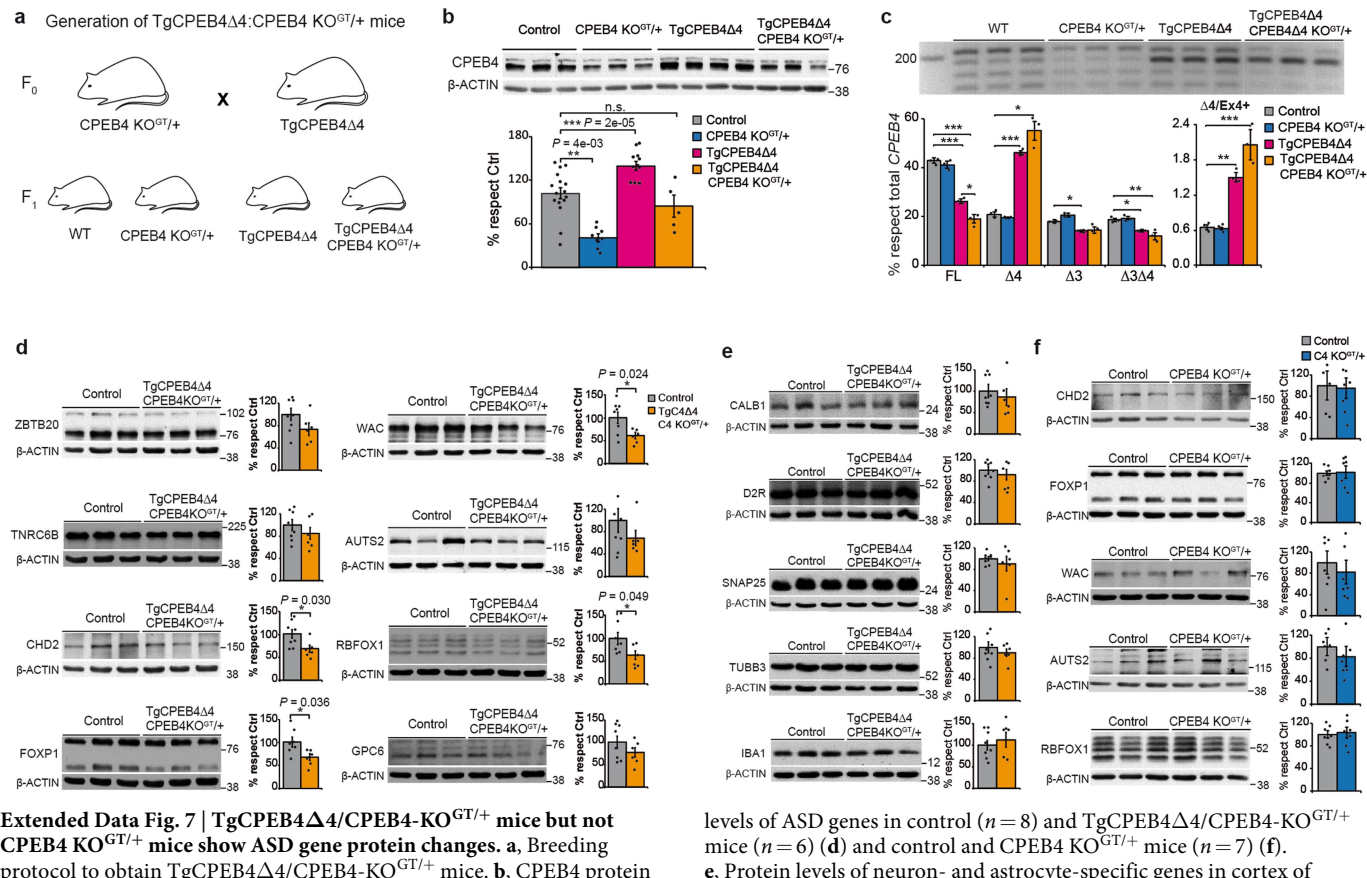
Extended Data Fig. 5 | Supplementary characterization of TgCPEB4Δ4 mice. **a**, Breeding protocol to obtain TgCPEB4Δ4 mice. Number of mice and percentages of births observed and expected for the four experimental genotypes. **b**, Kaplan–Meier curve for cumulative survival (continuous line) and probability of developing cranial dysmorphology (dashed line) ($n = 44$ for control, $n = 39$ for TgCPEB4Δ4 mice). **c**, Evolution of body weight (grams). Males (continuous line), $n = 25$ controls, $n = 9$ TgCPEB4Δ4 mice. Females (dashed line), $n = 26$ control, $n = 7$ TgCPEB4Δ4 mice. **d**, β -GAL nuclear staining in forebrain neurons from 1.5-month-old controls ($n = 6$) and TgCPEB4Δ4 mice ($n = 4$). LV, lateral

ventricle. Scale bars, 250 μ m. **e**, Striatal CPEB4 immunohistochemistry shows cytoplasm pattern in control ($n = 6$), no staining in CPEB4 KO ($n = 2$) and overexpressing neurons in TgCPEB4Δ4 mice ($n = 4$). Scale bars, 50 μ m. **f, g**, Protein (**f**) and mRNA (**g**) expression levels of CPEB1–4 in forebrain at embryonic day 18 ($n = 3$) and cortex at 1.5 months ($n = 6$), 1 year ($n = 4$) and 2 years ($n = 5$) of control and TgCPEB4Δ4 mice. For gel source data, see Supplementary Fig. 1. **a**, Pearson's chi-squared test. **c, f, g**, Two-sided unpaired *t*-test. Data are mean \pm s.e.m. * $P < 0.05$, ** $P < 0.01$, *** $P < 0.001$.

a Comparison of poly(A) changes in human ASD vs.TgCPEB4Δ4**b Enrichment of shortened poly(A) transcripts****c Enrichment of ASD genes with poly(A) length changes****e****d ASD-gene protein levels in St of TgCPEB4 $\Delta 4$ mice**

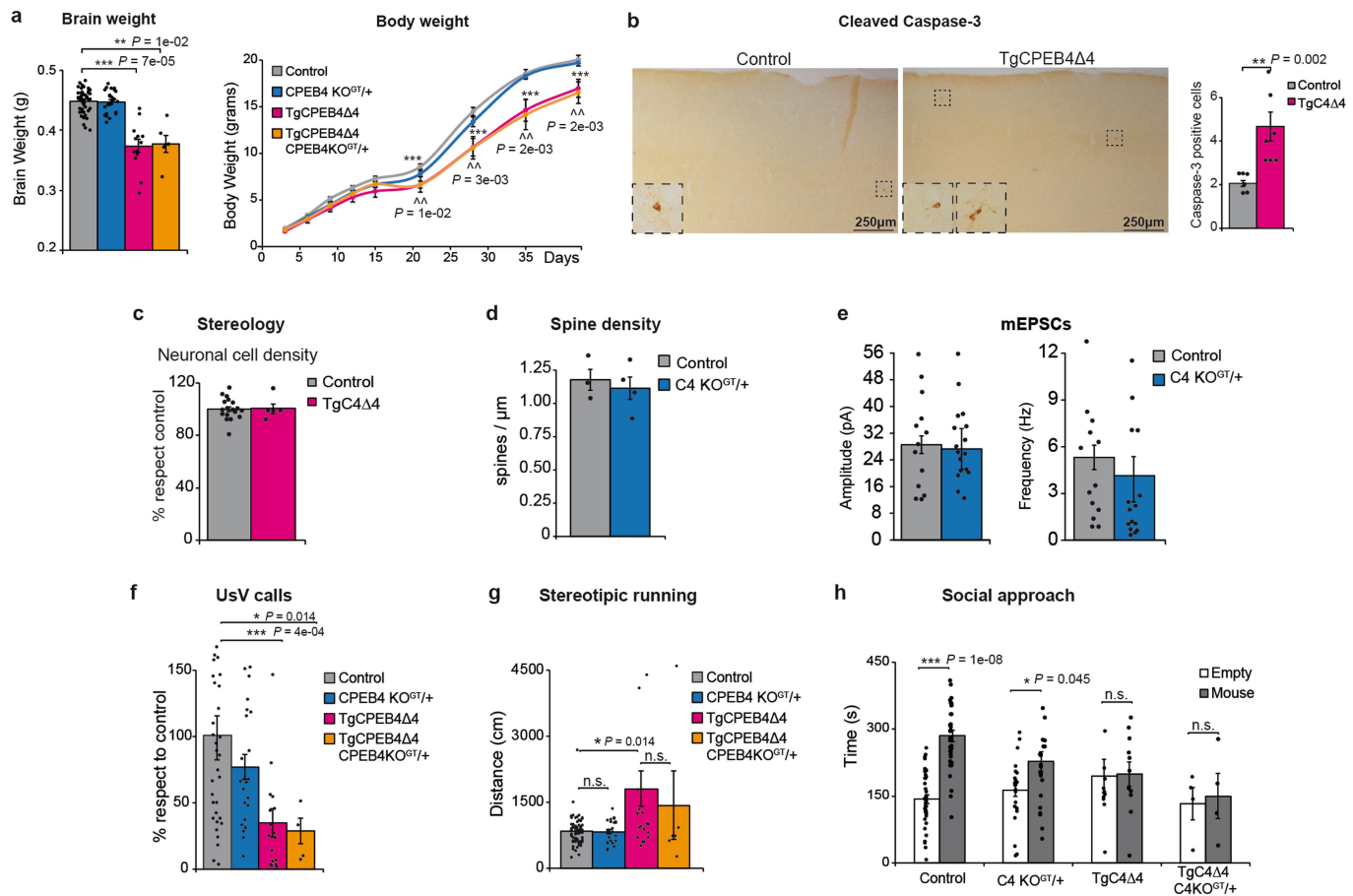
Extended Data Fig. 6 | Supplementary data showing global poly(A)-alterations and protein levels in TgCPEB4 $\Delta 4$ mice. **a**, Comparison of genes with poly(A) changes in the same or the opposite direction between humans with ASD and TgCPEB4 $\Delta 4$ mice. **b**, FC enrichment of brain-, oligodendrocyte-, astrocyte-, neuron-, synapse- and ASD-specific (SFARI categories 1–2) genes with shortened poly(A)-tails with respect to total genome in TgCPEB4 $\Delta 4$ mice. **c**, FC enrichment of ASD (SFARI categories 1–2, n = 62) genes shortened in TgCPEB4 $\Delta 4$ mice and lengthened in CPEB4 KO $^{GT/+}$ and CPEB4 KO mice versus total genome stratified by 5' UTR, 3' UTR, CDS and gDNA length, and ratio of neuronal-to-glial

expression. **d**, Protein levels in striatum of 1.5-month-old control and TgCPEB4 $\Delta 4$ mice (n = 7). **e**, Hire-PAT assay of *Auts2* poly(A)-tail in control and TgCPEB4 $\Delta 4$ mice (n = 3). **f**, Protein levels of neuron- and astrocyte-specific genes in cortex of control and TgCPEB4 $\Delta 4$ mice (n = 7). For gel source data, see Supplementary Fig. 1. **a**, Hypergeometric test. **b**, One-sided Fisher's exact test, P values of genes with shortened poly(A) in each group with respect to ASD genes. **c**, Statistical details in simulations in Methods. **d–f**, Two-sided unpaired t-test. Data are mean \pm s.e.m. *P < 0.05, **P < 0.01, ***P < 0.001.



Extended Data Fig. 7 | TgCPEB4 Δ 4/CPEB4-KO $^{GT/+}$ mice but not CPEB4 KO $^{GT/+}$ mice show ASD gene protein changes. **a**, Breeding protocol to obtain TgCPEB4 Δ 4/CPEB4-KO $^{GT/+}$ mice. **b**, CPEB4 protein levels in cortex of control 1.5-month-old ($n = 16$), CPEB4 KO $^{GT/+}$ ($n = 8$), TgCPEB4 Δ 4 ($n = 11$) and TgCPEB4 Δ 4/CPEB4-KO $^{GT/+}$ mice ($n = 5$). **c**, Percentage of CPEB4 splicing isoforms and Δ 4/Ex4 $^+$ ratio in cortex of control, CPEB4 KO $^{GT/+}$, TgCPEB4 Δ 4 and TgCPEB4 Δ 4/CPEB4-KO $^{GT/+}$ mice ($n = 3$) by PCR with primers annealing to exons 2 and 5. **d-f**, Protein

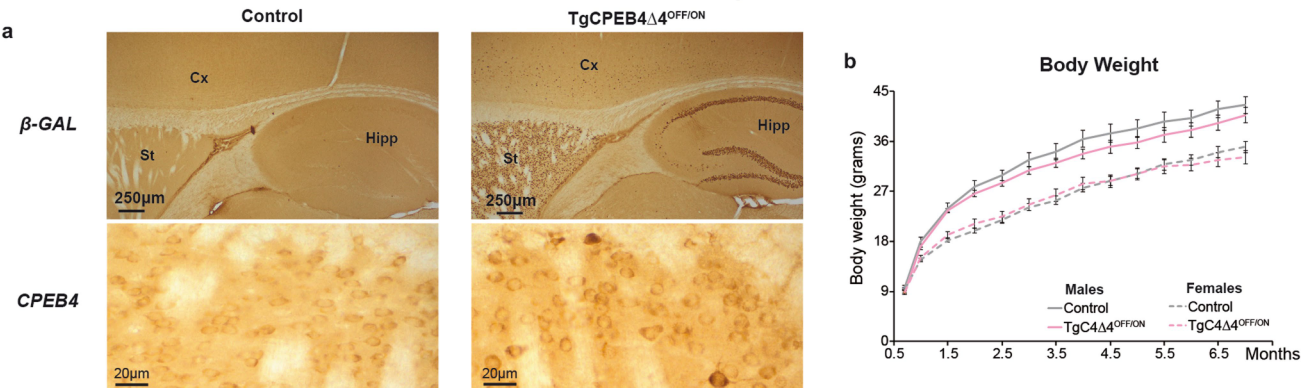
levels of ASD genes in control ($n = 8$) and TgCPEB4 Δ 4/CPEB4-KO $^{GT/+}$ mice ($n = 6$) (**d**) and control and CPEB4 KO $^{GT/+}$ mice ($n = 7$) (**f**). **e**, Protein levels of neuron- and astrocyte-specific genes in cortex of control ($n = 8$) and TgCPEB4 Δ 4/CPEB4-KO $^{GT/+}$ mice ($n = 6$). For gel source data, see Supplementary Fig. 1. **b**, One-way ANOVA followed by Games-Howell post hoc test. **c**, One-way ANOVA followed by Tukey's post hoc test. **d-f**, Two-sided unpaired t-test. Data are mean \pm s.e.m. * $P < 0.05$, ** $P < 0.01$, *** $P < 0.001$.



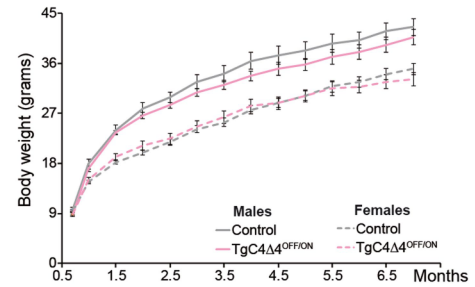
Extended Data Fig. 8 | TgCPEB4Δ4/CPEB4-KO^{GT/+} mice, but not CPEB4 KO^{GT/+} mice, show anatomical and behavioural alterations.

a, Brain weight in 6-week-old control ($n=45$), CPEB4 KO^{GT/+} ($n=25$), TgCPEB4Δ4 ($n=13$) and TgCPEB4Δ4/CPEB4-KO^{GT/+} ($n=6$) mice and evolution of body weight of control ($n=74$), CPEB4 KO^{GT/+} ($n=27$), TgCPEB4Δ4 ($n=18$) and TgCPEB4Δ4/CPEB4-KO^{GT/+} ($n=6$) mice. **b**, Immunohistochemistry against anti-cleaved caspase-3 in cortex ($n=3$ slices from six controls and six TgCPEB4Δ4 mice). Scale bars, 250 μm. **c**, Striatal neuronal cell density in control ($n=19$) and TgCPEB4Δ4 mice ($n=5$). **d**, Spine density (spines per μm) in cortical layers II/III of pyramidal neurons in CPEB4 KO^{GT/+} mice ($n=5$ cells from three controls, and $n=5$ cells from four CPEB4 KO^{GT/+} mice). **e**, Amplitude (pA) and frequency (Hz) of mEPSCs recorded from pyramidal neurons of the somatosensory cortex, in CPEB4 KO^{GT/+} mice ($n=13$ cells from five controls, and $n=17$ cells from six CPEB4 KO^{GT/+} mice). **f**, Ultrasonic

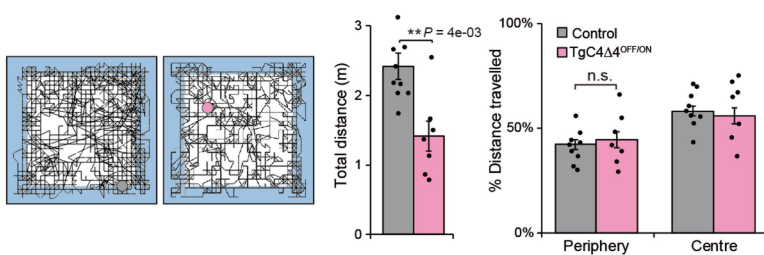
calls of pups during 5 min after separation from their mothers as mean of data from postnatal days 6 and 12 in control ($n=36$), CPEB4 KO^{GT/+} ($n=22$), TgCPEB4Δ4 ($n=17$) and TgCPEB4Δ4/CPEB4-KO^{GT/+} ($n=4$) pups. **g**, Stereotypical running represented as distance travelled (cm) in the periphery in the open field test in control ($n=74$), CPEB4 KO^{GT/+} ($n=25$), TgCPEB4Δ4 ($n=19$) and TgCPEB4Δ4/CPEB4-KO^{GT/+} ($n=6$) mice. **h**, Time interacting with empty cage or an unfamiliar mouse during 10 min for control ($n=40$), CPEB4 KO^{GT/+} ($n=24$), TgCPEB4Δ4 ($n=11$) and TgCPEB4Δ4/CPEB4-KO^{GT/+} ($n=4$) mice. **a**, One-way ANOVA followed by Games–Howell post hoc test. **b**, Two-sided Mann–Whitney–Wilcoxon test. **c, e**, Two-sided unpaired *t*-test. **f, g**, Kruskal–Wallis one-way ANOVA. **h**, Two-sided Wilcoxon signed-rank test. Data are mean ± s.e.m. n.s., non-significant, $*P < 0.05$, $**P < 0.01$, $***P < 0.001$.

OFF/ON - CPEB4 Δ 4 expression

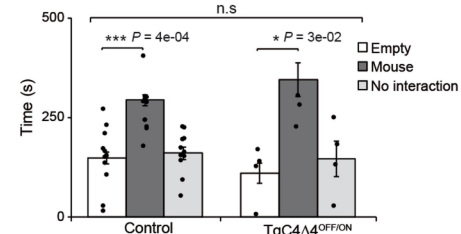
Body Weight



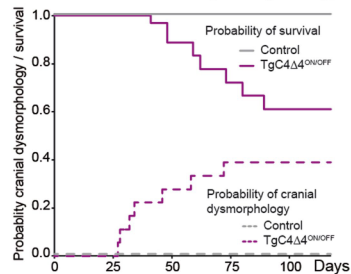
c Open Field



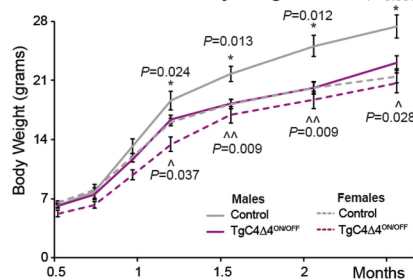
d Social Approach

ON/OFF - CPEB4 Δ 4 expression

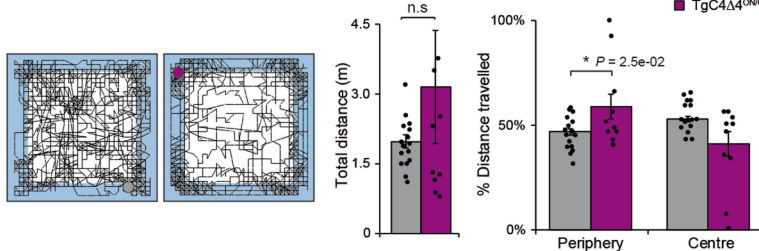
e Survival / Cranial dysmorphology



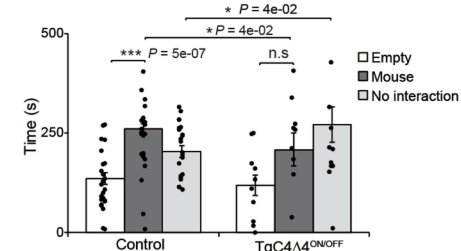
Body Weight



g Open Field



h Social Approach



Extended Data Fig. 9 | Effect on ASD-like behaviours of doxycycline-mediated temporal regulation of transgene expression in TgCPEB4 Δ 4 mice. **a-d**, TgCPEB4 Δ 4 mice with transgene expression starting at the age of 3 weeks (OFF/ON-TgCPEB4 Δ 4 mice) do not display ASD-like behavioural phenotypes. **a**, β -GAL nuclear staining in forebrain neurons and CPEB4 immunohistochemistry in 3-month-old control and TgCPEB4 Δ 4 mice ($n=3$). **b**, Evolution of body weight (grams) of male ($n=29$ controls, $n=11$ OFF/ON-TgCPEB4 Δ 4) and female mice ($n=29$ control, $n=10$ OFF/ON-TgCPEB4 Δ 4). No premature death or cranial dysmorphology was observed in OFF/ON-TgCPEB4 Δ 4 mice. **c**, Total distance travelled by control ($n=9$) and OFF/ON-TgCPEB4 Δ 4 ($n=7$) mice and percentage of their distance in the periphery and in the centre in open field test. **d**, Time interacting with either an empty cage, an unfamiliar mouse or without any interaction during 10 min for control ($n=12$) and OFF/ON-TgCPEB4 Δ 4 mice ($n=5$). **e-h**, Silencing transgene

expression in TgCPEB4 Δ 4 mice that have expressed the transgene during embryonic development does not revert ASD-like behaviours (ON/OFF-TgCPEB4 Δ 4 mice). **e**, Kaplan-Meier curve for cumulative survival (solid line) and percentage of mice developing cranial dysmorphology (dashed line), $n=21$ for controls, $n=16$ for ON/OFF-TgCPEB4 Δ 4 mice. **f**, Evolution of body weight (grams) in male ($n=19$ controls and $n=10$ ON/OFF-TgCPEB4 Δ 4) and female mice ($n=12$ control and $n=6$ ON/OFF-TgCPEB4 Δ 4). **g**, Total distance travelled by control ($n=16$) and ON/OFF-TgCPEB4 Δ 4 ($n=10$) mice and percentage of their distance in the periphery and in the centre in open field test. **h**, Time interacting with either an empty cage, an unfamiliar mouse or without any interaction during 10 min for control ($n=20$) and ON/OFF-TgCPEB4 Δ 4 mice ($n=13$). **b-d, f**, Two-sided unpaired t -test. **g, h**, Two-sided Mann-Whitney-Wilcoxon test. **h**, Two-sided Wilcoxon signed-rank test. Data are mean \pm s.e.m. n.s., non-significant; * $P<0.05$, ** $P<0.01$, *** $P<0.001$.

Cryo-EM structure of the insect olfactory receptor Orco

Joel A. Butterwick¹, Josefina del Mármlol^{1,3}, Kelly H. Kim^{2,3}, Martha A. Kahlson¹, Jackson A. Rogow¹, Thomas Walz² & Vanessa Ruta^{1*}

The olfactory system must recognize and discriminate amongst an enormous variety of chemicals in the environment. To contend with such diversity, insects have evolved a family of odorant-gated ion channels comprised of a highly conserved co-receptor (Orco) and a divergent odorant receptor (OR) that confers chemical specificity. Here, we present the single-particle cryo-electron microscopy structure of an Orco homomer from the parasitic fig wasp *Apocrypta bakeri* at 3.5 Å resolution, providing structural insight into this receptor family. Orco possesses a novel channel architecture, with four subunits symmetrically arranged around a central pore that diverges into four lateral conduits that open to the cytosol. The Orco tetramer has few inter-subunit interactions within the membrane and is bound together by a small cytoplasmic anchor domain. The minimal sequence conservation among ORs maps largely to the pore and anchor domain, shedding light on how the architecture of this receptor family accommodates its remarkable sequence diversity and facilitates the evolution of odour tuning.

Insects are the most diverse group of multicellular organisms on Earth, representing over half of all identified animal species on the planet¹. The success of insects reflects their remarkable capacity to adapt to a wide range of ecological niches. The rapid evolution of insect olfactory receptors is thought to contribute to this adaptation², endowing each insect species with the ability to selectively detect volatile chemicals associated with its specialized habitat and lifestyle.

The olfactory systems of insects and mammals share a similar logic for odour detection and discrimination^{3,4}. Each olfactory sensory neuron generally expresses just one member of a large family of receptors, an organizational principle that allows odours to be encoded by the combinatorial activation of different sensory neuron ensembles^{5,6}. However, insect olfactory receptors are unrelated to the G-protein-coupled chemoreceptors that are found in other animals. Instead, they have been proposed to form a unique class of heteromeric cation channels^{7,8} composed of two related heptahelical subunits: a divergent odorant receptor (OR) subunit that confers odour specificity, and a highly conserved co-receptor (Orco) subunit. Most species express just one Orco and a distinct complement of ORs⁹, ranging from just four members in the damselfly¹⁰ to more than 350 in some ants¹¹. Variation in receptor number is paralleled by their striking sequence diversity, with an average of only about 20% amino-acid identity shared between ORs, either within or across species¹². Indeed, orthologous ORs are rarely apparent between insect orders, highlighting how different species have evolved unique repertoires of receptors suited to their specific chemical environments.

Orco was initially identified as a member of the OR family in *Drosophila*¹³. However, in contrast to other ORs, Orco is broadly expressed in olfactory sensory neurons and is almost invariant in sequence across distant insect lineages, underscoring its essential role in olfactory transduction. ORs cannot assemble, traffic, or function in the absence of Orco^{14,20} and the loss of this single receptor results in markedly impaired olfactory behaviours^{14–17}. Orco is present in the olfactory sensory neurons of evolutionarily basal insects that lack ORs⁹, suggesting that it may represent the ancestral form of the

olfactory receptor complex. Indeed, in the absence of ORs, Orco forms autonomous cation channels that can be activated by synthetic agonists¹⁸.

As insect olfactory receptors lack homology to any other protein family, many of their most elementary functional and structural characteristics have remained unknown, including their stoichiometry and how odour binding is transduced to ion flux. Moreover, in the absence of a structural model, how a single Orco can assemble with such a wide array of highly divergent ORs has remained unclear. Here, we present the structure of an Orco homomer from the parasitic fig wasp *A. bakeri*¹⁹. Orco forms a tetrameric channel comprised of four loosely assembled transmembrane domains surrounding a central ion-conduction pathway, and a small intracellular anchor domain through which most inter-subunit interactions are formed. The minimal sequence conservation across ORs is largely localized to the pore and anchor domain, revealing how diverse Orco-OR heterotetramers can assemble. The structure of Orco thus defines the architecture of an archetypal insect olfactory receptor and provides insight into how this large family can rapidly diversify, allowing insects to adapt to different chemical landscapes.

Structure determination of an Orco-Fab complex

Insect olfactory receptors function as obligate multimers²⁰. We therefore screened Orco orthologues by size-exclusion chromatography to find those that stably formed higher-order complexes, and identified Orco from *A. bakeri* as a promising candidate. *A. bakeri* Orco¹⁹ exhibits the sequence and functional conservation characteristic of Orcos²¹: it shares more than 60% sequence identity with Orco orthologues spanning the majority of insect orders and could couple to ORs from evolutionary distant species to mediate odour-gated signalling (Extended Data Fig. 1). Furthermore, when expressed independently, *A. bakeri* Orco formed a cation channel activated by the agonist VUAA1¹⁸ (Fig. 1a, b; Extended Data Fig. 2). Chemical cross-linking suggested that Orco assembles into a tetramer, a stoichiometry further supported by its migration on native gels (Extended Data Fig. 3a–d).

¹Laboratory of Neurophysiology and Behavior, The Rockefeller University, New York, NY, USA. ²Laboratory of Molecular Electron Microscopy, The Rockefeller University, New York, NY, USA. ³These authors contributed equally: Josefina del Mármlol, Kelly H. Kim. *e-mail: ruta@rockefeller.edu

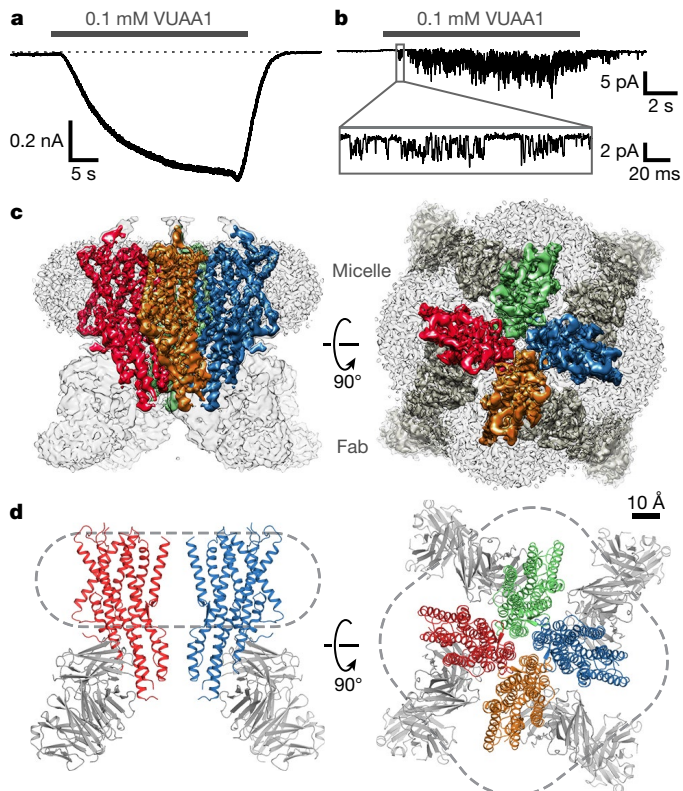


Fig. 1 | Channel activity, cryo-EM density and model of the Orco–Fab complex. **a**, Whole-cell voltage-clamp recording from a cell expressing Orco with local perfusion of VUAA1 (holding potential of -80 mV). Dotted line represents 0 pA. **b**, Outside-out patch recording at -80 mV. Inset shows single channel openings. **c**, Cryo-EM density of the Orco–Fab complex shown from the side (within the plane of the membrane; left) and from the top (the extracellular surface; right). Density of each Orco subunit (contoured at 6σ) is coloured differently. In the top view, Fab density is dark grey. Density of the detergent micelle (contoured at 4σ) is light grey. **d**, Ribbon diagrams of Orco corresponding to views shown in **c**. Two subunits are shown in the side view (left) while four are present in the top view (right). Dashed lines indicate the border of the micelle. The Fabs were not modelled and are included in **d** for illustrative purposes only.

Two-dimensional class averages calculated from an initial cryogenic electron microscopy (cryo-EM) data set of purified Orco failed to show coherent structural features (data not shown). To increase the effective molecular mass of the protein particle (210 kDa), we raised monoclonal antibodies against Orco and purified a 1:1 complex, in which each of the four Orco subunits was bound by an antigen-binding fragment (Fab). Isothermal titration calorimetry (ITC) experiments confirmed that the Orco–Fab complex retained its binding affinity for VUAA1 (Extended Data Fig. 3e, f). A vitrified sample of the purified Orco–Fab complex generated homogenous and mono-dispersed particles with a tetrameric organization that was immediately apparent from the raw cryo-EM images and 2D class averages (Extended Data Fig. 4a, b). Three-dimensional reconstruction imposing C4 symmetry yielded a density map with approximately 4 Å overall resolution. Further refinement after masking out the Fab and micelle regions improved the resolution to 3.5 Å (Fig. 1c; Extended Data Fig. 4c–g; Extended Data Table 1). Side-chain density was clearly resolved for most of the Orco channel and 82% of the protein could be accurately modelled, with the exception of the second extracellular loop (Val156–Ile170) and second intracellular loop (Leu244–Asn312). Density for the Fab was generally weaker, especially for the constant region, and was not modelled.

Architecture of the Orco homotetramer

The architecture of Orco represents a novel fold. Viewed from the extracellular surface, Orco forms a tetrameric pinwheel approximately 100 Å

in diameter and 80 Å axially, with four subunits encircling a central pore (Fig. 1d). The majority of the protein resides within the micelle, with only short loops projecting from the extracellular surface and a small intracellular domain extending below. We term this protruding cytoplasmic helical bundle the ‘anchor domain’, as it contains the majority of inter-subunit interactions as described below and thus ‘anchors’ the four loosely packed subunits within the micelle or lipid membrane.

Each Orco subunit has seven membrane-spanning helical segments (S1–S7), with an intracellular amino terminus and an extracellular carboxy terminus (Fig. 2a, b), a topology proposed by previous studies²⁰. A short helix (S0) contributes to a re-entrant loop at the amino terminus that packs underneath S4 at the outer perimeter of the channel. Multiple helical segments (S1, S2, S4, S5) traverse the membrane at an angle (approximately 30° relative to the membrane normal), facilitated by kinks in S2 and S5 at the intracellular membrane surface that transform the largely parallel helical bundle of the anchor domain to the tilted helices within the membrane. S7 resides nearest the central four-fold axis and is divided into two helices—a cytoplasmic segment (S7a) and a transmembrane segment (S7b)—separated by a 15-residue β -hairpin loop. S7b lines the central pore, while S7a forms the core of the anchor domain. The S4, S5, and S6 helices extend well beyond the membrane, projecting up to 40 Å into the cytosol where they surround S7a to complete the anchor domain.

The transmembrane domain of each subunit is stabilized by multiple charged and polar amino acids in S2, S4, S5 and S6 that coalesce to form a dense network of hydrophilic interactions within the intracellular membrane leaflet (Fig. 2c). Several of these interactions, including the salt bridge between Lys86 and Asp213 and the hydrogen bond between Asp213 and Gln392, have been previously identified as amino acid pairs with high co-evolutionary coupling across ORs²².

Within the extracellular leaflet, the S1–S6 helices splay apart to form a 10 Å-deep crevice, approximately 20 Å long. Several residues that have been implicated in determining the sensitivity of Orco to VUAA1 line this pocket²³, suggesting that it may serve as a binding site for small molecule ligands that gate the channel (Extended Data Fig. 5). Mutations that alter odour specificity in ORs^{24–27} also map to residues within this pocket, pointing to a potentially shared structural locus for ligand binding in Orcos and ORs. In the Orco structure, an ordered section of the S3–S4 extracellular loop restricts access to the pocket, which may prevent odour binding to Orco, thus preserving the specificity of odour tuning in Orco–OR complexes.

Within the membrane, the S1–S6 helices of each subunit are narrowly tethered to S7b and separated from their neighbouring subunits by deep inlets that would be filled with lipid within the membrane (Fig. 2e, f). Thus, interactions between subunits are largely confined to the pore-forming helices, while the peripheral portions of each subunit are isolated from each other, an arrangement reminiscent of the extensively studied superfamily of tetrameric cation channels^{28,29} (Extended Data Fig. 6a). However, whereas each subunit of a tetrameric cation channel contributes multiple helices to the central ion pathway, creating extensive contacts that intertwine the subunits together, the Orco pore is comprised of just a single helix (S7b), with far fewer amino acids linking the tetramer within the plane of the membrane (Fig. 2d–f; Extended Data Fig. 6b, c). The limited interactions between Orco subunits result in a small 7 Å gap between neighbouring subunits, suggesting that the lipid membrane forms an integral part of the inter-subunit interface that completes the structural boundary of the pore.

In contrast to the minimal contacts between Orco subunits within the membrane, the helices of the cytosolic anchor domain are densely packed, forming an interface that buries $1,740$ Å² of surface area, accounting for nearly 70% of the contacts between subunits (Fig. 2g). Orco can therefore be coarsely divided into two domains—four loosely attached peripheral transmembrane domains and a single tightly packed central anchor domain. The elongated helices within each Orco subunit link these domains. In particular, the S4 and S5 helices are each more than 50 residues long, forming linchpins that moor the transmembrane domains to the cytoplasmic anchor.

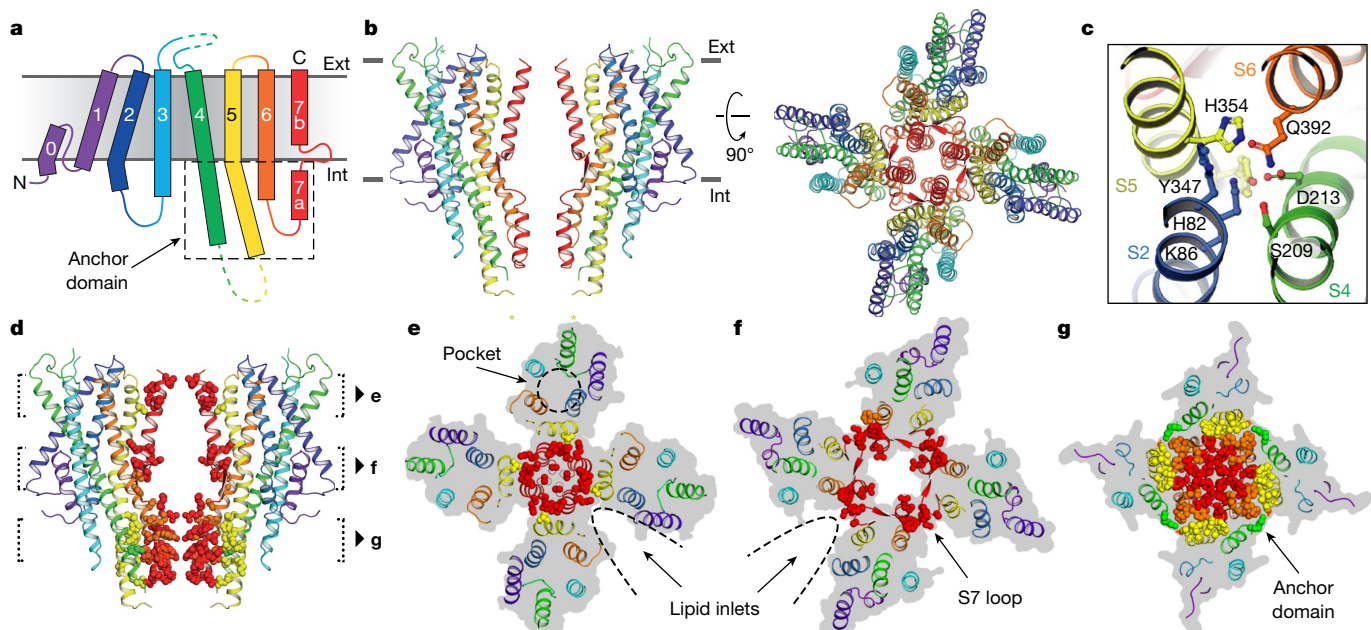


Fig. 2 | Architecture of the Orco homotetramer. **a**, Topology of an Orco subunit. **b**, Ribbon representation of Orco shown from the side (left, two subunits) and top (right, four subunits). Asterisks represent residues that were not modelled. Grey lines indicate membrane boundaries.

c, Hydrophilic network in the intracellular leaflet. **d**, Side view of two Orco subunits with residues within 5 Å of another subunit shown as spheres. **e–g**, 15 Å cross-sections as indicated in **d**.

The channel pore

At the centre of the Orco tetramer, the S7b segment from each subunit lines the ion-conduction pathway (Fig. 3a). The pore is narrowest near the extracellular end, where it is tapered to 2 Å in diameter by a pair of hydrophobic residues, Leu473 and Val469 (Fig. 3b, c). As this narrowing is too small to allow hydrated ions to pass, the structure of Orco appears to represent a closed state. From this extracellular constriction, the pore opens to a large aqueous vestibule lined largely by polar residues. The anchor domain occludes the vestibule at the intracellular face of the membrane, presenting a barrier to the flow of ions into the cytosol. One possibility is that upon channel opening, the extensive inter-subunit interactions within the anchor domain rupture to generate a continuous, approximately 80 Å pathway along the central four-fold axis of the channel. However, this structural rearrangement is not required for ion permeation: four lateral conduits formed at the interfaces between subunits provide a continuous passageway for ions between the central vestibule and the cytosol (Fig. 3). Each lateral conduit is lined by the structured S7 loop and the S5 and S6 segments from adjacent subunits forming a 6 Å-long channel that runs roughly parallel to the plane of the membrane. The diameter of this lateral pathway is greater than 5 Å throughout its length, which would allow partially hydrated cations to pass unhindered. Thus, the pore of Orco appears to exhibit a quadrivial architecture with a single extracellular entryway that diverges to four equivalent intracellular outlets.

The branched nature of Orco's ion pathway resembles acid-sensing ion channels (ASICs)³⁰ and ATP-gated P2X channels³¹. The loosely packed pores of these unrelated channels are also stabilized by soluble domains that reside at the membrane surface and must be circumnavigated to allow ions to pass. ASIC and P2X channels therefore display a similarly complex permeation pathway, in which ions access the central pore through lateral portals formed at the interfaces between adjacent subunits.

Ion selectivity and the extracellular gate

To investigate how amino acids lining the Orco pore contribute to its ion-conduction properties (Fig. 4a), we heterologously expressed the channel in mammalian cells and assessed the relative permeability of different cations. Under bi-ionic conditions, the measured reversal potential (E_{rev}) of ionic currents through a channel will shift towards that of its most permeant ion. In the presence of intracellular Cs⁺ and

extracellular Na⁺ or K⁺, we found the E_{rev} for VUAA1-evoked currents to be near 0 mV, suggesting that all three cations pass through Orco equivalently (Fig. 4b, Extended Data Fig. 7). By contrast, in the presence of extracellular Ca²⁺ or Mg²⁺, VUAA1-evoked currents reversed at more negative potentials³², indicating that these ions do not pass through the pore as readily as Cs⁺, probably as a consequence of their larger hydrated radii.

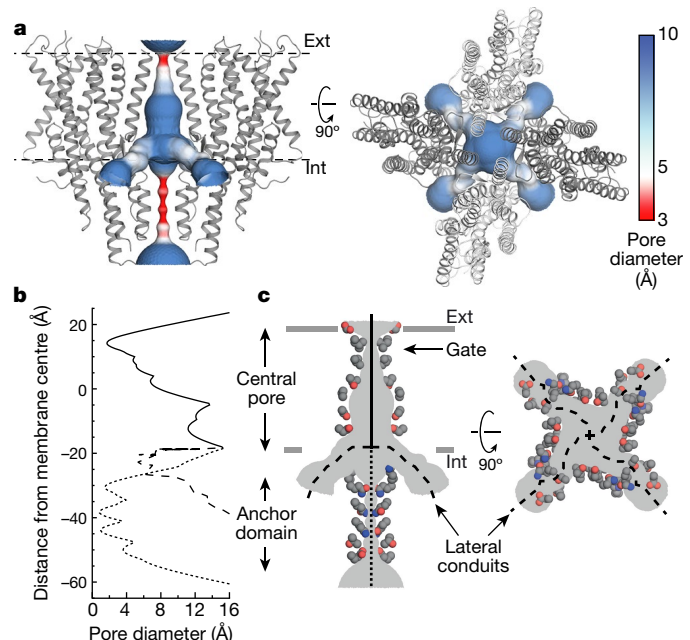


Fig. 3 | The ion-permeation pathway. **a**, The channel pore, coloured according to pore diameter, is shown from the side (left) and top (right). Orco subunits are shown as grey ribbons. **b**, The diameter along the central pore (solid line), anchor domain (dotted line) and lateral conduits (dashed line) are plotted along the membrane normal. **c**, Side chains of residues that line the ion-conduction pathway are shown as coloured spheres (grey carbons, blue nitrogens and red oxygens). The gate corresponds to the constriction formed by Val469 and Leu473.

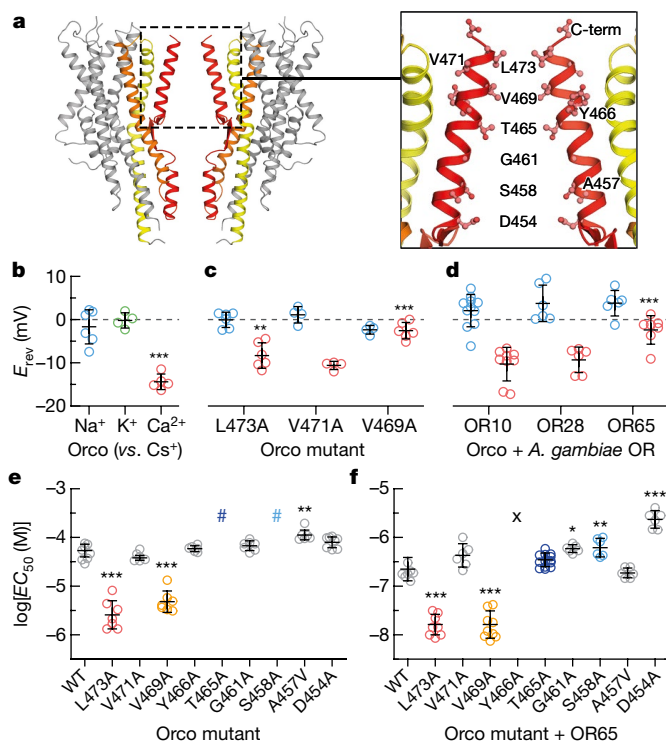


Fig. 4 | A hydrophobic gate contributes to ion selectivity. **a**, Location of residues lining the central pore. **b–d**, Reversal potentials (E_{rev} ; independent replicates and mean \pm s.d.) for wild-type and mutant Orcos alone or with *A. gambiae* ORs (intracellular CsCl with extracellular NaCl (blue), KCl (green) or CaCl₂ (red)). Asterisks represent E_{rev} values that are significantly different from 0 mV (**b**) or from those of wild-type Orco with the same ions (**c**, **d**). **e**, **f**, Average fitted concentrations for half-maximal response (EC_{50} ; independent replicates and mean \pm s.d.) for wild-type (WT) and mutant Orco alone (**e**) or with OR65 (**f**). Hash sign indicates dose-response curves that did not saturate; a lower-bound EC_{50} estimate is approximately 3×10^{-4} M. Crosses indicate no binding observed. Asterisks indicate values of EC_{50} that are significantly different from those of wild-type Orco or Orco–OR. In **b–f**, statistical significance was determined using one-way ANOVA tests followed by Tukey–Kramer multiple comparison tests; * $P < 0.05$, ** $P < 0.01$, *** $P < 0.001$. See Extended Data Figs. 7, 8 for additional statistical information.

Val469 and Leu473 form the narrowest constriction along the quadrivial pathway (Fig. 4a). Mutation of either of these residues to alanine resulted in channels that were more permissive towards Ca²⁺, suggesting that a smaller hydrophobic amino acid at either position generates a larger ion-conduction pathway (Fig. 4c). By contrast, mutation of the nearby Val471, which lies on the opposite face of S7b and points into the lipid membrane, had no effect on ion selectivity. We found that the Ca²⁺ permeability of Orco–OR complexes depended on the identity of the OR (Fig. 4d), consistent with the notion that both subunits contribute to the ion pathway in the heteromeric receptor^{32,33}. Although Val469 and Leu473 are highly conserved among Orcos, ORs show a broader distribution of hydrophobic residues, which could underlie the distinct permeation properties of different Orco–OR assemblies.

To investigate whether Val469 and Leu473 also contribute to gating of the ion pathway, we compared signalling in wild-type and alanine-mutant receptors by co-expressing a genetically encoded Ca²⁺ indicator, GCaMP6s, in mammalian cells. Mutation of either Val469 or Leu473 enhanced the apparent sensitivity of Orco homomers to VUAA1 tenfold (Fig. 4e; Extended Data Fig. 8). A similar shift was evident when these mutant Orcos were co-expressed with OR65 from the mosquito *Anopheles gambiae* and activated by its cognate odorant, eugenol (Fig. 4f). Because Val469 and Leu473 line the ion-conduction pathway, it is unlikely that these residues bind VUAA1 directly; rather,

they are likely to shape the energetics of gating by modulating the relative stability of the open versus closed states.

Immediately below the hydrophobic gate, conserved threonine (Thr465) and serine (Ser458) residues form two rings of hydroxyls that point into the pore, where they may stabilize permeant cations (Fig. 4a). Mutation of either Thr465 or Ser458 to alanine strongly attenuated VUAA1 responses in Orco homomers (Fig. 4e). However, co-expression of OR65 restored the functional sensitivity of these mutants (Fig. 4f), demonstrating that Orco and OR subunits can compensate for each other in the heteromeric receptor. Conversely, mutation of S7b residues at the interface between neighbouring subunits (Tyr466 and Asp454) resulted in functional Orco homomers but significantly impaired heteromeric channels. Mutation of this tyrosine in *Drosophila* Orco has been shown to differentially impact *in vivo* odour signalling, depending on the identity of the OR³³, suggesting that interactions between subunits are not strictly conserved across different Orco–OR assemblies. Mutation of nearby hydrophobic residues that point towards either the lipid (Val471 and Ala457) or the aqueous cavity of the pore (Gly461) did not strongly alter channel gating, either alone or in combination with OR65. Together, these results highlight how Orco and OR subunits cooperate to transduce odourant binding into ion flux within the heteromeric complex.

OR conservation maps to key interaction motifs

An Orco subunit from one species can interact with ORs from another²¹, yielding thousands, if not millions, of possible Orco–OR heteromeric channels, each with distinct ion-conduction properties and odour tuning. To investigate how a single Orco can assemble with such a diverse array of ORs, we aligned OR sequences from four distantly related insect species separated by nearly 400 million years of evolution and defined whether each residue was evolving more slowly or rapidly than the overall average amino acid substitution rate³⁴ (Fig. 5a, b; Extended Data Fig. 9). While the ORs from these four species exhibit the low sequence identity characteristic of this receptor family (average approximately 20%), the pattern of relative sequence conservation resembled that found in Orco and was concentrated along stretches in the carboxy-terminal half of these proteins (Fig. 5b).

When mapped onto the structure of Orco, residues with higher conservation principally line the pore and cluster within the anchor domain (Fig. 5c–f). In the extracellular leaflet, conserved residues from S7b and S5 form a ring that encompasses most of the inter-subunit contacts that stabilize the central pore (Fig. 5d, g). Near the intracellular surface, conserved residues in S7b form an extensive hydrophobic interface with residues lining S6, securing the base of the S7b pore helix (Fig. 5i). Likewise, the anchor domain contains an intricate network of many conserved residues. Notably, highly conserved tyrosine (Tyr415) and tryptophan (Trp419) residues from the cytosolic end of S6 project into a pocket formed by a conserved histidine (His333) and hydrophobic residues from S5 and S7a of a neighbouring subunit (Fig. 5j). Thus, OR sequence conservation preferentially maps to inter-subunit interfaces that could serve to stabilize interactions between Orco and ORs in the heteromer. However, most ORs possess only a subset of these conserved residues, which might explain why ORs cannot assemble in the absence of Orco.

As in other membrane proteins, more variable residues tend to be distributed along the protein surface exposed to the lipid membrane³⁴. Indeed, the most rapidly evolving OR residues map to the perimeter of the channel at the extensive protein–lipid interface surrounding each subunit. Residues within the transmembrane regions of S1–S5 are generally poorly conserved, except for a subset that comprises the hydrophilic network and bridges S2, S4, S5, and S6; residues equivalent to Lys86, Asp213, His354 and Gln392 are among the most highly conserved in ORs (Fig. 5h). The conservation of this hydrophilic network suggests that it forms an important structural motif that maintains the organization of the transmembrane helices within OR subunits.

Viewed through the lens of the Orco structure, the limited sequence conservation of ORs can be understood as largely concentrated at key

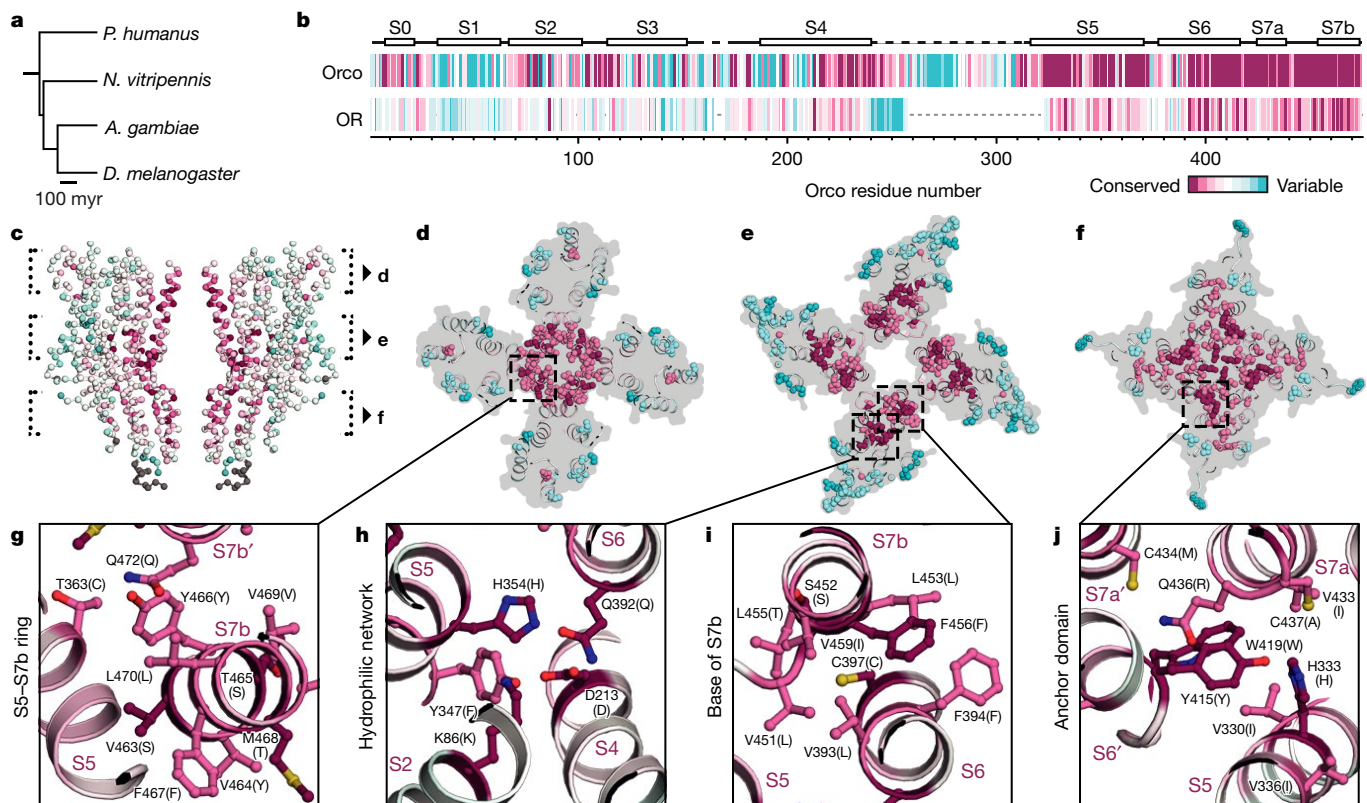


Fig. 5 | OR conservation maps to key interaction domains in Orco.
a, Phylogenetic tree of insects whose OR sequences were used in the alignment. **b**, Residue conservation among 176 Orcos from 174 species (top) and 361 ORs from the species in **a** (bottom), calculated using ConSurf³⁴, are plotted using a colour scale (far right) and aligned to *A. bakeri* Orco. Orco and OR conservation scores are independently

normalized. Orco secondary structure is indicated above the plot. **c–f**, 15 Å cross-sections as indicated in **c**. The most conserved and variable amino acids are shown as spheres. **g–j**, Selected regions from **d–f** shown in greater detail. Residues are labelled according to *A. bakeri* Orco, with the most common OR amino acid at that position indicated in parentheses.

structural and functional nodes in the channel. The striking correspondence between OR sequence conservation and Orco structural elements highlights their evolutionary relatedness and suggests that the Orco homotetramer can serve as a structural template for highly divergent Orco–OR receptor complexes. We thus propose that heteromeric insect olfactory receptors adopt the same overall architecture as the Orco homomeric channel, with one or more (probably two²⁰) Orco subunits being replaced by an OR.

Discussion

Olfactory detection poses a unique challenge. For example, while only a few photoreceptors are necessary to detect the entire visible spectrum, large repertoires of olfactory receptors are required to discriminate among the myriad of molecularly distinct chemicals in the environment^{3,4}. Diverse species, from insects to mammals, have evolved families of tens to thousands of receptors dedicated to the task of odorant detection. Our data provide structural and functional confirmation that insect olfactory receptors form a novel class of heteromeric ligand-gated ion channels, structurally and mechanistically distinct from other chemoreceptors.

Our work supports a model in which Orco and OR subunits assemble into a heterotetramer and work in concert to gate a central shared ion-conduction pathway^{32,33}. Each subunit contributes only a single helix, S7b, to a central pore, which is encircled by four loosely tethered S1–S6 transmembrane domains. The central pore diverges near the intracellular membrane surface and connects to the cytosol through four lateral conduits formed at the interfaces between subunits. We propose a simple gating mechanism in which either VUAA1 binding to Orco or odorant binding to the OR dilates the hydrophobic aperture at the extracellular end of S7b to allow passage of cations through the

quadrivial pore. This small conformational change presents a relatively low energetic barrier to channel opening, consistent with the weak affinity of VUAA1 and most odorants³⁵. One potential site for odorant binding is the extracellular pocket—a distinctive crevice formed by the loose packing of helices S1–S6. Residues lining this pocket are required for VUAA1 sensitivity²³ and have also been previously implicated in defining odorant specificity^{24–27}. However, many ORs bind multiple structurally distinct odorants with varying affinities³⁵, a biophysical property integral to the combinatorial coding of odours by the olfactory system. The extensive sequence diversity of ORs may reflect the existence of additional odorant-binding sites distributed throughout the protein that broaden a receptor's tuning.

A hallmark of insect olfactory receptors is their inordinate diversity within and across insect lineages. Several features of the architecture of Orco provide a framework for understanding how this receptor family accommodates such diversity. First, the organization of the homotetrameric Orco channel offers an explanation for how a single Orco can assemble and function with an array of distinct OR subunits. The transmembrane domains of each subunit are largely isolated from each other and sequestered within the lipid membrane, leaving only a minimal element—a single helix—linking neighbouring subunits at the centre of the channel. The majority of inter-subunit interactions reside in the small cytoplasmic anchor domain, which secures the subunits together. Conserved OR residues are concentrated within the anchor domain, leaving the majority of residues relatively unconstrained and free to diversify. Second, Orco affords flexibility to ORs by contributing highly conserved structural and functional elements to the heteromeric complex. Orco can complement and compensate for OR diversity, thereby relaxing evolutionary constraints on the ORs so that they are not competitive to assemble and function in its absence.

The ability of an OR to functionally rescue an Orco pore mutation shows how deleterious sequence variation can be tolerated within the heteromer. Since a single Orco must assemble and function with up to hundreds of distinct OR partners within a given species, the strict conservation of Orco is likely to be required to preserve functionality across these diverse complexes. Thus, conservation and variability are largely segregated to separate protein subunits in the heteromer, allowing for the modular assembly of an enormous number of receptors with distinct chemical tuning.

Our work offers structural insight into what is likely to be the largest family of ion channels found in nature, with many hundreds of thousands of different variants distributed across the hundreds of thousands of insect species. The structure of Orco provides an inroad to consider how protein variation can be selected through evolution to detect and perceive the vast chemical world.

Online content

Any methods, additional references, Nature Research reporting summaries, source data, statements of data availability and associated accession codes are available at <https://doi.org/10.1038/s41586-018-0420-8>

Received: 22 January 2018; Accepted: 20 June 2018;

Published online 15 August 2018.

1. Mora, C., Tittensor, D. P., Adl, S., Simpson, A. G. B. & Worm, B. How many species are there on Earth and in the ocean? *PLoS Biol.* **9**, e1001127 (2011).
2. Hansson, B. S. & Stensmyr, M. C. Evolution of insect olfaction. *Neuron* **72**, 698–711 (2011).
3. Bargmann, C. I. Comparative chemosensation from receptors to ecology. *Nature* **444**, 295–301 (2006).
4. Kaupp, U. B. Olfactory signalling in vertebrates and insects: differences and commonalities. *Nat. Rev. Neurosci.* **11**, 188–200 (2010).
5. Malnic, B., Hirono, J., Sato, T. & Buck, L. B. Combinatorial receptor codes for odors. *Cell* **96**, 713–723 (1999).
6. Wang, J. W., Wong, A. M., Flores, J., Vosshall, L. B. & Axel, R. Two-photon calcium imaging reveals an odor-evoked map of activity in the fly brain. *Cell* **112**, 271–282 (2003).
7. Sato, K. et al. Insect olfactory receptors are heteromeric ligand-gated ion channels. *Nature* **452**, 1002–1006 (2008).
8. Wicher, D. et al. *Drosophila* odorant receptors are both ligand-gated and cyclic-nucleotide-activated cation channels. *Nature* **452**, 1007–1011 (2008).
9. Missbach, C. et al. Evolution of insect olfactory receptors. *eLife* **3**, e02115 (2014).
10. Ioannidis, P. et al. Genomic features of the damselfly *Calopteryx splendens* representing a sister clade to most insect orders. *Genome Biol. Evol.* **9**, 415–430 (2017).
11. McKenzie, S. K., Fetter-Pruneda, I., Ruta, V. & Kronauer, D. J. C. Transcriptomics and neuroanatomy of the clonal raider ant implicate an expanded clade of odorant receptors in chemical communication. *Proc. Natl. Acad. Sci. USA* **113**, 14091–14096 (2016).
12. Vosshall, L. B. Olfaction in *Drosophila*. *Curr. Opin. Neurobiol.* **10**, 498–503 (2000).
13. Vosshall, L. B., Wong, A. M. & Axel, R. An olfactory sensory map in the fly brain. *Cell* **102**, 147–159 (2000).
14. Larsson, M. C. et al. Or83b encodes a broadly expressed odorant receptor essential for *Drosophila* olfaction. *Neuron* **43**, 703–714 (2004).
15. Yan, H. et al. An engineered orco mutation produces aberrant social behavior and defective neural development in ants. *Cell* **170**, 736–747.e9 (2017).
16. Trible, W. et al. orco mutagenesis causes loss of antennal lobe glomeruli and impaired social behavior in ants. *Cell* **170**, 727–735.e10 (2017).
17. DeGennaro, M. et al. orco mutant mosquitoes lose strong preference for humans and are not repelled by volatile DEET. *Nature* **498**, 487–491 (2013).
18. Jones, P. L., Pask, G. M., Rinker, D. C. & Zwiebel, L. J. Functional agonism of insect odorant receptor ion channels. *Proc. Natl. Acad. Sci. USA* **108**, 8821–8825 (2011).
19. Lu, B. et al. Expression and evolutionary divergence of the non-conventional olfactory receptor in four species of fig wasp associated with one species of fig. *BMC Evol. Biol.* **9**, 43 (2009).
20. Benton, R., Sachse, S., Michnick, S. W. & Vosshall, L. B. Atypical membrane topology and heteromeric function of *Drosophila* odorant receptors *in vivo*. *PLoS Biol.* **4**, e20 (2006).
21. Jones, W. D., Nguyen, T.-A. T., Kloss, B., Lee, K. J. & Vosshall, L. B. Functional conservation of an insect odorant receptor gene across 250 million years of evolution. *Curr. Biol.* **15**, R119–R121 (2005).

22. Hopf, T. A. et al. Amino acid coevolution reveals three-dimensional structure and functional domains of insect odorant receptors. *Nat. Commun.* **6**, 6077 (2015).
23. Corcoran, J. A., Sonntag, Y., Andersson, M. N., Johanson, U. & Löfstedt, C. Endogenous insensitivity to the Orco agonist VUAA1 reveals novel olfactory receptor complex properties in the specialist fly *Mayetiola destructor*. *Sci. Rep.* **8**, 3489 (2018).
24. Yang, K., Huang, L.-Q., Ning, C. & Wang, C.-Z. Two single-point mutations shift the ligand selectivity of a pheromone receptor between two closely related moth species. *eLife* **6**, 155 (2017).
25. Hughes, D. T., Wang, G., Zwiebel, L. J. & Luetje, C. W. A determinant of odorant specificity is located at the extracellular loop 2-transmembrane domain 4 interface of an *Anopheles gambiae* odorant receptor subunit. *Chem. Senses* **39**, 761–769 (2014).
26. Nichols, A. S. & Luetje, C. W. Transmembrane segment 3 of *Drosophila melanogaster* odorant receptor subunit 85b contributes to ligand-receptor interactions. *J. Biol. Chem.* **285**, 11854–11862 (2010).
27. Leary, G. P. et al. Single mutation to a sex pheromone receptor provides adaptive specificity between closely related moth species. *Proc. Natl. Acad. Sci. USA* **109**, 14081–14086 (2012).
28. Long, S. B., Tao, X., Campbell, E. B. & MacKinnon, R. Atomic structure of a voltage-dependent K⁺ channel in a lipid membrane-like environment. *Nature* **450**, 376–382 (2007).
29. Liao, M., Cao, E., Julius, D. & Cheng, Y. Structure of the TRPV1 ion channel determined by electron cryo-microscopy. *Nature* **504**, 107–112 (2013).
30. Bacongus, I., Bohlen, C. J., Goehring, A., Julius, D. & Gouaux, E. X-ray structure of acid-sensing ion channel 1-snake toxin complex reveals open state of a Na⁺-selective channel. *Cell* **156**, 717–729 (2014).
31. Gonzales, E. B., Kawate, T. & Gouaux, E. Pore architecture and ion sites in acid-sensing ion channels and P2X receptors. *Nature* **460**, 599–604 (2009).
32. Pask, G. M., Jones, P. L., Rützler, M., Rinker, D. C. & Zwiebel, L. J. Heteromeric Anophele odorant receptors exhibit distinct channel properties. *PLoS One* **6**, e28774 (2011).
33. Nakagawa, T., Pellegrino, M., Sato, K., Vosshall, L. B. & Touhara, K. Amino acid residues contributing to function of the heteromeric insect olfactory receptor complex. *PLoS One* **7**, e32372 (2012).
34. Landau, M. et al. ConSurf 2005: the projection of evolutionary conservation scores of residues on protein structures. *Nucleic Acids Res.* **33**, W299–W302 (2005).
35. Hallem, E. A. & Carlson, J. R. Coding of odors by a receptor repertoire. *Cell* **125**, 143–160 (2006).

Acknowledgements We thank R. Axel, R. MacKinnon, B. Noro and L. Vosshall for advice on the manuscript, A. Siliciano and C. Monnier for technical advice and preliminary biochemistry, other members of the Ruta laboratory for discussions, and R. Boggavarapu for help with initial negative-stain EM experiments. We are grateful to M. Ebrahim and J. Sotiris at The Rockefeller University Evelyn Gruss Lipper Cryo-Electron Microscopy Resource Center for assistance with microscope operation, F. Weis-Garcia and S. L. Bourne at the MSKCC Antibody & Biorepository Core Facility for hybridoma generation, and R. Lavoisier and C. Adura at The Rockefeller University High Throughput & Spectroscopy Resource Center for support on functional assays. This work was supported by a Helmsley Postdoctoral Fellowship (to K.H.K.) and a Sinsheimer Foundation Award, the National Institutes of Health (R01-AI103171-01A1) and New York Stem Cell Foundation Robertson Neuroscience Investigator Award (to V.R.).

Reviewer information *Nature* thanks R. Benton, E. Gouaux and the other anonymous reviewer(s) for their contribution to the peer review of this work.

Author contributions J.A.B. and M.A.K. expressed and purified Orco, screened monoclonal antibody lines and purified Fab fragments. J.A.B. and K.H.K. collected and analysed cryo-EM data with input from T.W. J.A.B. built and refined the Orco model and performed ITC measurements. J.d.M. performed electrophysiology experiments. J.A.R. performed calcium imaging assays. V.R. contributed to all aspects of the project and wrote the paper with J.A.B. and input from all authors.

Competing interests The authors declare no competing interests.

Additional information

Extended data is available for this paper at <https://doi.org/10.1038/s41586-018-0420-8>.

Supplementary information is available for this paper at <https://doi.org/10.1038/s41586-018-0420-8>.

Reprints and permissions information is available at <http://www.nature.com/reprints>.

Correspondence and requests for materials should be addressed to V.R.

Publisher's note: Springer Nature remains neutral with regard to jurisdictional claims in published maps and institutional affiliations.

METHODS

Expression and purification of Orco. A synthetic construct consisting of residues Lys2–Lys474 (the native C terminus) of *A. bakeri* Orco (also known as Or2¹⁹) was cloned into a pEG BacMam vector³⁶ along with an N-terminal Strep II tag, superfolder GFP³⁷ and an HRV 3C protease site. Baculovirus containing the Orco-coding sequence was created in SF9 cells (ATCC CRL-1711) and used to infect HEK293S GrnT⁻ cells (ATCC CRL-3022)³⁶. Cells were grown in suspension at 37 °C in Freestyle 293 medium (Gibco) supplemented with 2% (v/v) fetal bovine serum (FBS; Gibco) with 8% (v/v) carbon dioxide until they reached a density of ~3 × 10⁶ cells/ml and then infected at a multiplicity of infection of 1. After 12 h, 10 mM sodium butyrate (Sigma-Aldrich) was added to the medium and the temperature was reduced to 30 °C. The cells were harvested ~48 h later by centrifugation and washed once in phosphate-buffered saline (pH 7.5; Gibco). Cell pellets were frozen in liquid nitrogen and stored at -80 °C until needed.

Cell pellets were thawed on ice and resuspended in 10 mL of lysis buffer per gram of cells. Lysis buffer was composed of 50 mM HEPES/NaOH (pH 7.5), 375 mM NaCl, 1 μg/mL leupeptin, 1 μg/mL aprotinin, 1 μg/mL pepstatin A, 1 mM phenylmethylsulfonyl fluoride (all from Sigma-Aldrich). Orco was extracted by adding 0.25% (w/v) lauryl maltose neopentyl glycol (LMNG; Anatrace) with 0.05% (w/v) cholesterol hemisuccinate (CHS; Sigma-Aldrich) for 2 h at 4 °C. The mixture was clarified by centrifugation at 90,000g and the supernatant was added to 0.2 mL StrepTactin Sepharose resin (GE Healthcare) per gram of cells and rotated at 4 °C for 1 h. The resin was collected, washed with 10 column volumes (cv.) of 20 mM HEPES/NaOH (pH 7.5), 150 mM NaCl (HBS) with 0.01% (w/v) LMNG, 0.002% (w/v) CHS, and then with 10 cv. of HBS with 0.05% (w/v) digitonin (Sigma-Aldrich). Orco was eluted by adding 2.5 mM desthiobiotin (DTB; Sigma-Aldrich) to the digitonin buffer. The Strep-GFP tag was cleaved by HRV 3C protease (Novagen) added at 10 U/mg of Orco overnight at 4 °C. DTB was removed by using a PD-10 column (GE Healthcare) and the desalted sample was re-applied to the StrepTactin Sepharose resin (regenerated and re-equilibrated following the manufacturer's instructions) to remove uncut material. Fab was added to Orco at a 1.5-fold molar excess and incubated on ice for 30 min. Orco and Fab concentrations were calculated from their absorbances at 280 nm assuming extinction coefficients (ϵ_{280}) of 57.3 and 73.1 mM⁻¹ cm⁻¹, respectively (calculated by ProtParam³⁸). The complex was concentrated to ~5 mg/mL (Amicon Ultra; 50 kDa cutoff) and injected onto a Superose 6 Increase column (GE Healthcare) equilibrated in HBS with 0.05% (w/v) digitonin.

Purification of Fab. Monoclonal antibodies were produced by culturing hybridoma line 9G11/C7 in hybridoma serum-free medium (Gibco) supplemented with 1% (v/v) ultra-low IgG FBS (Gibco) and 1% (v/v) Nutridoma-SP (Roche) using CELLINE disposable bioreactors (Argos Technologies). Medium supernatant from the bioreactor was dialysed against 10 mM Tris/HCl (pH 7.5), 10 mM NaCl (Spectra/Por 6; 10 kDa cutoff) overnight at 4 °C. Precipitates were removed by centrifugation and the supernatant was passed through a 0.2 μm filter and onto a 5 mL HiTrap Q HP column (GE Healthcare) equilibrated in 10 mM Tris/HCl (pH 7.5), 10 mM NaCl. The antibody was eluted from the column using a linear gradient to 10 mM Tris/HCl (pH 7.5), 0.3 M NaCl. Fractions containing the antibody were pooled and digested for 3 h at 37 °C by papain (Worthington) at a 1:50 (w:w) papain:antibody ratio with L-cysteine and EDTA added at 10 mM each (Sigma-Aldrich). The digestion was terminated by the addition of 10 mM iodoacetamide (Sigma-Aldrich) for 20 min. The mixture was dialysed twice against 10 mM Tris/HCl (pH 7.5), 50 mM NaCl overnight at 4 °C and applied to a HiTrap Q HP equilibrated in the same buffer. Fab was collected from the flow-through and concentrated to ~10 mg/mL (Amicon Ultra; 10 kDa cutoff).

Cryo-EM sample preparation and data acquisition. Peak fractions containing the Orco-Fab complex were concentrated to 4–5 mg/mL (assuming $\epsilon_{280} = 130$ mM⁻¹ cm⁻¹). Cryo-EM grids were frozen using a Vitrobot Mark IV (FEI) as follows: 3 μL of the concentrated sample was applied to a glow-discharged Quantifoil R1.2/1.3 holey carbon 400 mesh gold grid, blotted for 3–4 s in >90% humidity at room temperature, and plunge frozen in liquid ethane cooled by liquid nitrogen.

Cryo-EM data were recorded on a Titan Krios (FEI) operated at 300 kV, equipped with a Gatan K2 Summit camera. SerialEM³⁹ was used for automated data collection. Movies were collected at a nominal magnification of 29,000 × in super-resolution mode resulting in a calibrated pixel size of 0.5 Å/pixel, with a defocus range of approximately -0.8 to -2.0 μm. Fifty frames were recorded over 10 s of exposure at a dose rate of 1.6 electrons per Å² per frame.

Movie frames were aligned and binned over 2 × 2 pixels using MotionCor²⁰ and the contrast transfer function parameters for each motion-corrected image were estimated using CTFFIND4⁴¹. Particles were auto-picked using Gautomatch⁴² using templates derived from averages that were generated from an initial data set of 5,000 particles from 116 images. A total of 82,614 particles from 1,221 images were extracted into 384 × 384-pixel boxes, binned over 3 × 3 pixels, and subjected to 2D classification using RELION-2.0⁴³. After removal of junk particles, the remaining 53,141 particles were re-extracted without binning and subjected to

3D refinement in RELION with C4 symmetry imposed, using, as initial reference, a 3D map that was calculated in EMAN2⁴⁴ from a subset of 2D-class averages. The four-fold symmetry was immediately evident from the individual particles and 2D-class averages, and refinement imposing no symmetry produced an equivalent map. Subsequent 3D classification into four classes showed a single dominant class containing 47,934 particles (90% of the data set), suggesting that the Orco–Fab complex was highly homogeneous with limited structural variability. The orientation parameters of the particles from all four classes were further refined using Frealign⁴⁵ employing a soft mask that excluded the Fab and micelle. The map was sharpened using a B-factor of -160 Å² yielding a final resolution of 3.5 Å, estimated using the Fourier shell correlation (FSC) = 0.143 cutoff criterion⁴⁶. The images in Fig. 1d were created using Chimera⁴⁷.

Model building. The 3.5 Å density map was of sufficient quality for de novo atomic model building. A poly-alanine model for Orco was built in Coot⁴⁸ and subsequent amino-acid assignments were made based on side-chain densities. Since the entire Fab was masked out during particle alignment, density for the Fab was much weaker and therefore was not modelled. The Orco tetramer was refined using real-space refinement implemented in PHENIX⁴⁹ with fourfold non-crystallographic symmetry applied. The structure was compared to existing structures in the Protein Data Bank using the Dali server⁵⁰ and no significant hits were obtained, suggesting that Orco adopts a novel fold. All images of the model were created using PyMOL⁵¹.

Structure analyses. Residues at subunit interfaces were identified using PyMOL as any residue within 5 Å of a neighbouring subunit (Fig. 2d–g). The inter-subunit surface area was calculated as the solvent-accessible surface area (SA) that would be occluded upon tetramer formation (SA of a single Orco subunit minus one-quarter the SA of the Orco tetramer).

The pore diameters along the central axis and lateral conduits were calculated using the program HOLE⁵² (Fig. 3a). Two calculations were performed: one along the central four-fold axis (central pore) and another between subunits near the cytosolic membrane interface (lateral conduits). The pores overlapped in the central vestibule.

Isothermal titration calorimetry. Samples of Orco and Orco–Fab complex were expressed and purified as described above, and concentrated to ~10 μM (monomer). A VUAA1 (Princeton Biomedical Research) stock was prepared in dimethylsulfoxide (DMSO; Sigma-Aldrich) at 100 mM and diluted to 0.5 mM in the same buffer as Orco. 0.5% (v/v) DMSO was added to Orco and buffer samples to match the amount of DMSO originating from the VUAA1 stock solution. ITC experiments were performed using a MicroCal Auto-iTC200 (Malvern) at 25 °C. Each experiment began with a single injection of 0.4 μL followed by 19 injections of 2 μL each (at 0.5 μL/s, 150 s apart) into a 0.2-mL Orco sample. The experiments were repeated using Orco samples obtained from independent purifications (biological replicates).

The raw heat evolutions were baseline-corrected and a single binding site model was fit to the integrated data using AFFINImeter (<https://www.affinimeter.com>), excluding the first injection. The number of binding sites per monomer was fixed to be 1 and a dissociation constant (K_d), enthalpy of binding (ΔH) and heat of sample dilution (ΔQ_{dil}) were fit. Separate experiments injecting VUAA1 into buffer alone showed no significant heats of dilution and were not subtracted from the Orco data before fitting.

Electrophysiological experiments. Experiments on wild-type Orco alone were conducted with a Flp-In T-Rex 293 cell line (Invitrogen) with a stably integrated GFP-tagged Orco cloned into pcDNA6/TR. Cells were maintained in high-glucose DMEM supplemented with 10% (v/v) tetracycline-free FBS (Takara Bio), 1% (v/v) MEM (Sigma-Aldrich), 1% (v/v) GlutaMAX (Gibco), 15 μg/ml blasticidin (Gibco) and 100 μg/ml hygromycin B (Invitrogen), and Orco expression was induced with 0.1 μg/ml tetracycline (Gold Biotechnology). Constructs for mutant Orco or Orco-OR experiments used pEG BacMam vectors, cloned as described above except that OR proteins were tagged with mCherry. HEK293 cells were maintained in high-glucose DMEM supplemented with 10% (v/v) FBS, 1% (v/v) MEM and 1% (v/v) GlutaMAX. Cells were plated on 12 mm poly-D-lysine-coated coverslips (Corning) and induced or transfected 24 h before recording. Experiments were repeated using separate cells (biological replicates).

Electrodes were drawn from borosilicate patch glass (Sutter Instruments) and polished (MF-83, Narishige Co.) to a resistance of 3–6 MΩ when filled with pipette solution. Analogue signals were filtered at 2 kHz using the built-in 4-pole Bessel filter of a Multiclamp 700B patch-clamp amplifier (Molecular Devices) in patch mode and digitized at 20 kHz (Digidata 1440A, Molecular Devices). Signals were further filtered offline at 1 kHz for analysis and representations.

Whole-cell and single-channel recordings in Fig. 1 and Extended Data Fig. 2 were performed using an extracellular (bath) solution composed of 135 mM NaCl, 5 mM KCl, 2 mM MgCl₂, 2 mM CaCl₂, 10 mM glucose, 10 mM HEPES-Na/HCl (pH 7.3, 310 mOsm/kg) and an intracellular (pipette) solution composed of 150 mM KCl, 10 mM NaCl, 1 mM EDTA-Na, 10 mM HEPES-Na/HCl (pH 7.45, 310 mOsm/kg). Single-channel recordings were done in excised outside-out mode.

VUAA1 (100 mM in DMSO) was diluted to the final concentrations using the extracellular solution. Solutions were locally perfused using a microperfusion system (ALA Scientific Instruments).

For the ion-selectivity studies in Fig. 4, the intracellular (pipette) solution consisted of 150 mM CsCl, 10 mM HEPES-Cs (pH 7.3). The extracellular solutions for monovalent cations ($X = \text{Na}, \text{K}$) consisted of 150 mM XCl, 10 mM HEPES-X/HCl (pH 7.3). The extracellular solutions for divalent cations ($X = \text{Ca}, \text{Mg}$) consisted of 100 mM XCl_2 , 10 mM HEPES-Cs/HCl (pH 7.3). VUAA1 and odorants were diluted to the appropriate concentration in extracellular solution. Wild-type and mutant Orco alone used 0.1 mM VUAA1, while Orco with *A. gambiae* OR10, OR28 and OR65 used 0.3 mM o-cresol, 0.3 mM 2,4,5-trimethylthiazole, and 10 μM eugenol, respectively (odours were from Sigma-Aldrich). Solutions were perfused locally in a bath composed of 150 mM NaCl, 10 mM HEPES-Na/HCl (pH 7.3). Motility differences between the caesium-filled pipette and the sodium-filled bath were measured to be 3 mV and the measured reversal potentials (E_{rev}) were corrected for this liquid junction potential. The ion-permeability ratios (P_X/P_{Cs}) in Extended Data Fig. 7 were calculated from E_{rev} using the simplified Goldman–Hodgkin–Katz equations:

$$E_{\text{rev}} = \frac{RT}{F} \ln \frac{P_X [\text{X}]_o}{P_{\text{Cs}} [\text{Cs}]_i} \quad \text{for } X = \text{Na} \text{ or K, and}$$

$$E_{\text{rev}} = \frac{RT}{2F} \ln \frac{4P_X [\text{X}]_o}{P_{\text{Cs}} [\text{Cs}]_i} \quad \text{for } X = \text{Ca} \text{ or Mg}$$

Cell-based calcium sensor fluorescence assay. Constructs used in this assay were cloned into a modified pME18s vector. HEK293 cells were maintained in FluoroBrite DMEM (Gibco) supplemented with 10% (v/v) FBS, 1% (v/v) MEM, and 1% (v/v) GlutaMAX. For each transfection, 0.5 μg of GCaMP6s (Addgene #40753⁵³) and 1.5 μg of the appropriate construct(s) were diluted in 250 μL Opti-MEM, 1% GlutaMAX (Gibco), mixed with an equal volume of medium containing 7 μL lipofectamine 2000 (Invitrogen), and incubated for 20 min at room temperature. HEK293 cells were detached with trypsin and resuspended at 1×10^6 cells/mL, mixed with the transfection solution and 42 μL added to 2×16 wells in a 384-well plate (Greiner CELLSTAR). After 4 h, the transfection medium was replaced with fresh medium, and after another 24 h, the medium was replaced with 20 μL of reading buffer composed of 1 \times HBSS (Gibco) supplemented with 20 mM HEPES/NaOH (pH 7.4), 5 mM CaCl_2 , 1 mM MgSO_4 , and 3 mM Na_2CO_3 . The fluorescence emission at 527 nm (excited at 480 nm) was continuously recorded by a Hamamatsu FDSS plate reader set to 37 °C. After 34 s, 20 μL of VUAA1 or odorant solution, diluted in reading buffer, was added and recording was continued for 2 min. All solutions were pre-warmed to 37 °C before use.

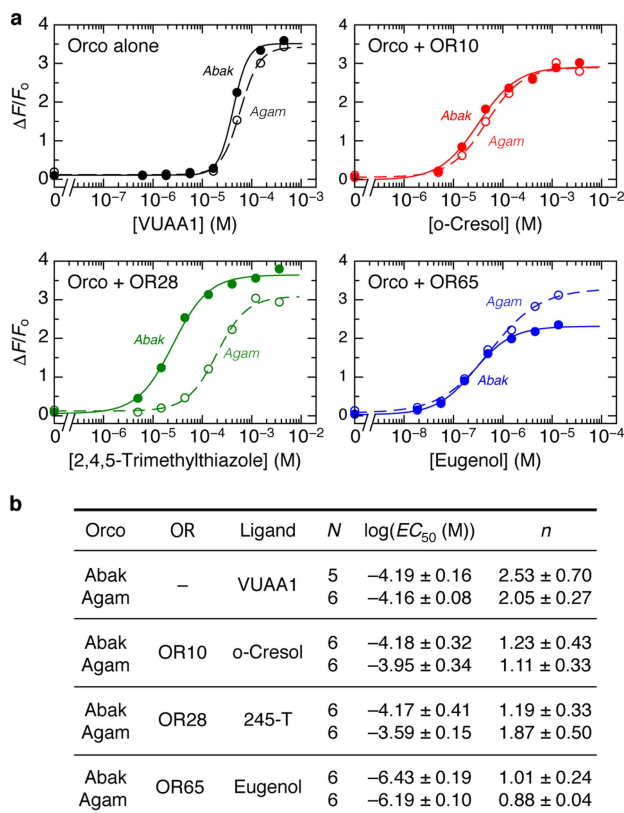
Seven VUAA1 or odour concentrations were used (plus one without ligand); each repeated four times on the plate covering 2×16 wells per construct and together considered a single biological replicate. The baseline fluorescence (F_0) was the average fluorescence of the 30 s before VUAA1 or odour delivery. ΔF was the fluorescence difference from baseline. The Hill equation was fitted to $\Delta F/F_0$ values using GraphPad Prism. In Extended Data Fig. 8 ($\Delta F/F_0$)_{norm} is the fitted maximum $\Delta F/F_0$ value relative to a separate wild-type Orco (or Orco-OR) control experiment from the same plate. In Extended Data Figs. 1, 8, averages of the four repeats at each ligand concentration are plotted.

Sequence alignment of Orco and OR proteins. For the sequence alignment of Orco proteins, 176 Orco sequences from 174 different organisms were aligned using Clustal Omega^{54,55} with minimal manual adjustment. For the sequence alignment of OR proteins, 361 sequences were included from four insect species: *A. gambiae* (72/79 ORs⁵⁶) *D. melanogaster* (61/62 ORs⁵⁷), *Nasonia vitripennis* (221/301 ORs⁵⁸) and *Pediculus humanus* (7/10 ORs⁵⁹). Not all OR sequences from each insect were used, as those with large insertions or deletions, or with regions of unknown residues were removed. The alignment was initially generated using MAFFT^{60,61} with subsequent manual adjustment, primarily to reduce the number of gaps, using the Orco alignment as a guide. The sequence alignments are included as Supplementary Data. Sequence alignments of Orcos and ORs were analysed independently using ConSurf^{34,62}.

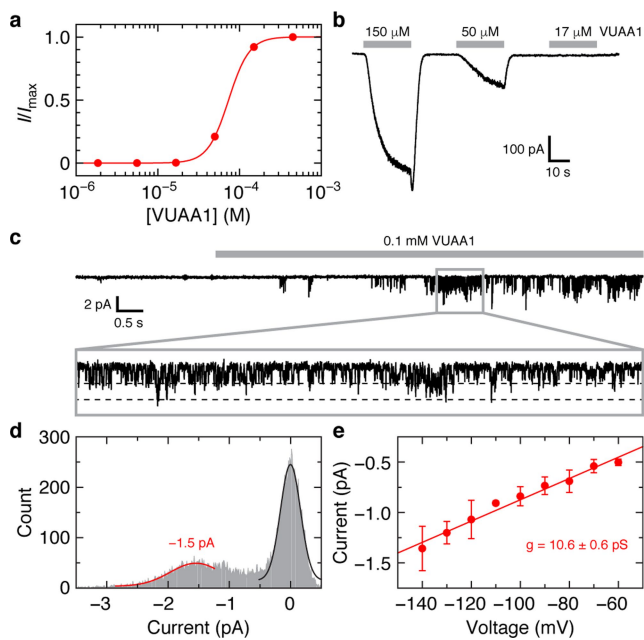
Reporting summary. Further information on experimental design is available in the Nature Research Reporting Summary linked to this paper.

Data availability. The 3D cryo-EM density map of the Orco–Fab complex has been deposited in the Electron Microscopy Data Bank under accession number EMD-7352. The coordinates of the atomic model of Orco have been deposited in the Protein Data Bank under accession number 6C70.

36. Goehring, A. et al. Screening and large-scale expression of membrane proteins in mammalian cells for structural studies. *Nat. Protoc.* **9**, 2574–2585 (2014).
37. Pédelacq, J.-D., Cabantous, S., Tran, T., Terwilliger, T. C. & Waldo, G. S. Engineering and characterization of a superfolder green fluorescent protein. *Nat. Biotechnol.* **24**, 79–88 (2006).
38. Gasteiger, E. et al. in *The Proteomics Protocols Handbook* 571–607 (Humana, New York, 2005).
39. Mastronarde, D. N. Automated electron microscope tomography using robust prediction of specimen movements. *J. Struct. Biol.* **152**, 36–51 (2005).
40. Zheng, S. Q. et al. MotionCor2: anisotropic correction of beam-induced motion for improved cryo-electron microscopy. *Nat. Methods* **14**, 331–332 (2017).
41. Rohou, A. & Grigorieff, N. CTFFIND4: Fast and accurate defocus estimation from electron micrographs. *J. Struct. Biol.* **192**, 216–221 (2015).
42. Zhang, K. Gautomatch <https://www.mrc-lmb.cam.ac.uk/kzhang/Gautomatch/> (2016).
43. Fernandez-Leiro, R. & Scheres, S. H. W. A pipeline approach to single-particle processing in RELION. *Acta Crystallogr. D Struct. Biol.* **73**, 496–502 (2017).
44. Tang, G. et al. EMAN2: an extensible image processing suite for electron microscopy. *J. Struct. Biol.* **157**, 38–46 (2007).
45. Grigorieff, N. Frealign: an exploratory tool for single-particle cryo-EM. *Methods Enzymol.* **579**, 191–226 (2016).
46. Rosenthal, P. B. & Henderson, R. Optimal determination of particle orientation, absolute hand, and contrast loss in single-particle electron cryomicroscopy. *J. Mol. Biol.* **333**, 721–745 (2003).
47. Pettersen, E. F. et al. UCSF Chimera—a visualization system for exploratory research and analysis. *J. Comput. Chem.* **25**, 1605–1612 (2004).
48. Emsley, P., Lohkamp, B., Scott, W. G. & Cowtan, K. Features and development of Coot. *Acta Crystallogr. D Biol. Crystallogr.* **66**, 486–501 (2010).
49. Adams, P. D. et al. PHENIX: a comprehensive Python-based system for macromolecular structure solution. *Acta Crystallogr. D Biol. Crystallogr.* **66**, 213–221 (2010).
50. Holm, L. & Laakso, L. M. Dali server update. *Nucleic Acids Res.* **44**, W351–W355 (2016).
51. The PYMOL Molecular Graphics System, Version 2.0 Schrödinger, LLC.
52. Smart, O. S., Neduvilil, J. G., Wang, X., Wallace, B. A. & Sansom, M. S. HOLE: a program for the analysis of the pore dimensions of ion channel structural models. *J. Mol. Graph.* **14**, 354–360, 376 (1996).
53. Chen, T.-W. et al. Ultrasensitive fluorescent proteins for imaging neuronal activity. *Nature* **499**, 295–300 (2013).
54. Sievers, F. et al. Fast, scalable generation of high-quality protein multiple sequence alignments using Clustal Omega. *Mol. Syst. Biol.* **7**, 539 (2011).
55. Goujon, M. et al. A new bioinformatics analysis tools framework at EMBL-EBI. *Nucleic Acids Res.* **38**, W695–W699 (2010).
56. Hill, C. A. et al. G protein-coupled receptors in *Anopheles gambiae*. *Science* **298**, 176–178 (2002).
57. Vosshall, L. B., Amrein, H., Morozov, P. S., Rzhetsky, A. & Axel, R. A spatial map of olfactory receptor expression in the *Drosophila* antenna. *Cell* **96**, 725–736 (1999).
58. Robertson, H. M., Gadau, J. & Wanner, K. W. The insect chemoreceptor superfamily of the parasitoid jewel wasp *Nasonia vitripennis*. *Insect Mol. Biol.* **19** (Suppl. 1), 121–136 (2010).
59. Pelletier, J., Xu, P., Yoon, K. S., Clark, J. M. & Leal, W. S. Odorant receptor-based discovery of natural repellents of human lice. *Insect Biochem. Mol. Biol.* **66**, 103–109 (2015).
60. Katoh, K., Misawa, K., Kuma, K. & Miyata, T. MAFFT: a novel method for rapid multiple sequence alignment based on fast Fourier transform. *Nucleic Acids Res.* **30**, 3059–3066 (2002).
61. Katoh, K., Rozewicki, J. & Yamada, K. D. MAFFT online service: multiple sequence alignment, interactive sequence choice and visualization. *Brief. Bioinform.* **30**, 3059 (2017).
62. Ashkenazy, H. et al. ConSurf 2016: an improved methodology to estimate and visualize evolutionary conservation in macromolecules. *Nucleic Acids Res.* **44**, W344–W350 (2016).
63. Wittig, I., Braun, H.-P. & Schägger, H. Blue native PAGE. *Nat. Protoc.* **1**, 418–428 (2006).
64. Hou, X., Pedi, L., Diver, M. M. & Long, S. B. Crystal structure of the calcium release-activated calcium channel Orai. *Science* **338**, 1308–1313 (2012).
65. Whicher, J. R. & Mackinnon, R. Structure of the voltage-gated K^+ channel Eag1 reveals an alternative voltage sensing mechanism. *Science* **353**, 664–669 (2016).

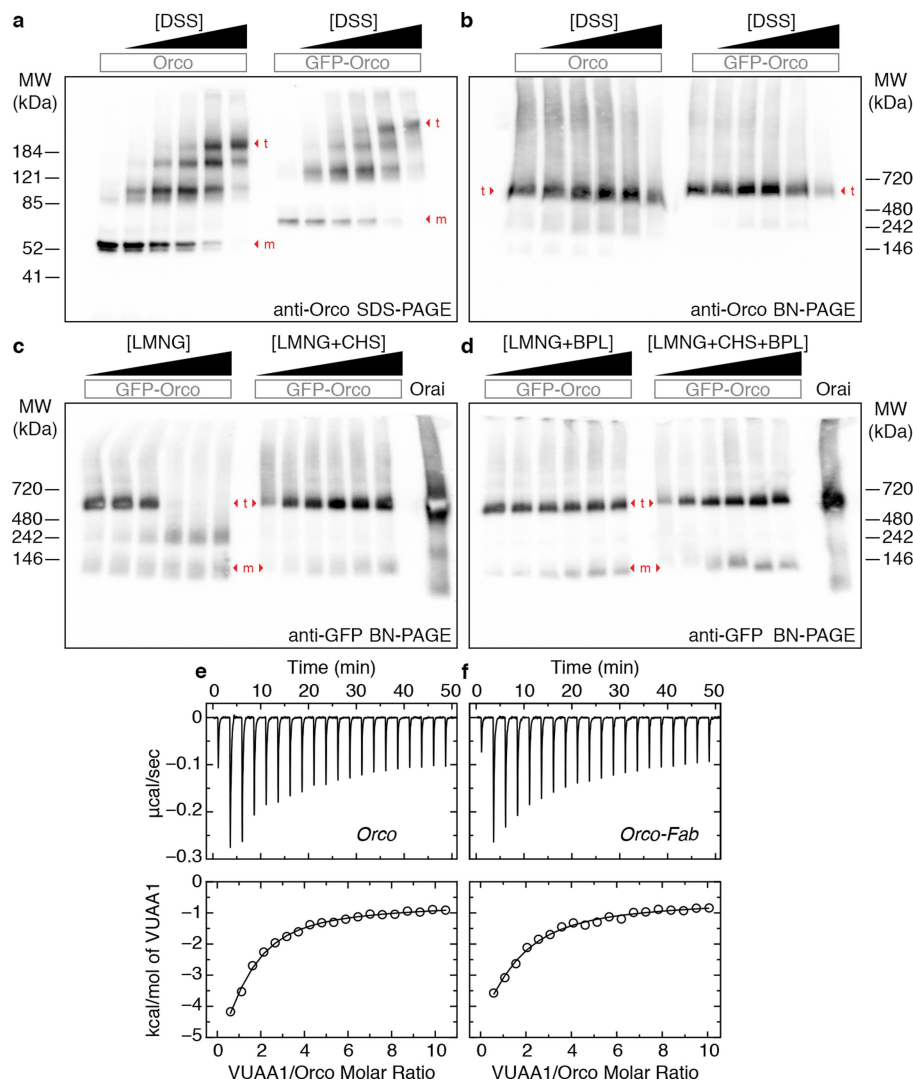


Extended Data Fig. 1 | Ligand-gated signalling of *A. bakeri* and *A. gambiae* Orcos. **a**, Fluorescence changes in HEK293 cells transfected with a genetically encoded Ca^{2+} indicator, GCaMP6s, and Orco from *A. bakeri* (Abak; closed circles) or *A. gambiae* (Agam; open circles) alone, or with an *A. gambiae* OR. Dose-response curves were obtained by titrating with VUAA1 or the cognate odour of the OR. **b**, Average fitted Hill equation parameters from N number of independent replicates. EC_{50} is the concentration for half-maximal response and n is the Hill coefficient (both mean \pm s.d.). 245-T is 2,4,5-trimethylthiazole.



Extended Data Fig. 2 | Electrophysiological characterization of Orco.

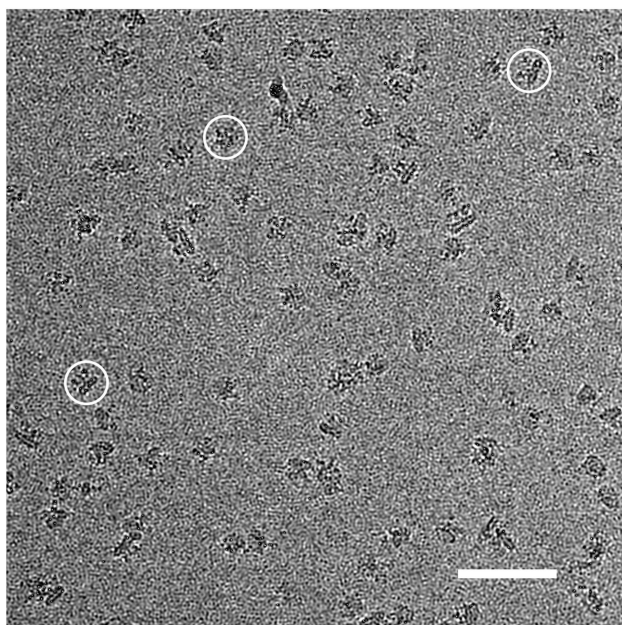
a, Example VUAA1 dose-response curve using whole-cell current from a HEK293 cell expressing Orco. I/I_{\max} is the measured current relative to the maximum current obtained at the highest concentration of VUAA1. The titration experiment was repeated using four independent cells with equivalent results. The average fitted Hill equation parameters are (mean \pm s.d.): $EC_{50} = 64 \pm 7 \mu\text{M}$, $n = 3.5 \pm 0.5$. **b**, Inward whole-cell current for a subset of the VUAA1 concentrations used in **a** (held at -80 mV). **c**, VUAA1-evoked Orco currents recorded from an outside-out membrane patch from a HEK293 cell expressing Orco (held at -140 mV). Inset (0.9 s) highlights single channel openings. **d**, Amplitude histogram determined from the inset in **c**. Fitted Gaussian distributions for single-channel Orco current (red) and baseline current (black) are shown. **e**, Amplitude histograms were obtained at multiple voltages and the single-channel conductance of $10.6 \pm 0.6 \text{ pS}$ was determined from the slope of the current-voltage plot (mean \pm s.d. for 2–6 data points per voltage from 9 patches). The specific numbers of replicates at each voltage were: 5 (-140 mV), 4 (-130 mV), 5 (-120 mV), 3 (-110 mV), 6 (-100 mV), 4 (-90 mV), 4 (-80 mV), 3 (-70 mV), 2 (-60 mV).



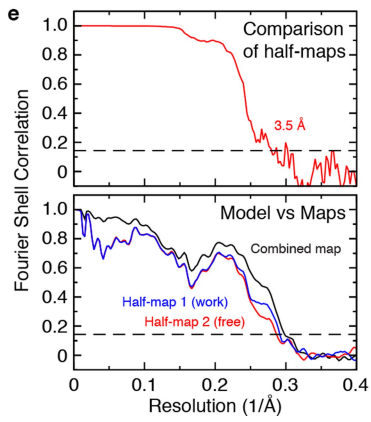
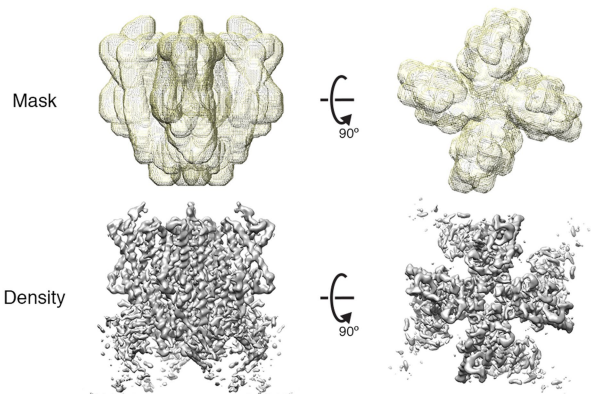
Extended Data Fig. 3 | Stoichiometry and ligand binding of the Orco homotetramer. **a**, Western blot of cross-linked Orco in transfected HEK293 cells. SDS-PAGE showing a ladder of four bands that appears with both GFP-tagged and untagged Orco after treatment with increasing concentration of the amine cross-linker disuccinimidyl suberate (DSS). Monomer (m) and tetramer (t) bands are indicated. DSS concentrations were (μM): 0, 25, 75, 125, 250, 2,500. **b**, Western blot of a Blue Native (BN)-PAGE⁶³ gel of the same samples as in **a** showing that tetrameric Orco is present in all samples and higher-order aggregates are not induced by cross-linking. **c, d**, Western blot of Orco extracted with increasing concentrations of detergent (LMNG) showed gradual loss of the tetrameric species. Addition of CHS (**c**), porcine brain polar lipid extract (**d**) (BPL; Anatrace) or the combination of the two stabilized the Orco tetramer. LMNG concentrations were (% w/v): 0.01, 0.05, 0.1, 0.25, 0.5, 1. Concentration of CHS, BPL and the sum of CHS + BPL were added at one-fifth that of LMNG. GFP-labelled Orai (55 kDa)⁶⁴ was used as a molecular weight marker as it is a hexamer with a similar total size as the Orco-GFP tetramer (340 kDa). The larger apparent molecular

weights observed in BN-PAGE gels (**b–d**) reflect the additional mass of the micelle. Primary antibodies used were: anti-Orco clone 20F7 and anti-GFP (Life Technologies). Each experiment in this figure was repeated three times with similar results. The molecular weight markers on the native gels are approximate: they are from a separate gel run under the same conditions (see Supplementary Data). **e, f**, Representative baseline-corrected isothermal titration calorimetry (ITC) data for Orco (**e**, 11 μM) and Orco-Fab complex (**f**, 10 μM) titrated with VUAA1. Integrated heats and fitted single-site binding isotherms are shown at the bottom. The number of binding sites per monomer was fixed at 1 and the dissociation constant (K_d), enthalpy of binding (ΔH), and heat associated with sample dilution (ΔQ_{dil}) were fit. The experiments were repeated three times each using Orco samples obtained from independent purifications. The average fitted thermodynamic parameters are as follows (mean \pm s.d.). Orco: $K_d = 13 \pm 1 \mu\text{M}$, $\Delta H = -8.3 \pm 0.6 \text{ kcal/mol}$, $\Delta Q_{\text{dil}} = -1.0 \pm 0.1 \text{ kcal/mol}$. Orco-Fab: $K_d = 18 \pm 2 \mu\text{M}$, $\Delta H = -9.7 \pm 0.4 \text{ kcal/mol}$, $\Delta Q_{\text{dil}} = -1.0 \pm 0.2 \text{ kcal/mol}$.

a 82,614 particles autopicked from 1,221 micrographs

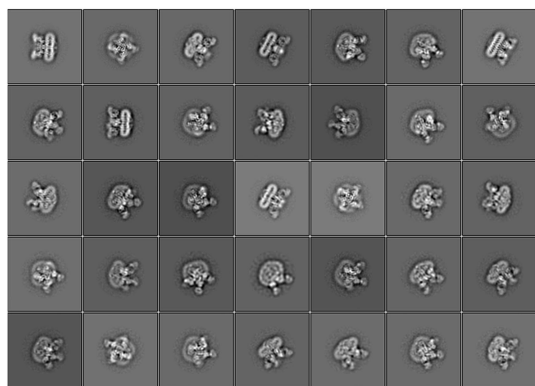


d Refine 3D model using a mask that excludes the Fab and micelle

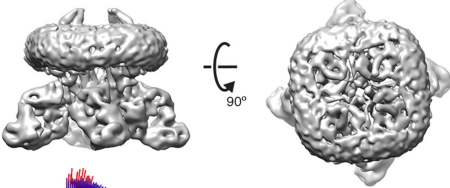


Extended Data Fig. 4 | Cryo-EM data analysis. **a**, A representative motion-corrected micrograph showing the distribution of Orco–Fab single particles (three particles are circled). Scale bar, 50 nm. **b**, 2D averages of classes selected for further processing. **c**, Initial density map from 3D refinement in RELION using all of the particles in **b** with C4 symmetry imposed. **d**, Soft mask and final density map after refinement in Frealign. **e**, Fourier shell correlation (FSC) curves for the final cryo-EM density maps. The horizontal dashed line represents the 0.143 cutoff value.

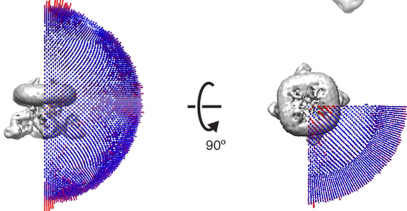
b 53,141 particles from best reference-free 2D classes



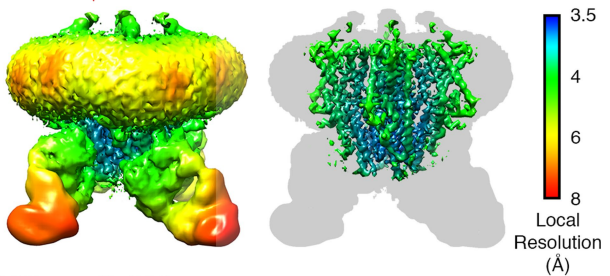
c initial 3D model with C4 symmetry (4.4 Å)



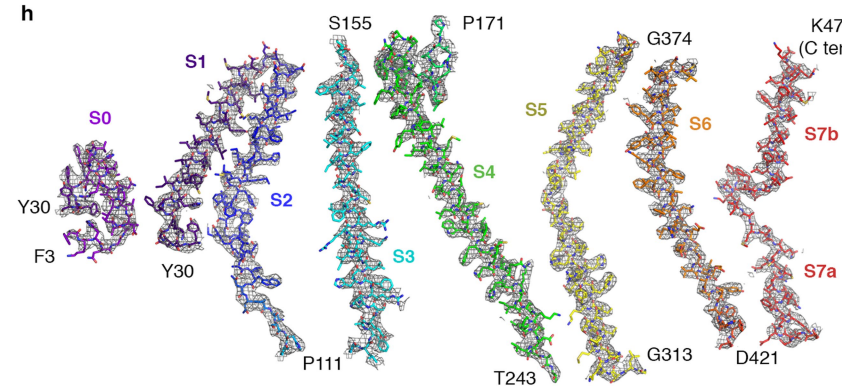
f



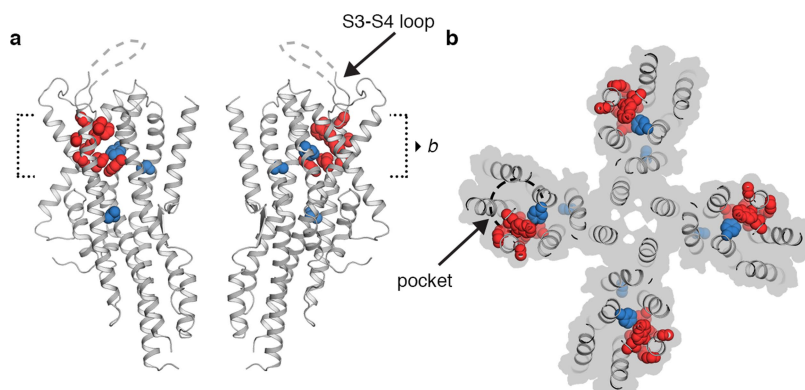
g



h

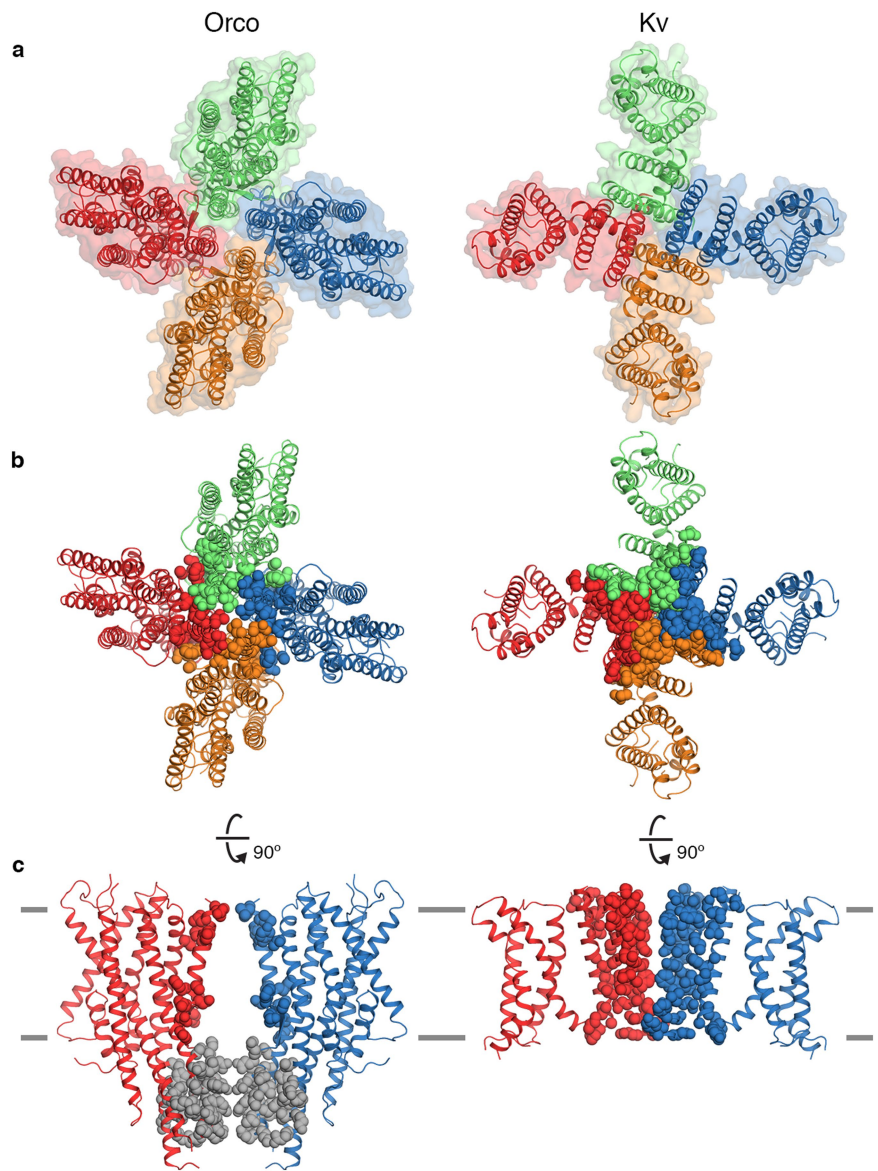


f, Orientation distribution of the particles included in the final 3D map of the Orco–Fab complex in **d** (as reported by RELION). **g**, Approximate local resolution of the entire Orco–Fab density map (left) and only Orco (right). **h**, Cryo-EM densities for the modelled regions are shown as grey mesh. Orco models are drawn as sticks with carbon atoms coloured according to Fig. 2, and oxygen, nitrogen and sulfur atoms coloured red, blue and yellow, respectively.



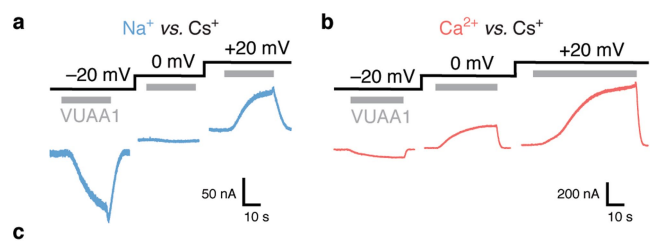
Extended Data Fig. 5 | Potential extracellular facing odour-binding pocket. **a**, Side view of Orco highlighting the location of residues in Orco or ORs that, when mutated, alter ligand-binding specificity. Orco residues that are equivalent to point mutations that alter odour specificity in *Helicoverpa assulta* OR14b²⁴, *A. gambiae* OR15²⁵, *D. melanogaster*

OR85b²⁶ or *Ostrinia furnacalis* OR3²⁷ are shown as red spheres. Residues required for VUAA1 sensitivity in Orco²³ are shown as blue spheres. In Orco, the S3–S4 extracellular loop is positioned above the pocket. **b**, A 15 Å cross-section through the pocket from **a**.



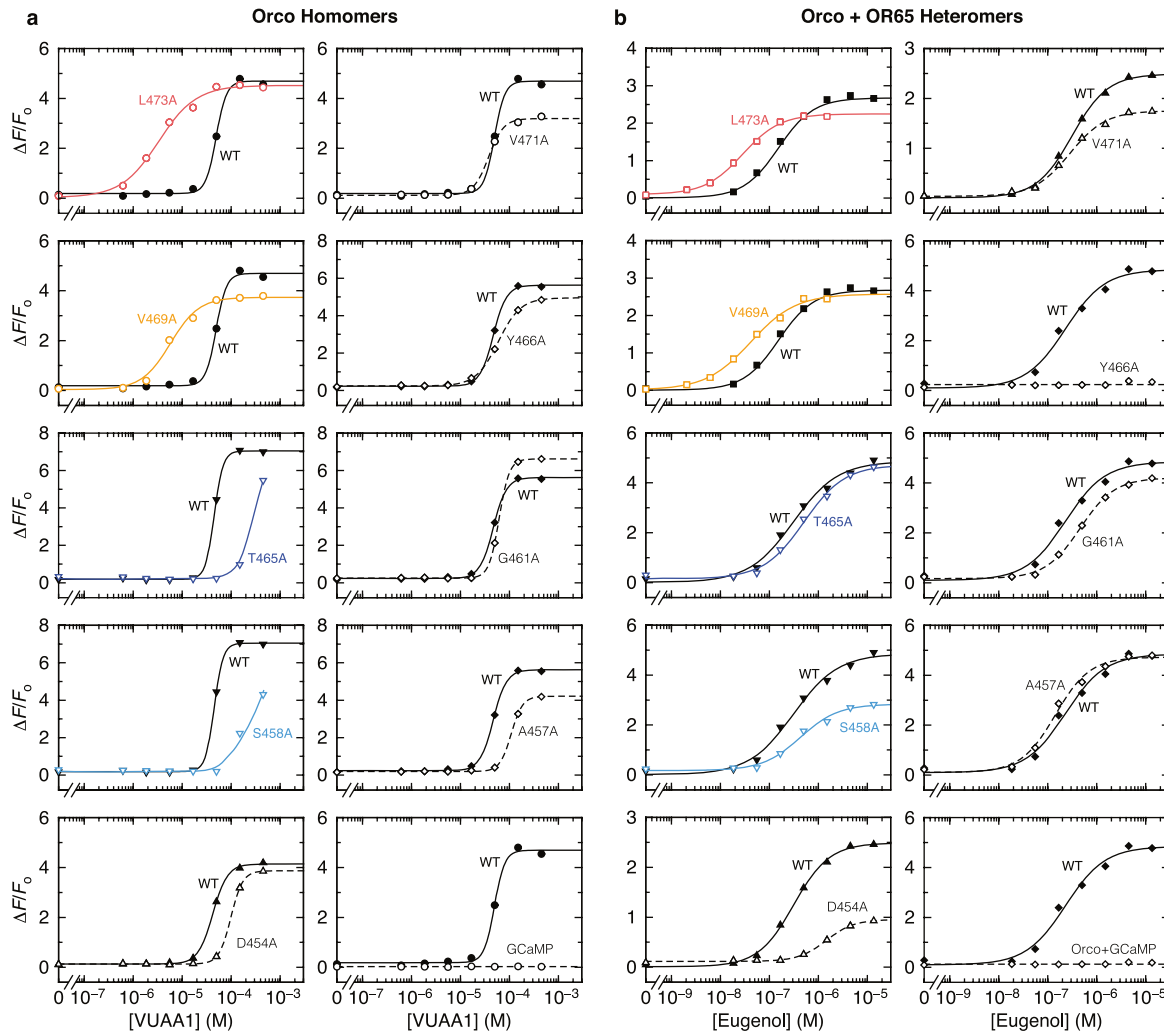
Extended Data Fig. 6 | Inter-subunit interactions in Orco and Kv channels. **a**, Top views of Orco (left) and Kv10.1 (Eag1)⁶⁵ (right) highlighting the overall organization of these tetrameric cation channels. In this Kv channel, the pore and voltage-domains are not domain-swapped and so it more closely resembles the quaternary structure of Orco compared to other Kv channels. **b, c**, Top (**b**) and side (**c**) views

showing inter-subunit interactions. Residues within 5 Å of a different subunit within the transmembrane region are shown as coloured spheres (16 residues in Orco, 58 residues in Kv10.1). In Orco, residues at subunit interfaces in the anchor domain are grey spheres (35 residues). The extracellular and intracellular domains of Kv10.1 are not shown.



Receptor(s)	Ligand	Ion	N	E_{rev} (mV)	P_{ion}/P_{Cs}	P value
Orco	VUAA1	Na ⁺	6	-1.7 ± 4.0	0.94 ± 0.15	-
		K ⁺	4	-1.2 ± 1.8	0.99 ± 0.17	0.79
		Ca ²⁺	5	-14.4 ± 1.8	0.12 ± 0.02	2x10 ⁻⁵
		Mg ²⁺	6	-20.7 ± 2.9	0.07 ± 0.02	1x10 ⁻⁷
Orco L473A	VUAA1	Na ⁺	6	-0.1 ± 1.8	1.00 ± 0.07	0.84
		Ca ²⁺	6	-8.3 ± 3.0	0.19 ± 0.05	0.005
Orco V471A	VUAA1	Na ⁺	4	1.1 ± 1.9	1.05 ± 0.08	0.49
		Ca ²⁺	4	-10.6 ± 1.0	0.16 ± 0.01	0.29
Orco V469A	VUAA1	Na ⁺	4	-2.4 ± 1.0	0.91 ± 0.04	1.00
		Ca ²⁺	6	-2.6 ± 1.9	0.31 ± 0.05	1x10 ⁻⁷
Orco + OR10	o-Cresol	Na ⁺	11	2.1 ± 3.7	1.08 ± 0.16	0.33
		Ca ²⁺	9	-10.3 ± 3.9	0.17 ± 0.05	0.46
Orco + OR28	245-T	Na ⁺	6	3.7 ± 4.2	1.16 ± 0.19	0.12
		Ca ²⁺	6	-9.3 ± 3.0	0.18 ± 0.04	0.28
Orco + OR65	Eugenol	Na ⁺	6	3.8 ± 3.7	1.16 ± 0.14	0.11
		Ca ²⁺	7	-2.4 ± 3.3	0.31 ± 0.08	1x10 ⁻⁵

Extended Data Fig. 7 | Reversal potentials and ion-permeability ratios. **a, b**, VUAA1-evoked whole-cell current from HEK293 cells expressing Orco with 150 mM intracellular CsCl and 150 mM extracellular NaCl (**a**, blue), or 100 mM extracellular CaCl₂ (**b**, red). **c**, Summary of reversal potentials (E_{rev}) and permeability ratios (P_{ion}/P_{Cs}) for wild-type and mutant Orco and Orco–OR complexes measured under bi-ionic conditions (mean ± s.d.). E_{rev} were measured using N independent cells and corrected for the measured junction potential. P_{ion}/P_{Cs} were calculated from E_{rev} using Goldman–Hodgkin–Katz equations (see Methods) with their errors determined by propagation of the standard deviations. Three one-way ANOVA tests were performed using these E_{rev} data followed by Tukey–Kramer multiple comparison tests. (1) Orco selectivity of Na⁺, K⁺, Ca²⁺ and Mg²⁺ (P values are from comparisons to Na⁺ E_{rev}). (2) Wild-type and mutant Orco Na⁺ and Ca²⁺ selectivity (P values are from comparisons to wild-type Orco with the same ion, Na⁺ or Ca²⁺, as appropriate). (3) Orco homomer and Orco–OR heteromer Na⁺ and Ca²⁺ selectivity (P values are from comparisons to the Orco homomer with the same ion, Na⁺ or Ca²⁺, as appropriate). 245-T is 2,4,5-trimethylthiazole.

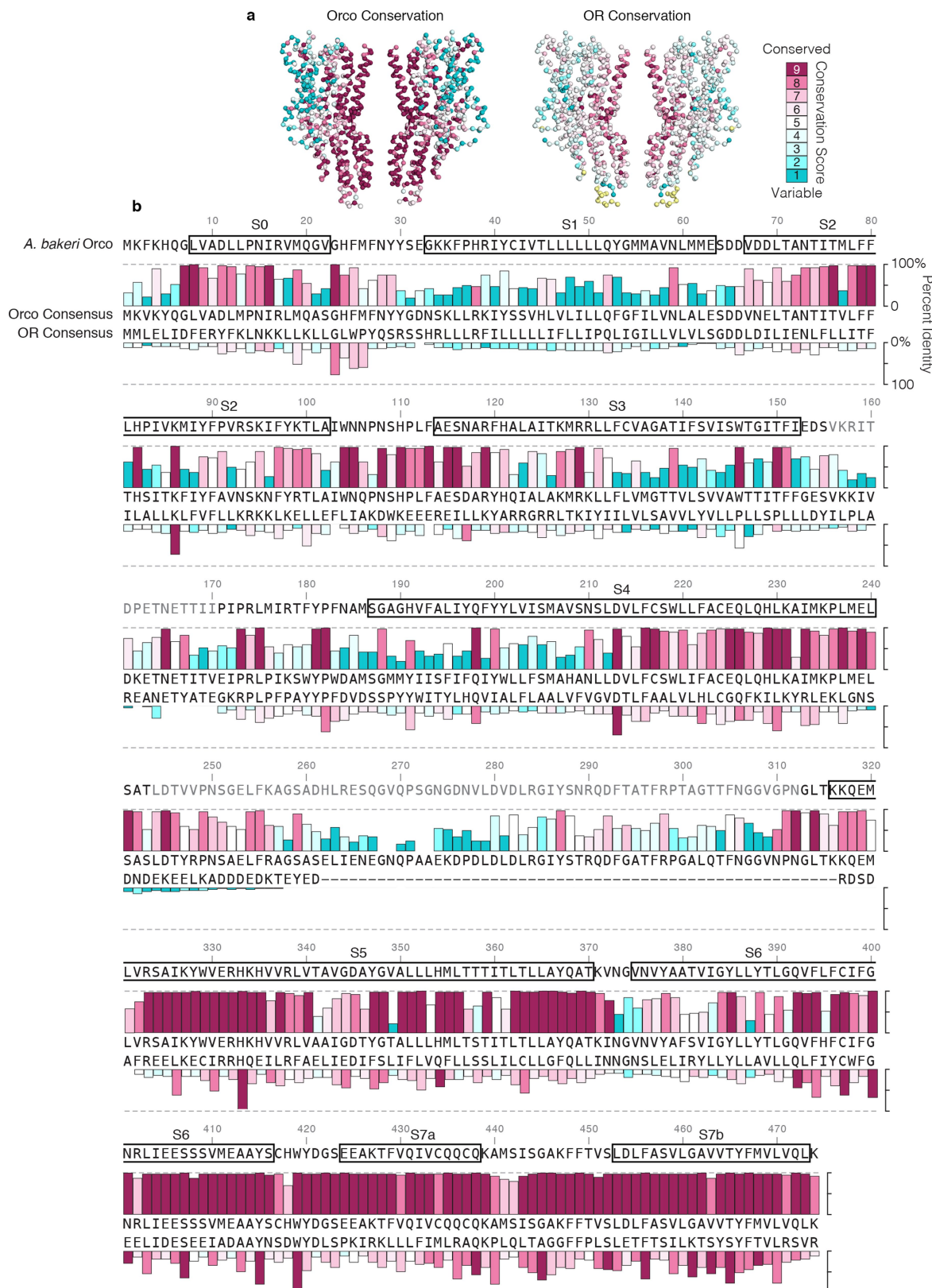


Extended Data Fig. 8 | Cell-based GCaMP assay. **a, b,** Relative fluorescence changes in HEK293 cells transfected with GCaMP plus wild-type (WT) or mutant Orco alone (**a**, titrated with VUAA1) or in the presence of *A. gambiae* OR65 (**b**, titrated with eugenol). Plots using the same symbols were collected on the same day. **c, d,** Fitted Hill equation parameters for Orco and Orco–OR65 (mean \pm s.d.). The assays were repeated N independent times to obtain the maximum $\Delta F/F_0$ response, concentration for half-maximal response (EC_{50}) and Hill coefficient (n). $(\Delta F/F_0)_{\text{norm}}$ is the fitted maximum $\Delta F/F_0$ response relative to a wild-type control Orco or Orco–OR65 experiment from the same plate (for

mutations that could not be accurately fit, the measured maximum $\Delta F/F_0$ response was used). Two one-way ANOVA tests were performed using these EC_{50} data followed by Tukey–Kramer multiple comparison tests.

(1) Wild-type and mutant Orco homomers (P values are from comparisons to wild-type Orco). (2) Wild-type and mutant Orco co-transfected with OR65 (P values are from comparisons to wild-type Orco with OR65).

*Fitted parameters for Orco T465A or S458A homomers + VUAA1 could not be obtained as the dose–response curves did not saturate: a lower-bound estimate for their EC_{50} is approximately 3×10^{-4} M. **No binding was observed for Orco Y466A in the presence of OR65.



Extended Data Fig. 9 | Conservation of Orco and OR sequences. **a**, Orco (left) and OR (right) conservation scores mapped onto the structure of Orco. **b**, Consensus sequences from Orco and OR amino-acid alignments (see Supplementary Data) are aligned to *A. bakeri* Orco. In total, 176 Orco

sequences and 361 OR sequences were used in the alignments. The percent identities (bar height) and ConSurf⁶² conservation scores (bar colour) are plotted for each consensus sequence. Only residues that align to *A. bakeri* Orco are included.

Extended Data Table 1 | Cryo-EM data collection, refinement and model validation statistics

Orco-Fab	
Data deposition	
PDB	6C70
EMDB	7352
Cryo-EM Data Collection	
Voltage (kV)	300
Magnification (x)	29,000
Pixel size (Å)	1.0
Electron exposure (e ⁻ /Å ² /frame)	1.6
Defocus range (μm)	-0.8 to -2.0
Number of image stacks	1,221
Number of frames per stack	50
Cryo-EM Data Processing	
Initial number of particles	82,614
Final number of particles	53,141
Symmetry imposed	C4
Map sharpening <i>B</i> factor (Å ²)	-160
Map resolution (Å)	3.5
Map resolution range (Å)	3-8
FSC threshold	0.143
Model Refinement	
Number of Orco amino acids	388
Number of Fab amino acids	0
Total non-hydrogen atoms	3092
Average <i>B</i> factor (Å ²)	104
Bond length r.m.s.d. (Å)	0.01
Bond angle r.m.s.d. (°)	1.07
Ramachandran Plot:	
Favoured (%)	97.4
Allowed (%)	2.6
Outliers (%)	0
Rotamer outliers (%)	0
MolProbity score	1.7
MolProbity clash score	7.6

Atomic iron and titanium in the atmosphere of the exoplanet KELT-9b

H. Jens Hoeijmakers^{1,2}, David Ehrenreich¹, Kevin Heng^{2*}, Daniel Kitzmann², Simon L. Grimm², Romain Allart¹, Russell Deitrick², Aurélien Wyttenbach¹, Maria Oreshenko², Lorenzo Pino¹, Paul B. Rimmer^{3,4}, Emilio Molinari^{5,6} & Luca Di Fabrizio⁵

To constrain the formation history of an exoplanet, we need to know its chemical composition^{1–3}. With an equilibrium temperature of about 4,050 kelvin⁴, the exoplanet KELT-9b (also known as HD 195689b) is an archetype of the class of ultrahot Jupiters that straddle the transition between stars and gas-giant exoplanets and are therefore useful for studying atmospheric chemistry. At these high temperatures, iron and several other transition metals are not sequestered in molecules or cloud particles and exist solely in their atomic forms⁵. However, despite being the most abundant transition metal in nature, iron has not hitherto been detected directly in an exoplanet because it is highly refractory. The high temperatures of KELT-9b imply that its atmosphere is a tightly constrained chemical system that is expected to be nearly in chemical equilibrium⁵ and cloud-free^{6,7}, and it has been predicted that spectral lines of iron should be detectable in the visible range of wavelengths⁵. Here we report observations of neutral and singly ionized atomic iron (Fe and Fe^+) and singly ionized atomic titanium (Ti^+) in the atmosphere of KELT-9b. We identify these species using cross-correlation analysis⁸ of high-resolution spectra obtained as the exoplanet passed in front of its host star. Similar detections of metals in other ultrahot Jupiters will provide constraints for planetary formation theories.

Motivated by theoretical predictions⁵, we conducted a search for metal lines in the high-resolution transmission spectrum of KELT-9b, which was observed using the HARPS-North (HARPS-N) spectrograph during a single transit of the exoplanet. HARPS-N is a fibre-fed spectrograph, stabilized in pressure and temperature and mounted on the 3.58-m Telescopio Nazionale Galileo (TNG), which is located on the Canary Island of La Palma, Spain. We recorded 19 and 30 spectra during the 3.9-h-long transit and outside of this transit, respectively, covering the whole night from 31 July 2017 to 1 August 2017. Spectra were reduced with the HARPS-N data reduction software, version 3.8. They consist of 69 orders covering the wavelength range 3,874–6,909 Å and overlapping partially at their edges. Orders were extracted individually, flat-fielded using calibrations obtained during twilight, and deblazed and wavelength-calibrated in the Solar System barycentric rest frame. We built a common reference-wavelength grid with a spectral resolution of 0.01 Å, on which the calibrated orders were then binned. Pixels in overlapping orders at the same wavelength were then averaged to conserve the flux. Contamination of the spectra by absorption lines of Earth's atmosphere (mainly by water) were corrected using established methods (see Methods). The optical range of wavelengths is populated with electronic transitions of atoms and ions of metals. With a spectral resolving power of about 115,000, these data are ideal for searching for the absorption signatures associated with metals present in the atmosphere of KELT-9b, by cross-correlating the high-resolution spectra^{8,9} with theoretical templates constructed from the cross-sections of the relevant species¹⁰ (Fig. 1).

We searched specifically for the spectral lines of Fe , Fe^+ , neutral titanium (Ti) and Ti^+ in the data because the relative abundances of these species vary by many orders of magnitude between atmospheric temperatures of 2,500 K and 6,000 K (Fig. 1). Fe^+ becomes more abundant than

Fe at about 3,900–4,300 K, depending on whether chemical equilibrium is assumed (Fig. 1c) or whether photochemistry and vertical mixing are present (Fig. 1d); Ti^+ becomes more abundant than Ti at about 3,000–3,400 K. These estimates assume that the elemental abundances (C/H, O/H, N/H, Ti/H and Fe/H) are equal to those of the Sun; that is, they assume solar metallicity. The abundances of Fe^+ and Ti^+ stabilize above the transition temperatures quoted above (Fig. 1), meaning that only lower bounds on the atmospheric temperature of KELT-9b may be obtained.

Observing through the atmosphere of Earth means that the measured transmission spectrum lacks an absolute empirical normalization. This lack of an absolute empirical normalization implies that absolute atomic abundances cannot be extracted from the data, which in turn implies that the metallicity cannot be inferred from these data alone. In addition, model transmission spectra lack an absolute theoretical normalization^{11–13}. In most hot Jupiters, the spectral continuum is dominated by a combination of Rayleigh scattering associated with molecular hydrogen, the spectral line wings of molecules and the alkali metals (which are mediated by pressure broadening), collision-induced absorption associated with helium and molecular hydrogen, and clouds or hazes. For KELT-9b, the unusually high temperatures imply that all species are in the gas phase and that opacity as a result of bound-free absorption associated with hydrogen anions (H^-)¹⁴ is the dominant source of the spectral continuum¹⁵ rather than Rayleigh scattering associated with atomic and molecular hydrogen (Fig. 1). The line wings of Fe , Fe^+ , Ti and Ti^+ are also subdominant (Fig. 1), which implies that pressure-broadening is not a source of uncertainty.

This rather peculiar property of KELT-9b, and of ultrahot Jupiters in general, allows us to meaningfully compute the relative differences between the line peaks of Fe , Fe^+ , Ti and Ti^+ and the spectral continuum provided by H^- . We construct four templates, using theoretical transmission spectra¹³ that consist separately of Fe , Fe^+ , Ti and Ti^+ lines, each with a H^- continuum. The ability to determine the relative normalization between the line peaks and the continuum means that we are able to give more weight to strong lines and less weight to weak lines in our templates, which results in a higher signal-to-noise ratio in our cross-correlations compared to an analysis using templates in which all of the lines are weighted equally (a so-called binary mask).

Encoded in the data are two distinct signatures: the rotation of the star ($v\sin i = 111.4 \text{ km s}^{-1}$, where v is the rotational velocity and i is the projected angle of the spin axis) and the orbital velocity of the exoplanet ($\pm 81 \text{ km s}^{-1}$), both projected along the line of sight to the observer. Each location on the stellar disk corresponds to a different projected rotational velocity of the star. As the exoplanet moves across the stellar disk, it traces out a range of projected rotational velocities with time (Fig. 2). This leaves an imprint on each stellar absorption line that shows up as an enhancement in flux at the wavelength that corresponds to the projected rotational velocity. When the time-averaged stellar spectrum is subtracted from the data and the cross-correlation analysis is performed, a time-dependent residual known as a Doppler shadow remains (Fig. 2). The tilt of the Doppler shadow with respect to the axes of time and

¹Observatoire astronomique de l'Université de Genève, Versoix, Switzerland. ²University of Bern, Center for Space and Habitability, Bern, Switzerland. ³University of Cambridge, Cavendish Astrophysics, Cambridge, UK. ⁴MRCC Laboratory of Molecular Biology, Cambridge, UK. ⁵INAF FGG, Telescopio Nazionale Galileo, Breña Baja, Spain. ⁶INAF Osservatorio Astronomico di Cagliari, Selargius, Italy. *e-mail: kevin.heng@csh.unibe.ch

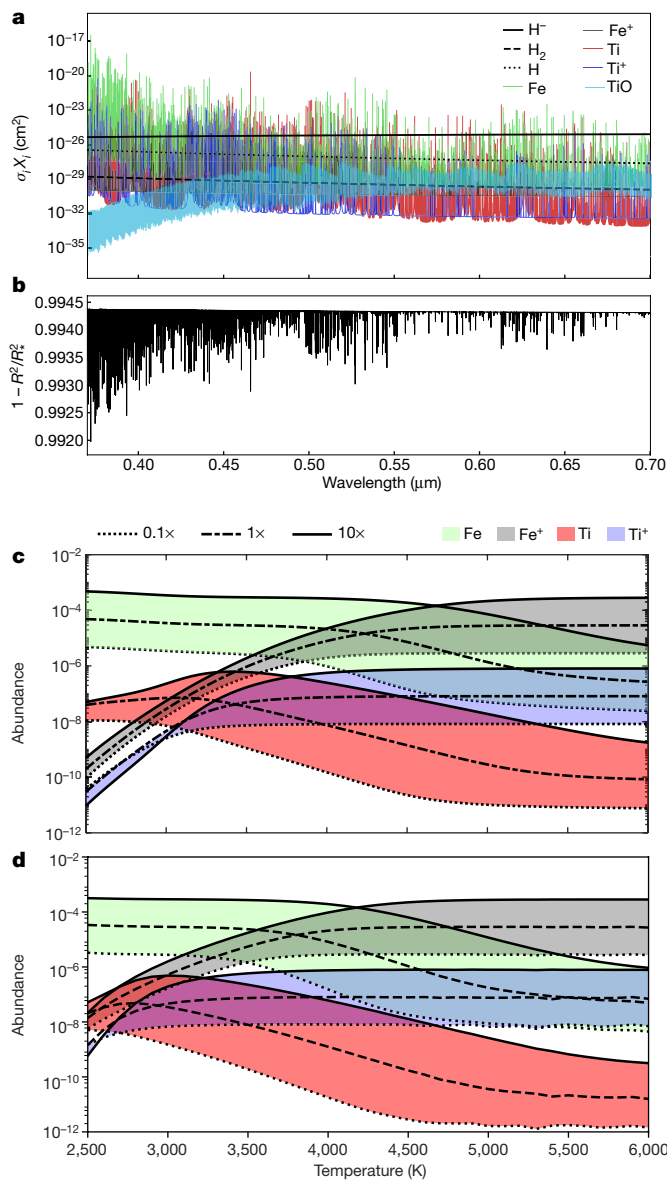


Fig. 1 | Theoretical cross-sections and chemistry. **a**, Cross-sections σ_i of Rayleigh scattering associated with atomic and molecular hydrogen (H and H_2), bound-free absorption associated with the hydrogen anion (H^-) and the spectral lines of neutral and singly ionized iron and titanium (Fe , Fe^+ , Ti and Ti^+) and of titanium oxide (TiO), weighted by their relative abundances by number (volume mixing ratios X_i), assuming chemical equilibrium, a temperature of 4,000 K and solar metallicity. The dominance of H^- absorption implies that the spectral continuum can be used to estimate the pressure associated with the transit chord probed in KELT-9b, which we compute to be about 10 mbar. **b**, The theoretical transmission spectrum corresponding to the cross-sections shown. R and R_0 denote the exoplanetary and stellar radii, respectively. **c**, Mixing ratios of Fe , Fe^+ , Ti and Ti^+ as a function of temperature, assuming chemical equilibrium and for metallicities of 0.1, 1 and 10 times the solar metallicity. **d**, Same as **c**, but including photochemistry and a representative vertical mixing strength of $10^{10} \text{ cm}^2 \text{ s}^{-1}$.

wavelength can be used to infer the angle between the rotational axis of the star and the orbital plane of the exoplanet. This Doppler tomography technique was used previously to infer that KELT-9b resides in a near-polar orbit⁴. Superimposed on the Doppler shadow is the time-dependent absorption spectrum of the atmosphere of KELT-9b (Fig. 2). The spectrum shifts in wavelength with time because it is associated with the varying projected orbital velocity of the exoplanet.

To perform the cross-correlations, we subdivided the reduced spectra into 20-nm bins (for computational efficiency), each to be treated

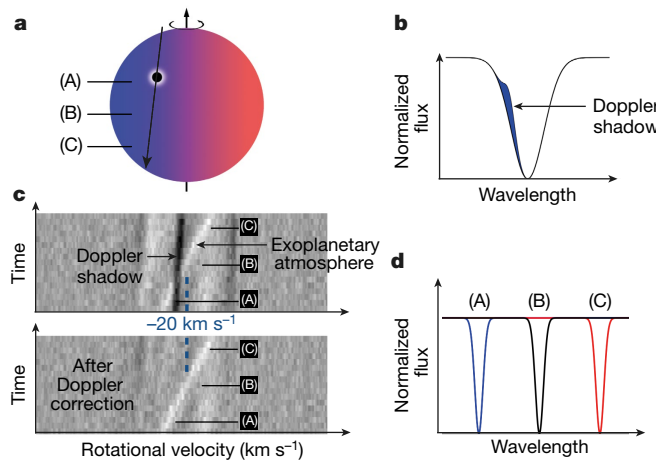


Fig. 2 | Geometry of the KELT-9 system. **a**, Schematic of the orbital geometry of the exoplanet (represented by the black filled circle). The arrow indicates the orbital trajectory of the exoplanet as it transits across the stellar disk. The blue and red shading represent the blue- and redshifted regions on the stellar disk caused by stellar rotation. **b**, The obscuration of part of the stellar disk results in an enhancement in flux of the stellar absorption line, as indicated by the blue shaded area. **d**, Furthermore, as the exoplanet progresses in its orbit, its projected orbital velocity shifts from being blueshifted (at point A) to being redshifted (at point C). **c**, These two distinct signatures show up in the cross-correlation function (CCF; grey scale; top) as a Doppler shadow (deficit in the CCF at the instantaneous velocity of the obscured part of the stellar disk) and a bright streak (enhancement in the CCF at the instantaneous radial component of the orbital velocity of the planet), respectively. To isolate the signature of the planet, we model and subtract the Doppler shadow from the CCF (bottom). The systemic radial velocity of the KELT-9 system (-20 km s^{-1}) is indicated.

independently in the analysis. We measured the stellar spectrum by averaging the out-of-transit exposures, divided the master stellar spectrum that we obtained out of each exposure and corrected for residual fluctuations in the continuum by normalizing each spectrum using a smoothing filter (with a width of 0.75 \AA). Each spectral pixel is weighted by the reciprocal of its variance in time⁸. The Doppler shadow is subtracted to isolate the atmospheric signal from the exoplanet (see Methods). We cross-correlated the residuals between radial velocities of $\pm 1,000 \text{ km s}^{-1}$ with the templates.

The peaks in the cross-correlation function (CCF) of Fe , Fe^+ and Ti^+ are seen as bright streaks across the axes of time and systemic radial velocity (Fig. 3). These streaks were also seen in the discovery study⁴ and are presumably caused by spectral lines that the exoplanet and the star have in common, notably Fe^+ . Co-adding the signal along these streaks, in the rest frame of the exoplanet, results in significant detections of CCF peaks for Fe , Fe^+ and Ti^+ with signal-to-noise ratios of 7, 14 and 9, respectively. The CCFs are normalized by the standard deviation at velocities away from the rest frame of the exoplanet to produce the signal-to-noise ratios of the detections. By fitting Gaussians to these CCFs, we find weighted average line contrasts of $(0.28 \pm 0.03) \times 10^{-3}$ (9.3σ), $(2.21 \pm 0.08) \times 10^{-3}$ (26σ) and $(1.28 \pm 0.07) \times 10^{-3}$ (18σ) for Fe , Fe^+ and Ti^+ , respectively. The Gaussian standard deviation is denoted by σ and the uncertainties quoted are 1σ . There is no significant detection of the CCF for Ti , which has an average line contrast of $(0.18 \pm 0.05) \times 10^{-3}$ (3.3σ).

That the lines of Fe^+ show up more prominently than those of Fe suggests that the atmospheric temperatures probed exceed about 4,000 K. The non-detection of Ti (Fig. 3) supports this interpretation. The discovery of Fe , Fe^+ and Ti^+ in KELT-9b sets the stage for future searches for carbon monoxide (CO) and water (H_2O) in the near-infrared range of wavelengths. At these elevated temperatures, CO is expected to be the dominant molecule, which would imply that its abundance directly mirrors the value of C/H (for $\text{C}/\text{O} < 1$) or O/H (for $\text{C}/\text{O} > 1$)⁵. Detecting H_2O would enable the carbon-poor and carbon-rich scenarios

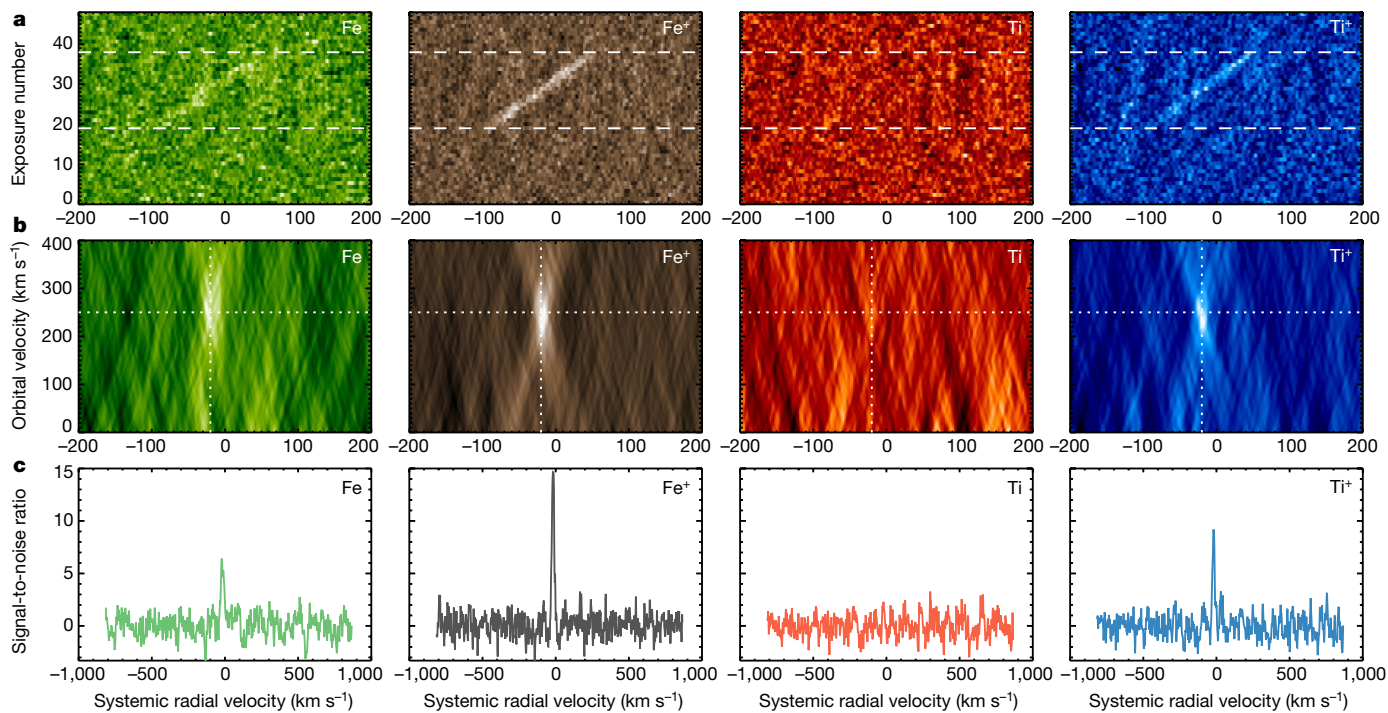


Fig. 3 | Analysis of observations. Separate cross-correlation analyses were performed using templates with Fe, Fe^+ , Ti and Ti^+ . Each template assumes a spectral continuum associated with H^- . **a**, CCFs (colour scale) with the Doppler shadow subtracted. The absorption spectrum of the exoplanetary atmosphere shows up as a bright streak. The horizontal dashed lines mark the start and end

of transit. **b**, The CCFs co-added along each streak (that is, in the rest frame of the exoplanet). The horizontal and vertical dotted lines denote the expected orbital velocity of KELT-9b and the systemic velocity of the KELT-9 system, respectively. **c**, The signal-to-noise ratio of cross-correlation extracted at an orbital velocity of 254 km s^{-1} . Fe, Fe^+ and Ti^+ are clearly detected, but Ti is not.

to be distinguished^{16,17}. Inferring C/H and O/H would allow the metallicity to be constrained. These prospects ensure that KELT-9b will remain important for studying extrasolar atmospheric chemistry using both space- and ground-based telescopes.

Online content

Any Methods, including any statements of data availability and Nature Research reporting summaries, along with any additional references and Source Data files, are available in the online version of the paper at <https://doi.org/10.1038/s41586-018-0401-y>.

Received: 1 May 2018; Accepted: 20 June 2018;

Published online 15 August 2018.

- Öberg, K. I., Murray-Clay, R. & Bergin, E. A. The effects of snowlines on C/O in planetary atmospheres. *Astrophys. J.* **743**, L16 (2011).
- Madhusudhan, N., Amin, M. A. & Kennedy, G. M. Toward chemical constraints on hot Jupiter migration. *Astrophys. J.* **794**, L12 (2014).
- Öberg, K. I. & Bergin, E. A. Excess C/O and C/H in outer protoplanetary disk gas. *Astrophys. J.* **831**, L19 (2016).
- Gaudi, B. S. et al. A giant planet undergoing extreme-ultraviolet irradiation by its hot massive-star host. *Nature* **546**, 514–518 (2017).
- Kitzmann, D. et al. The peculiar atmospheric chemistry of KELT-9b. *Astrophys. J.* (in the press); preprint at <https://arxiv.org/abs/1804.07137> (2018).
- Heng, K. A cloudiness index for transiting exoplanets based on the sodium and potassium lines: tentative evidence for hotter atmospheres being less cloudy at visible wavelengths. *Astrophys. J.* **826**, L16 (2016).
- Stevenson, K. B. Quantifying and predicting the presence of clouds in exoplanet atmospheres. *Astrophys. J.* **817**, L16 (2016).
- Snellen, I. A. G., de Kok, R. J., de Mooij, E. J. W. & Albrecht, S. The orbital motion, absolute mass and high-altitude winds of exoplanet HD209458b. *Nature* **465**, 1049–1051 (2010).
- Brogi, M. et al. The signature of orbital motion from the dayside of the planet τ Boötis b. *Nature* **486**, 502–504 (2012).
- Kurucz, R. L. Including all the lines: data releases for spectra and opacities. *Can. J. Phys.* **95**, 825–827 (2017).
- Benneke, B. & Seager, S. Atmospheric retrieval for super-Earths: uniquely constraining the atmospheric composition with transmission spectroscopy. *Astrophys. J.* **753**, 100 (2012).
- Griffith, C. A. Disentangling degenerate solutions from primary transit and secondary eclipse spectroscopy of exoplanets. *Philos. Trans. R. Soc. Lond. A* **372**, 20130086 (2014).
- Heng, K. & Kitzmann, D. The theory of transmission spectra revisited: a semi-analytical method for interpreting WFC3 data and an unresolved challenge. *Mon. Not. R. Astron. Soc.* **470**, 2972–2981 (2017).

- John, T. L. Continuous absorption by the negative hydrogen ion reconsidered. *Astron. Astrophys.* **193**, 189–192 (1988).
- Arcangeli, J. et al. H^- opacity and water dissociation in the dayside atmosphere of the very hot gas giant WASP-18b. *Astrophys. J.* **855**, L30 (2018).
- Madhusudhan, N. C/O ratio as a dimension for characterizing exoplanetary atmospheres. *Astrophys. J.* **758**, 36 (2012).
- Heng, K. & Tsai, S.-M. Analytical models of exoplanetary atmospheres. III. Gaseous C–H–O–N chemistry with nine molecules. *Astrophys. J.* **829**, 104 (2016).

Acknowledgements This project has received funding from the European Research Council (ERC) under the European Union's Horizon 2020 research and innovation programme (projects Four Aces and EXOKLEIN with grant agreement numbers 724427 and 771620, respectively). This work was carried out in the framework of the PlanetS National Centre of Competence in Research (NCCR) supported by the Swiss National Science Foundation (SNSF).

Reviewer information *Nature* thanks D. Deming and the other anonymous reviewer(s) for their contribution to the peer review of this work.

Author contributions H.J.H. led the data reduction and analysis, designed the cross-correlation templates, co-wrote the manuscript, co-led the scientific vision and coordination, sourced database information for opacity calculations and made all of the plots in Fig. 3. D.E. is the principal investigator of the HARPS-N dataset (A35DDT4) and co-wrote the manuscript. K.H. led the scientific vision, coordination and interpretation, and the writing of the manuscript. D.K. performed chemical-equilibrium calculations using the FastChem computer code and made the corresponding plot in Fig. 1. S.L.G. sourced database information for and performed opacity calculations using HELIOS-K computer code. R.A. performed the telluric subtraction using Molecfit and confirmed detections of Fe, Fe^+ and Ti^+ by repeating the cross-correlation analysis with binary masks. R.D. compiled cross-sections for spectral lines and continuum and made the corresponding plot in Fig. 1. A.W. led the data acquisition and observation, performed the extraction of the spectra, and confirmed the Doppler-shadow measurement and performed its removal. M.O. made the schematic plot in Fig. 2. L.P. co-designed the cross-correlation templates and performed additional checks on the outcome. P.B.R. performed chemical-kinetics calculations using ARGO computer code and made the corresponding plot in Fig. 1. E.M. provided a night of Director's Discretionary Time to make the project possible. L.D.F. performed the TNG/HARPS-N observations.

Competing interests The authors declare no competing interests.

Additional information

Extended data is available for this paper at <https://doi.org/10.1038/s41586-018-0401-y>.

Reprints and permissions information is available at <http://www.nature.com/reprints>.

Correspondence and requests for materials should be addressed to K.H.

Publisher's note: Springer Nature remains neutral with regard to jurisdictional claims in published maps and institutional affiliations.

METHODS

Telluric lines are the main contaminant in the observed spectrum, with strong spectral lines of water and molecular oxygen in the visible range of wavelengths. To perform decontamination, we used version 1.5.1 of Molecfit¹⁸, an ESO tool for correcting for the tellurics in ground-based spectra following established procedures¹⁹. We tested the performance of our telluric correction by cross-correlating the corrected and uncorrected in-transit spectra with a telluric water-absorption template spectrum (at 296 K). Extended Data Fig. 1 demonstrates that our correction efficiently removes the telluric water signal.

To remove the Doppler shadow, we cross-correlated the data with a PHOENIX stellar model template that matches the effective temperature of the star²⁰. We modelled and fitted the main Doppler shadow that occurs near -35 km s^{-1} , as well as three aliases near $+80 \text{ km s}^{-1}$, $+20 \text{ km s}^{-1}$ and -125 km s^{-1} , as time-dependent Gaussians. The best-fit parameters (central radial velocity, width and amplitude) are described by first-, second-, third- or fourth-degree polynomials in time. The resulting model of the Doppler shadow was adjusted in amplitude to the CCF obtained for each species and subtracted. We applied a cross-correlation formalism as used previously¹⁹ to measure the average line strengths of Fe, Fe⁺, Ti and Ti⁺. For this purpose, the templates that were used to detect the species were continuum-subtracted to act as weighted binary masks that measure the average spectral line present in each spectral bin and each exposure. The final one-dimensional CCFs were obtained by a weighted co-addition of the 20 bins and 19 in-transit exposures following the same strategy as used previously²¹. The weights were obtained by injecting the templates into the data at the start of the analysis at a low level as to not affect the statistics of the CCF²², and subsequently measuring the resulting increase in the CCF. Wavelength regions with poorer data quality or fewer spectral lines of the target species were thereby implicitly given a low weight.

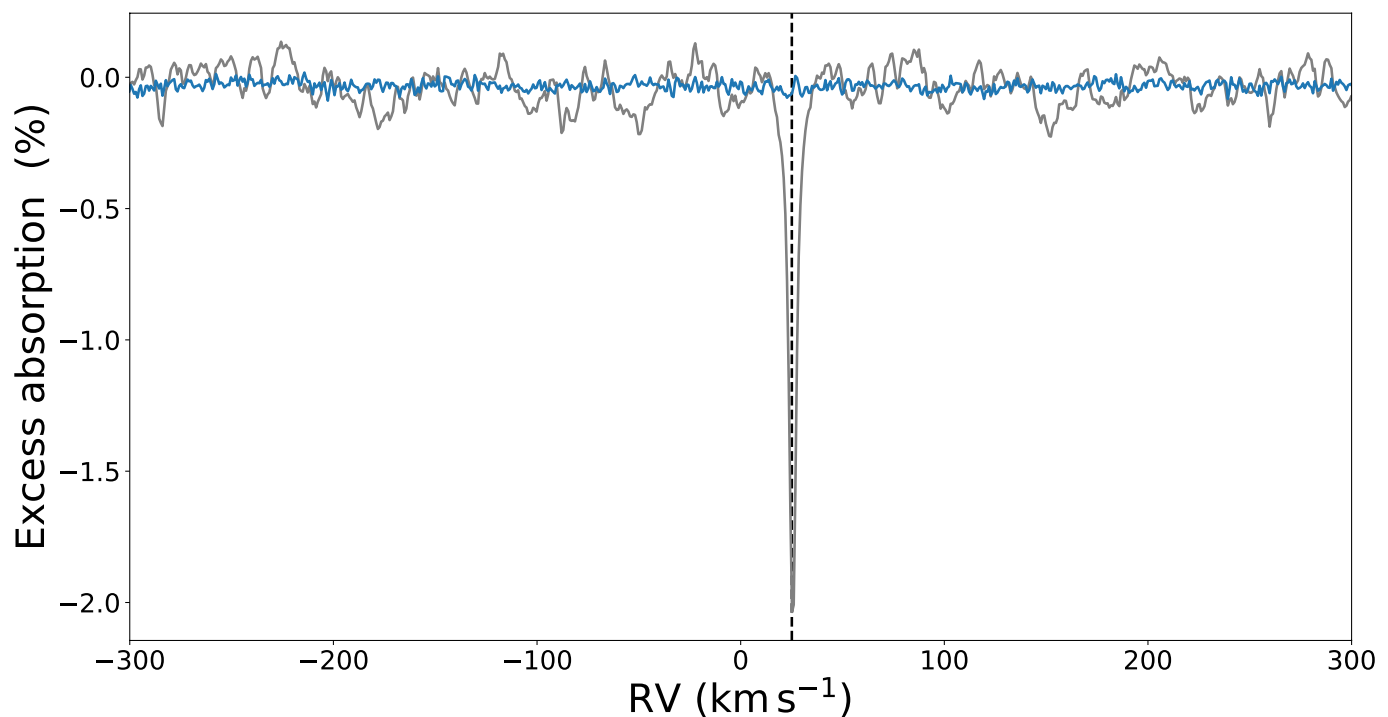
The opacities¹⁰ of Fe, Fe⁺, Ti and Ti⁺ were computed using standard methods^{23,24} and the open-source HELIOS-K opacity calculator²⁵. Equilibrium-chemistry calculations were performed using the FastChem code²⁶. We note that the JANAF database (<https://janaf.nist.gov>) supplies the Gibbs free energies needed to perform the equilibrium-chemistry calculations up to only 6,000 K. Chemical-kinetics calculations were performed using the ARGO code²⁷. The templates for the neutrals (Fe, Ti) and ions (Fe⁺, Ti⁺) assume atmospheric temperatures of 3,500 K and 4,500 K, respectively; assuming different temperatures results in slight changes to the signal-to-noise ratio of each detection. The bright CCF streaks associated

with each species were co-added along each streak, in the rest frame of the exoplanet, by using the measured orbital parameters⁴ and experimenting with a range of values for the orbital velocity of the exoplanet. We estimate the signal-to-noise ratios of the individually detected species by measuring the standard deviation of the CCF at velocities more than 50 km s^{-1} away from the exoplanet's rest frame. Water was not detected below the 200 p.p.m. level (3σ).

Data availability. The observations that support the findings of this study were obtained as part of DDT programme A35DDT4 and are available in the public archive of the TNG (<http://ia2.oats.inaf.it/archives/tng>).

Code availability. All codes, programs and algorithms that were used to support the findings of this study are described in previously published literature. The codes to calculate the opacity functions and to model atmospheric chemistry are publicly available at <https://github.com/exoclime>.

18. Smette, A. et al. Molecfit: a general tool for telluric absorption correction. I. Method and application to ESO instruments. *Astron. Astrophys.* **576**, A77 (2015).
19. Allart, R. et al. Search for water vapor in the high-resolution transmission spectrum of HD 189733b in the visible. *Astron. Astrophys.* **606**, A144 (2017).
20. Husser, T.-O. et al. A new extensive library of PHOENIX stellar atmospheres and synthetic spectra. *Astron. Astrophys.* **553**, A6 (2013).
21. Hoeijmakers, H. J. et al. A search for TiO in the optical high-resolution transmission spectrum of HD 209458b: hindrance due to inaccuracies in the line database. *Astron. Astrophys.* **575**, A20 (2015).
22. Brogi, M. et al. Rotation and winds of exoplanet HD 189733 b measured with high-dispersion transmission spectroscopy. *Astrophys. J.* **817**, 106 (2016).
23. Rothman, L.S. et al. The HITRAN molecular spectroscopic database and HAWKS (HITRAN atmospheric workstation): 1996 edition. *J. Quant. Spectrosc. Rad. Trans.* **60**, 665–710 (1998).
24. Heng, K. *Exoplanetary Atmospheres: Theoretical Concepts and Foundations* 74–81 (Princeton Univ. Press, Princeton, 2017).
25. Grimm, S. L. & Heng, K. HELIOS-K: an ultrafast, open-source opacity calculator for radiative transfer. *Astrophys. J.* **808**, 182 (2015).
26. Stock, J. W., Kitzmann, D., Patzer, A. B. C. & Sedlmayr, E. FastChem: a computer program for efficient complex chemical equilibrium calculations in the neutral/ionized gas phase with applications to stellar and planetary atmospheres. *Mon. Not. R. Astron. Soc.* **479**, 865–874 (2018).
27. Rimmer, P. B. & Helling, Ch. A chemical kinetics network for lightning and life in planetary atmospheres. *Astrophys. J. Suppl. Ser.* **224**, 9 (2016).



Extended Data Fig. 1 | Telluric water-absorption correction. Cross-correlation analysis performed on the in-transit spectrum with a telluric water-absorption template spectrum (at 296 K). The blue and grey curves are the transit depths with and without the telluric correction,

respectively. The data are shifted to the rest frame of the star, such that the signal dominated by telluric water absorption occurs near +25 km s⁻¹ (corresponding to the barycentric Earth radial velocity (BERV) systemic velocity), as indicated by the dashed vertical line.

Observation of topological phenomena in a programmable lattice of 1,800 qubits

Andrew D. King^{1*}, Juan Carrasquilla², Jack Raymond¹, Isil Ozfidan¹, Evgeny Andriyash¹, Andrew Berkley¹, Mauricio Reis¹, Trevor Lanting¹, Richard Harris¹, Fabio Altomare¹, Kelly Boothby¹, Paul I. Bunyk¹, Colin Enderud¹, Alexandre Fréchette¹, Emile Hoskinson¹, Nicolas Ladizinsky¹, Travis Oh¹, Gabriel Poulin-Lamarre¹, Christopher Rich¹, Yuki Sato¹, Anatoly Yu. Smirnov¹, Loren J. Swenson¹, Mark H. Volkmann¹, Jed Whittaker¹, Jason Yao¹, Eric Ladizinsky¹, Mark W. Johnson¹, Jeremy Hilton¹ & Mohammad H. Amin^{1,3}

The work of Berezinskii, Kosterlitz and Thouless in the 1970s^{1,2} revealed exotic phases of matter governed by the topological properties of low-dimensional materials such as thin films of superfluids and superconductors. A hallmark of this phenomenon is the appearance and interaction of vortices and antivortices in an angular degree of freedom—typified by the classical XY model—owing to thermal fluctuations. In the two-dimensional Ising model this angular degree of freedom is absent in the classical case, but with the addition of a transverse field it can emerge from the interplay between frustration and quantum fluctuations. Consequently, a Kosterlitz–Thouless phase transition has been predicted in the quantum system—the two-dimensional transverse-field Ising model—by theory and simulation^{3–5}. Here we demonstrate a large-scale quantum simulation of this phenomenon in a network of 1,800 *in situ* programmable superconducting niobium flux qubits whose pairwise couplings are arranged in a fully frustrated square-octagonal lattice. Essential to the critical behaviour, we observe the emergence of a complex order parameter with continuous rotational symmetry, and the onset of quasi-long-range order as the system approaches a critical temperature. We describe and use a simple approach to statistical estimation with an annealing-based quantum processor that performs Monte Carlo sampling in a chain of reverse quantum annealing protocols. Observations are consistent with classical simulations across a range of Hamiltonian parameters. We anticipate that our approach of using a quantum processor as a programmable magnetic lattice will find widespread use in the simulation and development of exotic materials.

Richard Feynman's vision of simulating quantum systems with a quantum computer^{6,7} has motivated the field of quantum information since its inception. In the absence of large-scale programmable universal quantum computers, advances in quantum simulation are bound by available technology. Nevertheless, remarkable progress has been made using near-term approaches such as ultracold atoms⁸, superconducting qubits⁹, Bose–Einstein condensates¹⁰, trapped ions¹¹ and quantum dots¹², among others¹³. Owing to the possibility of noise-tolerant applications, quantum simulation has been identified as an area of potential commercial value for near-term quantum computing technologies^{14,15}. Quantum annealing (QA) processors^{16–18} can be used to simulate systems in the transverse-field Ising model (TFIM) described by the Hamiltonian

$$H = \sum_i h_i \sigma_i^z + \sum_{i < j} J_{ij} \sigma_i^z \sigma_j^z - \Gamma \sum_i \sigma_i^x$$

where h_i are longitudinal fields, J_{ij} are coupling terms, σ_i^x and σ_i^z are Pauli matrices acting on the i th spin, and Γ is the transverse field. Evolution of this Hamiltonian in a low-temperature environment allows sampling of low-energy solutions, with applications to optimization and machine learning^{14,19,20}. This in turn allows estimation of

equilibrium statistics of various phases dictated by the parameters h_i , J_{ij} and Γ at a given temperature T .

Geometrically frustrated magnets²¹ are systems described by spin Hamiltonians with competing terms that cannot be minimized simultaneously. These systems give rise to a broad spectrum of exotic phases of matter. The TFIM exhibits a particular type of topological phenomenon on certain frustrated lattices: a Kosterlitz–Thouless (KT) phase transition separates a disordered paramagnetic phase from a phase in which complementary topological defects—vortices and antivortices—form bound pairs, resulting in polynomial decay of correlations^{1,2,4}. This phase transition has been predicted in theory and simulation, but to our knowledge never observed experimentally in the TFIM. Other KT phase transitions have, however, been observed in many systems including superconducting and superfluid films²², trapped atomic gases¹⁰ and hybrid tin–graphene Josephson junction arrays²³.

Here we exhibit this phenomenon in a large-scale programmable quantum simulation. We perform this simulation using a superconducting QA processor consisting of 2,048 radio-frequency superconducting quantum interference device (SQUID) flux qubits fabricated as an integrated circuit, in which the Hamiltonian terms h_i and J_{ij} are specified with programmable on-chip control circuitry^{16–18}. The topology of the available non-zero coupling terms J_{ij} consists of a regular bipartite grid. On this programmable substrate we define a sequence of fully frustrated square-octagonal lattices having a cylindrical boundary condition (Fig. 1a), with the largest system using 1,800 qubits (see Methods). This lattice features chains of four ferromagnetically coupled qubits. In the large ferromagnetic (FM) coupling limit, the low-energy description of this lattice follows the same Landau–Ginzburg–Wilson theory as the widely studied^{3–5,24–26} triangular antiferromagnetic (AFM) lattice (Fig. 1b). We therefore use the same analytic machinery, which is valuable even outside the large FM coupling, low-temperature limit.

Central to this analysis is a mapping from each plaquette in the triangular lattice to a two-dimensional pseudospin that can be represented by a complex number ψ_j . This gives the local angular degree of freedom in which topological features, including vortices and antivortices, can emerge. To first-order perturbation in the small- Γ limit, an AFM triangle has six degenerate ground states, each consisting of an up-spin ($| \uparrow \rangle$), a down-spin ($| \downarrow \rangle$), and a spin aligned with the transverse field ($| \rightarrow \rangle = (| \uparrow \rangle + | \downarrow \rangle)/\sqrt{2}$). These six ground states map to complex six-state XY pseudospins (Fig. 1c) via the mapping

$$\psi_j = \langle \sigma_{j1}^z \rangle + \langle \sigma_{j2}^z \rangle e^{2\pi i/3} + \langle \sigma_{j3}^z \rangle e^{4\pi i/3}$$

As with a single AFM triangle, the triangular lattice has, to first-order perturbation, a six-fold-degenerate ground state. One-third of the spins align with the transverse field, one-third take spin-up and one-third take spin-down (Fig. 1d). The square-octagonal lattice has a

¹D-Wave Systems Inc., Burnaby, British Columbia, Canada. ²Vector Institute, MaRS Centre, Toronto, Ontario, Canada. ³Department of Physics, Simon Fraser University, Burnaby, British Columbia, Canada. *e-mail: aking@dwavesys.com

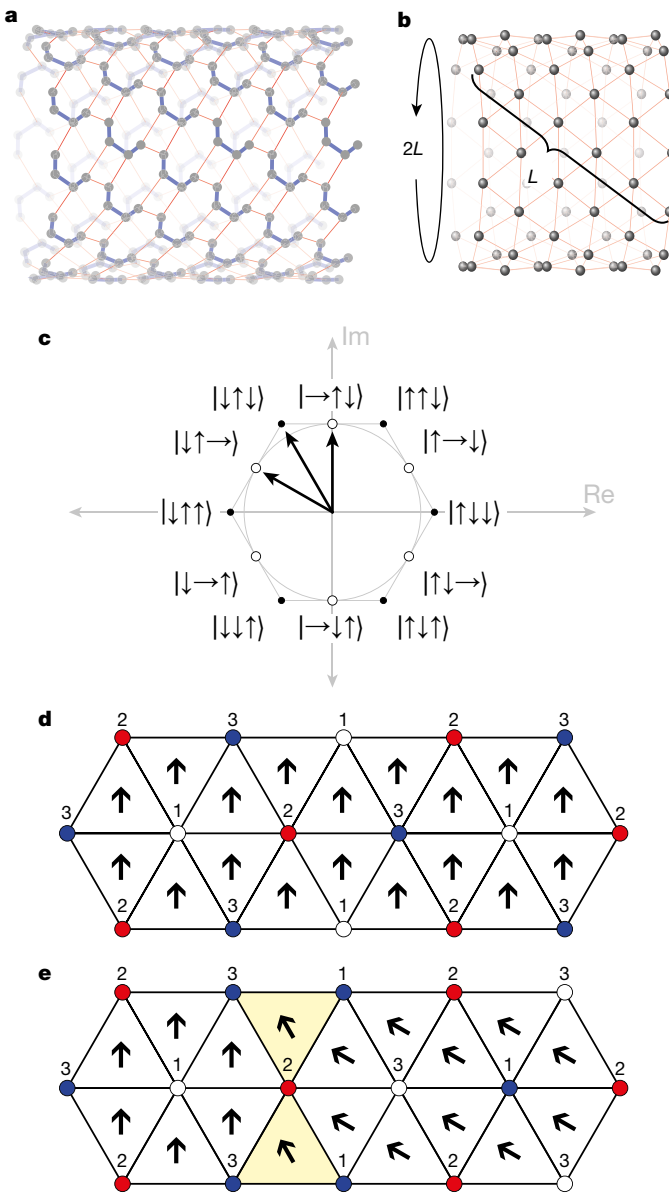


Fig. 1 | Geometrically frustrated lattices. **a, b,** We study the fully frustrated square-octagonal (**a**) and triangular (**b**) lattices with cylindrical boundary condition and width L up to 15 ($L = 6$ shown). FM couplers ($J_{ij} = -1.8$) are indicated with blue lines in **a**; AFM couplers ($J_{ij} = 1$) except on the boundary, where $J_{ij} = 1/2$) are indicated with red lines in **a** and **b**. **c,** Owing to the combination of frustration and superposition, the AFM triangle has six classical ground states and under a small transverse field has six perturbative ground states. These states map to complex pseudospins as shown, indicated with black and white circles, respectively (real and imaginary axes are indicated by 'Re' and 'Im', respectively). Spin states of up, down and transverse-field-aligned superposition are denoted by \uparrow , \downarrow and \rightarrow , respectively, in **c** and by red, blue and white circles in **d** and **e**. **d, e,** Each plaquette in the triangular lattice has a pseudospin (indicated by arrows) defined by the spins of the plaquette. In a perturbative ground state (**d**), all spins in a given sublattice (indicated by numbers) take the same state, and consequently all pseudospins have the same orientation. The state shown in **e** has a shift in pseudospin orientation, which corresponds to an excitation: the two yellow triangles are in a classical ground state but have no energetic contribution from qubits aligning with the transverse field. The pseudospins seen in **d** and **e** are indicated in **c**.

corresponding set of six perturbative ground states that require four-qubit chains to be in delocalized superpositions of their computational basis states $|\uparrow\uparrow\uparrow\uparrow\rangle$ and $|\downarrow\downarrow\downarrow\downarrow\rangle$. Thus the addition of quantum fluctuations selects an ordered subset from the highly degenerate ground-state manifold, reducing entropy and imposing long-range correlations;

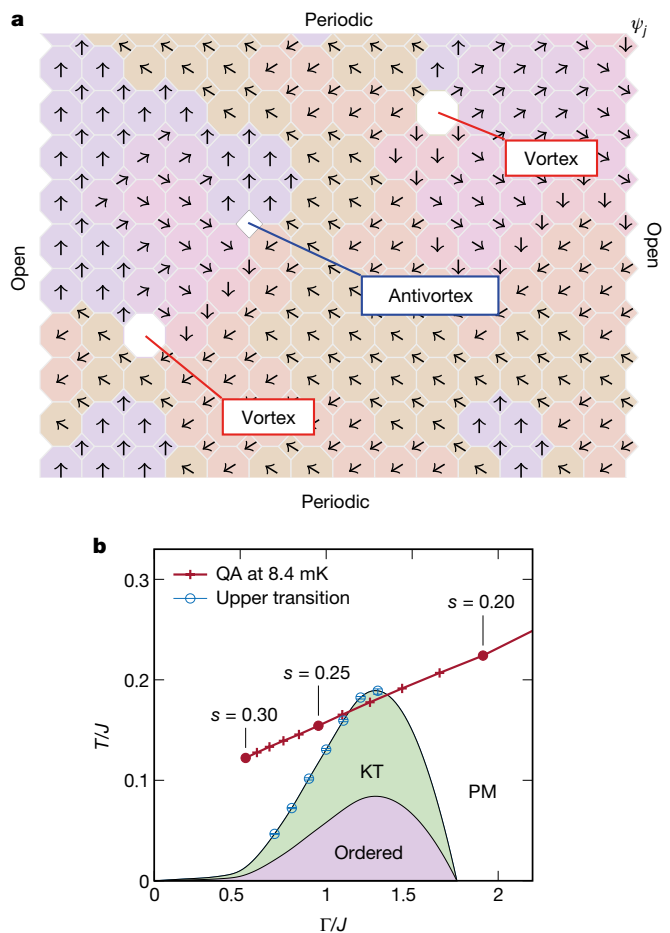


Fig. 2 | Topological features in the transverse-field Ising model. **a,** In the fully frustrated square-octagonal lattice, the spins of a classical state map naturally to a complex pseudospin field ψ_j on the plaquettes, revealing topological features. A swath of an output state from the QA processor, cropped at the top and bottom, is shown from this perspective, with arrows indicating values of ψ_j in the complex plane. Vortices and antivortices (marked in white) can be identified by the clockwise or anticlockwise winding of ψ_j along a closed clockwise path. These topological defects occur in the presence of all-up or all-down plaquettes and frustrated FM couplers. Unpaired vortices and antivortices can appear, owing to the open boundary. **b,** The phase diagram of the square-octagonal lattice in the temperature/transverse-field (T/Γ) plane is determined by QMC simulation on toroidal systems (see Methods). Below a disordered paramagnetic (PM) phase, an ordered region and a critical KT region with $\Gamma > 0$ are bounded by KT phase transitions; circles indicate one of two methods of determining the upper KT transition. The quantum processor follows an annealing schedule that passes through the KT region at sufficiently low temperature of about $T < 9$ mK. Experiments are performed between 8.4 mK and 21.4 mK.

this phenomenon is a form of ‘order by disorder’⁴, and naturally divides the spins into three sublattices categorized by their magnetization in the six perturbative ground states. The sublattice magnetizations m_1 , m_2 and m_3 , defined as the average of $\langle \sigma_i^z \rangle$ over spins in the sublattice, give a complex order parameter²⁶

$$\psi = m e^{i\theta} = (m_1 + m_2 e^{i2\pi/3} + m_3 e^{i4\pi/3}) / \sqrt{3}$$

In the absence of open boundary effects, ψ is simply the average of pseudospin ψ_j over all plaquettes in the system. Figure 1d, e shows pseudospins in the triangular lattice; a full explanation is given in the Methods.

In the square-octagonal lattice, we use the same order parameter with the three sublattices defined according to the natural mapping: two FM-coupled spins must be in the same sublattice, and two

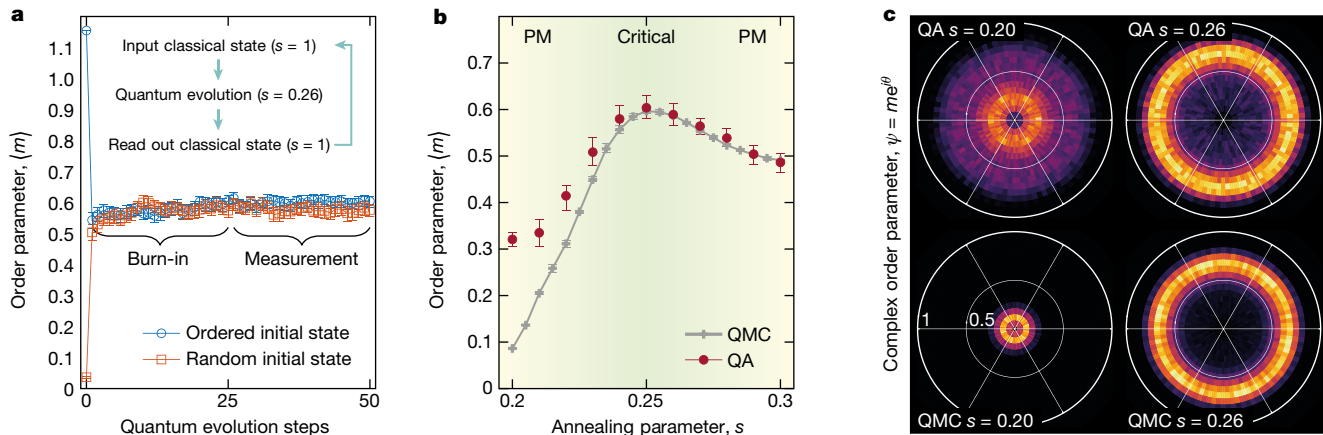


Fig. 3 | Measurement of complex order parameter ψ in quantum simulation. **a**, We estimate statistics of the quantum system using a quantum evolution Monte Carlo approach: the previous classical state is input to the QA processor, evolved for 65 ms in a reverse annealing protocol (see Methods), and read out as a new classical state. A call to the processor consists of 50 evolution steps; we discard the first 25 output samples as correlation with the initial state decays and heating from experimental setup dissipates. Statistics (here, $\langle m \rangle = \langle |\psi| \rangle$) are estimated from the remaining 25 samples, averaged over 240 independent experiments. Error bars are bootstrap 95% confidence intervals. **b**, Order parameter magnitude $\langle m \rangle$ for 1,800-spin square-octagonal lattice ($L = 15$) with cylindrical boundaries. As s increases, quantum and thermal

AFM-coupled spins must be in different sublattices. Figure 2a shows ψ evaluated on each plaquette for an output state from the QA processor.

Figure 2b shows the phase diagram of the square-octagonal lattice in the Γ - T plane, which resembles that of the triangular lattice⁵ (see Methods). At high temperature the system is in a disordered paramagnetic phase. As T drops, for $\Gamma < 1.76$, the system enters a KT phase, in which vortices and antivortices form bound pairs. At even lower temperature, the system transitions into an ordered phase, where U(1) symmetry is broken and ψ concentrates around the six low-temperature clock states (white circles in Fig. 1c; see Methods). While the generation of vortices and antivortices relies on competing quantum and classical fluctuations in the TFIM, the upper KT phase transition belongs to the classical two-dimensional XY universality class⁴ and both transitions are also seen in the classical six-state XY model²⁷; we discuss this relationship further in the Methods.

Having described the lattice and its phase diagram, we now turn to the task of simulating the physics with the QA processor. The processor Hamiltonian is parameterized by a time-dependent annealing parameter s that varies between 0 and 1, and for this particular lattice can be written as

$$H(s) = J(s) \sum_{i,j} J_{ij} \sigma_i^z \sigma_j^z - \Gamma(s) \sum_i \sigma_i^x$$

where J_{ij} is 1.0 for AFM couplers and -1.8 for FM couplers. Details of implementing this Hamiltonian are given in the Methods. As s increases, $J(s)$ increases and $\Gamma(s)$ decreases: $J(0) \approx 0$, $J(1) \gg T$, $\Gamma(0) \gg T$ and $\Gamma(1) \approx 0$. Figure 2b shows the set of points in the Γ - T plane realized by varying s at the operating temperature of 8.4 ± 0.2 mK; points above or below this line can be reached by either rescaling J_{ij} or changing the QA operating temperature.

To estimate the distribution of ψ we use the QA processor as a quantum evolution update operator in a ‘quantum evolution Monte Carlo’ method, where each evolution follows a reverse annealing protocol²⁸ (Fig. 3a; details in Methods). This protocol involves initializing the system in a classical state at $s = 1$, quickly reducing s to a target value between 0.20 and 0.30 over approximately 3.5 μ s, and pausing for up to 65 ms before quenching back to $s = 1$ over 1 μ s and reading the classical output. Repetition of this protocol resembles a Markov chain by which

fluctuations are reduced and the system displays a peak in $\langle m \rangle$ where order is maximal. Peak location deviates slightly from Fig. 2b, which is generated using toroidal rather than cylindrical systems; the fact that this deviation is reflected in QMC results indicates that this is a finite-size effect related to boundary conditions. For $s \geq 0.24$, QA estimates of $\langle m \rangle$ are close to equilibrium values as confirmed by QMC. Overestimation of $\langle m \rangle$ from QA for small s , where the dynamics is fast, arises from evolution during the 1- μ s pre-readout quench. **c**, Monte Carlo histogram of the complex order parameter $\psi = me^{i\theta}$ from QA (top) and QMC (bottom) for small ($s = 0.20$) and large ($s = 0.26$) values of $\langle m \rangle$. Brightness indicates relative frequency of values; ψ shows rotational U(1) symmetry consistent with the expected paramagnetic and KT phases (see Methods).

we generate Monte Carlo estimates of ψ . This is a departure from the traditional use case of QA, in which s is steadily increased from 0 to 1. As is typical in Markov chain Monte Carlo methods, we discard the first half of samples in each experiment as ‘burn-in’ to minimize correlation with the initial state; a further motivation is that we observe around 0.1 mK of cooling at low temperatures, as heat from the QA programming cycle dissipates. We estimate statistics using both an ordered initial state and a random initial state ($m = |\psi|$ large and small, respectively). Deviations between the two estimators are small and included in the error bars.

We experimentally probe values of s between 0.20 and 0.30 at physical temperature T between 8.4 mK and 21.4 mK. Figure 3b shows the expectation $\langle m \rangle$ as a function of s for the 1,800-spin lattice (lattice width $L = 15$) at 8.4 mK, compared with estimates from continuous-time path-integral quantum Monte Carlo (QMC) simulations as detailed in the Methods. In agreement with QMC, QA shows a peak in $\langle m \rangle$ close to where the QA schedule cuts through the KT phase in the large system limit, with a small shift caused by the open boundary condition and finite-size effects—the phase diagram is determined using toroidal rather than cylindrical instances (see Methods). For $s \geq 0.24$, QA shows good agreement with QMC. For smaller s , the dynamics of the system is fast (see Methods) and the system orders during the 1- μ s quench, leading to an overestimate of $\langle m \rangle$; results are almost unchanged between $s = 0$ and $s = 0.2$.

The histogram of the complex order parameter ψ is plotted in Fig. 3c for two points along the QA schedule. As s increases from 0.20 to 0.26, both QA and QMC show the emergence of order: ψ concentrates around a ring with the characteristic U(1) symmetry of the two-dimensional XY model despite the discrete \mathbb{Z}_2 symmetry of the Ising model^{5,24,25,27}.

In the thermodynamic limit, the KT phase transition is marked by a change of correlation decay from exponential to power-law at the critical temperature. In the critical phase, correlations C_{ij} decrease with distance x_{ij} as $C_{ij} \propto x_{ij}^{-b}$ with an exponent b bounded above by the universal two-dimensional XY critical exponent²⁹ $\eta = 1/4$. At finite sizes, the transition is expected to be broadened, and the apparent transition point can be affected by boundary conditions. To probe the onset of critical behaviour we study correlations in the complex field ψ_j on the plaquettes of the largest lattice on 1,800 spins; correlation is measured

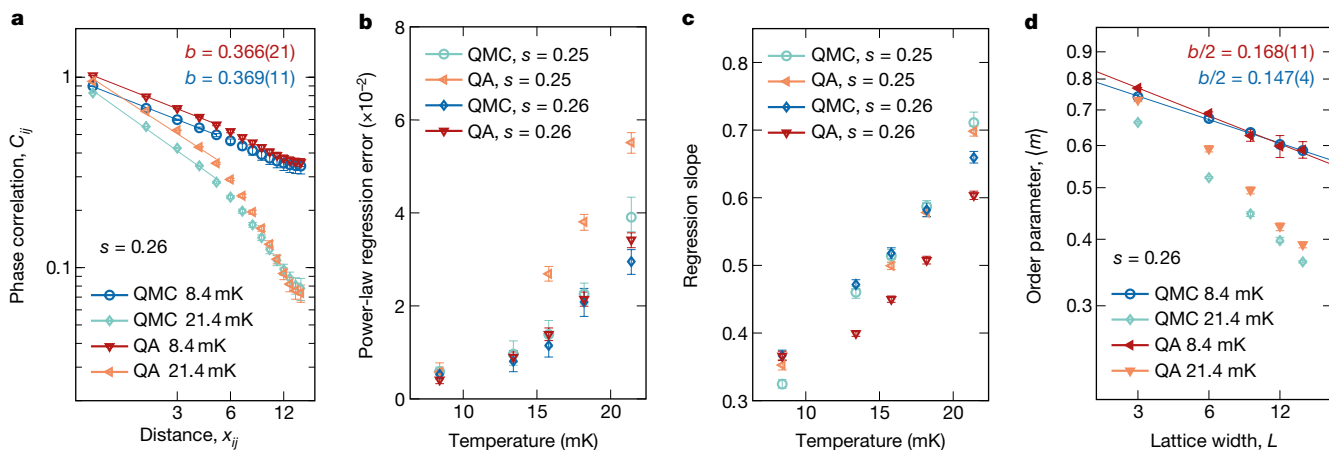


Fig. 4 | Power-law correlation decay near the KT crossover.

a, Correlations in the complex field ψ_j , calculated as $C_{ij} = \langle \text{Re}(\psi_i \psi_j^*) \rangle$ and measured between plaquettes along the periodic dimension far from the open boundary. Data for QMC and QA are shown near the critical temperature (8.4 mK) and above the critical temperature (21.4 mK). In the thermodynamic limit these correlations should decay with a power-law exponent close to $\eta = 1/4$ near the critical temperature. We perform power-law regression fitting on distances 1 to 5, where boundary effects are minimal. Although correlation scaling is asymptotically exponential

as $C_{ij} = \langle \text{Re}(\psi_i \psi_j^*) \rangle$ on plaquettes along the periodic dimension, half-way between the open boundaries.

Figure 4a shows C_{ij} as a function of distance for two temperatures at $s = 0.26$, with good agreement between QMC and QA. The absolute shift between QMC and QA correlations is explained by evolution during the quench (see Methods). As temperature decreases, correlations increase, approaching power-law decay: the quality of power-law fit on distances 1 to 5—where boundary effects are minimal—improves as temperature decreases. This is shown in Fig. 4b for $s = 0.25$ and 0.26, near the peak of $\langle m \rangle$ in s (Fig. 3b). The exponent b of this power-law regression decreases with temperature (Fig. 4c), reaching a minimum value of $b \approx 0.35$ for QA and $b \approx 0.32$ for QMC.

In the vicinity of the critical region, the same onset of power-law behaviour is expected for $\langle m \rangle$ as a function of size with a halved exponent; that is, $\langle m \rangle \propto L^{-b/2}$. This is shown in Fig. 4d, where QA shows agreement with QMC over a range of system sizes. Scaling exponents of $b \approx 0.34$ and $b \approx 0.29$ for QA and QMC, respectively, are close to the values extracted from phase correlations in Fig. 4c.

We have presented a large-scale quantum simulation of an exotic phase of matter. Our experimental results show clear signatures of topological phenomena: a complex order parameter with rotational symmetry that responds as expected to changes in Γ and T , and the onset of power-law scaling of correlations. Taken together, these constitute the experimental observation of topological order in a frustrated two-dimensional transverse-field Ising model, as theoretically predicted^{3,4} and simulated in QMC⁵. Agreement with QMC over a range of system sizes and Hamiltonian parameters—individually extracted with no fitting parameters—validates the flux qubit implementation of the transverse-field Ising model at large scales.

The reverse annealing technique used in this work promises to greatly expand the utility of quantum annealing processors. The ability of a QA processor to reverse anneal from an input state allowed us to validate convergence of our statistical estimators to a steady state, but its importance is far more general: quantum evolution of an input state is crucial to the implementation of hybrid quantum-classical algorithms³⁰. Quantum evolution Monte Carlo is perhaps the simplest such algorithm.

This programmable magnetic material has allowed us to study the many-body dynamics of matter that is time-consuming to simulate classically and difficult to implement physically. The methods used here can be applied to explore other exotic phases of matter in a variety

above the critical temperature, the short-range behaviour starts to show a crossover as the temperature is lowered; this is captured by the regression slope. **b**, As temperature is reduced, the root-mean-squared regression error drops, indicating the onset of power-law decay. **c**, In both QA and QMC, the regression slope moves towards the expected critical exponent $\eta = 1/4$ as temperature decreases. **d**, The decay of m versus L is expected to go from exponential in the paramagnetic phase to power-law with exponent $b/2$ near the KT crossover.

of lattices. Several future developments will improve our simulation approach. First, greater qubit connectivity will allow more flexibility in lattice geometry and realization of fully periodic boundary conditions. Second, faster projective readout will enable more accurate sampling from systems with fast dynamics, and any advances in noise and control error will improve the accuracy of these simulations. And finally, with the addition of non-stoquastic couplings^{31,32}, quantum annealing processors could foreseeably simulate systems of which classical simulations are intractable even at modest scale.

Online content

Any Methods, including any statements of data availability and Nature Research reporting summaries, along with any additional references and Source Data files, are available in the online version of the paper at <https://doi.org/10.1038/s41586-018-0410-x>.

Received: 16 February 2018; Accepted: 22 June 2018;

Published online 22 August 2018.

- Berezinskii, V. L. Destruction of long-range order in one-dimensional and two-dimensional systems having a continuous symmetry group II: quantum systems. *Sov. Phys. JETP* **34**, 610–616 (1972).
- Kosterlitz, J. M. & Thouless, D. J. Ordering, metastability and phase transitions in two-dimensional systems. *J. Phys. C* **6**, 1181–1203 (1973).
- Moessner, R., Sondhi, S. L. & Chandra, P. Two-dimensional periodic frustrated Ising models in a transverse field. *Phys. Rev. Lett.* **84**, 4457–4460 (2000).
- Moessner, R. & Sondhi, S. L. Ising models of quantum frustration. *Phys. Rev. B* **63**, 224401 (2001).
- Isakov, S. V. & Moessner, R. Interplay of quantum and thermal fluctuations in a frustrated magnet. *Phys. Rev. B* **68**, 104409 (2003).
- Feynman, R. P. Simulating physics with computers. *Int. J. Theor. Phys.* **21**, 467–488 (1982).
- Lloyd, S. Universal quantum simulators. *Science* **273**, 1073–1078 (1996).
- Gross, C. & Bloch, I. Quantum simulations with ultracold atoms in optical lattices. *Science* **357**, 995–1001 (2017).
- Paraoanu, G. S. Recent progress in quantum simulation using superconducting circuits. *J. Low Temp. Phys.* **175**, 633–654 (2014).
- Hazdibaric, Z., Kriger, P., Cheneau, M., Battelier, B. & Dalibard, J. Berezinskii–Kosterlitz–Thouless crossover in a trapped atomic gas. *Nature* **441**, 1118–1121 (2006).
- Zhang, J. et al. Observation of a many-body dynamical phase transition with a 53-qubit quantum simulator. *Nature* **551**, 601–604 (2017).
- Henggels, T. et al. Quantum simulation of a Fermi–Hubbard model using a semiconductor quantum dot array. *Nature* **548**, 70–73 (2017).
- Georgescu, I. M., Ashhab, S. & Nori, F. Quantum simulation. *Rev. Mod. Phys.* **86**, 153–185 (2014).
- Mohseni, M. et al. Commercialize quantum technologies in five years. *Nature* **543**, 171–175 (2017).

15. Preskill, J. Quantum Computing in the NISQ era and beyond. Preprint at <https://arxiv.org/abs/1801.00862> (2018).
16. Johnson, M. W. et al. Quantum annealing with manufactured spins. *Nature* **473**, 194–198 (2011).
17. Harris, R. et al. Experimental investigation of an eight-qubit unit cell in a superconducting optimization processor. *Phys. Rev. B* **82**, 024511 (2010).
18. Bunyk, P. I. et al. Architectural considerations in the design of a superconducting quantum annealing processor. *IEEE Trans. Appl. Supercond.* **24**, 1–10 (2014).
19. Mott, A., Job, J., Vlimant, J.-r., Lidar, D. & Spiropulu, M. Solving a Higgs optimization problem with quantum annealing for machine learning. *Nature* **550**, 375–379 (2017).
20. Amin, M. H., Andriyash, E., Rolfe, J., Kulchytskyy, B. & Melko, R. Quantum Boltzmann machine. *Phys. Rev. X* **8**, 021050 (2018).
21. Moessner, R. & Ramirez, A. P. Geometrical frustration. *Phys. Today* **59**, 24–29 (2006).
22. Kosterlitz, J. M. & Thouless, D. J. Early work on defect driven phase transitions. *Int. J. Mod. Phys. B* **30**, 1630018 (2016).
23. Han, Z. et al. Collapse of superconductivity in a hybrid tin-graphene Josephson junction array. *Nat. Phys.* **10**, 380–386 (2014).
24. Jiang, Y. & Ernig, T. Ordering of geometrically frustrated classical and quantum triangular Ising magnets. *Phys. Rev. B* **73**, 104452 (2006).
25. Wang, Y.-C., Qi, Y., Chen, S. & Meng, Z. Y. Caution on emergent continuous symmetry: a Monte Carlo investigation of the transverse-field frustrated Ising model on the triangular and honeycomb lattices. *Phys. Rev. B* **96**, 115160 (2017).
26. Blankschtein, D., Ma, M., Berker, A. N., Grest, G. S. & Soukoulis, C. M. Orderings of a stacked frustrated triangular system in three dimensions. *Phys. Rev. B* **29**, 5250–5252 (1984).
27. José, J. V., Kadanoff, L. P., Kirkpatrick, S. & Nelson, D. R. Renormalization, vortices, and symmetry-breaking perturbations in the two-dimensional planar model. *Phys. Rev. B* **16**, 1217–1241 (1977).
28. Lanting, T., King, A. D., Evert, B. & Hoskinson, E. Experimental demonstration of perturbative anticrossing mitigation using nonuniform driver Hamiltonians. *Phys. Rev. A* **96**, 042322 (2017).
29. Herbut, I. *A Modern Approach to Critical Phenomena* (Cambridge Univ. Press, Cambridge, 2007).
30. Chancellor, N. Modernizing quantum annealing using local searches. *New J. Phys.* **19**, 023024 (2017).
31. Babbush, R., Love, P. J. & Aspuru-Guzik, A. Adiabatic quantum simulation of quantum chemistry. *Sci. Rep.* **4**, 6603 (2014).
32. Nishimori, H. & Takada, K. Exponential enhancement of the efficiency of quantum annealing by non-stochastic Hamiltonians. *Front. ICT* **4**, 1–11 (2017).

Acknowledgements We thank I. Affleck, S. Boixo, E. Farhi, M. Franz, I. Herbut, S. Isakov, S. Lloyd, R. Melko, M. Mohseni, H. Neven and Y. Wan for discussions. We are grateful to the research, engineering and operations staff at D-Wave Systems for directly and indirectly supporting this research.

Reviewer information *Nature* thanks A. Kerman, M. Troyer and the other anonymous reviewer(s) for their contribution to the peer review of this work.

Author contributions A.D.K., J.C., J.R., I.O., E.A. and M.H.A. conceived and designed the experiment. J.R., E.A., I.O. and A.D.K. conducted classical simulations. A.D.K. and I.O. conducted the main QA experiments. A.B. and M.R. calibrated the QA processor. T.L., R.H., K.B., A.F., G.P.-L., A.Y.S., K.B. and A.F. conducted supporting experiments and theoretical analysis. A.B., M.R., T.L., R.H., C.R., F.A., P.I.B., T.O., J.Y., C.E., N.L., J.W., L.J.S., E.H., Y.S., M.H.V., E.L., M.W.J. and J.H. designed, developed and fabricated the QA apparatus. M.H.A., A.D.K., J.C., J.R., I.O., E.A., T.L., R.H. and A.Y.S. contributed to writing the manuscript.

Competing interests All authors are current or recent employees of D-Wave Systems Inc.

Additional information

Extended data is available for this paper at <https://doi.org/10.1038/s41586-018-0410-x>.

Reprints and permissions information is available at <http://www.nature.com/reprints>.

Correspondence and requests for materials should be addressed to A.D.K.

Publisher's note: Springer Nature remains neutral with regard to jurisdictional claims in published maps and institutional affiliations.

METHODS

Pseudospin phase and topological features in the TFIM. In the TFIM, the triangular AFM lattice and fully frustrated square-octagonal lattice admit an approximate mapping to the two-dimensional XY model that is essential to the topological phenomena we observe. Here we provide a description of this mapping, which has its origins in the study of the stacked magnet²⁶ and has since been described in the quantum case^{3–5,24,25}. We begin with a description of the XY model and the upper KT phase transition intersected by the QA schedule.

The two-dimensional XY model describes an interaction of classical spins. Each spin is a unit vector described by an angle θ_i . The interaction between spins is given by the XY Hamiltonian

$$H = -J_{XY} \sum_{\langle i,j \rangle} \cos(\theta_i - \theta_j) \quad (1)$$

where the sum is taken over all coupled pairs of spins. The ground state of this system is one in which all spins are aligned (see Extended Data Fig. 1); note that the system described by equation (1) has continuous O(2) or U(1) symmetry.

In a ground state, the angle θ does not change as we traverse a closed path in the plane in a clockwise direction. Given a perturbation of a ground state, θ may fluctuate along this path but will not wind in a full rotation. A clockwise or anticlockwise winding is known as a vortex or an antivortex, respectively; these topological defects imply an excitation that diverges with the radius R of the encircling path:

$$E_{\text{vortex}} = \pi J_{XY} \log \frac{R}{r} \quad (2)$$

where r is the lattice spacing. The entropy S_{vortex} also grows proportionally to $\log(R/r)$ since there are $(R/r)^2$ possible locations of the vortex in an area of R^2 . A competition of these two terms leads to a sign-variable expression for the free energy contribution of a vortex:

$$\Delta F = E_{\text{vortex}} - TS_{\text{vortex}} = (\pi J_{XY} - 2k_B T) \log \frac{R}{r} \quad (3)$$

The critical vortex unbinding temperature T_2 at which the KT phase transition occurs is given by the sign change of ΔF :

$$T_2 = \frac{\pi}{2k_B} J_{XY}$$

Above this temperature, the free energy favours isolated vortices; below this temperature vortices and antivortices are attracted to one another and appear in bound pairs.

The mapping from the TFIM to the XY model arises from the interaction of frustration and quantum fluctuations. We first consider the effect of a perturbative transverse field on a single AFM triangle. In the classical case, the AFM triangle has six ground states. In each, one of two floppy spins can be flipped without changing the energy. Extended Data Fig. 2 shows two such states differing by a flip of spin 1. The addition of a perturbative transverse field Γ lifts this degeneracy, allowing a superposition of these two states in which spin 1 aligns with the transverse field. We denote this superposition by $|-\rangle = (|\uparrow\rangle + |\downarrow\rangle)/\sqrt{2}$ and note that this lowers the energy from $-J$ to $-J - \Gamma$.

To first-order perturbation, this quantum ground state is six-fold degenerate, with the three spins taking values $|\uparrow\rangle, |\downarrow\rangle, |-\rangle$ in any permutation. We map these six states to the complex plaquette pseudospins ψ_j as described by equation (2): $\psi_j = \langle \sigma_1^z \rangle + \langle \sigma_2^z \rangle e^{2\pi i/3} + \langle \sigma_3^z \rangle e^{4\pi i/3}$. This is shown in Extended Data Fig. 3 for the state $|-\uparrow\downarrow\rangle$. Pseudospins for six quantum and six classical states are shown in Extended Data Fig. 3d. Also shown are the classical excited states $|\uparrow\uparrow\uparrow\rangle$ and $|\downarrow\downarrow\downarrow\rangle$, which have $\psi_j = 0$. As vanishing points of the pseudospin phase, these magnetized triangles correspond to vortices and antivortices in the lattice.

As shown in Fig. 1d, the triangular AFM lattice can be tiled with a single clock state, resulting in a pseudospin that is constant across the lattice. This tiling naturally divides the sites of the lattice into three sublattices, which we use to determine the complex order parameter ψ as in equation (3). The introduction of a twist in the pseudospin phase, as shown in Fig. 1e, leads to a state where two of the triangles contain no spin aligned with the transverse field. This excitation can be described in terms of an effective XY model on the dual lattice, with effective XY coupling proportional to Γ . This is consistent with the linear scaling of T_2 in Γ seen in the small- Γ limit³³. The corresponding phase boundary in the square-octagonal lattice, which is defined by the energy splitting of four-qubit chains, has a quartic form as presented with the details of the phase diagram below. To compute the pseudospin of a plaque in the square-octagonal phase we use all 12 spins in the three FM-coupled chains intersecting the plaque, whether it is a square or an octagon.

The pseudospin emerges from the six perturbative ground states of an AFM triangle, and thus the XY pseudospin at low temperatures is related not to the U(1)-symmetric XY model, but to the six-state clock model with \mathbb{Z}_6 symmetry.

In the six-state clock model studied by Jose et al.²⁷, there are three phases: as temperature drops from the paramagnetic phase, we first see the vortex unbinding KT transition described above. Then, at even lower temperature, the system enters an ordered phase where the complex order parameter concentrates around one of the six clock states. Throughout the critical phase between the paramagnetic and ordered phases, U(1) symmetry is observed because the symmetry-breaking term does not become relevant until the lower transition^{4,27}. The same three phases are seen in the triangular⁴ and square-octagonal lattices in the TFIM (we map out the phase diagram later in the Methods section). Thus at the regions of the $(T/J, \Gamma/J)$ plane probed by QA experiments, the observation of U(1) symmetry is consistent with both QMC simulations and theory.

The effective pseudospin XY model is derived from the perturbative limit $T \approx 0, \Gamma \rightarrow 0$, and only serves to provide the universal properties in the large-system limit. So while it is an effective means of understanding the KT transition in the triangular and square-octagonal lattices, it cannot provide the non-universal details of the TFIM outside the perturbative regime, and even at intermediate system sizes its universal properties deviate noticeably from expected values⁵.

Quantum processor and experimental methods. The quantum annealing processor used in this work is a D-Wave 2000Q system operated in a non-annealing mode. Operating temperatures ranging between 8.4 ± 0.2 mK and 21.4 ± 0.2 mK are measured with a cryostat thermometer and independently verified using single-qubit susceptibility measurements.

We focus on the region of the annealing schedule between $s=0.20$ and $s=0.30$ (Extended Data Fig. 4a). In quantum annealing, the annealing parameter s is typically increased smoothly from 0 to 1, bringing the system from a single-well superposition at $s=0$ to a low-temperature classical system at $s=1$ (Extended Data Fig. 4b). In our experiments we take a different approach, using the reverse-annealing protocol described in section III.D of Lanting et al.²⁸. In this protocol we initialize the system at $s=1$ with a classical state loaded into the qubits. We then reduce s quickly, bringing the system to the quantum model we want to simulate. We let this model relax for a fixed evolution time, 65 ms except in the relaxation timing experiments (see Methods section ‘Non-equilibrium dynamics of QA and QMC’), before quickly quenching s to 1 (Extended Data Fig. 4c). The evolution time of 65 ms was chosen to be roughly as long as possible within the constraints of the control electronics, to ensure that the operating temperature is as low as possible.

Each call to the processor consists of 50 reverse anneals for all data in the main text, and between 50 and 200 reverse anneals in the relaxation timing experiments. In the relaxation timing experiments the same initial state is used for every reverse anneal. In all other runs, a single initial state (clock or random) is loaded for the first anneal, and each subsequent anneal is initialized with the final state of the previous anneal. This allows us to perform quantum evolution Monte Carlo to estimate the equilibrium statistics of the target system. From each processor call, we discard the first 25 of 50 samples as described in the main text. Data shown in the main text represent 480 processor calls (with the exception of Fig. 3c, which represents 720 processor calls) divided equally between clock initial state and random initial state, each of which is further divided equally between two physical embeddings of the lattice.

In the Monte Carlo runs, a single initial state (clock or random) is loaded for the first anneal, and each subsequent anneal is initialized with the final state of the previous anneal (Extended Data Fig. 4c). This allows us to perform quantum evolution Monte Carlo to estimate equilibrium statistics of the target system. From each processor call, we discard the first 25 of 50 samples as described in the main text. Data for additional temperatures and values of s are shown in Extended Data Fig. 5. **Compensation of qubit nonidealities.** When Γ is small, the radio-frequency SQUID flux qubits faithfully model two-level Ising spins. Since our experiments are performed in a region of the schedule where Γ is large, behaviour deviates from a two-level Ising system. To mitigate this nonideality we make two adjustments.

The first adjustment is a compensation of transverse and coupling energy scales, which are given to high accuracy using eight energy levels per SQUID instead of the two levels of an ideal Ising spin¹⁷. Since order in the square-octagonal lattice arises via tunnelling of 4-qubit FM chains, our approach is to determine a compensation $f(s)$ such that a chain of four FM-coupled 8-level SQUIDS at s has the same first eigengap $E_1 - E_0$ as a chain of four FM-coupled 2-level SQUIDS at $f(s)$. These gaps are shown in Extended Data Fig. 4d, and the compensation is shown in Extended Data Fig. 4e. To confirm that this shift in s makes sense as a compensation approach, we probe the spectra more generally by adding a bias on the first SQUID of the chain and examining the first three eigengaps in Extended Data Fig. 4f. The compensation approach is validated by the agreement of the first eigengap across a range of biases and s values. Higher energy levels, which show more deviation, are less important.

The second adjustment is a compensation of effective next-nearest-neighbour couplings. Beyond the issue of energy scales just addressed, the radio-frequency SQUID flux qubits in the QA processor provide an imperfect implementation of

Ising spins early in the anneal. The primary deviation is that every qubit mediates a coupling between any two of its neighbouring qubits. This introduces next-nearest-neighbour couplings, meaning that for any spins i, j, k , there is an effective coupling term $\chi_b J_{ij} J_{jk}$ added to J_{ik} ; the strength is denoted χ_b , representing normalized background susceptibility: $\chi_b = M_{\text{AFM}} \chi_q$ where M_{AFM} is the maximum available AFM mutual inductance and χ_q is the physical qubit susceptibility. The value of χ_b varies from -0.07 ± 0.02 early in the anneal to -0.03 ± 0.01 late in the anneal where single-spin dynamics freeze out, as measured by independent experiments.

In the QA experiments, we compensate for χ_b based on the fact that FM couplers are most often unfrustrated in the systems studied. We consider the application of next-nearest-neighbour terms as a function f applied to the coupling Hamiltonian J_{QA} supplied to the processor, and seek a choice of J_{QA} such that $f(J_{\text{QA}})$ approximates αJ for some constant $\alpha > 0$. This gives us the following constraints on the classical Hamiltonians:

(1) Any two chains have the same total coupling between them in $f(J_{\text{QA}})$ and αJ . In the absence of boundary conditions, this coupling is αJ .

(2) If a chain has a single break (domain wall), the total strength of frustrated couplers is the same in $f(J_{\text{QA}})$ and αJ . In the absence of boundary conditions, this coupling is $-1.8\alpha J$.

We use an iterative method to determine J_{QA} given an average AFM coupling strength ρ ; it follows that α is a function of ρ and χ_b (in turn, χ_b is a function of s). For $\rho = 0.95$ the value of α ranges monotonically from 1.27 at $s = 0.20$ to 1.13 at $s = 0.30$.

Embedding the square-octagonal lattice. The cylindrical topology of the square-octagonal lattice is realized as two square sheets coupled together at the top and bottom (Extended Data Fig. 6). In the processor used, the graph of available couplings is a 16×16 grid of eight-qubit complete bipartite ‘Chimera’ unit cells¹⁸; only a 7×7 block of cells is shown in Extended Data Fig. 6b. Each FM-coupled chain of four qubits consists of two qubits in one unit cell, and one qubit in each of two other unit cells. If the size of the unit cell were doubled, it would be possible to embed a toroidal square-octagonal lattice with fully periodic boundary conditions. The halving of the antiferromagnetic couplers on the open boundaries of the cylinder ensures that the classical ground-state space is highly degenerate and includes the ordered clock states (Extended Data Fig. 8a) as well as striped states (Extended Data Fig. 8b) in each orientation.

Calibration refinement. The QA processor was calibrated as a general-purpose quantum annealer, with the goal of good performance across a variety of inputs. Given our focus on one particular input type, we can improve performance by exploiting structure and symmetries in the input. After compensating for background susceptibility as described above, we exploit symmetries in the lattice.

The first symmetry is spin-flip invariance: since there is no longitudinal field h , the expected magnetization of each spin in the absence of systematic biases should be zero. To maintain this degeneracy we apply flux-offset biases to qubits in a gradient descent method, greatly improving the distribution of qubit magnetizations (Extended Data Fig. 7a). The required offset is a function of annealing schedule, so we maintain an independent compensation for each schedule based on forward-annealing results.

The second symmetry is rotational symmetry about the periodic dimension. For lattice width L (with $4L \cdot 2L$ spins), each coupler is in an equivalence class of $2L$ rotationally equivalent couplers that should be frustrated equiprobably. More generally, two couplers should have the same statistics if there is a graph automorphism over the lattice that maps one to the other. We make fine adjustments to individual coupling terms to tighten the frustration distributions of these equivalence sets (Extended Data Fig. 7b).

There are no further trivial symmetries in the square-octagonal lattice; both the triangular lattice with semi-open boundary and the square-octagonal lattice with fully periodic boundary have richer automorphism groups that might be exploited in future research. The symmetries that we use for calibration refinement apply at every point in the phase diagram, so the calibration refinement used here does not result in overfitting.

Spin-bath polarization. The persistent current flowing in the qubit bodies during the QA protocol produces a magnetic field that can partially align or polarize the spin environment. For long evolution times, the polarized environment can produce sample-to-sample correlations, biasing the QA towards previously achieved spin configurations. To reduce sample-to-sample correlations, we introduce a pause of 10 ms between anneals to give the spin-bath time to depolarize. However, in the reverse annealing protocol we start in a polarized state, and the QA system will be biased towards the initial state by polarization in the spin-bath. This leads to the small systematic difference in estimators of $\langle m \rangle$ using a clock initial state versus a random initial state. This effect is particularly relevant to the benchmarking experiments, where we measure evolution time to escape from an initial state.

Classical Monte Carlo methods. Quantum Monte Carlo is a classical method for estimating the equilibrium statistics of a quantum system. For all QMC experiments in this work we use continuous-time path-integral Monte Carlo³⁴ with

Swendsen–Wang³⁵ updates. For a given spin system, a model is parameterized by T and Γ , where $J=1$.

For the benchmarking experiments summarized in Extended Data Fig. 8, a single model was initialized with a classical ground state with no interfaces in imaginary time. In other words, each Trotter slice initially contains the same classical ground state. This is analogous to the QA setup wherein a classical state is loaded into the processor. The static model (T, T) is then evolved for some number of Monte Carlo sweeps, up to 2^{18} .

For the experiments in which we want equilibrium estimates of a model, we employ parallel tempering using a series of models that vary in T , with either Γ or Γ/T fixed. We also employ a specialized chain update, in which every other Monte Carlo sweep attempts flipping of all spins in a four-qubit FM-coupled chain, rather than one spin at a time. We find that this speeds up convergence by up to three orders of magnitude.

Convergence for a set of Hamiltonians is determined via standard error on $\langle m^2 \rangle$ and convergence of absolute sublattice magnetizations to at most 0.04 from a fully magnetized clock initial state (Extended Data Fig. 8a), which is then checked for consistency with the same experiment given a random initial state. Convergence of the Binder cumulant and moments of the order parameter are tested with respect to initialization in several different types of classical ground state. Error is determined self-consistently between independent runs; error bars on QMC results are 95% bootstrap confidence intervals. Pseudospin correlations are computed from 5120 classical states projected from QMC in ten independent runs. Experimental lengths are up to 2^{22} Monte Carlo sweeps.

Non-equilibrium dynamics of QA and QMC. We now turn our attention to the non-equilibrium dynamics of the system in relation to its QMC counterpart: continuous-time path-integral Monte Carlo with imaginary-time cluster updates described above. We measure evolution timescales by initializing each system in two classical ground states. The first is a clock state (Extended Data Fig. 8a) in which the scalar field ψ is uniform and $m = 2/\sqrt{3}$; the second is a striped state (Extended Data Fig. 8b) in which ψ is staggered and $m = 0$. As evolution time of QA and QMC is increased, the expectation of m at the end of a single evolution converges in expectation towards a single value regardless of initial condition (Extended Data Fig. 8c).

We compare the evolution time required by QA and QMC to bring the clock-initialization and striped-initialization estimates of m to within 0.3 of each other (Extended Data Fig. 8d). Both QA and QMC become slower as s increases, as quantum and thermal fluctuations are reduced. The scaling of evolution time in s is far steeper for QMC than for QA, indicating that in this case QMC provides accurate equilibrium statistics of the quantum statistics, but does not simulate the dynamics³⁶. To reduce these onerous QMC timescales we employed parallel tempering and developed a lattice-specific cluster update method (not used in Extended Data Fig. 8)—a future study will analyse the impact of these and other advanced methods.

Phase diagram of square-octagonal lattice. Here we provide evidence for the claimed phase diagram of the square-octagonal lattice. We show critical behaviour and give estimates of the upper and lower critical temperatures bounding the critical KT region in the phase diagram of the square-octagonal lattice, and give an estimate of the quantum critical point at $T = 0$. We follow the methods used by Isakov and Moessner⁵ on the triangular lattice. We study $L \times L$ lattices (on $4L^2$ spins) with fully periodic (toroidal) boundary conditions with L ranging from 3 to 21. Our results are presented in Extended Data Fig. 9.

For a range of transverse fields we use two methods to determine the lower (T_1) and upper (T_2) critical temperatures using properties of the two-dimensional XY universality class.

First, we use the expected power-law decay of correlations—and consequently m —as system size increases. Within the critical region and for fixed Γ , m_L is expected to scale as $L^{-\eta/2}$, with critical exponents $\eta_1 = 1/9$ and $\eta_2 = 1/4$. From this we determine T_1 and T_2 using a power-law fit on values of L between 6 and 21 (Extended Data Fig. 9).

Second, we additionally determine T_1 and T_2 by fitting our data to universal scaling curves. For the lower transition, we have

$$m_L L^b = m_0 (L^{-1} e^{at^{-1/2}})$$

where m_0 is a universal function, a is a non-universal constant, and $t = (T_1 - T)/T_1$ is the residual temperature approaching T_1 from below. For the lower transition, we have

$$\chi_L L^{-c} = \chi_0 (L^{-1} e^{at^{-1/2}})$$

where χ_0 is a universal function, a is a non-universal constant, and $t = (T - T_2)/T_2$ is the residual temperature approaching T_2 from above. We expect from universality that in these fits, $b \approx (1/9)/2$ and $c \approx 7/4$.

For the upper transition, we obtain good collapses for Γ between 0.7 and 1.3. These values are in fairly good agreement with values of T_1 determined from η , as in the triangular lattice⁵. For the lower transition, fitting is generally poor and we obtain only a reasonably convincing collapse for $\Gamma \in [1.1, 1.2]$ by discarding data for $L < 15$. Values of T_1 deviate noticeably from those given by η . A study of larger instances would clarify the picture.

Again extending from the triangular lattice, we anticipate a quantum phase transition consistent with the three-dimensional XY universality class^{5,25,26} with dynamical exponent $z=1$ and universal exponent $\nu=2/3$. To estimate the quantum critical point, we measure the normalized Binder cumulant

$$U = 2 \left(1 - \frac{\langle m^4 \rangle}{2 \langle m^2 \rangle^2} \right)$$

We do so for system sizes up to $L=15$ using inverse temperature $\beta(L, \Gamma) = 3.5L^z/\Gamma$. The Binder cumulant U crosses near a critical point $\Gamma_c \approx 1.76$. Scaling of U in the vicinity of the quantum critical point collapses as $U_L = L^{1/\nu}(\Gamma - \Gamma_c)/\Gamma_c$ using $\nu=2/3$. The dynamical exponent $z=1$ was verified by fitting the peak susceptibility as a function³⁷ of L .

The mapping between the square-octagonal model and the six-state XY model in the perturbative limit $\Gamma \rightarrow 0$ admits an effective XY coupling proportional to the tunnelling energy of a four-qubit FM chain; this will have a fourth-order polynomial form in Γ (Extended Data Fig. 9f).

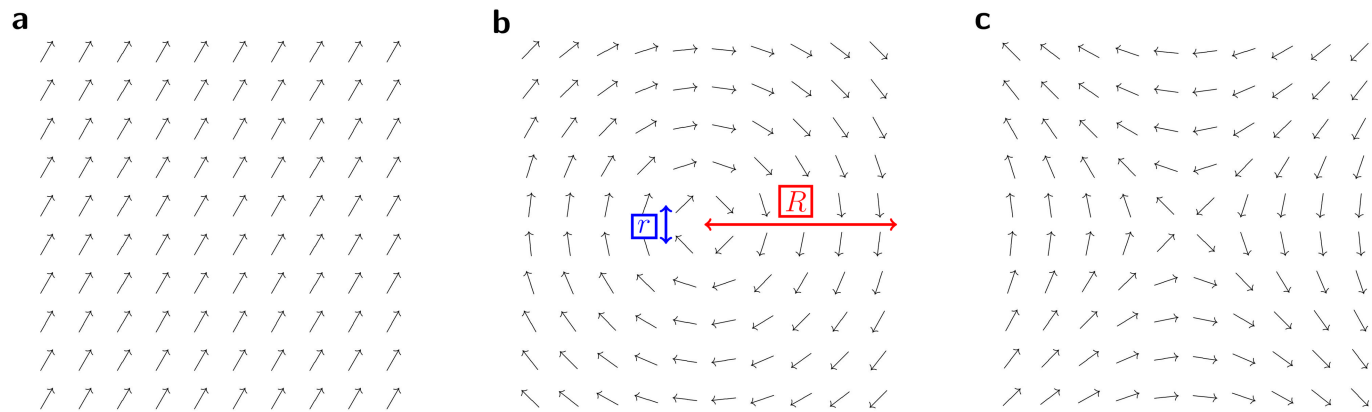
Effect of quench. The QA simulation generally shows good agreement with QMC in estimates of $\langle m \rangle$, consistent with the formation and annihilation of vortex–antivortex pairs. However, these excitations appear far less often in QA output states than in projected QMC states. Here we show that this can be explained by evolution during the 1-μs QA quench. As quantum and thermal fluctuations are reduced, tightly bound vortex–antivortex pairs are annihilated. Extended Data Fig. 10

compares the mean residual classical energy per spin of QA and QMC. QMC projected states have many more excitations than QA states. We model a local classical quench in QMC output by repairing classical excitations at the single-qubit level and four-qubit chain level. After this classical quench is applied to QMC output, residual energies of QMC states resemble those of QA states. Effect on ψ is minimal. This is consistent with the hypothesis that similar annihilation of defects occurs during the QA quench. We therefore expect that faster QA quench should lead to a greater population of classical excitations—vortices and antivortices—in QA output.

Statistical methods. All error bars show 95% bootstrap confidence intervals over 1,000 bootstrap samples. For QA results in Figs. 3b and 4, independent confidence intervals are generated for the Monte Carlo estimators with ordered initial state and random initial state, and the union of these intervals is shown. For every data point analysed in Fig. 3c we also show the equivalent data points under reversal of all spins and/or rotation (but not flipping) of the cylinder. Thus we show 27,000 effective samples for QA and 30,720 effective samples for QMC.

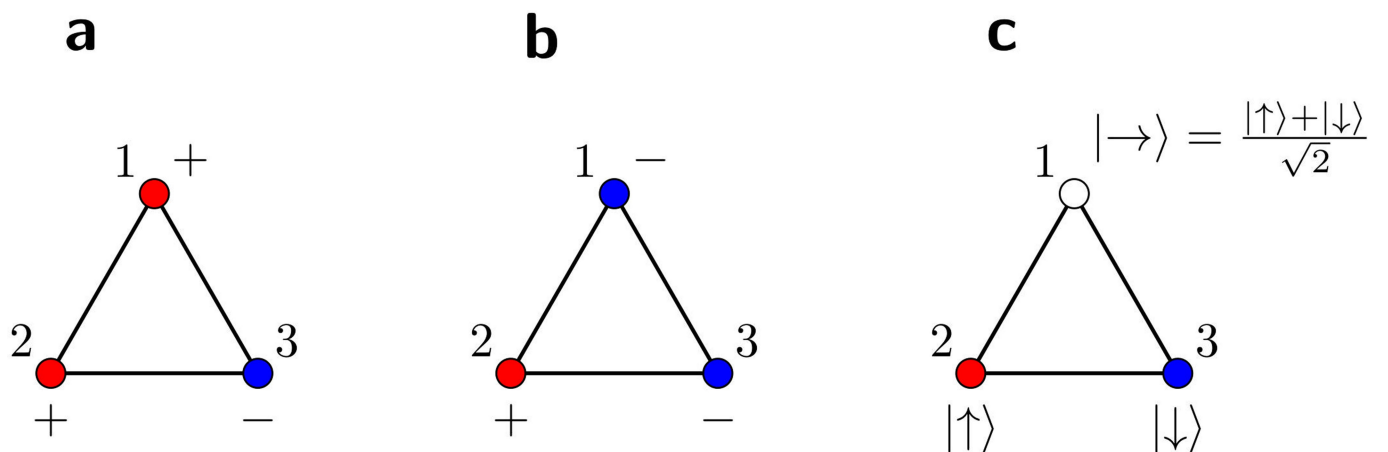
Data availability. The datasets generated and analysed during this study are available from the corresponding author on reasonable request.

33. Korshunov, S. E. Finite-temperature phase transitions in the quantum fully frustrated transverse-field Ising models. *Phys. Rev. B* **86**, 014429 (2012).
34. Rieger, H. & Kawashima, N. Application of a continuous time cluster algorithm to the two-dimensional random quantum Ising ferromagnet. *Eur. Phys. J. B* **9**, 233–236 (1999).
35. Swendsen, R. H. & Wang, J.-S. Replica Monte Carlo simulation of spin-glasses. *Phys. Rev. Lett.* **57**, 2607–2609 (1986).
36. Andriyash, E. & Armin, M. H. Can quantum Monte Carlo simulate quantum annealing? Preprint at <https://arxiv.org/abs/1703.09277> (2017).
37. Guo, M., Bhatt, R. N. & Huse, D. A. Quantum critical behavior of a three-dimensional Ising spin glass in a transverse magnetic field. *Phys. Rev. Lett.* **72**, 4137–4140 (1994).



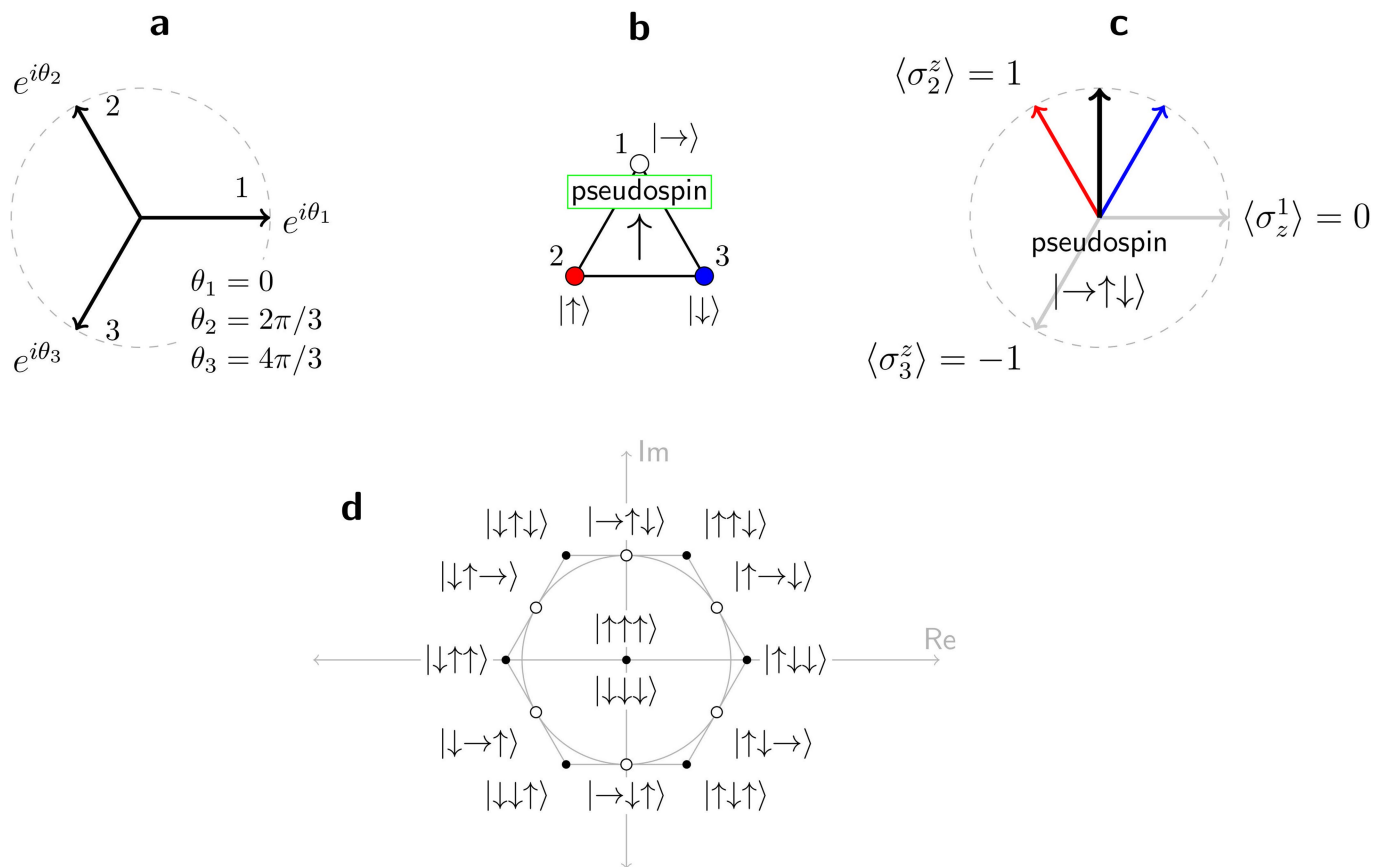
Extended Data Fig. 1 | Topological features in the two-dimensional XY model. **a**, The ground state, in which all rotors have equal angle θ , has continuous U(1) symmetry, as a universal rotation of θ will not change the energy of the system. **b**, **c**, A vortex or antivortex (**b** and **c**, respectively) is a point around which the angle winds (rotates completely) clockwise or

anticlockwise, respectively, when traversing a closed loop around the point in a clockwise direction. Both the energy and the entropy of an isolated vortex or antivortex region of radius R are proportional to $\log(R/r)$, where r is the lattice spacing.


Extended Data Fig. 2 | Floppy spin aligns with the transverse field.

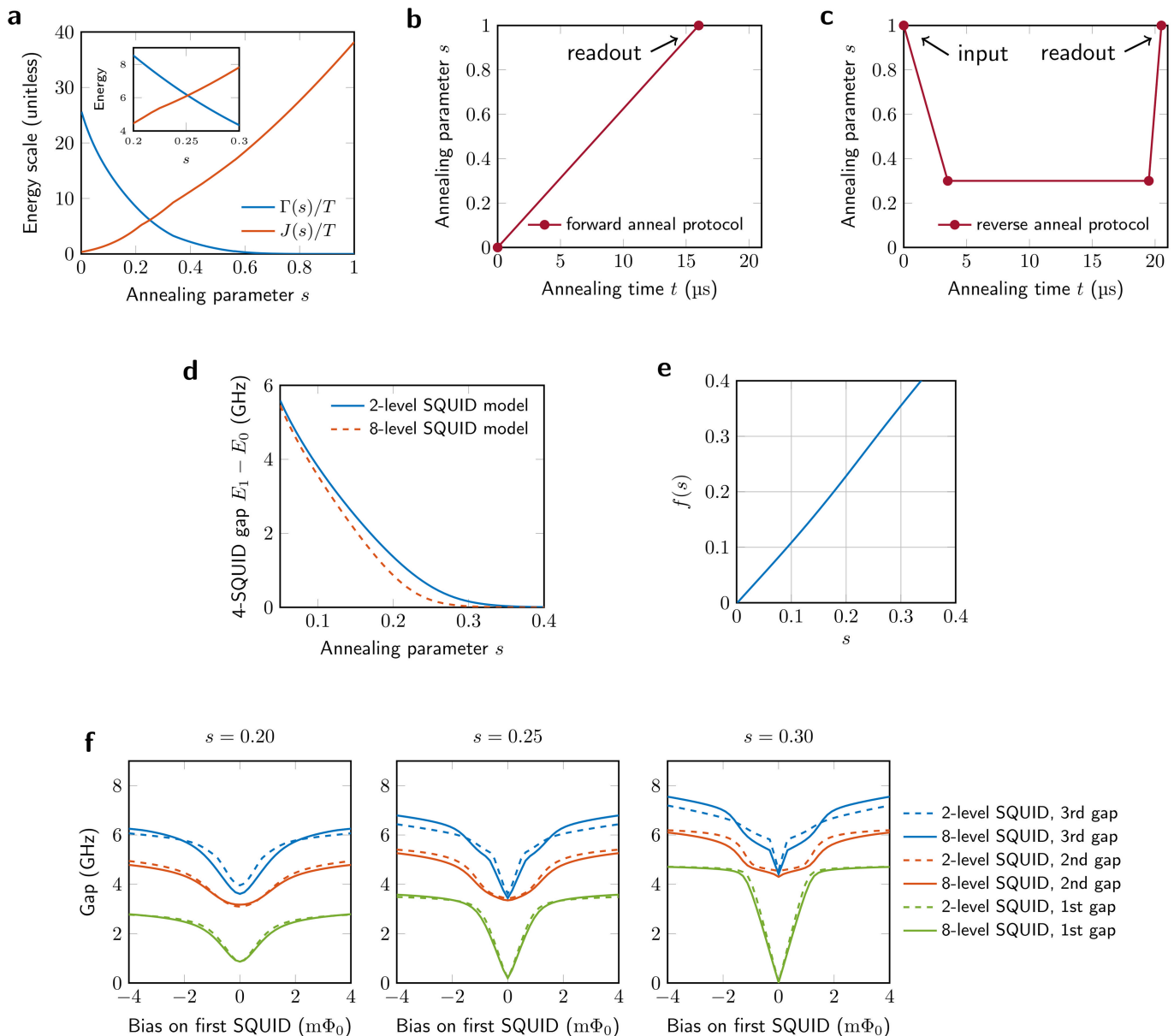
a, b, Two of six degenerate classical ground states differ by a flip of spin 1.
c, With the addition of a perturbative transverse field Γ , spin 1 aligns with

the transverse field in a symmetric superposition $|\rightarrow\rangle = (|\uparrow\rangle + |\downarrow\rangle)/\sqrt{2}$, reducing the energy from $-J$ to $-J - \Gamma$. Red and blue represent spin-up and spin-down, respectively.


Extended Data Fig. 3 | Pseudospins from classical and quantum states.

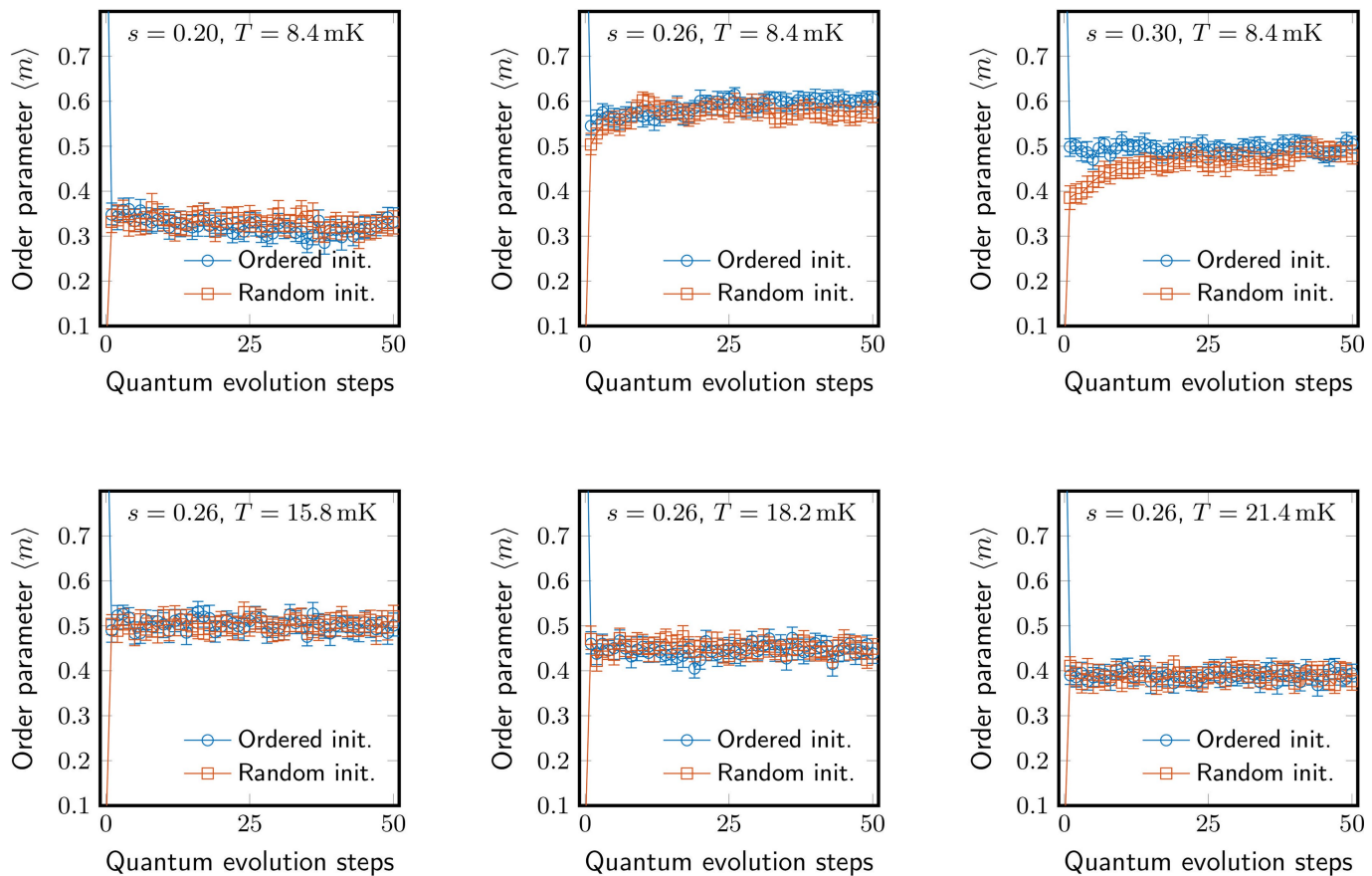
a, Each pseudospin ψ_j is determined as a linear combination of basis vectors with weights given by σ^z operators. **b, c**, the pseudospin of the clock state $|\rightarrow\uparrow\downarrow\rangle$ is $e^{i\pi/2}$. **d**, The six-fold-degenerate perturbative quantum ground states (white, with magnitude 1) and six-fold-degenerate

classical ground states (black, with magnitude $2/\sqrt{3}$) admit twelve ‘clock’ pseudospins in the complex plane. Also shown are the classical excited states $|\uparrow\uparrow\uparrow\rangle$ and $|\downarrow\downarrow\downarrow\rangle$, which have pseudospin 0 and therefore correspond to a vortex or antivortex.



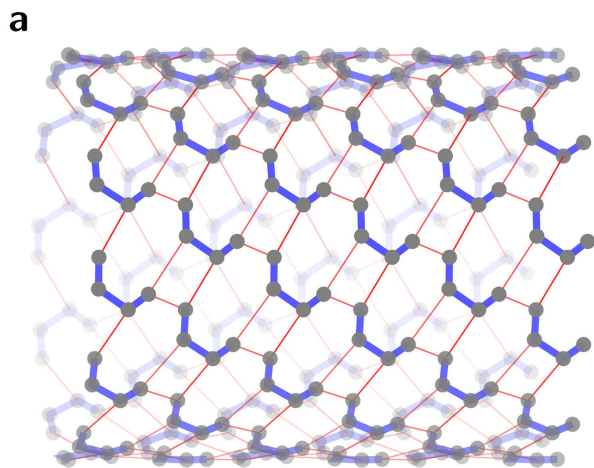
Extended Data Fig. 4 | Annealing schedule and protocols. **a**, Unitless energy scales for transverse field Γ and Ising couplings J as a function of annealing parameter s , compared with temperature $T = 8.4$ mK (the inset is a detail of the region studied: $0.2 \leq s \leq 0.3$). **b**, Standard 16- μs forward anneal protocol given as $s(t)$, which increases linearly from 0 to 1. **c**, 16- μs evolution in a reverse annealing protocol, where s drops from 1 to $s = 0.3$ over 3.5 μs , dwells at s for 16 μs , and quenches to 1 over 1 μs . Experiments, with the exception of relaxation time measurements, are performed with 2¹⁶ μs (65 ms) dwells at target model s . **d**, The first eigengap $E_1 - E_0$ for a chain of four FM-coupled SQUIDs given by a physically realistic 8-level

SQUID model deviates from the gap given by the desired 2-level SQUID model of Ising spins. **e**, To compensate for this deviation, we determine a nonlinear shift in s so that the gap of the chain of 8-level SQUIDS at s matches the gap of the chain of 2-level SQUIDs at $f(s)$. This shift in s is roughly 0.03 to 0.05 in the region of interest, and is reflected in the effective schedule (a). **f**, To evaluate this compensation more generally, we place a flux bias on the first device of the chain and compare the eigenspectra of the 8-level SQUID model at s with the compensated 2-level SQUID model at $f(s)$, for three values of s . Agreement in the first eigengap is good across a range of biases and s values.

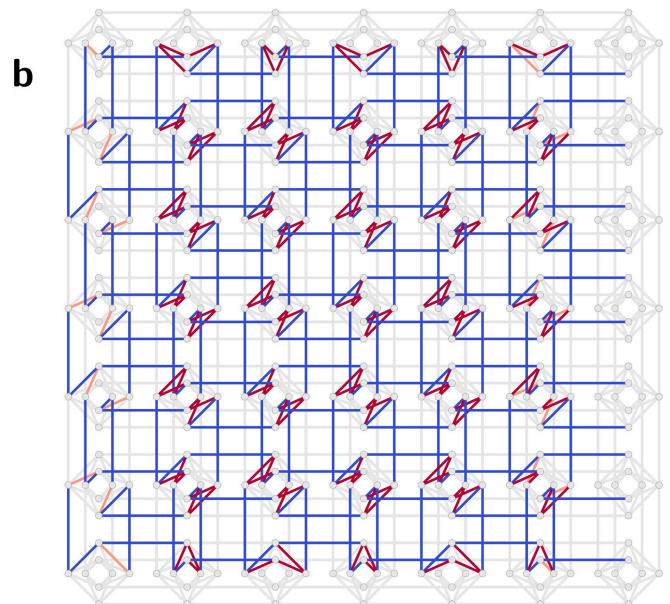


Extended Data Fig. 5 | Convergence of quantum evolution Monte Carlo. Our quantum evolution Monte Carlo sampling approach involves making a chain of 50 reverse annealing evolutions starting from an ordered state and a random state. At 8.4 mK, cooling of around 0.1 mK is observed during the first 25 evolutions. This cooling lowers m at $s = 0.26$, as the lower temperature slows evolution during the 1- μs quench. The same cooling increases the order parameter at $s = 0.26$, where the lower

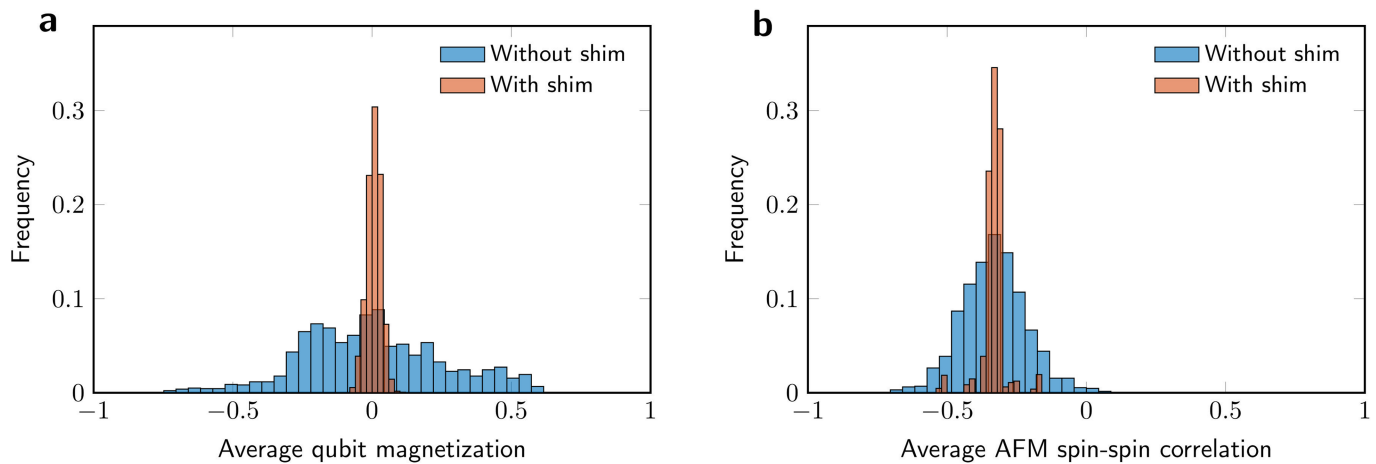
temperature results in evolution of a more ordered model. Shown are experimental results for increasing values of s (top row) and for $s = 0.26$ at increasing temperatures (bottom row). At $s = 0.30$, $T = 8.4$ mK, evolution is slow and the estimates of $\langle m \rangle$ are far from the equilibrium value of $\langle m \rangle$ after a single 65-ms evolution. Spin-bath polarization, which biases the estimators towards the initial condition at low temperatures, disappears as temperature is increased.



Extended Data Fig. 6 | Embedding a cylindrical lattice into the qubit connectivity graph. **a, b,** The cylindrical square-octagonal lattice with length $L = 6$ (**a**) is embedded into a region of the Chimera qubit connectivity graph (**b**). The embedding consists of two square sheets that

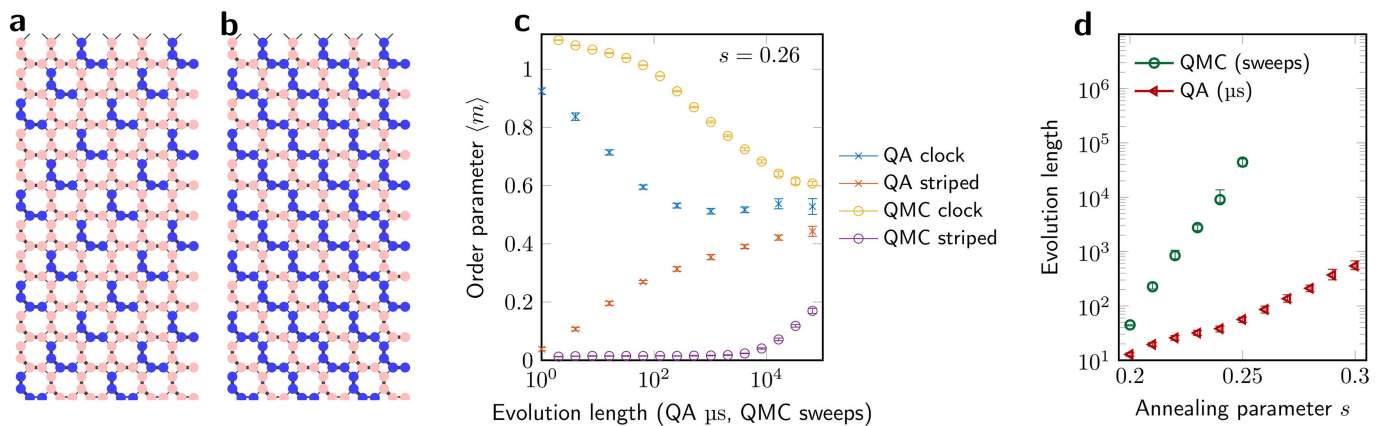


are coupled together at the top and bottom. The largest instance studied with $L = 15$ uses 1,800 of the 2,048 qubits in the processor, with unused qubits along the outside boundary of the processor. FM couplers are in blue and AFM couplers are in red.



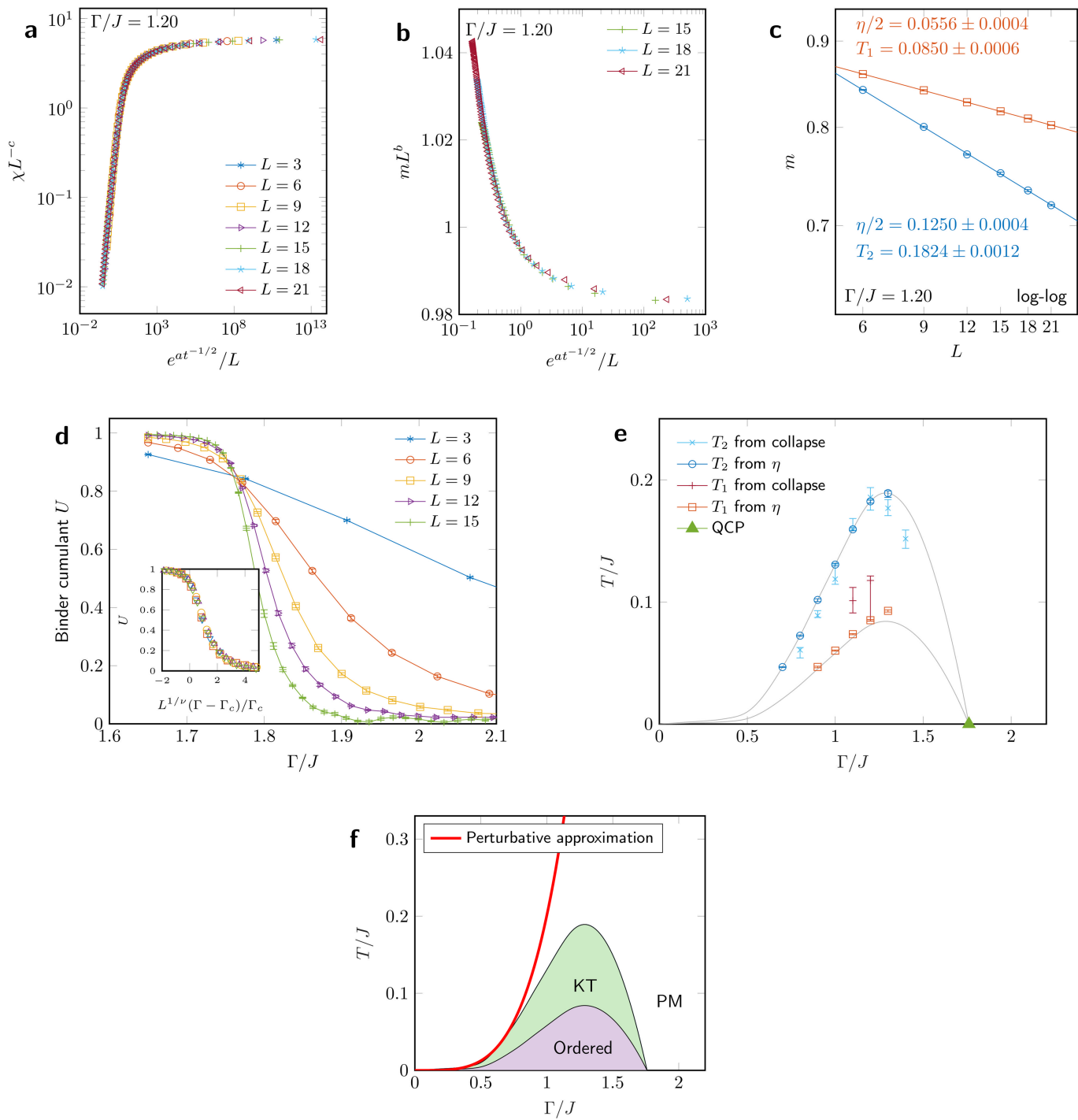
Extended Data Fig. 7 | Effect of calibration refinement. **a, b,** Symmetries in the lattice dictate that each qubit should have an average magnetization of zero (**a**) and that each AFM coupler should be frustrated with the same probability as other couplers in its rotational symmetry equivalence class of $2L$ couplers (**b**). We use a gradient-descent shim method (code available from the corresponding author on reasonable request) to maintain

degeneracy among qubits and equivalent couplers with flux offsets and small adjustments to specified coupling energies. Data are taken for $L = 15$, with 1,800 qubits and 1,290 AFM couplers, over 120 experiments with and without shim. Both magnetization and correlation distributions are tightened substantially. Outliers in shimmed spin–spin correlation are symmetry classes near the boundary of the lattice.



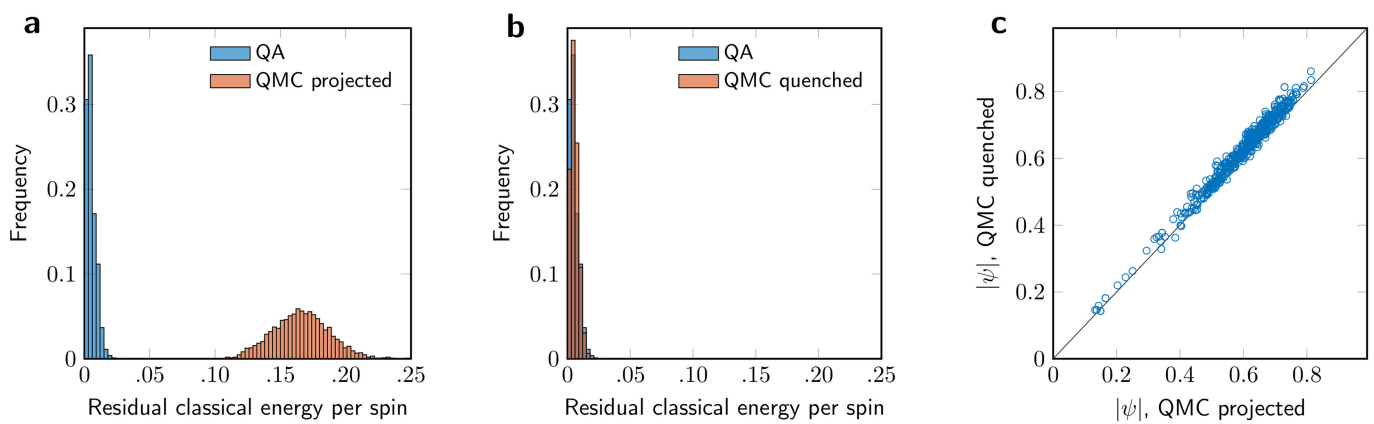
Extended Data Fig. 8 | Evolution time required to converge from two distant initial states in an 1,800-spin lattice. **a–c**, We initialize the quantum simulation (QA) and the classical Monte Carlo simulation (QMC) with single-spin updates (that is, no cluster updates) in two classical ground states, shown for $L = 6$ with pink and blue representing up and down Ising spins, respectively. One is a clock state (**a**) with order parameter $m = 2/\sqrt{3}$. The other is a striped state (**b**), which has $m = 0$ and is far from other classical ground states in Hamming distance. As these

initial states are evolved in either QA or QMC for increasing evolution times, m converges towards a steady state (**c**) regardless of initial condition. The uptick of m for long QA evolution may be a signature of on-chip cooling during evolution. **d**, The time required to converge m for the two initial conditions to within 0.3 of each other increases with s , as thermal and quantum fluctuations drop and dynamics slow. This indicates that QMC simulates only the equilibrium statistics of quantum evolution—not the dynamics.



Extended Data Fig. 9 | Phase diagram of the square-octagonal lattice from Monte Carlo simulations with toroidal boundary conditions.
a, b, We estimate the upper (a) and lower (b) KT phase transition via universal collapse of susceptibility data, varying temperature for several values of Γ/J (shown: $\Gamma/J = 1.2$); lower collapse is imperfect. **c**, Power-law scaling of m with L at upper and lower critical temperatures with critical exponents from two-dimensional XY universality. Lines show power-law regression. **d**, Crossing of the normalized Binder cumulant for models with $\beta = 3.5L/\Gamma$ gives an estimate of the quantum critical point $\Gamma/J \approx 1.76$

(the inset shows the collapse of Binder cumulant across system sizes). **e**, From this data we derive a picture of the phase diagram of the square-octagonal lattice with $J_{FM} = -1.8J_{AFM}$. **f**, In the perturbative limit, the critical temperature of the square-octagonal lattice is determined by the energy splitting of four-qubit FM chains. Therefore, the perturbative phase boundary corresponding to the triangular lattice's linear perturbative phase boundary has a quartic form (boundary shown is proportional to Γ^4 , fitted by eye).


Extended Data Fig. 10 | Effect of classical quench on QMC samples.

a, Distributions of classical energy differ greatly between QA and QMC output, with QA giving much lower classical energies. **b**, When a local quench is performed on QMC output, removing local excitations at the

single-qubit level and the four-qubit chain level, the energy distribution matches QA closely. **c**, Quenching increases $\langle |\psi| \rangle$ by 0.02 in these QMC samples. Samples are collected for $s = 0.26$, $T = 8.4$ mK.

Photonic topological Anderson insulators

Simon Stützer¹, Yonatan Plotnik², Yaakov Lumer³, Paraj Titum⁴, Netanel H. Lindner², Mordechai Segev², Mikael C. Rechtsman⁵ & Alexander Szameit^{1*}

The hallmark property of two-dimensional topological insulators is robustness of quantized electronic transport of charge and energy against disorder in the underlying lattice¹. That robustness arises from the fact that, in the topological bandgap, such transport can occur only along the edge states, which are immune to backscattering owing to topological protection. However, for sufficiently strong disorder, this bandgap closes and the system as a whole becomes topologically trivial: all states are localized and all transport vanishes in accordance with Anderson localization^{2,3}. The recent suggestion⁴ that the reverse transition can occur was therefore surprising. In so-called topological Anderson insulators, it has been predicted⁴ that the emergence of protected edge states and quantized transport can be induced, rather than inhibited, by the addition of sufficient disorder to a topologically trivial insulator. Here we report the experimental demonstration of a photonic topological Anderson insulator. Our experiments are carried out in an array of helical evanescently coupled waveguides in a honeycomb geometry with detuned sublattices. Adding on-site disorder in the form of random variations in the refractive index of the waveguides drives the system from a trivial phase into a topological one. This manifestation of topological Anderson insulator physics shows experimentally that disorder can enhance transport rather than arrest it.

In parallel to investigations into electronic topological insulators, the recent demonstration of photonic topological insulators^{5–7} has shown that topological phenomena are not limited to the motion of electrons in solid-state materials. In fact, topological protection is a general wave phenomenon that applies equally well to many wave systems, including electromagnetic waves^{5–15}, acoustic waves^{16,17}, mechanical waves^{18,19} and cold atoms^{20,21}. Among these, photonic topological systems have been found to be useful in demonstrating effects that would otherwise be unreachable in the context of condensed-matter physics, such as Anderson localization^{22,23}, very strong strain²⁴, non-Hermitian behaviour²⁵ and the concept of topological bound states in the continuum²⁶. Furthermore, topological photonic systems provide a complementary set of potential technological applications, including new mechanisms for integrated optical isolation and general robustness to imperfections in the fabrication of photonic devices.

Here we demonstrate a topological Anderson insulator. Our experiments are carried out in a photonic platform, as proposed theoretically²⁷, based on a two-dimensional time-reversal-symmetry-broken Floquet topological insulator. In particular, when sufficient disorder is introduced, we enter the topological phase and observe unidirectional edge transport. Our key result, which demonstrates the possibility of inducing a topological phase using disorder, is universal and carries over to different dimensions²⁸ and to symmetry-protected topological phases^{4,35}. The experimental platform that we use is an array of evanescently coupled helical waveguides²⁹, where the diffraction of light through the system is described by the paraxial wave equation, which is mathematically equivalent to the Schrödinger equation. A closely related system has been used for the observation of Floquet photonic topological insulators⁵.

To explain the mechanism that underlies our photonic topological Anderson insulator, we start with a honeycomb lattice of helical waveguides⁵, which is a photonic Floquet topological insulator. The equation that describes the diffraction of a paraxial beam of light in this lattice can be written, under the tight-binding approximation, as

$$i\partial_z \psi_i = c \sum_{j(\text{nn } i)} e^{-i\mathbf{A}(z) \cdot \mathbf{r}_{i,j}} \psi_j + m_\delta \delta_i \psi_i \equiv \sum_j \hat{H}_{ij}(z) \psi_j \quad (1)$$

where z is the distance of propagation along the waveguide axis, ψ_i is the envelope function of the electric field in the i th waveguide, c is the coupling strength between waveguides, $\mathbf{A}(z) = kR\Omega a (\cos(\Omega z), \sin(\Omega z), 0)$ is the gauge field induced by the helicity, k is the wavenumber of the light in the medium (fused silica), R is the radius of the helix, Ω is the longitudinal frequency associated with the helix, a is the nearest-neighbour spacing and $\mathbf{r}_{i,j}$ is the displacement vector pointing from waveguide i to waveguide j . The honeycomb lattice comprises two triangular sublattices. The parameter δ_i takes the value 1 in one sublattice and -1 in the other, such that the on-site energies of the two are separated by the detuning $2m_\delta$. Equation (1) defines $\hat{H}(z)$ as the Hamiltonian at propagation distance z , and the summation therein is taken over nearest-neighbour waveguides. This is exactly the Schrödinger equation, where z takes the role of time. Because $\mathbf{A}(z)$ is z -dependent and periodic, solutions to equation (1) can be obtained by using Floquet's theorem. Thus, the band structure can be obtained by diagonalizing the unitary evolution operator for one period³⁰. Detuning the two triangular sublattices breaks the inversion symmetry of the structure and opens a trivial bandgap. This can be quantified with a mass m_δ associated with the effective Dirac equation of the honeycomb lattice in the absence of the periodic driving. In the undetuned case ($m_\delta=0$), the Dirac-cone dispersion is equivalent to that of massless relativistic particles. Such detuning can be realized experimentally in waveguide arrays by allowing the two honeycomb sublattices to have different refractive indices.

The mechanism according to which we realize the photonic topological Anderson insulator is depicted schematically in Fig. 1a. The band structure of the honeycomb lattice with straight and identical waveguides, so that the induced gauge field $\mathbf{A}(z)=\mathbf{0}$ and $m_\delta=0$, is shown in Fig. 1b. This band structure corresponds to that of a ribbon (associated with the zigzag edge of graphene³¹). As known in graphene physics, the ribbon band structure exhibits two Dirac cones (red ellipses in Fig. 1b) that are connected by a flat band of edge states³¹. When the waveguides follow a helical trajectory such that $\mathbf{A}(z)$ is non-zero (Fig. 1c), the z -reversal symmetry is broken and a bandgap opens. In this case, each valley acquires an opposite mass: m_τ and $-m_\tau$ for the left and right valleys, respectively. These opposite masses imply that the edge states cross the bandgap, with each edge state localized to opposite sides of the ribbon. Therefore, the bandgap is topological; the edge states form a single backscattering-free chiral edge state that is localized to the edge of the structure. This is the essence of a Floquet topological insulator in the honeycomb system⁵.

¹Institute for Physics, Rostock University, Rostock, Germany. ²Physics Department and Solid State Institute, Technion – Israel Institute of Technology, Haifa, Israel. ³Department of Electrical and Systems Engineering, University of Pennsylvania, Philadelphia, PA, USA. ⁴Joint Quantum Institute and Joint Center for Quantum Information and Computer Science, NIST/University of Maryland, College Park, MD, USA. ⁵Department of Physics, The Pennsylvania State University, University Park, PA, USA. *e-mail: alexander.szameit@uni-rostock.de

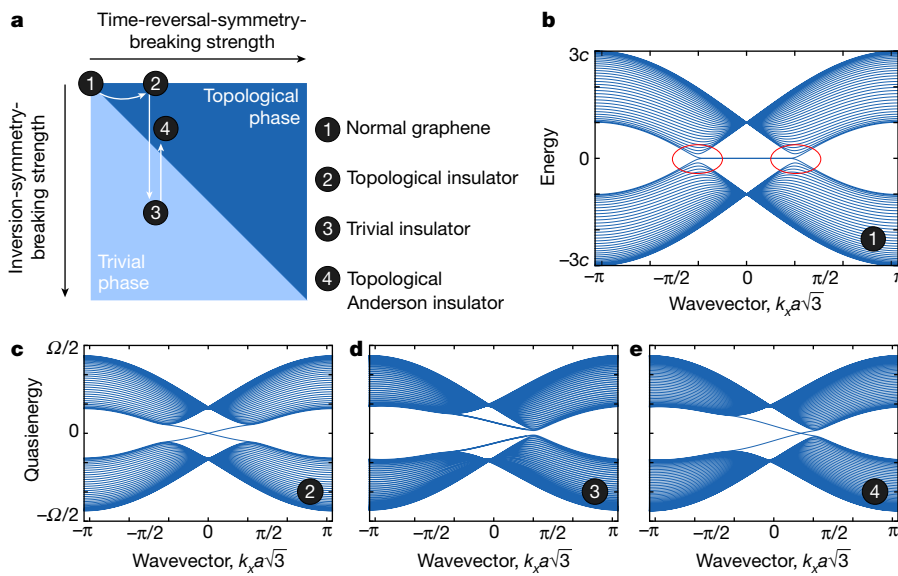


Fig. 1 | Floquet topological Anderson insulator in a detuned honeycomb lattice. **a**, Mechanism for realizing the topological insulator phase in a photonic waveguide lattice. The white arrows indicate the trajectory through the phase diagram in the experimental protocol. The parameters for the band-structure calculations are chosen for illustration purposes. **b**, Band structure for a trivial honeycomb lattice with straight waveguides. The red ellipses indicate the Dirac cones. **c**, Time-reversal

symmetry is broken by helical waveguide trajectories, opening a topological bandgap. **d**, Breaking the parity symmetry of the structure by detuning the sublattices sufficiently causes a trivial bandgap to form. **e**, Sufficiently strong disorder suppresses the effect of the parity-symmetry-breaking terms and moves the system into the topological Anderson insulator phase. The band structure shown in this case is for illustration purposes; there is no well defined band structure in the disordered case.

Consider now what happens when the sublattices of the Floquet topological insulator are detuned so that the two sublattices exhibit different refractive indices. Introducing non-zero detuning breaks the inversion symmetry of the lattice, which adds a positive mass term m_δ to each valley. If the detuning is large enough ($m_\delta > m_\tau$), then the masses $m_\tau + m_\delta$ and $-m_\tau + m_\delta$ in both valleys become positive and the bandgap becomes trivial (Fig. 1d). In other words, the outcome of a sufficiently detuned honeycomb lattice of helical waveguides is a topologically trivial system with broken inversion and time-reversal symmetry. This is where disorder comes into play: as was recently proposed²⁷, this system can be brought into a topologically non-trivial phase using disorder. More specifically, it has been shown²⁷ (using the Born approximation) that introducing on-site disorder, which is achieved by randomizing the refractive-index contrasts of the waveguides, causes an effective decrease in the detuning m_δ . The decrease in m_δ grows stronger as the strength of the disorder is increased. Therefore, upon introducing disorder and increasing its strength, the mobility gap closes when $m_\tau = m_\delta$ and reopens for $m_\tau > m_\delta$. When the gap reopens, the system is topological (Fig. 1e). This is precisely the effect of photonic topological Anderson insulators: adding disorder brings the system from being topologically trivial ($m_\delta > m_\tau$) to topologically non-trivial ($m_\tau > m_\delta$).

A schematic depiction of the waveguide configuration is shown in Fig. 2a. In this setting, it is essential to control which states are excited. We do that by adding a one-dimensional auxiliary array—a ‘straw’—through which we selectively excite the modes of the system at a fixed energy (k_z). More specifically, in a one-dimensional waveguide array, tilting the phase front of the wave that illuminates the input facet determines the momentum of the excited Bloch mode. Here, such selective excitation is especially important because we would like to excite states entirely within the gap, to determine whether the gap exists and whether it is trivial or topological. By controlling the tilt angle of input of the beam, we can control k_x , the Bloch wavevector in the horizontal direction. The band structure (k_z versus k_x) of the straw is shown in the inset in Fig. 2a. We fix k_z (the Floquet quasienergy) by choosing k_x , and k_z is conserved as the beam travels through the straw and enters the honeycomb array. Thus, simply by changing the incidence angle of the beam, we can tune the quasienergy of the modes that are excited in the structure.

The bandwidth in k_z of the straw depends on k_x and is relatively wide (determined by the number of sites in the straw and input beam), limiting our ability to perform precise spectroscopy. However, it remains a highly useful tool for selective excitation of wave packets in the honeycomb lattice.

We first consider a system that breaks z -reversal symmetry ($m_\tau \neq 0$) with identical (non-detuned) waveguides ($m_\delta = 0$), and repeat the previous realization of a Floquet topological insulator⁵ (see Methods for details). Owing to the helicity of the waveguides, the system has a topological bandgap at quasienergy $k_z = 0$, and we expect to find a chiral edge state in this bandgap (the Floquet band structure is shown in the inset to Fig. 2a). This is precisely what we see. In Fig. 2b we show the output facet of the array in the case where k_z lies in the bandgap (top) and the case where it lies in the band (bottom). When k_z is in the gap, a chiral edge state is excited: the optical wave packet is launched from the straw and couples to the chiral edge state, where it propagates unidirectionally upwards in a clockwise direction around the honeycomb lattice, but does not penetrate into the lattice. On the other hand, when k_z lies in the band, the wave packet couples to bulk states; hence, it penetrates into the lattice and spreads into the array, so does not stay confined to the edge. The evolution of the edge state is shown in Fig. 2c. As the input beam is brought closer to the array, the edge state travels farther along the edge until it passes the top corner. The fact that it moves only upwards, and stays confined to the edge, is a signature of the chirality of the edge state. We note that for the choice of parameters of the waveguide array used in the experiment the longitudinal frequency of the helix Ω is smaller than the total bandwidth (6c) in the absence of the helix. This results in an additional topological gap, which opens at a quasienergy of around $k_z = \Omega/2$ and hosts chiral edge states, as shown in Fig. 2a. However, by using the selective excitation through the straw, in this experiment we always excite states with quasienergies close to $k_z = 0$ and do not probe states with quasienergy near $k_z = \Omega/2$.

We now describe the probing of a series of helical photonic lattices, where we introduce detuning between the sublattices ($m_\delta \neq 0$) of the honeycomb structure by making their refractive indices different. In practice, this is done by changing the speed of the laser-writing beam during the fabrication process (a higher writing speed results in a lower refractive index of the waveguides). In a series of six waveguide arrays, we systematically increase this detuning, decreasing the gap size as

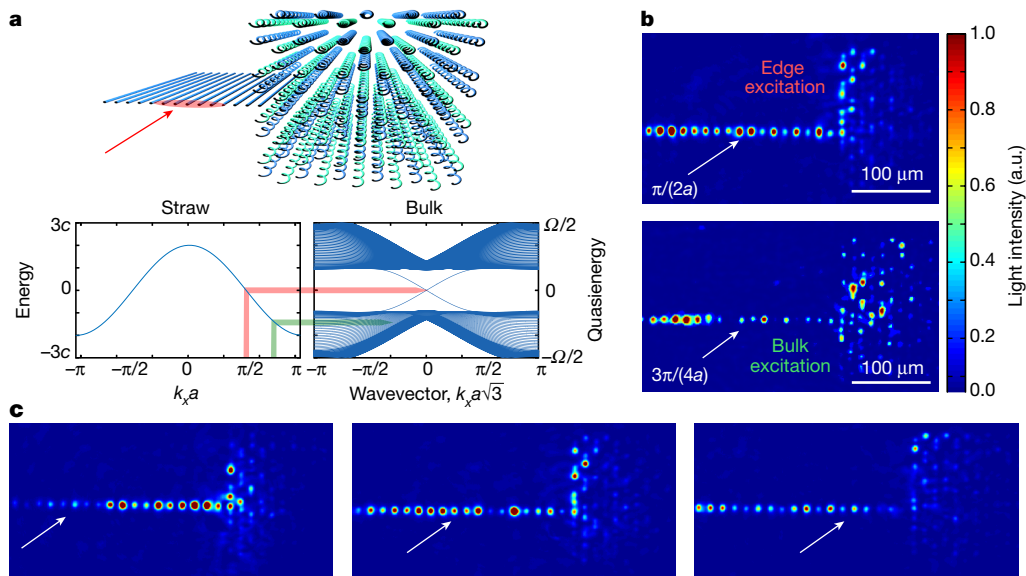


Fig. 2 | Set-up and functionality of the lattice system. **a**, Hybrid structure composed of a one-dimensional straw and a two-dimensional honeycomb lattice of helical waveguides (top), along with the corresponding dispersion relations (bottom). **b**, Determining the correct input angle for the incident light, such that a chiral edge state in the topological gap is excited. Two experimental images are shown, for $k_x = \pi/(2a)$ and $k_x = 3\pi/(4a)$; the excitation in the dispersion relation is sketched in the bottom plots of **a**. If the launch angle does not correspond to excitation in the gap, extensive coupling into the lattice bulk is observed. a.u., arbitrary units. **c**, Changing the input position (indicated by the white arrows) facilitates the observation of the evolution of the edge states as they propagate along the edge and pass the upper corner, never penetrating into the bulk.

m_δ increases, and examine how much the wavefunction launched through the straw penetrates into the lattice (plotted in Fig. 3). To do that, we choose $k_x = \pi/(2a)$, where the Bloch wavenumber in the

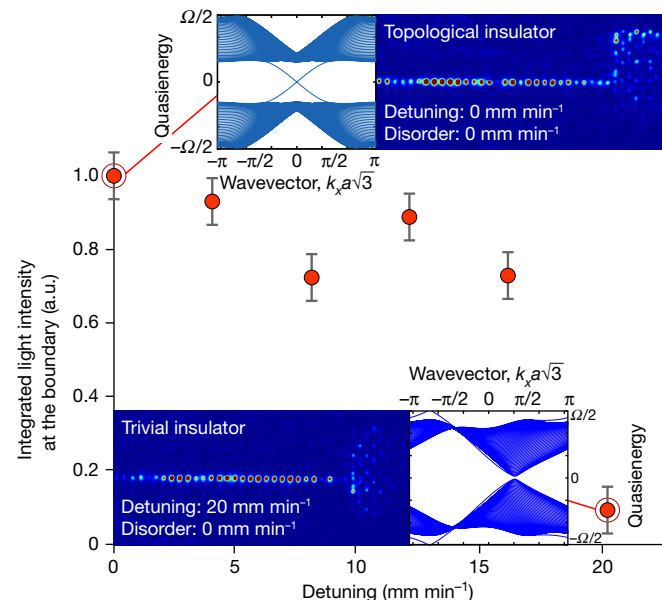


Fig. 3 | Engineering the topologically trivial phase. For sufficiently strong detuning between the sublattices of the honeycomb lattice, a trivial gap opens, such that the chiral edge state ceases to exist and all incident light is reflected back into the straw. The experiments show the light-intensity pattern as it exits the helical waveguide array (insets; colour scale as in Fig. 2) and the measured integrated intensity at the boundary as a function of detuning (main panel; in units of translation velocity of the writing laser). For zero detuning, the incident light resides only on the edge (indicating the topological insulator phase). When the detuning is small, the system is still in the topological phase and almost all the incident light resides on the edge. When the detuning is increased further, the system becomes topologically trivial and the incident light does not penetrate along the edge. There is no disorder in this lattice. The error bars indicate measurement uncertainty, and the confidence interval is about 0.06 of the maximum intensity observed (normalized to unity).

straw corresponds to the value of k_z in the centre of the bandgap of the honeycomb lattice. For sufficiently strong detuning m_δ , we observe a sharp decrease in the penetration of light along the edge, which corresponds to the closing of the topological bandgap and the reopening of the trivial bandgap at $k_z=0$. This observation constrains m_δ to be larger than 1.57 cm^{-1} , although precise determination of the on-site waveguide propagation constants within the array is not possible (owing to the exponential sensitivity of the refractive index to write speed and the effect of the lattice environment on the individual waveguides). Indeed, in the trivial gap, no states are present, and there is a dramatic drop in the penetration into the array along the edge. The inability to couple to edge states establishes that we have introduced sufficiently strong detuning, m_δ , to have opened the trivial bandgap, which does not support edge modes.

Next, we introduce on-site disorder and demonstrate the formation of the photonic topological Anderson insulator by observing whether the mid-gap excitation gives rise to coupling to a topological edge state. The disorder enters equation (1) on the right-hand side via an additional term, $w r_i \psi_i$, where r_i is a uniformly distributed random variable between -0.5 and 0.5 and w is the strength of the disorder. We find that for sufficiently strong disorder (corresponding to a maximum variation in laser write speed of 8 mm min^{-1}), the mid-gap excitation is able to couple into the lattice, staying largely confined to the edge (see Fig. 4a–c). As we move the input beam closer to the array, the light coupled into the array propagates farther along the edge, much as in the non-disordered topological system (with $m_\delta=0$) of Fig. 2c. The beam moves up along the left edge, implying the presence of a chiral edge state (that was not present when the system was not disordered). We find the group velocity of the edge state to be $21 \mu\text{m cm}^{-1}$. We fit the profile of the excited wavefunction and find that it decays exponentially away from the edge, consistent with having excited predominantly the edge states (see Methods). For comparison, we show the same scenario but with no disorder and with the same m_δ in Fig. 4d–f. When no disorder is present, there is no observable edge excitation and minimal bulk penetration; that is, the beam launched into the topologically trivial photonic bandgap is reflected. The small amount of bulk penetration seen in Fig. 4d–f probably arises from the finite bandwidth of the input beam in k_z . The appearance of the chiral edge state when the disorder is sufficiently strong is evidence of the photonic

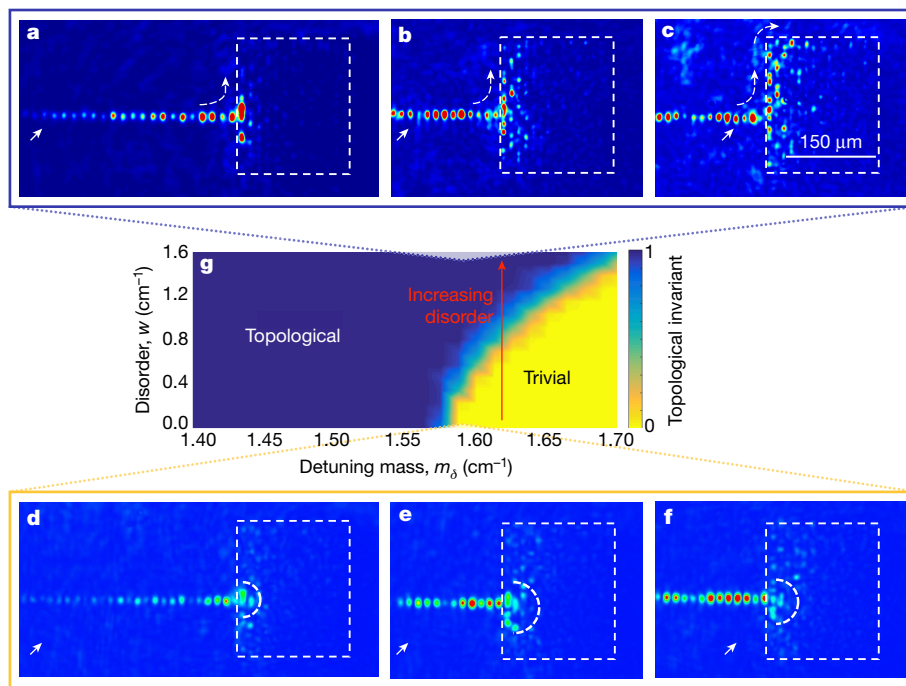


Fig. 4 | Formation of the photonic topological Anderson insulator. **a–c**, When sufficient disorder is added, the system is driven into the topological Anderson insulator phase and chiral edge states form. This is demonstrated by moving the excitation in the straw (solid arrows) close to the (disordered) honeycomb lattice, so that the edge state crawls up the edge (dashed arrows). The excitation in the straw is far from the honeycomb lattice (22 waveguides away; **a**); the excitation is at an intermediate distance from the lattice (11 waveguides away; **b**); and the excitation is close to the lattice (4 waveguides away; **c**). The dashed boxes indicate the honeycomb waveguide array. **d–f**, By contrast, in the fully ordered, detuned helical honeycomb lattice, essentially all light is

reflected into the straw, with only a small part penetrating into the bulk without exciting any edge mode. The excitation in the straw is far from the honeycomb lattice (**d**); the excitation is at an intermediate distance from the lattice (**e**); and the excitation is close to the lattice (**f**) (distances as in **a–c**). **g**, Phase diagram showing the trivial and topological phases as a function of the detuning mass, m_δ , and disorder strength, w , obtained using experimental parameters (see Methods). The red arrow indicates the trajectory through the phase diagram as the system starts from the trivial phase and enters the topological phase with increasing disorder strength.

topological Anderson insulator phase²⁷. In Fig. 4g we show a phase diagram that indicates the topological invariant that counts the number of edge states at quasienergy $k_z=0$ as a function of detuning m_δ and disorder strength w (a full description of the topological invariant^{32,33} that we use is provided in Methods). The phase diagram shows that adding sufficiently strong disorder to the detuned lattice in the trivial phase necessarily takes the system into the topological phase. For considerably stronger disorder, localization sets in, making the system Anderson-localized⁴.

The experiments presented here demonstrate the observation of a topological Anderson insulator using a photonic platform. Specifically, we have shown that a topologically trivial system can undergo a transition and become topological when disorder is added. This was carried out by observing the emergence of a chiral edge state upon introducing sufficiently strong disorder (where there was none with no disorder). The topological Anderson insulator phase is a clear example of the complex relationship between topology and disorder: it goes beyond the usual notion whereby sufficiently strong disorder destroys topologically protected transport¹. It shows that disorder is a key variable in probing topological phases, in the sense that even in trivial systems topological behaviour can emerge when disorder is introduced at sufficient strengths. We expect that our experimental realization of this phase will stimulate a range of theoretical and experimental studies to explore the role of disorder in topological systems. This prompts various important questions, such as what happens to the topological Anderson insulator phase in the presence of interactions in optical, atomic and condensed-matter systems, and whether there is a topological Anderson insulator phase in the quantum many-body regime. The answers to these questions are now being brought within experimental reach.

After this paper was submitted, a related paper³⁴ appeared on arXiv that reported the observation of a topological Anderson insulator in one-dimensional atomic wires.

Online content

Any Methods, including any statements of data availability and Nature Research reporting summaries, along with any additional references and Source Data files, are available in the online version of the paper at <https://doi.org/10.1038/s41586-018-0418-2>.

Received: 18 October 2017; Accepted: 20 June 2018;
Published online 22 August 2018.

- Hasan, M. Z. & Kane, C. L. Colloquium: Topological insulators. *Rev. Mod. Phys.* **82**, 3045–3067 (2010).
- Anderson, P. W. Absence of diffusion in certain random lattices. *Phys. Rev.* **109**, 1492–1505 (1958).
- Segev, M., Silberberg, Y. & Christodoulides, D. N. Anderson localization of light. *Nat. Photon.* **7**, 197–204 (2013).
- Li, J., Chu, R.-L., Jain, J. K. & Shen, S.-Q. Topological Anderson insulator. *Phys. Rev. Lett.* **102**, 136806 (2009).
- Rechtsman, M. C. et al. Photonic Floquet topological insulators. *Nature* **496**, 196–200 (2013).
- Hafezi, M., Mittal, S., Fan, J., Migdall, A. & Taylor, J. M. Imaging topological edge states in silicon photonics. *Nat. Photon.* **7**, 1001–1005 (2013).
- Cheng, X. et al. Robust reconfigurable electromagnetic pathways within a photonic topological insulator. *Nat. Mater.* **15**, 542–548 (2016).
- Haldane, F. D. M. & Raghu, S. Possible realization of directional optical waveguides in photonic crystals with broken time-reversal symmetry. *Phys. Rev. Lett.* **100**, 013904 (2008).
- Wang, Z., Chong, Y., Joannopoulos, J. D. & Soljacic, M. Observation of unidirectional backscattering-immune topological electromagnetic states. *Nature* **461**, 772–775 (2009).
- Umucalilar, R. O. & Carusotto, I. Artificial gauge field for photons in coupled cavity arrays. *Phys. Rev. A* **84**, 043804 (2011).

11. Hafezi, M., Demler, E. A., Lukin, M. D. & Taylor, J. M. Robust optical delay lines with topological protection. *Nat. Phys.* **7**, 907–912 (2011).
12. Fang, K., Yu, Z. & Fan, S. Realizing effective magnetic field for photons by controlling the phase of dynamic modulation. *Nat. Photon.* **6**, 782–787 (2012).
13. Khanikaev, A. B. et al. Photonic topological insulators. *Nat. Mater.* **12**, 233–239 (2013).
14. Maczewsky, L. J., Zeuner, J. M., Nolte, S. & Szameit, A. Observation of photonic anomalous Floquet topological insulators. *Nat. Commun.* **8**, 13756 (2017).
15. Mukherjee, S. et al. Experimental observation of anomalous topological edge modes in a slowly driven photonic lattice. *Nat. Commun.* **8**, 13918 (2017).
16. Khanikaev, A. B., Fleury, R., Mousavi, S. H. & Alù, A. Topologically robust sound propagation in an angular-momentum-biased graphene-like resonator lattice. *Nat. Commun.* **6**, 8260 (2015).
17. Yang, Z. et al. Topological acoustics. *Phys. Rev. Lett.* **114**, 114301 (2015).
18. Süsstrunk, R. & Huber, S. D. Observation of phononic helical edge states in a mechanical topological insulator. *Science* **349**, 47–50 (2015).
19. Nash, L. M. et al. Topological mechanics of gyroscopic metamaterials. *Proc. Natl. Acad. Sci. USA* **112**, 14495–14500 (2015).
20. Jotzu, G. et al. Experimental realization of the topological Haldane model with ultracold fermions. *Nature* **515**, 237–240 (2014).
21. Aidelsburger, M. et al. Measuring the Chern number of Hofstadter bands with ultracold bosonic atoms. *Nat. Phys.* **11**, 162–166 (2014).
22. Schwartz, T., Bartal, G., Fishman, S. & Segev, M. Transport and Anderson localization in disordered two-dimensional photonic lattices. *Nature* **446**, 52–55 (2007).
23. Lahini, Y. et al. Anderson localization and nonlinearity in one-dimensional disordered photonic lattices. *Phys. Rev. Lett.* **100**, 013906 (2008).
24. Rechtsman, M. C. et al. Strain-induced pseudomagnetic field and photonic Landau levels in dielectric structures. *Nat. Photon.* **7**, 153–158 (2013).
25. Weimann, S. et al. Topologically protected bound states in photonic parity-time-symmetric crystals. *Nat. Mater.* **16**, 433–438 (2017).
26. Plotnik, Y. et al. Experimental observation of optical bound states in the continuum. *Phys. Rev. Lett.* **107**, 183901 (2011).
27. Titum, P., Lindner, N. H., Rechtsman, M. C. & Refael, G. Disorder-induced Floquet topological insulators. *Phys. Rev. Lett.* **114**, 056801 (2015).
28. Guo, H.-M., Rosenberg, G., Refael, G. & Franz, M. Topological Anderson insulator in three dimensions. *Phys. Rev. Lett.* **105**, 216601 (2010).
29. Szameit, A. & Nolte, S. Discrete optics in femtosecond-laser-written photonic structures. *J. Phys. B* **43**, 163001 (2010).
30. Lindner, N. H., Refael, G. & Galitski, V. Floquet topological insulator in semiconductor quantum wells. *Nat. Phys.* **7**, 490–495 (2011).
31. Castro Neto, A. H., Guinea, F., Peres, N. M. R., Novoselov, K. S. & Geim, A. K. The electronic properties of graphene. *Rev. Mod. Phys.* **81**, 109–162 (2009).
32. Rudner, M. S., Lindner, N. H., Berg, E. & Levin, M. Anomalous edge states and the bulk-edge correspondence for periodically driven two-dimensional systems. *Phys. Rev. X* **3**, 031005 (2013).
33. Titum, P., Berg, E., Rudner, M. S., Refael, G. & Lindner, N. H. Anomalous Floquet-Anderson insulator as a nonadiabatic quantized charge pump. *Phys. Rev. X* **6**, 021013 (2016).
34. Meier, E. J. et al. Observation of the topological Anderson insulator in disordered atomic wires. Preprint at <https://arxiv.org/abs/1802.02109> (2018).
35. Groth, C. W. et al. Theory of the topological Anderson insulator. *Phys. Rev. Lett.* **103**, 196805 (2019).

Acknowledgements A.S. and M.S. thank the German-Israeli DIP (project BL 574/13-1). A.S. acknowledges funding from the German Research Foundation (project SZ 276/9-1). M.S. thanks the European Research Council for financial support. N.L. acknowledges financial support from the European Research Council under the European Union Horizon 2020 Research and Innovation Programme (grant agreement number 639172), from the People Programme (Marie Curie Actions) of the European Union's Seventh Framework Programme (FP7/2007–2013) under REA grant agreement number 631696 and from the Israeli Center of Research Excellence (I-CORE) Circle of Light, funded by the Israeli Science Foundation. M.C.R. acknowledges support from the National Science Foundation under grant number DMS-1620422, as well as the Sloan (FG-2016-6418) and Kaufman (KA2017-91788) foundations. P.T. is supported by an NRC postdoctoral fellowship. The authors acknowledge the University of Maryland supercomputing resources made available for conducting the research reported in this paper.

Author contributions All authors contributed substantially to this work.

Competing interests The authors declare no competing interests.

Additional information

Extended data is available for this paper at <https://doi.org/10.1038/s41586-018-0418-2>.

Reprints and permissions information is available at <http://www.nature.com/reprints>.

Correspondence and requests for materials should be addressed to A.S.

Publisher's note: Springer Nature remains neutral with regard to jurisdictional claims in published maps and institutional affiliations.

METHODS

Details of the fabricated lattice. In our waveguide structures, we use a helix pitch of $Z = 1\text{ cm}$, a radius of $R = 10\text{ }\mu\text{m}$ and a nearest-neighbour spacing of $a = 14\text{ }\mu\text{m}$; at our probe wavelength ($\lambda = 633\text{ nm}$), this corresponds to a dimensionless gauge field strength of $|A| = kR\Omega a = 1.26$, with $k = 2\pi n_0/\lambda$, $\Omega = 2\pi/Z$, an ambient refractive index $n_0 = 1.45$ and $a = 14\text{ }\mu\text{m}$ nearest-neighbour spacing, which gives rise to a nearest-neighbour coupling strength of 1.8 cm^{-1} . The waveguides are written at an average writing speed of 90 mm min^{-1} . A broad input probe beam is incident on the straw, with a beam waist of approximately $100\text{ }\mu\text{m}$.

Discussion of the topological invariant that characterizes the photonic topological Anderson insulator phase. The topological invariant that characterizes the non-interacting two-dimensional periodically driven systems (in the absence of any additional symmetry besides particle number conservation) is the winding number W_{k_z} , which depends on the quasienergy k_z . For each quasienergy k_z , the value W_{k_z} is equal to the number of chiral edge states at that quasienergy^{32,33}. To compute the winding number for $k_z = 0$, we first compute the Bott index of the Floquet band²⁷, which lies in the quasienergy interval $0 \leq k_z \leq \Omega/2$. This Bott index essentially counts²⁷ the number of chiral edge states that traverse the gap at $k_z = \Omega/2$ less the number of chiral edge states that traverse the gap at $k_z = 0$. In addition, we verify that for the range of m_δ shown in Fig. 4 ($m_\delta > 1.4\text{ cm}^{-1}$), the gap at $k_z = \Omega/2$ hosts a single chiral edge state for the entire range of parameters with no disorder. Therefore, we conclude that, throughout the range of parameters shown in Fig. 4g, a Bott index of 0 corresponds to a topological gap at $k_z = 0$ and a Bott index of 1 corresponds to a trivial gap at $k_z = 0$.

Decay length of the edge state. We extract the decay length of the edge state from the experimental data. To achieve this, we analyse the intensity profile of the light propagating along the edge. To average over the disorder potential, we integrate the intensity per pixel along a direction parallel to the edge, and obtain the averaged intensity as a function of distance from the edge. The intensity profile (Extended Data Fig. 1a) decays with increasing distance from the edge, with peaks at the waveguide positions. We fit the envelope of the intensity profile to an exponential decay, which results in a decay length of the edge state of $47\text{ }\mu\text{m}$ (Extended Data Fig. 1b). This length scale is much smaller than the system size ($158\text{ }\mu\text{m}$). This result demonstrates that the system is sufficiently large for us to have observed the edge state. We do not observe any light at the far edge of the sample (the edge opposite the point at which the straw meets the sample), which indicates that the system size is sufficiently large that there is no considerable coupling between edge states on opposite sides.

We compare the experimentally obtained value of the decay length of the edge states with theoretical values obtained from a numerical simulation of a tight-binding model. The simulations are run for lattices with 60×30 unit cells with periodic

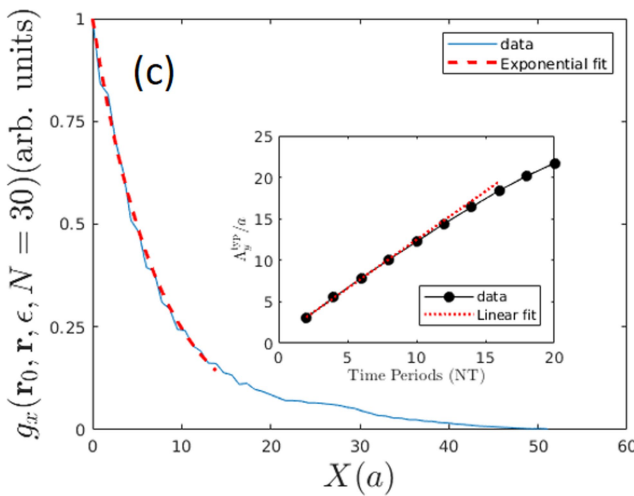
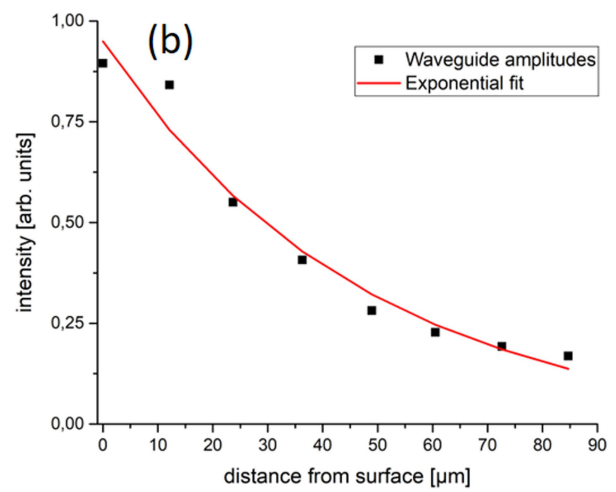
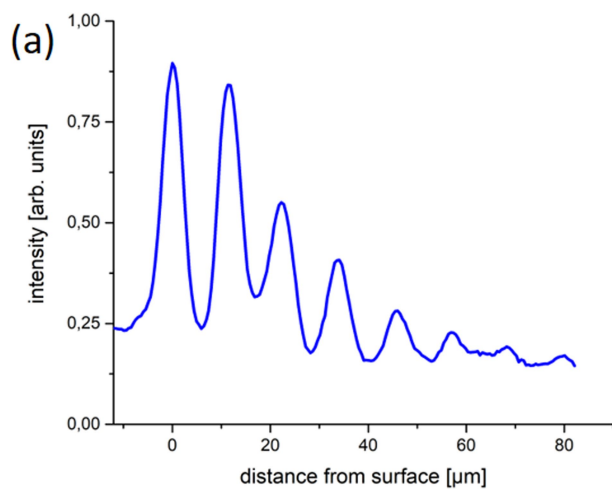
boundary conditions along y and open boundary conditions along x for a total time of $N = 30$ periods of rotation of the helices. The parameters for the tight-binding model are chosen as $c = 1.8\text{ cm}^{-1}$, $c_{\text{nnn}} = 0.234\text{ cm}^{-1}$, $m_\delta = 1.6\text{ cm}^{-1}$, $\Omega = 2\pi\text{ cm}^{-1}$, $kR\Omega a = 1.26$ and $w = 1.6\text{ cm}^{-1}$, where c_{nnn} is the next-nearest-neighbour hopping strength. To extract the decay length from the numerical simulation, we numerically compute the Green's function $G_N(\mathbf{r}_0, \mathbf{r}, NT) = \langle \mathbf{r}|U(t=NT, 0)|\mathbf{r}_0\rangle$, where $U(t=NT, 0)$ is the evolution operator over N periods. From the Fourier transform of the Green's function in time, we compute $g_N(\mathbf{r}_0, \mathbf{r}, \varepsilon) = \langle |G_N(\mathbf{r}_0, \mathbf{r}, \varepsilon)|^2 \rangle$, where the angle brackets denote averaging over multiple realizations of the disorder. (For more details on the definition of these quantities, see ref.²⁷; in short, $U(t, t_0)$ is the time-dependent propagator from time t_0 to t , $|\mathbf{r}_0\rangle$ and $|\mathbf{r}\rangle$ are position eigenstates and ε is the quasienergy, equivalent to k_z in the experiment.) For initial positions \mathbf{r}_0 localized on the edge and ε in the mobility gap (near quasienergy $\varepsilon = 0$), the function $g_N(\mathbf{r}_0, \mathbf{r}, \varepsilon)$ shows propagation along the edge and an exponentially localized profile confined to the edge. We integrate $g_N(\mathbf{r}_0, \mathbf{r}, \varepsilon = 0)$, averaged over 100 realizations, along the direction parallel to the edge (that is, we integrate over the y component of \mathbf{r}). We extract the decay length from the decay profile of the result (which is a function of only the distance from the edge). The results (Extended Data Fig. 1c) give a decay length of $7a$.

From our numerical simulations, we can also extract the group velocity along the edge. This is achieved by examining the dependence of g_N , averaged along the x direction (perpendicular to the edge), as a function of time. The spread of this function along the y direction (parallel to the edge) can be quantified using a typical length scale³⁶ $\Lambda_y^{\text{typ}}(N)$, which is obtained by examining the inverse participation ratio of the disorder-averaged Green's function (integrated over the x direction)³. In the inset of Extended Data Fig. 1c, we show the dependence of $\Lambda_y^{\text{typ}}(N)$ on N , which clearly shows a linear growth indicating the ballistic nature of the edge state. The slope gives the velocity, which is $1.2a\text{ cm}^{-1}$.

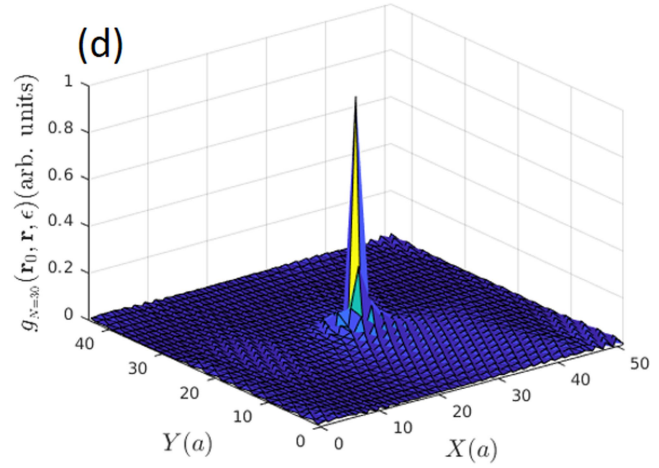
From the numerically obtained disorder-averaged Green's function, we also extract the localization length of the bulk states. We take an initial position \mathbf{r}_0 in the bulk of the system and plot the corresponding function $g_N(\mathbf{r}_0, \mathbf{r}, \varepsilon) = \langle |G_N(\mathbf{r}_0, \mathbf{r}, \varepsilon)|^2 \rangle$ (Extended Data Fig. 1d). This yields a bulk localization length of $4a$. Our numerical analysis thus shows that quasienergies near $\varepsilon = 0$ are indeed in a mobility gap. Furthermore, the bulk localization length in the mobility gap near $\varepsilon = 0$ is indeed sufficiently smaller than the system size.

Data availability. All data generated or analysed during this study are available from the corresponding author upon reasonable request.

36. Titum, P., Lindner, N. H. & Refael, G. Disorder-induced transitions in resonantly driven Floquet topological insulators. *Phys. Rev. B* **96**, 054207 (2017).



Extended Data Fig. 1 | Experimental and numerical results for the disordered system. **a**, The averaged intensity profile of the edge state, which peaks at the waveguide positions. **b**, A fit through the waveguide peak intensities decays exponentially, with a decay length of $47\text{ }\mu\text{m}$. **c**, The function $g_N(\mathbf{r}_0, \mathbf{r}, \epsilon)$, integrated along the edge, showing a decay length of



about $7a$. The inset shows the simulated displacement of the wavefunction along the edge for the parameters listed in Methods, from which the group velocity can be extracted. **d**, The function $g_N(\mathbf{r}_0, \mathbf{r}, \epsilon)$, for an initial position \mathbf{r}_0 deep in the bulk of the system, showing that the bulk localization length is approximately $4a$.

Magnetoelectric inversion of domain patterns

N. Leo^{1,2,12}, V. Carolus^{3,12}, J. S. White⁴, M. Kenzelmann⁴, M. Hudl⁵, P. Tolédano⁶, T. Honda⁷, T. Kimura⁸, S. A. Ivanov⁹, M. Weil¹⁰, Th. Lottermoser¹, D. Meier¹¹ & M. Fiebig^{1*}

The inversion of inhomogeneous physical states has great technological importance; for example, active noise reduction relies on the emission of an inverted sound wave that interferes destructively with the noise of the emitter¹, and inverting the evolution of a spin system by using a magnetic-field pulse enables magnetic resonance tomography². In contrast to these examples, inversion of a distribution of ferromagnetic or ferroelectric domains within a material is surprisingly difficult: field poling creates a single-domain state, and piece-by-piece inversion using a scanning tip is impractical. Here we report inversion of entire ferromagnetic and ferroelectric domain patterns in the magnetoelectric material Co₃TeO₆ and the multiferroic material Mn₂GeO₄, respectively. In these materials, an applied magnetic field reverses the magnetization or polarization, respectively, of each domain, but leaves the domain pattern intact. Landau theory indicates that this type of magnetoelectric inversion is universal across materials that exhibit complex ordering, with one order parameter holding the memory of the domain structure and another setting its overall sign. Domain-pattern inversion is only one example of a previously unnoticed effect in systems such as multiferroics, in which several order parameters are available for combination. Exploring these effects could therefore advance multiferroics towards new levels of functionality.

Since their discovery in the 1950s, multiferroics—materials in which magnetic and ferroelectric order coexist—have undergone tremendous development^{3,4}. This is partly due to the desire to control magnetism by using electric rather than magnetic fields. However, any such magnetoelectric correlation must be permitted by the order and symmetry of the material. Particularly complex magnetoelectric coupling may therefore require the presence of several, often multidimensional, order parameters; for example, the coexistence of a large magnetization and polarization in hybrid improper ferroelectrics involves three order parameters⁵. Even more parameters are required if an additional condition that the magnetization and polarization are parallel is introduced⁶. In addition to coupled magnetic and electric order, the interplay of so many order parameters could yield other valuable properties, which have yet to be discovered.

Here, we use the versatility that results from the large number of magnetic and electric order parameters to achieve inversion of an entire ferromagnetic or ferroelectric multi-domain pattern in a single step: a homogeneous field reverses the magnetization or polarization of each domain, but preserves the original domain pattern. To demonstrate the universal nature of such inversion, we select two materials with different properties—magnetoelectric Co₃TeO₆ and multiferroic Mn₂GeO₄. Using these materials, we demonstrate inversion of a ferromagnetic and a ferroelectric domain pattern, respectively, by imaging the domain structure using optical second-harmonic generation (SHG)^{7,8}. Analysis of the free energy reveals that in both compounds, one order parameter holds the memory of the domain structure and another determines its overall sign. The magnetoelectric inversion of domain patterns is one

of many imaginable examples of the as-yet-unexplored functionalities in systems with many complex order parameters.

Co₃TeO₆ forms monoclinic crystals (space group C2/c1'). Below 17.7 K, the magnetic order^{9–11} is defined by two propagation vectors, $\mathbf{k}_0 = (0, 0, 0)$ and $\mathbf{k}_{\perp 0} \approx (0, 0.5, 0.25)$, which lead to order parameters $\zeta(\mathbf{k}_0)$ and $\eta(\mathbf{k}_{\perp 0})$, respectively (Methods, Extended Data Fig. 1)^{12,13}. The magnetic point group symmetry is 2', which permits a spontaneous magnetization $M_{x,z}(\zeta(\mathbf{k}_0), \eta(\mathbf{k}_{\perp 0}))$ and a spontaneous polarization $P_y(\zeta(\mathbf{k}_0), \eta(\mathbf{k}_{\perp 0}))$. Experiments^{9,10,12} yield $M_{x,z} = 0.57 \times 10^{-3} \mu_B$ per Co²⁺, where μ_B is the Bohr magneton, but $P_y = 0$.

Mn₂GeO₄ forms orthorhombic crystals (space group Pnma1'). The multiferroic phase below 5.5 K is characterized by four magnetic order parameters associated with the coexisting magnetic propagation vectors $\mathbf{k}_0 = (0, 0, 0)$ and $\mathbf{k}_{\perp 0} = (\pm 0.136, \pm 0.211, 0)$. Two order parameters, $X_1(\mathbf{k}_0)$ and $X_3(\mathbf{k}_0)$, describe commensurate antiferromagnetic and ferromagnetic contributions, respectively, while two others, $M^{D1}(\mathbf{k}_{\perp 0})$ and $M^{D2}(\mathbf{k}_{\perp 0})$, describe incommensurate spiral components^{6,14,15}. The magnetic point group symmetry is 2, and a spontaneous magnetization $M_z \propto X_3(\mathbf{k}_0)$ and a magnetically induced electric polarization $P_z \propto M^{D1,2}(\mathbf{k}_{\perp 0})$ coexist (Methods, Extended Data Fig. 2). Experiments^{5,16} yield $M_z = 7 \times 10^{-3} \mu_B$ per Mn²⁺ and $P_z = 6 \mu_C m^{-2}$.

We image the spatial distributions of domains by using SHG—that is, frequency doubling of light in a material⁷. The relationship between the polarizations of the incident and emitted light, at frequencies ω and 2ω , respectively, depends on the symmetry of the material. Because any type of ferroic order changes the point group symmetry, characteristic SHG contributions emerge that allow us to image the associated domain patterns⁸ with a resolution of about 1 μm. In particular, SHG detects the small spontaneous magnetization or polarization that is often associated with multiferroic materials (see Methods for details on the SHG coupling and experiment)⁴.

SHG spectra from a z-oriented Co₃TeO₆ sample (Fig. 1a) yield maxima at 2.56 eV and 2.65 eV from electronic transitions within the Co²⁺ (3d) band. The polarization of the SHG light and its presence below 17.4 K (Fig. 1b) are in line with coupling to $M_{x,z}$ (Methods). We use this SHG signal to image the ferromagnetic $M_{x,z}$ domain distribution in a zero-field-cooled z-oriented Co₃TeO₆ sample. Interference with a crystallographic SHG background signal reveals domains at $+M_{x,z}$ and $-M_{x,z}$ as regions of different brightness in Fig. 1c (Methods).

In Fig. 2 we show the evolution of an $M_{x,z}$ domain structure for a magnetic field H_y , sweeping $\mu_0 H_y$ across the range -2.4 T to $+2.4$ T. Because $H_y \perp M_{x,z}$ the field does not convert the $\pm M_{x,z}$ domains into a single-domain state. Zero-field cooling reveals many domains, whereas the application of $+2.4$ T yields a simplified pattern with only a few dominant domains (Fig. 2b). When the field is reversed, the number of domains increases at around 0 T (Fig. 2c). However, at -2.4 T we obtain a domain pattern that is nearly identical to that at $+2.4$ T (Fig. 1a), but with the brightness of each domain inverted (Fig. 1d). Apparently, $M_{x,z}$ is reversed in each individual domain, but without affecting the shape

¹Department of Materials, ETH Zurich, Zurich, Switzerland. ²Laboratory for Multiscale Materials Experiments, Paul Scherrer Institut, Villigen, Switzerland. ³Helmholtz-Institut für Strahlen- und Kernphysik, Universität Bonn, Bonn, Germany. ⁴Laboratory for Neutron Scattering and Imaging, Paul Scherrer Institut, Villigen, Switzerland. ⁵Department of Physics, Stockholm University, Stockholm, Sweden. ⁶Physique des Systèmes Complexes, Université de Picardie, Amiens, France. ⁷Institute of Materials Structure Science, High Energy Accelerator Research Organization (KEK), Tsukuba, Japan. ⁸Department of Advanced Materials Science, University of Tokyo, Kashiwa, Japan. ⁹Department of Multifunctional Materials, Karpov Institute of Physical Chemistry, Moscow, Russia. ¹⁰Institute for Chemical Technology and Analytics, Division of Structural Chemistry, TU Wien, Vienna, Austria. ¹¹Department of Materials Science and Engineering, Norwegian University of Science and Technology (NTNU), Trondheim, Norway. ¹²These authors contributed equally: N. Leo, V. Carolus. *e-mail: manfred.fiebig@mat.ethz.ch

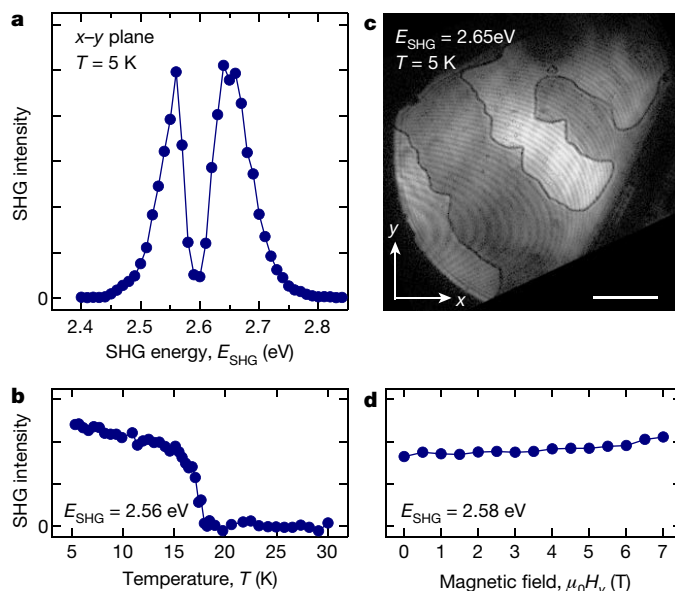


Fig. 1 | Probing ferromagnetism in Co_3TeO_6 by using SHG. **a**, SHG intensity spectrum at $T = 5\text{ K}$ for x -polarized frequency-doubled and y -polarized incident light (proportional to the nonlinear susceptibility component χ_{xyy}) on a z -oriented sample. Henceforth, photon energies at the intensity maxima at $E_{\text{SHG}} = 2.56\text{ eV}$ and $E_{\text{SHG}} = 2.65\text{ eV}$ are used. Data noise in all SHG measurements is shot noise of the digital camera. All measurements were reproduced multiple times. **b**, Temperature dependence of the χ_{xyy} -related SHG intensity. The signal is observed in the magnetoelectric phase only below 17.4 K . **c**, Distribution of ferromagnetic domains in a z -oriented Co_3TeO_6 sample. An SHG interference technique visualizes the $\pm M_{x,z}$ domains as regions with different brightness (Methods, Extended Data Fig. 3). Scale bar, $500\text{ }\mu\text{m}$. **d**, Dependence of the χ_{xyy} -related SHG intensity on a magnetic field H_y . μ_0 is the vacuum permeability. In contrast to the image in **c**, the SHG yield is independent of the domain state because the SHG interference technique that generates the contrast between opposite domain states in **c** is not applied. Thus, unperturbed by the domain state, **d** reveals the H_y dependence of the magnitude of $M_{x,z}$.

and distribution of the domains. We thus find a striking inversion of an entire inhomogeneous distribution of ferromagnetic domains by a homogeneous field.

The reversal occurs via intermittent formation and shifts of domain walls (Fig. 1c). This and the approximate H_y independence of the magnitude of $M_{x,z}$ (Fig. 1d) rule out the possibility that the brightness inversion is an optical artefact. Furthermore, the domain-wall mobility excludes the possibility that the protection of the domain pattern is caused by pinning effects. According to the magnetic-field dependence of the SHG interference shown in Fig. 1e, integrated over the range -3 T to $+3\text{ T}$ over two spots of about $500\text{ }\mu\text{m}$, the most substantial domain variations occur between -0.2 T and $+0.2\text{ T}$. The protection of the domain pattern at high fields is in stark contrast to its variability at low fields.

The inversion of the $M_{x,z}$ domain pattern by the homogeneous H_y field is resolved by a free-energy term that couples $M_{x,z}(\zeta(\mathbf{k}_0), \eta(\mathbf{k}_{\neq 0}))$ to H_y in a sign-sensitive way. An analysis of Landau invariants reveals the lowest-order term that enables such coupling as

$$F_{\text{inv}} \propto \mathcal{C}(\mathbf{k}_{\neq 0}) M_y(H_y) M_{x,z} \quad (1)$$

Here, $\mathcal{C}(\mathbf{k}_{\neq 0})$ is a product of the components of $\eta(\mathbf{k}_{\neq 0})$ that establishes the invariance of the free-energy contribution F_{inv} (see Methods for its derivation)¹⁷. Because a magnetic field H_y induces a proportional magnetization M_y and does not act on $\mathcal{C}(\mathbf{k}_{\neq 0})$, a reversal of $H_y \propto M_y$ entails reorientation of $M_{x,z}$ to retain $F_{\text{inv}} < 0$ for ground-state energy minimization. This sensitivity of the orientation of $M_{x,z}$ to H_y does not contradict the aforementioned near-insensitivity of the magnitude of $M_{x,z}$ to H_y , because these two properties originate from different coupling terms. Hence, the same order parameters that are responsible for magnetoelectric coupling in Co_3TeO_6 provide the basis for other intriguing cross-correlations, here the inversion of an entire ferromagnetic domain pattern.

To support our claim of generality for the domain-inversion behaviour, we now turn to Mn_2GeO_4 , a material that differs from Co_3TeO_6 in crystal structure as well as magnetic and electric order. The SHG spectrum of a z -oriented Mn_2GeO_4 platelet (Fig. 3a) yields a peak at 1.83 eV . The signal is present in the multiferroic phase below 5.5 K (Fig. 3b), implying coupling to M_z or P_z . Zero-field cooling resolves many domains and domain walls (Fig. 3c), but application of an electric field $E_z = 144\text{ kV cm}^{-1}$ transforms this phase into a single-domain state (Fig. 3d). By contrast, a magnetic field H_z above the coercive field leaves the sample in a multi-domain state (Fig. 4a). Therefore, we conclude that SHG couples to the spontaneous polarization P_z but not to the magnetization M_z .

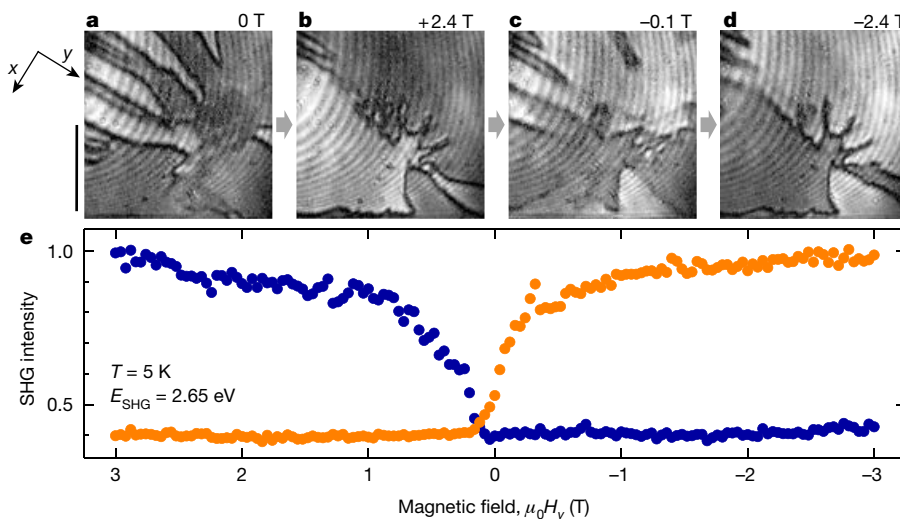


Fig. 2 | Inversion of the ferromagnetic domain pattern in Co_3TeO_6 . **a–d**, Sequentially taken SHG images of the $\pm M_{x,z}$ domain pattern on a z -oriented Co_3TeO_6 sample at the given magnetic fields H_y . Scale bar, $500\text{ }\mu\text{m}$. **e**, Dependence of the $M_{x,z}$ domain state on a magnetic field H_y . The domain-state-sensitive SHG interference (Methods) was measured on two spots of $500\text{ }\mu\text{m}$ diameter that lie in opposite domain states (blue and

orange data points) outside the area shown in **a–d**. Tuning the magnetic field between positive and negative values reverses the magnetization of each domain while the domain pattern remains intact. The interchange is mainly limited to the field interval -0.2 T to $+0.2\text{ T}$. The inversion progresses via transient formation and shifts of domains and domain walls.

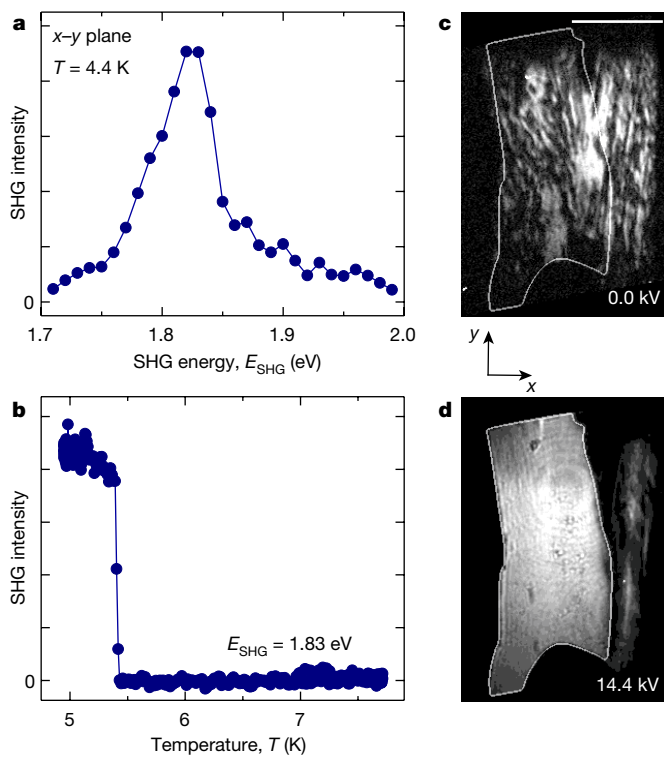


Fig. 3 | Probing ferroelectricity in Mn_2GeO_4 by using SHG. **a**, SHG intensity spectrum at $T = 4.4$ K for z -polarized frequency-doubled and y -polarized incident light (proportional to the nonlinear susceptibility component χ_{zyy}) on a z -oriented and slightly tilted sample. The peak at $E_{\text{SHG}} = 1.83$ eV identifies the photon energy that we used for the subsequent measurements. **b**, Temperature dependence of the χ_{zyy} -related SHG intensity after subtracting temperature-independent background contributions from the surface and higher-order-multipole SHG. A signal is observed in the multiferroic phase below 5.5 K. **c**, The domain structure of a zero-field-cooled sample reveals an inhomogeneous distribution of bright and dark regions, indicating a large number of domains and domain walls. Scale bar, 500 μm . **d**, After applying an electric field $E_z = 144$ kV cm^{-1} , the SHG image exhibits homogeneous brightness, indicating a ferroelectric single-domain state in the region in which the transparent electrodes overlap (white outline).

The evolution of the ferroelectric P_z domains with an applied magnetic field H_z is shown in Fig. 4. First, the sample is field-cooled at $H_z = -230$ mT, which induces a single-domain $-M_z$ state⁶, but, according to the SHG image at $H_z = 0$ in Fig. 4a, retains a ferroelectric multi-domain state. As H_z is increased towards positive values, additional ferroelectric domain walls are formed and move across the sample. At +150 mT we obtain a ferroelectric domain pattern that is nearly identical to the one observed initially, except that P_z in each domain is reversed (Fig. 4h). Increasing H_z yields no additional change, and further field cycles corroborate the reproducibility of the local P_z inversion without changes to the domain pattern.

We thus encounter a situation for the ferroelectric order in Mn_2GeO_4 that is analogous to the ferromagnetic order in Co_3TeO_6 . The order in each domain is reversed, but the domain pattern is unchanged—a phenomenon that goes beyond the magnetoelectric switching between single-domain states discussed so far^{6,18}. To explain the domain inversion in Mn_2GeO_4 , we require a sign-sensitive coupling between P_z and H_z . An analysis of Landau invariants involving the order parameters $X_{1,3}(\mathbf{k}_0)$ and $M^{D1,2}(\mathbf{k}_{\pm 0})$ reveals

$$F_{\text{inv}} \propto \mathcal{C}(\mathbf{k}_0) M_z(H_z) P_z \quad (2)$$

with $\mathcal{C}(\mathbf{k}_0) \propto X_1(\mathbf{k}_0)$ (see Methods for the Landau theory developed by Harris)^{14,15}. Cooling in a magnetic field H_z sets a uniform magnetization $M_z \propto H_z$. This still allows a $\pm P_z$ domain distribution because $F_{\text{inv}} < 0$ can be retained by the sign of $\mathcal{C}(\mathbf{k}_0)$. Because $\mathcal{C}(\mathbf{k}_0)$ remains invariant under the application of H_z , the free energy is minimized only if P_z switches simultaneously with the reversal of $M_z \propto H_z$. Thus, in two different materials, we have demonstrated the inversion of ferromagnetic or ferroelectric domain patterns with a single sweep of a homogeneous, non-conjugated field.

To generalize our two examples, Co_3TeO_6 and Mn_2GeO_4 , we express the inversion using a trilinear coupling term in the free energy:

$$F_{\text{inv}} \propto \hat{I} \hat{S}(H_S) \hat{O} \quad (3)$$

The effect of this coupling term is illustrated in Fig. 5. \hat{O} represents the experimentally observed domain distribution (magnetization or polarization). \hat{I} contains the memory of the domain pattern that is preserved, because it remains invariant under the applied field H_S . By contrast, $\hat{S} = \hat{S}(H_S)$ can be switched by H_S . For $H_S \ll 0$, \hat{S} is in a single-domain -1 state and the observable \hat{O} assumes the domain structure of \hat{I} . When

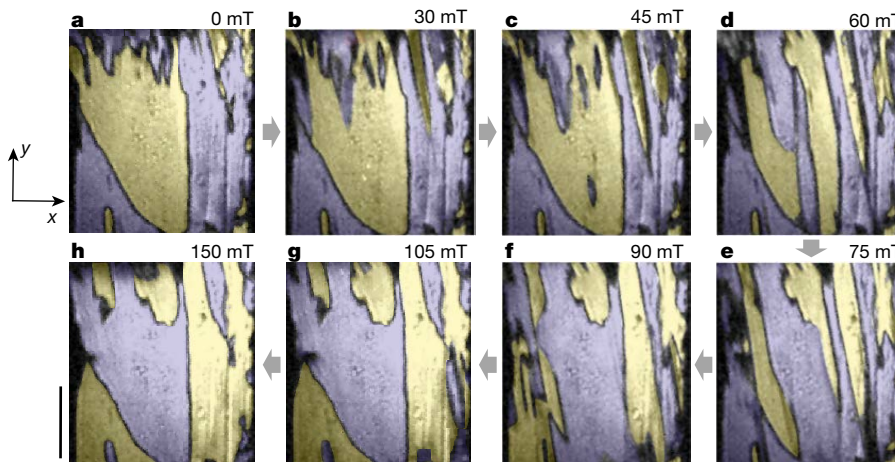


Fig. 4 | Inversion of the ferroelectric domain pattern in Mn_2GeO_4 . Sequentially taken SHG images of $\pm P_z$ domains on a z -oriented Mn_2GeO_4 sample at the given magnetic fields H_z (see Extended Data Fig. 4 for the corresponding experiment on an x -oriented sample). Because of the small SHG contrast, domain states at $+P_z$ and $-P_z$ are highlighted by yellow and purple shading, respectively. Scale bar, 500 μm . **a**, After field-cooling

at $\mu_0 H_z = -230$ mT, followed by setting $\mu_0 H_z = 0$, the sample is in a ferroelectric multi-domain state. **b–g**, Application of $\mu_0 H_z > 0$ leads to additional nucleation and movement of domain walls. **h**, In the saturated state at +150 mT, almost the same domain distribution as in **a** (after the original field cooling) is obtained, but with the orientation of the ferroelectric polarization reversed in each domain.

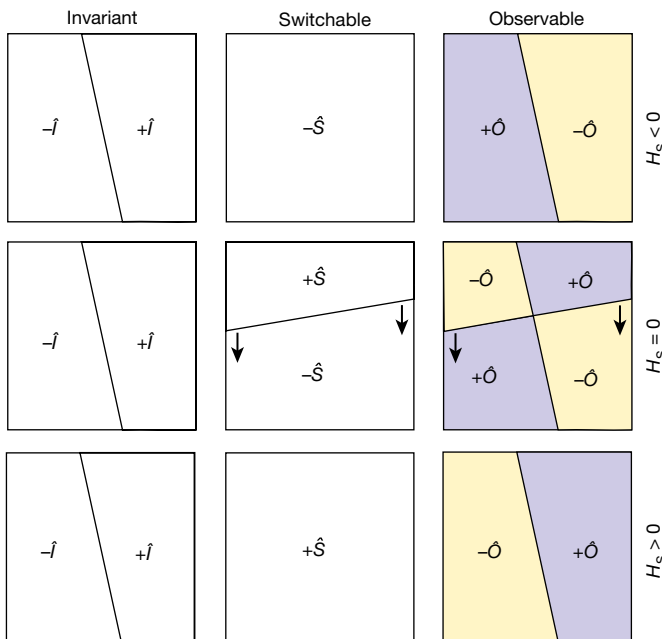


Fig. 5 | Multi-order-parameter model for domain-pattern inversion.

\hat{O} represents the domain distribution observed in the experiment: magnetization for Co_3TeO_6 or polarization for Mn_2GeO_4 (reflected in Fig. 4 by the colour shading). \hat{I} contains the memory of the domain pattern to be preserved in \hat{O} . Then, $\hat{S} = \hat{S}(H_s)$ is switched between a uniform -1 state and a uniform $+1$ state by ramping the applied field H_s between its maximum negative and positive values. Reversal of \hat{S} by H_s entails reversal of \hat{O} to minimize the free energy in equation (3), because \hat{I} is immutable under H_s . Thus, the field H_s reverses the orientation of the order parameter of \hat{O} in each domain, but preserves the domain structure. When crossing $H_s = 0$, \hat{S} enters a transient multi-domain state with the nucleation and propagation of $(-1)/(+1)$ domain walls. This leads to the observed transient increase in the number of domain walls and their propagation in \hat{O} . The propagation of \hat{O} and \hat{S} domain walls is indicated by arrows. The sample-specific expressions for \hat{I} , \hat{S} and \hat{O} are listed in Table 1.

crossing $H_s = 0$, \hat{S} becomes transiently multi-domain; consequently, new domain walls appear in \hat{O} and propagate across the sample. For $H_s \gg 0$, \hat{S} resumes the single-domain state (now $+1$) and the initial domain configuration of \hat{I} is recovered in \hat{O} , albeit with the orientation of \hat{O} reversed in each domain because of the H_s -controlled sign change of \hat{S} . The deterministic interchange of domain patterns expressed by equation (3) distinguishes our experiment from the non-deterministic switching between multi-domain patterns found, for example, in partial ferroics¹⁹. The expressions for \hat{I} , \hat{S} and \hat{O} are sample-specific (Table 1, Methods); however, supported by the independence of our two chosen examples, Co_3TeO_6 and Mn_2GeO_4 , we argue that the inherent complexity of any system that is characterized by several multidimensional order parameters at different magnetic propagation vectors \mathbf{k} makes their widespread existence and coupling likely.

Multiferroics are ideal for domain-pattern inversion because of the inherent order-parameter complexity required to achieve strongly coupled magnetic and electric order. CoCr_2O_4 or, at room temperature, hexaferrites may be candidates for such inversion^{18,20–22}. Aside from symmetry, material parameters need to be satisfied. Coupling between

\hat{I} and \hat{S} beyond that in equation (3), such as by strain, must be small. Furthermore, the \hat{I} walls must not pin the motion of the \hat{S} walls during the inversion. On the other hand, an alternative domain-inversion mechanism to the one presented here may be entirely rooted in domain-wall coupling and be absent within the domains. GdFeO_3 or the hexagonal manganites are possible candidates for this behaviour^{18,23}. These other examples confirm the idea that we have presented only one of many conceivable examples of order-parameter coupling beyond magnetoelectric phase control; many other multi-order-parameter functionalities remain to be explored.

Online content

Any methods, additional references, Nature Research reporting summaries, source data, statements of data availability and associated accession codes are available at <https://doi.org/10.1038/s41586-018-0432-4>

Received: 13 February; Accepted: 27 June 2018;

Published online 22 August 2018.

1. Hansen, C. H. *Understanding Active Noise Cancelation* (Spon Press, New York, 2001).
2. Jung, B. A. & Weigel, M. Spin echo magnetic resonance imaging. *J. Magn. Reson. Imaging* **37**, 805–817 (2013).
3. Wang, K. F., Liubab, J.-M. & Renc, Z. F. Multiferroicity: the coupling between magnetic and polarization orders. *Adv. Phys.* **58**, 321–448 (2009).
4. Fiebig, M., Lottermoser, Th., Meier, M. & Trassin, M. The evolution of multiferroics. *Nat. Rev. Mater.* **1**, 16046 (2016).
5. Benedek, N. A. & Fennie, C. J. Hybrid improper ferroelectricity: a mechanism for controllable polarization-magnetization coupling. *Phys. Rev. Lett.* **106**, 107204 (2011).
6. White, J. S. et al. Coupling of magnetic and ferroelectric hysteresis by a multicomponent magnetic structure in Mn_2GeO_4 . *Phys. Rev. Lett.* **108**, 077204 (2012).
7. Pershan, P. S. Nonlinear optical properties of solids: energy considerations. *Phys. Rev.* **130**, 919–929 (1963).
8. Fiebig, M., Pavlov, V. V. & Pisarev, R. V. Second-harmonic generation as a tool for studying electronic and magnetic structures of crystals. *J. Opt. Soc. Am. B* **22**, 96–118 (2005).
9. Singh, H. et al. Short range ferromagnetic, magneto-electric, and magneto-dielectric effect in ceramic Co_3TeO_6 . *J. Appl. Phys.* **119**, 044104 (2016).
10. Hudl, M. et al. Complex magnetism and magnetic-field-driven electrical polarization in Co_3TeO_6 . *Phys. Rev. B* **84**, 180404 (2011).
11. Li, W.-H. et al. Interplay between the magnetic and electric degrees of freedom in multiferroic Co_3TeO_6 . *Phys. Rev. B* **85**, 094431 (2012).
12. Tolédano, P. et al. First-order multi-k phase transitions and magnetoelectric effects in multiferroic Co_3TeO_6 . *Phys. Rev. B* **85**, 214439 (2012).
13. Ivanov, S. A. et al. Temperature-dependent multi-k magnetic structure in multiferroic Co_3TeO_6 . *Mater. Res. Bull.* **47**, 63–72 (2012).
14. Honda, T. et al. Coupled multiferroic domain switching in the canted conical spin spiral system Mn_2GeO_4 . *Nat. Commun.* **8**, 15457 (2017).
15. Harris, A. B. Identifying Landau order parameters and their transformation properties for complex multiferroics: the case of Mn_2GeO_4 . *Phys. Rev. B* **96**, 054422 (2017).
16. Honda, T., Ishiguro, Y., Nakamura, H., Wakabayashi, Y. & Kimura, T. Structure and magnetic phase diagrams of multiferroic Mn_2GeO_4 . *J. Phys. Soc. Jpn.* **81**, 103703 (2012).
17. Carolus, V. *Topography and Manipulation of Magnetic Domains in Cobalt Tellurite*. PhD thesis, Bonn Univ. (2014).
18. Tokunaga, Y. et al. Composite domain walls in a multiferroic perovskite ferrite. *Nat. Mater.* **8**, 558–562 (2009).
19. Aizu, K. Possible species of ferromagnetic, ferroelectric, and ferroelastic crystals. *Phys. Rev. B* **2**, 754–772 (1970).
20. Yamasaki, Y. et al. Magnetic reversal of the ferroelectric polarization in a multiferroic spinel oxide. *Phys. Rev. Lett.* **96**, 207204 (2006).
21. Tokunaga, Y. et al. Multiferroic M-type hexaferrites with a room-temperature conical state and magnetically controllable spin helicity. *Phys. Rev. Lett.* **105**, 257201 (2010).
22. Zhai, K. et al. Giant magnetoelectric effects achieved by tuning spin cone symmetry in Y-type hexaferrites. *Nat. Commun.* **8**, 51 (2017).
23. Fiebig, M., Lottermoser, Th., Fröhlich, D., Goltsev, A. V. & Pisarev, R. V. Observation of coupled magnetic and electric domains. *Nature* **419**, 818–820 (2002).

Table 1 | Material-specific terms and order parameters

Material	\hat{I}	$\hat{S}(H_s)$	\hat{O}
Co_3TeO_6	$C(\mathbf{k}_0) \mapsto \eta$	$M_y(H_y) \mapsto \zeta$	$M_{x,z} \mapsto \eta, \zeta$
Mn_2GeO_4	$C(\mathbf{k}_0) \mapsto X_1$	$M_z(H_z) \mapsto X_3$	$P_z \mapsto X_1, X_3$

The table shows the values of the terms \hat{I} , $\hat{S}(H_s)$ and \hat{O} in equations (1) and (2) and their relationship to the order parameters of Co_3TeO_6 and Mn_2GeO_4 , respectively. See Methods for explicit definitions of the order parameters and of \hat{I} , \hat{S} and \hat{O} .

Acknowledgements J.S.W. thanks the SNSF for support via grant 200021_153451. M.K. acknowledges financial support by SNSF grant 200021_165855. S.A.I. acknowledges financial support from the Russian Foundation for Basic Research. M.F. is grateful for support by SNSF grant 200021_178825. We thank B. Harris for a discussion of the Landau theory for Mn_2GeO_4 in refs^{14,15}, prior to their publication.

Reviewer information *Nature* thanks V. Gopalan and the other anonymous reviewer(s) for their contribution to the peer review of this work.

Author contributions All authors contributed to the discussion and interpretation of the experiment and to the completion of the manuscript. N.L. and V.C. performed the experiments. N.L., J.S.W. and M.K. interpreted the domain-pattern inversion on the basis of a previously published^{14,15} Landau-theoretical description of the order parameters. V.C., M.H. and P.T. performed the Landau-theoretical analysis of the Co₃TeO₆ experiments. M.W. grew single crystals of Co₃TeO₆ and S.A.I. analysed their stoichiometry and structure. T.H. and T.K. prepared single crystals of Mn₂GeO₄. Th.L. supervised the experiments on Co₃TeO₆. D.M. and M.F. initiated the experiment and supervised the work.

Competing interests The authors declare no competing interests.

Additional information

Extended data is available for this paper at <https://doi.org/10.1038/s41586-018-0432-4>.

Reprints and permissions information is available at <http://www.nature.com/reprints>.

Correspondence and requests for materials should be addressed to M.F.

Publisher's note: Springer Nature remains neutral with regard to jurisdictional claims in published maps and institutional affiliations.

METHODS

Sample preparation. Single crystals of Co_3TeO_6 were grown by using the chemical vapour transport method. The chemical composition and the homogeneity of the crystals were analysed by using energy-dispersive spectroscopy using a JEOL 840A scanning electron microscope and INCA 4.07 (Oxford Instruments) software. For the sample prepared for diffraction measurements, the cation content was also determined by inductively coupled plasma atomic emission spectroscopy performed with an ARL Fusions 3410 spectrometer. According to the elemental analysis done on 20 different crystallites, the stoichiometry is $\text{Co}_{2.98(3)}\text{Te}_{1.02(3)}$ and $\text{O}_{5.99(2)}$ (oxygen value derived from iodometric titration). A room-temperature X-ray diffraction pattern on a Bruker D8 Advance diffractometer yielded $a = 14.8117(4)$ Å, $b = 8.8392(3)$ Å, $c = 10.3587(4)$ Å and $\beta = 94.84(1)$ ° as monoclinic unit-cell parameters. Single crystals of Mn_2GeO_4 were grown by using the floating-zone method as described elsewhere^{13,16}. All crystals were oriented by using Laue diffraction, cut, lapped to a thickness of about 50 µm and polished from both sides with silica slurry.

Second-harmonic generation (SHG). SHG denotes the doubling of the frequency of a light wave in a material. Restricting ourselves to the (leading) electric-dipole approximation, SHG is described by⁷ $P_i(2\omega) \propto \chi_{ijk} E_j(\omega) E_k(\omega)$. Here, $E_{j,k}(\omega)$ denote the electric-field components of the incident light and $P_i(2\omega)$ is the induced *i*-polarized nonlinear polarization that acts as source for the emitted SHG wave at intensity $I \propto |\mathbf{P}(2\omega)|^2$. The nonlinear susceptibility tensor χ characterizes the symmetry of the host material²⁴. Because ferroic order changes the point group symmetry, it leads to the emergence of ordering-induced contributions to the SHG yield, which we use to probe this order with spectral and spatial resolution⁸. Domain states with opposite orientation of the order parameter differ in the sign of the corresponding SHG light waves, equivalent to a 180° phase shift. This allows us to image opposite domain states as regions of different brightness via an interference technique²⁵ illustrated in Extended Data Fig. 3. The detailed set-up for transmission SHG experiments is described elsewhere⁸.

SHG experiments on Co_3TeO_6 . The 2' magnetic point group symmetry of the phase below 17.4 K permits a set of time-reversal-symmetry-violating ('c-type') electric-dipole SHG contributions proportional to $M_{x,z}$. According to symmetry tables²⁴, this set includes 14 tensor components. We observed all of these and verified that they display the same $M_{x,z}$ -related temperature dependence as in Fig. 1b. In turn, no other tensor components yielding an order parameter coupling were identified, consistent with the 2' point group symmetry and the earlier observation that P_y , although allowed, is measured as zero^{9,10,12}. According to theory, the coupling to the magnetic order parameter by SHG is typically the result of the low-symmetry environment of the paramagnetic ions in combination with spin-orbit interaction⁸. Experiments were performed in a liquid-helium-operated split-coil magnetic-field cryostat on a *z*-cut sample with light in perpendicular incidence. We used light pulses of 5 ns emitted from an optical parametric oscillator pumped by the frequency-tripled light emitted from a Nd:YAG laser. Superposition of the SHG wave from the χ_{xyy} component with a constant crystallographic SHG reference contribution from the χ_{yyy} component was used for the aforementioned interference technique that identifies opposite domain states by their different brightness²⁵.

SHG experiments on Mn_2GeO_4 . The 2 point group symmetry of the multiferroic phase below 5.5 K allows a set of time-reversal-symmetry-conserving ('i-type') electric-dipole SHG contributions proportional to P_z . This set includes 13 components²⁴, from which we selected χ_{zyy} and χ_{yyz} . Experiments were performed on a *z*-cut sample onto which transparent electrodes were sputtered to apply large electric fields. To access the *z*-polarized SHG contribution in χ_{zyy} , the sample was tilted with respect to the direction of the incident light. In addition, we show experiments for χ_{yyz} on an *x*-cut sample in Extended Data Fig. 4. We used light pulses of 120 fs emitted from an optical parametric amplifier pumped by an amplified Ti:sapphire laser system. Destructive interference of SHG waves from opposite $\pm P_z$ domain states at the position of the domain walls reveals the domain boundaries as black lines meandering through the SHG image²⁶. These are used to identify the ferroelectric domain pattern.

Landau theory for the low-temperature phase of Co_3TeO_6 . Here we provide the link between our qualitative treatment of the propagation vectors, order parameters and invariants that describe the magnetoelectric order of Co_3TeO_6 and the full group-theoretical derivation; see also refs^{12,17} for the latter. Using the notation of ref.¹², the phase of Co_3TeO_6 below 17.4 K is characterized by two magnetic order parameters associated with the coexisting magnetic modulations vectors $\mathbf{k}_0 = \mathbf{k}_2 = (0, 0, 0)$ and $\mathbf{k}_{\neq 0} = \mathbf{k}_3 \approx (0, 0.5, 0.25)$ (ref.¹³). \mathbf{k}_0 is associated with the

one-dimensional magnetic order parameter $\zeta(\mathbf{k}_0)$ and from the one-dimensional little group of the four-armed star of $\mathbf{k}_{\neq 0}$ we can construct the four-dimensional order parameter $\eta(\mathbf{k}_{\neq 0}) = (\rho_1 e^{i\theta_1}, \rho_1 e^{-i\theta_1}, \rho_2 e^{i\theta_2}, \rho_2 e^{-i\theta_2})$ (ref.¹²). The latter is simplified by assuming $\rho_1 = \rho_2 = \rho_e$ and $\theta_1 = \theta_2 = \theta_e$ because of the (approximate¹¹) commensurability of $\mathbf{k}_{\neq 0}$. The coexisting antiferromagnetic order parameters $\zeta(\mathbf{k}_0)$ and $\eta(\mathbf{k}_{\neq 0})$ yield the magnetic point group symmetry 2', which permits a spontaneous magnetization $M_{x,z} \propto \zeta \rho_e^4 \cos(4\theta_e)$ and a spontaneous electric polarization $P_y \propto \zeta^2 \rho_e^4 \cos(4\theta_e)$. However, the latter was not detected at zero magnetic field, which indicates that Co_3TeO_6 is a magnetoelectric rather than a multiferroic compound^{10,12}.

To explain the inversion of the $M_{x,z}$ domains under the application of a magnetic field H_y , we require a coupling connecting $M_{x,y}(\zeta(\mathbf{k}_0), \eta(\mathbf{k}_{\neq 0}))$ and $M_y(H_y)$ in a sign-sensitive way that complies with the invariance of the free energy under the symmetry operations of the parent phase. In particular, translational invariance poses the following restrictive constraint: for order parameters at incommensurate propagation vectors, here $\mathbf{k}_{\neq 0}$, translational invariance can be retained only if these order parameters enter the free energy in even powers. However, the even power preserves time-reversal symmetry so that another—time-reversal-symmetry-violating—order parameter associated with a commensurate propagation vector, here \mathbf{k}_0 , has to enter the trilinear term in equation (1).

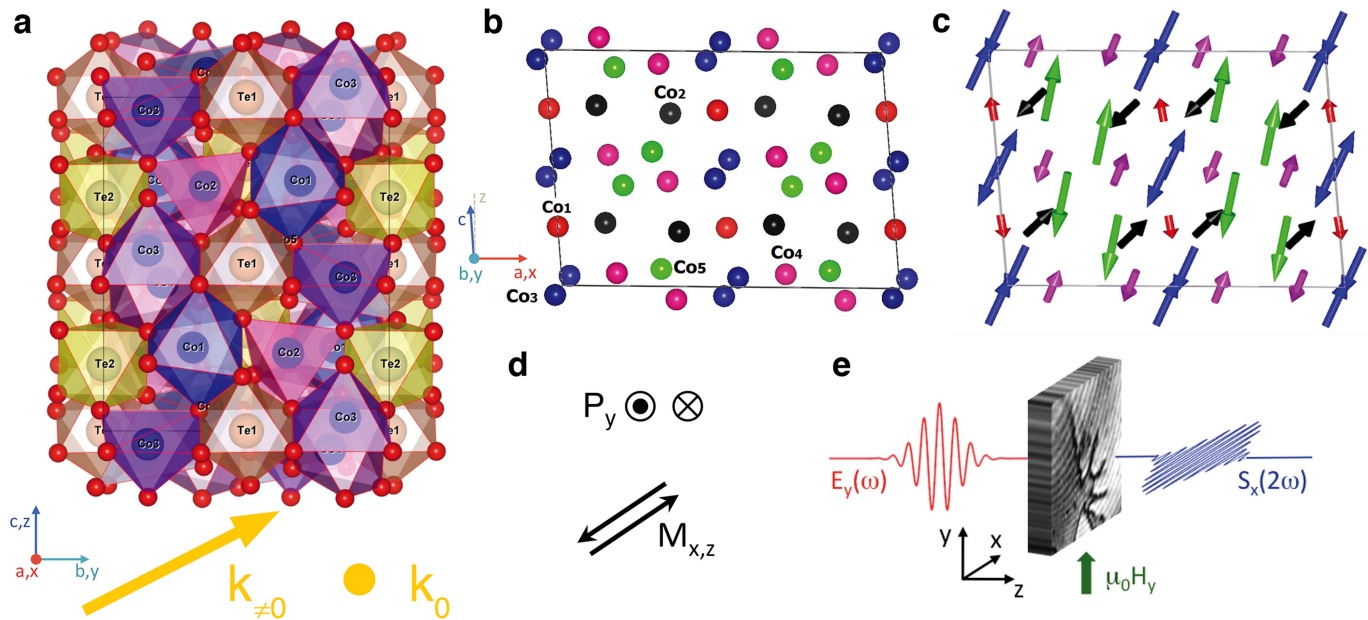
Using the transformation behaviour of the order parameters $\eta(\mathbf{k}_{\neq 0})$ and $\zeta(\mathbf{k}_0)$, described by the irreducible representations¹² $\tau_1(\mathbf{k}_{\neq 0})$ and $\Gamma_4(\mathbf{k}_{\neq 0})$, respectively, we find $F_{\text{inv}} \propto \sigma_4(\mathbf{k}_{\neq 0}) \zeta(\mathbf{k}_0) M_y(H_y)$ as the simplest coupling term to the free energy. Here, $\sigma_4(\mathbf{k}_{\neq 0}) = [\rho_1^4 \sin(4\theta_e) - \rho_2^4 \sin(4\theta_e)]$ is a fourth-order product of the elements of $\eta(\mathbf{k}_{\neq 0})$, which transforms like the irreducible representation $\tau_1(\mathbf{k}_{\neq 0})$ and retains the invariance of F_{inv} . Because $M_{x,z} \propto \zeta(\mathbf{k}_0)$, we have thus reconstructed the expression in equation (1), finding $C(\mathbf{k}_{\neq 0}) = \sigma_4 / [\rho_e^4 \cos(4\theta_e)]$. Note that $\sigma_4(\mathbf{k}_{\neq 0})$ is non-zero only if $\mathbf{k}_{\neq 0}$ is incommensurate so that the degeneracy of ρ_e and θ_e is lifted (that is, $\rho_1 \neq \rho_2$ and $\theta_1 \neq \theta_2$). A small incommensurate modulation was indeed observed¹¹ in Co_3TeO_6 , but is usually neglected because of the smallness of this correction¹². However, in the domain-inversion mechanism, this correction generates the leading-order coupling term.

Landau theory for the multiferroic phase of Mn_2GeO_4 . Here we provide the link between the qualitative treatment of the propagation vectors, order parameters and invariants that describe the magnetoelectric order of Mn_2GeO_4 and the full group-theoretical derivation; see also refs^{14,15} for the latter. Using the notation of refs^{14,15}, the multiferroic phase of Mn_2GeO_4 below 5.5 K is characterized by four magnetic order parameters associated with the coexisting magnetic modulation vectors $\mathbf{k}_0 = \mathbf{Q}_c = (0, 0, 0)$ and $\mathbf{k}_{\neq 0} = \mathbf{Q}_{ic} = (\pm 0.136, \pm 0.211, 0)$. The two one-dimensional order parameters related to $\mathbf{k}_{\neq 0}$ are X_1 and X_3 . From the two-dimensional little group of the four-armed star of $\mathbf{k}_{\neq 0}$ we can construct two four-dimensional magnetic order parameters M_Q^{D1} and M_Q^{D2} with $M_Q^{Di} = (M_{QA}^{Di}, M_{QB}^{Di}, M_{QA}^{Di*}, M_{QB}^{Di*})$ and $i = 1, 2$. Here A and B refer to the two possible directions of the magnetic propagation vector $\mathbf{k}_{\neq 0}$. The corresponding magnetic point group^{6,14–16} is 2. Antiferromagnetic components proportional to $X_1(\mathbf{k}_0)$ and a spontaneous magnetization $M_z \propto X_3(\mathbf{k}_0)$ coexist with a spontaneous electric polarization $P_z \propto A_{ic} - B_{ic}$ so that $P_z \parallel M_z$ (corresponding to the term U in refs^{14,15}). Here, $J_{ic} = M_Q^{D1} M_Q^{D2*} - M_Q^{D2} M_Q^{D1*}$ for $J = A, B$.

For the domain inversion, a sign-sensitive coupling of $P_z(\mathbf{k}_{\neq 0})$ to H_z , and thus $M_z(H_z)(\mathbf{k}_0)$, is required. The lowest-order contribution that permits this is $F_{\text{inv}} \propto X_1 X_3 (A_{ic}^2 - B_{ic}^2) \propto X_1 (A_{ic} + B_{ic}) M_z P_z$. This reconstructs the expression in equation (2), yielding $C(\mathbf{k}_0) = X_1 (A_{ic} + B_{ic})$, and corresponds to the term W in refs^{14,15}. Note that $C(\mathbf{k}_0)$ contains contributions associated with \mathbf{k}_0 and $\mathbf{k}_{\neq 0}$. However, the term $A_{ic} + B_{ic} \propto \mathbf{k}_{\neq 0}$ merely retains the correct symmetry of the coupling, whereas $X_1(\mathbf{k}_0)$ holds the domain structure that determines the parallel or antiparallel orientation of M_z and P_z such that $F_{\text{inv}} < 0$ (refs^{14,15}). Reversal of the field H_z reverses the magnetization M_z . Microscopically, this swaps the orientation of the Mn^{2+} spin cones (Extended Data Fig. 2), corresponding to an exchange of A_{ic} and B_{ic} . Because $P_z \propto A_{ic} - B_{ic}$, this simultaneously reverses the direction of polarization^{14,15}.

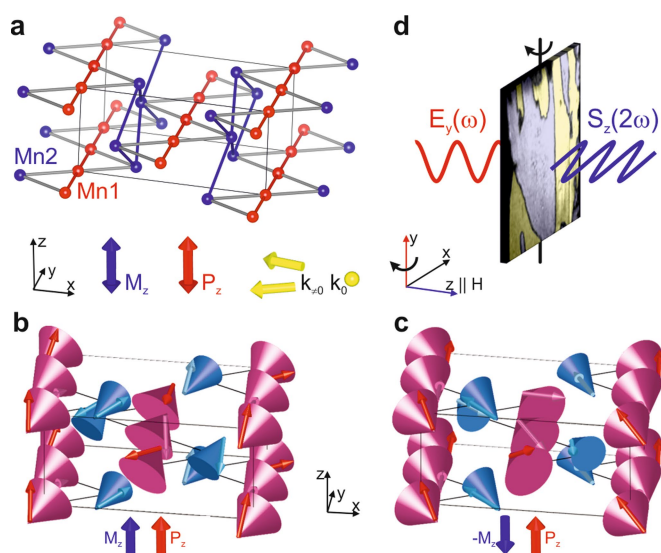
Data availability. The data that support the findings of this study are available from the corresponding author on reasonable request.

24. Birss, R. R. *Symmetry and Magnetism* Ch. 2, 3 (North-Holland, Amsterdam, 1966).
25. Leute, S., Lottermoser, Th. & Fröhlich, D. Nonlinear spatially resolved phase spectroscopy. *Opt. Lett.* **24**, 1520–1522 (1999).
26. Fiebig, M., Fröhlich, D., Lottermoser, Th. & Maat, M. Probing of ferroelectric surface and bulk domains in ferroelectric $RMnO_3$ ($R = Y, Ho$) by second harmonic generation. *Phys. Rev. B* **66**, 144102 (2002).

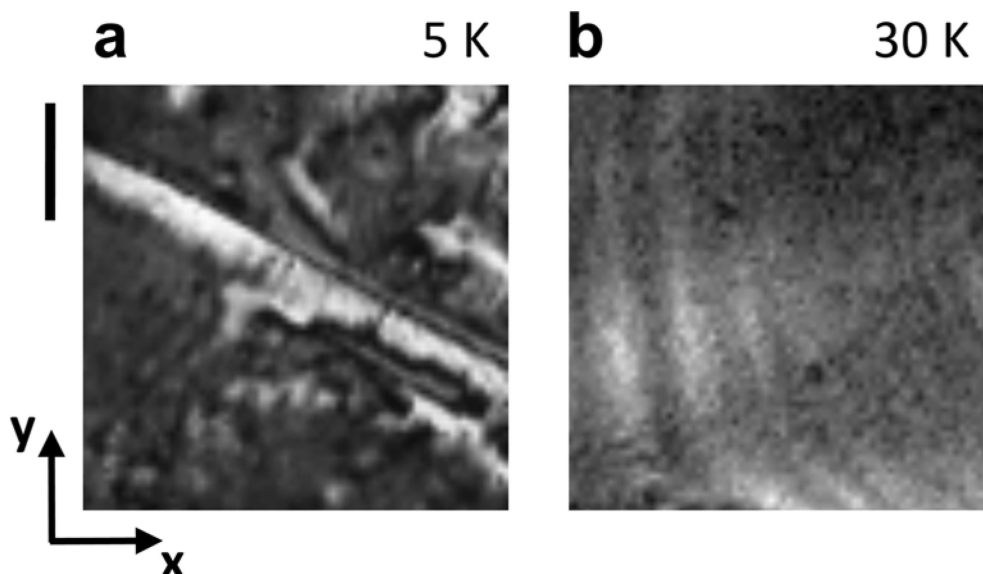


Extended Data Fig. 1 | Crystallographic structure, magnetic structure and optical excitation of Co_3TeO_6 . **a**, Three-dimensional view of the crystallographic unit cell along the x axis in relation to the magnetic propagation vectors k_0 and $k_{\neq 0}$. **b**, Section of the unit cell in the x - z plane showing the location of the paramagnetic Co^{2+} ions in five different positions. **c**, Magnetic moments of the Co^{2+} ions shown in **b**. **d**, Orientation of the spontaneous magnetization $M_{x,z}$

and the electric polarization P_y . The latter is symmetry-allowed as spontaneous polarization, yet observed only as a magnetic-field-induced contribution^{9,10,12}. **e**, Geometry of the SHG transmission experiment with light at ω and 2ω propagating along the z axis, probing a z -cut Co_3TeO_6 platelet in perpendicular incidence. The sample is exposed to a magnetic field H_y .

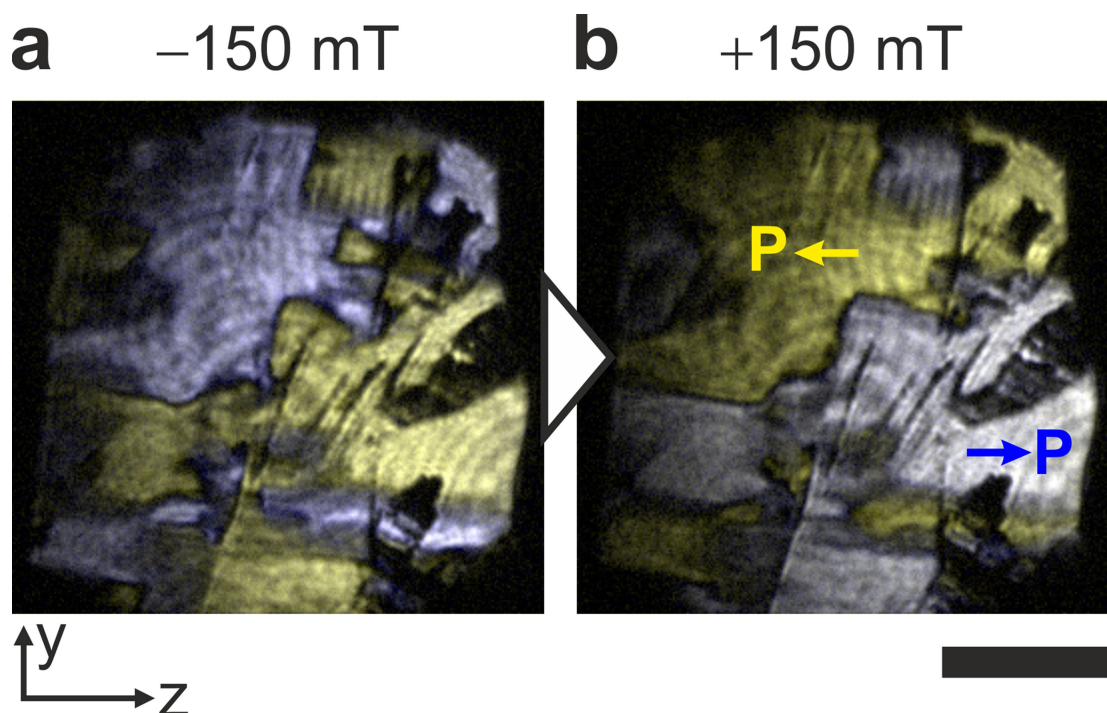


Extended Data Fig. 2 | Crystallographic structure, magnetic structure and optical excitation for Mn_2GeO_4 . **a**, Top, three-dimensional view of the crystallographic unit cell showing the location of the paramagnetic Mn^{2+} ions on the different positions ‘Mn1’ and ‘Mn2’. Bottom, orientation of the spontaneous magnetization M_z and spontaneous polarization P_z in relation to the magnetic propagation vectors k_0 and $k_{\neq 0}$. **b**, Conically modulated order of the magnetic Mn^{2+} moments on the Mn1 and Mn2 positions. Bold arrows show the resulting spontaneous magnetization M_z and spontaneous polarization P_z . **c**, As in **b**, but for reversed spontaneous magnetization. **d**, Geometry of the SHG transmission experiment with light incident onto a z -cut Mn_2GeO_4 platelet. The sample is exposed to a magnetic field H_z and it is rotated around the y axis so that the optical excitation does not occur in perpendicular geometry.



Extended Data Fig. 3 | SHG coupling and interference. **a**, Spatially resolved SHG image of a z -cut Co_3TeO_6 sample. At 5 K, a magnetization-induced SHG contribution from χ_{xyy} and a crystallographically induced SHG contribution from χ_{yyy} are present. The χ_{xyy} light waves from opposite domains differ by 180° because of proportionality to the spontaneous magnetization $\pm M_{x,z}$. The phase of the χ_{yyy} wave is homogeneous across the sample because it is blind to the magnetic order.

Constructive ($+M_{x,z}$) and destructive ($-M_{x,z}$) interference of the magnetic and crystallographic SHG contributions therefore yields the opposite magnetic domain states as regions of different brightness. **b**, Image of the same region as in **a** but at 30 K, at which $M_{x,z} = 0$ so that only the homogeneous crystallographic SHG contribution from χ_{yyy} remains. Scale bar, 500 μm .



Extended Data Fig. 4 | Inversion of the ferroelectric domain pattern in an x -cut Mn_2GeO_4 sample. Sequentially taken SHG images of $\pm P_z$ domains on an x -oriented Mn_2GeO_4 sample at the given magnetic fields H_z . The same domain-inversion behaviour as for the z -cut sample in Fig. 4

is observed. Because of the small SHG contrast, opposite polarization domain states are highlighted by colour shading. Darker or black areas are caused by cracks and pores in the Mn_2GeO_4 sample. Scale bar, $500 \mu\text{m}$.

Reverse weathering as a long-term stabilizer of marine pH and planetary climate

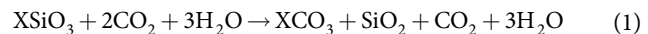
Terry T. Isson^{1*} & Noah J. Planavsky¹

For the first four billion years of Earth's history, climate was marked by apparent stability and warmth despite the Sun having lower luminosity¹. Proposed mechanisms for maintaining an elevated partial pressure of carbon dioxide in the atmosphere (P_{CO_2}) centre on a reduction in the weatherability of Earth's crust and therefore in the efficiency of carbon dioxide removal from the atmosphere². However, the effectiveness of these mechanisms remains debated^{2,3}. Here we use a global carbon cycle model to explore the evolution of processes that govern marine pH, a factor that regulates the partitioning of carbon between the ocean and the atmosphere. We find that elevated rates of 'reverse weathering'—that is, the consumption of alkalinity and generation of acidity during marine authigenic clay formation^{4–7}—enhanced the retention of carbon within the ocean–atmosphere system, leading to an elevated P_{CO_2} baseline. Although this process is dampened by sluggish kinetics today, we propose that more prolific rates of reverse weathering would have persisted under the pervasively silica-rich conditions^{8,9} that dominated Earth's early oceans. This distinct ocean and coupled carbon–silicon cycle state would have successfully maintained the equitable and ice-free environment that characterized most of the Precambrian period. Further, we propose that during this time, the establishment of a strong negative feedback between marine pH and authigenic clay formation would have also enhanced climate stability by mitigating large swings in P_{CO_2} —a critical component of Earth's natural thermostat that would have been dominant for most of Earth's history. We speculate that the late ecological rise of siliceous organisms⁸ and a resulting decline in silica-rich conditions dampened the reverse weathering buffer, destabilizing Earth's climate system and lowering baseline P_{CO_2} .

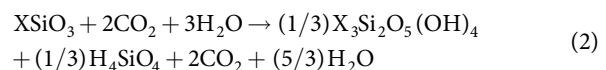
Stability was a hallmark feature of Earth's early climate. Solar luminosity was only 80%–95% as intense as it is today during the Proterozoic eon (2,500 to 542 million years (Myr) ago)¹. Yet geologic evidence suggests a persistence of ice-free conditions. Low-latitude glaciations that bookend the Proterozoic, although anomalously severe in extent, account for only a small fraction of Precambrian time. The extensive interval of clement climate that characterized Earth's middle ages diverges from the frequent and rapid icehouse–greenhouse cycles that are characteristic of the more mercurial Phanerozoic (<541 Myr ago) climate system¹⁰. This fundamental shift in the stability of Earth's climate regime suggests the operation of a much more robust natural thermostat¹¹ during the Precambrian. Further, most proposed mechanisms for maintaining a warm early Earth, in spite of a 'faint young Sun', require an atmosphere with a more potent greenhouse effect¹². While a range of atmospheric compositions have been proposed for this greenhouse cocktail, a high- P_{CO_2} baseline stands out as an essential ingredient¹². Proterozoic P_{CO_2} of about 10 to 1,000 times pre-industrial atmospheric levels (PIAL; 280 parts per million, p.p.m.) have been proposed from proxy reconstructions^{13,14}. Simulations of Proterozoic climate, using a fully coupled ocean–atmosphere general circulation model, likewise suggest a vital role for high P_{CO_2} —even with much higher levels of methane (CH_4), a P_{CO_2} of more than ten times PIAL would have been required to mitigate runaway global glaciations¹⁵.

Traditionally proposed mechanisms for maintaining elevated P_{CO_2} during the Precambrian centre on a reduction in the weatherability of Earth's crust linked to changes in its composition, rates of uplift, sea level or the intensity of erosional processes (for example, biological modification)². However, the effectiveness of these mechanisms in sustaining high atmospheric P_{CO_2} has been debated^{2,3}. Receiving limited attention, however, are processes that influence marine pH, a property that regulates the partitioning of carbon between the ocean and atmosphere reservoirs, and carbon sequestration on geologic timescales. Here we provide a new assessment of the factors leading to a persistently stable and CO_2 -rich early atmosphere by exploring the role of reverse weathering as a pH and climate regulator.

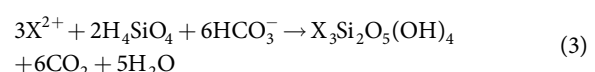
Reverse weathering is a key parameter of Earth's surficial coupled silicon–carbon cycle that can play a major part in controlling atmospheric composition and the chemistry of seawater^{4–6}. Classically defined as a 'back-reaction' that recombines dissolved silica and alkali metal cations, generating acidity in the process, reverse weathering simply describes the in situ formation (authigenesis) of non-kaolinite-type (cation-poor) phyllosilicate minerals (clays)^{4–6}. Early conjectures of this process were provoked by large imbalances in the modern marine budgets of major cations (Mg^{2+} , K^+), alkalinity and $[H^+]$ ^{4–6}. Reverse weathering can be illustrated as an alternative pathway to the canonical Urey silicate weathering reaction (equation (1))¹⁶ for the export of dissolved silica and alkalinity, as follows:



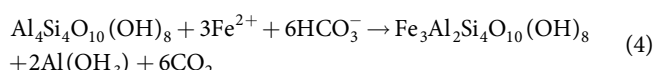
or



where X is a divalent cation (for example, Fe^{2+} , Mg^{2+}). While the weathering of silicate rock coupled to the eventual precipitation of dissolved silica as chert (SiO_2) and carbon as carbonate (XCO_3) sequesters carbon from the ocean–atmosphere system (equation (1)), the removal of dissolved silica and cations through clay authigenesis generates acidity (H^+), and quantitatively re-releases CO_2 (equation (2))⁷. Where cations are hydrothermally sourced (for example, Fe^{2+} , K^+ , Na^+), reverse weathering can be expressed as:



An alternative mode of clay authigenesis occurs via the transformation of a pre-existing (detrital) cation-poor clay mineral, involving either cation enrichment or substitution¹⁷. Classic examples include the expansion of smectite clays to form mix-layered or pure glauconite phases¹⁸, and the transformation of kaolinite to berthierine:



¹Department of Geology and Geophysics, Yale University, New Haven, CT, USA. *e-mail: terry.t.issone@gmail.com

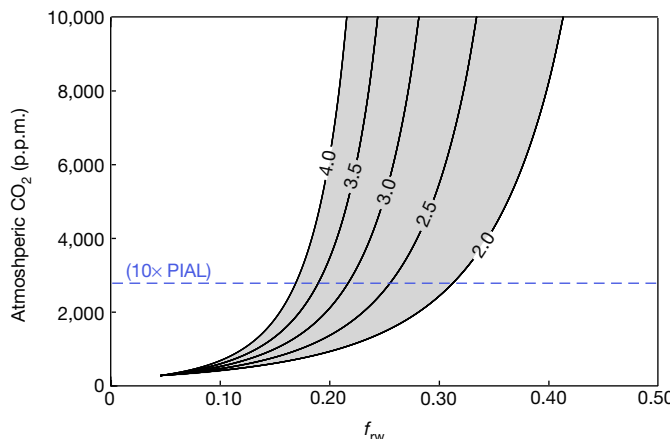
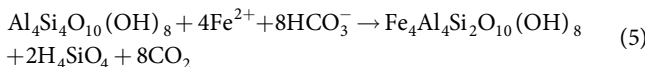


Fig. 1 | Atmospheric p_{CO_2} as a function of reverse weathering, f_{rw} , at steady state. Each contour represents a different alkalinity to silica consumption ratio (Alk:Si). The root of each curve indicates preindustrial p_{CO_2} at 280 p.p.m. and a reverse-weathering silica flux of about 0.5 Tmol yr⁻¹ ($f_{\text{rw}} = 0.05$)^{27,29}. ‘10× PIAL’ denotes the estimated minimum threshold that mitigates runaway icehouse conditions¹⁵. The strength of the silicate weathering feedback (n_{Si}) was set at 0.3.



that liberate framework Al (equation (4)) or Si (equation (5))¹⁹. This enrichment style of authigenesis deviates from that of nucleation and growth (equations (2) and (3)) since no ‘new’ dissolved Si is consumed.

Simply put, reverse weathering acts to retain carbon within the ocean–atmosphere system, effectively reducing the efficiency of silicate weathering in sequestering carbon. In contrast to Al and all other clay-forming cations, Si is unique in that it forms the basis of all authigenic clay reactions. Because Si sequestration follows only one of two main mineralization pathways, the impact of reverse weathering in altering the global carbon cycle can be expressed as $f_{\text{rw}} = \frac{F_{\text{rw}}}{F_{\text{rw}} + F_{\text{opal}}}$, where F_{rw} and F_{opal} represent export via clay authigenesis and SiO_2 (amorphous silica; opal), respectively. Here we investigate the effects of reverse weathering on the marine acid–base balance and climate, questioning the assumption that silicate weathering has operated at near-maximum efficiency (that is, $f_{\text{rw}} = 0$) throughout Earth’s history—a stance adopted by the current generation of carbon cycle models²⁰.

To that end, we used a global carbon cycle model (LOSCAR²⁰), modified to incorporate global silica cycling and alkalinity consumption through reverse weathering. In this model the operation of reverse

weathering in conjunction with the stabilizing silicate weathering climate feedback means that any transient increase in f_{rw} will ultimately be balanced by more intense weathering of silicate rock until a new stable state—at lowered marine pH and elevated p_{CO_2} —is achieved to balance outgassing rates (Fig. 1). In other words, the ocean’s capacity to store carbon is reduced, inducing degassing to the atmosphere until equilibrium is achieved. Because the total flux of acidity generated through reverse weathering is primarily set by the chemical makeup of the globally integrated authigenic clay assemblage, we explore a range of compositions typical of the assortment of authigenic clays found within Earth’s sedimentary archive^{18,19,21–24}. Specifically, this can be described as a ratio of the total flux of alkalinity to Si consumed during clay formation (Alk:Si) (see Methods, Table 1). Figure 1 demonstrates that p_{CO_2} is highly sensitive to changes in f_{rw} , and that at modern outgassing rates, a 20%–25% increase in f_{rw} could have maintained p_{CO_2} at more than ten times PIAL (Fig. 1). While variations in the strength of the silicate weathering feedback (n_{Si} ; Extended Data Fig. 9) can alter the sensitivity of this relationship²⁰, we find that using a broader range of values does not alter our primary conclusion that reverse weathering is an important process that can regulate marine pH levels, and that increasing f_{rw} will sustain an elevated p_{CO_2} baseline.

Evidence that reverse weathering can have a dramatic effect on Earth’s climate system forces an evaluation of the factors controlling the extent of this process. While robust evidence for marine clay authigenesis in the modern has emerged^{22,25–27}, both laboratory studies²² and analysis of natural marine sediments^{18,25,27} suggest that reverse-weathering rates are currently sluggish. Low rates of reverse weathering have been attributed to the silica-depleted conditions that characterize modern seawater²⁸, restricting reverse weathering both kinetically and spatially almost exclusively to environments characterized by extremely high rates of biogenic opal remineralization^{25,28}. Consequently, reverse weathering is generally estimated to constitute only a relatively minor (<10%) component of total dissolved silica export in the modern oceans^{27,29}.

Within this framework, the secular evolution of dissolved marine silica concentrations would have been critical in determining rates of authigenic clay formation. The dissolved marine concentrations of clay-forming elements have varied dramatically through time. In particular, there is strong evidence that ocean interiors were both ferruginous (anoxic and Fe-rich)³⁰ and globally rich in silica^{8,9} for the majority of Earth’s history. Dissolved silica in Precambrian seawater is estimated to have been at least an order of magnitude higher than in today’s oceans^{8,9}. This drop in dissolved silica concentrations has been directly linked to the emergence of silica biominerilizers. Specifically, the radiation of silicifying sponges in the early Cambrian, radiolarians in the Ordovician, and the Cretaceous–Cenozoic rise of diatoms are key evolutionary events that are believed to have shaped the temporal trajectory of dissolved Si concentrations^{8,9}. Rapid biominerilization

Table 1 | Reverse-weathering reactions

Species	Formula	Alk: Si
Greenalite	$3\text{Fe}^{2+} + 2\text{H}_4\text{SiO}_4 + 6\text{HCO}_3^- \rightarrow \text{Fe}_3\text{Si}_2\text{O}_5(\text{OH})_4 + 6\text{CO}_2 + 5\text{H}_2\text{O}$	3.00
Minnesotait	$3\text{Fe}^{2+} + 4\text{H}_4\text{SiO}_4 + 6\text{HCO}_3^- \rightarrow \text{Fe}_3\text{Si}_4\text{O}_{10}(\text{OH})_2 + 6\text{CO}_2 + 10\text{H}_2\text{O}$	1.50
Berthierine	$2\text{Fe}^{2+} + \text{H}_4\text{SiO}_4 + 2\text{Al}(\text{OH})_3 + 4\text{HCO}_3^- \rightarrow \text{Fe}_2\text{Al}_2\text{SiO}_5(\text{OH})_4 + 4\text{CO}_2 + 5\text{H}_2\text{O}$	4.00
Chamosite	$5\text{Fe}^{2+} + 3\text{H}_4\text{SiO}_4 + 2\text{Al}(\text{OH})_3 + 10\text{HCO}_3^- \rightarrow \text{Fe}_5\text{Al}_2\text{Si}_3\text{O}_{10}(\text{OH})_8 + 10\text{CO}_2 + 10\text{H}_2\text{O}$	3.33
Sepiolite	$4\text{Mg}^{2+} + 6\text{H}_4\text{SiO}_4 + 8\text{HCO}_3^- \rightarrow \text{Mg}_4\text{Si}_6\text{O}_{15}(\text{OH})_2 + 8\text{CO}_2 + 15\text{H}_2\text{O}$	1.33
Clinochlore	$5\text{Mg}^{2+} + 3\text{H}_4\text{SiO}_4 + 2\text{Al}(\text{OH})_3 + 10\text{HCO}_3^- \rightarrow \text{Mg}_5\text{Al}_2\text{Si}_3\text{O}_{10}(\text{OH})_8 + 10\text{CO}_2 + 10\text{H}_2\text{O}$	3.33
Sudoite	$2\text{Mg}^{2+} + 3\text{H}_4\text{SiO}_4 + 4\text{Al}(\text{OH})_3 + 4\text{HCO}_3^- \rightarrow \text{Mg}_2\text{Al}_4\text{Si}_3\text{O}_{10}(\text{OH})_8 + 4\text{CO}_2 + 10\text{H}_2\text{O}$	1.33
Glaucite	$0.55\text{K}^+ + 0.05\text{Na}^+ + 1.4\text{Fe}^{3+} + 0.2\text{Fe}^{2+} + 0.5\text{Mg}^{2+} + 3.8\text{H}_4\text{SiO}_4 + 0.2\text{Al}(\text{OH})_3 + 6.2\text{HCO}_3^- \rightarrow \text{K}_{0.55}\text{Na}_{0.05}\text{Fe}^{3+}_{1.4}\text{Mg}_{0.5}\text{Fe}^{2+}_{0.2}\text{Al}_{0.2}\text{Si}_{3.8}\text{O}_{10}(\text{OH})_2 + 6.2\text{CO}_2 + 10\text{H}_2\text{O}$	1.63
Saponite	$0.15\text{Ca}^{2+} + 0.1\text{Na}^+ + 2.5\text{Mg}^{2+} + 0.8\text{Fe}^{2+} + 3\text{H}_4\text{SiO}_4 + \text{Al}(\text{OH})_3 + 7\text{HCO}_3^- \rightarrow \text{Ca}_{0.15}\text{Na}_{0.1}\text{Mg}_{2.5}\text{Fe}^{2+}_{0.8}\text{Si}_3\text{AlO}_{10}(\text{OH})_2 + 7\text{CO}_2 + 10\text{H}_2\text{O}$	2.38
Odinite	$0.7\text{Fe}^{3+} + 0.7\text{Mg}^{2+} + 0.3\text{Fe}^{2+} + 0.1\text{Ti}(\text{OH})_4 + 0.1\text{Mn}^{2+} + 1.8\text{H}_4\text{SiO}_4 + 0.7\text{Al}(\text{OH})_3 + 4.3\text{HCO}_3^- \rightarrow \text{Fe}^{3+}_{0.7}\text{Mg}_{0.7}\text{Fe}^{2+}_{0.3}\text{Ti}_{0.1}\text{Mn}_{0.1}\text{Al}_{0.7}\text{Si}_{1.8}\text{O}_5(\text{OH})_4 + 4.3\text{CO}_2 + 5\text{H}_2\text{O}$	2.61
Corrensite	$0.4\text{Ca}^{2+} + 0.1\text{Na}^+ + 0.1\text{K}^+ + 5\text{Mg}^{2+} + 3\text{Fe}^{2+} + 6\text{H}_4\text{SiO}_4 + 3\text{Al}(\text{OH})_3 + 17\text{HCO}_3^- \rightarrow \text{Ca}_{0.4}\text{Na}_{0.1}\text{K}_{0.1}\text{Mg}_5\text{Fe}^{2+}_{3}\text{Al}_3\text{Si}_6\text{O}_{20}(\text{OH})_{10} + 17\text{CO}_2 + 20\text{H}_2\text{O}$	2.83

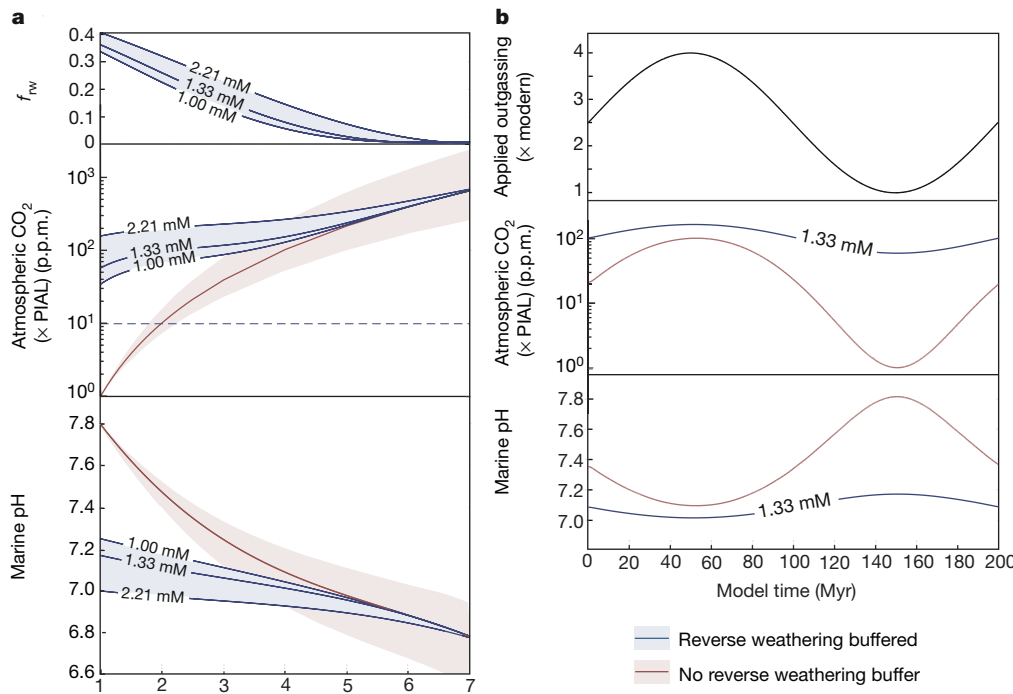


Fig. 2 | p_{CO_2} and pH results for systems buffered by reverse weathering under silica-rich conditions (blue) versus unbuffered low-silica systems (red). **a**, Steady-state results. The compensating feedback between clay authigenesis (f_{rw}) and outgassing is reflected by their inverse relationship. Blue contours represent dissolved silica levels, $n_{\text{Si}} = 0.3$, Alk:Si = 2.5. The red-shaded envelope denotes sensitivity to n_{Si} between 0.25–0.35. **b**, Time-dependent results. The same outgassing scenario (baseline outgassing 2.5 times modern; amplitude ± 1.5 ; period 200 Myr) was applied to both systems. The results highlight the stabilizing effect of reverse weathering when subject to climatic perturbations, preventing extreme p_{CO_2} swings.

rates ensure that >90% of today's global Si export is sequestered as biogenic opal²⁹, enforcing a strong disequilibrium between dissolved silica and siliceous phases at the seafloor—enhancing the dissolution of cation-rich silicate minerals within both sedimentary and basaltic systems (that is, marine weathering)^{27,31}.

In contrast, the lack of a Precambrian skeletal sink suggests that dissolved Si would have been maintained via abiotic processes at levels between 1.00 mM and 2.21 mM (whereas modern marine dissolved Si levels are <0.1 mM) set by sorption equilibrium with detrital particulates (for example, clays and zeolites), organic matter⁹ and authigenic Fe-oxyhydroxides²³. The solubility of amorphous silica (opal-A) at about 2.21 mM provides an upper limit on the activity of seawater silica, with sedimentological evidence suggesting that such levels could have been achieved at least locally within Precambrian evaporative environments (if not globally)⁹. With inorganic regulation of the Precambrian Si cycle, there would have been an efflux from seawater to the sediment pile, where dissolved Si would have been consumed through reverse-weathering reactions⁹—in direct contrast to modern times, in which there is a strong influx of dissolved Si from interstitial waters to the water column, linked to biogenic silica dissolution and marine weathering^{27,29,31}. This is consistent with observed marine authigenic clay enrichments in Precambrian sediments that indicate distinctively elevated rates of reverse weathering.

To explore the effects of reverse weathering under sustained anoxic and silica-rich Precambrian conditions, we coupled our modified version of LOSCAR to an early diagenetic model (LOSCAR-RW; see Methods). Thermodynamic and experimental work both indicate that rates of clay authigenesis are strongly dependent on ambient pH conditions (for example, ref. ²⁴). As such, we explicitly relate reverse weathering to the pH of sedimentary porewaters, establishing a stabilizing feedback—more basic conditions promote clay authigenesis, generating acidity that in turn lowers the pH of porewaters (in diffusional exchange with seawater). Clay authigenesis essentially acts as an Earth thermostat through the regulation of marine pH, that is, in equilibrium with the atmosphere on geologic timescales (Extended Data Fig. 1).

red-shaded envelope denotes sensitivity to n_{Si} between 0.25–0.35. **b**, Time-dependent results. The same outgassing scenario (baseline outgassing 2.5 times modern; amplitude ± 1.5 ; period 200 Myr) was applied to both systems. The results highlight the stabilizing effect of reverse weathering when subject to climatic perturbations, preventing extreme p_{CO_2} swings.

Within all model runs, there are distinctly higher p_{CO_2} and lower pH baselines for a climate system buffered by reverse weathering when compared to an unbuffered system. For instance, at modern outgassing rates and proposed Precambrian levels of dissolved silica^{8,9,23}, new baseline marine pH and p_{CO_2} of around 7.0–7.2 and around 35–110 times PIAL respectively would have been achieved at steady state (versus modern PIAL values of about 7.8 and 280 p.p.m.) (Fig. 2a). Under these conditions, the buffering capacity of authigenic clays would have also dramatically enhanced the stability of Earth's climate system—through the establishment of a marine system that is much more resistant to pH change. This is exemplified over a range of outgassing rates between 1 and 7 times the modern value, where the sensitivity of global marine pH at steady state is more than halved (± 0.4) compared to a system without a reverse-weathering buffer (± 1.0) (Fig. 2). Simply stated, an elevated acidity flux from reverse weathering compensates for dampened outgassing rates and vice versa. Accordingly, the sensitivity of p_{CO_2} to outgassing is similarly reduced to a degree that would mitigate runaway to catastrophic climate states (when subject to intervals of extreme outgassing or crustal weatherability, for instance) (Fig. 2).

We note that the standard LOSCAR model does not incorporate marine weathering—a process that generates marine alkalinity, particularly within the methanogenic zone of the sediment pile²⁷ and in sea-floor basalts³¹—that has the potential to further alter global carbon cycle budgets (see Methods, Extended Data Fig. 4). For instance, under elevated silica levels, increased saturation states (or a reduced degree of undersaturation) of common primary and secondary silicate minerals within marine porewaters could have acted to dampen marine weathering rates (that is, further elevating p_{CO_2}) (Extended Data Fig. 2–4).

Placed in the context of climatic evolution, an overall decrease in volcanic outgassing rates³² through Earth's history warrants a compensating increase in f_{rw} , resulting in fairly constant p_{CO_2} and pH baselines between 3.5 and 0.54 billion years (Gyr) ago (Fig. 3). Within this protracted interval, we find that enhanced reverse weathering, relative to the modern level, would have been capable of sustaining above-freezing

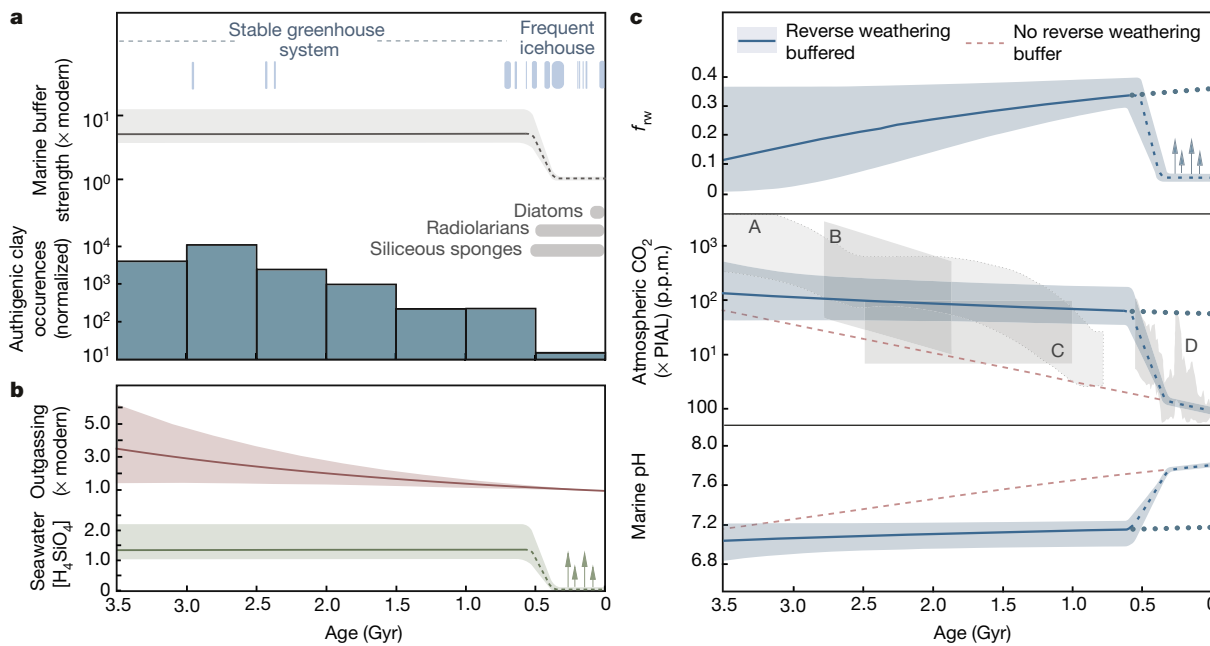


Fig. 3 | Evolution of reverse weathering and climate stability. **a**, Glacial intervals (blue bars). Marine buffer strength (the sensitivity of marine pH to a change in outgassing; estimates are derived from between 1 and 3 times the modern outgassing level). Marine authigenic clay (greenalite and minnesotaite) occurrences normalized to the proportion of sediment coverage (Extended Data Fig. 5). **b**, Applied outgassing and dissolved silica

temperatures^{12,15} over a broad range of stable state conditions (p_{CO_2} of up to 140 times PIAL). This model highlights the role of marine chemistry in regulating global carbon cycle evolution, and provides an alternative to invoking extreme reductions to crustal weatherability for sustaining high p_{CO_2} .

Evidence from the geochemical record suggests that organisms have had a critical role in shaping the composition of Earth's oceans and atmosphere, which in turn also structures the biosphere. Perhaps most notably, methanogens and oxygenic phototrophs have transformed Earth's surface environments since the Archean era³³. The most recent chapter of Earth's history, the Phanerozoic, was one shaped foremost by eukaryotic life. If our estimates are correct, then the switch to a biologically controlled silicon cycle with the rise of silica-biomimeticizing eukaryotes would have initiated a substantial waning of reverse-weathering rates. This transition would have led to a drop in baseline p_{CO_2} and the establishment of a more volatile (responsive) climate system, directly linked to a decrease in the pH buffering strength of oceans (Fig. 3). This view of Earth's history is consistent with geologic evidence for a decline in authigenic marine clays and the weakening of Earth's thermostat as indicated by the onset of more frequent greenhouse-icehouse oscillations since the latest Precambrian (Fig. 3). Had siliceous organisms never evolved, Earth's surface environment would be much warmer and oceans far more acidic than they are today (Fig. 3). In this light, our results suggest that Phanerozoic p_{CO_2} trends¹⁰ could

reflect, at least in part, variations in the ecological success of siliceous organisms. Future models seeking to explore climatic evolution on terrestrial bodies should consider both forward (weathering) and backward (reverse weathering) processes governing global alkalinity budgets.

Online content

Any Methods, including any statements of data availability and Nature Research reporting summaries, along with any additional references and Source Data files, are available in the online version of the paper at <https://doi.org/10.1038/s41586-018-0408-4>

Received: 24 July 2017; Accepted: 7 June 2018;

Published online 8 August 2018.

1. Gough, D. Solar interior structure and luminosity variations. *Sol. Phys.* **74**, 21–34 (1981).
2. Kump, L. R., Brantley, S. L. & Arthur, M. A. Chemical weathering, atmospheric CO_2 , and climate. *Annu. Rev. Earth Planet. Sci.* **28**, 611–667 (2000).
3. Keller, C. & Wood, B. Possibility of chemical weathering before the advent of vascular land plants. *Nature* **364**, 223–225 (1993).
4. Mackenzie, F. T. & Garrels, R. M. Chemical mass balance between rivers and oceans. *Am. J. Sci.* **264**, 507–525 (1966).
5. Garrels, R. M. Silica: role in the buffering of natural waters. *Science* **148**, 69 (1965).
6. Sillén, L. G. The physical chemistry of sea water. *Oceanography* **67**, 549–581 (1961).
7. Mackenzie, F. T. & Garrels, R. M. Silica-bicarbonate balance in the ocean and early diagenesis. *J. Sedim. Petrol.* **36**, 1075–1084 (1966).
8. Maliva, R. G., Knoll, A. H. & Simonson, B. M. Secular change in the Precambrian silica cycle: insights from chert petrology. *Geol. Soc. Am. Bull.* **117**, 835–845 (2005).
9. Siever, R. The silica cycle in the Precambrian. *Geochim. Cosmochim. Acta* **56**, 3265–3272 (1992).
10. Royer, D. L., Berner, R. A., Montañez, I. P., Tabor, N. J. & Beerling, D. J. CO_2 as a primary driver of Phanerozoic climate. *GSA Today* **14**, 4–10 (2004).
11. Walker, J. C., Hays, P. & Kasting, J. F. A negative feedback mechanism for the long-term stabilization of Earth's surface temperature. *J. Geophys. Res. Oceans* **86**, 9776–9782 (1981).
12. Kasting, J. F. Theoretical constraints on oxygen and carbon dioxide concentrations in the Precambrian atmosphere. *Precambr. Res.* **34**, 205–229 (1987).
13. Sheldon, N. D. Precambrian paleosols and atmospheric CO_2 levels. *Precambr. Res.* **147**, 148–155 (2006).

Table 2 | Modern global silica budget

Fluxes and reservoirs	Symbol	Flux	Unit
Total Si input	F_{in}	10.9	Tmol Si yr ⁻¹
Si output into reverse weathering	F_{rw}	0.5	Tmol Si yr ⁻¹
Si output into chert	F_{opal}	10.4	Tmol Si yr ⁻¹
Fraction of total Si consumed through reverse weathering	f_{rw}	0.05	–
Total alkalinity consumed through reverse weathering (or acidity generated) (Alk:Si = 1–2.5)	Alk_{rw}	0.5–1.25	Tmol yr ⁻¹

14. Kanzaki, Y. & Murakami, T. Estimates of atmospheric CO₂ in the Neoarchean-Paleoproterozoic from paleosols. *Geochim. Cosmochim. Acta* **159**, 190–219 (2015).
15. Fiorella, R. P. & Sheldon, N. D. Equable end Mesoproterozoic climate in the absence of high CO₂. *Geology* **45**, 231–234 (2017).
16. Urey, H. C. On the early chemical history of the Earth and the origin of life. *Proc. Natl Acad. Sci. USA* **38**, 351–363 (1952).
17. Mackin, J. E. & Aller, R. C. Dissolved Al in sediments and waters of the East China Sea: implications for authigenic mineral formation. *Geochim. Cosmochim. Acta* **48**, 281–297 (1984).
18. Baldermann, A., Warr, L., Letofsky-Papst, I. & Mavromatis, V. Substantial iron sequestration during green-clay authigenesis in modern deep-sea sediments. *Nat. Geosci.* **8**, 885–889 (2015).
19. Bhattacharyya, D. P. Origin of berthierine in ironstones. *Clays Clay Miner.* **31**, 173–182 (1983).
20. Zeebe, R. LOSCAR: long-term ocean-atmosphere-sediment carbon cycle reservoir model v2.0.4. *Geosci. Model Dev.* **5**, 149–166 (2012).
21. Hazen, R. M. et al. Clay mineral evolution. *Am. Mineral.* **98**, 2007–2029 (2013).
22. Michalopoulos, P. & Aller, R. C. Rapid clay mineral formation of Amazon delta sediments: reverse weathering and oceanic elemental cycles. *Science* **270**, 614–617 (1995).
23. Halevy, I., Alesker, M., Schuster, E., Popovitz-Biro, R. & Feldman, Y. A key role for green rust in the Precambrian oceans and the genesis of iron formations. *Nat. Geosci.* **10**, 135–139 (2017).
24. Tosca, N. J., Guggenheim, S. & Pufahl, P. K. An authigenic origin for Precambrian greenalite: implications for iron formation and the chemistry of ancient seawater. *Geol. Soc. Am. Bull.* **128**, 511–530 (2016).
25. Ehlert, C. et al. Stable silicon isotope signatures of marine pore waters—biogenic opal dissolution versus authigenic clay mineral formation. *Geochim. Cosmochim. Acta* **191**, 102–117 (2016).
26. Rahman, S., Aller, R. & Cochran, J. Cosmogenic ³²Si as a tracer of biogenic silica burial and diagenesis: major deltaic sinks in the silica cycle. *Geophys. Res. Lett.* **43**, 7124–7132 (2016).
27. Wallmann, K. et al. Silicate weathering in anoxic marine sediments. *Geochim. Cosmochim. Acta* **72**, 2895–2918 (2008).
28. Michalopoulos, P. & Aller, R. C. Early diagenesis of biogenic silica in the Amazon delta: alteration, authigenic clay formation, and storage. *Geochim. Cosmochim. Acta* **68**, 1061–1085 (2004).
29. Tréguer, P. J. & De La Rocha, C. L. The world ocean silica cycle. *Annu. Rev. Mar. Sci.* **5**, 477–501 (2013).
30. Poulton, S. W. & Canfield, D. E. Ferruginous conditions: a dominant feature of the ocean through Earth's history. *Elements* **7**, 107–112 (2011).
31. Coogan, L. A. & Dosso, S. E. Alteration of ocean crust provides a strong temperature dependent feedback on the geological carbon cycle and is a primary driver of the Sr-isotopic composition of seawater. *Earth Planet. Sci. Lett.* **415**, 38–46 (2015).
32. Tajika, E. & Matsui, T. Evolution of terrestrial proto-CO₂ atmosphere coupled with thermal history of the Earth. *Earth Planet. Sci. Lett.* **113**, 251–266 (1992).
33. Holland, H. D. Volcanic gases, black smokers, and the Great Oxidation Event. *Geochim. Cosmochim. Acta* **66**, 3811–3826 (2002).

Acknowledgements This research was supported by the NASA Astrobiology Institute under Cooperative Agreement number NNA15BB03A issued through the Science Mission Directorate. We thank R. Zeebe for access to LOSCAR v.2.0.4. We also thank M. Zhao, K. Daviau and D. Pennman for model discussions.

Reviewer information *Nature* thanks L. Coogan and Y. Godderis for their contribution to the peer review of this work.

Author contributions T.T.I. conceived the research ideas, developed and analysed the model, and wrote the paper. N.J.P. contributed to discussion and writing.

Competing interests The authors declare no competing interests.

Additional information

Extended data is available for this paper at <https://doi.org/10.1038/s41586-018-0408-4>.

Supplementary information is available for this paper at <https://doi.org/10.1038/s41586-018-0408-4>.

Reprints and permissions information is available at <http://www.nature.com/reprints>.

Correspondence and requests for materials should be addressed to T.T.I.

Publisher's note: Springer Nature remains neutral with regard to jurisdictional claims in published maps and institutional affiliations.

METHODS

Reverse weathering and the silicon–carbon cycle. As a context for exploring the evolution of reverse weathering, it is useful to consider past key contributions to the field and several aspects of the modern silicon–carbon cycle. To our knowledge, the idea that clay minerals could act as a buffer of seawater pH stems from a seminal paper by Sillén in 1961⁶. Here and in subsequent articles, Sillén challenged the traditional framework of a carbonate system operating as the sole buffer of seawater pH^{6,34}. Several supporting articles followed within the decade, highlighting the importance of the reverse-weathering process for the budgets of not only H⁺ but also major cations^{4,5,7,35,36}. Perhaps most notably, Mackenzie and Garrels in 1966^{4,7} constructed a mass balance for river water inputs, such that the major constituents were precipitated from seawater as mineral phases commonly found in marine sediments—balancing the budgets required for Na, Mg, K and Si removal through clay authigenesis. Since then, both field and laboratory work have provided mounting evidence for the operation of this process in nature today^{17,18,22,25–28,37–42}, prompting greater acceptance within the broader community. However, when placed in the context of the global carbon²⁷ and silica budgets^{29,43–45}, it is generally agreed that reverse-weathering fluxes in modern systems account for a non-negligible, yet small, fraction of either budget. Consequently, this has led to the general exclusion of reverse weathering from the current generation of global carbon cycle models designed to reconstruct past climate states and the composition of seawater (for example, refs^{20,46,47}). However, because reverse weathering can lead to the long-term sequestration of various elements (for example, Fe, Mg, K, Li, Si and O), secular variations in rates of early diagenetic clay synthesis throughout Earth's history can alter global mass and isotope balance budgets.

As there have been multiple reviews of the modern global silica budget^{29,43,44}, we provide only a brief overview here (Table 2). The total marine influx of dissolved silica every year is about 10.9 Tmol. Rivers contribute about 7.3 Tmol yr⁻¹ of this source flux, and the remainder are attributed to hydrothermal, aeolian, groundwater and marine weathering sources. In terms of outputs, biogenic silica is responsible for >90% of the flux and the rest is sequestered through reverse-weathering reactions (<10%)²⁹. Strikingly, the magnitude of the recycled flux within modern oceans is far greater than that of net marine input and outputs. The residence time of silica in the oceans is estimated to be 15,000 yr to 20,000 yr, with dissolved silica cycling through the biological system approximately 40 times before sequestration^{29,43}. The uptake of dissolved silica by organisms in surface waters, estimated at 240 Tmol yr⁻¹, is around 30 times larger than the river influx. These rates of biological fixation are so rapid that dissolved silica levels (typically <0.1 mM) are forced into extreme disequilibrium with respect to its amorphous phase (opal-A; equilibrium at about 2.21 mM). This essentially sets up an autocannibalistic system, such that about 56% and about 10% of biogenic silica is remineralized in surface and deep waters respectively and reincorporated into siliceous tests or spicules. Of the remaining 34% or so transported to the sediment–water interface (in highly localized zones), only about 2.5% escapes dissolution and the rest is diffused back into seawater^{25,29,48}. Critically, silicate mineral undersaturation is not limited to biogenic silica—dissolution extends to the majority of common silicate minerals at the seafloor (fed by riverine and aeolian systems) and primary phases within basaltic ocean crust—a process referred to as marine weathering^{27,31,49}. Exceptions include certain select species within the montmorillonite, nontronite and glauconite group of clay minerals that remain saturated at the seafloor despite low dissolved silica levels (Extended Data Fig. 2). In other words, modern seawater conditions are less suitable for reverse-weathering reactions and instead favour marine weathering reactions.

Modern porewater systems, on the other hand, can facilitate reverse weathering. Silica derived from dissolving mineral phases is sometimes re-precipitated as authigenic clays^{25,27,28}, in ‘pockets’ of marine porewater systems with favourable conditions (for example, elevated pH, dissolved silica or clay-forming cations). However, such conditions are rarely observed in modern systems. As illustrated in a compilation of porewater dissolved silica concentrations ($n = 6,245$) from 453 sediment cores globally, the occurrence of elevated porewater-dissolved silica levels (of >0.5 mM) are globally uncommon in modern systems even where biogenic silica content is high. Estimated Precambrian-like conditions are rarely observed (Extended Data Fig. 3)⁴⁸. Several key factors contribute to this: (1) about 70% of biogenic silica is remineralized in the water column and does not make it to the sediment–water interface²⁹; (2) the localizing nature of biogenic silica production—meaning that substantial export occurs in specific bands or regions (for example, the Southern Ocean), leaving the rest of the ocean floor largely devoid of biogenic silica^{50,51}; (3) the kinetics of diffusional exchange (between porewater and depleted seawater) is much more rapid than the dissolution of solid particulate phases (horizontal inputs), rendering it difficult to sustain elevated porewater concentrations⁴⁸. In sum, biotic regulation of the global silicon cycle essentially ‘locks up’ silica in solid phases^{8,9}, forcing a decoupling of the available silica from clay-forming cations that renders reverse-weathering reactions both spatially and kinetically limited.

In the absence of silica-secreting biota, geologic evidence suggest that dissolved silica was sequestered, via saturation and precipitation of inorganic phases, under pervasively enriched Precambrian ocean and porewater systems^{8,9,52–55}. The stratigraphic, mineralogical and textural features of Precambrian and Phanerozoic siliceous sediments are distinct^{8,9,55–57}. Early diagenetic peritidal and subtidal chert deposits that form authigenically through direct precipitation within pore-fluids, are common features of Precambrian successions, and disappear from the record roughly coincident with the Paleozoic ecological rise of radiolarians^{8,9}. These shallow-water authigenic sediments often facilitate the exceptional preservation of non-skeletal Precambrian microfossils^{8,58,59}. The inference is that Precambrian porewater conditions fostered rapid silica ‘entombment’, allowing organic-walled microfossils to escape degradation^{8,60}. Today, such extreme rates of microbial silification are only observed in silica-rich hot springs⁶¹ or reproduced experimentally under elevated silica conditions⁶². Perhaps more notably, authigenic silicate minerals that form only under silica-enriched conditions are also ubiquitous during this time, as predicted by thermodynamic and experimental guidelines (Fig. 3; Extended Data Fig. 5). For instance the Fe-clay minerals greenalite and minnesotaite are abundant, occurring not only in distinct units but also as impurities within ‘cloudy’ cherts as clay nanoparticles^{63–69}. The inclusion of authigenic clays within early precipitating diagenetic cherts highlights extremely early formation within porewaters^{63–69}. These authigenic clays are often regarded as precursor phases of other Fe- and Si-bearing minerals such as hematite, magnetite, siderite, dolomite-ankerite and chert that form at the expense of these early diagenetic clays during later diagenesis, indicating that these authigenic clays were originally even more widespread than current mineralogical records suggest^{63–69}. Early diagenetic Mg-bearing minerals have also been noted in Proterozoic successions^{70,71}. During this time, dissolved silica would have been maintained between 1.0 mM to 2.21 mM through sorption equilibrium with detrital particles (for example, clays and zeolites), organic matter⁹, authigenic Fe oxyhydroxides^{23,72} or saturation with Si-bearing phases. With sorption controlling marine Si levels, dissolved Si concentrations are likely to have been buffered, with any transient shift in dissolved Si inputs or outputs from the marine realm compensated for by exchange (sorption–desorption) from the sorbed pool^{9,23,72,73}. Saturation with amorphous silica^{9,74} provides an upper, but often invoked, bound on dissolved silica at 2.21 mM^{8,9,75,76}.

The evolution of continental exposure and composition through Earth's history are likely to have altered the global silicon cycle. The extent of continental exposure can influence weathering intensities, and potentially the balance between marine and terrestrial silicate weathering (see, for example, ref.⁷⁷). With lower continental exposure, as has been proposed for the Archean⁷⁸, two end-member outcomes are possible: either (1) the ratio of terrestrial to marine silicate weathering would have been lowered or (2) terrestrial weathering intensities would have been elevated for a given silicate weathering flux to match an outgassing flux. Nonetheless, recent modelling efforts indicate substantial continental exposure since the Mesoarchean⁷⁷, which is consistent with recent empirical evidence suggesting extensive terrestrial weathering in the Mesoarchean⁷⁹. In other words, this work suggests that continental exposure was modern-like for the majority of Earth's history. The transition from a more mafic to a more felsic upper continental crust would have also changed the ratio of Si released per mole of CO₂ consumed. For instance, at sustained outgassing rate, a more mafic upper continental crust would release less Si during weathering. Under these conditions, the cation to Si ratio released from weathering would be much higher. Traditionally, the transition to a more felsic upper continental crust was proposed to have occurred near the Archean–Proterozoic boundary^{80,81}. However, more recent Ti isotope work suggests a Mesoarchean transition⁸². Additionally, any increase in Si fluxes linked to changes in continental composition could have been directly offset by decreasing outgassing rates through time^{32,83,84}. Therefore, it is very likely that both of these factors were limited to early to mid-Archean times. As such, we do not explicitly model the effects of continental area and continental composition on global Si input flux. However, we note that it is the f_{rw} ratio (the fraction of alkalinity and the fraction of silica that is sequestered through the reverse-weathering process, as opposed to carbonate and silica precipitation) that governs the impact of reverse weathering on atmospheric P_{CO₂} levels and climate (not total fluxes). Further, it is possible that altering the total input flux of dissolved Si may not dramatically affect the total flux of reverse weathering, given that dissolved Si concentrations are set at constant levels (for example, about 2.2 mM) through (non-reverse weathering) abiotic equilibrium (or pseudo-equilibrium) Si reactions within the oceans⁹.

In a transformative paper, Wallmann and others²⁷ highlighted that the weathering of primary silicate minerals in marine sediments is likely to be a very large CO₂ sink that is not traditionally included in global carbon budgets. In addition, this study also concluded that while reverse-weathering processes can dominate within the upper portion (typically 1–2 m) of the sediment pile, marine weathering processes become more prominent at depth²⁷. Specifically, it was revealed from two sediment cores from the northern slope of Sakhalin Island, Sea of Okhotsk,

(1) that limited consumption of cations (Mg^{2+} , Na^+ , K^+ and Li^+) through reverse weathering in the upper portion of the sediment pile and (2) that the abundances of primary silicate minerals such as plagioclase feldspar, olivine, pyroxene and volcanic ash decrease down-core into the methanogenic zone and are transformed into smectite. Here, the elevated rates of marine weathering were attributed to the elevated concentrations of dissolved organic humic and fulvic acid anions that complex cations, initiating more rapid dissolution through further undersaturation of primary silicate phases, generating alkalinity in the process. Critically, such elevated total alkalinity levels have also been observed within the methanogenic zones of numerous other sites globally²⁷.

This work also opens the possibility that the by-products of reverse weathering could be subjected to marine weathering deeper in the sediment pile. It is therefore critical to consider the effects of marine weathering in Earth's geologic past. A general increase in porewater and seawater dissolved silica levels back in time would reduce the degree of undersaturation of primary silicate minerals relative to the modern value (Extended Data Fig. 2). While the degree of saturation of these primary minerals would have still been reduced passing through the methanogenic zone, the starting baseline saturation state in the upper portion of the sediment pile would have been elevated relative to the modern saturation state. Critically, it is unlikely that reverse-weathering products will reach equilibrium in the sediment pile as reverse weathering proceeds, given the strong kinetic limitation on clay formation^{24,70}. Stated in other words, porewaters are likely to remain supersaturated with respect to the clay phases forming in the upper portion of the sediment pile. Thus the journey of authigenic clay minerals would have begun as being supersaturated both in seawater and the upper portion of the sedimentary pile and although there would be a decrease in saturation state within the methanogenic zone, this drop is not likely to drive undersaturation. In contrast, modern systems typically begin with phases in the upper portion of the sediment pile being strongly undersaturated or close to equilibrium (such as albite, anorthite, olivine, pyroxene), and achieve an even greater degree of undersaturation when passing though the methanogenic zone. Whether there is undersaturation for clay phases will depend on the degree of kinetic inhibition for the mineral species and the degree of complexation of the clay-forming elements. In sum, regardless of complexities in this process, under elevated Precambrian-like silica conditions, a much larger degree of cation complexation would be required to facilitate the same degree of marine weathering as in the modern era under silica-depleted conditions. The preservation of these reverse-weathering products in the Precambrian sedimentary record (Fig. 3, Extended Data Fig. 5), is consistent with super-saturation through the sediment pile.

To explore further the importance of marine weathering, we incorporate this process into LOSCAR-RW, parameterized as a production flux of alkalinity at the sediment–water interface (that is, CO_2 consumption). We explore the full proposed range of global CO_2 consumption through marine weathering of around 2–20 Tmol per year^{27,31}. Specifically, we conducted analysis for both modern and Precambrian-like (elevated reverse-weathering buffer) systems (Extended Data Fig. 4). In both systems, the overall trend with increasing marine weathering is towards lowered CO_2 and increased marine pH. A more potent Precambrian reverse-weathering buffer acts to dampen this effect, resulting in a smaller net stable state shift given the same change in marine weathering (that is, a more stable system). Similarly, the Precambrian system also achieves a lower pH stable state and a higher CO_2 at the same marine weathering rate compared to the modern system. In other words, it is possible for Earth to achieve a high- CO_2 state with elevated marine weathering and reverse-weathering rates.

Authigenic clays through time. Clay authigenesis has long been recognized as a critical process that governs the mineralogical and textural make-up of marine sediments²¹. A wide range of different clay species has been reported to form authigenically in the marine environment (such as palygorskite, montmorillonite, glauconite, saponite, berthierine, greenalite and minnesotaite)^{18,19,21,68,69,85–87}. Of these species, many (for example, palygorskite, saponite and montmorillonite) also form authigenically in lacustrine and soil environments, thereby rendering it a challenge to distinguish marine and terrestrial sources^{85,88}. As such, for a representative marine framework, we turn to the minerals greenalite and minnesotaite, which are both common in the record and are generally regarded to form exclusively in marine environments^{13,63–69,86,87}. Stilpnomelane is another phyllosilicate mineral that has recently been shown to form under early-diagenetic conditions²³, despite being traditionally viewed to be of metamorphic origin. Stilpnomelane has also been observed to replace early-diagenetic minerals such as greenalite^{89,90}.

We present an extensive compilation of the reported occurrences of greenalite, minnesotaite and stilpnomelane through time (Extended Data Fig. 5, Supplementary Table 2). Our compilation is based on an extensive literature review, with a survey of over 3,500 individual papers and reports mentioning greenalite, minnesotaite or stilpnomelane, for unique occurrences of these minerals. Members, formations, and groups were all considered unique occurrences. Given the nature of our findings, and that the stratigraphy of Phanerozoic units is

typically much more finely divided than the Precambrian, this scheme for what merits consideration of an individual occurrence is conservative. As highlighted by ref. ⁹¹, the geologic record becomes less voluminous the further back in time it reaches. Accounting for increasing rock quantity through time is thus necessary for any meaningful result. As such, we normalize our data to the proportion of marine sediment coverage (for a given geologic age) after ref. ⁹², per time bin (500 Myr; see also the Macrostrat database at <https://macrostrat.org>). Greenalite and minnesotaite data only are shown in Fig. 3, given the possible metamorphic origins of stilpnomelane (Extended Data Fig. 5). Full raw and normalized data are presented in Extended Data Fig. 5. We find the results of our compilation to be consistent with several previous studies that have noted that authigenic clay minerals are more common in Precambrian than Phanerozoic aged sediments^{24,57,63,68,69,76,87,93,94}.

The composition of the globally integrated authigenic clay assemblage plays a part in determining the absolute flux of acidity generated through reverse weathering. To maintain charge balance during the formation of authigenic clays, the total charge (of dissolved cations) must be balanced by the consumption of an equal amount of alkalinity (herein represented as HCO_3^-) in the reaction. For our modelling purposes, this can be expressed as the ratio of the total amount of alkalinity to the Si consumed during reverse weathering (Alk:Si). We find that this ratio varies between 1 and 4, for common authigenic clay minerals found within Earth's sedimentary archive²¹ (Table 1). The common Precambrian clay greenalite, for instance, has an Alk:Si of 3.0. Our model centres on linking the global carbon and silicon cycles because silica forms the basic framework of all clay minerals, and helps in controlling rates of reverse weathering^{22,25,26,28,37}. Although aluminium (Al) can limit the formation of some clay minerals^{17,39}, Al is not required for the formation of non-aluminous clays. Thus, any attempt to track reverse weathering through the global Al (or any other cation such as Mg, Fe and K) mass budget will yield an incomplete estimate of both the extent of reverse weathering and its effect on the global carbon cycle and marine pH.

Modifications to LOSCAR. For this work, we modified the Long-term Ocean-atmosphere-Sediment CArbon Cycle Reservoir Model version 2.0.4 (LOSCAR), which was designed to compute carbon partitioning between the ocean-atmosphere and sedimentary reservoirs on timescales ranging from centuries to millions of years²⁰. The preindustrial ocean geometry was adopted for all model runs. Modifications to LOSCAR for the modelling purposes of this contribution are as follows. In LOSCAR, the terrestrial weathering of silicate rock is simply related to atmospheric P_{CO_2} levels via the expression:

$$F_s = F_s^o \left(\frac{P_{CO_2}}{P_{CO_2}^o} \right)^{n_{Si}} \quad (6)$$

where F_s refers to the weathering flux of silicate rock from continents, the superscript 'o' denotes the initial steady-state value, and n_{Si} controls the strength of the silicate weathering feedback. We calibrate the model according to the most recent global silica budget compilation after ref. ²⁹ (Table 2). In addition to sources of silica that are sensitive to atmospheric P_{CO_2} levels (riverine, groundwater and aeolian sources). We also include marine silica sources (seafloor weathering and hydrothermal; F_n). The total marine silica input (F_{in}) is therefore:

$$F_{in} = F_s^o \left(\frac{P_{CO_2}}{P_{CO_2}^o} \right)^{n_{Si}} + F_n \quad (7)$$

At steady state, this input value equals outputs through reverse weathering and opal ($F_{out} = F_{rw} + F_{opal}$).

Carbonate precipitation was switched from a biotic (Phanerozoic) to an abiotically controlled Precambrian ocean system, to account for the onset of carbonate biomobilization at the Cambrian–Precambrian boundary⁹⁵ and the Mesozoic rise of planktic calcifiers^{96–98}. In our Precambrian mode carbonate precipitation occurs only at high degrees of supersaturation, consistent with geologic evidence for mineralogically ‘anomalous’ carbonates including marine cements, calcified cyanobacteria and thick precipitated beds with fibrous textures that are extremely rare in Phanerozoic aged sediments^{98,99}. More specifically, in contrast to the standard LOSCAR parameterization where calcite supply to the sediment water interface is tied to the biological pump, we modified the carbonate supply term within all ocean basins to be driven by the degree of saturation, using the experimental kinetic data presented in ref. ¹⁰⁰. Net accumulation (preservation) in each ocean basin is achieved only if formation exceeds chemical erosion (dissolution) in the model.

Modelling reverse weathering using LOSCAR-RW. To parameterize reverse weathering we coupled an early diagenetic model (for example, see Extended Data Figs. 6 and 7) with our modified version of LOSCAR. Building from the accepted view of anoxic and iron-rich Precambrian oceans, the upwelling of

dissolved phosphorus (P) and ferrous iron governs the export of organic matter and Fe-oxyhydroxides from surface waters respectively^{57,76,101}. With deep iron-rich seawater there would be inorganic scavenging of bioavailable P from surface oceans (a deep-sea P trap), for which, following ref. ¹⁰¹, we have modelled a percentage scavenging efficiency. We used a modified anoxic organic remineralization power law^{102,103} to determine the export efficiency of organic matter to the sediment–water interface, with water column remineralization coupled directly to the reduction of sinking Fe-oxyhydroxide particulates. Tracers in the diagenetic model include solid (organic matter, Fe-oxyhydroxide and calcite) and dissolved phases ($\text{CO}_2 \text{ HCO}_3^-$, CO_3^{2-} , pH, alkalinity, Ca and Si) within the topmost metre of the sediment column. We assume that anaerobic respiration governs organic matter remineralization (tied to the reduction of Fe-oxyhydroxide) and reverse weathering governs the consumption of dissolved Si.

$$\frac{\partial [X]}{\partial t} = D \frac{\partial^2 [X]}{\partial z^2} - \omega \frac{\partial [X]}{\partial z} - \text{rxn} \quad (8)$$

The sum reaction of the time rate of change of any dissolved constituent (X) in porewaters can be described as the sum of the diffusion term ($D \frac{\partial^2 [X]}{\partial z^2}$), the advection term ($\omega \frac{\partial [X]}{\partial z}$), and the reaction term (rxn), where D is the diffusion coefficient, ω is the sedimentation rate and z the depth in the sediment^{104,105}. Steady state ($\frac{\partial [X]}{\partial t} = 0$) is achieved in all model runs. The reverse-weathering reaction term is described as $k_{\text{rw}} [\text{Si} - \text{Si}_0]$, where k_{rw} is the reverse-weathering reaction rate constant and Si_0 is the lower boundary dissolved silica condition (equilibrium concentration). From first principles there should be a pH control on authigenic clay formation (for example, refs ^{23,24,70,106–110}), which has been observed in experimental work (for example, refs ^{19,24,70,111–114}). The degree (order) of dependence on pH scales with the Alk:Si consumption ratio of the clay species. As such, we relate k_{rw} and Si_0 to porewater pH conditions according to the expressions $k_{\text{rw}} = 1.01 \times 10^{-19} \times \text{pH}^{2.4} \text{ yr}^{-1}$ and $\text{Si}_0 = 2.02 \times 5.57 \times \text{pH} \text{ mol l}^{-1}$, based on previously presented experimental data²⁴, which explicitly relate pH and the extent of reverse weathering. This formulation is the basis for a stabilizing feedback on p_{CO_2} . These expressions determine the strength of the reverse-weathering pH buffering effect within marine porewater systems (which are in diffusional exchange with bottom seawater; for instance, Extended Data Fig. 6) and thus controls the buffering capacity of the whole ocean system. The reaction term for calcite is described as $k_{\text{calc}} [\Omega_{\text{calc}} - 1]$, where Ω_{calc} is the saturation state. Organic matter remineralization is parameterized as $k_{\text{org}} \times [\text{org}] \times \frac{[\text{Fe(OH)}_3]}{[\text{Fe(OH)}_3] + [\text{Fe(OH)}_3]_{\text{lim}}}$, where $[\text{Fe(OH)}_3]_{\text{lim}}$ is the limiting concentration¹¹⁵ and ‘[org]’ is the concentration of organic matter. The total flux of dissolved silica consumed in sedimentary porewater systems can be described according to Fick’s first law at the sediment–water interface such that:

$$F_{\text{rw}} = -\varphi D \frac{\partial [\text{Si}]}{\partial z} \Lambda \quad (9)$$

where φ is sediment porosity and Λ is the authigenically ‘active’ area of the seafloor. The total flux of alkalinity consumed (or acidity generated) is then simply:

$$\text{Alk}_{\text{rw}} = -(\text{Alk} : \text{Si}) F_{\text{rw}} \quad (10)$$

Alk:Si relates total alkalinity to the flux of dissolved silica consumed through reverse weathering in porewaters. In LOSCAR-RW, reverse weathering is parameterized as the removal flux of alkalinity (Alk_{rw}) across the sediment–water interface within each environment. Specifically, the deep sea, slope and shelf sedimentary environments are linked to the deep, intermediate and surface ocean boxes respectively. Steady-state outputs of marine pH, total dissolved inorganic carbon (DIC), total alkalinity and calcite saturation state that correspond to the results presented in Fig. 1 are presented in Extended Data Fig. 8. Sensitivity analyses to changes in the strength of the silicate weathering feedback (n_{Si}) between 0.1–0.5^{11,20,46,116–119}, are presented in Extended Data Fig. 9. We base all our preferred model runs on experimental data and previous constraints on Precambrian marine conditions (see Supplementary Table 1 for full list of parameter values). We find that rates of reverse weathering over the range of conditions previously predicted for the Precambrian are most sensitive to changes in marine pH and the concentration of dissolved silica in seawater (Extended Data Figs. 4, 6–10). We note, however, that any changes to the globally integrated authigenic clay assemblage through time have the potential to alter the pH, dissolved Si, reaction rate law relationships, and hence the extent and pH buffering potential of the reverse-weathering process that was adopted in this study. For instance, from a thermodynamic viewpoint, the sensitivity of clay authigenesis to ambient pH conditions ought to increase with a global assemblage with a higher Alk:Si consumption ratio, potentially altering the buffering strength of the entire ocean system. Reconstructing the evolution of the Alk:Si consumption ratio throughout Earth’s history is therefore a critical topic for future work. Nonetheless, these sensitivity tests suggest that our central conclusion—that reverse weathering rates would have been elevated in Si-rich

oceans leading to more stable and elevated atmospheric CO₂ conditions—is robust over a broad range of parameter space.

Data availability. All data collected for this study are included in this published article (and the Supplementary Information).

34. Sillén, L. G. The ocean as a chemical system. *Science* **156**, 1189–1197 (1967).
35. Mackenzie, F. T. & Garrels, R. M. Silicates: reactivity with sea water. *Science* **150**, 57–58 (1965).
36. Holland, H. D. The history of ocean water and its effect on the chemistry of the atmosphere. *Proc. Natl Acad. Sci. USA* **53**, 1173–1183 (1965).
37. Michalopoulos, P., Aller, R. C. & Reeder, R. J. Conversion of diatoms to clays during early diagenesis in tropical, continental shelf muds. *Geology* **28**, 1095–1098 (2000).
38. Presti, M. & Michalopoulos, P. Estimating the contribution of the authigenic mineral component to the long-term reactive silica accumulation on the western shelf of the Mississippi River Delta. *Cont. Shelf Res.* **28**, 823–838 (2008).
39. Mackin, J. E. & Aller, R. C. The effects of clay mineral reactions on dissolved Al distributions in sediments and waters of the Amazon continental shelf. *Cont. Shelf Res.* **6**, 245–262 (1986).
40. Ristvet, B. L. Reverse Weathering Reactions Within Recent Nearshore Marine Sediments, Kaneohe Bay, Oahu. PhD thesis, <https://scholarspace.manoa.hawaii.edu/bitstream/10125/18151/1/ristvet.pdf>, Northwestern Univ. Illinois, Chicago (1978).
41. Higgins, J. & Schrag, D. Constraining magnesium cycling in marine sediments using magnesium isotopes. *Geochim. Cosmochim. Acta* **74**, 5039–5053 (2010).
42. Baldermann, A., Warr, L. N., Grathoff, G. H. & Dietzel, M. The rate and mechanism of deep-sea glauconite formation at the Ivory Coast–Ghana marginal ridge. *Clays Clay Miner.* **61**, 258–276 (2013).
43. Treguer, P. et al. The silica balance in the world ocean: a reestimate. *Science* **268**, 375–379 (1995).
44. Laruelle, G. G. et al. Anthropogenic perturbations of the silicon cycle at the global scale: key role of the land–ocean transition. *Glob. Biogeochem. Cycles* **23**, <https://doi.org/10.1029/2008GB003267> (2009).
45. Holland, H. D. Sea level, sediments and the composition of seawater. *Am. J. Sci.* **305**, 220–239 (2005).
46. Berner, R. A. & Kothavala, Z. GEOCARB III: a revised model of atmospheric CO₂ over Phanerozoic time. *Am. J. Sci.* **301**, 182–204 (2001).
47. Mills, B., Lenton, T. M. & Watson, A. J. Proterozoic oxygen rise linked to shifting balance between seafloor and terrestrial weathering. *Proc. Natl Acad. Sci. USA* **111**, 9073–9078 (2014).
48. Frings, P. Revisiting the dissolution of biogenic Si in marine sediments: a key term in the ocean Si budget. *Acta Geochim.* **36**, 429–432 (2017).
49. Brady, P. V. & Carroll, S. A. Direct effects of CO₂ and temperature on silicate weathering: possible implications for climate control. *Geochim. Cosmochim. Acta* **58**, 1853–1856 (1994).
50. Pichevin, L., Ganeshram, R., Geibert, W., Thunell, R. & Hinton, R. Silica burial enhanced by iron limitation in oceanic upwelling margins. *Nat. Geosci.* **7**, 541–546 (2014).
51. Soppa, M. A. et al. Global retrieval of diatom abundance based on phytoplankton pigments and satellite data. *Remote Sens.* **6**, 10089–10106 (2014).
52. Siever, R. The silica budget in the sedimentary cycle. *Am. Mineral.* **42**, 821–841 (1957).
53. Drever, J. I. Geochemical model for the origin of Precambrian banded iron formations. *Geol. Soc. Am. Bull.* **85**, 1099–1106 (1974).
54. Holland, H. D. *The Chemical Evolution of the Atmosphere and Oceans* (Princeton Univ. Press, 1984).
55. Perry, E. C. J. & Leftcariu, L. Formation and Geochemistry of Precambrian Cherts. In *Treatise on Geochemistry Vol. 7* (eds Holland, H. D. & Turekian, K. K.) 1–21 (Elsevier, New York, 2003).
56. Maliva, R. G., Knoll, A. H. & Siever, R. Secular change in chert distribution: a reflection of evolving biological participation in the silica cycle. *Palaios* **4**, 519–532 (1989).
57. Fischer, W. W. & Knoll, A. H. An iron shuttle for deepwater silica in Late Archean and early Paleoproterozoic iron formation. *Geol. Soc. Am. Bull.* **121**, 222–235 (2009).
58. Knoll, A. Exceptional preservation of photosynthetic organisms in silicified carbonates and silicified peats. *Phil. Trans. R. Soc. Lond. B* **311**, 111–122 (1985).
59. Knoll, A., Swett, K. & Mark, J. Paleobiology of a Neoproterozoic tidal flat complex: the Draken Conglomerate Formation, Spitsbergen. *J. Paleontol.* **65**, 531–570 (1991).
60. Callow, R. H. & Brasier, M. D. Remarkable preservation of microbial mats in Neoproterozoic siliciclastic settings: implications for Ediacaran taphonomic models. *Earth Sci. Rev.* **96**, 207–219 (2009).
61. Renaut, R., Jones, B. & Tiercelin, J. J. Rapid in situ silicification of microbes at Loburu hot springs, Lake Bogoria, Kenya Rift Valley. *Sedimentology* **45**, 1083–1103 (1998).
62. Newman, S. et al. Experimental fossilization of mat-forming cyanobacteria in coarse-grained siliciclastic sediments. *Geobiology* **44**, 579–582 (2017).
63. Klein, C. Some Precambrian banded iron-formations (BIFs) from around the world: Their age, geologic setting, mineralogy, metamorphism, geochemistry, and origins. *Am. Mineral.* **90**, 1473–1499 (2005).
64. Kaufman, A. J., Hayes, J. & Klein, C. Primary and diagenetic controls of isotopic compositions of iron-formation carbonates. *Geochim. Cosmochim. Acta* **54**, 3461–3473 (1990).

65. Morris, R. Genetic modelling for banded iron-formation of the Hamersley Group, Pilbara Craton, Western Australia. *Precambrian Res.* **60**, 243–286 (1993).

66. Ewers, W. & Morris, R. Studies of the Dales Gorge member of the Brockman iron formation, Western Australia. *Econ. Geol.* **76**, 1929–1953 (1981).

67. Eugster, H. & Chou, I. The depositional environments of Precambrian banded iron-formations. *Econ. Geol.* **68**, 1144–1168 (1973).

68. Rasmussen, B., Muhling, J. R., Suvorova, A. & Krapež, B. Greenalite precipitation linked to the deposition of banded iron formations downslope from a late Archean carbonate platform. *Precambrian Res.* **290**, 49–62 (2017).

69. Rasmussen, B., Krapež, B., Muhling, J. R. & Suvorova, A. Precipitation of iron silicate nanoparticles in early Precambrian oceans marks Earth's first iron age. *Geology* **43**, 303–306 (2015).

70. Tosca, N. J., Macdonald, F. A., Strauss, J. V., Johnston, D. T. & Knoll, A. H. Sedimentary talc in Neoproterozoic carbonate successions. *Earth Planet. Sci. Lett.* **306**, 11–22 (2011).

71. Noack, Y., Decarreau, A., Boudzoumou, F. & Trompette, R. Low-temperature oolitic talc in upper Proterozoic rocks, Congo. *J. Sediment. Res.* **59**, 717–723 (1989).

72. Davis, C. C., Chen, H.-W. & Edwards, M. Modeling silica sorption to iron hydroxide. *Environ. Sci. Technol.* **36**, 582–587 (2002).

73. Siever, R. & Woodford, N. Sorption of silica by clay minerals. *Geochim. Cosmochim. Acta* **37**, 1851–1880 (1973).

74. Konhauser, K. O., Lalonde, S. V., Amskold, L. & Holland, H. D. Was there really an Archean phosphate crisis? *Science* **315**, 1234 (2007).

75. Siever, R. Silica solubility, 0°–200° C, and the diagenesis of siliceous sediments. *J. Geol.* **70**, 127–150 (1962).

76. Konhauser, K. O. et al. Iron formations: a global record of Neoarchaean to Palaeoproterozoic environmental history. *Earth Sci. Rev.* **172**, 140–177 (2017).

77. Korenaga, J., Planavsky, N. J. & Evans, D. A. Global water cycle and the coevolution of the Earth's interior and surface environment. *Phil. Trans. R. Soc. Lond. A* **375**, 20150393 (2017).

78. Flament, N., Coltice, N. & Rey, P. F. A case for late-Archaean continental emergence from thermal evolution models and hypsometry. *Earth Planet. Sci. Lett.* **275**, 326–336 (2008).

79. Satkoski, A. M., Lowe, D. R., Beard, B. L., Coleman, M. L. & Johnson, C. M. A high continental weathering flux into Paleoproterozoic seawater revealed by strontium isotope analysis of 3.26 Ga barite. *Earth Planet. Sci. Lett.* **454**, 28–35 (2016).

80. Lee, C.-T. A. et al. Two-step rise of atmospheric oxygen linked to the growth of continents. *Nat. Geosci.* **9**, 417–424 (2016).

81. Tang, M., Chen, K. & Rudnick, R. L. Archean upper crust transition from mafic to felsic marks the onset of plate tectonics. *Science* **351**, 372–375 (2016).

82. Greber, N. D. et al. Titanium isotopic evidence for felsic crust and plate tectonics 3.5 billion years ago. *Science* **357**, 1271–1274 (2017).

83. Holland, H. D. Why the atmosphere became oxygenated: a proposal. *Geochim. Cosmochim. Acta* **73**, 5241–5255 (2009).

84. O'Neill, C., Lenardic, A., Höink, T. & Coltice, N. Mantle convection and outgassing on terrestrial planets. In *Comparative Climatology of Terrestrial Planets* (eds Mackwell, S. J. et al.) 473–446 (Univ. of Arizona Press, Tucson, 2014).

85. Pletsch, T. Palaeoenvironmental implications of palygorskite clays in Eocene deep-water sediments from the western central Atlantic. *Geol. Soc. Lond. Spec. Publ.* **183**, 307–316 (2001).

86. Rasmussen, B., Meier, D. B., Krapež, B. & Muhling, J. R. Iron silicate microgranules as precursor sediments to 2.5-billion-year-old banded iron formations. *Geology* **41**, 435–438 (2013).

87. Johnson, J. E., Muhling, J. R., Cosmidis, J., Rasmussen, B. & Templeton, A. S. Low-Fe (III) greenalite was a primary mineral from Neoarchean oceans. *Geophys. Res. Lett.* **45**, 3182–3192 (2018).

88. Huang, J., Chu, X., Lyons, T., Planavsky, N. & Wen, H. A new look at saponite formation and its implications for early animal records in the Ediacaran of South China. *Geobiology* **11**, 3–14 (2013).

89. LaBerge, G. L. Development of magnetite in iron formations of the Lake Superior region. *Econ. Geol.* **59**, 1313–1342 (1964).

90. French, B. M. Progressive contact metamorphism of the Biwabik Iron-formation, Mesabi Range, Minnesota. *Minn. Geol. Surv.* **49**, 1–103 https://conservancy.umn.edu/bitstream/handle/11299/57071/MGS_B_45.pdf?sequence=1 (University of Minnesota Digital Conservancy, Univ. Minnesota Press, Minneapolis, 1968).

91. Garrels, R. M. & Mackenzie, F. T. Sedimentary rock types: relative proportions as a function of geological time. *Science* **163**, 570–571 (1969).

92. Peters, S. E. & Husson, J. M. Sediment cycling on continental and oceanic crust. *Geology* **45**, 323–326 (2017).

93. James, H. L. Sedimentary facies of iron-formation. *Econ. Geol.* **49**, 235–293 (1954).

94. Klein, C. Greenalite, stilpnomelane, minnesotaite, crocidolite and carbonates in a very low-grade metamorphic Precambrian iron formation. *Can. Mineral.* **12**, 475–498 (1974).

95. Wood, R. A., Grotzinger, J. P. & Dickson, J. Proterozoic modular biomineralized metazoan from the Nama Group, Namibia. *Science* **296**, 2383–2386 (2002).

96. Martin, R. E. Cyclic and secular variation in microfossil biomineralization: clues to the biogeochemical evolution of Phanerozoic oceans. *Global Planet. Change* **11**, 1–23 (1995).

97. Ridgwell, A. Mid Mesozoic revolution in the regulation of ocean chemistry. *Mar. Geol.* **217**, 339–357 (2005).

98. Grotzinger, J. P. & Knoll, A. H. Anomalous carbonate precipitates: is the Precambrian the key to the Permian? *Palaios* **10**, 578–596 (1995).

99. Sumner, D. Y. & Grotzinger, J. P. Were kinetics of Archean calcium carbonate precipitation related to oxygen concentration? *Geology* **24**, 119–122 (1996).

100. Burton, E. A. & Walter, L. M. Relative precipitation rates of aragonite and Mg calcite from seawater: temperature or carbonate ion control? *Geology* **15**, 111–114 (1987).

101. Reinhard, C. T. et al. Evolution of the global phosphorus cycle. *Nature* **541**, 386–389 (2017).

102. Katsev, S. & Crowe, S. A. Organic carbon burial efficiencies in sediments: the power law of mineralization revisited. *Geology* **43**, 607–610 (2015).

103. Middelburg, J. J. A simple rate model for organic matter decomposition in marine sediments. *Geochim. Cosmochim. Acta* **53**, 1577–1581 (1989).

104. Berner, R. A. *Principles of Chemical Sedimentology* (McGraw-Hill, 1971).

105. Boudreau, B. P. *Diagenetic Models and their Implementation* (Springer, 1997).

106. Wilson, J., Savage, D., Cuadros, J., Shibata, M. & Ragnarsdóttir, K. V. The effect of iron on montmorillonite stability. (I) Background and thermodynamic considerations. *Geochim. Cosmochim. Acta* **70**, 306–322 (2006).

107. Fritz, S. J. & Toth, T. A. An Fe-berthierine from a Cretaceous laterite; Part II. Estimation of Eh, pH and p_{CO_2} conditions of formation. *Clays Clay Miner.* **45**, 580–586 (1997).

108. Weaver, C. E. & Beck, K. C. Miocene of the SE United States: a model for chemical sedimentation in a peri-marine environment. *Sedim. Geol.* **17**, 1–234 (1977).

109. Tosca, N. J. & Wright, V. P. Diagenetic pathways linked to labile Mg-clays in lacustrine carbonate reservoirs: a model for the origin of secondary porosity in the Cretaceous pre-salt Barra Velha Formation, offshore Brazil. *Geol. Soc. Lond. Spec. Publ.* **435**, 435 (2015).

110. Birsoy, R. Formation of sepiolite-palygorskite and related minerals from solution. *Clays Clay Miner.* **50**, 736–745 (2002).

111. Baldermann, A., Mavromatis, V., Frick, P. M. & Dietzel, M. Effect of aqueous Si/Mg ratio and pH on the nucleation and growth of sepiolite at 25°C. *Geochim. Cosmochim. Acta* **227**, 211–226 (2018).

112. Wollast, R., Mackenzie, F. T. & Bricker, O. P. Experimental precipitation and genesis of sepiolite at Earth-surface conditions. *Am. Mineral.* **53**, 1645–1662 (1968).

113. Tosca, N. & Masterson, A. Chemical controls on incipient Mg-silicate crystallization at 25°C: implications for early and late diagenesis. *Clay Miner.* **49**, 165–194 (2014).

114. Sharma, G. D. Influence of CO₂ on silica in solution. *Geochem. J.* **3**, 213–223 (1970).

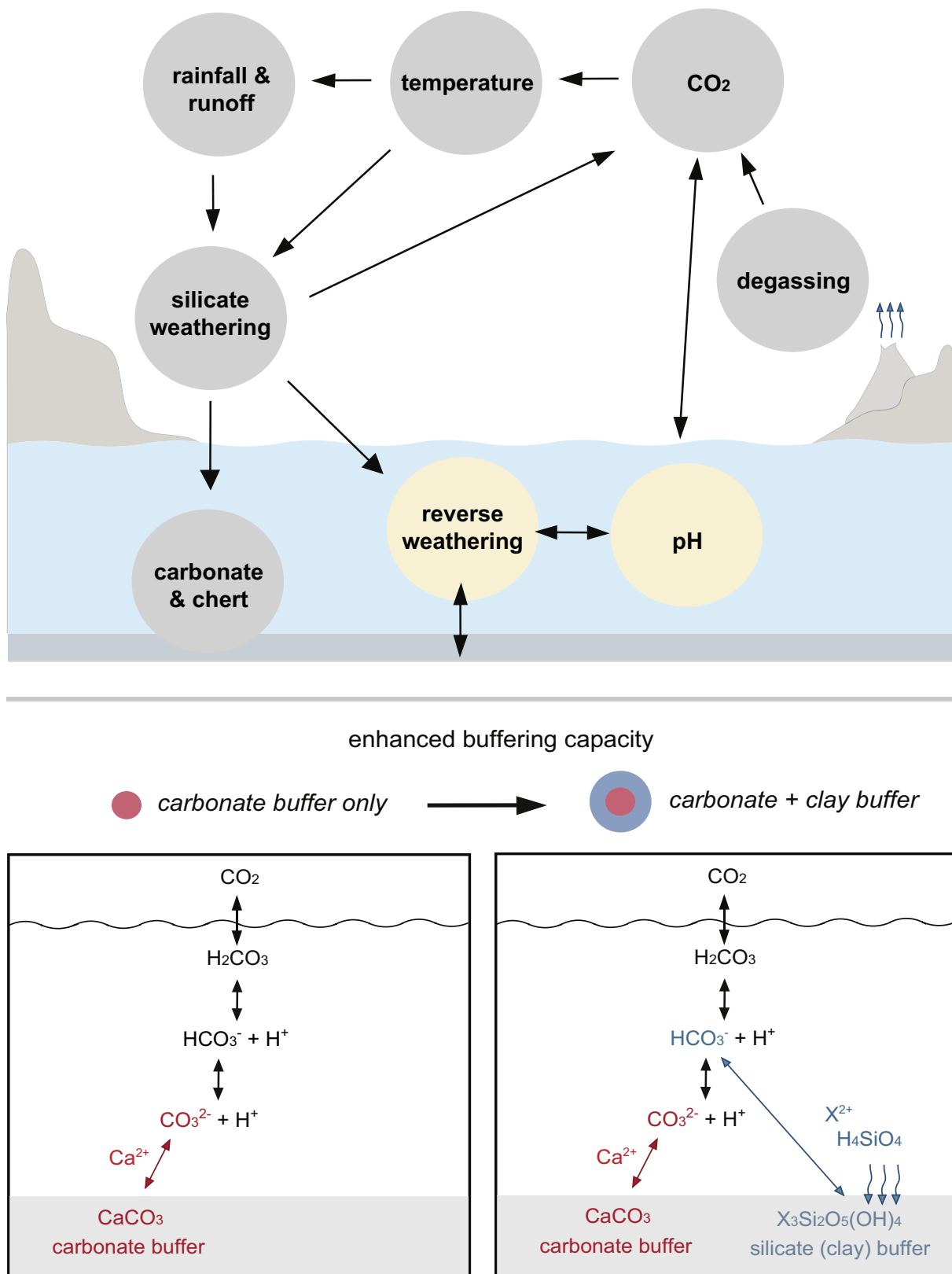
115. Reed, D. C., Slomp, C. P. & Gustafsson, B. G. Sedimentary phosphorus dynamics and the evolution of bottom-water hypoxia: a coupled benthic–pelagic model of a coastal system. *Limnol. Oceanogr.* **56**, 1075–1092 (2011).

116. Uchikawa, J. & Zeebe, R. E. Influence of terrestrial weathering on ocean acidification and the next glacial inception. *Geophys. Res. Lett.* **35**, <https://doi.org/10.1029/2008GL035963> (2008).

117. Sleep, N. H. & Zahnhle, K. Carbon dioxide cycling and implications for climate on ancient Earth. *J. Geophys. Res. Planets* **106**, 1373–1399 (2001).

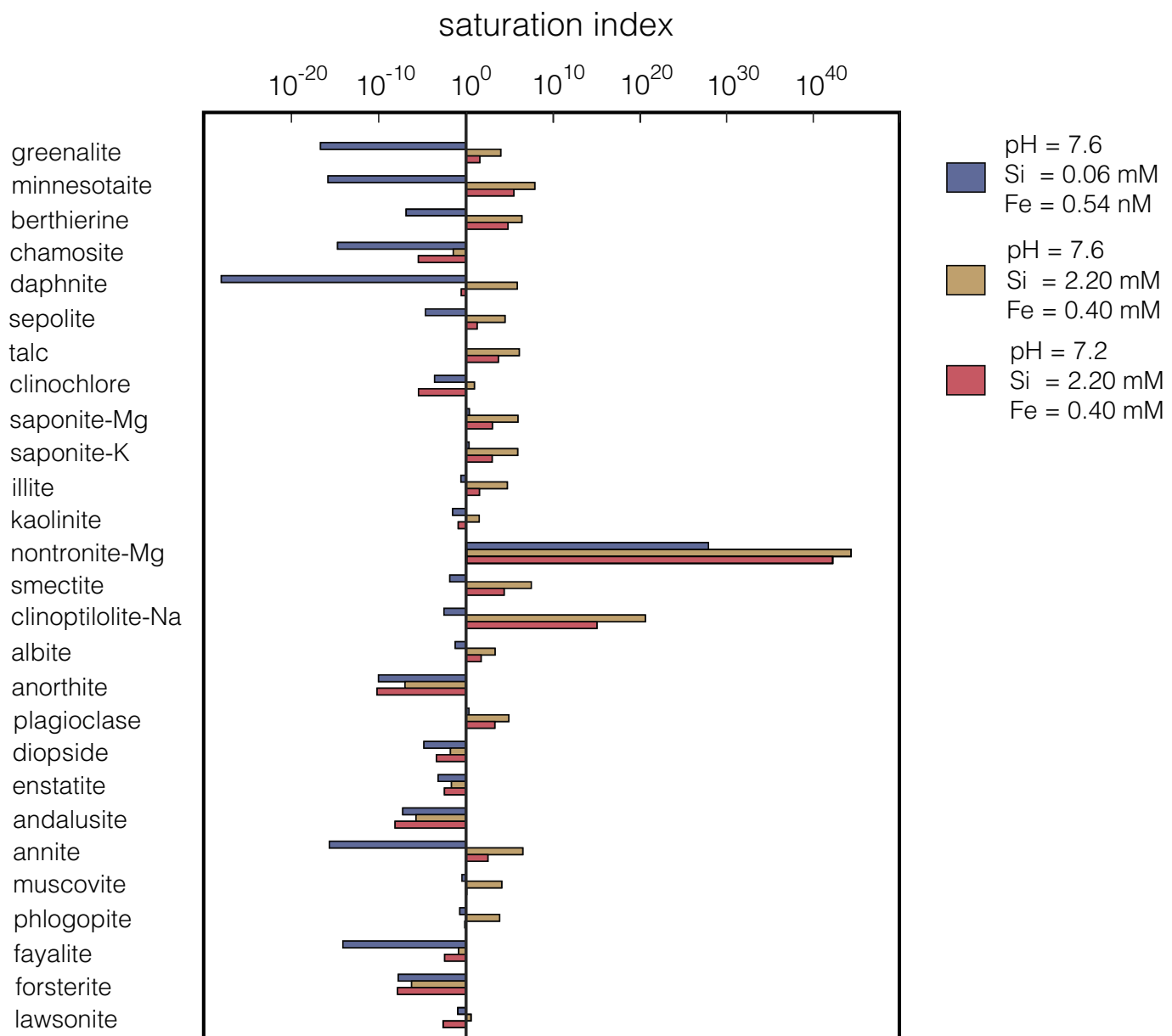
118. Walker, J. C. & Kasting, J. F. Effects of fuel and forest conservation on future levels of atmospheric carbon dioxide. *Global Planet. Change* **5**, 151–189 (1992).

119. Volk, T. Feedbacks between weathering and atmospheric CO₂ over the last 100 million years. *Am. J. Sci.* **287**, 763–779 (1987).



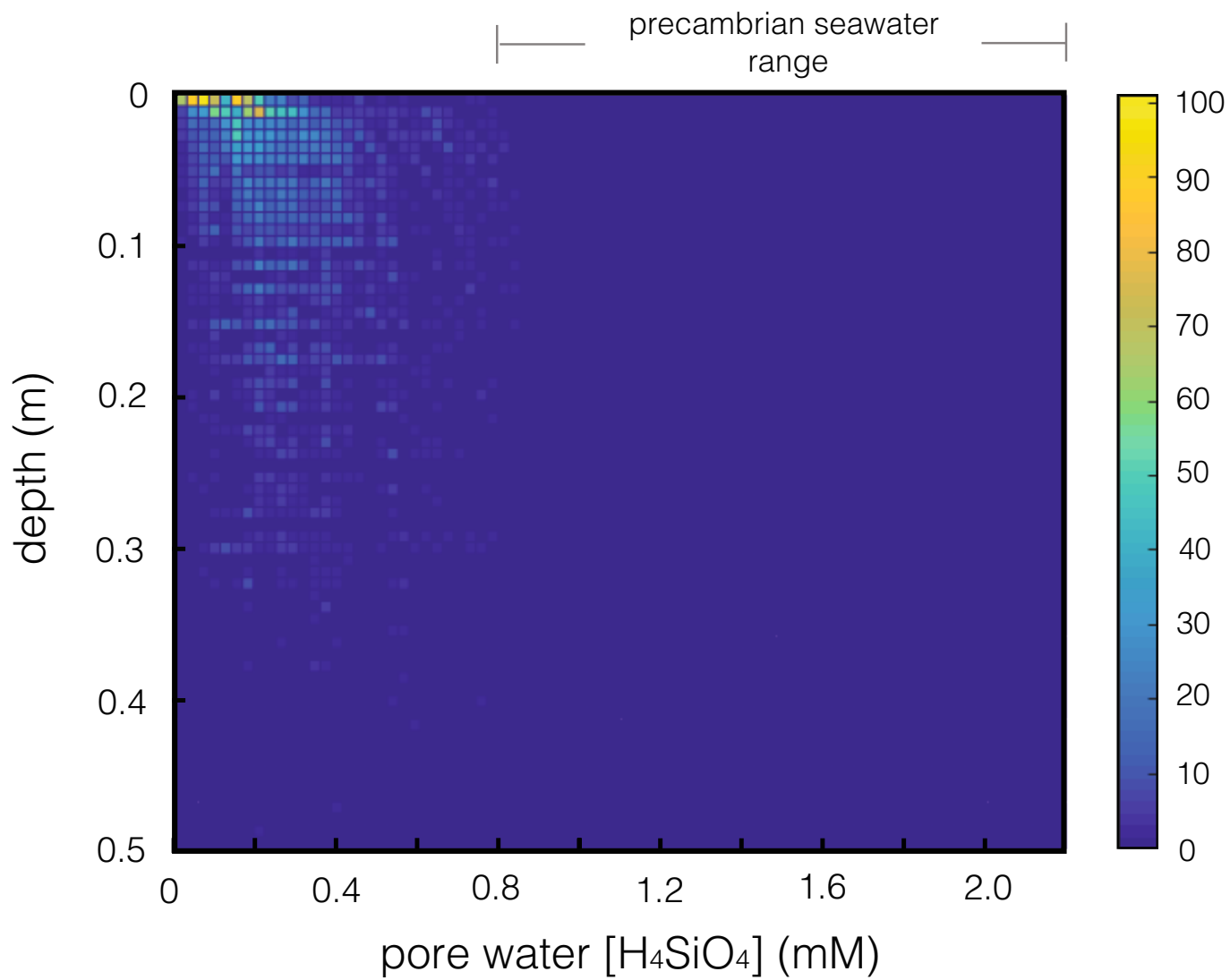
Extended Data Fig. 1 | Conceptual model for reverse weathering as a stabilizer of the long-term global carbon cycle and climate. Reverse weathering regulates atmospheric P_{CO_2} through the establishment of a stabilizing feedback with marine pH (a pH thermostat). This feedback operates in conjunction with the silicate weathering feedback (dependence

of chemical weathering and erosion on temperature and rainfall) to stabilize climate. A more potent reverse-weathering buffer, which is to be expected under high-silica Precambrian conditions, greatly strengthens the pH buffering capacity of oceans.



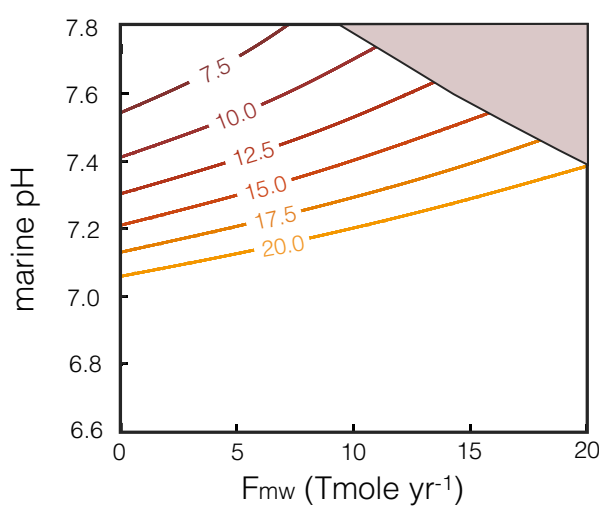
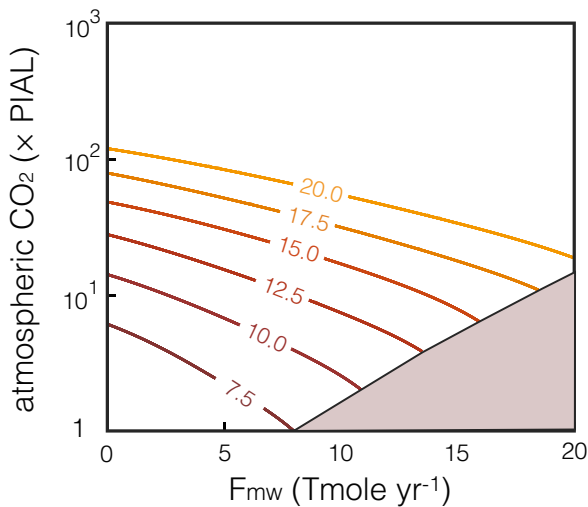
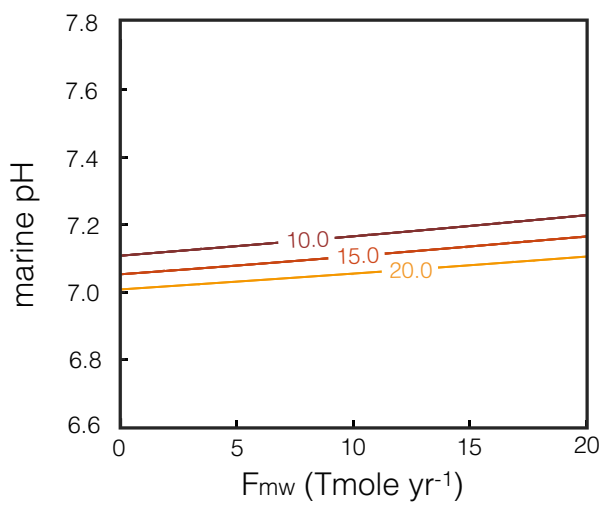
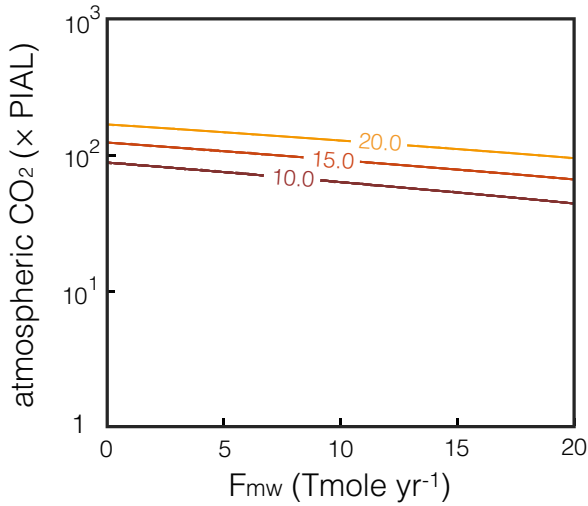
Extended Data Fig. 2 | Saturation index of some common rock forming silicates in modern and Precambrian bottom waters. The baseline conditions of the dissolved species are $\text{Na} = 0.48 \text{ M}$; $\text{Fe} = 540 \times 10^{-12} \text{ M}$; $\text{Mg} = 52.7 \text{ mM}$; $\text{K} = 10.2 \text{ mM}$; $\text{Al} = 1 \times 10^{-15} \text{ M}$; $\text{Ca} = 10.3 \text{ mM}$.

Dissolved silica and iron concentrations are varied between modern-like (blue) and estimated Precambrian-like conditions (yellow and red). Thermodynamic database is Geochimists Workbench 10.0 (<https://www.gwb.com/pdf/GWB10/GWBessentials.pdf>).



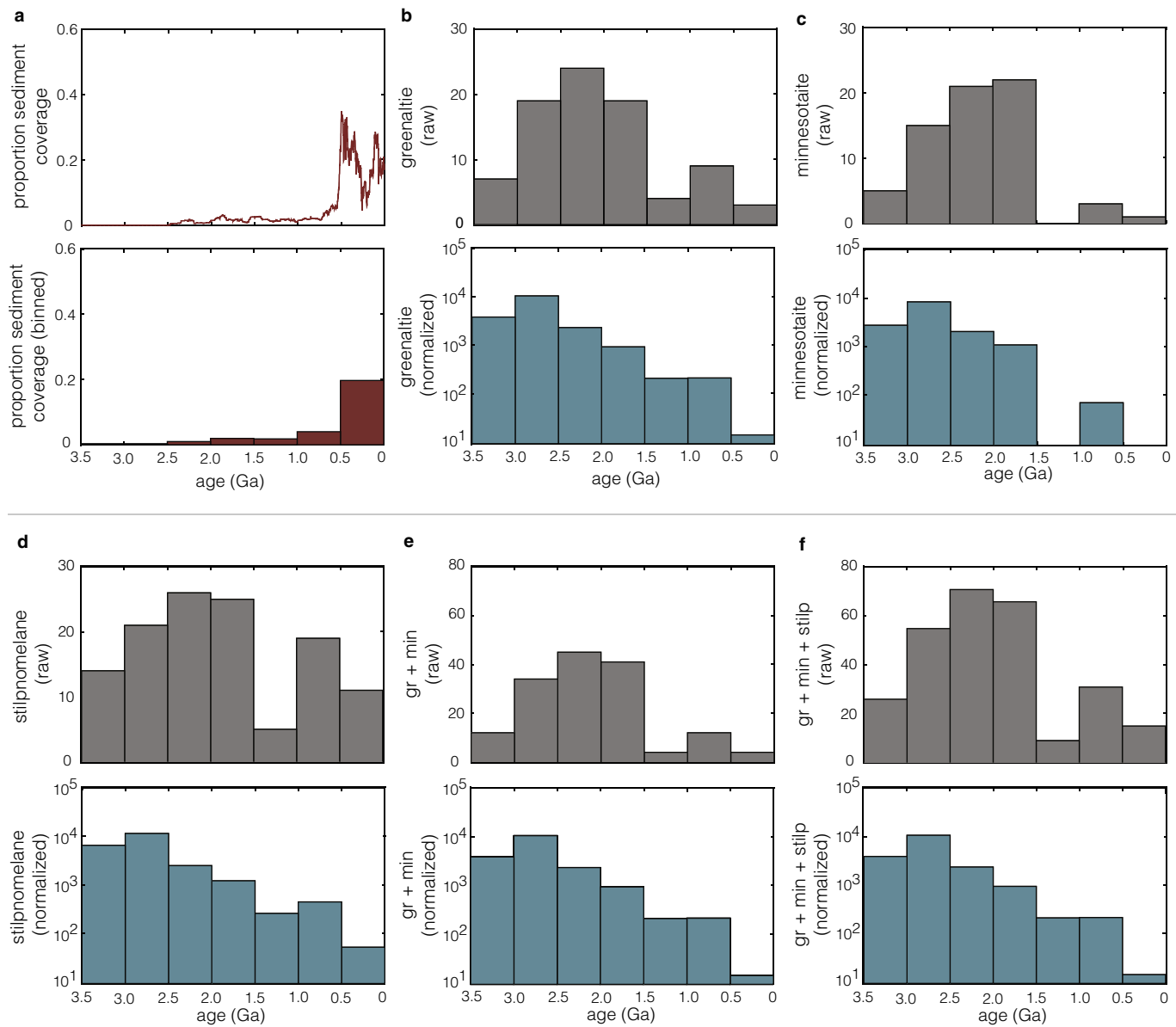
Extended Data Fig. 3 | An occurrence density plot of modern marine porewater dissolved silica levels. The plot is based on dissolved silica concentrations ($n = 6,245$) from 453 sediment cores globally⁴⁸. The map

plots dissolved Si levels with sediment depth (depth = 0 indicates the sediment–water interface). Warmer colours indicate elevated occurrences.

a**b**

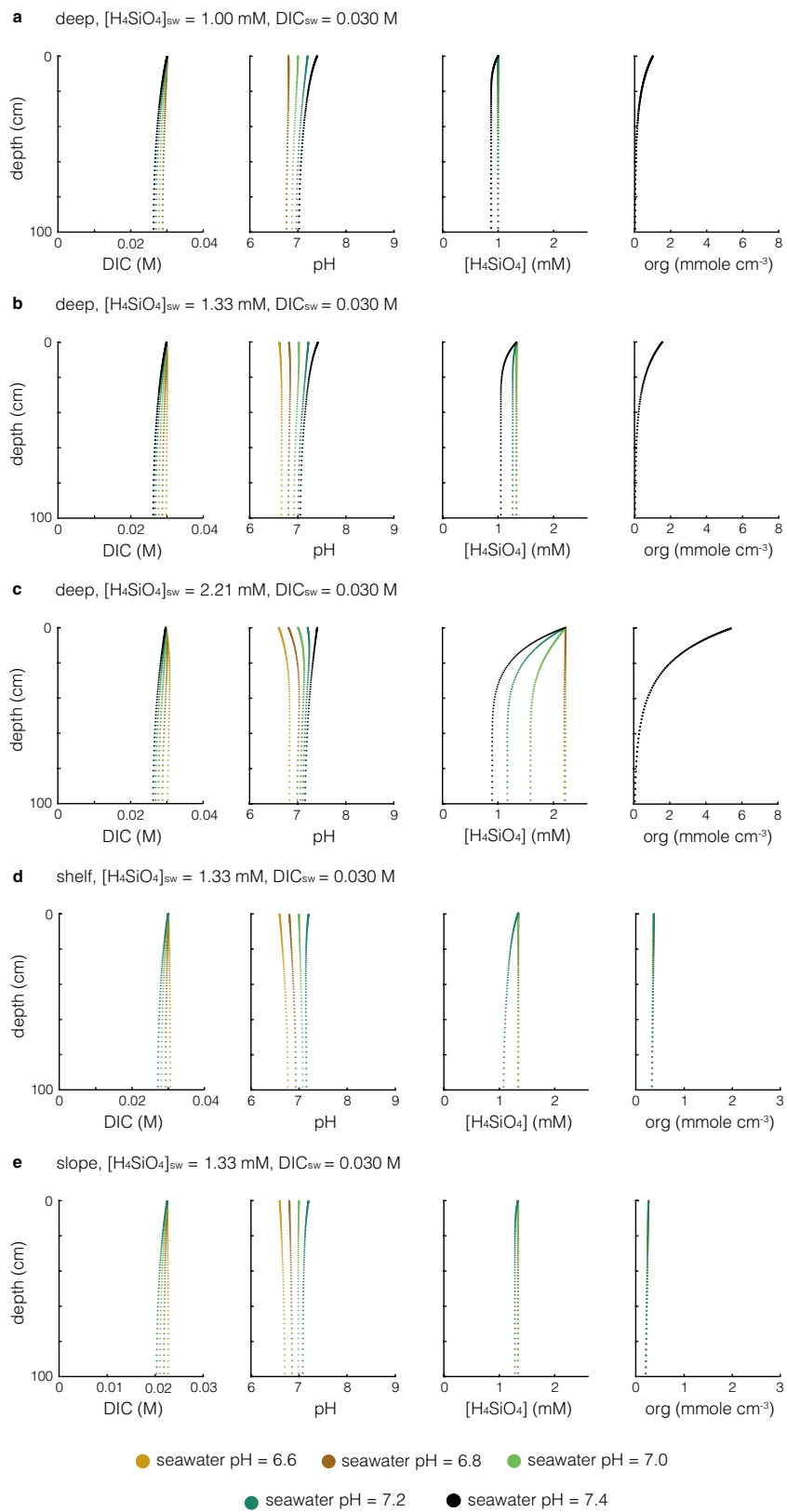
Extended Data Fig. 4 | Sensitivity analysis to marine weathering fluxes. Steady-state results for P_{CO_2} and pH over the estimated range of marine weathering CO_2 consumption flux (F_{mw}) after ref. ²⁷. **a**, Simulating modern Earth states. Acidity release through reverse weathering is fixed at 1 Tmol yr^{-1} . **b**, Simulating Precambrian Earth states with elevated

reverse-weathering buffer at dissolved silica of 1.33 mM. Contours highlight the variation of volcanic outgassing rates in teramoles per year. Shaded areas indicate parameter space that is unattainable for a steady-state system (marine weathering exceeds the sum of CO_2 fluxes from degassing and extent of reverse weathering).



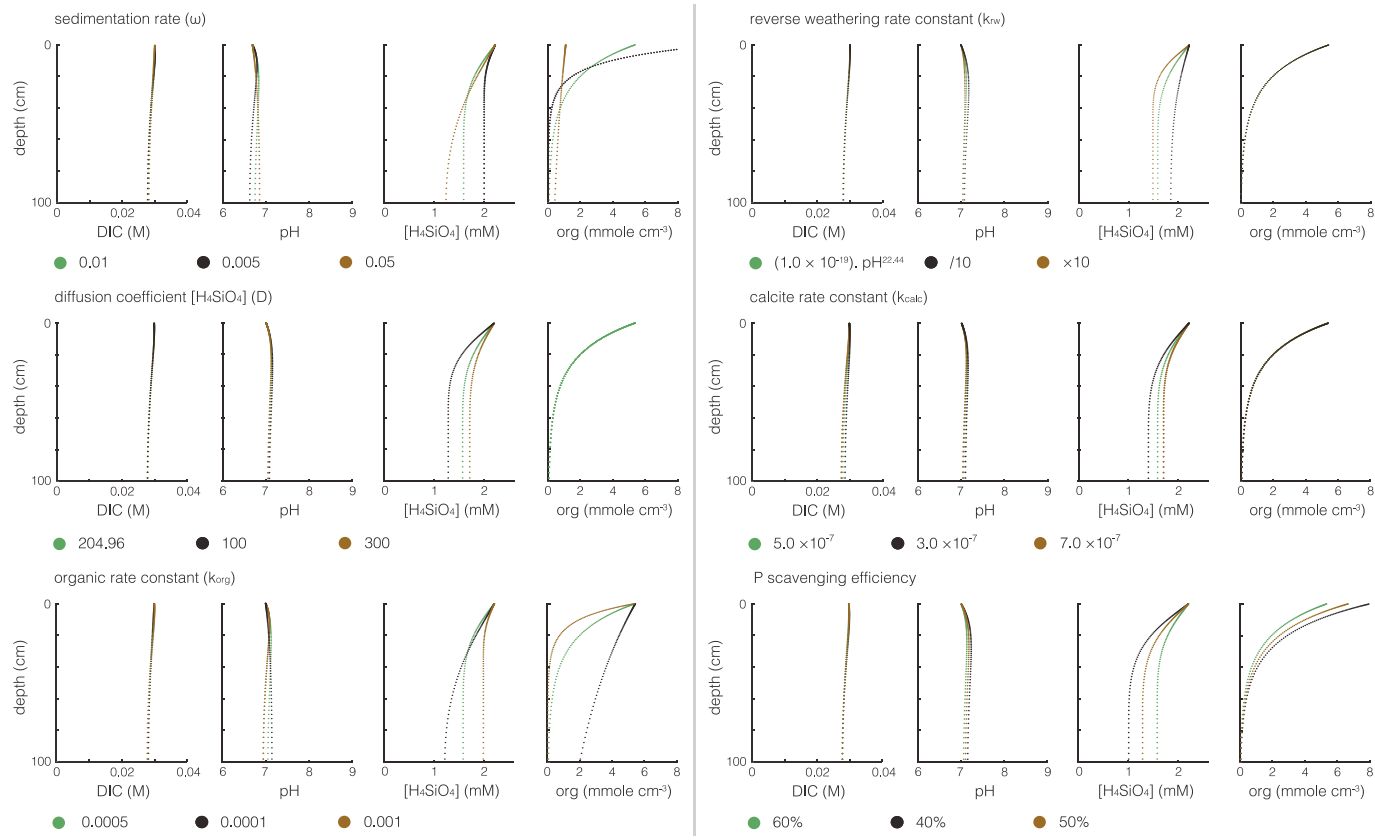
Extended Data Fig. 5 | Literature compilation of greenalite (gr), minnesotaite (min) and stilpnomelane (stilp) in marine sedimentary units through time. **a**, Proportion of marine sediment coverage through

time⁹². **b–f**, Raw data for the minerals given, and data normalized to the proportion of marine sediment coverage.



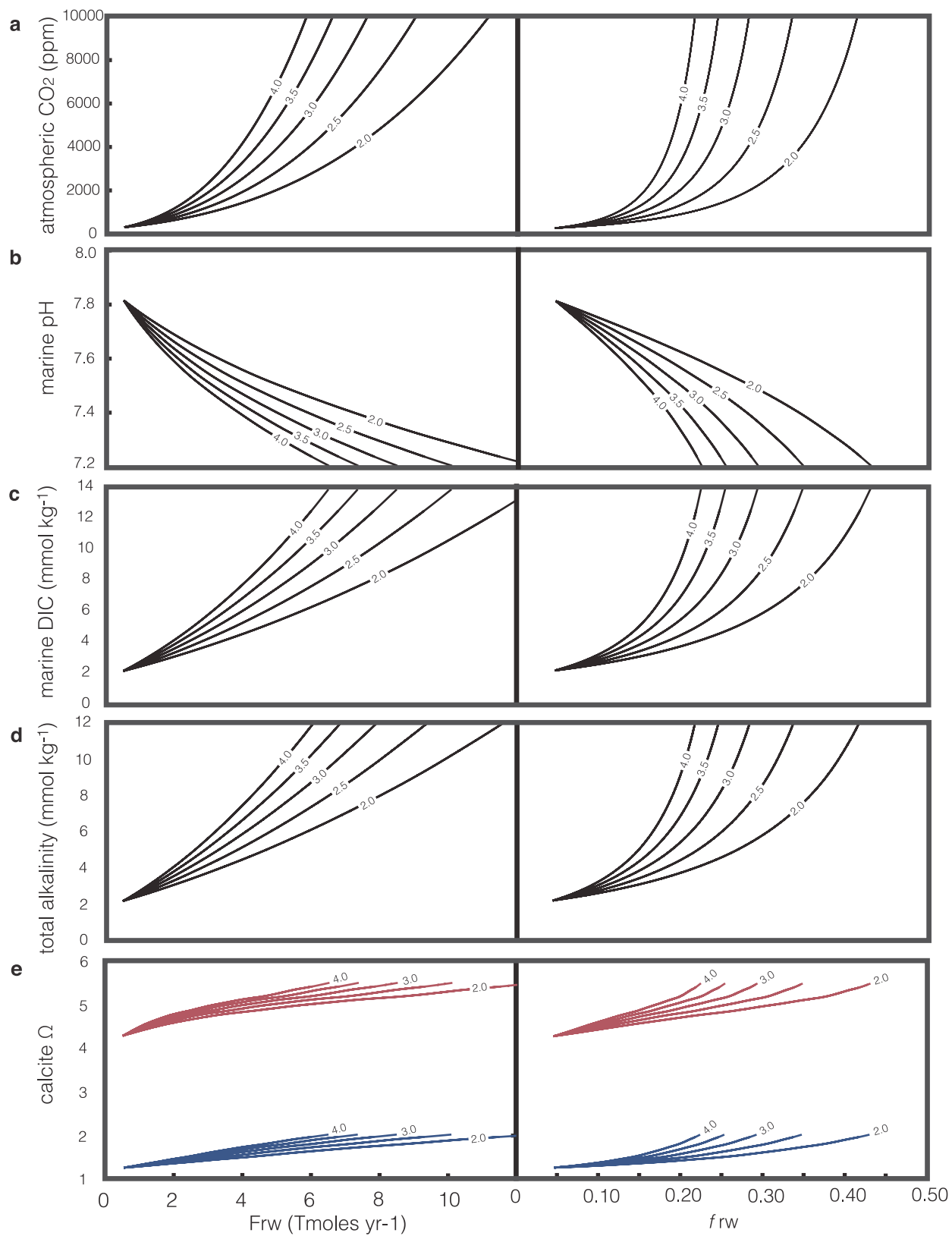
Extended Data Fig. 6 | Example porewater profiles of DIC, pH, $[H_4SiO_4]$ and organic (org) matter at steady state. Curves represent results from model runs at varying bottom seawater pH (6.6–7.4)

and $[H_4SiO_4]$ (1.00–2.21 mM) conditions in diffusional exchange with sediment porewaters in deep sea (a–c), slope (d) and shelf (e) environments. Subscript 'sw' indicates seawater.

**Extended Data Fig. 7 | Analysis of sensitivity to diagenetic model parameters.**

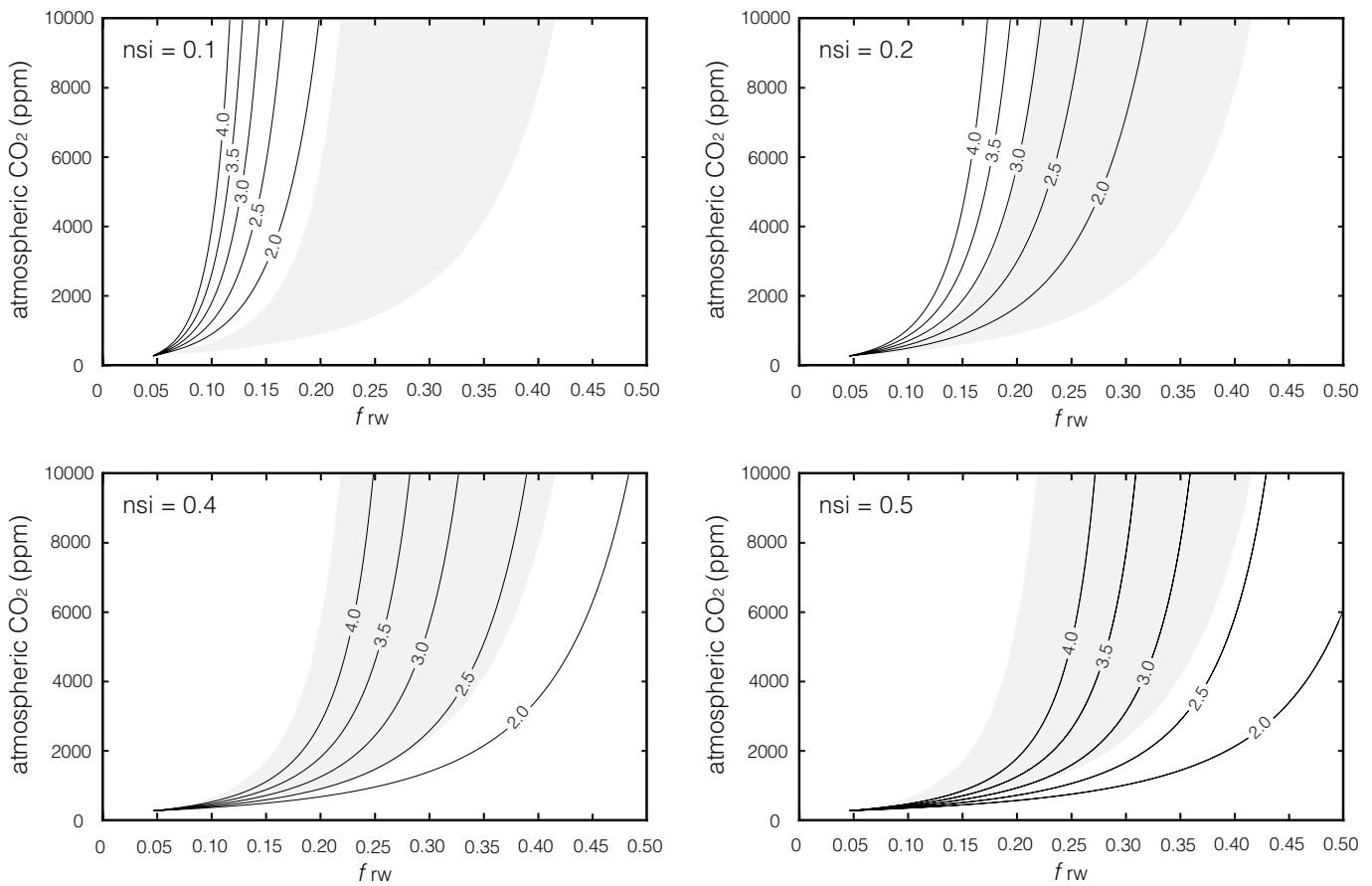
parameters. Baseline conditions (green) are the deep-sea environment, with marine $[H_4SiO_4] = 2.21\text{ mM}$ and marine DIC = 0.030 M . Shown are sensitivity to sedimentation rate ω (yr^{-1}), diffusion coefficient of $[H_4SiO_4]$

($\text{cm}^2 \text{yr}^{-1}$), organic matter rate constant k_{org} (yr^{-1}), reverse-weathering rate constant k_{rw} (yr^{-1}), calcite rate constant k_{calc} ($\text{mol cm}^{-3} \text{yr}^{-1}$) and the efficiency of water column P scavenging.

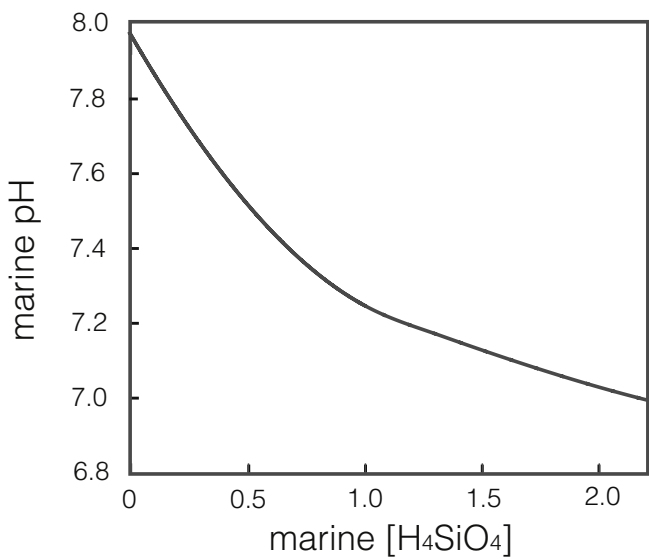
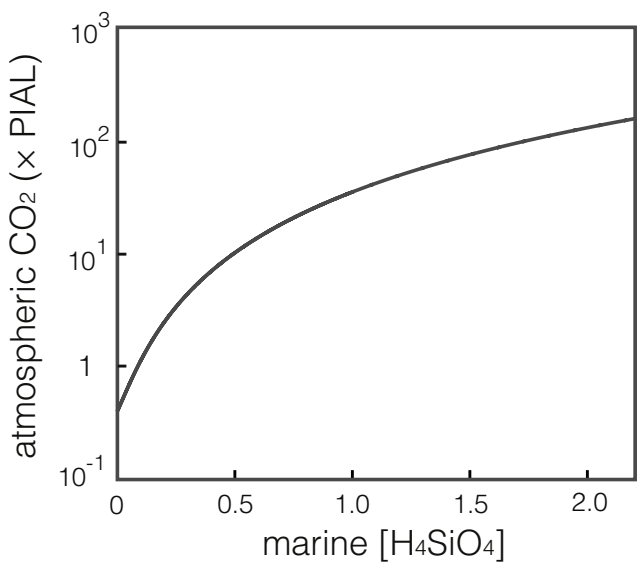


Extended Data Fig. 8 | Steady-state outputs for reverse weathering versus the given parameters. **a**, Atmospheric P_{CO_2} ; **b**, marine pH; **c**, marine DIC; **d**, total alkalinity; **e**, calcite saturation, Ω . F_{rw} is the total silica consumption flux and f_{rw} is the fraction of the consumption flux of the total marine silica input. Within panel **e**, shallow-water values are

plotted in red and global ocean mean values in blue. Contours represent variations to Alk:Si. The strength of the silicate weathering feedback (n_{si}) is set at 0.3. The root of each curve depicts preindustrial estimates and a reverse-weathering silica flux of about 0.5 Tmol yr^{-1} ($f_{\text{rw}} = 0.05$)²⁹.



Extended Data Fig. 9 | Sensitivity analysis to the strength of the silicate weathering feedback. $n_{si} = 0.1\text{--}0.5$. Data are from refs^{11,20,46,116–119}. The grey-shaded area highlights the range where $n_{si} = 0.3$ (Fig. 1). Contours represent variations to Alk:Si.



Extended Data Fig. 10 | The relationship between marine $[\text{H}_4\text{SiO}_4]$ and p_{CO_2} and marine pH at modern outgassing rates.

A Triassic stem turtle with an edentulous beak

Chun Li^{1,2*}, Nicholas C. Fraser³, Olivier Rieppel⁴ & Xiao-Chun Wu^{5*}

The early evolution of turtles continues to be a contentious issue in vertebrate palaeontology. Recent reports have suggested that they are diapsids^{1–6}, but the position of turtles within Diapsida is controversial^{7–12} and the sequence of acquisition of turtle synapomorphies remains unclear^{1–3}. Here we describe a Triassic turtle from China that has a mixture of derived characters and plesiomorphic features. To our knowledge, it represents the earliest known stem turtle with an edentulous beak and a rigid puboischiadic plate. The discovery of this new form reveals a complex early history of turtles.

The turtle is represented by a nearly complete skeleton from the lower Carnian (about 228 million years ago) of the Guanling District, Guizhou Province, southwestern China (Fig. 1a); it was collected from sediments approximately 7.5 m below the horizon that contained the stem turtle *Odontochelys*¹³ (Extended Data Fig. 1). The most notable features of the newly described taxon are the edentulous beak formed by the anterior parts of the upper and lower jaws, the closure of the supratemporal fenestra by the contact of the parietal with the postorbital and postfrontal, the reduced number of the dorsal vertebrae with the transversely broadened ribs, and the formation of a rigid puboischiadic plate, whereas a carapace and plastron are absent.

Reptilia Laurenti, 1768

Pantestudines Joyce, Parham and Gauthier, 2004¹⁴

Eorhynchochelys sinensis gen. et sp. nov.

Etymology. *Eo-* (dawn), *rhyhncho-* (beak), *chelys* (turtle): the earliest turtle with a beak; *sinensis*, from China.

Holotype. Sanya Museum of Marine Paleontology (SMMMP) 000016 in Hainan Province, China, an articulated specimen displaying the postcranium in dorsal view, and the skull in ventral view (the skull and pelvis were prepared from both sides).

Locality. Heshangjing of Baiyuncun, Xinpuxiang, Guanling District, Guizhou Province, southwestern China.

Horizon. The upper unit of the lower part of the Wayao Member of the Falang Formation, approximately 8.5 m above the top of the Zhuganpo Member; Late Triassic (Carnian age).

Diagnosis. A stem pantestudine of large size; proportionately small skull broadly triangular in outline; supratemporal fenestra closed; infratemporal fenestra partially open; edentulous beak; pleurodont tooth implantation; teeth on parabasisphenoid; 12 dorsal vertebrae; neural spines with disc-like dorsal tables in cervical vertebra 8 to caudal 5; dorsal ribs 1 through 10 horizontally (anteroposteriorly) broadened, T-shaped in cross-section; rigid puboischiadic plate with median ventral keel; and ischium with posterior elongation.

The edentulous premaxillae and the anterior parts of the dentaries show a noticeably rugose surface with small pits and fine grooves, indicating the presence of a keratinous beak in *Eorhynchochelys* (Fig. 2a, c, e, f and Extended Data Fig. 2a–d). The exposed anterior teeth of the right maxilla are conical, but the exposed posterior teeth of the left maxilla are pleurodont, column-like and have a blunt tip (Extended Data Fig. 2a, e). The supratemporal fenestra is closed and the supratemporal bone is absent (Fig. 2a, c and Extended Data Fig. 3).

The pterygoid exhibits a distinct transverse flange and numerous conical teeth scattered across its entire ventral surface. The prominent parabasisphenoid has well-developed basipterygoid processes, and anteriorly extends into a broad-based, dentigerous cultriform process (Fig. 2b, d). The large basioccipital displays robust basal tubera. The sutures remain unfused in the exoccipital–opisthotic complex, which extends into a robust paroccipital process. The disarticulated supraoccipital shows a concave inner (ventral) surface.

There are 9 cervical, 12 dorsal, 2 sacral and 56 caudal vertebrae, all of which are non-notochordal and amphicoelous. The vertebral column is characterized by mid-dorsals that bear elongate prezygapophyses with a small, concave articular facet and short postzygapophyses and by neural spines that have broadened dorsal tables in posterior cervical vertebrae through anterior caudal vertebrae (Figs. 1a–c, 3a, b and Extended Data Fig. 4).

Cervical ribs 7 to 9 are complete and lack an anterior process (Fig. 1b, c). Cervical rib 9 has a much more elongate distal shaft of uniform diameter, a sharp transition that occurs at the eighth vertebra in *Proganochelys*¹⁵. Dorsal ribs 1 to 10 are dichotomous and approximately T-shaped in cross-section as they expand to form prominent anterior and posterior horizontal flanges. These ribs extend laterally with minimal ventral curvature and together form a flattened carapace-like shield (Fig. 1a). There is, however, no contact or overlap of successive ribs. Dorsal ribs 11 and 12 are shorter and much less expanded than the more anterior ones. The sacral ribs are stout and fused to the sacral vertebrae (Fig. 3a, b and Extended Data Fig. 5).

The scapular blade is long and narrow with a slight distal expansion. There is a very weak development of an acromion (Fig. 1b, c). The clavicle is broad and stout anteromedially along its articulation with the rather narrow lateral process of the dorsoventrally expanded interclavicle; posterolaterally the scapular process of the clavicle becomes more slender.

With a pronounced postacetabular process, the ilium is similar to that of *Pappochelys* and *Odontochelys* (Fig. 3a, b). As preserved, the puboischiadic plate was broken, the right portion partially obscuring the left portion in ventral view. The rounded anterior edge of the pubis shows no evidence of an epipubic process; however, an incipient lateral process is present (Fig. 3c–e). A deep incision in the posterior margin of the pubis, closed posteriorly by the ischium, marks the obturator foramen. A second foramen piercing the ischium lies immediately behind the latter. In ventral view the ischium is practically indistinguishable from that of *Odontochelys* (Fig. 3c–g), exhibiting a prominent lateral tubercle behind the acetabulum. Posteromedial to the lateral tubercle, the ischium narrows to form an elongate process. The pubes and ischia meet in a broad suture along the ventral midline, thus forming a robust and solid puboischiadic plate with a distinct medioventral keel, as is also the case in *Odontochelys* (Fig. 3c–g). The posterior elongation of the ischium terminates in a blunt tip, similar to *Odontochelys*; however, *Eorhynchochelys* lacks a separate hypischium that is present in *Odontochelys* and *Proganochelys* (Extended Data Fig. 6).

The arrangement of the gastralia remains unclear. Some rod-like gastralia elements are loosely scattered below the dorsal ribs (Fig. 3a, b),

¹Key Laboratory of Vertebrate Evolution and Human Origins, Institute of Vertebrate Paleontology and Paleoanthropology (IVPP), Chinese Academy of Sciences, Beijing, China. ²Center for Excellence in Life and Paleoenvironment, Chinese Academy of Sciences, Beijing, China. ³National Museums Scotland, Edinburgh, UK. ⁴Field Museum of Natural History, Chicago, IL, USA. ⁵Canadian Museum of Nature, Ottawa, Ontario, Canada. *e-mail: lichun@ivpp.ac.cn; xcwu@nature.ca

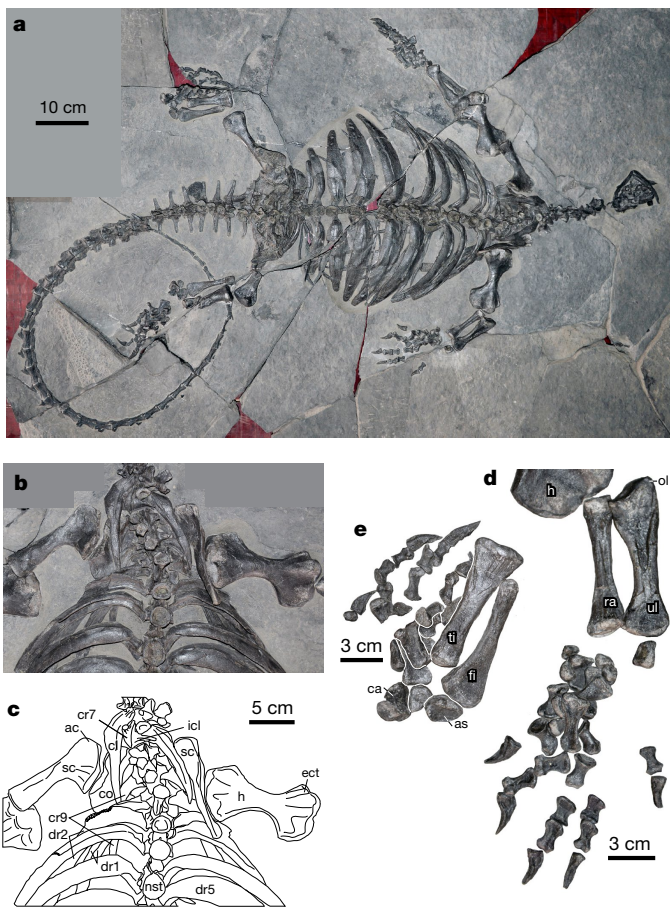


Fig. 1 | The holotype of *E. sinensis* (SMMP 000016). **a**, Complete articulated skeleton, as preserved. **b, c**, Photograph and interpretative drawing of anterior axial skeleton, pectoral girdle and right zeugopodium in dorsal view with elongate and narrow scapula blade and enlarged, circular neural spine tables that are deeply concave. **d**, Right autopodium of forelimb in posteroventral view. **e**, Right autopodium of hindlimb in posterior view. *Eorhynchochelys* is only known from a single specimen, reaching almost 2.3 m in total length including the conspicuously long tail, and is much larger than *Odontochelys* in size. The relatively small, broad and triangular skull, approximately 9.0 cm long, was separated from the neck by about two centimetres, and is exposed in ventral view, whereas most of the postcranial skeleton is articulated and exposed in dorsal view. The fusion of the neural arches to their centra and well-ossified ends of all long bones suggest that the specimen represents a fully grown adult. ac, acromion; as, astragalus; ca, calcaneum; cl, clavicle; co, coracoid; cr9, cervical rib 9; dr1, dr2, dr5, dorsal ribs 1, 2, 5; ect, ectepicondylar groove; fi, fibula; h, humerus; icl, interclavicle; nst, neural spine table; ol, olecranon; ra, radius; sc, scapula; tib, tibia; ul, ulna.

however, it was not possible to determine whether there was any fusion of some of the gastral ribs, similar to *Pappochelys*.

The fore- and hindlimbs are approximately equal in length and generally very robust. Both the humerus and femur have well-developed proximal and distal heads. The humerus exhibits a shallow S-shaped flexure and a prominent ectepicondylar groove (Fig. 1b, c). The femur has a distinct internal trochanter and the proximal head is offset from the shaft. The carpals and tarsals are well-ossified, but unlike in *Odontochelys*, the astragalus and calcaneum, both of irregular contours, remain separate. Each digit terminates in an ungual that is always longer than the penultimate phalanx (Fig. 1d, e).

Eorhynchochelys exhibits a mosaic of characters, some of which are shared with *Pappochelys* and others with *Odontochelys* and more derived turtles. *Eorhynchochelys* and *Pappochelys* have double-headed and expanded dorsal ribs with gently tapering distal ends, whereas in *Odontochelys*, the single-headed dorsal ribs have blunter distal terminations and in *Eunotosaurus*⁹ the weakly double-headed dorsal

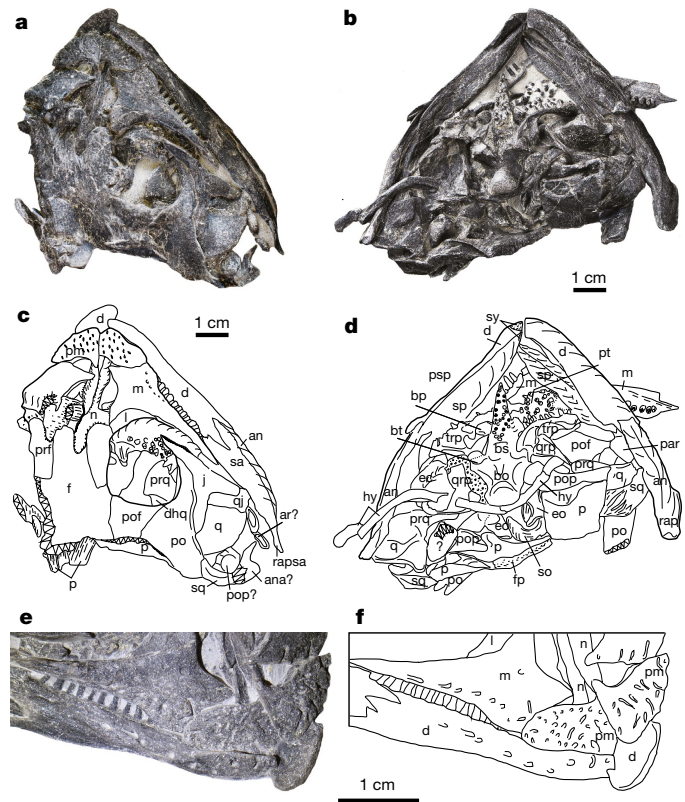


Fig. 2 | Skull of *E. sinensis* (SMMP 000016). **a–d**, Photographs and interpretative line drawings of the skull in dorsal and ventral views. **e, f**, The snout in dorsal and slightly lateral view. As shown in **a–d**, the maxilla meets the premaxilla in a broad suture and the posterior region of the skull has been crushed so that the squamosals, parietals and associated occipital region have been pushed underneath the back end of the skull; nevertheless, it is clear that the much-enlarged postorbital, postfrontal and parietal broadly contact each other, indicating the absence of a supratemporal fenestra; the large quadrate and associated quadratojugal have been displaced anteriorly and crushed, leaving the extent of the lower temporal fenestra equivocal; and the jugal has a distinct posterior process but there is no indication that it established a sutural contact with the quadratojugal. an, angular; ana, atlantal neural arch; ar, articular; bo, basioccipital; bp, basipterygoid process; bs, basisphenoid; bt, basal tubera; d, dentary; dhq, dorsal head of quadrate; ec, ectopterygoid; eo, exoccipital; f, frontal; fp, articular facet of parietal; hy, hyoid; j, jugal; l, lachrymal; m, maxilla; n, nasal; p, parietal; pm, premaxilla; po, postorbital; pof, postfrontal; pop, paroccipital process; prf, prefrontal; pt, pterygoid; q, quadrate; qj, quadratojugal; qrp, quadrate ramus of pterygoid; rap, retroarticular process; rapsa, retroarticular process of surangular; sa, surangular; so, supraoccipital; sp, splenial; sq, squamosal; trp, transverse process of pterygoid; ?, an undetermined bone. Zigzag lines denote broken surfaces.

ribs show a strongly curved shaft with narrowed distal portions. In *Eorhynchochelys*, the trunk is noticeably broader in the mid-dorsal region, whereas in *Pappochelys* the trunk is approximately parallel sided. As in *Odontochelys*, *Proganochelys*, and all crown-group turtles, the supratemporal fenestra is closed in *Eorhynchochelys*, but the infratemporal fenestra would seem to have been partially open ventrally. The acromion is slightly more prominent than in *Pappochelys*, but not as pronounced as in *Odontochelys*. In the absence of a plastron, the ventrolateral process of the pubis is only minimally developed and, unlike in *Pappochelys* and *Odontochelys*, there is no trace of an ossified epipubic process in *Eorhynchochelys*. The presence of a lateral tubercle and a posterior elongation in the ischium are features that are shared with *Odontochelys*; the rigid puboischiadic plate is a feature that is shared with *Odontochelys* and more derived turtles. There is no trace of a separately ossified hypoischium in either *Eorhynchochelys* or *Pappochelys*.

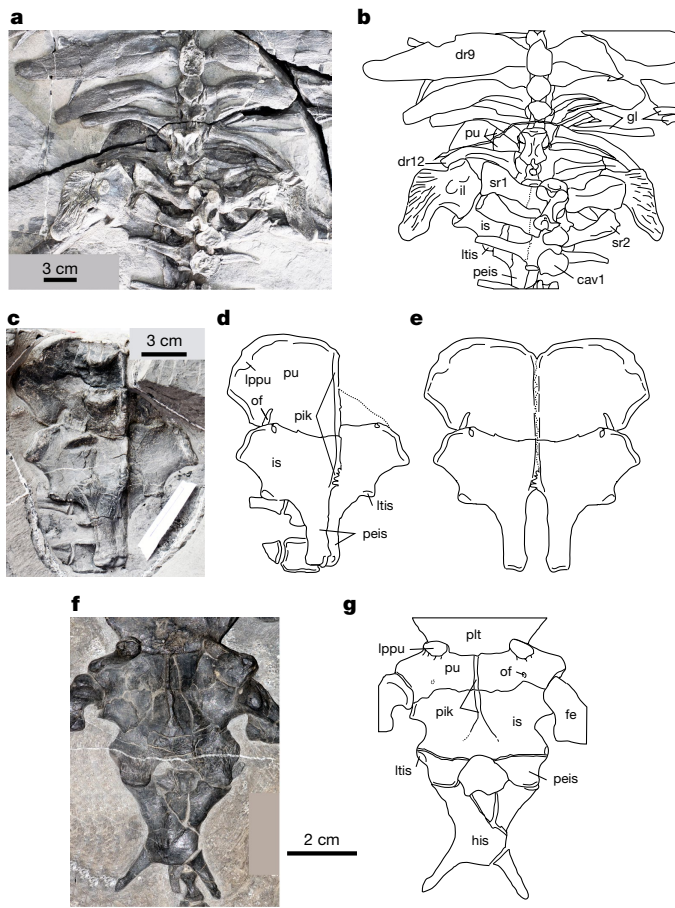


Fig. 3 | Posterior dorsal vertebrae and pelvic girdle of stem turtles. a, b, Photographs and interpretative drawings of the holotype of *E. sinensis* (SMMP 000016) in dorsal view, showing very low neural spines that, at their tips, expand to form extensively broadened dorsal tables with a circular-to-subcircular circumference and a distinctly concave surface in dorsal view in posterior cervicals (Fig. 1b, c) through anterior caudals. The unusually extensive and prominent dorsal tables of the neural spines differ from the convex or flat surface of the dorsal tables supporting dermal osteoderms in armored diapsids, such as extant crocodylians. The condition in *E. sinensis* seems to be unique and may represent a hitherto unknown evolutionary stage of the formation of neurals in more derived turtles. In addition, the stout sacral ribs are fused to the sacral vertebrae (as they are also in *Odontochelys* and *Pappochelys*) and their distinctly expanded distal ends are detached from the ilium, in contrast to the tightly fused condition in *Proganochelys*. c–e, The pubes and ischium in ventral view. f, g, The paratype of *Odontochelys semitestacea* (IVPP V 13240) in ventral view. cav1, caudal rib 1; dr9, dr12, dorsal ribs 9, 12; fe, femur; gl, gastralia; his, hypopophysis; il, ilium; is, ischium; lppu, lateral process of pubis; ltis, lateral tubercle of ischium; of, obturator foramen; peis, posterior elongation of pubis; pik, puboischiadic keel; plt, plastron; pu, pubis; sr1, sr2, sacral ribs 1, 2.

A phylogenetic analysis using TNT v.1.0¹⁶ based on a data matrix derived from the reduced, previously published dataset⁴ (Supplementary Information) recovered a phylogeny in which Pantestudines, including a *Claudiosaurus*–*Acerosodontosaurus* clade, appears as the sister group of a clade including Archosauromorphia, Lepidosauria, Kuehneosauridae and aquatic groups (Fig. 4; see Extended Data Fig. 7, in which Pantestudines is less inclusive based on the large data matrix derived from the previously published datasets^{3,4}). Within Pantestudines, the phylogenetic position of *Eorhynchochelys* is more derived than that of *Pappochelys*, whereas *Eunotosaurus* retains its position more basal than that of the latter^{2–4}. With a Bremer support value of 11, the monophyly of an ingroup formed by *Eunotosaurus* and more derived turtles is strongly supported. The sister-group relationship of *Eorhynchochelys* with the *Odontochelys*–*Proganochelys* clade

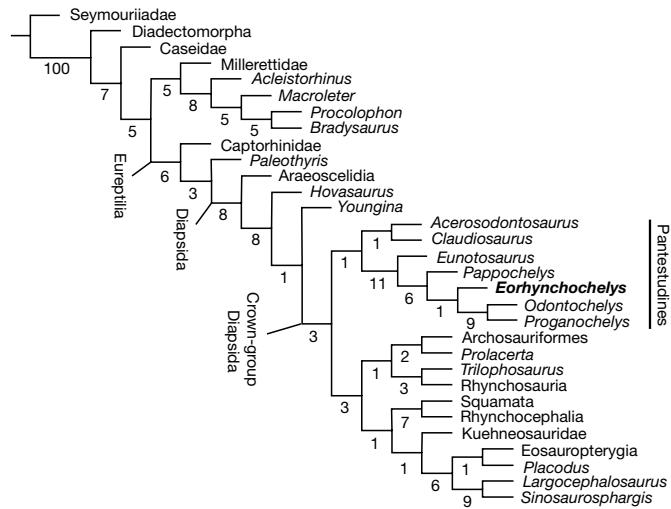


Fig. 4 | Phylogenetic position of *Eorhynchochelys* among amniotes. A single most parsimonious tree (930 steps, consistency index = 0.342, retention index = 0.564) was generated using a new technology search (for details see Extended Data Fig. 7) of TNT v.1.0¹⁶ based on the data matrix (31 taxa including *Eorhynchochelys* and *Largocephalosaurus* and 280 characters) derived from the previously published, reduced dataset⁴. Bremer supporting values (numbers) are indicated for each node. For the synapomorphies of main clades, see Supplementary Data. We suggest that *Eorhynchochelys* was adapted to an amphibian way of life, which is also supported by its phylogenetic position, which is bracketed by *Pappochelys* (phylogenetically more basal) and *Odontochelys* (phylogenetically more derived), both of which have been considered to be semi-aquatic^{2,13}.

in the group is supported by the following unequivocal synapomorphies: absence of supratemporal fenestra, presence of bony symphysis (sutured) of pubes and ischia, and rigid puboischiadic plate with a medioventral keel in adult.

Turtles, including *Odontochelys*, typically have a reduced count of 9 dorsal vertebrae with 9 pairs of expanded ribs. The same count was also given for *Pappochelys*^{2,4} and *Eunotosaurus*⁹, although we note that it is difficult to provide a definitive vertebral count for *Pappochelys* based on disarticulated and sometimes disassociated material. The count of 12 dorsal vertebrae in *Eorhynchochelys* represents an evolutionary reversal and so does the toothed premaxilla of *Odontochelys*.

The development of broadened ribs in stem turtles has recently been associated with digging habits^{17–19}. For *Eorhynchochelys*, digging activity is further supported by the stout limbs, prominent condyles on the humerus and femur, moderately developed olecranon of the ulna and the enlarged claws. Taken together, these characters seem to indicate predominantly terrestrial habits. It has been argued that the oldest turtles with a fully developed shell were terrestrial^{17,20}. The occurrence of *Eorhynchochelys* in marine sediments and the failure of the astragalus and calcaneum to fuse in an adult are features consistent with aquatic habits. However, although found in marine black shaly marlstones, this may not reflect a local biocoenosis (Supplementary Information). The new form may have been an inhabitant of coastal waters foraging on land as well as in the water, searching the mud along the shore using its powerful limbs in a way that many living pond turtles also do (Fig. 4 and Supplementary Information).

Reporting summary

Further information on experimental design is available in the Nature Research Reporting Summary linked to this paper.

Data availability

The authors declare that the data supporting the findings of this study are available within the paper and its Supplementary Information. Extra data are available from the corresponding authors upon reasonable request. *Eorhynchochelys sinensis* has been deposited in the ZooBank database (<http://zoobank.org/>) with Life Science Identifier urn:lsid:zoobank.org:act:71E36186-0305-46ED-9985-1EF3987B7D14.

Online content

Any Methods, including any statements of data availability and Nature Research reporting summaries, along with any additional references and Source Data files, are available in the online version of the paper at <https://doi.org/10.1038/s41586-018-0419-1>.

Received: 1 March 2018; Accepted: 15 June 2018;

Published online 22 August 2018.

1. Bever, G. S., Lyson, T. A. & Bhullar, B.-A. Fossil evidence for a diapsid origin of the anapsid turtle skull. *Soc. Vert. Paleont. Abstr.* **2014**, 91 (2014).
2. Schoch, R. R. & Sues, H.-D. A Middle Triassic stem-turtle and the evolution of the turtle body plan. *Nature* **523**, 584–587 (2015).
3. Bever, G. S., Lyson, T. R., Field, D. J. & Bhullar, B.-A. Evolutionary origin of the turtle skull. *Nature* **525**, 239–242 (2015).
4. Schoch, R. R. & Sues, H.-D. Osteology of the Middle Triassic stem-turtle *Pappochelys rosinae* and the early evolution of the turtle skeleton. *J. Syst. Palaeonto.* **16**, 927–965 (2017).
5. de Braga, M. & Rieppel, O. Reptile phylogeny and the affinities of turtles. *Zool. J. Linn. Soc.* **120**, 281–354 (1997).
6. Rieppel, O. & Reisz, R. R. The origin and early evolution of turtles. *Annu. Rev. Ecol. Syst.* **30**, 1–22 (1999).
7. Hedges, S. B. & Poling, L. L. A molecular phylogeny of reptiles. *Science* **283**, 998–1001 (1999).
8. Lyson, T. R., Bever, G. S., Bhullar, B.-A. S., Joyce, W. G. & Gauthier, J. A. Transitional fossils and the origin of turtles. *Biol. Lett.* **6**, 830–833 (2010).
9. Lyson, T. R., Bever, G. S., Scheyer, T. M., Hsiang, A. Y. & Gauthier, J. A. Evolutionary origin of the turtle shell. *Curr. Biol.* **23**, 1113–1119 (2013).
10. Rieppel, O. in *Morphology and Evolution of Turtles* (eds Brinkman, D. B. et al.) 51–61 (Springer, Dordrecht, 2013).
11. Lee, M. S. Y. Turtle origins: insights from phylogenetic retrofitting and molecular scaffolds. *J. Evol. Biol.* **26**, 2729–2738 (2013).
12. Hirasawa, T. et al. The evolutionary origin of the turtle shell and its dependence on the axial arrest of the embryonic rib cage. *J. Exp. Zool. B Mol. Dev. Evol.* **324**, 194–207 (2015).
13. Li, C., Wu, X.-C., Rieppel, O., Wang, L.-T. & Zhao, L.-J. An ancestral turtle from the Late Triassic of southwestern China. *Nature* **456**, 497–501 (2008).
14. Joyce, W. G. & Gauthier, J. A. Palaeoecology of Triassic stem turtles sheds new light on turtle origins. *Proc. R. Soc. B* **271**, 1–5 (2004).
15. Gaffney, E. S. The comparative osteology of the Triassic turtle *Proganochelys*. *Bull. Am. Mus. Nat. Hist.* **194**, 1–263 (1990).
16. Goloboff, P., Farris, J. & Nixon, K. TNT. A free program for phylogenetic analysis. *Cladistics* **24**, 774–786 (2008).
17. Lyson, T. R. et al. Fossil origin of the turtle shell. *Curr. Biol.* **26**, 1887–1894 (2016).
18. Jenkins, F. A. Jr. Anatomy and function of expanded ribs in certain edentates and primates. *J. Mamm.* **51**, 288–301 (1970).
19. Fraser, N. C. Palaeontology: a hook to the past. *Curr. Biol.* **26**, R922–R925 (2016).
20. Scheyer, T. M. & Sander, P. M. Shell bone histology indicates terrestrial palaeoecology of basal turtles. *Proc. R. Soc. B* **274**, 1885–1893 (2007).

Acknowledgements We thank Z.-Y. Sun and Sanya Museum of Marine Paleontology for access to the specimen, J.-Z. Ding (IVPP) for skilful preparation of the specimen, W. Gao (IVPP) for photographic assistance, Y.-S. Lou (IVPP) for laboratory assistance during the course of the study, L.-T. Wang (Guizhou Geological Survey) for field assistance, and R.R. Schoch, H.-D. Sues, G.S. Bever and T.R. Lyson for providing information or references. X.-C.W., N.F. and O.R. thank the IVPP for hospitality during their visits. This work was supported by the Strategic Priority Research Programs of Chinese Academy of Sciences (XDA19050102 and XDB26000000 to C.L.), the National Science Foundation of China (41772006 to C.L.) together with support from the IVPP and the Canadian Museum of Nature (RCPO9 to X.-C.W.).

Reviewer information *Nature* thanks G. S. Bever, R. R. Schoch and H.-D. Sues for their contribution to the peer review of this work.

Author contributions All authors conceived the project and participated in the writing of the text and Supplementary Information. C.L. led the field work and acquired the specimen for study. X.-C.W. drafted the figures with input from all authors.

Competing interests The authors declare no competing interests.

Additional information

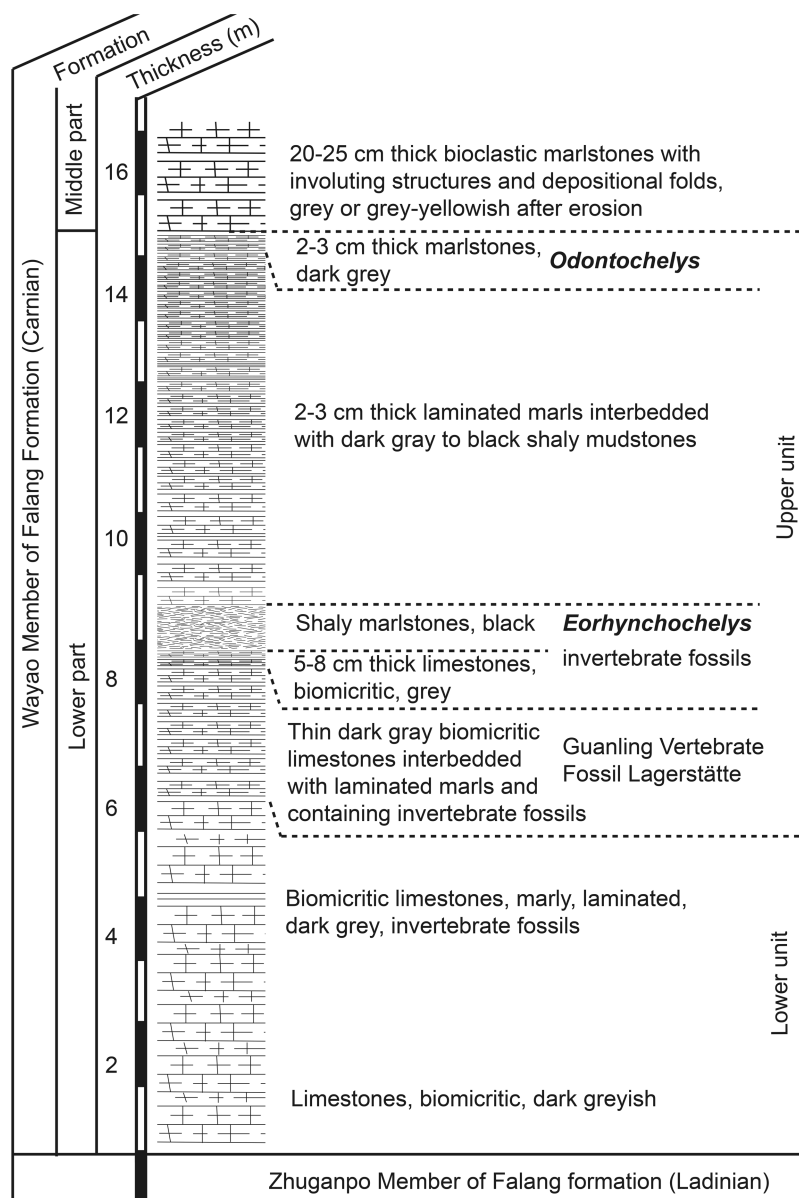
Extended data is available for this paper at <https://doi.org/10.1038/s41586-018-0419-1>.

Supplementary information is available for this paper at <https://doi.org/10.1038/s41586-018-0419-1>.

Reprints and permissions information is available at <http://www.nature.com/reprints>.

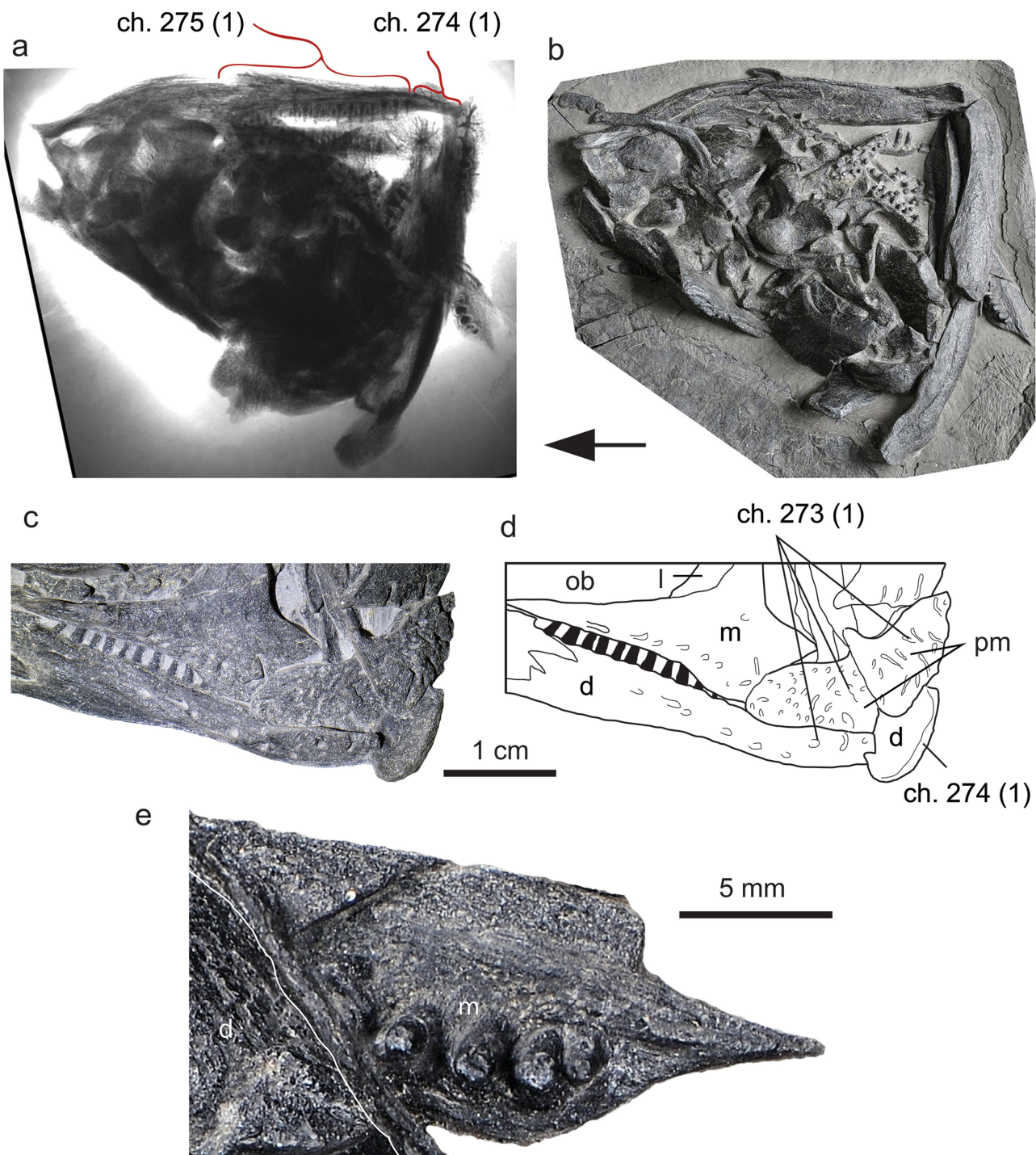
Correspondence and requests for materials should be addressed to C.L. or X.-C.W.

Publisher's note: Springer Nature remains neutral with regard to jurisdictional claims in published maps and institutional affiliations.



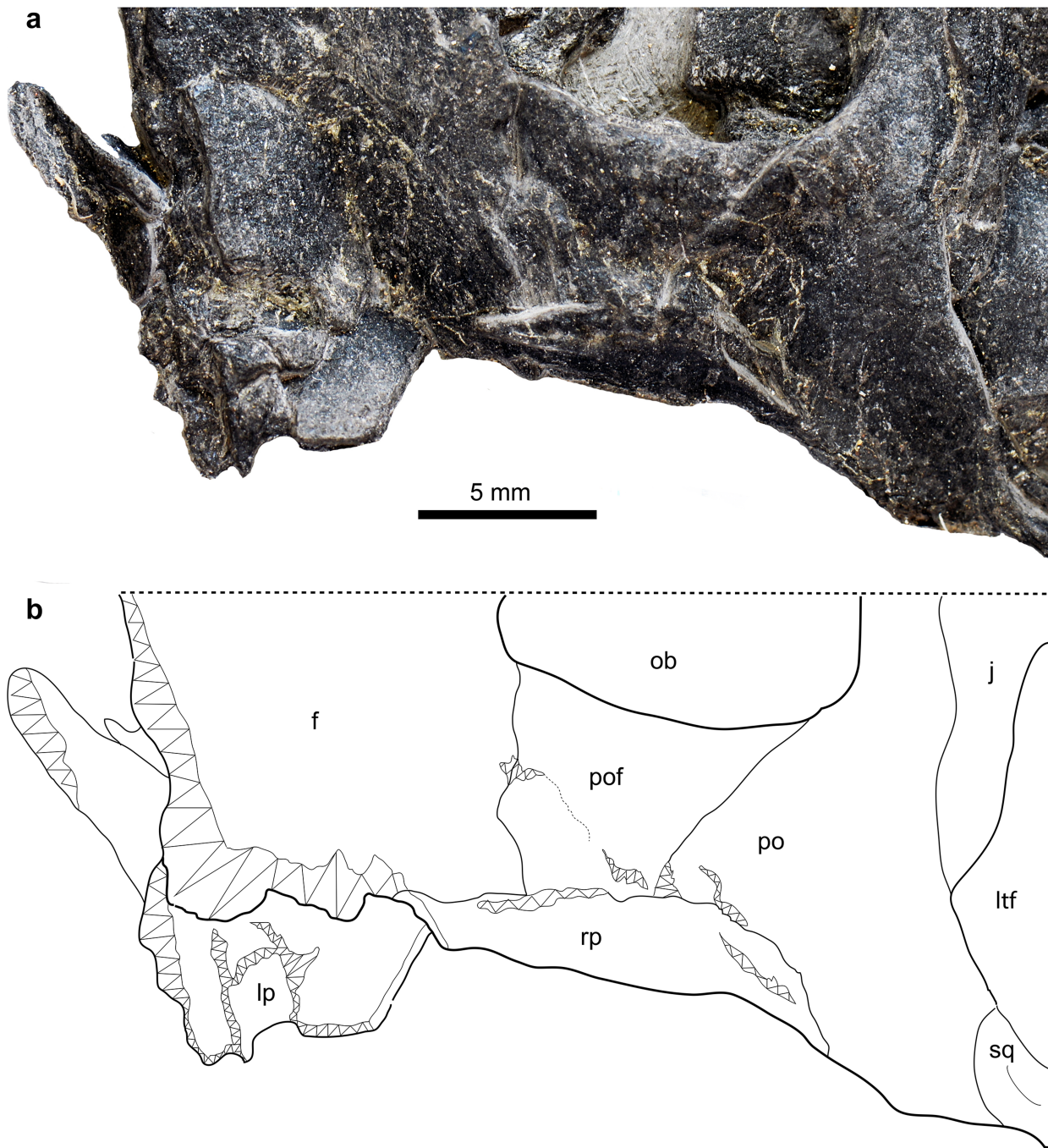
Extended Data Fig. 1 | Stratigraphic section of the Lower Wayao Member (LWM) of the Falang Formation. The section was found at Heshangjing, Baiyuncun of Xinpuxiang in Guanling of Guizhou Province, near the locality of *E. sinensis*. The Guanling biota originates in the lower part of the upper unit in the LWM. The LWM is about 14.5 m thick in this section, nearly 2.5 m thicker than that of the Wolonggang quarry section near the village of Xiaowa (Supplementary Information). The block of the black shaly marlstone containing *E. sinensis* is full of small bivalves,

whereas the block of thin marlstones containing *O. semitestacea* has large bivalves (species of *Halobia* and *Daonella*) and also scattered ammonites (species of *Trachyceras* and *Paratrachyceras*). The horizon where *E. sinensis* originated is 7.5 m below the one that contained *O. semitestacea* but slightly above the dark grey, marly, laminated micritic limestones that produce abundant skeletons of ichthyosaurs, thalattosaurs and placodonts as well as other fossils (Supplementary Information).



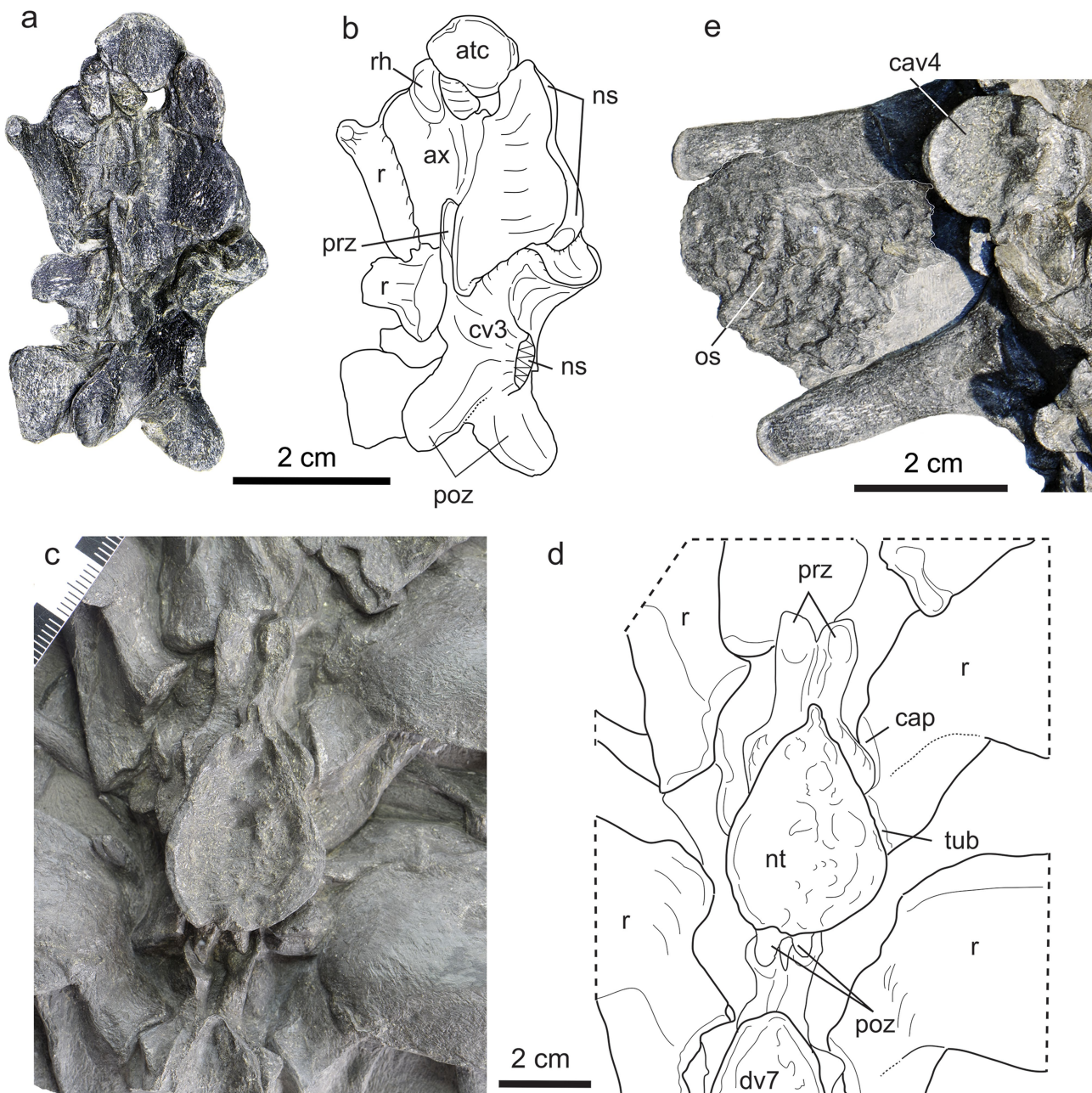
Extended Data Fig. 2 | Extra information on the skull of *E. sinensis* (SMMP 000016). a, b, X-radiograph and photograph of the skull in ventral view. c, d, Photograph and line drawing of the snout portion of the skull in right-lateral view, showing the ornamentation on the external surface of the edentulous premaxillae, the anterior portions of the right dentary and maxilla; the absence of teeth and the surface ornamentation suggest the presence of a rhamphotheca in *E. sinensis* in life. e, Close-up photograph of the posterior portion of the left maxilla, showing column-like pleurodont posterior teeth with blunt tips and the teeth deeply inset

from the labial margin and ankylosed to the labial base, which differs from the subthecodont implantation in *Eunotosaurus africanus* and *Pappochelys rosinae*; the implantation pattern of the teeth is unknown for *O. semitestacea*, because the lingual side of the dentition is not exposed in the known specimens. New characters: ch. 273 (1), keratinous beak present, as indicated by surface ornamentation; ch. 274 (1), anterior end of the dentary edentulous; ch. 275 (1), dentary tooth number fewer than 30. d, dentary; l, lacrimal; m, maxilla; ob, orbit; pm, premaxilla.



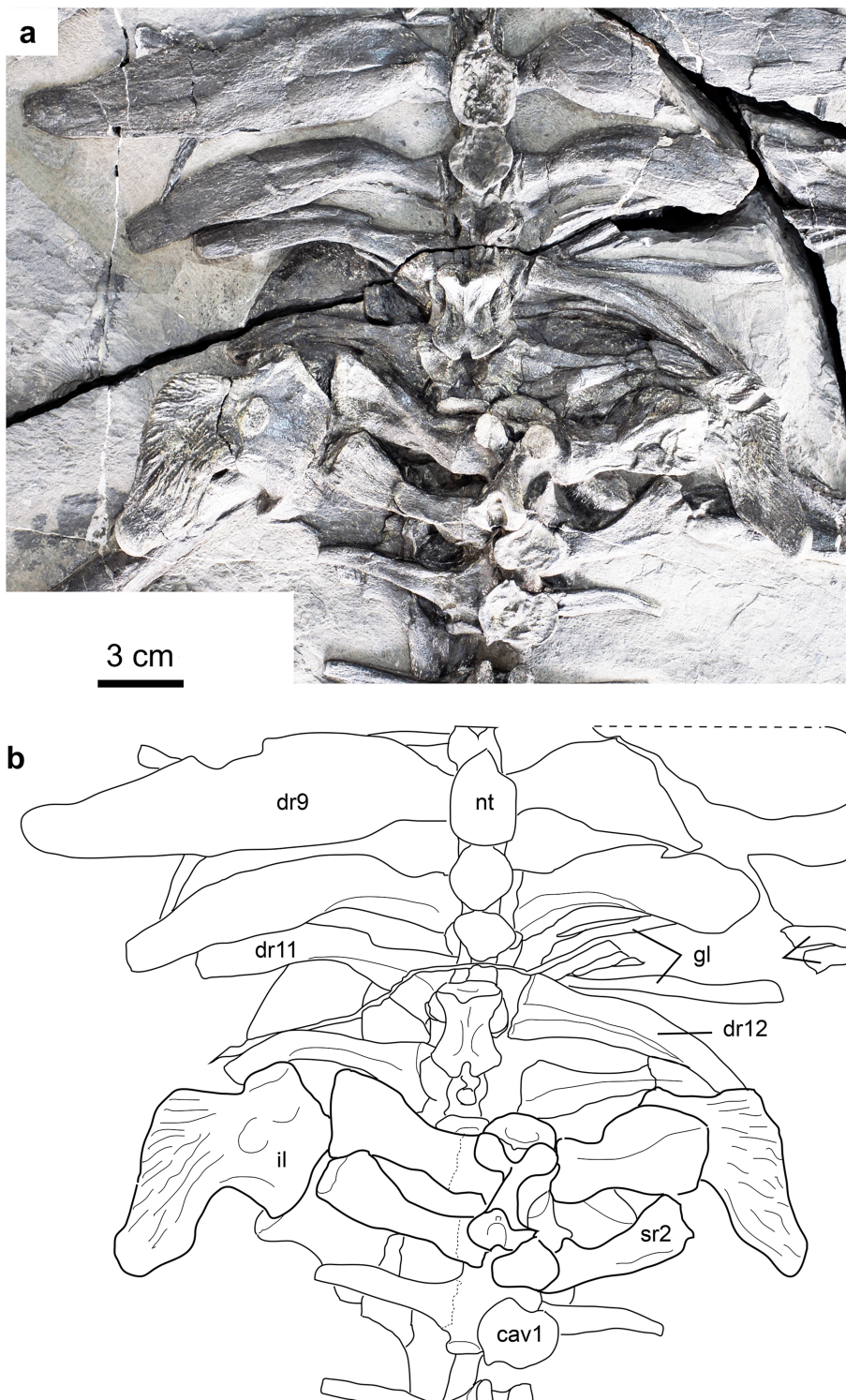
Extended Data Fig. 3 | A close-up of the postorbital portion of the skull roof of *E. sinensis* (SMMMP 000016) in dorsal view. **a**, Photograph. **b**, Line drawing, showing no supratemporal or trace of a supratemporal fenestra between the frontal, postfrontal, postorbital and parietal. Zigzag

lines denote broken surfaces. f, frontal; j, jugal; lp, left parietal; ltf, lower temporal fenestra; ob, orbit, po, postorbital; pof, postfrontal; rp, right parietal; sq, squamosal.



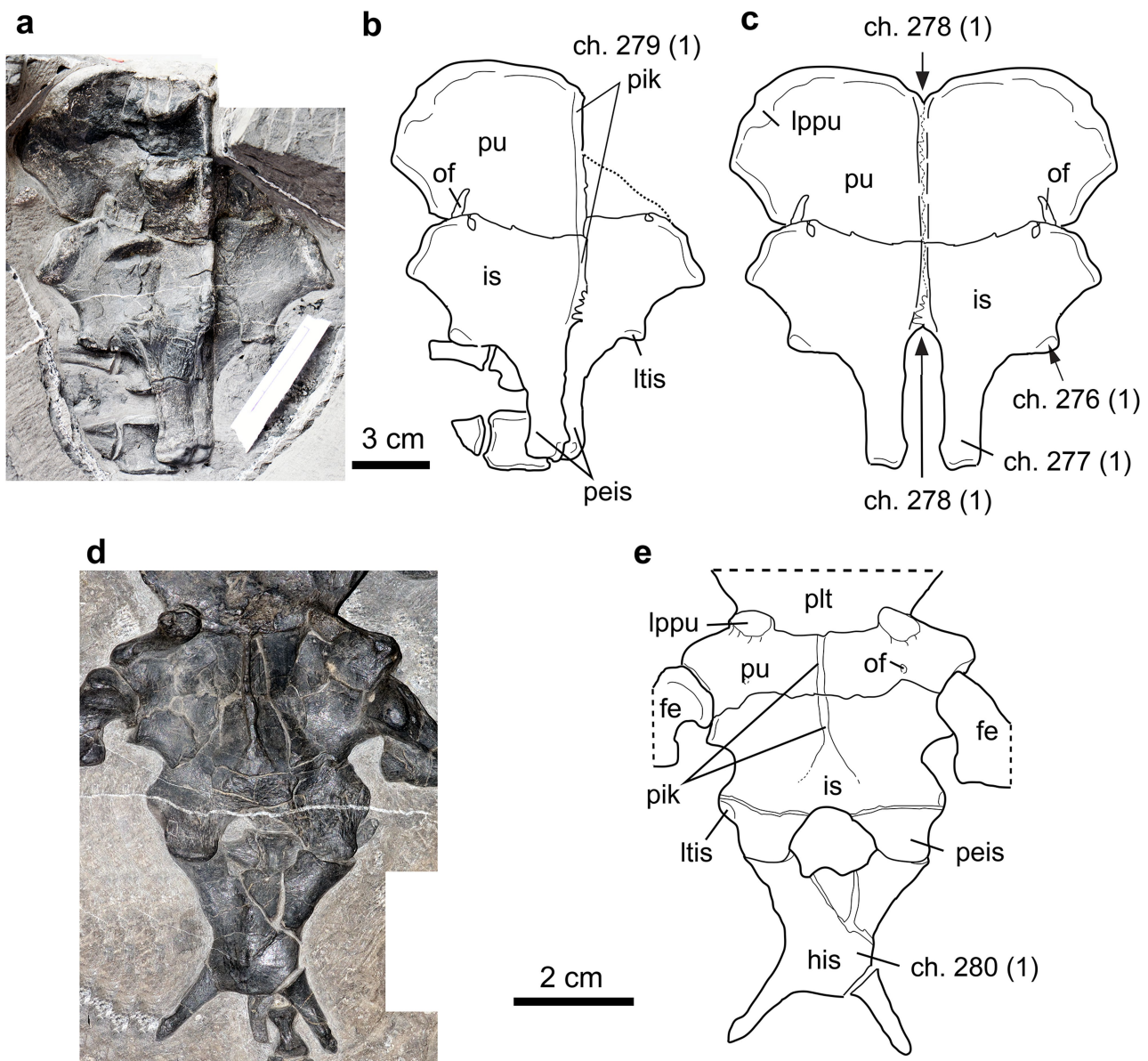
Extended Data Fig. 4 | Cervical and dorsal vertebrae of *E. sinensis* (SMMP 000016). a, b, Axis and cervical 3 in dorsal and left-lateral views, showing that the axis is characterized by an anteroposteriorly broadened neural spine that is higher posteriorly than anteriorly, unlike *Proganochelys quenstedti* and other turtles that show an anterior midline projection on the axis neural spine. c, d, Dorsals 6 and 7 in dorsal view, showing the prezygapophyses and postzygapophyses that are unusually different in size, unlike those of the post-axial cervicals and the first two dorsal vertebrae that are similar in size and robustness. e, An incomplete osteoderm in dorsal view. There is no evidence of extensive dermal armour. The single

fragment of an osteoderm with surface ornamentation located between the transverse processes of the fourth and fifth caudal vertebrae is, however, inconsistent with the otherwise excellent preservation and articulation of the skeleton and almost certainly represents a different taxon and individual. Zigzag lines denote broken surfaces. atc, atlantal centrum; ax, axis; cap, capitulum; cav4, caudal vertebra 4; cv3, cervical vertebra 3; dv7, dorsal vertebra 7; ns, neural spine; nt, neural table; os, osteoderm; poz, postzygapophysis; prz, prezygapophysis; r, rib; rh, rib head; tub, tuberculum.



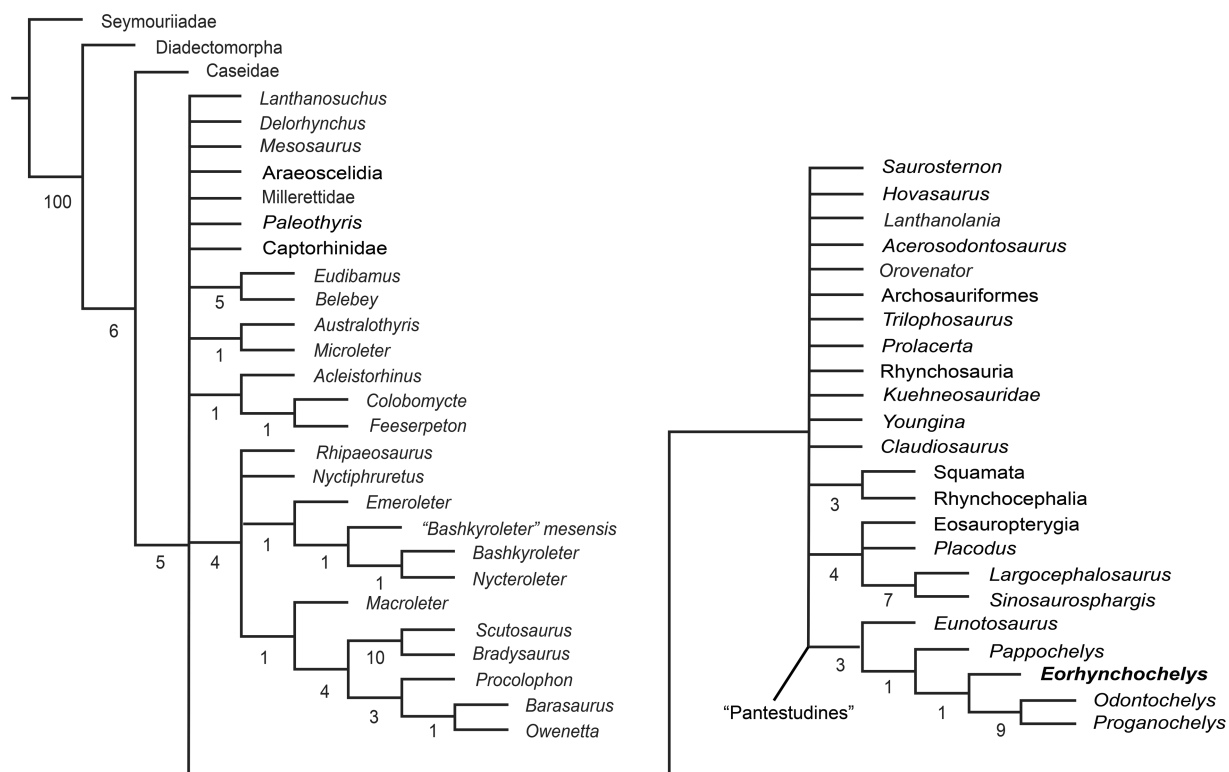
Extended Data Fig. 5 | Posterior trunk of *E. sinensis* (SMMP 000016) in dorsal view. **a**, Photograph. **b**, Line drawing showing that the dorsal surface of the distinctly broadened dorsal ribs is faintly ornamented by a series of striations. In addition, the stout sacral ribs are fused to the sacral

vertebrae (as they are in *O. semitestacea* and *P. rosinae*) and their distinctly expanded distal ends are detached from the ilium, in contrast to the tightly fused condition in *P. quenstedti*. Dorsal ribs 11 and 12 of *E. sinensis* are not specialized and are very different from dorsal ribs 1–9 in morphology.



Extended Data Fig. 6 | Puboischiadic plate in stem turtles.
a–c, Photograph, line drawing and reconstruction of the puboischiadic plate of *E. sinensis* (SMMP 000016) in ventral view. **d, e**, Photograph and line drawing of the puboischiadic plate of *O. semitestacea* (the paratype, IVPP V 13240) with the ossified hypoischium in ventral view. New characters: ch. 276 (1), lateral process of the ischium present; ch. 277 (1), posterior directed process of the ischium present; ch. 278 (1),

bony symphysis (a sutural midventral contact) between pubes and ischia present; ch. 279 (1), the rigid puboischiadic plate with a ventromidline keel present in adults; ch. 280 (1), hypoischium present. fem., femur; his, hypoischium; is, ischium; lppu, lateral process of the pubis; latis, lateral tubercle of the ischium; of, obturator foramen; peis, posterior elongation of the ischium; pik, puboischiadic keel; plt, plastron; pu, pubis.

**Extended Data Fig. 7 | Strict consensus of 16 most parsimonious trees.**

The 16 trees (with a tree length of 1,207, a consistency index of 0.269, and a retention index of 0.582) were generated using a new technology search of TNT v.1.0¹⁶ based on the large data matrix (52 taxa and 280 characters) derived from previously published datasets^{3,4}, showing that the monophly of 'Pantestudines' with *Claudiosaurus* and *Acerosodontosaurus* excluded and the interrelationships of *Eorhynchochelys* within the clade are the same as produced by the analysis based on the reduced dataset⁴ (see the clade formed by *Eunotosaurus* and more derived turtles in Fig. 4). As

in the analysis of the reduced dataset, the new technology search based on 100 random addition sequence replicates and 1,000 random seeds was implemented, and the advanced search settings were changed to ensure enough iterations: 100 sectorial search drifting cycles, 100 ratchet iterations, 100 drift cycles and 100 rounds of tree fusion for every replicate. Multistate characters were treated as unordered and all characters were equally weighted. Bremer supporting values (numbers) are shown for each node.

Estimating global agricultural effects of geoengineering using volcanic eruptions

Jonathan Proctor^{1,2,7*}, Solomon Hsiang^{1,3,7}, Jennifer Burney⁴, Marshall Burke^{3,5} & Wolfram Schlenker^{3,6}

Solar radiation management is increasingly considered to be an option for managing global temperatures^{1,2}, yet the economic effects of ameliorating climatic changes by scattering sunlight back to space remain largely unknown³. Although solar radiation management may increase crop yields by reducing heat stress⁴, the effects of concomitant changes in available sunlight have never been empirically estimated. Here we use the volcanic eruptions that inspired modern solar radiation management proposals as natural experiments to provide the first estimates, to our knowledge, of how the stratospheric sulfate aerosols created by the eruptions of El Chichón and Mount Pinatubo altered the quantity and quality of global sunlight, and how these changes in sunlight affected global crop yields. We find that the sunlight-mediated effect of stratospheric sulfate aerosols on yields is negative for both C4 (maize) and C3 (soy, rice and wheat) crops. Applying our yield model to a solar radiation management scenario based on stratospheric sulfate aerosols, we find that projected mid-twenty-first century damages due to scattering sunlight caused by solar radiation management are roughly equal in magnitude to benefits from cooling. This suggests that solar radiation management—if deployed using stratospheric sulfate aerosols similar to those emitted by the volcanic eruptions it seeks to mimic—would, on net, attenuate little of the global agricultural damage from climate change. Our approach could be extended to study the effects of solar radiation management on other global systems, such as human health or ecosystem function.

Geoengineering—the purposeful alteration of the climate to offset changes induced by greenhouse gas emissions—is a proposed, but still poorly understood, approach to limit future warming⁵. One of the most widely suggested geoengineering strategies is solar radiation management (SRM). SRM proposals typically involve spraying precursors to sulfate aerosols into the stratosphere to produce particles that cool the earth by reflecting sunlight back into space⁶. The closest natural analogues to these SRM proposals are major volcanic eruptions⁷. Eruptions of El Chichón (1982, Mexico) and Mount Pinatubo (1991, the Philippines) injected 7 and 20 Mt of sulfur dioxide, respectively, into the atmosphere, which was then oxidized to form stratospheric sulfate aerosols (SSAs)⁸. These particles propagated throughout the tropics over several weeks and spread latitudinally over the following months, increasing the opacity of the stratosphere—as measured by optical depth—more than an order of magnitude above baseline levels for multiple years (Fig. 1a–c, e).

The eruptions of El Chichón and Pinatubo had substantial effects on the global optical environment and climate. We analyse daily data from 859 insolation stations⁹ ($n = 3,311,553$ station-days; Fig. 1d) paired with stratospheric aerosol optical depth (SAOD)¹⁰ and cloud fraction data under all-sky conditions. We find that the Pinatubo eruption (global average of +0.15 SAOD) reduced direct sunlight by 21%, increased diffuse sunlight by 20% and reduced total sunlight by 2.5% (Fig. 1f, Extended Data Table 1, Supplementary Information, section II).

These global all-sky results generalize previous clear-sky estimates at individual stations¹¹. Globally, this reduction in insolation led to cooling of about 0.5°C ⁸ and redistribution and net reduction in precipitation¹², effects that were partially offset by a concurrent El Niño event (Fig. 2). On the basis of these observations, it has previously been suggested that SRM cooling could mitigate agricultural damages from global warming⁴. The net effect of SRM, however, remains uncertain owing to possible unintended consequences from SSA-induced changes. Here we empirically estimate how the alteration of sunlight by SSAs may directly affect agricultural yields, after accounting for effects mediated by temperature, precipitation and clouds.

The sign of the ‘insolation effect’ of SRM on agriculture is theoretically ambiguous^{13–16}. Scattering light decreases total available sunlight—which tends to decrease photosynthesis—but increases the fraction of light that is diffuse, which can increase photosynthesis by redistributing light from sun-saturated canopy leaves to shaded leaves below^{15,17}. It is unknown whether damages from decreasing total light or benefits from increasing diffuse light dominate in crop production. The sign of this insolation effect will depend primarily on two factors: the forward-scattering properties of the aerosol and the relative benefit of diffuse light for the growth of edible yield (Supplementary Information, section III.5). The latter may depend on canopy geometry, photosynthetic pathway (for example, C3 or C4) and ambient conditions^{13,18}. Previous studies of unmanaged ecosystems have tended to find that scattering increases biomass growth^{15,19}—although not always¹⁸—and, importantly, that edible yield production may not directly correlate with biomass growth. Studies of agricultural systems tend to estimate the negative effects of tropospheric aerosol scattering^{13,16} and positive effects of solar brightening²⁰ on yields. Simulations of potential SRM effects focus on cooling and precipitation effects²¹ and suggest global yields may increase owing to cooling⁴, although these analyses do not account for the full effect of scattering. To our knowledge, this is the first study to estimate and account for the net effects of SSA radiative scattering on yields, thereby testing whether the benefits of SSA scattering demonstrated in unmanaged ecosystems^{15,19} also apply to agricultural production, as has often been hypothesized^{4,14}. This analysis is also, to our knowledge, the first global empirical study of the insolation effect on crops as well as the first study to leverage a quasi-experimental design to estimate the total effect of SRM on any economic sector.

The theoretically ideal experiment would measure the total effect of SRM on yields using many identical Earths, half of them treated with SSAs. In practice, we approximate this experiment with one Earth during sequential periods of high and low SSA exposure, exogeneously determined by volcanic eruptions. We identify the insolation effect of SSAs on yields²² (Extended Data Fig. 1) by comparing countries to themselves over time, with changing SSA treatment—measured in SAOD composited from satellite and other observations¹⁰ (Fig. 1e)—while controlling flexibly for potentially confounding climate variables, including temperature, precipitation, cloud fraction and the El

¹Global Policy Laboratory, Goldman School of Public Policy, University of California, Berkeley, Berkeley, CA, USA. ²Department of Agricultural and Resource Economics, University of California, Berkeley, Berkeley, CA, USA. ³National Bureau of Economic Research, Cambridge, MA, USA. ⁴School of Global Policy and Strategy, University of California, San Diego, San Diego, CA, USA.

⁵Department of Earth System Science, Stanford University, Stanford, CA, USA. ⁶School of International and Public Affairs and The Earth Institute, Columbia University, New York, NY, USA. ⁷These authors contributed equally: Jonathan Proctor, Solomon Hsiang. *e-mail: proctor@berkeley.edu

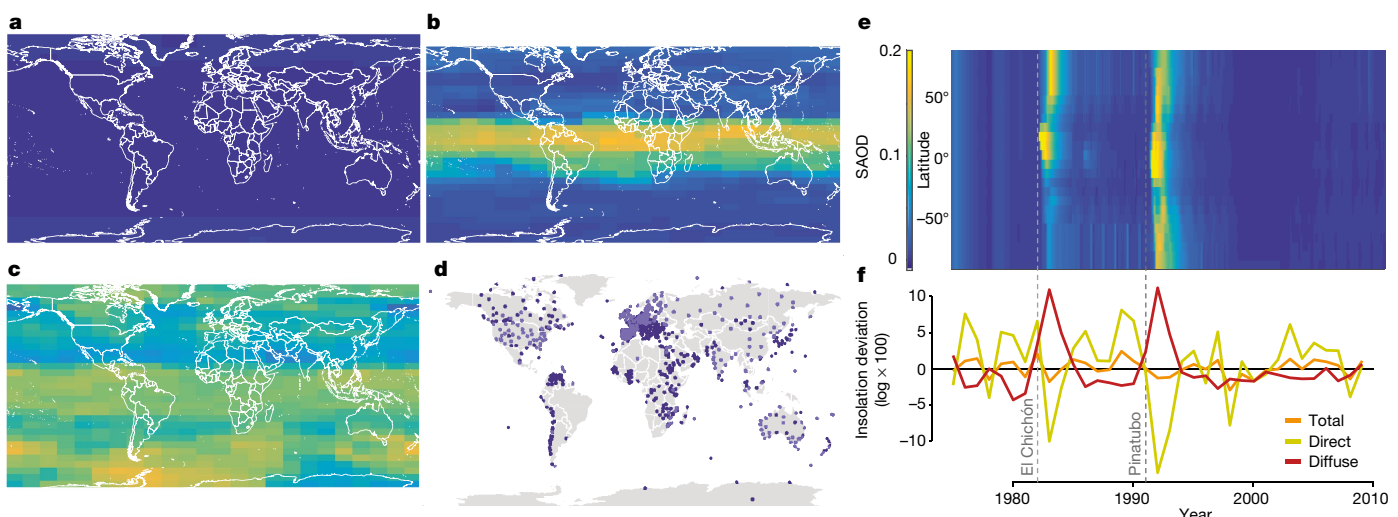


Fig. 1 | Large volcanic eruptions alter the global optical environment. a–c, SAOD (1,000 nm) before the Pinatubo eruption (March 1991) (a), two months after the eruption (August 1991) (b) and the next year, after the aerosol cloud had spread (March 1992) (c). d, Surface insolation observing stations used in our analysis of the effect of SAOD on insolation; light blue stations additionally measure diffuse light. e, SAOD (550 nm)

Niño–Southern Oscillation (ENSO) (Supplementary Information, section III.3). Our multivariate fixed-effects panel estimation strategy (equation (16) in Supplementary Information) accounts for unobserved time-invariant factors—such as soil type or historical propensity for civil unrest—as well as country-specific time-trending variables, such as access to fertilizers or trends in damaging tropospheric ozone²³. Our primary analysis focuses on the Pinatubo eruption because the concentration and distribution of resulting SSAs were measured with substantially more accuracy than were those of earlier eruptions²⁴. We validate the model by verifying that the estimated responses of crop yields to temperature and precipitation are consistent with previous studies²⁵ (Extended Data Fig. 2).

We find that the changes in sunlight from SSAs reduce both C4 (maize; $P < 0.01$, $n = 2,501$ country-years) and C3 (soy, rice and wheat; $P < 0.05$, $n = 4,828$ crop-country-years) yields, by 48% and 28%, respectively, per unit SAOD (Fig. 3a, model 1). This indicates that the global average scattering from Pinatubo (+0.15 SAOD) reduced C4 yields by 9.3% and C3 yields by 4.8% (Fig. 3b), although some of this loss was probably offset by SSA-induced cooling, making it difficult to observe directly. By contrast, process models¹⁹ and empirical analyses of unmanaged-ecosystem biomass growth¹⁵ tend to estimate a positive insolation effect, which suggests that either the diffuse fertilization effect is weaker for crops than ecosystems or scattering light alters the relative production of biomass and edible yield.

Our finding that SSA scattering from Pinatubo negatively affected yields is robust to removing temperature, precipitation, ENSO and cloud controls (Fig. 3a, models 2–5), estimating the effect separately for each crop, accounting for the zenith angle of incoming sunlight, using two alternative datasets of SSA SAOD, dropping observations from the countries in which the major eruptions occurred and adding surface CO₂ as a control (Extended Data Table 2). We examine the effect of future, current and past SSAs on current yields, finding that only contemporaneous exposure to SSAs matters (Fig. 3d). We estimate the yield–insolation response flexibly, and fail to reject that the response is linear over the support of our data (Extended Data Fig. 3).

Extending the analysis back in time increases the sample size but also the measurement error, owing to weaknesses in the historical observational system. The estimated insolation effect for both C3 and C4 crops becomes smaller, and remains significant for C4 crops, as we sequentially include data from the eruptions of El Chichón (1982) (Fig. 3a, model 6) and Agung (1963) (Extended Data Table 2 column 9). This

from 1975–2010¹⁰. f, Annual average daily total (orange), direct (yellow) and diffuse (red) sunlight across all stations; before averaging, each measurement at a given station on a given day-of-year was de-meaned (by subtracting the mean of all observations from the respective station and day-of-year), to remove seasonal effects as well as differences in geography and observational protocols.

pattern is consistent with both systematic ‘attenuation bias’ from the mis-measurement of SAOD before the satellite era²⁶ and differences in the radiative properties of the SSAs generated by Pinatubo and El Chichón, discussed below.

Two results support the idea that our analysis captures a sunlight-mediated effect. First, the response of C3 crops is less negative than that of C4 crops ($P < 0.01$). C3 crops benefit from scattering more than

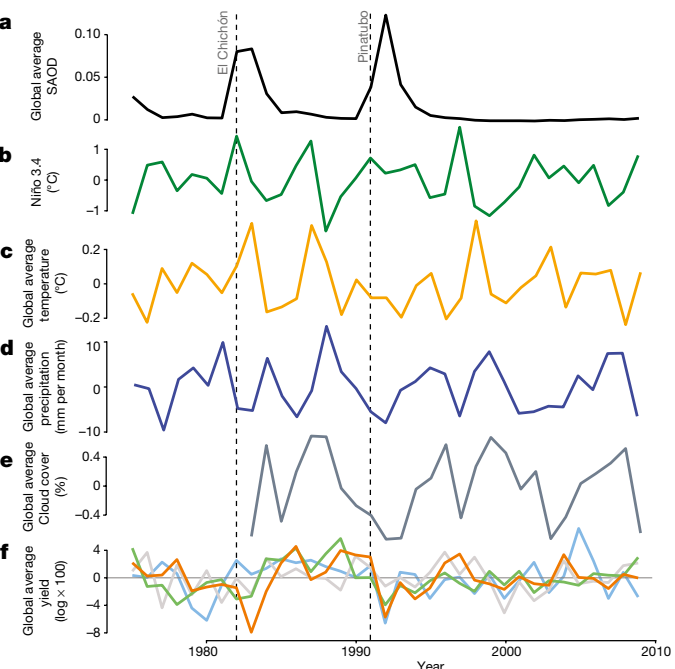


Fig. 2 | Global summary statistics of key model variables. a, SAOD for years after the eruptions of El Chichón (March to April 1982) and Pinatubo (June 1991) (dotted lines). b–e, The ENSO 3.4 index (b), surface air temperature (c), precipitation (d) and cloud fraction (e) during the same period. f, Yields of maize (orange), wheat (grey), soy (blue) and rice (green) decline after the eruptions. Climate and yield values are growing-season averages, de-trended by country-specific quadratic time trends and averaged over countries in the sample. SAOD data are processed similarly, but are not de-trended.

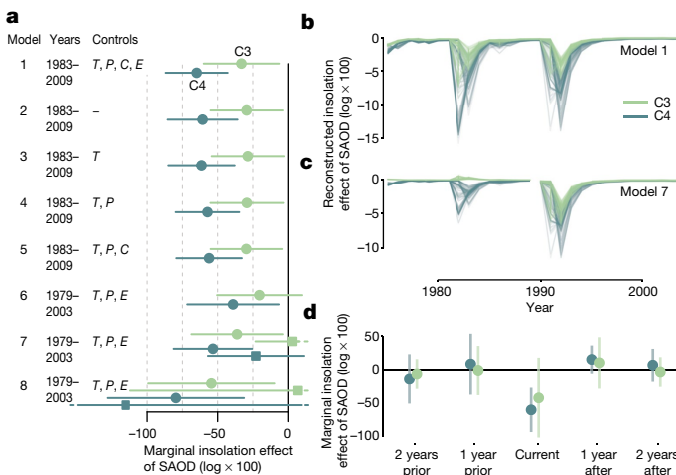


Fig. 3 | Empirical estimates of the insolation effect of SSAs on crop yield. **a**, The estimated effect of increasing SSA optical depth by one unit on C4 (blue) and C3 (green) yields, owing to changes in sunlight (model 1, equation (16) in Supplementary Information, and Extended Data Table 2). Models 2–5 drop and then sequentially add temperature (T), precipitation (P), cloud (C) and ENSO (E) controls. Models 7–8 estimate effects separately for Pinatubo (year ≥ 1990 , circles) and Chichón (year < 1990 , squares); Model 8 uses a different SAOD dataset (SPARC). **b**, Reconstructions of the SSA insolation effect using model 1. Each line represents a single country over time. **c**, As in **b**, but using model 7. **d**, Simultaneously estimated insolation effects two years before and two years after the current growing season. See Supplementary Information sections III.2.3, III.2.2 and III.4. In **a**, **d**, whiskers represent 95% confidence intervals.

C4 crops because the C3 photosynthetic rate saturates at lower light levels¹³. Second, per unit of SAOD, aerosols from El Chichón are both more forward scattering (Extended Data Tables 1, 3) and less damaging to yields (Fig. 3a, models 7, 8) than those of Pinatubo. This pattern is consistent with diffuse fertilization increasing edible yield. It also suggests that aerosol radiative properties may explain some heterogeneity in the estimated insolation effect across these eruptions. This heterogeneity substantially affects reconstructed yield losses from SSA scattering (Fig. 3c). We are, however, unable to determine whether this difference in the estimated insolation effect across eruptions is due to a difference in the radiative properties of the SSAs or to a differing degree of measurement error and, in turn, attenuation bias (Supplementary Information, section III.6).

To calculate the total effect of SSAs on yields for a future SRM scenario, we apply our empirical results (Fig. 3a, model 1) to output

from an earth system model and compare future yields under two scenarios: (1) climate change under Representative Concentration Pathway 4.5 (RCP4.5)—a modest mitigation pathway—and (2) the same, but with sulfur dioxide injection to balance all additional anthropogenic forcing after 2020²⁷.

Over cropped areas in this simulation (2050–2069), the SRM treatment (average $+0.084$ SAOD) decreases the average temperature by 0.88°C , reduces precipitation by 0.26 mm per month and increases the cloud fraction by 0.0081 relative to the control during the maize growing season (Extended Data Fig. 4). In turn, average maize yields increase by 6.3% owing to this cooling (Fig. 4a), decrease by 5.3% owing to SRM-induced dimming (Fig. 4b) and change by $<0.2\%$ owing to altered precipitation and clouds (Fig. 4c, d). We sum these partial effects to construct the total effect of SRM, and repeat the analysis for soy, rice and wheat (Extended Data Fig. 5). We find that, relative to the control, SRM treatment has no statistically discernible effect on yields once we have accounted for optical effects ($P > 0.1$ for all crops; Fig. 4e, Extended Data Fig. 6). Failing to account for the insolation effect, as was done in the only previous global estimate⁴, substantially overestimates the benefits of SRM to agriculture.

Our analysis finds that volcanogenic SSAs have statistically significant and economically substantial insolation-mediated costs that are roughly equal in magnitude to their benefits from cooling. This suggests that anthropogenic SSAs used in SRM may not be able to substantially lessen the risks that climate change poses to global agricultural yields and food security (Extended Data Fig. 7).

Our finding that SSAs from El Chichón were more forward scattering and less damaging than SSAs from Pinatubo indicates that optimizing the radiative properties of particles used in SRM might mitigate insolation-mediated damages. However, we cannot rule out the possibility that this difference was due instead to poor observation of the SSAs from El Chichón.

Farmer-level adaptations, such as switching to varieties more resistant to dimming, could theoretically mitigate the insolation-mediated damage of SRM. However, given that farmer-level adaptations to extreme heat have been modest²⁸, it is not clear that adaptation to dimming will be easier.

Our quasi-experimental results are consistent with the sunlight-mediated effect of tropospheric aerosols¹⁶ and emissions of their precursors²⁹ on Indian wheat and rice yields, further supporting the notion that we capture a sunlight-mediated response. It is however possible that other factors, such as increased ultraviolet-light exposure from stratospheric ozone destruction, could explain part of the estimated effect. Notably, changes in tropospheric ozone concentrations due to Pinatubo are thought to be negative³⁰, which would increase yields—suggesting that our results might underestimate the SSA insolation effect.

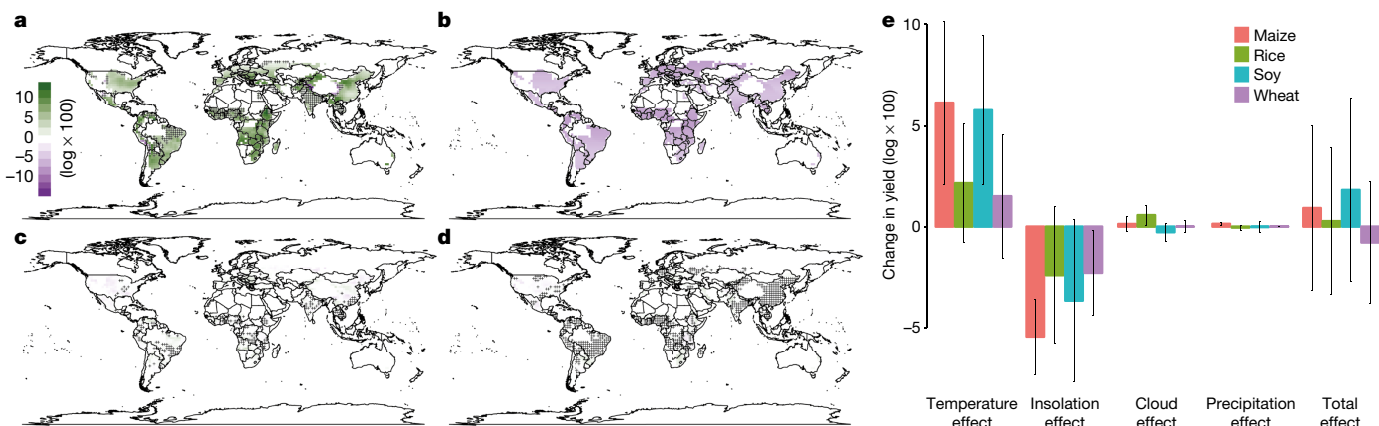


Fig. 4 | Partial and total effects of SRM on yields. **a–d**, The partial effects of SRM—relative to a climate-change-only scenario (RCP4.5)—on expected maize yields from 2050–2069, owing to changes in temperature (a), insolation (b), precipitation (c) and cloud fraction (d). Statistically insignificant changes ($P > 0.05$) are hatched. Changes in uncropped land

have been masked out by setting the values to zero. **e**, Global partial and total effects of SRM (cropped-fraction weighted average) for maize (red), soy (turquoise), rice (green) and wheat (purple). Error bars show 95% confidence intervals for the predicted effect.

Online content

Any Methods, including any statements of data availability and Nature Research reporting summaries, along with any additional references and Source Data files, are available in the online version of the paper at <https://doi.org/10.1038/s41586-018-0417-3>.

Received: 18 June 2017; Accepted: 29 June 2018;
Published online 8 August 2018.

1. Crutzen, P. J. Albedo enhancement by stratospheric sulfur injections: a contribution to resolve a policy dilemma? *Clim. Change* **77**, 211–219 (2006).
2. Ocean Studies Board. *Climate Intervention: Reflecting Sunlight to Cool the Earth* (The National Academies, Washington DC, 2015).
3. MacMartin, D. G., Kravitz, B., Long, J. C. S. & Rasch, P. J. Geoengineering with stratospheric aerosols: what do we not know after a decade of research? *Earth's Future* **4**, 543–548 (2016).
4. Pongratz, J., Lobell, D. B., Cao, L. & Caldeira, K. Crop yields in a geoengineered climate. *Nat. Clim. Change* **2**, 101–105 (2012).
5. Pachauri, R. K. et al. *Climate Change 2014: Synthesis Report. Contribution of Working Groups I, II and III to the Fifth Assessment Report of the Intergovernmental Panel on Climate Change* (eds Core Writing Team, Pachauri, R. K. & Meyer, L. A.) (IPCC, Geneva, 2015).
6. Robock, A., Marquardt, A., Kravitz, B. & Stenchikov, G. Benefits, risks, and costs of stratospheric geoengineering. *Geophys. Res. Lett.* **36**, L19703 (2009).
7. Robock, A., MacMartin, D. G., Duren, R. & Christensen, M. W. Studying geoengineering with natural and anthropogenic analogs. *Clim. Change* **121**, 445–458 (2013).
8. Robock, A. Volcanic eruptions and climate. *Rev. Geophys.* **38**, 191–219 (2000).
9. World Radiation Data Centre. 'Global radiation. Daily sums, monthly sums and means' and 'Diffuse radiation. Daily sums, monthly sums and means'. *World Meteorological Organization* <http://wrdc.mgo.rssi.ru/> (accessed 1 August 2015).
10. Sato, M., Hansen, J. E., McCormick, M. P. & Pollack, J. B. Stratopheric aerosol optical depths 1850–1990. *J. Geophys. Res.* **98**, 22987–22994 (1993).
11. Dutton, E. G. & Christy, J. R. Solar radiative forcing at selected locations and evidence for global lower tropospheric cooling following the eruptions of El Chichón and Pinatubo. *Geophys. Res. Lett.* **19**, 2313–2316 (1992).
12. Trenberth, K. E. & Dai, A. Effects of Mount Pinatubo volcanic eruption on the hydrological cycle as an analog of geoengineering. *Geophys. Res. Lett.* **34**, L15702 (2007).
13. Greenwald, R. et al. The influence of aerosols on crop production: a study using the CERES crop model. *Agric. Syst.* **89**, 390–413 (2006).
14. Roderick, M. L. & Farquhar, G. D. Geoengineering: hazy, cool and well fed? *Nat. Clim. Change* **2**, 76–77 (2012).
15. Gu, L. et al. Response of a deciduous forest to the Mount Pinatubo eruption: enhanced photosynthesis. *Science* **299**, 2035–2038 (2003).
16. Gupta, R., Somanathan, E. & Dey, S. Global warming and local air pollution have reduced wheat yields in India. *Clim. Change* **140**, 593–604 (2017).
17. Roderick, M. L., Farquhar, G. D., Berry, S. L. & Noble, I. R. On the direct effect of clouds and atmospheric particles on the productivity and structure of vegetation. *Oecologia* **129**, 21–30 (2001).
18. Alton, P. B. Reduced carbon sequestration in terrestrial ecosystems under overcast skies compared to clear skies. *Agric. For. Meteorol.* **148**, 1641–1653 (2008).
19. Mercado, L. M. et al. Impact of changes in diffuse radiation on the global land carbon sink. *Nature* **458**, 1014–1017 (2009).
20. Tolleenar, M., Fridgen, J., Tyagi, P., Stackhouse, P. W. Jr. & Kumudini, S. The contribution of solar brightening to the US maize yield trend. *Nat. Clim. Change* **7**, 275–278 (2017).
21. Xia, L. et al. Solar radiation management impacts on agriculture in China: a case study in the Geoengineering Model Intercomparison Project (GeoMIP). *J. Geophys. Res. Atmos.* **119**, 8695–8711 (2014).
22. Food and Agriculture Organization of the United Nations. Crops, NationalProduction. FAOSTAT <http://www.fao.org/faostat/en/#data/QC> (accessed 1 January 2016).
23. Hsiang, S. Climate econometrics. *Annu. Rev. Resour. Econ.* **8**, 43–75 (2016).
24. Thomason, L. & Peter, T. (eds) *SPARC Assessment of Stratospheric Aerosol Properties (ASAP)*. SPARC Report No. 4 <http://www.sparc-climate.org/publications/sparc-reports/> (SPARC Scientific Steering Group, 2006).
25. Schlenker, W. & Lobell, D. B. Robust negative impacts of climate change on African agriculture. *Environ. Res. Lett.* **5**, 014010 (2010).
26. Wooldridge, J. M. *Econometric Analysis of Cross Section and Panel Data* (MIT Press, Cambridge, 2002).
27. Niemeier, U., Schmidt, H., Alterskjær, K. & Kristjánsson, J. E. Solar irradiance reduction via climate engineering: impact of different techniques on the energy balance and the hydrological cycle. *J. Geophys. Res. Atmos.* **118**, 11905–11917 (2013).
28. Carleton, T. A. & Hsiang, S. M. Social and economic impacts of climate. *Science* **353**, aad9837 (2016).
29. Burney, J. & Ramanathan, V. Recent climate and air pollution impacts on Indian agriculture. *Proc. Natl. Acad. Sci. USA* **111**, 16319–16324 (2014).
30. Tang, Q., Hess, P. G., Brown-Steiner, B. & Kinnison, D. E. Tropospheric ozone decrease due to the Mount Pinatubo eruption: reduced stratospheric influx. *Geophys. Res. Lett.* **40**, 5553–5558 (2013).

Acknowledgements We thank M. Anderson, M. Auffhammer, D. Baldocchi, K. Caldeira, C. Field, A. Goldstein, D. Keith, P. Huybers, R. Kopp, D. Lobell, K. Ricke, J. Sallee and seminar participants at Berkeley, Chicago, Columbia, Cornell, Harvard, Johns Hopkins and Stanford universities, the Massachusetts Institute of Technology and the Allied Social Science Association Annual Meeting for useful comments. We thank I. Bolliger for his contributions to the project and all the members of the Global Policy Laboratory for their valuable feedback. We thank L. Thomason for generously sharing SAOD data used in Fig. 1a–c. This material is based upon work supported by the National Science Foundation Grant No. CNH-L 1715557 and the National Science Foundation Graduate Research Fellowship under Grant No. DGE 1752814.

Reviewer information *Nature* thanks L. Gu and the other anonymous reviewer(s) for their contribution to the peer review of this work.

Author contributions S.H. conceived the study; J.P., S.H., J.B., M.B. and W.S. designed the study; J.P. collected and analysed the data with contributions from J.B.; J.P., S.H., J.B., M.B. and W.S. interpreted results; J.P. and S.H. wrote the paper.

Competing interests The authors declare no competing interests.

Additional information

Extended data is available for this paper at <https://doi.org/10.1038/s41586-018-0417-3>.

Supplementary information is available for this paper at <https://doi.org/10.1038/s41586-018-0417-3>.

Reprints and permissions information is available at <http://www.nature.com/reprints>.

Correspondence and requests for materials should be addressed to J.P.

Publisher's note: Springer Nature remains neutral with regard to jurisdictional claims in published maps and institutional affiliations.

METHODS

No statistical methods were used to predetermine sample size.

To link national annual yield data from the Food and Agricultural Organization of the United Nations to climatological data, we aggregate all gridded temperature, precipitation, cloud and SAOD datasets to the annual-country level by averaging values over cropped area³¹ to the growing season³² using a methodology that is similar to those previously published^{25,33}.

Our analysis of the effect of SSAs on log insolation ($n = 3,311,553$ station-days for total insolation and 889,327 for direct and diffuse insolation) models SAOD, cloud fraction³⁴ and ENSO (current and lagged) linearly (equation (2) in Supplementary Information). We include station by day-of-year fixed effects. Our analysis of the effect of SSAs on atmospheric forward scattering shares the same specification (equation (5) in Supplementary Information).

Our analysis of the effect of SSAs on log yields models the effect of SAOD linearly (nonlinear estimates do not significantly differ from the linear estimate; Extended Data Fig. 3), the response of temperature³⁵, precipitation³⁶ and clouds³⁷ using restricted cubic splines, and allows the response of ENSO (current and lagged) to differ between teleconnected and non-teleconnected regions³⁸ (equation (16) in Supplementary Information). We include country fixed effects and country-specific quadratic time trends. For all empirical insolation and yield analyses we calculate standard errors to account for serial correlation within countries across years and for spatial autocorrelation within years across countries²³.

To calculate the total effect of SRM relative to a climate change scenario, we average results over three ensemble members from the Max Planck Institute Earth System Model²⁷. Uncertainty in the total effect represents uncertainty in the estimated parameters of the empirical yield model (Supplementary Information, section IV.4). We do not consider carbon fertilization effects in calculation

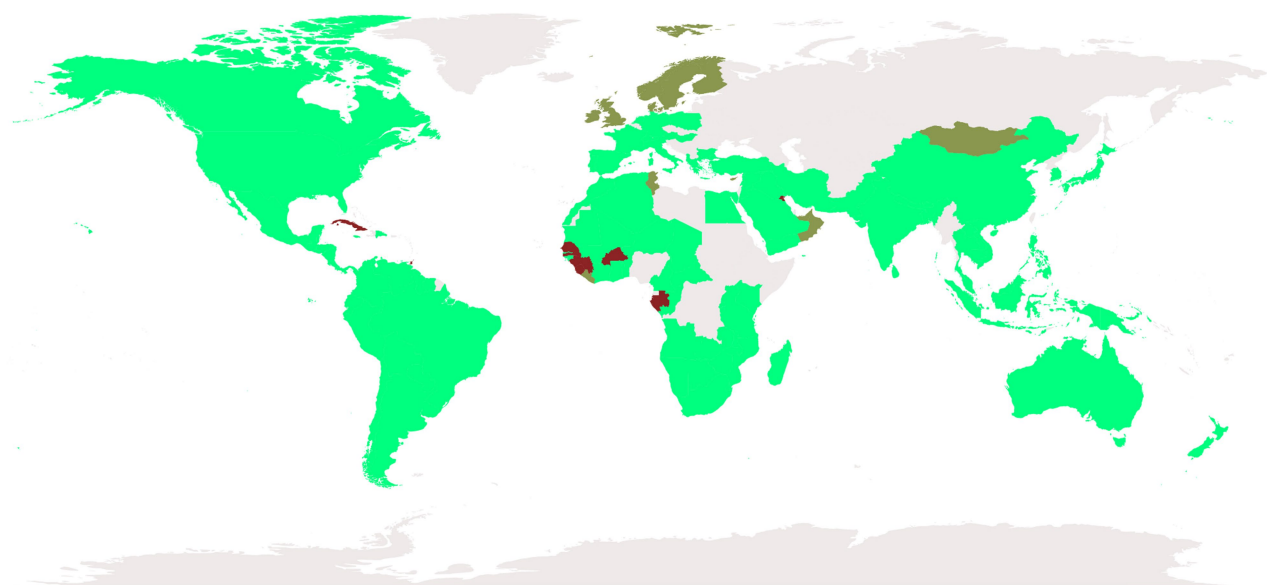
of the total effect because carbon dioxide levels are the same in the SRM and climate-change-only scenarios.

Reporting summary. Further information on experimental design is available in the Nature Research Reporting Summary linked to this paper.

Code availability. Replication code is available at <https://zenodo.org/communities/global-agricultural-effects-of-geoengineering-volcanic-eruptions/> as well as upon request from the corresponding author.

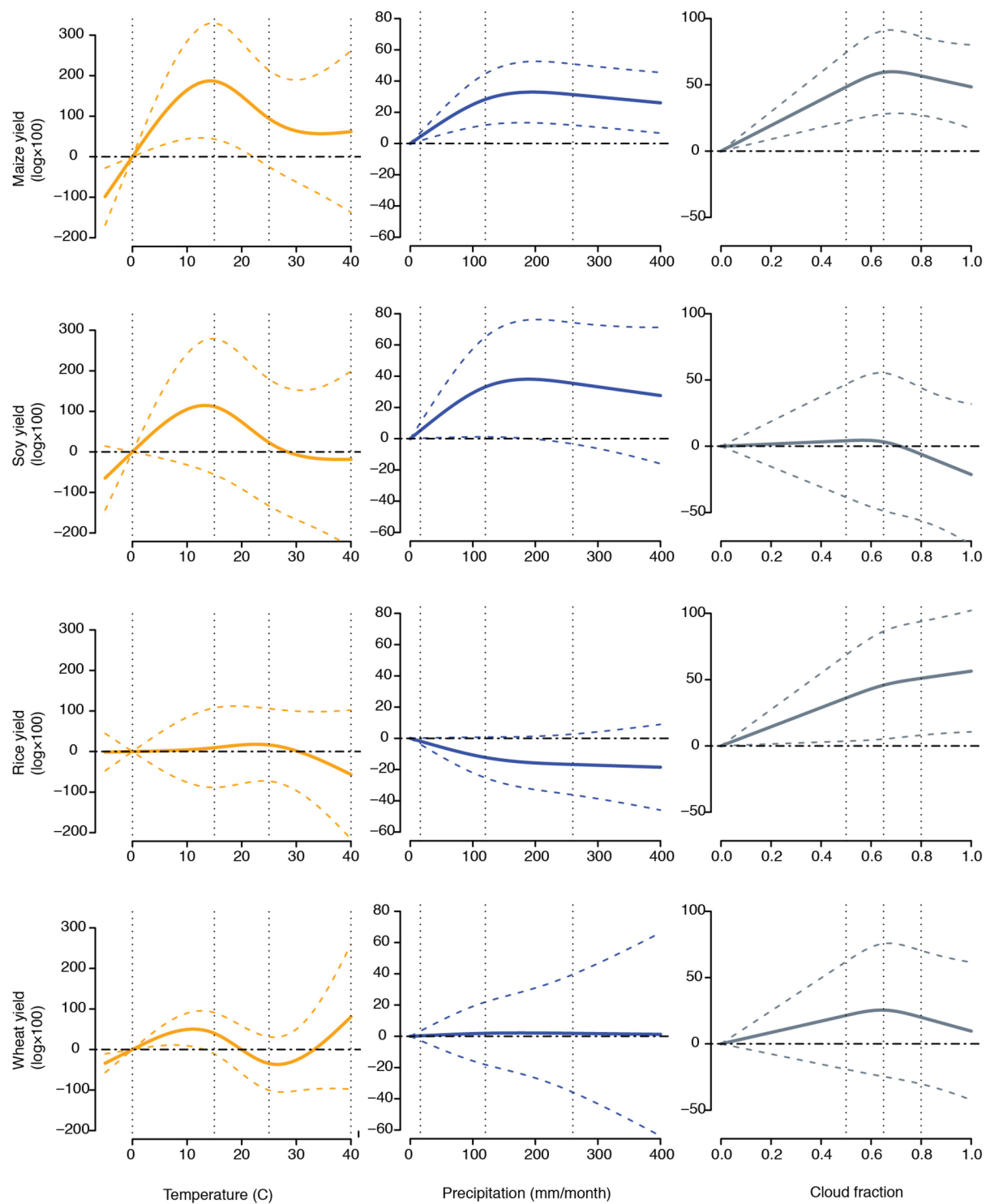
Data availability. All data used in this analysis is from free, publicly available sources and is available upon request from the corresponding author.

31. Ramankutty, N., Evan, A. T., Monfreda, C. & Foley, J. A. Farming the planet: 1. geographic distribution of global agricultural lands in the year 2000. *Glob. Biogeochem. Cycles* **22**, GB1003 (2008).
32. Sacks, W. J., Deryng, D., Foley, J. A. & Ramankutty, N. Crop planting dates: an analysis of global patterns. *Glob. Ecol. Biogeogr.* **19**, 607–620 (2010).
33. Burke, M. & Emerick, K. Adaptation to climate change: evidence from US agriculture. *Am. Econ. J. Econ. Policy* **8**, 106–140 (2016).
34. ISCCP Science Team. ISCCP data and information. *NASA Atmospheric Science Data Center* https://eosweb.larc.nasa.gov/project/isccp/isccp_table (accessed 7 February 2016) (1999).
35. Rohde, R. et al. A new estimate of the average Earth surface land temperature spanning 1753 to 2011. *Geoinfor. Geostat. Overview* **1**, 1000101 (2013).
36. Willmott, C. & Matsurra, K. Terrestrial air temperature and precipitation: monthly and annual time series (1950–1999). *Earth System Research Laboratory* <http://www.esrl.noaa.gov/psd/> (accessed 1 January 2016) (2001).
37. Norris, J. R. & Evan, A. T. Empirical removal of artifacts from the ISCCP and PATMOS-x satellite cloud records. *J. Atmos. Ocean. Technol.* **32**, 691–702 (2015).
38. Hsiang, S. M. & Meng, K. C. Tropical economics. *Am. Econ. Rev.* **105**, 257–261 (2015).



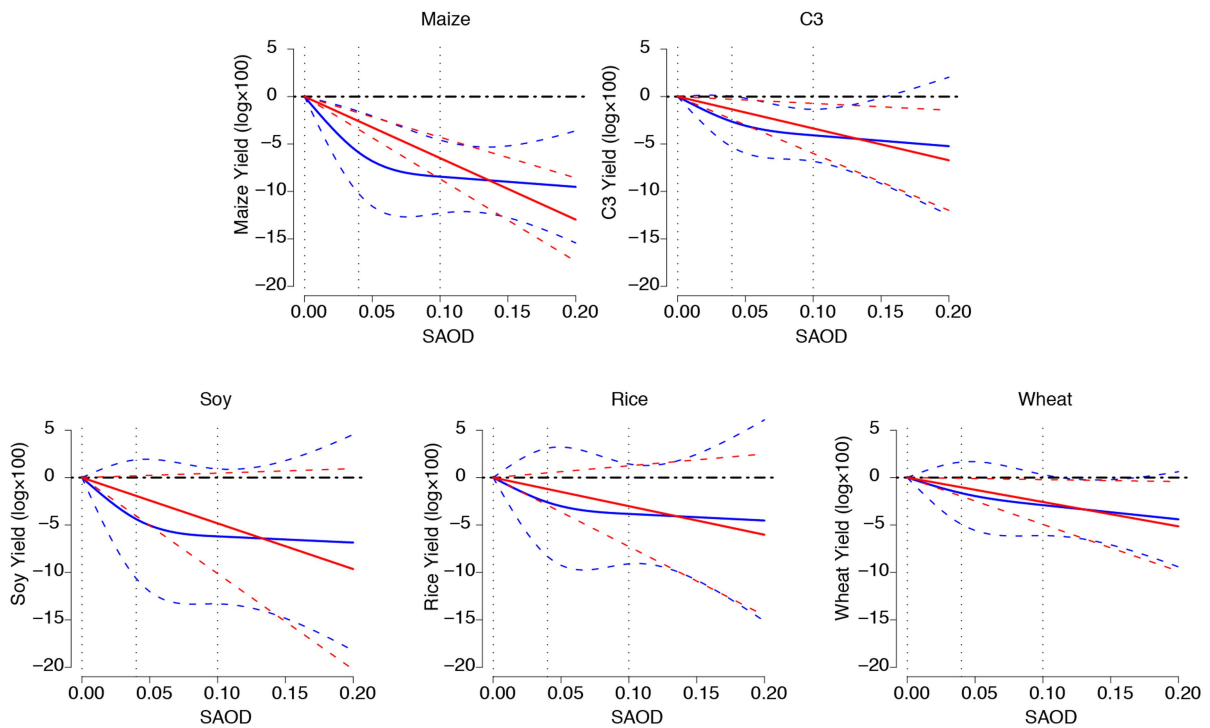
Extended Data Fig. 1 | Countries included in the estimation of the insolation-mediated effect of SAOD on crop yield. Countries in light green are included in the estimation of the insolation-mediated effect of SSAs on yields for both C3 (soy, rice and wheat) and C4 (maize) crops.

Countries in dark green are included only in estimation of the insolation effect for C3 crops, and countries in red are included only in estimation of the insolation effect for maize. Countries in grey are not included in the analysis owing to missing data.



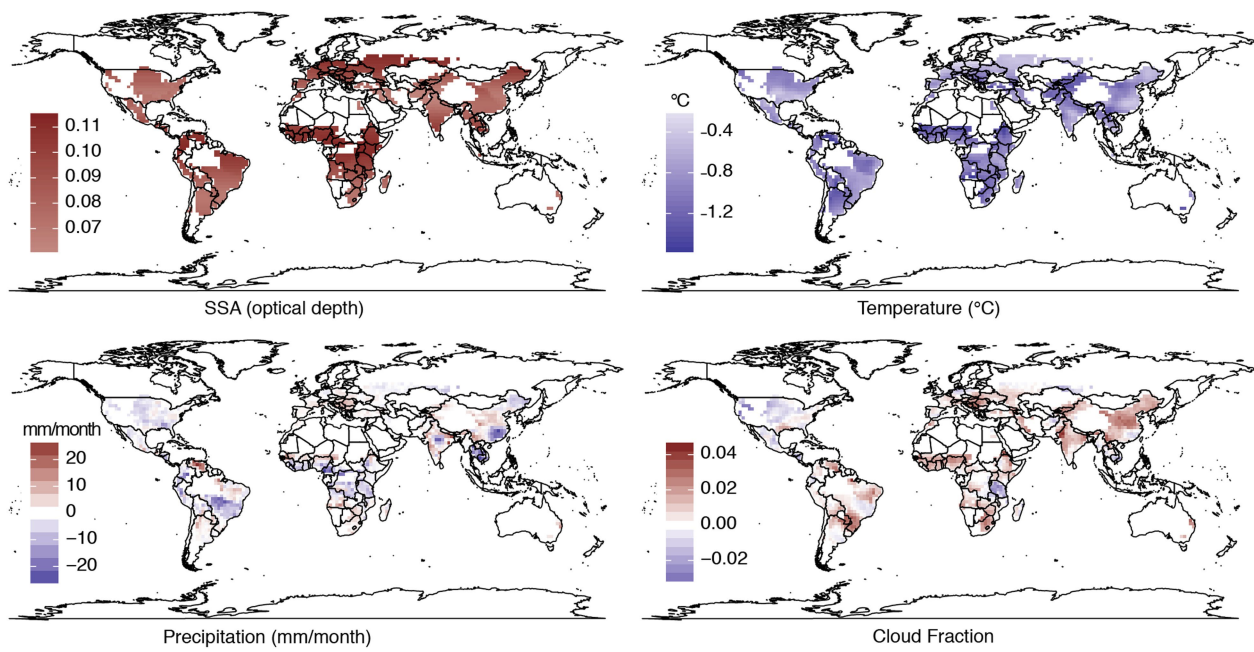
Extended Data Fig. 2 | Estimated response of yields to changes in growing-season average temperature (orange), precipitation (blue) and cloud fraction (grey). Temperature, precipitation and cloud fraction axes show growing-season means. The y axes show partial effects on yield relative to a value of zero for each climatological variable ($f_T(T_{it})$, $f_P(P_{it})$

and $f_C(C_{it})$ in equation (16) in Supplementary Information). Vertical dotted lines show the placement of the knots for the restricted cubic splines specification. Dashed lines show the 95% confidence intervals. $n = 2,501, 1,256, 1,562$ and $2,010$ country-years for maize, soy, rice and wheat, respectively.



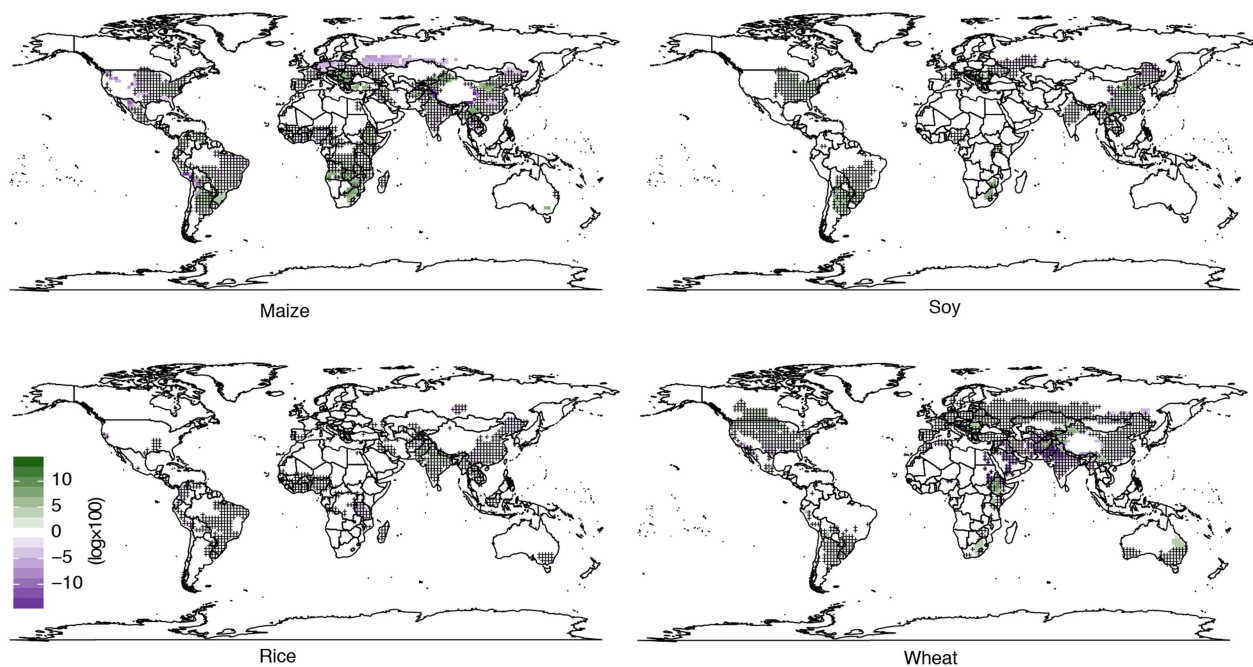
Extended Data Fig. 3 | Flexible (blue) and linear (red) estimation of the insolation-mediated effect of SSAs on crop yields. The SAOD axes show growing-season means. Each point on a curve gives the optical effect of SAOD, relative to a value of zero (the slope of the red lines is β in

equation (16) in Supplementary Information). Vertical dotted lines show the placement of the knots for the restricted cubic splines specification. Dashed lines show the 95% confidence intervals.



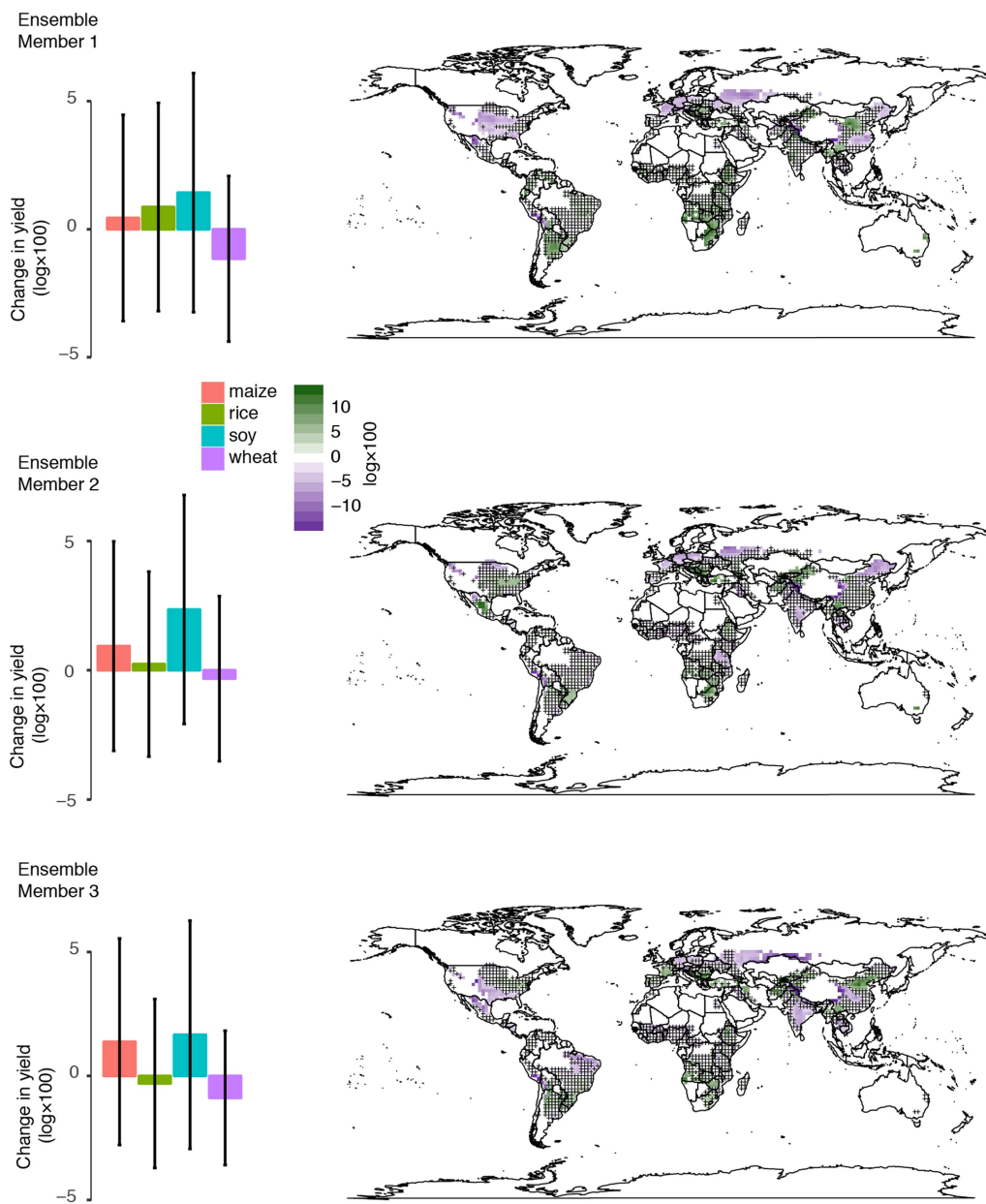
Extended Data Fig. 4 | Effect of SRM on climatological determinants of yield. SRM-induced changes in maize growing-season average SAOD, temperature, precipitation and cloud fraction, relative to the

climate-change-only scenario. Changes in uncropped land have been masked out by setting the values to zero.



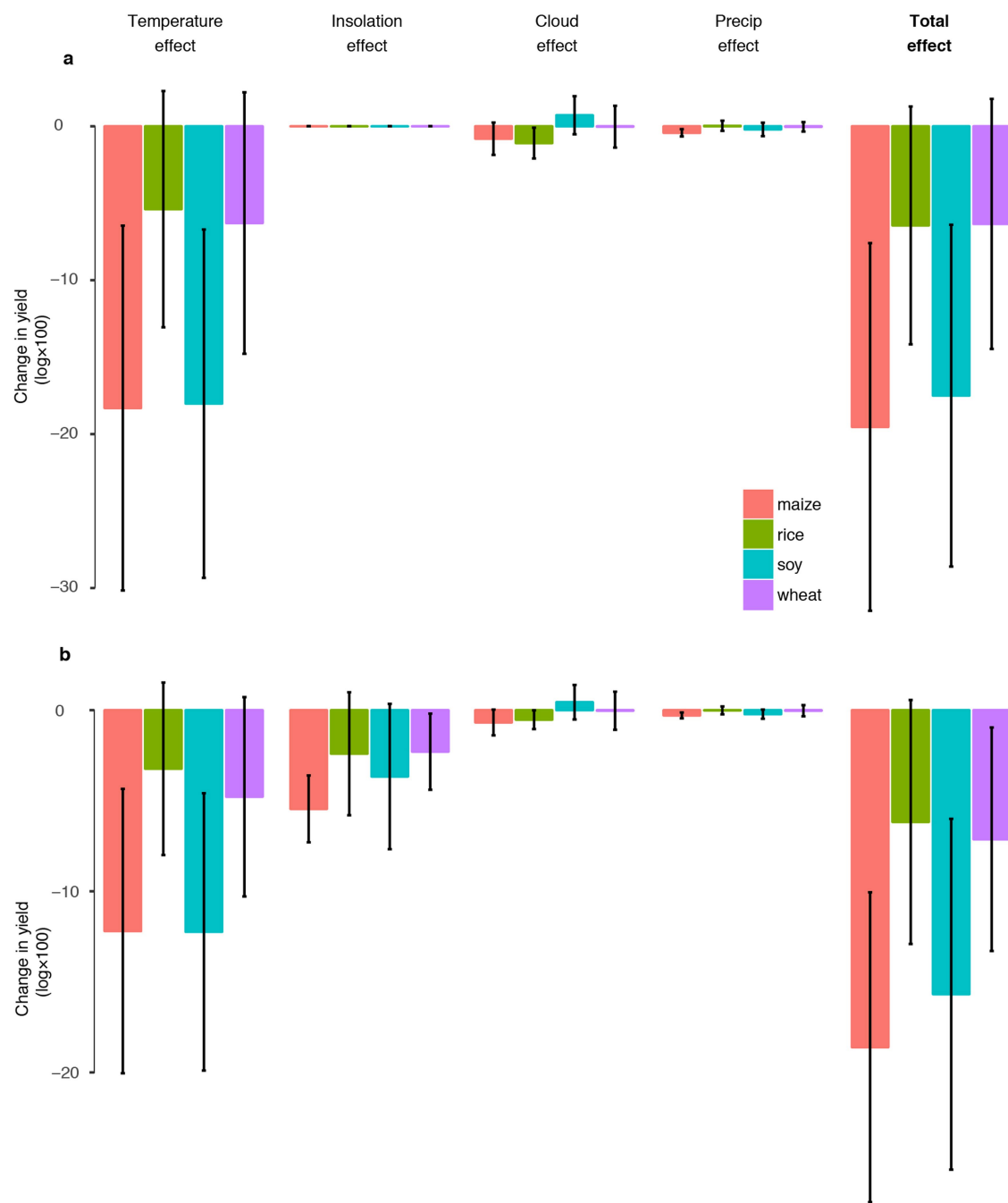
Extended Data Fig. 5 | Total effect of SRM on maize, soy, rice and wheat yields. Total effects are constructed by summing the partial effects from insolation, temperature, precipitation and clouds. Effects are relative to the climate-change-only scenario. Changes in uncropped land have been masked out by setting the values to zero. Statistically insignificant effects ($P > 0.05$) are hatched. We calculate P values using a two-sided

t-test comparing the estimated effect of SRM to a null hypothesis of zero effect. When calculating the distribution of the estimated SRM effect, we consider only statistical uncertainty. This uncertainty is shown in Extended Data Table 2, Extended Data Fig. 2, and the calculations are described in Supplementary Information, section IV.4.



Extended Data Fig. 6 | The finding that SRM mitigates little of the damages of climate change is consistent across three ensemble runs. Bar graphs show the total effect of SRM on global yields (cropped-fraction weighted average), relative to the climate change control, for each of the three Earth system model runs. Results are similar across ensemble member runs. Maps on the right show the total effect of SSAs on maize yields for each of the ensemble runs. Error bars in the bar graphs show 95% confidence intervals for estimated mean effects for each crop.

Statistically insignificant effects ($P > 0.05$) are hatched in the maps. Changes in uncropped land have been masked out by setting the values to zero. We calculate P values using a two-sided t -test comparing the estimated effects to a null hypothesis of zero effect. Within each ensemble member, we calculate the distributions of the estimated effects considering only statistical uncertainty. This uncertainty is shown in Extended Data Table 2, Extended Data Fig. 2, and the calculations are described in Supplementary Information, section IV.4.



Extended Data Fig. 7 | Effects of climate change and SRM relative to historical scenario. **a**, As in Fig. 4e, but comparing a climate change scenario (RCP 4.5) to an historical scenario (Supplementary Information, section IV.3). **b**, As in Fig. 4e, but comparing a climate-change-with-SRM scenario to an historical scenario. Note that these calculations consider

only climatological and sunlight-mediated effects; changes in yields owing to carbon fertilization, or other factors that may differ between scenarios, are not included. Error bars show 95% confidence intervals around the estimated mean effect.

Extended Data Table 1 | Effect of SSAs on total, direct and diffuse insolation

Radiation Type: Years in Sample:	(1) Total [83-09]	(2) Total [79-09]	(3) Total [79-09]	(4) Direct [83-09]	(5) Direct [79-09]	(6) Direct [79-09]	(7) Diffuse [83-09]	(8) Diffuse [79-09]	(9) Diffuse [79-09]
SAOD	−0.172*** (0.062)	−0.067 (0.058)		−1.580*** (0.320)	−1.395*** (0.295)		1.199*** (0.122)	1.197*** (0.125)	
SAOD × (yr≤89) [Chichón]		−0.024 (0.079)			−1.039 (0.760)			2.063*** (0.102)	
SAOD × (yr>89) [Pinatubo]		−0.100* (0.054)			−1.406*** (0.301)			1.171*** (0.115)	
Cloud Fraction	−0.946*** (0.041)			−2.792*** (0.179)			0.499*** (0.085)		
Nino 3.4	0.002 (0.002)	0.002 (0.003)	0.002 (0.003)	0.018** (0.009)	0.017 (0.012)	0.017 (0.012)	−0.001 (0.003)	0.0004 (0.003)	0.001 (0.003)
Nino 3.4 (lagged)	0.004 (0.003)	−0.001 (0.003)	−0.001 (0.003)	0.006 (0.010)	−0.011 (0.013)	−0.011 (0.013)	−0.003*** (0.001)	0.001 (0.001)	0.0003 (0.002)
Observations	3,311,553	4,371,586	4,371,586	889,327	1,000,776	1,000,776	889,327	1,000,776	1,000,776
Adjusted R ²	0.766	0.750	0.750	0.552	0.413	0.413	0.722	0.744	0.744

Coefficients on SAOD describe the effect of increasing SSA optical depth by 1 unit on the log of total, direct or diffuse sunlight. Columns 1, 4 and 7 show the preferred specification (equation (2) in Supplementary Information). Columns 2, 5 and 8 include data from 1979–2009 to capture the effect of both the Pinatubo and El Chichón eruptions. Columns 3, 6 and 9 estimate the effect separately for El Chichón and Pinatubo (Supplementary Information, section II.1). We do not control for cloud fraction in columns 2, 3, 5, 6, 8 and 9 because the cloud data are available only beginning in 1983. All models account for station-by-day-of-year fixed effects. Standard errors of the mean, shown in parentheses, are clustered by country and by year to account for serial correlation over time within a country and for autocorrelation across space within a year. We calculate *P* values using a two-sided *t*-test. **P*<0.1, ***P*<0.05, ****P*<0.01.

Extended Data Table 2 | Robustness of the insolation effect of SSAs on yields to changes in model specification, data sample and data source

Years in Sample	(1) [83-09]	(2) [83-09]	(3) [83-09]	(4) [83-09]	(5) [83-09]	(6) [83-09]	(7) [83-03]	(8) [83-05]	(9) [61-09]	(10) [83-09]	(11) [83-09]	(12) [79-03]	(13) [79-03]
Climate Controls	None	T	TP	TPC	TPCE	TPCE	TPCE	TPCE	TPE	TPCE	TPCEO	TPE	TPE
SAOD Data					Cos(SZA)	SPARC	SPARC2		Drop Mex. & Phil.	Add CO ₂		SPARC	
Maize (C4)													
SAOD	-0.607*** (0.127)	-0.615*** (0.120)	-0.572*** (0.115)	-0.561*** (0.118)	-0.649*** (0.112)	-0.392*** (0.0656)	-0.901*** (0.252)	-0.776*** (0.162)	-0.258** (0.125)	-0.672*** (0.116)	-0.644*** (0.119)		
SAOD x (yr≤89) [Chichón]												-0.229 (0.173)	-1.073 (0.764)
SAOD x (yr>89) [Pinatubo]												-0.533*** (0.142)	-0.796*** (0.247)
Observations	2,501	2,501	2,501	2,501	2,501	2,501	1,868	2,025	3,867	2,447	2501	2,322	2,211
R-squared	0.950	0.952	0.953	0.953	0.954	0.954	0.953	0.955	0.939	0.953	0.954	0.948	0.949
C3 - pooled													
SAOD	-0.294** (0.131)	-0.286** (0.131)	-0.293** (0.132)	-0.297** (0.129)	-0.331** (0.136)	-0.183** (0.0741)	-0.559** (0.232)	-0.439** (0.192)	-0.0638 (0.135)	-0.349** (0.140)	-0.325** (0.144)		
SAOD x (yr≤89) [Chichón]												0.0283 (0.132)	0.0669 (0.606)
SAOD x (yr>89) [Pinatubo]												-0.362** (0.165)	-0.545** (0.228)
Observations	4,828	4,828	4,828	4,828	4,828	4,828	3,618	3,916	7,431	4,694	4828	4,480	4,297
R-squared	0.940	0.941	0.941	0.942	0.942	0.942	0.946	0.946	0.928	0.941	0.942	0.942	0.943
Soy (C3)													
SAOD	-0.313 (0.287)	-0.327 (0.282)	-0.335 (0.276)	-0.356 (0.288)	-0.482* (0.270)	-0.319* (0.160)	-0.848** (0.381)	-0.860*** (0.268)	-0.152 (0.280)	-0.541* (0.270)	-0.483* (0.271)		
SAOD x (yr≤89) [Chichón]												0.227 (0.236)	1.888 (1.290)
SAOD x (yr>89) [Pinatubo]												-0.630** (0.233)	-0.843** (0.324)
Observations	1,256	1,256	1,256	1,256	1,256	1,256	937	1,026	1,897	1,202	1,256	1,169	1,118
R-squared	0.883	0.888	0.889	0.890	0.890	0.890	0.905	0.903	0.868	0.891	0.890	0.894	0.894
Rice (C3)													
SAOD	-0.395* (0.196)	-0.407* (0.198)	-0.424** (0.201)	-0.412* (0.202)	-0.301 (0.217)	-0.158 (0.118)	-0.298 (0.372)	-0.203 (0.267)	-0.191 (0.143)	-0.321 (0.228)	-0.283 (0.225)		
SAOD x (yr≤89) [Chichón]												-0.149 (0.244)	-1.125 (1.059)
SAOD x (yr>89) [Pinatubo]												-0.225 (0.251)	-0.353 (0.368)
Observations	1,562	1,562	1,562	1,562	1,562	1,562	1,179	1,278	2,474	1,509	1,562	1,448	1,396
R-squared	0.935	0.935	0.935	0.935	0.936	0.935	0.941	0.941	0.907	0.935	0.936	0.932	0.933
Wheat (C3)													
SAOD	-0.201 (0.127)	-0.164 (0.122)	-0.161 (0.122)	-0.164 (0.118)	-0.257** (0.121)	-0.126** (0.0600)	-0.594** (0.249)	-0.352* (0.200)	0.103 (0.114)	-0.253** (0.123)	-0.256** (0.114)		
SAOD x (yr≤89) [Chichón]												0.0672 (0.156)	0.0118 (0.564)
SAOD x (yr>89) [Pinatubo]												-0.295* (0.158)	-0.529** (0.232)
Observations	2,010	2,010	2,010	2,010	2,010	2,010	1,502	1,612	3,060	1,983	2,010	1,863	1,783
R-squared	0.939	0.940	0.940	0.941	0.941	0.941	0.944	0.944	0.934	0.940	0.941	0.942	0.943

The table above shows the insolation effect of SSAs for maize, C3 crops pooled, and soy, rice and wheat yields individually across a range of robustness checks (Supplementary Information, section III.4). The C3 response is estimated assuming that crops that share the C3 photosynthetic pathway (soy, rice and wheat) have a common insolation effect (equation (18) in Supplementary Information). Columns 1–5 drop all climate controls and then add temperature (T), precipitation (P), cloud fraction (C) and ENSO (E) controls back in one at a time; column 5 is our preferred specification (equation (16) in Supplementary Information); column 6 accounts for the angle at which incoming light passes through the SSA layer by dividing SAOD by the cosine of the solar zenith angle (SZA); columns 7 and 8 use two alternative SSA datasets, SPARC and SPARC2 (Supplementary Information, section I.4); column 9 includes data from 1961–2009 to span the eruption of Agung; column 10 drops Mexico and the Philippines, where the El Chichón and Pinatubo eruptions occurred, from the analysis; column 11 adds surface CO₂ concentration as a control; column 12 estimates the effects for El Chichón and Pinatubo separately; and column 13 does the same using the SPARC dataset. All models account for country fixed effects and country-specific quadratic time trends. Standard errors of the mean, shown in parentheses, are clustered by country and by year to account for serial correlation over time within a country and for autocorrelation across space within a year. We calculate P values using a two-sided t-test. *P<0.1, **P<0.05, ***P<0.01.

Extended Data Table 3 | Effect of SSAs on atmospheric forward scattering

	(1)	(2)	(3)
Dep. Var. = $\text{Pr}(\text{photon reaches the surface} \mid \text{photon hits a particle})$			
Year	[83-09]	[79-09]	[79-09]
SAOD	0.233*** (0.030)	0.243*** (0.030)	
SAOD x (yr≤89) [Chichón]		0.345*** (0.031)	
SAOD x (yr>89) [Pinatubo]		0.240*** (0.029)	
Cloud Fraction	-0.047*** (0.018)		
Nino 3.4	0.001 (0.001)	0.001 (0.001)	0.001 (0.001)
Nino 3.4 (lagged)	-0.0004 (0.001)	-0.001 (0.001)	-0.001 (0.001)
Observations	886,287	997,142	997,142
Adjusted R ²	0.228	0.227	0.227

The dependent variable is the probability that a photon of light makes it to the surface, conditional on hitting a particle (w in equation (3) in Supplementary Information). Coefficients on SAOD represent the effect of increasing SAOD by 1 unit on w for the entire atmospheric column. Column 1 is our preferred specification (equation (5) in Supplementary Information). Column 2 drops cloud controls and includes both the Pinatubo and El Chichón eruptions. Column 3 estimates the effects for El Chichón and Pinatubo separately. All models account for station-by-day-of-year fixed effects. Standard errors of the mean, shown in parentheses, are clustered by country and by year to account for serial correlation over time within a country and for autocorrelation across space within a year. We calculate P values using a two-sided t -test. *** $P < 0.01$.

Restoration of vision after de novo genesis of rod photoreceptors in mammalian retinas

Kai Yao¹, Suo Qiu^{1,2}, Yanbin V. Wang^{3,4}, Silvia J. H. Park³, Ethan J. Mohns⁵, Bhupesh Mehta^{4,6}, Xinran Liu⁷, Bo Chang⁸, David Zenisek^{3,4}, Michael C. Crair^{3,5}, Jonathan B. Demb^{3,4} & Bo Chen^{1,9,10*}

In zebrafish, Müller glia (MG) are a source of retinal stem cells that can replenish damaged retinal neurons and restore vision¹. In mammals, however, MG do not spontaneously re-enter the cell cycle to generate a population of stem or progenitor cells that differentiate into retinal neurons. Nevertheless, the regenerative machinery may exist in the mammalian retina, as retinal injury can stimulate MG proliferation followed by limited neurogenesis^{2–7}. Therefore, there is still a fundamental question regarding whether MG-derived regeneration can be exploited to restore vision in mammalian retinas. Gene transfer of β-catenin stimulates MG proliferation in the absence of injury in mouse retinas⁸. Here we report that following gene transfer of β-catenin, cell-cycle-reactivated MG can be reprogrammed to generate rod photoreceptors by subsequent gene transfer of transcription factors essential for rod cell fate specification and determination. MG-derived rods restored visual responses in *Gnat1*^{rd17}/*Gnat2*^{epf13} double mutant mice, a model of congenital blindness^{9,10}, throughout the visual pathway from the retina to the primary visual cortex. Together, our results provide evidence of vision restoration after de novo MG-derived genesis of rod photoreceptors in mammalian retinas.

In cold-blooded vertebrates such as zebrafish, Müller glia (MG) act as retinal stem cells that readily proliferate to replenish damaged retinal neurons, establishing a powerful self-repair mechanism^{11–13}. In mammals, however, MG lack regenerative capability as they do not spontaneously re-enter the cell cycle. Injuring the mammalian retina does activate the proliferation of MG, but with limited neurogenesis^{2–7}, and the required injury is obviously counterproductive for regeneration as it kills retinal neurons. Furthermore, there has been no convincing evidence that MG-derived regeneration improves vision in mammals. To test whether MG-derived neurogenesis improves vision without the necessity for retinal injury, we reprogrammed MGs *in vivo* to generate new rod photoreceptors in mature mouse retinas. We previously reported that gene transfer of β-catenin under control of the GFAP promoter using the ShH10 adeno-associated virus (AAV; ShH10-GFAP-β-catenin) in MG stimulates these cells to re-enter the cell cycle in uninjured mouse retina⁸. To reprogram the cell-cycle-reactivated MG into rod photoreceptors, we tested a combination of three transcription factors (*Otx2*, *Crx* and *Nrl*) that are essential for determining rod cell fate during development^{14–17}.

In the developing mouse retina, generation of cell types is complete by two postnatal weeks¹⁸. To investigate whether new rod photoreceptors could be generated from MG in the mature retina, we used a two-step reprogramming method to first stimulate MG proliferation by intravitreal injection of ShH10-GFAP-β-catenin at four weeks of age. This was followed two weeks later by a second injection of ShH10-GFAP-mediated gene transfer of *Otx2*, *Crx* and *Nrl*. We first examined whether MG could undergo successive rounds of cell division after

the initial gene transfer of β-catenin. Following a double-labelling procedure using 5-ethynyl-2'-deoxyuridine (EdU) and 5-bromo-2'-deoxyuridine (BrdU), developed to analyse the clonal expansion of horizontal cells¹⁹, proliferating MG were labelled with EdU 10 days after the injection of ShH10-GFAP-β-catenin, and 24 h later S phase cells were labelled with BrdU. Retinas were collected four days later to determine whether EdU⁺ cells had progressed through another cell division, into a second round of S phase. Very few cells were labelled with both EdU and BrdU (Extended Data Fig. 1), indicating that the vast majority of MG undergo only one cell division after β-catenin gene transfer.

To identify MG that may undergo rod photoreceptor differentiation after the second injection of ShH10-GFAP-mediated gene transfer of *Otx2*, *Crx* and *Nrl*, we included ShH10-rhodopsin-tdTomato—a 2.1-kb rhodopsin promoter²⁰ driving the expression of tdTomato—in the first injection, together with ShH10-GFAP-GFP to label all transduced MG (Fig. 1a). On the basis of morphological changes observed from different retinal samples after the second injection for rod induction, the progression of MG-derived rod differentiation was categorized into initial, intermediate and terminal stages. At the initial stage, tdTomato⁺ cells resembled MG, with the upper processes ending at the outer limiting membrane, and the lower processes (MG endfeet) extending to the nerve-fibre layer (Fig. 1b–d). At the intermediate stage, there was an asymmetric cell division whereby each tdTomato⁺ cell produced two daughter cells with different fates (Fig. 1e–g). One daughter cell apparently differentiated to a rod photoreceptor with its soma localized to the outer nuclear layer (ONL), and, notably, the MG-derived rod cell generated outer and inner segments, a specialized cellular structure that is essential for phototransduction. The second daughter cell remained in the inner nuclear layer (INL) with a typical MG morphology. At the terminal stage, the tdTomato⁺ cell appeared to have differentiated to a mature rod, resembling native rods with outer and inner segments, and an enlarged synaptic-bouton-like terminal. The second daughter cell remained as an MG and shut off tdTomato expression (as it is driven by the rod-specific rhodopsin promoter) (Fig. 1h–j). MG-derived rod differentiation was observed throughout the treated retina, whereas no tdTomato⁺ cells were observed in control retinas that received the same treatments except for ShH10-GFAP-β-catenin, which was omitted from the first injection (Extended Data Fig. 2).

We quantified the progression of rod differentiation over time (1,000–1,200 tdTomato⁺ cells, 6–8 retinas per time point; with additional examples in Extended Data Fig. 3). One week after the second injection (Fig. 1k), most tdTomato⁺ cells (73.5%) were in the initial stage, with a smaller number in the intermediate (20.6%) and terminal stages (5.9%). Two weeks after the second injection (Fig. 1l), most tdTomato⁺ cells (74.8%) were in the terminal stage. Four weeks after the second injection (Fig. 1m), nearly all tdTomato⁺ cells were in the

¹Department of Ophthalmology, Icahn School of Medicine at Mount Sinai, New York, NY, USA. ²State Key Laboratory of Ophthalmology, Zhongshan Ophthalmic Center, Sun Yat-sen University, Guangzhou, China. ³Department of Ophthalmology and Visual Science, Yale University School of Medicine, New Haven, CT, USA. ⁴Department of Cellular and Molecular Physiology, Yale University School of Medicine, New Haven, CT, USA. ⁵Department of Neuroscience, Yale University School of Medicine, New Haven, CT, USA. ⁶Department of Biophysics, National Institute of Mental Health and Neuro Sciences, Bangalore, India. ⁷Department of Cell Biology, Center for Cellular and Molecular Imaging, Yale University School of Medicine, New Haven, CT, USA. ⁸The Jackson Laboratory, Bar Harbor, ME, USA. ⁹Department of Neuroscience, Icahn School of Medicine at Mount Sinai, New York, NY, USA. ¹⁰Department of Developmental and Regenerative Biology, Icahn School of Medicine at Mount Sinai, New York, NY, USA. *e-mail: bo.chen@mssm.edu

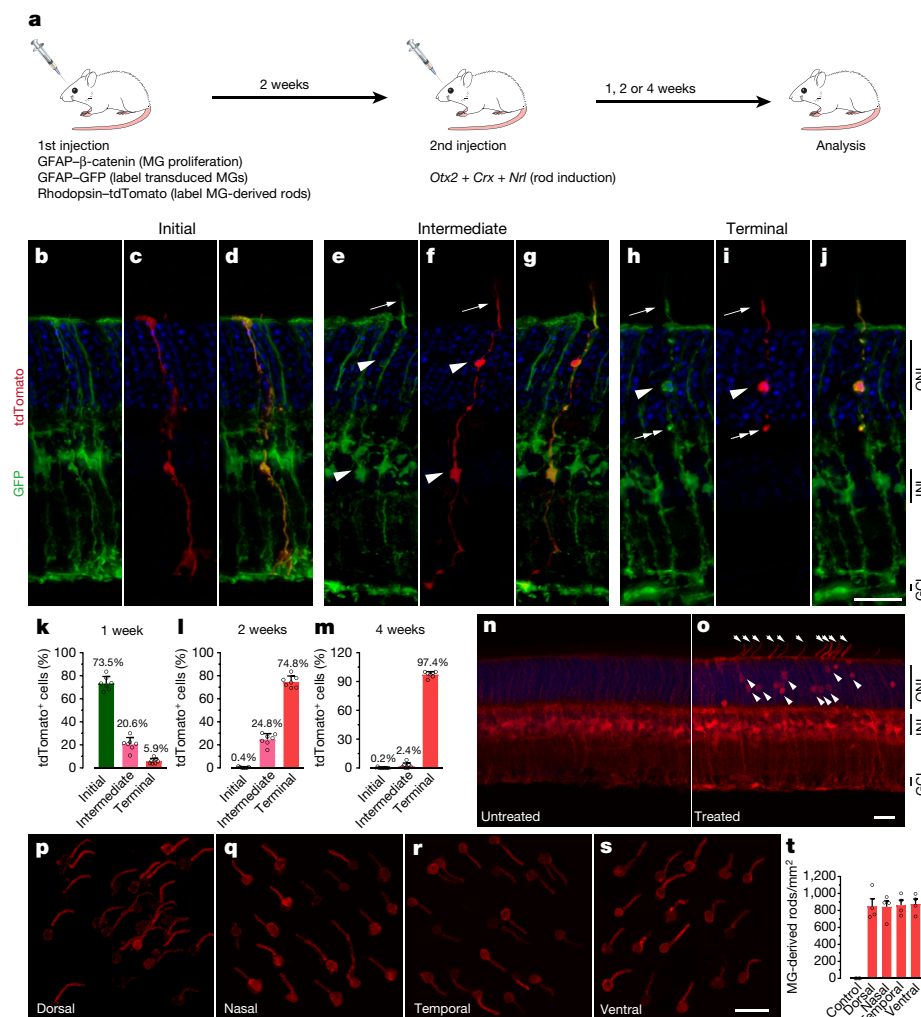


Fig. 1 | Generation of rod photoreceptors by reprogramming MG in the mouse retina. **a**, Schematic of the two-step reprogramming method to generate rod photoreceptors. **b–j**, Characterization of MG-derived rod differentiation through initial (**b–d**), intermediate (**e–g**) and terminal (**h–j**) stages. Arrowheads, cell soma; arrows, rod outer segments; double arrows, synaptic terminals. GCL, ganglion cell layer; INL, inner nuclear layer; ONL, outer nuclear layer. Scale bar, 25 μ m. Experiments were repeated 6 times independently with similar results. **k–m**, Quantification of MG-derived rod differentiation at 1 (**k**), 2 (**l**) and 4 weeks (**m**) after the second injection of ShH10-GFAP-mediated gene transfer of *Otx2*, *Crx* and *Nrl* for rod induction. Data are presented as mean \pm s.e.m.,

$n = 7$ retinas. **n, o**, Lineage analysis of MG-derived rod photoreceptors: untreated MG fate-mapping mice with MG labelled by tdTomato (**n**); treated MG fate-mapping mice using the two-step reprogramming method (**o**). Arrowheads, rod soma; arrows, rod outer segments. Scale bar, 20 μ m. Experiments were repeated 4 times independently with similar results. **p–t**, Quantification of MG-derived rod photoreceptors in the dorsal (**p**), nasal (**q**), temporal (**r**) and ventral (**s**) quadrants of retinal flat-mount preparations at 4 weeks after the second injection for rod induction. Scale bar, 20 μ m. Experiments were repeated 4 times independently with similar results. Data in **t** show mean \pm s.e.m., $n = 4$ retinas. Control measurements were combined across quadrants.

terminal stage (97.4%). The tdTomato⁺ cells were also positive for GFP (Fig. 1e, h), indicating that they were indeed derived from MG, as gene transfer using the ShH10 AAV serotype and GFAP gene promoter should selectively transduce MG but not photoreceptors⁸. GFP expression decreased in MG-derived rods over time, and no GFP signal was detected in tdTomato⁺ cells 12 weeks after the second injection (Extended Data Fig. 4). We also tested whether expression of *Otx2*, *Crx* and *Nrl* individually or in pairs was sufficient for rod induction (Extended Data Fig. 5). Four weeks after the second injection, only the combination of *Crx* and *Nrl* yielded tdTomato⁺ cells, which were restricted to the initial stage of rod differentiation (Extended Data Fig. 6).

To trace the lineages of MG following our two-step reprogramming method, we generated a MG fate-mapping mouse strain (GFAP-Cre \times Rosa26-tdTomato reporter line), which permanently labels MG with tdTomato⁸ (Fig. 1n). We injected the MG fate-mapping mice at four weeks of age with ShH10-GFAP-β-catenin to stimulate MG proliferation, followed two weeks later by ShH10-GFAP-mediated

gene transfer of *Otx2*, *Crx* and *Nrl* for rod induction. Four weeks after the second injection, tdTomato⁺ cells were observed in the ONL and appeared to have differentiated into mature rods with outer and inner segments (Fig. 1o), further demonstrating that the rod cells were derived from MG in the treated retina. We occasionally observed MG-derived tdTomato⁺ cells with a horizontal cell morphology (Extended Data Fig. 7), consistent with a role for *Otx2* in promoting the fate of both photoreceptors and horizontal cells²¹.

To assess the efficiency of rod induction, we quantified the number of tdTomato⁺ cells at four weeks after the second injection. tdTomato⁺ cells were evenly distributed across the retina, with more than 800 cells per mm² in each retinal quadrant (Fig. 1p–t). By contrast, no MG-derived rods were observed in control retinas (in which ShH10-GFAP-β-catenin was omitted from the first injection) (Fig. 1t). We also examined regenerative capability of MG in retinas of seven-month-old mice. In these mice, the density of rhodopsin-tdTomato⁺ cells was reduced to around 200 per mm² in each retinal quadrant (Extended Data Fig. 8).

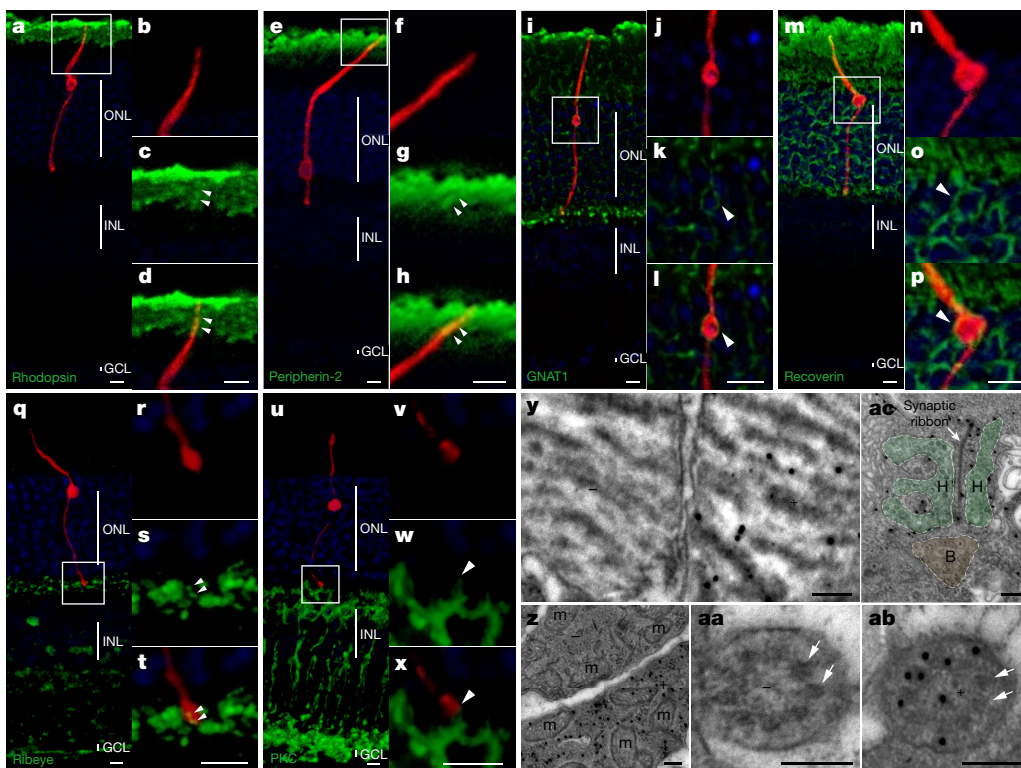


Fig. 2 | MG-derived rod photoreceptors express essential rod genes and are morphologically similar to native rod photoreceptors.

a–t, MG-derived rods (red) correctly expressed a set of essential rod proteins (green), including rhodopsin (a–d), peripherin-2 (e–h), GNAT1 (i–l), recoverin (m–p), and ribeye (q–t). Arrowheads indicate detection of immunoreactivity in MG-derived rods. u–x, MG-derived rods (red) had an enlarged bouton-like synaptic terminal in close apposition (arrowhead) to the $\text{PKC}\alpha^+$ rod bipolar cells (green). Scale bars, 20 μm (a, e, i, m, q, u), 10 μm (b–d, f–h, j–l, n–p), 5 μm (r–t, v–x). y–ac,

The rod consists of specialized structures for detection of photons and communication with downstream neurons. Using confocal microscopy and immunohistochemistry, we investigated whether MG-derived rod cells expressed rod proteins (rhodopsin, GNAT1 (also known as rod α -transducin), peripherin-2, recoverin and ribeye) that have important roles in the formation or maintenance of cellular structures and are essential for phototransduction. Wild-type mice at four weeks of age were first injected with ShH10-GFAP- β -catenin (to stimulate MG proliferation) and ShH10-rhodopsin-tdTomato (to label MG-derived rods). Four weeks after the second injection for ShH10-GFAP-mediated gene transfer of *Otx2*, *Crx* and *Nrl*, we observed that tdTomato $^+$ cells expressed rhodopsin and peripherin-2 in the outer segment (Fig. 2a–h), GNAT1 and recoverin in the soma and processes (Fig. 2i–p), and ribeye in the synaptic terminal (Fig. 2q–t), which was enlarged to form a bouton in close apposition to the post-synaptic specialties of $\text{PKC}\alpha^+$ rod bipolar cell dendrites (Fig. 2u–x). As the immunoreactivity for rhodopsin and peripherin-2 were present at high density and in close proximity to native rods, we confirmed the expression of both proteins in dissociated tdTomato $^+$ cells (Extended Data Fig. 9). The rod outer segment (ROS) consists of densely packed membrane discs housing essential proteins for phototransduction. The rod inner segment (RIS) is filled with long thin mitochondria, providing a main energy source to meet the high metabolic needs of the rod. Synthesized proteins and membranes are trafficked from the RIS to the ROS via the connecting cilium, a microtubule-based structure crucial for rod function and survival. Rods communicate with second-order neurons, bipolar cells and horizontal cells through a highly specialized triad synaptic structure. Ultrastructural analysis using transmission electron microscopy showed that the MG-derived rods correctly formed the ROS (Fig. 2y).

Ultrastructural analysis of MG-derived rods using transmission electron microscopy indicates correct formation of rod outer segments containing densely packed membrane discs (y), rod inner segments containing long thin mitochondria (z), connecting cilium with microtubule doublets (arrowheads) arranged in a circle (aa, ab) and classic triad synapse with horizontal cell axon terminals (H, green shading) and bipolar cell dendritic terminal (B, brown shading) (ac). +, immunogold-labelled MG-derived rods; –, native rods; m, mitochondrion. Scale bars (y–ac), 200 nm. Experiments were repeated 3 times independently with similar results.

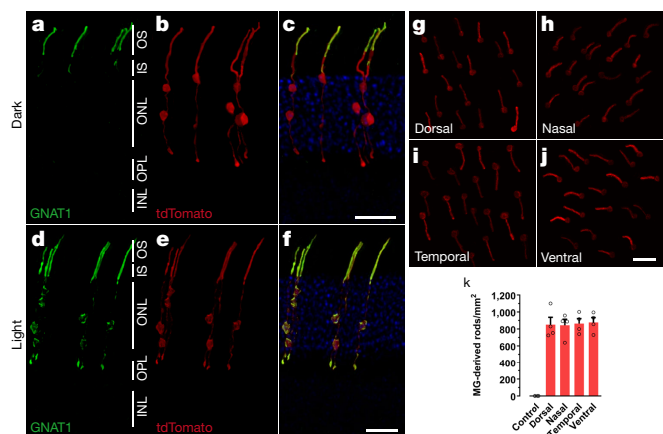


Fig. 3 | MG-derived regeneration of rod photoreceptors in *Gnat1*^{rd17} *Gnat2*^{cpf13} mice. a–f, GNAT1, detected by immunohistochemistry in tdTomato $^+$ MG-derived rods (b, e), translocated from the rod outer segments in the dark-adapted retina (a–c) to the rod inner segments, rod soma and synaptic terminals (d–f) upon light stimulation. Experiments were performed 4 weeks after the second injection for rod induction in *Gnat1*^{rd17} *Gnat2*^{cpf13} mice. Experiments were repeated 3 times independently with similar results. g–k, Effective generation of MG-derived rod photoreceptors in *Gnat1*^{rd17} *Gnat2*^{cpf13} mice, analysed by scoring the number of tdTomato $^+$ MG-derived rods per mm^2 (k) in the dorsal (g), nasal (h), temporal (i) and ventral (j) quadrants in retinal flat-mount preparations. Experiments were repeated 4 times independently with similar results. Scale bar, 20 μm . Data in k are mean \pm s.e.m., $n = 4$ retinas.

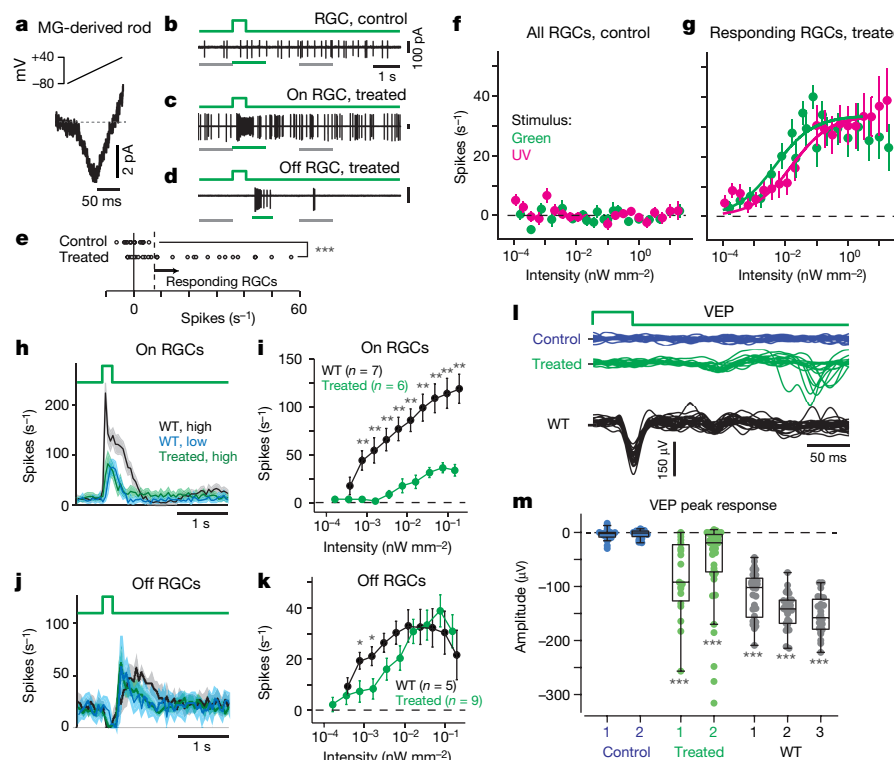


Fig. 4 | MG-derived rod photoreceptors integrate into retinal circuitry and restore visual function in *Gnat1^{d17}Gnat2^{cpf13}* mice. **a**, Averaged whole-cell current of MG-derived rods (11 recordings; 6 rods, 3 retinas) to a voltage ramp (-80 to $+40$ mV, 120 ms) shows evidence of Ca^{2+} current. **b–d**, RGC spikes to green light (1.0-mm diameter; 20 nW mm^{-2} in control cells and $3.6 \times 10^{-2} \text{ nW mm}^{-2}$ in treated cells) in response window (green line) relative to baseline windows (grey lines) showed either ‘on’- (c) or ‘off’-centre (d) polarity in treated retinas. **e**, Firing rates to green light (averaged over the range 2.1×10^{-2} to $2.1 \times 10^{-1} \text{ nW mm}^{-2}$) were higher in treated retina (26 cells; 10 retinas, 6 mice) relative to control retina (17 cells; 7 retinas, 4 mice). $***P = 2.7 \times 10^{-4}$, two-sided *t*-test. Responsive cells ($n = 15$) are those to the right of the dashed line. **f–g**, Average response ($\pm \text{s.e.m.}$ across cells) of RGCs from control ($n = 11$ (dim range), 17 (bright range) cells) and treated retinas ($n = 14$ (dim range), 9 (bright range) cells) with fitted sigmoids (see Methods). **h**, Post-stimulus time histogram for ‘on’-centre RGC responses in treated (6 cells) and wild-type (WT; C57BL/6 strain) mice (7 cells), at either high (averaged over the

range 1.6×10^{-2} to $2.1 \times 10^{-1} \text{ nW mm}^{-2}$) or low intensities (averaged over the range 3.8×10^{-4} to $7.6 \times 10^{-4} \text{ nW mm}^{-2}$) (mean $\pm \text{s.e.m.}$ across cells). **i**, ‘On’ RGC responses (mean $\pm \text{s.e.m.}$ across cells) were greater in wild-type mice relative to treated mice. $**P < 0.002$, one-sided *t*-tests; not adjusted for multiple comparisons. **j**, Same format as in **h**, for ‘off’-centre RGCs from treated (9 cells) and wild-type mice (5 cells). **k**, Same format as **i** for ‘off’-centre RGCs. $*P < 0.05$, one-sided *t*-tests. **l**, VEPs to a light flash ($\sim 1.4 \times 10^3 \text{ nW mm}^{-2}$, 50 ms) in primary visual cortex in *Gnat1^{d17}Gnat2^{cpf13}* mice of treatment (treated), sham (control) and wild-type groups. Responses across trials from a single mouse are shown, with additional mice in **m**. **m**, Response amplitude (VEP minimum) for control (2 mice), treated (2 mice) and wild-type groups (3 mice). Points represent single trials. Box plots show median \pm interquartile range, error bars indicate full range (minus outliers). All treated and wild-type mice showed significant responses (that is, median different from zero; $***P < 0.001$, Wilcoxon signed-rank test), whereas control mice did not.

RIS (Fig. 2z) connecting cilium (Fig. 2aa, ab) and classic triad synapse (Fig. 2ac), which were morphologically similar to those of native rods.

To unambiguously assess the functionality of newly generated rod photoreceptors, we reprogrammed MG in *Gnat1^{d17}Gnat2^{cpf13}* double mutant mice, which lack photoreceptor-mediated light responses. *Gnat1^{d17}* mice are deficient in GNAT1, an essential component for phototransduction, and are a model of congenital stationary night blindness^{9,22}. *Gnat2^{cpf13}* homozygotes express a mutant GNAT2 (also known as cone α -transducin), and exhibit poor cone-mediated responses that are evident by three weeks of age, and complete lack of cone-mediated responses at nine weeks of age¹⁰. Phototransduction occurs in the outer segment of photoreceptors. Light-driven translocation of GNAT1 enables rods to adapt over a wide range of light intensities²³, and also contributes to rod survival and synaptic transmission to rod bipolar cells²⁴. To reconstitute phototransduction in MG-derived rods in *Gnat1^{d17}Gnat2^{cpf13}* mice, we used ShH10-rhodopsin-mediated gene transfer of the wild-type *Gnat1* in MG. *Gnat1^{d17}Gnat2^{cpf13}* mice at four weeks of age were first injected with ShH10-GFAP- β -catenin (to stimulate MG proliferation), ShH10-rhodopsin-tdTomato (to label MG-derived rods) and ShH10-rhodopsin-*Gnat1* (to correct the *Gnat1* mutation in MG-derived rods). Four weeks after the second injection for ShH10-GFAP-mediated gene transfer of *Otx2*, *Crx* and *Nrl*, we observed that GNAT1 was localized to the ROS in the tdTomato⁺

MG-derived rods in dark-adapted retina (Fig. 3a). Following light stimulation (10,000 lx, 2 h), GNAT1 translocated towards the inner retina to other cellular compartments including the RIS, soma and synaptic terminal (Fig. 3d). However, co-expressed tdTomato—which served as an internal control—distributed to all cellular compartments regardless of light stimulation (Fig. 3b, e). Furthermore, MG-derived rods were generated as effectively in *Gnat1^{d17}Gnat2^{cpf13}* mice as in wild-type mice (Fig. 3g–k). By contrast, no MG-derived rods were observed in control *Gnat1^{r17}Gnat2^{cpf13}* retinas (in which ShH10-GFAP- β -catenin was omitted from the first injection) (Fig. 3k).

Vision is initiated by photoreceptors and propagated through synaptic transmission to bipolar cells. Synaptic release from rod photoreceptors requires a calcium current^{25,26}. We examined the calcium currents in MG-derived rods (GFP⁺ cells) with whole-cell voltage-clamp recordings in a retinal slice preparation from *Gnat1^{d17}Gnat2^{cpf13}* mice at four weeks after the second injection for rod induction. Prominent inward currents were recorded from treated retinas, with a peak near 0 mV (Fig. 4a), consistent with the expected L-type calcium currents in rods²⁷.

Visual information is integrated by retinal ganglion cells (RGCs), the retina’s output neurons. To examine whether MG-derived rods integrate into retinal circuits, we recorded light responses from RGCs of *Gnat1^{d17}Gnat2^{cpf13}* mice at four weeks after the second injection

for rod induction, using an *in vitro* preparation^{28,29}. To distinguish rod- from cone-mediated responses, we targeted RGCs in the ventral retina, where cones primarily express UV-sensitive cone opsin, with peak sensitivity at 360 nm, whereas rods express rhodopsin, with peak sensitivity at 500 nm^{28,30}. Large somas in the ganglion cell layer were targeted for action potential recordings in response to green and UV light (1-mm diameter). In control retinas (ShH10-GFAP-β-catenin omitted from the first injection), RGCs lacked light responses (Fig. 4b, e, f); whereas about half of RGCs from treated retinas responded following either light onset ('on' cells, $n=6$; Fig. 4c) or light offset ('off' cells, $n=9$; Fig. 4d, e, g). For the entire sample, RGCs from the treated retina showed stronger responses (18.0 ± 3.6 spikes per s, mean \pm s.e.m.) to green light at an intermediate intensity compared to RGCs from the control retina (-0.03 ± 0.76 spikes per s; Fig. 4e). For the responding RGCs ($n=15$; Fig. 4e), the firing rate was about 3.5 times more sensitive to green light as compared to UV light (Fig. 4g), consistent with a rod-mediated response. The responding RGCs from treated retinas showed lower sensitivity than RGCs from wild-type (C57BL/6 strain) retinas (Fig. 4h–k), especially for 'on' RGCs (Fig. 4i). For both 'on' and 'off' RGCs, responses to a high light level in the treated retina resembled RGC responses to a low light level in the wild-type retina (Fig. 4h, j), which is likely to be because of the relatively smaller number of responsive rods in the treated retina.

We next tested whether RGC responses in the treated *Gnat1^{rd17}* *Gnat2^{cpfl3}* mice could be transmitted to the primary visual cortex *in vivo*. We recorded visually evoked potentials (VEPs) in primary visual cortices of lightly anaesthetized *Gnat1^{rd17}* *Gnat2^{cpfl3}* mice at four weeks after the second injection for rod induction from the treated and control (ShH10-GFAP-β-catenin omitted from the first injection) groups. VEPs were identified as negative deflections in the cortical local field potentials (LFPs) following stimulus onset. At the brightest intensity tested ($1.42 \mu\text{W mm}^{-2}$ at the retina; see Methods), the stimulus drove a distinctive response in the LFP of the treated group, whereas no response was recorded in the control group (Fig. 4l, m). The responses of the treated group were delayed and smaller relative to responses of C57BL/6 wild-type controls (Fig. 4l), perhaps explained by the cortical integration of relatively lower outputs from RGCs in the treated mice. Nevertheless, the significant post-stimulus LFP amplitudes from the treated mice confirmed rescued light response in the primary visual cortices in comparison to the control group (Fig. 4m).

Our results demonstrate that MG, in the absence of retinal injury, can be reprogrammed *in vivo* to generate new rod photoreceptors that integrate into retinal circuits and restore vision in mammals.

Online content

Any Methods, including any statements of data availability and Nature Research reporting summaries, along with any additional references and Source Data files, are available in the online version of the paper at <https://doi.org/10.1038/s41586-018-0425-3>.

Received: 13 June 2017; Accepted: 3 July 2018;

Published online 15 August 2018.

- Goldman, D. Müller glial cell reprogramming and retina regeneration. *Nat. Rev. Neurosci.* **15**, 431–442 (2014).
- Elsaeidi, F. et al. Notch suppression collaborates with Ascl1 and Lin28 to unleash a regenerative response in fish retina, but not in mice. *J. Neurosci.* **38**, 2246–2261 (2018).
- Jorstad, N. L. et al. Stimulation of functional neuronal regeneration from Müller glia in adult mice. *Nature* **548**, 103–107 (2017).
- Karl, M. O. et al. Stimulation of neural regeneration in the mouse retina. *Proc. Natl Acad. Sci. USA* **105**, 19508–19513 (2008).
- Dyer, M. A. & Cepko, C. L. Control of Müller glial cell proliferation and activation following retinal injury. *Nat. Neurosci.* **3**, 873–880 (2000).
- Ooto, S. et al. Potential for neural regeneration after neurotoxic injury in the adult mammalian retina. *Proc. Natl Acad. Sci. USA* **101**, 13654–13659, (2004).
- Ueki, Y. et al. Transgenic expression of the proneural transcription factor Ascl1 in Müller glia stimulates retinal regeneration in young mice. *Proc. Natl Acad. Sci. USA* **112**, 13717–13722 (2015).
- Yao, K. et al. Wnt regulates proliferation and neurogenic potential of Müller glial cells via a Lin28/*let-7* miRNA-dependent pathway in adult mammalian retinas. *Cell Rep.* **17**, 165–178 (2016).

- Calvert, P. D. et al. Phototransduction in transgenic mice after targeted deletion of the rod transducin α-subunit. *Proc. Natl Acad. Sci. USA* **97**, 13913–13918, (2000).
- Chang, B. et al. Cone photoreceptor function loss-3, a novel mouse model of achromatopsia due to a mutation in *Gnat2*. *Invest. Ophthalmol. Vis. Sci.* **47**, 5017–5021 (2006).
- Fausett, B. V. & Goldman, D. A role for α1 tubulin-expressing Müller glia in regeneration of the injured zebrafish retina. *J. Neurosci.* **26**, 6303–6313 (2006).
- Bernardos, R. L., Barthel, L. K., Meyers, J. R. & Raymond, P. A. Late-stage neuronal progenitors in the retina are radial Müller glia that function as retinal stem cells. *J. Neurosci.* **27**, 7028–7040 (2007).
- Fimbel, S. M., Montgomery, J. E., Burkett, C. T. & Hyde, D. R. Regeneration of inner retinal neurons after intravitreal injection of ouabain in zebrafish. *J. Neurosci.* **27**, 1712–1724 (2007).
- Nishida, A. et al. *Otx2* homeobox gene controls retinal photoreceptor cell fate and pineal gland development. *Nat. Neurosci.* **6**, 1255–1263 (2003).
- Chen, S. et al. Crx, a novel *Otx*-like paired-homeodomain protein, binds to and transactivates photoreceptor cell-specific genes. *Neuron* **19**, 1017–1030 (1997).
- Furukawa, T., Morrow, E. M. & Cepko, C. L. Crx, a novel *otx*-like homeobox gene, shows photoreceptor-specific expression and regulates photoreceptor differentiation. *Cell* **91**, 531–541 (1997).
- Mears, A. J. et al. *Nrl* is required for rod photoreceptor development. *Nat. Genet.* **29**, 447–452 (2001).
- Livesey, F. J. & Cepko, C. L. Vertebrate neural cell-fate determination: lessons from the retina. *Nat. Rev. Neurosci.* **2**, 109–118 (2001).
- Ajioka, I. et al. Differentiated horizontal interneurons clonally expand to form metastatic retinoblastoma in mice. *Cell* **131**, 378–390 (2007).
- Matsuda, T. & Cepko, C. L. Electroporation and RNA interference in the rodent retina *in vivo* and *in vitro*. *Proc. Natl Acad. Sci. USA* **101**, 16–22 (2004).
- Emerson, M. M., Surzenko, N., Goetz, J. J., Trimarchi, J. & Cepko, C. L. *Otx2* and *Onecut1* promote the fates of cone photoreceptors and horizontal cells and repress rod photoreceptors. *Dev. Cell* **26**, 59–72 (2013).
- Deng, W. T. et al. Functional interchangeability of rod and cone transducin α-subunits. *Proc. Natl Acad. Sci. USA* **106**, 17681–17686 (2009).
- Sokolov, M. et al. Massive light-driven translocation of transducin between the two major compartments of rod cells: a novel mechanism of light adaptation. *Neuron* **34**, 95–106 (2002).
- Majumder, A. et al. Transducin translocation contributes to rod survival and enhances synaptic transmission from rods to rod bipolar cells. *Proc. Natl Acad. Sci. USA* **110**, 12468–12473 (2013).
- Schmitz, Y. & Witkovsky, P. Dependence of photoreceptor glutamate release on a dihydropyridine-sensitive calcium channel. *Neurosci.* **78**, 1209–1216 (1997).
- Thoreson, W. B., Nitzan, R. & Miller, R. F. Reducing extracellular Cl⁻ suppresses dihydropyridine-sensitive Ca²⁺ currents and synaptic transmission in amphibian photoreceptors. *J. Neurophysiol.* **77**, 2175–2190 (1997).
- Corey, D. P., Dubinsky, J. M. & Schwartz, E. A. The calcium current in inner segments of rods from the salamander (*Ambystoma tigrinum*) retina. *J. Physiol. (Lond.)* **354**, 557–575 (1984).
- Wang, Y. V., Weick, M. & Demb, J. B. Spectral and temporal sensitivity of cone-mediated responses in mouse retinal ganglion cells. *J. Neurosci.* **31**, 7670–7681 (2011).
- Ke, J. B. et al. Adaptation to background light enables contrast coding at rod bipolar cell synapses. *Neuron* **81**, 388–401 (2014).
- Nikonov, S. S., Khodenko, R., Lem, J. & Pugh, E. N. Jr. Physiological features of the S- and M-cone photoreceptors of wild-type mice from single-cell recordings. *J. Gen. Physiol.* **127**, 359–374 (2006).

Acknowledgements This research was supported by National Institutes of Health grants R01 EY024986, R01 EY021502, R01 EY014454, R01 EY021372, R01 EY015788, R01 EY023105, R01 EY021195, R01 EY014990, P30 EY026878, Pew Scholars Program in the Biomedical Sciences, Research to Prevent Blindness and the McGraw Family Foundation for Vision Research.

Reviewer information *Nature* thanks Z. He, A. Huberman and the other anonymous reviewer(s) for their contribution to the peer review of this work.

Author contributions K.Y. and S.Q. performed injections, immunohistochemistry and imaging analysis. Y.V.W., S.H.J.P. and J.B.D. performed retinal ganglion cell recordings. E.J.M. and M.C.C. performed cortical recordings. B.M. and D.Z. performed calcium current recordings. X.L. performed transmission electron microscopy analysis. B.Che. provided *Gnat1^{rd17}* *Gnat2^{cpfl3}* double mutant mice. B.Che. designed the study and wrote the paper with instrumental input from J.B.D.

Competing interests The authors declare no competing interests.

Additional information

Extended data is available for this paper at <https://doi.org/10.1038/s41586-018-0425-3>.

Supplementary information is available for this paper at <https://doi.org/10.1038/s41586-018-0425-3>.

Reprints and permissions information is available at <http://www.nature.com/reprints>.

Correspondence and requests for materials should be addressed to B.Che.

Publisher's note: Springer Nature remains neutral with regard to jurisdictional claims in published maps and institutional affiliations.

METHODS

Animals. All procedures involving the use of animals in this study were approved by the Institutional Animal Care and Use Committees of the Icahn School of Medicine at Mount Sinai and Yale University. Wild-type mice (strain C57BL/6J) and Rosa26-tdTomato reporter mice (strain B6.Cg-Gt(ROSA)26Sor^{tm1(CAG-tdTomato)Hze}/J) were obtained from the Jackson Laboratory (Bar Harbour). *Gnat1*^{d17}*Gnat2*^{cpfl3} double mutant mice were kindly provided by B. Chang (The Jackson Laboratory). For light adaptation, the mice were placed in the dark for at least 12 h and the pupils were dilated with 1% tropicamide and 1% atropine before exposure to 10,000 lx white light for 2 h. For dark adaptation, the mice were maintained in the dark for more than 12 h, and all procedures were performed under infrared illumination. Mice (males and females) were randomly assigned to groups. The sample size was chosen based on pilot studies for >80% power (*R*). Researchers were blinded to treatment conditions.

AAV production and intravitreal injection. cDNAs encoding GFP, tdTomato, β -catenin, *Otx2*, *Crx* and *Nrl* were subcloned and inserted into a AAV vector backbone where the expression was driven by the GFAP promoter (a gift from L. Tian at UC Davis), or the rhodopsin promoter (subcloned from pRho-DsRed; Addgene #11156). The *Gnat1* cDNA, reverse-transcribed and amplified from mouse retinal RNAs, was used to replace tdTomato in pAAV-rhodopsin-tdTomato to build the pAAV-Rho-*Gnat1* vector. Individual adeno-associated virus (AAV) was produced in HEK293T cells (ATCC, authenticated by AAV production and tested for mycoplasma contamination by PCR) by plasmid co-transfection and iodixanol gradient ultracentrifugation. Purified AAVs were concentrated with Amicon Ultra-15 Filter Units (Millipore) to a final titre of $1.0\text{--}5.0 \times 10^{13}$ genome copies per ml (Extended Data Table 1). Intravitreal injection was performed using a microsyringe equipped with a 33-gauge needle. The tip of the needle was passed through the sclera, at the equator and next to the dorsal limbus of the eye, into the vitreous cavity. Injection volume was 1 μl per eye for AAVs.

EdU and BrdU co-labelling and detection. EdU or BrdU solution (1 μl , 1 mg/ml) was intravitreally injected into the vitreous chamber. For BrdU detection, the retinas were rinsed with PBS after fixation with 4% paraformaldehyde and incubated with 2 M HCl for 30 min at room temperature. Retinas were rinsed with PBS and incubated with a blocking buffer containing 5% normal donkey serum, 0.1% Triton X-100, and 0.1% NaN₃ in PBS for 2 h at room temperature. Primary antibody for BrdU (Thermo Scientific) was added for overnight incubation at 4 °C. Retinas were washed with PBS and incubated with secondary antibody (DyLight594-conjugated AffiniPure Donkey Anti-Mouse IgG, Jackson ImmunoResearch) for 2 h at room temperature. Analysis of EdU incorporation was performed using Click-iT EdU Kit (Thermo Scientific). EdU detection components were re-suspended according to manufacturer's instructions and applied directly to retinal samples. In brief, the solution for each EdU reaction has a total volume of 250 μl composed of 215 μl 1 × Click-iT reaction buffer, 10 μl CuSO₄, 0.6 μl Alexa Fluor azide, and 25 μl 1 × reaction buffer additive. After incubation in the reaction solution for 30 min at room temperature, samples were washed with PBS and mounted with Fluoromount-G for detection.

Immunohistochemistry and imaging. Retinas were fixed with 4% paraformaldehyde in PBS for 30 min at room temperature, and sectioned at 20- μm thickness. Sample slides were washed with PBS before incubation with a blocking buffer containing 5% normal donkey serum, 0.1% Triton X-100, and 0.1% NaN₃ in PBS for 2 h at room temperature. Primary antibodies were added for overnight incubation at 4 °C. Primary antibodies used: rhodopsin (1:250, Thermo Scientific, MS-1233-P1), peripherin-2 (1:500, Millipore, MABN293), recoverin (1:500, Millipore, AB5585), GNAT1 (1:1,000, Santa Cruz, sc-389), PKC α (1:100, Santa Cruz, sc-8393), and ribeye (1:500, Synaptic Systems, 192103). Sections were washed with PBS and incubated with secondary antibodies (Jackson ImmunoResearch) for 2 h at room temperature. Cell nuclei were counterstained with DAPI (Sigma). Confocal images were acquired using a Zeiss LSM 510 EXCITER microscope.

Transmission electron microscopy. The whole eye was fixed in 2.5% glutaraldehyde and 2% paraformaldehyde in 0.1 M sodium cacodylate buffer pH 7.4 with for 1 h at room temperature. After the cornea was removed, samples were post-fixed in 1% osmium tetroxide for 1 h, stained en bloc in 2% aqueous uranyl acetate for a further hour then rinsed, dehydrated in ethanol and propylene oxide and infiltrated with Embed 812 (Electron Microscopy Science). The blocks were hardened overnight at 60 °C. 60-nm sections were cut with a Leica ultramicrotome and collected on formvar/carbon-coated nickel grids. Grids were placed section side down on drops of 1% hydrogen peroxide for 5 min, blocked for nonspecific binding on 3% bovine serum albumin in PBS containing 1% triton-X for 30 min. Grids were incubated overnight as a primary antibody with either a rabbit anti-GFP (T. Südhof laboratory, Stanford University) at 1:200 or rabbit anti-TdTomato at 1:100 (Clontech, 632496), rinsed in buffer and then incubated with the secondary antibody and 10 nm protein A gold (Utrecht UMC) for 30 min. The grids were well rinsed in PBS, fixed in 1% glutaraldehyde for 5 min, rinsed again, dried and stained using 2% aqueous uranyl acetate and lead citrate. Sample grids were viewed using

FEI Tenca Biotwin TEM at 80 kV of accelerating voltage. Images were acquired with a Morada CCD camera and iTEM (Olympus) software.

Mouse retinal slice preparation and calcium current recordings. *Gnat1*^{d17}*Gnat2*^{cpfl3} mice were anaesthetized with isoflurane (Sigma), killed by cervical dislocation and their eyes enucleated. Whole retinas were isolated and placed on a 0.45- μm cellulose acetate/nitrate membrane filter (Millipore), which was secured with vacuum grease to a glass slide adjacent to the recording chamber. Slices were cut to a thickness of 150 μm using a tissue slicer and transferred to the recording chamber while remaining submerged. The recording chamber was immediately attached to a perfusion system, and the slices were perfused at a rate of 5 ml min⁻¹ with Ames media bubbled with 95% O₂ and 5% CO₂. All stages of retinal preparation were carried out at room temperature in a dark room. The standard recording solution for regenerated rods was composed of (in mM): 108 gluconic acid, 5 EGTA, 10 CsCl, 10 TEA, 4 MgATP, 1 LiGTP. The pH was adjusted to 7.4 with CsOH. The osmolarity of both extracellular and intracellular solutions was 289–293, with a pH of 7.35–7.40.

Patch pipettes (tip resistance, 10–12 M Ω) were fabricated from borosilicate glass (TFW150-4, WPI) using a two-stage vertical puller (Narishige). Pipettes were coated with Sticky Wax (Kerr Corp.). Whole-cell recordings were obtained using a dual EPC10/2 amplifier (HEKA Instruments). Slices were viewed with a Zeiss Axioskop 2FS plus equipped with a water-immersion 40 \times DIC objective and using an infrared filter for illumination. Regenerated rods were identified by their shape, GFP fluorescence and position in the slice. Illumination for epifluorescence was performed using an X-Cite 120Q lamp (EXFO) with a 488-nm bandpass excitation filter set for imaging GFP fluorescence or 590-bandpass filter set for imaging RFP. Images were acquired before whole-cell recording with Andor iXon camera controlled by a Shutter driver VCM-D1. Data were acquired using PatchMaster (HEKA Instruments), and analysis performed using Igor Pro (WaveMetrics) and Origin 7.5 (Microcal). Currents were elicited at 60-s intervals, collected at 20 kHz, and low-pass filtered at 1 kHz.

RGC recordings. Retinas from *Gnat1*^{d17}*Gnat2*^{cpfl3} double-mutant mice were prepared as previously described^{28,29}. After dissecting the retina under infrared light, the tissue was superfused with Ames' medium bubbled with 95% O₂ and 5% CO₂ in a chamber on a microscope (Olympus BX51WI) stage at ~34 °C. A patch pipette (tip resistance, ~3–5 M Ω) filled with Ames' medium was used to form a loose seal (~50–200 M Ω) on a large soma (>20- μm diameter) to record action potentials. Cells were targeted under microscopic control using infrared light, a 60 \times water objective lens (NA 0.9) and an infrared-sensitive camera (Retiga 1300, Qcapture software; Qimaging Corporation). Data were sampled at 10 kHz and recorded on a computer using a MultiClamp 700B amplifier and pClamp9 software (Molecular Devices).

A total of 12 mice were studied, six treated mice, four controls (that is, β -catenin delivery omitted from first virus injection) and two wild-type C57/BL6. Of these, six mice (three treated, three controls) were studied in a double blind fashion; the person performing the virus injection was not aware of the identity of the virus condition, and the person performing the recording did not know the treatment group of the mouse until the conclusion of all experiments.

Light stimuli were 1-mm-diameter spots generated by green (peak, 530 nm) or ultraviolet (UV; peak, 370 nm) LEDs that were diffused and windowed by the aperture in the microscope's fluorescence port and projected through a 4 \times objective lens (NA 0.13) onto the photoreceptor layer. In some experiments, light was attenuated with a 2.0 neutral density filter (NDF; Kodak Wratten, Edmund Optics) that attenuated green and UV light by 130- and 880-fold, respectively. Light was presented as 200-ms flashes on darkness every 10 s. In one block of trials, green and UV light flashes were alternated for 10 levels, with increasing intensity over time. For some cells, the entire block was repeated both with and without the NDF in place. For some cells with weak or absent responses, light flashes were presented in the brighter range only. For cells with sensitive responses, flashes were presented either in the dimmer range only or in both ranges. Firing rate (spikes per s) was recorded during a response window (300–500 ms) and normalized by subtracting the average firing rate measured during baseline periods before (500 ms) and after the flash (500 ms, Fig. 4b–d). If there was an obvious response to either light onset or offset, the response window was adjusted accordingly (Fig. 4c, d). If there was not an obvious response, the window for light onset was used by default (Fig. 4b).

RGC responses were quantified by averaging firing rates for green flashes in the intensity range of 2.1×10^{-2} to 2.1×10^{-1} nW mm⁻² (Fig. 4e), which included four flash levels for blocks with or without the NDF in place. From these averaged responses, we selected responding cells from the treated group that exceeded the largest response measured in the control group. For responding RGCs in the treated group, we averaged the response across cells and combined data over the dimmer and brighter stimulus ranges (Fig. 4g). We fit the flash intensity-response function using the equation $R(I) = AI^q(I^q + \sigma^q)^{-1}$, in which I is intensity (nW mm⁻²), A is the maximum response amplitude (spikes per s), σ is the intensity that drives a half-saturating response, and q determines the slope. Fitted sigmoidal curves

(Fig. 4g) shared amplitude (A , 33.8 spikes per s) and exponent (q , 0.705) parameters but had unique semi-saturation constants (σ for green, 4.6×10^{-3} nW mm $^{-2}$; σ for UV, 1.6×10^{-2} nW mm $^{-2}$). Fitting was performed using least-squares routines in MATLAB (The MathWorks).

VEPs and multi-unit activity recordings. Under isoflurane anaesthesia (2%; Baxter), an injection of xylocaine/epinephrine (1.0%; AstraZeneca) was delivered beneath the skin overlying the skull. The skull was then exposed, cleaned of tissue, and coated with a thin layer of cyanoacrylate adhesive (VetBond, 3M). A second layer of cyanoacrylate adhesive (Maxi-Cure, BSI) was used to attach two metal bars to the pretreated skull; these bars were then used to secure the head into a custom-built stereotaxic apparatus. A craniotomy was made over primary visual cortex, leaving the dura mater intact. Body temperature was maintained at 36°C during surgery and experiments via a heating pad placed below the subject. Pupils were dilated with 1% tropicamide and 1% atropine, and the eyes were then coated with a thin layer of silicone oil (Sigma) to prevent dehydration.

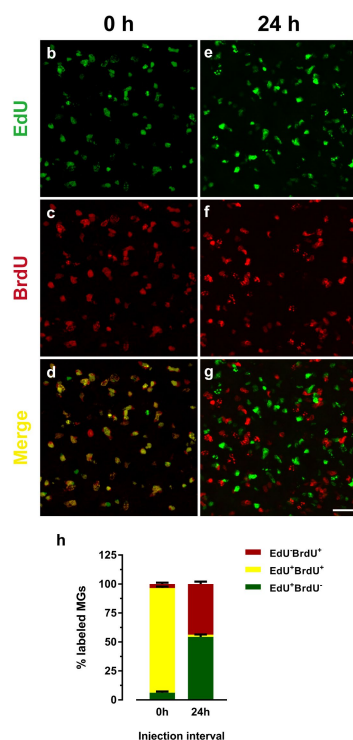
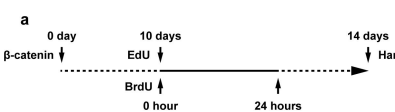
Neurophysiological signals were collected using a 16-site silicon probe with 4 recording sites on each of 4 shanks (100-μm vertical separation between recording sites; 125-μm horizontal spacing between shanks; 1-2-MΩ impedance; NeuroNexus Technologies). After the probe was lowered through the dura mater and into the cortex, a layer of agarose (1.5% in ACSF; Sigma) was applied to cover the craniotomy. An insulated silver wire (0.25-mm diameter; Medwire) was inserted above the cerebellum served as a reference electrode. Signals were preamplified 10× (MPA8I preamplifiers; Multi Channel Systems) before being amplified 200× and band-pass filtered at 0.3–5,000 Hz (Model 3500; A-M Systems). The amplified and filtered signals were sampled at 25 kHz using a digital interface (Power 1401 mk 2; Cambridge Electronic Design).

After the recording probe was implanted, isoflurane was lowered to 1.0–1.5% and mice were given 30 min to adapt to the dimly lit testing area before visual stimuli

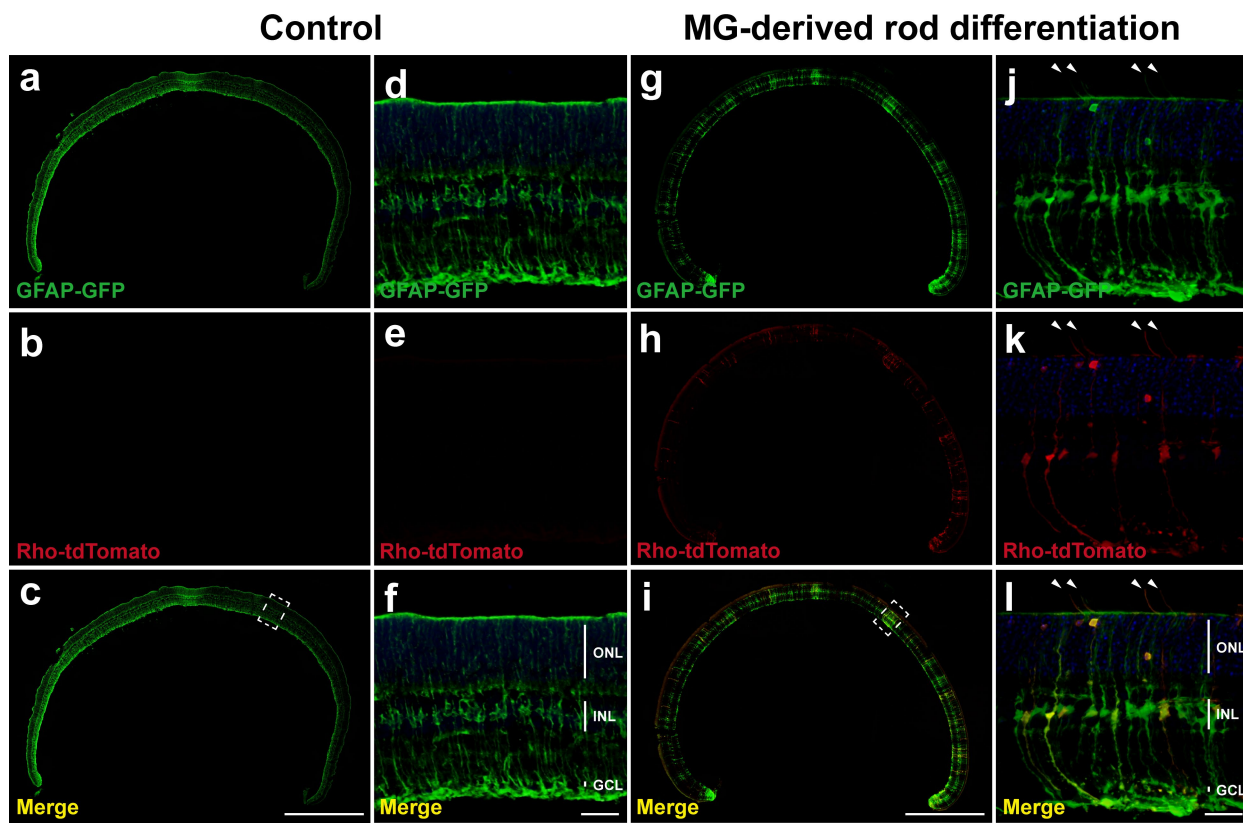
were delivered. Stimuli were 50-ms flashes of white light from a light-emitting diode (LED) that was placed 1 cm from the eye. The LED had two peaks, at ~460 and ~550 nm, with an integrated intensity of ~20 μW mm $^{-2}$; taking into account the spectral tuning of rhodopsin, this corresponded to an equivalent intensity at 500 nm (that is, the peak sensitivity of rhodopsin) of ~7.55 μW mm $^{-2}$ at the cornea and ~1.42 μW mm $^{-2}$ on the retina (assuming a 4-mm 2 dilated pupil area and evenly spread light over the ~21.2 mm 2 retinal area). Dimmer stimuli were also tested (~0.60 μW mm $^{-2}$ and ~1.4 nW mm $^{-2}$ on the retina). No response was observed to the dimmest intensity, whereas gradually stronger responses were observed to the two brighter intensities. VEPs were identified as negative deflections in the cortical local field potentials (LFPs) following stimulus onset, with greater negative amplitudes in deeper cortical layers than in superficial layers. For LFP analyses, the recording channel with the greatest negative amplitude in response to visual stimulation was used. Maximum negative deflections in the LFP during the 0.5 s following stimulus onset were measured, and, for each mouse, we tested whether the median of the response distribution differed from zero (Wilcoxon signed-rank test). Analyses were performed using MATLAB (The MathWorks), Spike2 (Cambridge Electronic Design) and GraphPad Prism 6 (GraphPad Software).

Statistical analysis. Statistical differences between different experimental groups were typically analysed by a Student's *t*-test or one-way ANOVA test except in cases where the data were not normally distributed (for example, LFP amplitudes), in which case a non-parametric test was used, as described above. Data are presented as mean ± s.e.m., except where data were skewed (for example, LFP amplitudes), in which case a box plot indicates median ± inter-quartile range. A value of $P < 0.05$ is considered significant.

Data availability. The datasets generated and/or analysed during the current study are available from the corresponding author on reasonable request.

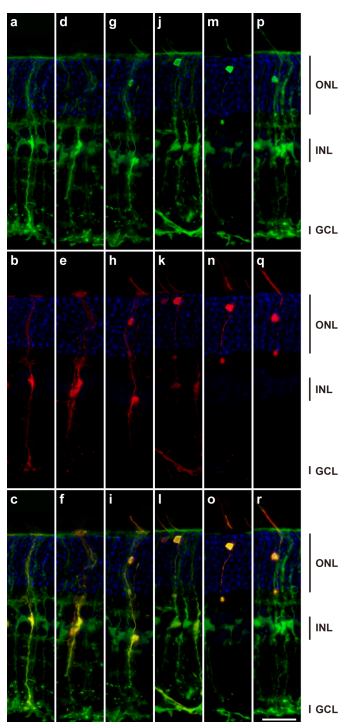


Extended Data Fig. 1 | MG may undergo only one cell division after β -catenin gene transfer. **a**, A schematic of the EdU/BrdU double-labelling experiment. Wild-type retinas were injected with ShH10-GFAP- β -catenin (0 day), followed by an injection of EdU (10 days). BrdU was either co-injected with EdU (0 h) or injected 24 h after EdU injection (24 h). Retinas were collected 14 days after β -catenin gene transfer. **b–g**, Detection of EdU and BrdU labelled MG. Scale bar, 20 μ m. **h**, Percentage of MG labelled by EdU (EdU⁺BrdU⁻, green), BrdU (red), or both (EdU⁺BrdU⁺, yellow). Experiments were repeated 3 times with similar results. Data are presented as mean \pm s.e.m., $n = 4$ retinas.

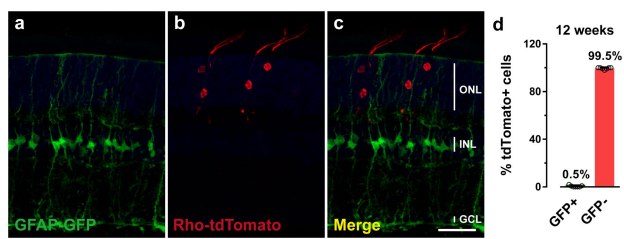


Extended Data Fig. 2 | A MG-derived rod differentiation was observed across the whole retinal section. Wild-type retinas at 4 weeks of age were first injected with ShH10-GFAP-GFP (label transduced MGs), and ShH10-rhodopsin-tdTomato (label MG-derived rods) in the absence (a–f) or presence (g–l) of ShH10-GFAP- β -catenin (to stimulate MG proliferation), followed 2 weeks later by the second injection of ShH10-GFAP-mediated

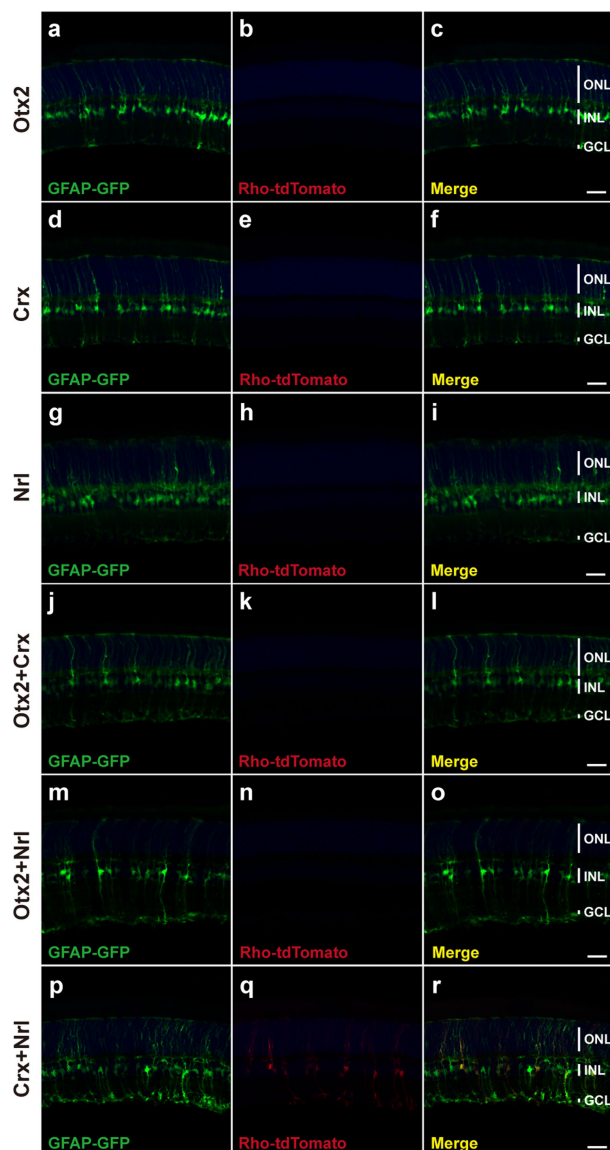
gene transfer of *Otx2*, *Crx* and *Nrl* for rod induction. Retinal samples were analysed by confocal microscopy 10 days after the second injection. The boxed areas in c and i are enlarged in d–f and j–l, respectively. Arrowheads, MG-derived rods. Scale bars, 750 μ m (a–c, g–i), 25 μ m (d–f, j–l). Experiments were repeated 4 times with similar results.



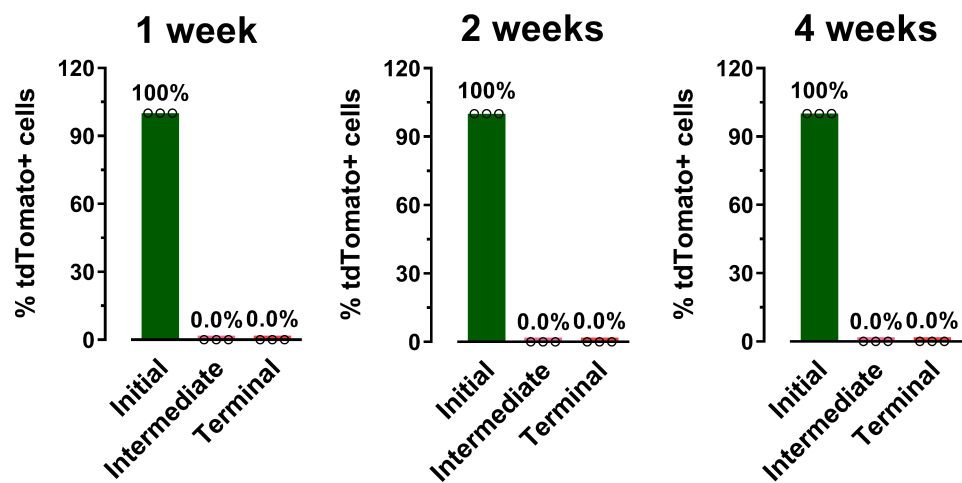
Extended Data Fig. 3 | Additional examples showing the progression of MG-derived rod differentiation. Wild-type retinas at 4 weeks of age were first injected with ShH10-GFAP- β -catenin, ShH10-GFAP-GFP and ShH10-rhodopsin-tdTomato, followed 2 weeks later by a second injection of ShH10-GFAP-mediated gene transfer of *Otx2*, *Crx* and *Nrl* for rod induction. MG-derived rod differentiation progressed through the initial (a–c), intermediate (d–l) and terminal (m–r) stages. Scale bar, 25 μ m. Experiments were repeated 6 times with similar results.



Extended Data Fig. 4 | MG-derived rods eventually turned off expression of GFAP-GFP over time. Wild-type retinas at 4 weeks of age were first injected with ShH10-GFAP- β -catenin, ShH10-GFAP-GFP and ShH10-rhodopsin-tdTomato, followed 2 weeks later by the second injection of ShH10-GFAP-mediated gene transfer of *Otx2*, *Crx* and *Nrl* for rod induction. **a–c**, Retinas were collected 12 weeks after the second injection and analysed for the expression of GFAP-GFP in tdTomato $^{+}$ MG-derived rods. Scale bar, 25 μ m. Experiments were repeated 3 times independently with similar results. **d**, Percentage of tdTomato $^{+}$ cells also expressing GFP. Data are presented as mean \pm s.e.m., $n = 7$ retinas.

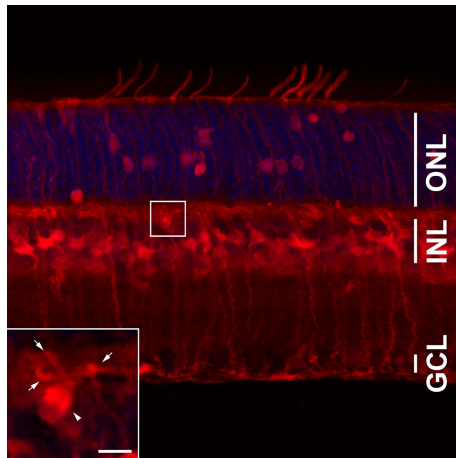


Extended Data Fig. 5 | Treatment with *Otx2*, *Crx* and *Nrl* individually or in pairs is not sufficient for rod induction. Wild-type retinas were injected with ShH10-GFAP- β -catenin (for MG proliferation), ShH10-GFAP-GFP (to label transduced MG) and ShH10-rhodopsin-tdTomato (to label MG-derived rods) at 4 weeks of age, followed 2 weeks later by a second injection of ShH10-GFAP-mediated gene transfer of transcription factors for rod induction. Samples were analysed by confocal microscopy in retinal sections at 4 weeks after the second injection. **a–c**, *Otx2* treatment. **d–f**, *Crx* treatment. **g–i**, *Nrl* treatment. **j–l**, *Otx2 + Crx* treatment. **m–o**, *Otx2 + Nrl* treatment. **p–r**, *Crx + Nrl* treatment. Scale bar, 20 μ m. Experiments were repeated 4 times with similar results.

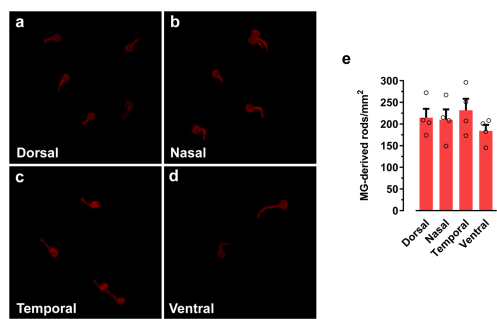


Extended Data Fig. 6 | Time-course analysis of MG-derived rod differentiation in wild-type retinas treated with *Crx* and *Nrl*. Wild-type retinas at 4 weeks of age were first injected with ShH10-GFAP- β -catenin, ShH10-GFAP-GFP and ShH10-rhodopsin-tdTomato, followed 2 weeks

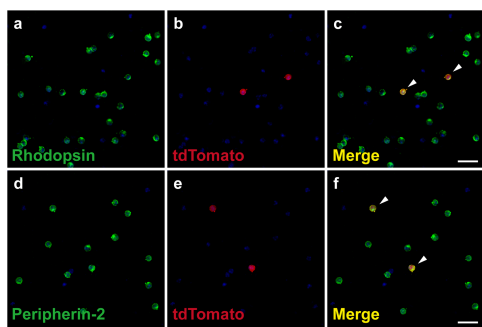
later by a second injection of ShH10-GFAP-mediated gene transfer of *Crx* and *Nrl*. tdTomato⁺ cells were only detected in the initial stage of rod differentiation at 1, 2 and 4 weeks after the second injection. Data are presented as mean \pm s.e.m., $n = 3$ retinas at each time point.



Extended Data Fig. 7 | Fate-mapping experiments indicate that the two-step reprogramming method may occasionally produce cells with a horizontal cell morphology. The boxed area is enlarged to show an MG-derived tdTomato⁺ cell with a horizontal cell morphology located in the outer region of the inner nuclear layer. Arrowhead, cell soma; arrows, cell processes. Scale bar, 5 μm. Experiments were repeated 4 times with similar results.



Extended Data Fig. 8 | MG-derived regeneration of rod photoreceptors decreases in aged mice. **a-d**, Generation of tdTomato⁺ MG-derived rod photoreceptors in 7-month-old-mouse retinas in the dorsal (**a**), nasal (**b**), temporal (**c**) and ventral (**d**) quadrants in retinal flat-mount preparations. Scale bar, 20 μ m. Experiments were repeated 4 times with similar results. **e**, Quantification of tdTomato⁺ MG-derived rods per mm² in the four retinal quadrants. Data are presented as mean \pm s.e.m., $n = 4$ retinas.



Extended Data Fig. 9 | MG-derived rod photoreceptors express rhodopsin and peripherin-2. Wild-type retinas were injected with ShH10-GFAP- β -catenin (for MG proliferation) and ShH10-rhodopsin-tdTomato (to label MG-derived rods) at 4 weeks of age, followed 2 weeks later by the second injection of ShH10-GFAP-mediated gene transfer of *Otx2*, *Crx* and *Nrl* for rod induction. Treated retinas were dissociated 4 weeks after the second injection and analysed for the expression of rhodopsin (a–c) and peripherin-2 (d–f) using immunohistochemistry and confocal microscopy. MG-derived rods were immunoreactive for rhodopsin (arrowheads, c) and peripherin-2 (arrowheads, f). Scale bar, 20 μ m. Experiments were repeated 3 times with similar results.

Extended Data Table 1 | Viral constructs, packaged viruses and virus titres after purification and concentration

Viral constructs	Virus	Titres
pAAV-GFAP-GFP	ShH10-GFAP-GFP	2.6×10^{13}
pAAV-GFAP-β-Catenin	ShH10-GFAP-β-Catenin	2.9×10^{13}
pAAV-Rho-tdTomato	ShH10-Rho-tdTomato	1.8×10^{13}
pAAV-GFAP-Otx2	ShH10-GFAP-Otx2	4.7×10^{13}
pAAV-GFAP-Crx	ShH10-GFAP-Crx	5.0×10^{13}
pAAV-GFAP-Nrl	ShH10-GFAP-Nrl	4.8×10^{13}
pAAV-Rho-Gnat1	ShH10-Rho-Gnat1	1.5×10^{13}

AAVs used in the study were purified, concentrated and quantified using quantitative real-time PCR.

Neonatal selection by Toll-like receptor 5 influences long-term gut microbiota composition

Marcus Fulde^{1,2}, Felix Sommer^{3,4,11}, Benoit Chassaing^{5,6,11}, Kira van Vorst², Aline Dupont⁷, Michael Hensel⁸, Marijana Basic⁹, Robert Klopfleisch¹⁰, Philip Rosenstiel⁴, André Bleich⁹, Fredrik Bäckhed³, Andrew T. Gewirtz⁶ & Mathias W. Hornef^{1,7*}

Alterations in enteric microbiota are associated with several highly prevalent immune-mediated and metabolic diseases^{1–3}, and experiments involving faecal transplants have indicated that such alterations have a causal role in at least some such conditions^{4–6}. The postnatal period is particularly critical for the development of microbiota composition, host–microbe interactions and immune homeostasis^{7–9}. However, the underlying molecular mechanisms of this neonatal priming period have not been defined. Here we report the identification of a host-mediated regulatory circuit of bacterial colonization that acts solely during the early neonatal period but influences life-long microbiota composition. We demonstrate age-dependent expression of the flagellin receptor Toll-like receptor 5 (TLR5) in the gut epithelium of neonate mice. Using competitive colonization experiments, we demonstrate that epithelial TLR5-mediated REG3 γ production is critical for the counter-selection of colonizing flagellated bacteria. Comparative microbiota transfer experiments in neonate and adult wild-type and *Tlr5*-deficient germ-free mice reveal that neonatal TLR5 expression strongly influences the composition of the microbiota throughout life. Thus, the beneficial microbiota in the adult host is shaped during early infancy. This might explain why environmental factors that disturb the establishment of the microbiota during early life can affect immune homeostasis and health in adulthood.

Before birth, the intestinal tract is devoid of viable bacteria. Upon rupture of the fetal membranes, the neonate's body surfaces become exposed to environmental bacteria¹⁰. During the early postnatal period, the microbiota shows high inter-individual variation and low diversity, and is strongly influenced by maternal contact and the environment^{11,12}. Ongoing environmental exposure steadily increases diversity, ultimately leading to a mature and relatively stable microbiota¹³. Recent studies have shown that the postnatal period and early infancy are a particularly important time window for immune cell maturation and homeostasis^{7–9}. In these studies, exposure to microbes early after birth had a major influence on immune maturation and disease susceptibility, whereas a first encounter with microorganisms at a later age failed to correct the dysfunctional immune system. This suggests that early infancy represents a critical 'window of opportunity' for the establishment of a mature and beneficial microbiota, and a priming period for the developing immune system¹⁴. We hypothesize that this non-redundant contribution of the postnatal period to host–microbiota homeostasis reflects a role for the developing immune system in shaping microbiota composition during the neonatal period. Such a mechanism might play a decisive role in the establishment of host–microbiota homeostasis and could influence susceptibility to inflammatory and metabolic diseases in later life.

To investigate how the microbiota is shaped postnatally, we systematically defined age-dependent differences in the expression of innate

immune receptor molecules by intestinal epithelial cells (IECs). Innate immune receptors facilitate the recognition of conserved microbial structures and induce the production of antimicrobial effector molecules. In addition to the previously described low expression of the double-stranded RNA receptor Toll-like receptor 3 (encoded by *Tlr3*) in the neonatal epithelium¹⁵, we observed that isolated IECs from neonatal (3-day-old) mice exhibited substantially enhanced expression of the flagellin receptor *Tlr5* as compared to cells from adult mice (Fig. 1a). Genes encoding inflammasome components that are known also to mediate responses to bacterial flagellin, such as *Naip5* and *Nlrc4*, did not exhibit an age-dependent expression pattern. Quantitative PCR with reverse transcription (RT-PCR) confirmed that *Tlr5* expression was high during the first two weeks of life but decreased sharply and reached baseline levels at weaning (on day 21 after birth; Fig. 1b). Of note, this age-dependent decrease was restricted to IECs; spleen cells did not exhibit age-dependent *Tlr5* expression (Fig. 1c).

Next, we tested the role of intestinal epithelial *Tlr5* expression during infection with a flagellated enteropathogenic microorganism using our recently described model of neonatal *Salmonella* infection¹⁶. However, we found no difference in intestinal colonization, spread to liver, spleen or lung tissue, or survival after oral administration of wild-type or isogenic non-flagellated ($\Delta fliB/fliC$) *Salmonella* to *Tlr5*-proficient and *Tlr5*-deficient neonatal mice (Extended Data Fig. 1a–e). Nevertheless, the absence of flagellin-mediated immune stimulation was illustrated by a significant ($P < 0.01$) reduction in the epithelial expression of *Cxcl2* following infection with non-flagellated bacteria or of *Tlr5*-deficient neonates (Extended Data Fig. 1f).

To analyse the effect of TLR5-mediated epithelial stimulation, we subsequently performed competitive colonization experiments by administering a 1:1 ratio of wild-type and non-flagellated *Salmonella* orally to wild-type or *Tlr5*-deficient neonates. Strikingly, intestinal colonization of wild-type but not *Tlr5*-deficient neonatal mice was strongly biased towards non-flagellated bacteria within the first 24 h after oral administration (Fig. 1d and Extended Data Fig. 2). Selection was independent of bacterial motility, as demonstrated by competition between wild-type and flagellin-expressing but non-motile $\Delta motA$ *Salmonella* (Fig. 1d). Notably, selection required TLR5 expression by the intestinal epithelium (Fig. 1e) and was limited to the postnatal period, correlating with the described age-restricted *Tlr5* expression (Fig. 1f). Transcriptional analysis following colonization of wild-type mice with flagellin-positive or -negative bacteria established the influence of the TLR5 ligand on epithelial expression of the antibacterial c-type lectin *Reg3g* (Fig. 1g). Also, mice deficient for *Reg3g* or for the TLR5 adaptor protein *Myd88* failed to exhibit bacterial selection (Fig. 1h). Thus, epithelial TLR5, MYD88 and REG3 γ constitute a counter-selective circuit for flagellated bacteria in the neonatal intestine.

¹Institute for Medical Microbiology and Hospital Epidemiology, Hannover Medical School, Hannover, Germany. ²Institute of Microbiology and Epizootics, Department of Veterinary Medicine at the Freie Universität Berlin, Berlin, Germany. ³Department of Molecular and Clinical Medicine/Wallenberg Laboratory, Institute of Medicine, University of Gothenburg and Sahlgrenska University Hospital, Gothenburg, Sweden. ⁴Institute of Clinical Molecular Biology (IKMB), Kiel University, Kiel, Germany. ⁵Neuroscience Institute, Georgia State University, Atlanta, GA, USA. ⁶Institute for Biomedical Sciences, Georgia State University, Atlanta, GA, USA. ⁷Institute for Medical Microbiology, RWTH University Hospital Aachen, Aachen, Germany. ⁸Division of Microbiology, University of Osnabrück, Osnabrück, Germany. ⁹Institute for Laboratory Animal Science, Hannover Medical School, Hannover, Germany. ¹⁰Institute of Veterinary Pathology, Department of Veterinary Medicine at the Freie Universität Berlin, Berlin, Germany. ¹¹These authors contributed equally: Felix Sommer, Benoit Chassaing. *e-mail: mhornef@ukaachen.de

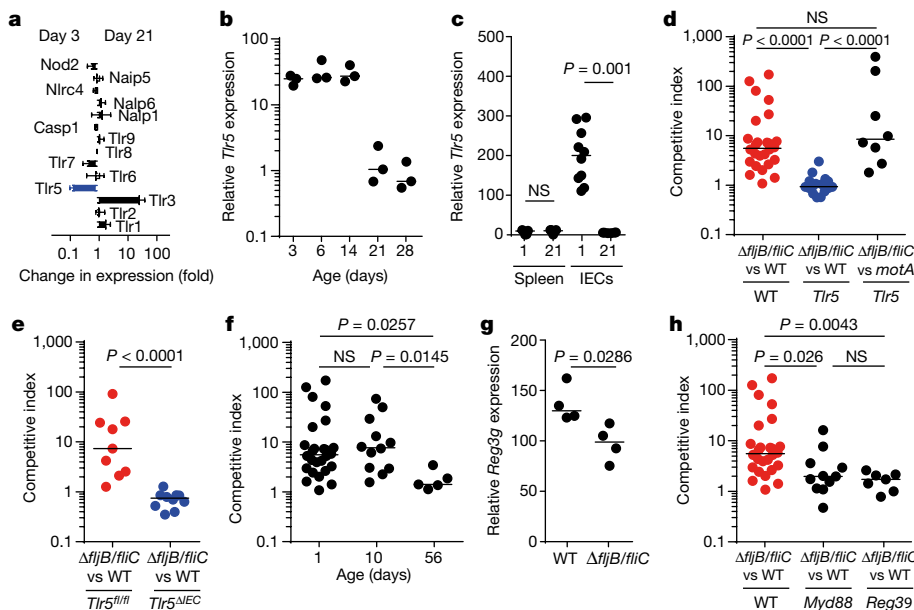


Fig. 1 | Age-dependent expression and function of epithelial TLR5.

a, Epithelial innate immune receptor expression measured by microarray analysis. Mean \pm s.d. ($n = 4$, from two litters). **b**, Epithelial *Tlr5* expression measured by qRT-PCR normalized to *Gapdh* expression. Median; $n = 3$, from three litters. **c**, *Tlr5* expression measured by qRT-PCR in spleen tissue and IECs from 1- and 21-day-old mice, normalized to *Hprt* expression. Median; $n = 5$ (two litters), $n = 7$ (two), $n = 10$ (three) and $n = 7$ (two) from left to right; NS, not significant; two-sided Mann-Whitney U-test. **d**, Competitive index of $\Delta fijB/fliC$ and wild-type (WT) S. Typhimurium (red or blue circles) or non-motile flagellated S. Typhimurium ($\Delta motA$, black circles) 24 h after infection of 1-day-old wild-type (red and black circles) or *Tlr5*-deficient (blue circles) mice. Median; $n = 26, 17, 8$ from six, four and one litters, respectively; Kruskal-Wallis test followed by Dunn's post-test. **e**, Competitive index of $\Delta fijB/fliC$ and wild-type S. Typhimurium 24 h after infection of 1-day-old floxed

Consistent with published results⁶, individually housed adult *Tlr5*-deficient mice exhibited a markedly altered enteric microbiota composition when compared with wild-type mice, associated with a metabolic phenotype illustrated by increased food intake, increased body weight and histological changes in liver and pancreatic tissue (Extended Data Fig. 3). Faecal transfer experiments had previously shown that microbiota alteration can cause metabolic dysregulation⁶. Here, we focused on the influence and specificity of neonatal epithelial TLR5 expression on altered microbiota composition.

We used two experimental approaches to analyse the influence of TLR5 expression on the establishment of the endogenous enteric microbiota in neonatal mice in the absence of cage-clustering. First, we cohoused *Tlr5*^{+/−} and *Tlr5*^{+/+} dams between conception and birth, and then housed them separately with their pups and analysed the neonates' microbiota. Here, neonates were housed only with animals of the same genotype (Fig. 2a). Eight days after birth, there was a significant difference ($P = 0.001$) in the composition of the enteric microbiota between *Tlr5*^{+/+} and *Tlr5*^{+/−} mice, consistent with an influence of TLR5 expression on the early enteric microbiota (Fig. 2c). Second, we crossbred heterozygous *Tlr5*^{+/−} mice derived from the same *Tlr5*^{+/+} and *Tlr5*^{+/−} parents and examined the offspring raised in the same litter for eight days after birth. Under these conditions, *Tlr5*^{+/−} neonates were cohoused with their *Tlr5*-proficient dam (*Tlr5*^{+/−}) and littermates (*Tlr5*^{+/+} and *Tlr5*^{+/−}) (Fig. 2b). Here, overall principal coordinate analysis revealed no significant difference ($P = 0.669$) in microbiota composition, in accordance with previous reports¹⁷ (Fig. 2d). These results illustrate the technical challenge of characterizing a gene-mediated effect on the establishment of the enteric microbiota in the early postnatal period, during which the dam, littermates and other environmental factors exert a strong and possibly dominant effect.

wild-type (*Tlr5*^{fl/fl}) and IEC-specific *Tlr5*-deficient (*Tlr5*^{ΔIEC}) littermates. Median; $n = 9$ and 10 each from at least four litters, respectively; two-sided Mann-Whitney U-test. **f**, Competitive index of wild-type and $\Delta fijB/fliC$ S. Typhimurium 24 h after infection of 1-day-old ($n = 26$ from six litters), 10-day-old ($n = 12$, three litters), and 56-day-old ($n = 5$) female wild-type mice. Median; Kruskal-Wallis test followed by Dunn's post-test. **g**, Epithelial *Reg3g* expression measured by qRT-PCR 24 h after infection of 1-day-old wild-type mice with $\Delta fijB/fliC$ or wild-type S. Typhimurium normalized to *Hprt* expression. Median; $n = 4$ (one litter), representative of two independent experiments; two-sided Mann-Whitney U-test. **h**, Competitive index of wild-type and $\Delta fijB/fliC$ S. Typhimurium 24 h after infection of wild-type, *Myd88*^{−/−} or *Reg3g*^{−/−} mice. Median; $n = 26, 11, 7$ from six, two and one litters, respectively; Kruskal-Wallis test followed by Dunn's post-test.

We therefore next turned to another approach and comparatively analysed the development of two different donor microbiota (from adult wild-type and *Tlr5*^{+/−} donor mice) following their transfer to germ-free *Tlr5*^{+/+} or *Tlr5*^{+/−} neonate or adult recipient mice. Initially, we compared the development of a *Tlr5*^{+/−}-derived microbiota (TLR5 microbiota) and a wild-type-derived microbiota (WT microbiota) within neonate and adult wild-type germ-free hosts housed in sterile microisolator cages at 14, 21, and 28 days after transfer. Whereas the difference between the WT and TLR5 microbiota remained constant in adult animals, in neonate mice they became more similar over time (Fig. 3a). Unifrac analysis confirmed a significant ($P < 0.0001$) decrease in the distance (that is, an increase in similarity) between the WT and TLR5 microbiota in the wild-type neonate host over time, whereas this distance did not decrease upon transfer to adult hosts (Fig. 3b).

We then repeated this experiment but transferred the WT and TLR5 microbiota to both germ-free wild-type and germ-free *Tlr5*-deficient mice. Additionally, we extended the study period in particular for the group of wild-type neonate hosts, in order to examine the influence of neonatal TLR5 expression on long-term microbiota composition. Although the clarity of the results is limited by the different sampling schedules, we again observed an increase in the similarity (and concomitant decrease in the Unifrac distance) of the donor WT and TLR5 microbiota upon transfer to wild-type neonate but not adult mice (Fig. 3c–f). However, the increase in similarity was observed only upon transfer to neonate wild-type mice and not to *Tlr5*-deficient neonate mice (Fig. 3c). Unifrac analysis confirmed a substantial decrease in the distance between the WT and TLR5 microbiota in the wild-type but not the *Tlr5*^{+/−} neonate hosts (Fig. 3e). Notably, the increase in similarity after transfer to neonate wild-type mice occurred early after transfer, consistent with the age-restricted expression of *Tlr5* in the intestinal

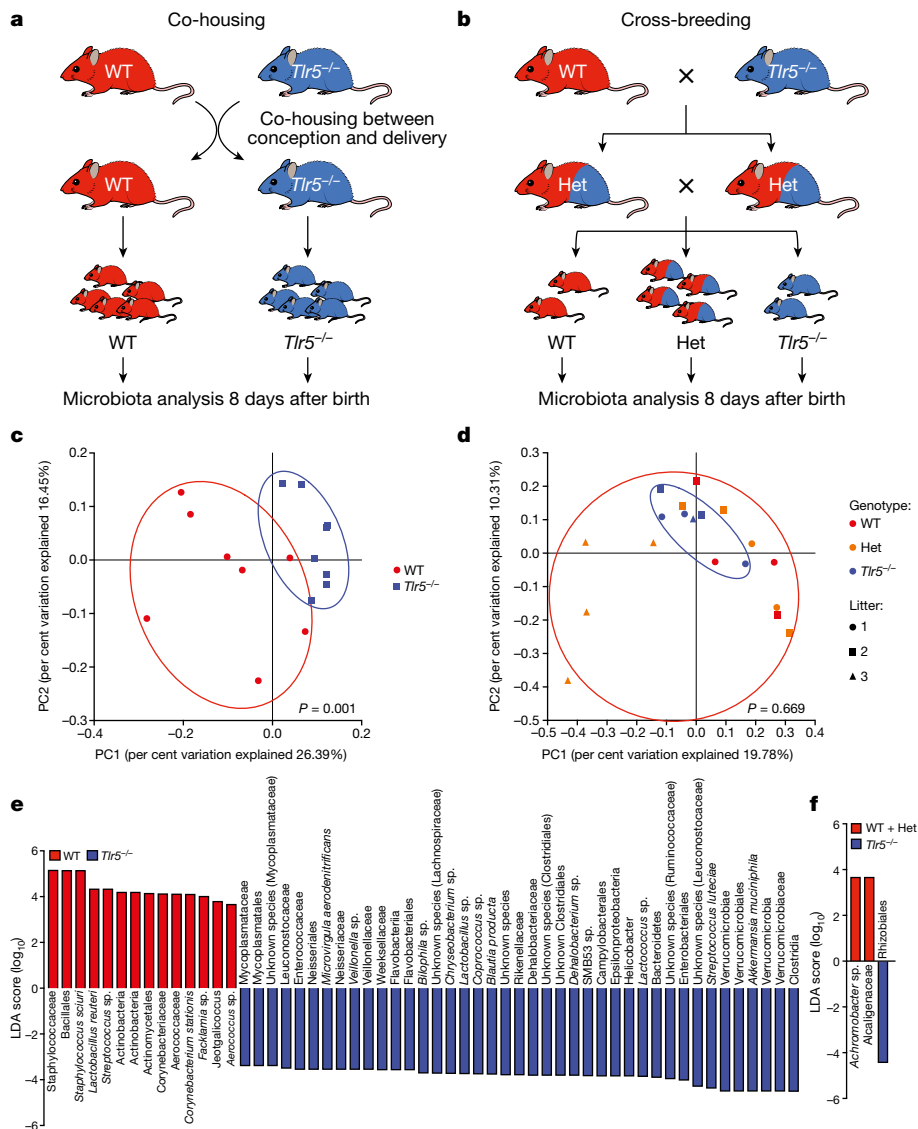


Fig. 2 | Microbiota composition in neonates from co-housed pregnant *Tlr5*-discordant dams or after crossbreeding in *Tlr5*-discordant siblings. **a**, Timed-bred wild-type and *Tlr5*^{-/-} deficient dams (three of each) were co-housed from the day after mating until conception in a separately ventilated isolator cage. At embryonic day 18 (E18), pregnant mice (two each of wild-type and *Tlr5*^{-/-} dams) were separated for delivery. Pups were euthanized eight days after birth. **b**, *Tlr5*^{+/-} (*Het*) mice from the same wild-type and *Tlr5*^{-/-} breeding pair were crossbred and offspring littermates were killed eight days after birth and genotyped. Bacterial DNA was isolated from the small intestine and analysed by 16S rDNA sequencing. **c, d**, PCoA plots illustrating the similarity in the microbiota composition between wild-type (red circles, $n = 8$) and *Tlr5*^{-/-} (blue squares, $n = 8$) mice from the co-housing experiment (c) and wild-type (red, $n = 4$), heterozygous *Tlr5*^{+/-} (orange, $n = 9$), and homozygous *Tlr5*^{-/-} (blue, $n = 6$) mice from three different litters (indicated by three different symbols) from the cross-breeding experiment. P values stated for group comparisons, calculated by permutational multivariate analysis of variance (PERMANOVA) using MacQIIME v1.8. **e, f**, Linear discriminant analysis (LDA) plots highlighting significantly different characteristic bacterial taxa for wild-type versus *Tlr5*^{-/-} comparison from the co-housing experiment (e) and combined wild-type and *Tlr5*^{+/-} versus *Tlr5*^{-/-} comparison from the cross-breeding experiment (f). Samples from c and d were included in the LDA.

epithelium (Fig. 1b, c). Unexpectedly, however, the increased similarity persisted for more than 140 days and thus greatly exceeded the period of intestinal counter-selection of flagellated bacteria (Fig. 1f), highlighting the importance of the early postnatal period for long-term microbiota composition.

One consequence of dysbiosis resulting from *Tlr5* deficiency is an increased level of flagellated bacteria, as reflected by increased levels of faecal flagellin¹⁸. Consistent with the notion that such dysbiosis is transmissible, transplant of microbiota from *Tlr5*-deficient mice to adult germ-free wild-type mice resulted in a markedly higher concentration of faecal flagellin than was found after transfer of WT microbiotas to adult germ-free wild-type mice (Fig. 3g). By contrast, faecal flagellin levels did not differ between neonate recipients after transfer of WT or *TLR5* microbiotas. Thus, the ability to reshape dysbiotic microbiotas during early colonization with flagellated bacteria appears to be restricted to the postnatal period but to exert a lasting influence on the enteric microbiota. Local induction of the antibacterial c-type lectin REG3 γ in the intestinal epithelium contributes to this phenotype, consistent with its TLR5-dependent expression pattern during the neonatal period and the enhanced content of biologically active flagellin in the faeces of *Reg3g*-deficient neonate mice (Extended Data Figs. 4, 5).

Together, our results identify a specific regulatory circuit in the neonatal host epithelium that shapes the establishment of the enteric microbiota and restricts the expansion of colonizing flagellated bacteria.

This specific selection mechanism is restricted to the early postnatal period but exerts an effect that lasts until adulthood. Our findings thus help to explain the critical importance of the postnatal period for life-long susceptibility to disease.

A range of additional exogenous and endogenous factors such as diet and the innate and adaptive immune systems influence the composition of the enteric microbiota. It is therefore not surprising that neonatal age per se, independent of *Tlr5* genotype, also plays an important role. Dietary factors such as the high lactose concentration, antibacterial substances and restricted range of carbon sources found in breast milk might account for this effect. On the other hand, an age-independent TLR5-mediated influence on the enteric microbiota is in line with previous studies demonstrating that TLR5 expression by professional immune cells strongly influences mucosal host immunity^{19,20}. Host immunity, in turn, has been shown to exert a substantial influence on host-microbiota homeostasis^{21,22}.

A number of studies have demonstrated the functional expression of *Tlr5* at the intestinal mucosa^{19,22–24}. TLR5 might act either directly via recognition of and response to a flagellated pathogen, or indirectly via an alteration of the microbiota that in turn confers metabolic or immunological consequences^{6,25,26}. Although the affinity of flagellin from different bacterial species to the TLR5 receptor varies widely, both commensal and pathogenic bacteria are recognized by TLR5²⁷. Flagellin is also recognized by the NAIP5–NLRC4 inflammasome (which is expressed independent of age); together with other

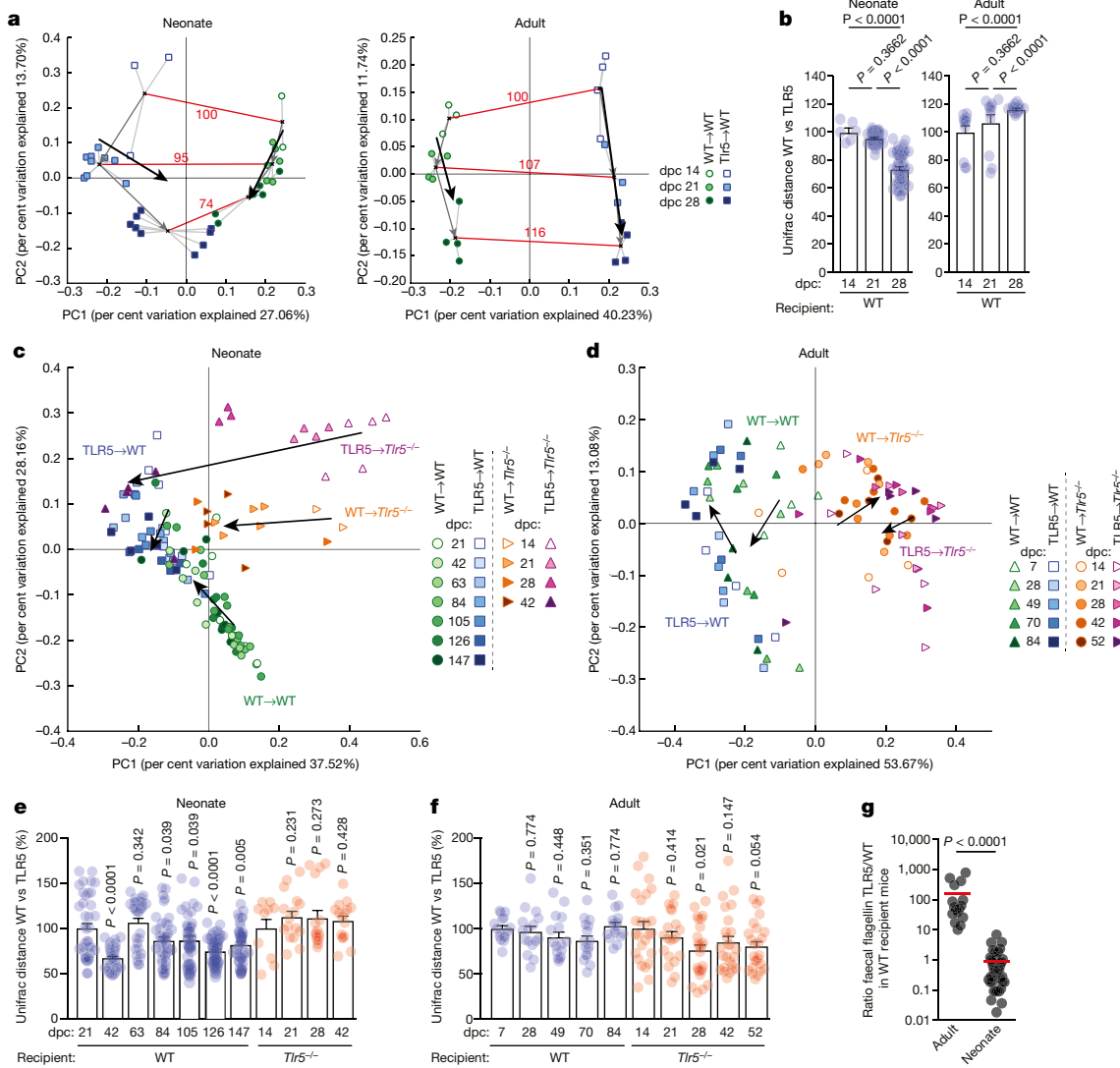


Fig. 3 | Influence of age and *Tlr5* expression on microbiota composition. **a**, PC1-PC2 plot showing the maturation of the WT (green) or TLR5 microbiota (blue) in wild-type neonates after transfer to germ-free dams at E18 (left: green, $n=6$; blue, $n=9$) and 6-week-old female germ-free wild-type mice (right: green, $n=4$; blue, $n=4$) monitored by 16S rDNA sequencing. Crosses indicate centroids of each group; thin grey arrows indicate microbiota changes between time points averaged to trend line arrows (thick black arrows); red lines indicate the Unifrac distance between the donor microbiota. dpc, days post colonization. **b**, Similarity between transferred microbiota by Unifrac distance analysis. One-way ANOVA followed by post-hoc FDR correction (Benjamini and Hochberg) ($*P < 0.05$; $**P < 0.01$; $***P < 0.001$; $****P < 0.0001$). **c, d**, PC1-PC2 plot showing maturation of microbiota derived from wild-type (green, orange) or *Tlr5*^{-/-} (TLR5; blue, purple) donor mice in wild-type (green, $n=8$; blue, $n=5$) or *Tlr5*^{-/-} (orange, $n=4$; purple, $n=4$) neonates after transfer to

homeostatic signalling pathways, the inflammasome might support and amplify the described selective mechanism.

A strong influence of TLR5 on the enteric microbiota has previously been demonstrated in adult mice and functionally linked to the development of metabolic syndrome with hyperphagia, hyperlipidaemia, insulin resistance, and obesity^{6,25}. The findings that antibiotic treatment abolished the metabolic phenotype, and that transfer of the TLR5 microbiota induced similar changes in adult wild-type germ-free mice, established a causal relationship between microbiota alteration and metabolic dysregulation⁶. The inability of the adult host to correct the alteration of the transferred microbiota despite the presence of the *Tlr5* gene is consistent with our description of a regulatory circuit that is restricted to the postnatal period.

germ-free dams at E18 (c) and in 6-week-old adult germ-free wild-type (green, $n=4$; blue, $n=4$, female) and *Tlr5*^{-/-} (orange, $n=5$; purple, $n=5$, in both cases, two females and three males) mice (d) monitored by 16S rDNA sequencing. Averaging trend line arrows (black arrows) illustrate microbiota changes. **e, f**, Similarity between the transferred microbiota in neonate (e) and adult (f) wild-type or *Tlr5*^{-/-} recipient mice by Unifrac distance analysis. Significances between the initial and successive time points were calculated using one-way ANOVA followed by post-hoc FDR correction (Benjamini and Hochberg) ($*P < 0.05$; $**P < 0.01$; $***P < 0.001$; $****P < 0.0001$). **g**, Ratio of faecal bioactive flagellin of wild-type mice that received the TLR5 microbiota (adult, female, $n=4$; neonate, $n=5$) divided by mice that received the WT microbiota (adult, female, $n=4$, neonate, $n=8$) determined using the HEK-Blue-mTLR5 biosensor cell line. Data represent the mean \pm s.e.m. ($****P < 0.0001$; two-sided Mann-Whitney U-test).

Two main cellular compartments, epithelial cells and CD103⁺ CD11b⁺ dendritic cells, have been shown to express *Tlr5* in the intestine^{28,29}. In adult mice, the expression of *Tlr5* in CD103⁺CD11b⁺ dendritic cells vastly exceeds its expression in the intestinal epithelium²⁸, consistent with our results. Upon flagellin recognition, CD103⁺CD11b⁺ dendritic cells promote an epithelial host response by enhanced production of cytokines such as IL-22, IL-23 and IL-18^{22,28,30}. Nevertheless, the TLR5-mediated effect on the microbiota and its influence on metabolism and mucosal inflammation was associated with a lack of *Tlr5* expression by IECs and not dendritic cells²⁹. How the low epithelial *Tlr5* expression in adult animals might induce the strong effect on the enteric microbiota, however, has remained unclear. Our data explain this enigma, demonstrating that intestinal

epithelial *Tlr5* expression restricted to the postnatal period substantially influences microbiota composition and might thus affect susceptibility to metabolic dysfunction and inflammation in adult mice.

Previous work has shed light on the possible beneficial effects of low intestinal epithelial TLR5 expression in adult mice. Microbial constituents, and in particular microbiota-derived flagellin, which acts simultaneously as an innate immune receptor agonist and an antigen for the adaptive immune response, have been shown to drive intestinal inflammation in patients with Crohn's disease³¹. Consistently, the presence of a loss-of-function *Tlr5* polymorphism (rs5744168) was negatively associated with Crohn's disease, whereas expression of a gain-of-function polymorphism in *Tlr5* (rs5744174) was associated with an increased risk of Crohn's disease in humans^{32,33}. Thus, reduced expression of intestinal epithelial TLR5 in adults might help to avoid excessive inflammation that can disrupt host-microbiota homeostasis.

Online content

Any Methods, including any statements of data availability and Nature Research reporting summaries, along with any additional references and Source Data files, are available in the online version of the paper at <https://doi.org/10.1038/s41586-018-0395-5>

Received: 14 March 2016; Accepted: 5 July 2018;

Published online 8 August 2018.

- Turnbaugh, P. J. et al. An obesity-associated gut microbiome with increased capacity for energy harvest. *Nature* **444**, 1027–1031 (2006).
- Qin, J. et al. A metagenome-wide association study of gut microbiota in type 2 diabetes. *Nature* **490**, 55–60 (2012).
- Frank, D. N. et al. Molecular-phylogenetic characterization of microbial community imbalances in human inflammatory bowel diseases. *Proc. Natl. Acad. Sci. USA* **104**, 13780–13785 (2007).
- Henao-Mejia, J. et al. Inflammation-mediated dysbiosis regulates progression of NAFLD and obesity. *Nature* **482**, 179–185 (2012).
- Schaubach, M. et al. Dysbiotic gut microbiota causes transmissible Crohn's disease-like ileitis independent of failure in antimicrobial defence. *Gut* **65**, 225–237 (2015).
- Vijay-Kumar, M. et al. Metabolic syndrome and altered gut microbiota in mice lacking Toll-like receptor 5. *Science* **328**, 228–231 (2010).
- Olszak, T. et al. Protective mucosal immunity mediated by epithelial CD1d and IL-10. *Nature* **509**, 497–502 (2014).
- Cahenzli, J., Kölner, Y., Wyss, M., Geuking, M. B. & McCoy, K. D. Intestinal microbial diversity during early-life colonization shapes long-term IgE levels. *Cell Host Microbe* **14**, 559–570 (2013).
- Wesemann, D. R. et al. Microbial colonization influences early B-lineage development in the gut lamina propria. *Nature* **501**, 112–115 (2013).
- Bäckhed, F. et al. Dynamics and stabilization of the human gut microbiome during the first year of life. *Cell Host Microbe* **17**, 852 (2015).
- Yatsunenko, T. et al. Human gut microbiome viewed across age and geography. *Nature* **486**, 222–227 (2012).
- Dominguez-Bello, M. G. et al. Delivery mode shapes the acquisition and structure of the initial microbiota across multiple body habitats in newborns. *Proc. Natl. Acad. Sci. USA* **107**, 11971–11975 (2010).
- Faith, J. J. et al. The long-term stability of the human gut microbiota. *Science* **341**, 1237439 (2013).
- Torow, N. & Hornef, M. W. The neonatal window of opportunity: Setting the stage for life-long host-microbial interaction and immune homeostasis. *J. Immunol.* **198**, 557–563 (2017).
- Pott, J. et al. Age-dependent TLR3 expression of the intestinal epithelium contributes to rotavirus susceptibility. *PLoS Pathog.* **8**, e1002670 (2012).
- Zhang, K. et al. Age-dependent enterocyte invasion and microcolony formation by *Salmonella*. *PLoS Pathog.* **10**, e1004385 (2014b).
- Ubeda, C. et al. Familial transmission rather than defective innate immunity shapes the distinct intestinal microbiota of TLR-deficient mice. *J. Exp. Med.* **209**, 1445–1456 (2012).
- Chassaing, B., Koren, O., Carvalho, F. A., Ley, R. E. & Gewirtz, A. T. AIEC pathobiont instigates chronic colitis in susceptible hosts by altering microbiota composition. *Gut* **63**, 1069–1080 (2014).
- Uematsu, S. & Akira, S. Immune responses of TLR5⁺ lamina propria dendritic cells in enterobacterial infection. *J. Gastroenterol.* **44**, 803–811 (2009).
- Oh, J. Z. et al. TLR5-mediated sensing of gut microbiota is necessary for antibody responses to seasonal influenza vaccination. *Immunity* **41**, 478–492 (2014).

- Kinnebrew, M. A. et al. Bacterial flagellin stimulates Toll-like receptor 5-dependent defense against vancomycin-resistant *Enterococcus* infection. *J. Infect. Dis.* **201**, 534–543 (2010).
- Kinnebrew, M. A. et al. Interleukin 23 production by intestinal CD103⁺CD11b⁺ dendritic cells in response to bacterial flagellin enhances mucosal innate immune defense. *Immunity* **36**, 276–287 (2012).
- Carvalho, F. A. et al. Transient inability to manage proteobacteria promotes chronic gut inflammation in TLR5-deficient mice. *Cell Host Microbe* **12**, 139–152 (2012).
- Vijay-Kumar, M. et al. Deletion of TLR5 results in spontaneous colitis in mice. *J. Clin. Invest.* **117**, 3909–3921 (2007).
- Singh, V. et al. Microbiota-dependent hepatic lipogenesis mediated by stearoyl CoA desaturase 1 (SCD1) promotes metabolic syndrome in TLR5-deficient mice. *Cell Metab.* **22**, 983–996 (2015).
- Lantier, L. et al. Poly(I:C)-induced protection of neonatal mice against intestinal *Cryptosporidium parvum* infection requires an additional TLR5 signal provided by the gut flora. *J. Infect. Dis.* **209**, 457–467 (2014).
- Andersen-Nissen, E. et al. Evasion of Toll-like receptor 5 by flagellated bacteria. *Proc. Natl. Acad. Sci. USA* **102**, 9247–9252 (2005).
- Uematsu, S. et al. Detection of pathogenic intestinal bacteria by Toll-like receptor 5 on intestinal CD11c⁺ lamina propria cells. *Nat. Immunol.* **7**, 868–874 (2006).
- Chassaing, B., Ley, R. E. & Gewirtz, A. T. Intestinal epithelial cell toll-like receptor 5 regulates the intestinal microbiota to prevent low-grade inflammation and metabolic syndrome in mice. *Gastroenterology* **147**, 1363–1377.e17 (2014).
- Zhang, B. et al. Viral infection. Prevention and cure of rotavirus infection via TLR5/NLRC4-mediated production of IL-22 and IL-18. *Science* **346**, 861–865 (2014).
- Lodes, M. J. et al. Bacterial flagellin is a dominant antigen in Crohn disease. *J. Clin. Invest.* **113**, 1296–1306 (2004).
- Gewirtz, A. T. et al. Dominant-negative TLR5 polymorphism reduces adaptive immune response to flagellin and negatively associates with Crohn's disease. *Am. J. Physiol. Gastrointest. Liver Physiol.* **290**, G1157–G1163 (2006).
- Bank, S. et al. Polymorphisms in the Toll-like receptor and the IL-23/IL-17 pathways were associated with susceptibility to inflammatory bowel disease in a Danish cohort. *PLoS ONE* **10**, e0145302 (2015).

Acknowledgements We thank D. Gütle, T. Albers, M. Nietschke, A. Smoczek, V. Tremaroli and M. Krämer for technical support and M. Rühlemann for discussions. The work was supported by the priority programs SPP1656 (Ho-2236/9-1 and BL953/5-1) and SPP1580 (Ho 2236/11-1, He 1964/18-2), SFB944 (P4 to M.H.) and SFB1182 (C2 to F.S. and P.R.) and the single grant Ho 2236/14-1 from the German Research Foundation (DFG), as well as the Lower Saxony-Israel Fond and the Niedersachsen-Research Network on Neuroinfectiology (N-RENNT) of the Ministry of Science and Culture of Lower Saxony, Germany, to M.F. and M.W.H. M.F. and K.v.V. were supported by the German Federal Ministry of Education and Research (BMBF) within the consortium InfectControl 2020 (Project NeoBiom, grant ID 03ZZ0829C). M.F. was supported by the Freie Universität Berlin within the Excellence Initiative of the DFG and P.R. by the ExC306 Inflammation at Interfaces. B.C. is supported by a Career Development Award from the Crohn's and Colitis Foundation and an Innovator Award from the Kenneth Rainin Foundation. F.B. is Torsten Söderberg Professor in Medicine and recipient of ERC consolidator Grant 2013 (European Research Council, Consolidator grant 615362-METABASE).

Reviewer information *Nature* thanks J. Kagan and the other anonymous reviewer(s) for their contribution to the peer review of this work.

Author contributions M.F. and M.W.H. performed and analysed colonization and infection experiments. M.F., M.B., B.C., A.B. and A.T.G. planned and performed microbiota transfer experiments. M.F., M.B., B.C. and A.D. performed conventional and germ-free mouse breeding and sample collection. F.S., F.B., P.R., and M.F. analysed the enteric microbiota samples. K.v.V., M.F. and A.D. analysed faecal flagellin content. M.H. generated bacterial mutants. R.K. performed histopathological analysis. M.W.H., A.T.G. and F.B. supervised the study.

Competing interests The authors declare no competing interests.

Additional information

Extended data is available for this paper at <https://doi.org/10.1038/s41586-018-0395-5>.

Supplementary information is available for this paper at <https://doi.org/10.1038/s41586-018-0395-5>.

Reprints and permissions information is available at <http://www.nature.com/reprints>.

Correspondence and requests for materials should be addressed to M.W.H.

Publisher's note: Springer Nature remains neutral with regard to jurisdictional claims in published maps and institutional affiliations.

METHODS

Mice. Adult C57BL/6J wild-type, B6.129S1-Tlr5^{tm1Flv}/J (Tlr5, stock no. 008377), B6.129-Reg3^{γtm1Lvh}/J (Reg3^γ, stock no. 017480), and B6.129P2(SJL)-Myd88^{tm1Defr}/J (Myd88, stock no. 009088) mice were obtained from the Jackson Laboratory. Mice were bred locally and held under specific pathogen-free (SPF) or germ-free conditions at the Hannover Medical School animal facility. Handling of animals was performed in accordance with regulations defined by FELASA and the national animal welfare body GV-SOLAS (<http://www.gv-solas.de>). For phenotypic characterization studies (weight and food intake) age- and sex-matched WT and *Tlr5*-deficient mice were used. The gender of neonate mice is not expected to influence the observed phenotype and was not determined. At Georgia State University, *Tlr5*-deficient mice were originally generated by S. Akira, Japan. Floxed *Tlr5* animals were crossed to Villin-Cre expressing animals (B6.Cg-Tg(Vill1-cre)997Gum/J) in order to generate epithelial cell-specific *Tlr5* deletion, as previously described²⁹. Germ-free WT and *Tlr5* deficient mice were kept under germ-free conditions in a Park Bioservices isolator in Georgia State University germ-free facility. All mice were bred and maintained under approved protocols (Institutional Animal Care and Use Committee, IACUC). No statistical methods were used to predetermine sample size. The experiments were not randomized and the investigators were not blinded to allocation during experiments and outcome assessment.

Bacteria. Bacterial strains used in this study are summarized in Supplementary Information Table 1. Gene deletions were generated by Red-mediated recombination as previously described using primers listed in Supplementary Information Table 2 and template plasmid pKD4 to synthesize targeting DNA by PCR³⁴. Deletion strains were generated based on ATC14028 and all strains used were isogenic. Proper insertion of the resistance cassette was confirmed by colony PCR. Mutant alleles were transferred to fresh strain background or into strains with further mutations by P22 transduction. If required, the *aph* resistance cassette was cured by FLP-mediated recombination as described³⁴. Before infection, strains were electroporated with plasmid pFPV25.1 (pGFP, AmpR, kindly provided by B. Cormack, Stanford, USA) for constitutive expression of enhanced green fluorescent protein (eGFP). Maintenance of the plasmid under *in vivo* conditions was confirmed previously¹⁶.

Infection model. Neonate (1-day-old) and juvenile (10-day-old) mice were orally infected with approximately 5×10^2 CFU S. Typhimurium essentially as described earlier¹⁶. Adult (56-day-old) mice were infected with S. Typhimurium after streptomycin pre-treatment (20 mg) as described³⁵. The health status of infected mice was monitored at least once daily. Mice were euthanized according to a clinical scoring system that was approved by the local authority (Lower Saxony State Office for Consumer Protection, Food Safety, and Animal Welfare Service). For competition experiments, isogenic bacterial strains were mixed in a 1:1 ratio before infection. After the indicated time points, mice were euthanized and the indicated organs (lung, liver, spleen, small intestine, and colon) were collected in PBS, homogenized, diluted, and plated on LB agar plates with the respective antibiotics. Small intestinal tissue homogenates from animals competitively infected with *Salmonella* WT and its flagellin-deficient *fliB/fliC* mutant strain were simultaneously plated on LB agar plates with 100 µg/mL Ampicillin (selecting for both, *Salmonella* WT and strain $\Delta fliB::FRT fliC::aph$ harbouring plasmid pFPV25.1) and 100 µg/mL ampicillin/25 µg/mL kanamycin (selecting for strain $\Delta fliB::FRT fliC::aph$). The competitive index (CI) was calculated as follows: CI = (mutant output/WT output)/(mutant input/WT input). A CI > 1 indicates that the mutant S. Typhimurium strain outcompeted its parental WT strain. Note that results from competition experiments with WT and flagellin-deficient ($\Delta fliB/fliC$) S. Typhimurium in WT mice presented in Fig. 1d, f, h and Extended Data Fig. 2 are identical and were pooled from five independent experiments conducted in two different laboratory animal facilities.

Ethics statement. This study was conducted in accordance with the German animal protection law and with the European Communities Council Directive 2010/63/EU for the protection of animals used for experimental purposes. All experiments were approved by the Local Institutional Animal Care and Research Advisory Committee and permitted by the local authority (Lower Saxony State Office for Consumer Protection, Food Safety, and Animal Welfare Service, A.Z. 07/1268a, 09/1639, 12/0697, 12/0693, 13/1097 and 14/1385).

Primary cell isolation. Primary intestinal epithelial cells were isolated from neonatal small intestines as described earlier. In brief, after euthanizing the mice, small intestinal tissue was collected on ice and subsequently minced with a scalpel. Then, the homogenate was incubated in 30 mM EDTA PBS at 37 °C for 10 min before passing the cells through a 100 µm nylon cell strainer (BD Falcon). Finally, cells were washed with 10% FCS/ PBS, collected by centrifugation, and immediately snap-frozen in liquid nitrogen. The isolation of small intestinal cells from adult mice was carried out essentially as described elsewhere³⁶.

Gene expression analysis. Total RNA was extracted from isolated, snap-frozen enterocytes using TRIzol (Ambion). Microarray analysis was performed in quadruplicate as recently described¹⁵. First strand complementary DNA (cDNA) for

quantitative real time (RT)-PCR was synthesized from 5 µg of RNA (determined on a NanoDrop 1000 spectrophotometer (Thermo Scientific)) with Oligo-dT primers and RevertAid reverse transcriptase (Fermentas). Taqman technology based RT-PCR was performed using absolute QPCR ROX mix (Thermo Scientific), sample cDNA and the Taqman probes *Hprt* (Mm00446368_m1), *Tlr5* (Mm00546288_m1), *Cxcl2* (Mm00436450_m1), and *Reg3γ* (Mm01181783_g1) from Life Technologies. SYBR green-based RT-PCRs were performed essentially as described earlier¹⁵. The following primers were used: *Tlr5* (forw: atggatggatgcgtttcc, rev: ggccatgaagatcacactta), *Gapdh* (forw: tgccaccacaactgttttc, rev: ggcatggatctggatcg). Values were normalized to the expression of the housekeeping genes *Hprt* or *Gapdh*.

Microbiota transplantation. Fresh stools were collected and pooled from four age- and gender-matched wild-type (WT) and *Tlr5*^{-/-} (TLR5) mice and subsequently suspended in 3 mL ice-cold PBS. After homogenization with glass beads, the extracts were centrifuged (300g, 4 °C, 10 min) and supernatants were administered (0.2 mL per mouse) immediately to pregnant and non-pregnant wild-type and *Tlr5*-deficient germ-free-housed mice. Recipient animals were housed under sterile conditions in microisolators (gnocages) throughout the experiment. Days post colonization (dpc) describe the time after birth (neonates) or the time after transfer (adults). Faeces of neonate and adult mice were taken at the indicated time points under sterile conditions. On some occasions, particularly young animals did not defecate and faecal samples could not be obtained.

Microbiota analysis. DNA was isolated from either small intestinal biopsies or faecal pellets using the QIAamp Fast DNA Stool Mini Kit (Qiagen) as described previously⁷. 16S profiling and MiSeq sequencing were performed as follows: the V4 region of the 16S gene was amplified using barcoded primers and the Hot Master Mix 2.5x PCR kit (5 Prime). PCR was carried out using the program [94 °C for 3 min, × (94 °C for 45 s, 50 °C for 60 s, 72 °C for 90 s), 72 °C for 10 min, hold at 4 °C] and the cycle number adjusted depending on the DNA type. MiSeq sequence data was analysed using MacQIIME v1.8 (<http://www.wernerlab.org/software/macqiime>). In brief, all sequencing reads were trimmed keeping only nucleotides with a Phred quality score of at least 20, then paired-end assembled and mapped onto the different samples using the barcode information. All samples within a single analysis were normalized to the minimum shared read count to account for differential sequencing depth among samples. Rarefaction was performed at 8,000 (Fig. 3c–f), 40,000 (Extended Data Fig. 3a), 30,000 (Fig. 2c), 12,000 (Fig. 2d) and 24,000 (Fig. 3a, b) reads per sample, respectively. Sequences were assigned to operational taxonomic units (OTUs) using uclust and the greengenes reference database (gg_13_8 release) with 97% identity. Representative OTUs were picked and taxonomy assigned using uclust and the greengenes database. Quality filtering was performed by removing chimaeric sequences using ChimeraSlayer and by removing singletons and sequences that failed to align with PyNAST. The reference phylogenetic tree was constructed using FastTree 2. Relative abundance was calculated by dividing the number of reads for an OTU by the total number of sequences in the sample. Unweighted Unifrac beta diversity was calculated and visualized by principal coordinate plots. Centroids of each group (neonate or adult *Tlr5*^{+/+} or *Tlr5*^{-/-} mice at one specific time point after colonization with either WT or TLR5 microbiota) were calculated by averaging the principal coordinates of all samples of a given group. Arrows connecting the centroids of two successive time points within a group receiving the same donor microbiota were calculated and averaged into a centroid trend line arrow thereby incorporating the time-lapse information. Unifrac distances, a measure of similarity of sample groups, were compared between WT and TLR5 microbiota recipient groups as indicated. Distances were calculated within each time point, then compared to the initial time point of that sample group using one-way ANOVA and *P* values were adjusted for multiple testing using FDR correction. This approach was used because of the high experimental group number and thus considers group variance only in the analysed combinations, but cannot assess all temporal fluctuations (age effect). Linear discriminant analysis (LDA) effect size (LEfSe)³⁸ was performed using the online tool available at <http://huttenhower.sph.harvard.edu/galaxy/>. LDA denotes taxa based on their contribution to the overall observed differences between groups, that is, taxa being significantly increased in abundance in TLR5 compared to WT.

Quantification of faecal flagellin. Bioactive, pro-inflammatory flagellin was quantified in faecal samples using human embryonic kidney (HEK)-Blue-mTLR5 cells (Invivogen) as described previously¹⁸. This assay detects similarly the *fliB* encoded and the *fliC* encoded flagellin³⁹. In brief, faecal material was resuspended in PBS to a final concentration of 100 mg/mL and homogenized for 10 s using a Mini-Beadbeater-24 without the addition of beads. The samples were centrifuged at 8,000g for 2 min and the supernatant was serially diluted and added to the cell culture medium of HEK-Blue-mTLR5 cells. Purified *Salmonella* Typhimurium flagellin (Invivogen) served as control and to establish a standard curve. Cell culture supernatant was collected after 24 h and transferred to QUANTI-Blue medium (Invivogen) and alkaline phosphatase activity was measured after 1 h at

620 nm using a spectrophotometer. Ratios were calculated from all values obtained from TLR5 microbiota recipients against all values obtained from WT microbiota recipients. HEK-Blue-mTr5 cells were free of mycoplasma; their authentication was confirmed by functional testing with different innate immune stimuli.

Histopathology. Liver and pancreas tissue samples were fixed in formaldehyde for 24 h and embedded in paraffin. Three-micrometre sections were stained with haematoxylin and eosin and evaluated by an American board-certified pathologist in a blinded fashion.

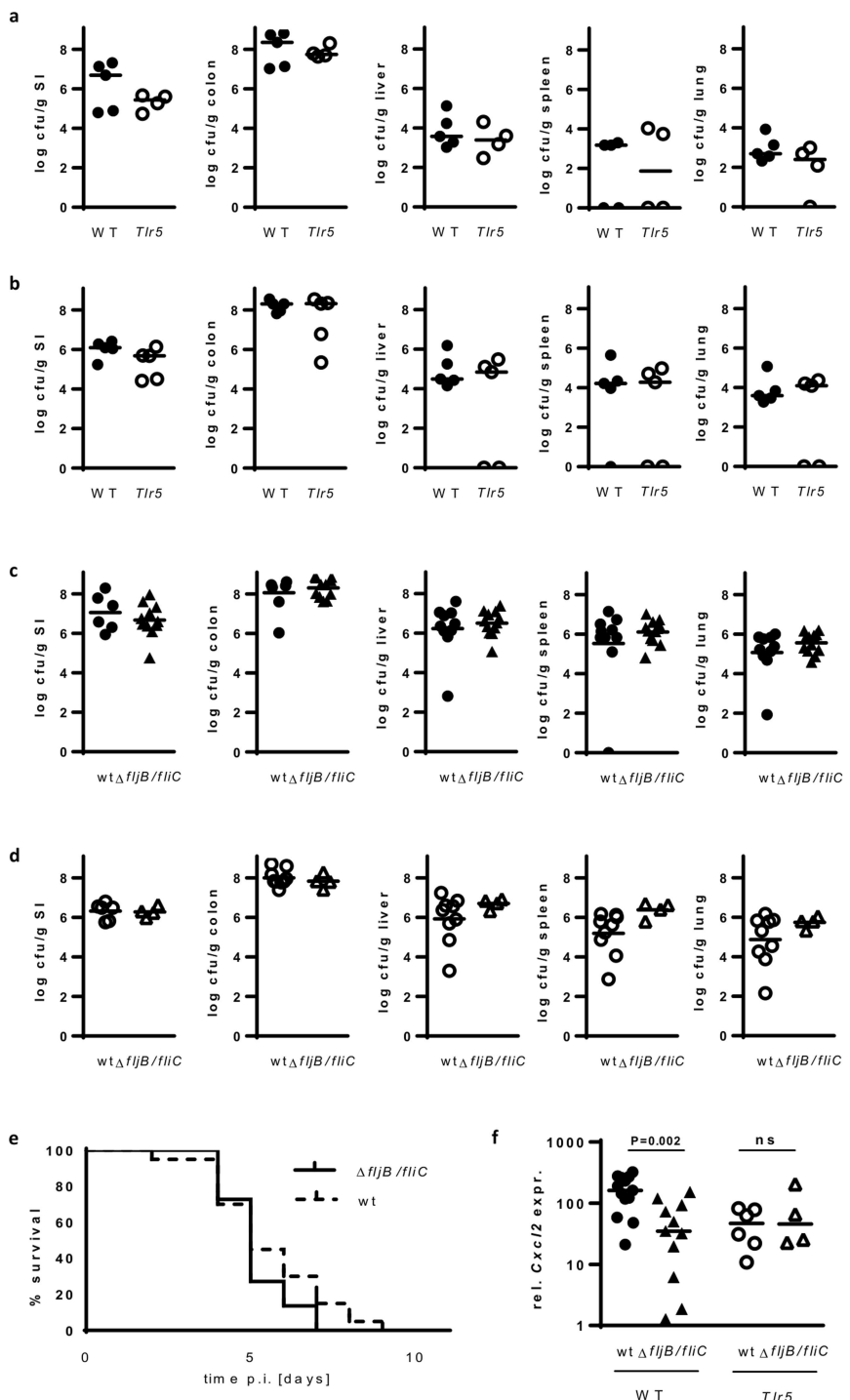
Statistical analysis and reproducibility. Sample sizes were chosen to reach statistical significance ($P < 0.05$) for a pre-specified effect based on the sample variation observed during previous studies. Sample sizes for microbiota analysis were chosen based on sample sizes published in other similar studies. In some occasions, DNA from faecal material did not yield sufficient DNA 16S amplicon or sequencing reads. No other pre-established inclusion/exclusion criteria, randomization protocols or blinded analysis were used. Bacterial growth in organ tissues or quantitative RT–PCR show counts for individual animals plus the median. One-way ANOVA Kruskal–Wallis test (with Dunn's post-test) and the Mann–Whitney test were used for statistical analysis of bacterial growth in organ tissues, comparative competitive indices and analysis of quantitative RT–PCR results. Unifrac results were evaluated using the one-way ANOVA followed by post-hoc FDR correction (Benjamini and Hochberg method). The sample variance was similar between statistically compared groups. The GraphPad Prism Software 7.03 was used for statistical evaluation. P values are indicated as follows: *** $P < 0.0001$; ** $P < 0.001$; ** $P < 0.01$; and * $P < 0.05$. The indicated mouse numbers should be considered biological replicates. In most cases animals from different litters were included to reflect inter-litter variation. All bacterial plating and RT–PCRs

were performed in duplicate; ELISA measurements were performed in triplicate (technical replicates).

Reporting summary. Further information on experimental design is available in the Nature Research Reporting Summary linked to this paper.

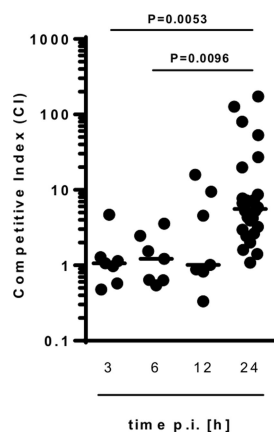
Data availability. Microarray data that support the findings of this study have been deposited in GEO with the accession code GSE35596. The microbiota results are accessible through the European Nucleotide Archive (ENA, <https://www.ebi.ac.uk/ena>) under the accession numbers ERS2087884–ERS2087899, ERS2088075–ERS2088093, ERS2088094–ERS2088150, and ERS2088348–ERS2088555. Additional data that support the findings of this study are available from the corresponding author upon reasonable request.

34. Datsenko, K. A. & Wanner, B. L. One-step inactivation of chromosomal genes in *Escherichia coli* K-12 using PCR products. *Proc. Natl Acad. Sci. USA* **97**, 6640–6645 (2000).
35. Barthel, M. et al. Pretreatment of mice with streptomycin provides a *Salmonella enterica* serovar *Typhimurium* *colitis* model that allows analysis of both pathogen and host. *Infect. Immun.* **71**, 2839–2858 (2003).
36. Lotz, M. et al. Postnatal acquisition of endotoxin tolerance in intestinal epithelial cells. *J. Exp. Med.* **203**, 973–984 (2006).
37. Sommer, F. et al. Altered mucus glycosylation in core 1 O-glycan-deficient mice affects microbiota composition and intestinal architecture. *PLoS ONE* **9**, e85254 (2014).
38. Segata, N. et al. Metagenomic biomarker discovery and explanation. *Genome Biol.* **12**, R60 (2011).
39. Simon, R. & Samuel, C. E. Activation of NF-κB-dependent gene expression by *Salmonella* flagellins FlIC and FljB. *Biochem. Biophys. Res. Commun.* **355**, 280–285 (2007).

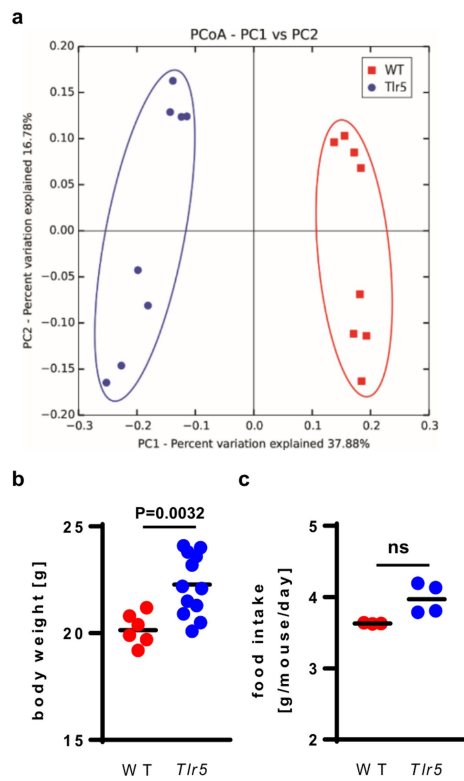


Extended Data Fig. 1 | Role of TLR5 and flagellin expression in the pathogenesis of neonatal *Salmonella* infection. **a, b,** Intestinal colonization and organ dissemination evaluated by serial dilution and plating two (**a**) or three (**b**) days after infection of 1-day-old wild-type (WT, filled circles, $n=5$) or *Tlr5*-deficient mice (*Tlr5*, open circles, $n=4$ or $n=5$, respectively) with approximately 10^2 CFU *S. Typhimurium*. Results from one litter at each time point. **c,** Intestinal colonization and organ dissemination evaluated by serial dilution and plating in small intestine ($n=6$ and 11), colon ($n=7$ and 11), liver ($n=10$ and 12), spleen ($n=10$ and 12) and lung ($n=10$ and 12) 4 days after infection of 1-day-old WT (filled symbols) mice with approximately 10^2 WT *S. Typhimurium* (circles, two litters) or $\Delta fliB/fliC$ mutant *S. Typhimurium* (triangles, three litters). **d,** Intestinal colonization and organ dissemination evaluated by serial dilution and plating in small intestine ($n=6$ and 4), colon ($n=9$ and 4), liver ($n=9$ and 4), spleen ($n=9$ and 4) and lung ($n=9$ and 4)

4 days after infection of 1-day-old *Tlr5*-deficient (open symbols) mice with approximately 10^2 WT *S. Typhimurium* (circles, 1 litter) or $\Delta fliB/fliC$ mutant *S. Typhimurium* (triangles, 1 litter). Data in **a-d** represent the median (two-sided Mann-Whitney test). **e**, Survival of 1-day-old WT mice infected orally with wild-type (wt, dashed line, $n = 20$, three litters) or isogenic flagellin-deficient ($\Delta fliB/fliC$, solid line, $n = 22$, three litters) *S. Typhimurium*. **f**, *Cxcl2* mRNA expression analysed by quantitative RT-PCR in intestinal epithelial cells (IECs) isolated 4 days after infection of 1-day-old wild-type mice (WT, filled symbols, $n = 13$ and 11 from each three litters) or *Tlr5*-deficient mice (*Tlr5*, open symbols, $n = 6$ and 4 from each two litters) with wild-type *S. Typhimurium* (wt, circles) or an isogenic flagellin mutant ($\Delta fliB/fliC$, triangles). Values were normalized to the expression of the housekeeping gene *Hprt*. Data represent the median (* $P < 0.05$; ** $P < 0.01$, two-sided Mann-Whitney test).

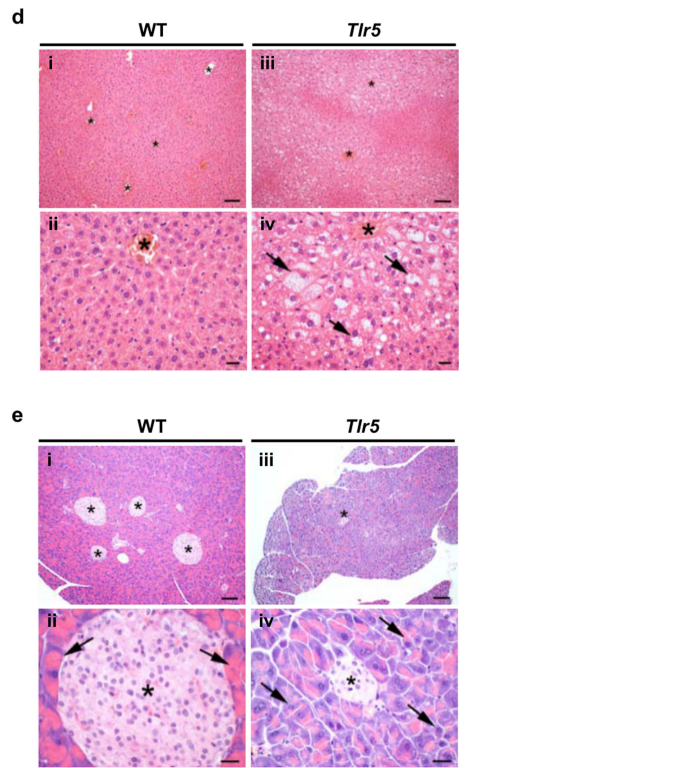


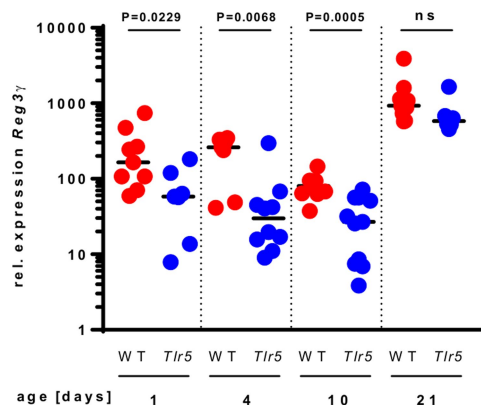
Extended Data Fig. 2 | Kinetics of counter-selection against flagellated *Salmonella* in *Tlr5*-proficient mice. Intestinal colonization (CI) at 3, 6, 12, and 24 h after oral infection of 1-day-old mice with a 1:1 ratio of wild-type and $\Delta fliB/fliC$ S. Typhimurium. Data represent the median; $n = 7$, 7, 7 (derived from 2 litters) and 26 (6 litters), respectively; ** $P < 0.01$, Kruskal–Wallis test followed by Dunn's post-test). Note that results from competition experiments with WT and flagellin-deficient ($\Delta fliB/fliC$) S. Typhimurium in WT mice after 24 h presented in Fig. 1d, f, h and Extended Data Fig. 2 are identical and were pooled from six independent experiments conducted in two different laboratory animal facilities.



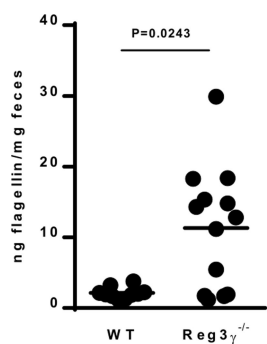
Extended Data Fig. 3 | Influence of TLR5 on microbiota composition and the metabolic phenotype in individually housed adult mice.

a, Bacterial DNA was extracted from the faeces of individually housed 6–8-week-old homozygous *Tlr5*^{+/+} (WT, red, $n = 8$) and homozygous *Tlr5*^{−/−} (*Tlr5*, blue, $n = 8$) mice. The microbiota composition was analysed by 16S rDNA sequencing and the overall difference is illustrated in a principal coordinate analysis (PCoA). **b**, Body weight was evaluated in 7-week-old male WT (red) and *Tlr5*-deficient (blue) mice. Data represent the median. Statistical analysis was performed using two-sided Mann–Whitney *U*-test ($n = 6$ and 12, respectively, $**P < 0.01$). **c**, Daily food intake was evaluated in 25-week-old female WT (red) and *Tlr5*-deficient (blue) mice. Data represent the median. Statistical analysis was performed using two-sided Mann–Whitney *U*-test ($n = 3$ and 4, respectively).





Extended Data Fig. 4 | Neonatal but not adult epithelial *Reg3g* mRNA expression is influenced by TLR5 expression. IECs from non-infected wild-type (WT, red) and *Tlr5*-deficient (*Tlr5*, blue) mice were collected at 1 ($n = 9$ from three litters and $n = 7$ from three litters), 4 ($n = 7$ from two litters and $n = 10$ from two litters), 10 ($n = 9$ from one litter and $n = 11$ from two litters) and 21 days ($n = 9$ from one litter and $n = 6$ from one litter) after birth and *Reg3g* mRNA expression was analysed by qRT-PCR. Values were normalized to the expression of the housekeeping gene *Hprt*. Data represent the median (* $P < 0.05$; ** $P < 0.01$; *** $P < 0.001$; two-sided Mann-Whitney *U*-test).



Extended Data Fig. 5 | REG3 γ expression influences the faecal bioactive flagellin load. Faecal pellets from age-matched WT ($n = 10$; 6 female, 4 male) and *Reg3g*-deficient ($n = 13$; 8 female, 5 male) 5–8-week-old mice housed in 3 and 4 separate isolator cages, respectively, were collected. The amount of bioactive, pro-inflammatory flagellin was determined using the HEK-Blue-mTLR5 cell line as described in the Methods section. Data represent the median from two independent measurements; * $P < 0.05$, two-sided Mann–Whitney *U*-test.

RNA velocity of single cells

Gioele La Manno^{1,2}, Ruslan Soldatov³, Amit Zeisel^{1,2}, Emelie Braun^{1,2}, Hannah Hochgerner^{1,2}, Viktor Petukhov^{3,4}, Katja Lidschreiber⁵, Maria E. Kastriti⁶, Peter Lönnerberg^{1,2}, Alessandro Furlan¹, Jean Fan³, Lars E. Borm^{1,2}, Zehua Liu³, David van Bruggen¹, Jimin Guo³, Xiaoling He⁷, Roger Barker⁷, Erik Sundström⁸, Gonçalo Castelo-Branco¹, Patrick Cramer^{5,9}, Igor Adameyko⁶, Sten Linnarsson^{1,2,*} & Peter V. Kharchenko^{3,10,*}

RNA abundance is a powerful indicator of the state of individual cells. Single-cell RNA sequencing can reveal RNA abundance with high quantitative accuracy, sensitivity and throughput¹. However, this approach captures only a static snapshot at a point in time, posing a challenge for the analysis of time-resolved phenomena such as embryogenesis or tissue regeneration. Here we show that RNA velocity—the time derivative of the gene expression state—can be directly estimated by distinguishing between unspliced and spliced mRNAs in common single-cell RNA sequencing protocols. RNA velocity is a high-dimensional vector that predicts the future state of individual cells on a timescale of hours. We validate its accuracy in the neural crest lineage, demonstrate its use on multiple published datasets and technical platforms, reveal the branching lineage tree of the developing mouse hippocampus, and examine the kinetics of transcription in human embryonic brain. We expect RNA velocity to greatly aid the analysis of developmental lineages and cellular dynamics, particularly in humans.

During development, differentiation occurs on a timescale of hours to days, which is comparable to the typical half-life of mRNA. The relative abundance of nascent (unspliced) and mature (spliced) mRNA can be exploited to estimate the rates of gene splicing and degradation, without the need for metabolic labelling, as previously shown in bulk^{2–4}. We reasoned that similar signals may be detectable in single-cell RNA sequencing (RNA-seq) data, and could reveal the rate and direction of change of the entire transcriptome during dynamic processes.

All common single-cell RNA-seq protocols rely on oligo-dT primers to enrich for polyadenylated mRNA molecules. Nevertheless, examining single-cell RNA-seq datasets based on the SMART-seq2, STRT/C1, inDrop and 10x Genomics Chromium protocols^{5–8}, we found that 15–25% of reads contained unspliced intronic sequences (Fig. 1a), in agreement with previous observations in bulk⁴ (14.6%) and single-cell⁵ (~20%) RNA-seq. Most such reads originated from secondary priming positions within the intronic regions (Extended Data Fig. 1). In 10x Genomics Chromium libraries, we also found abundant discordant priming from the more commonly occurring intronic-polyT sequences (Extended Data Fig. 1), which may have been generated during PCR amplification by priming on the first-strand cDNA. The substantial number of intronic molecules and their correlation with the exonic counts suggest that these molecules represent unspliced precursor mRNAs. This was confirmed by metabolic labelling of newly transcribed RNA⁹ followed by RNA sequencing using oligo-dT-primed single-cell-tagged reverse transcription (STRT)¹⁰ (Extended Data Fig. 2); 83% of all genes displayed expression time courses consistent with simple first-order kinetics, as expected if unspliced reads represent nascent mRNA.

To quantify the time-dependent relationship between the abundance of precursor and mature mRNA, we assumed a simple model

for transcriptional dynamics², in which the first time derivative of the spliced mRNA abundance (RNA velocity) is determined by the balance between production of spliced mRNA from unspliced mRNA, and the mRNA degradation (Fig. 1b and Supplementary Note 1). Under such a model, steady states are approached asymptotically when the rate of transcription α is constant, with the steady-state abundances of spliced (s) and unspliced (u) molecules determined by α , and constrained to a fixed-slope relationship where $u = \gamma s$ (Supplementary Note 2 Section 1). The equilibrium slope γ combines degradation and splicing rates, capturing gene-specific regulatory properties, the ratio of intronic and exonic lengths, and the number of internal priming sites. Using a recently published compendium of mouse tissues¹¹, we found that the steady-state behaviour of most genes across a wide range of cell types was consistent with a single fixed slope γ (Extended Data Fig. 3a–c). However, 11% of genes showed distinct slopes in different subsets of tissues (Extended Data Fig. 3d, e), suggesting tissue-specific alternative splicing (Extended Data Fig. 3f) or degradation rates.

During a dynamic process, an increase in the transcription rate α results in a rapid increase in unspliced mRNA, followed by a subsequent increase in spliced mRNA (Fig. 1c and Supplementary Note 2 Section 1) until a new steady state is reached. Conversely, a drop in the rate of transcription first leads to a rapid drop in unspliced mRNA, followed by a reduction in spliced mRNAs. During induction of gene expression, unspliced mRNAs are present in excess of the expectation based on the equilibrium rate γ , whereas the opposite is true during repression (Fig. 1d). The balance of unspliced and spliced mRNA abundance is, therefore, an indicator of the future state of mature mRNA abundance, and thus the future state of the cell.

To demonstrate how this simple model can be used to extrapolate the mature mRNA abundance into the future, we examined a time course of bulk RNA-seq measurements of the circadian cycle in the mouse liver¹². Unspliced mRNA levels at each time point were consistently more similar to the spliced mRNA of the subsequent time (Fig. 1e), and many circadian-associated genes showed the expected excess of unspliced mRNA relative to the slope γ during upregulation, and a corresponding deficit during downregulation (Fig. 1f, g). Solving the proposed differential equations for each gene allowed us to extrapolate each measurement throughout the circadian cycle, accurately capturing the expected direction of progression of the circadian cycle (Fig. 1h).

Next, to demonstrate the ability to predict transcriptional dynamics in single-cell measurements, we analysed recently published single-cell mRNA-seq data of mouse chromaffin cells¹³, obtained using SMART-seq2⁵ (Fig. 2). During development, a substantial proportion of chromaffin cells, which are neuroendocrine cells of the adrenal medulla, arise from Schwann cell precursors, providing a convenient test case in which the direction of differentiation can be validated by lineage tracing. Phase portraits of many genes showed the expected deviations

¹Laboratory of Molecular Neurobiology, Department of Medical Biochemistry and Biophysics, Karolinska Institutet, Stockholm, Sweden. ²Science for Life Laboratory, Solna, Sweden. ³Department of Biomedical Informatics, Harvard Medical School, Boston, MA, USA. ⁴Department of Applied Mathematics, Peter The Great St. Petersburg Polytechnic University, St. Petersburg, Russia.

⁵Department of Biosciences and Nutrition, Karolinska Institutet, Stockholm, Sweden. ⁶Department of Physiology and Pharmacology, Karolinska Institutet, Stockholm, Sweden. ⁷John van Geest Centre for Brain Repair, Department of Clinical Neurosciences, University of Cambridge, Cambridge, UK. ⁸Division of Neurodegeneration, Department of Neurobiology, Care Sciences and Society, Karolinska Institutet, Stockholm, Sweden. ⁹Max Planck Institute for Biophysical Chemistry, Department of Molecular Biology, Göttingen, Germany. ¹⁰Harvard Stem Cell Institute, Cambridge, MA, USA. *e-mail: sten.linnarsson@ki.se; peter_kharchenko@hms.harvard.edu

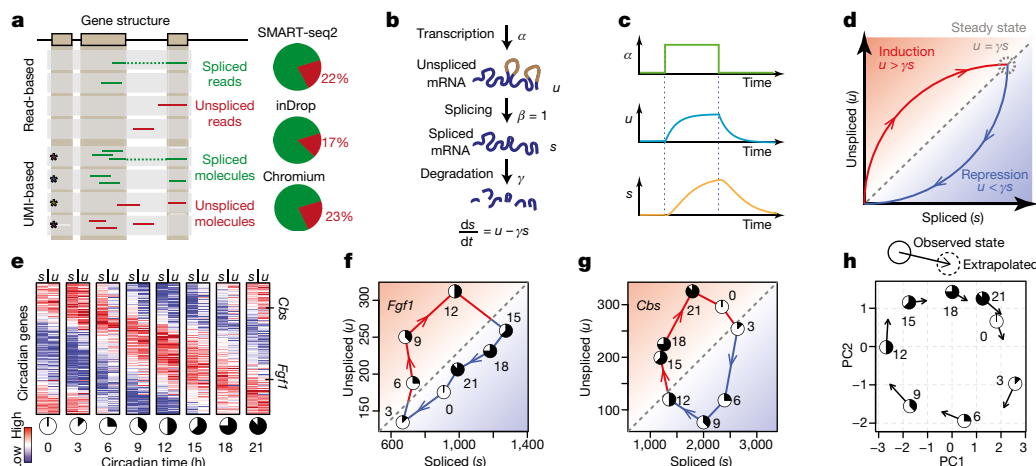


Fig. 1 | Balance between unspliced and spliced mRNAs is predictive of cellular state progression. **a**, Spliced and unspliced counts are estimated by separately counting reads that incorporate the intronic sequence. Multiple reads associated with a given molecule are grouped (boxes with asterisks) for unique molecular identifier (UMI)-based protocols. Pie charts show typical fractions of unspliced molecules. **b**, Model of transcriptional dynamics, capturing transcription (α), splicing (β) and degradation (γ) rates involved in production of unspliced (u) and spliced (s) mRNA products. **c**, Solution of the model in **b** as a function of time, showing unspliced and spliced mRNA dynamics in response to step changes in α . **d**, Phase portrait showing the same solution shown in **c** (solid curves). Steady states for different values of transcription rates α fall on the diagonal given by slope γ (dashed line). Levels of unspliced mRNA above or below this proportion indicate increasing (red shading) or

decreasing (blue shading) expression of a gene, respectively. **e**, Abundance of spliced (s) and unspliced (u) mRNAs for circadian-associated genes in the mouse liver over a 24-h time course¹². The unspliced mRNAs are predictive of spliced mRNA at the next time point. **f**, **g**, Phase portraits observed for a pair of circadian-driven genes: *Fgf1* (**f**) and *Cbs* (**g**). The circadian time of each point is shown using a clock symbol (corresponding to those in **e**). The dashed diagonal line shows the steady-state relationship, as predicted by γ fit. **h**, Change in expression state at a future time t , as predicted by the model, is shown in the space of the first two principal components (PCs), recapitulating the progression along the circadian cycle. Each circle shows the observed expression state, with the arrow pointing to the position of the future state, extrapolated from velocity estimates.

from the predicted steady-state relationship (Fig. 2b, c). RNA velocity estimates of the individual cells accurately recapitulated the transcriptional dynamics within this dataset, including general movement of the differentiating cells towards a chromaffin fate (Fig. 2d), as well as the movement towards and away from the intermediate differentiation state. The velocity also captured cell-cycle dynamics involved in the chromaffin differentiation, both in principle component analysis (PCA) projection and in a focused analysis of cell-cycle associated genes (Supplementary Note 2 Section 5).

Our velocity estimation procedure incorporates several features to accommodate the complexity of splicing biology (Supplementary Note 1). The estimation of the gene-specific equilibrium coefficient γ is performed using regression on the extreme expression quantiles, ensuring robust estimation even when most of the observed cells are outside of the steady state (Supplementary Note 2 Section 2). To accommodate genes observed far outside of their steady state, we also developed an alternative fit based on gene structure (Extended Data Fig. 4). A variety of techniques can be used to visualize the velocity estimates in low dimensions. The observed and extrapolated cell states can be jointly embedded in a common low-dimensional space (for example, PCA in Fig. 2d). Alternatively, velocities can be projected onto existing low-dimensional embeddings, such as *t*-distributed stochastic neighbour embedding (*t*-SNE), on the basis of the similarity of the extrapolated state to other cells in the local neighbourhood (Fig. 2h, see Supplementary Note 1). In large datasets, it is easier to visualize the prevalent pattern of cell velocities with locally averaged vector fields (Fig. 2i). Because cells can have RNA velocities along multiple independent components simultaneously, such as differentiation, maturation and proliferation, care must be taken when interpreting low-dimensional representations, as cells that lack apparent velocity in one particular embedding can nevertheless have substantial velocity in some subspace that is not visualized.

Cell-specific RNA velocity estimates provide a natural basis for quantitative modelling of cell fates. Metabolic labelling showed that for most genes, changes in the spliced/unspliced ratio would be detectable after 10–100 min (Extended Data Fig. 2). The effective timescale

of extrapolation, on the other hand, depends on the biological process that is analysed. On the basis of pulse labelling of chromaffin progenitor cells with 5-ethynyl-2'-deoxyuridine (EdU) (Supplementary Note 2 Section 6), we estimate that we were able to extrapolate 2.5–3.8 h into the future (Fig. 2f, g), which is also consistent with the ability to resolve cell-cycle events. Given the linear nature of the extrapolation, however, this predictive timescale will depend on the shape of the gene expression trajectory (that is, the curvature of the expression manifold). Cell fates can be predicted over longer time scales by tracing a sequence of small extrapolation steps on the observed expression manifold (Supplementary Note 2 Section 7).

To demonstrate the generality of our approach we analysed data generated using additional single-cell RNA-seq protocols. We observed the transcriptional dynamics of neutrophil maturation in mouse bone marrow, and of light-induced neuronal activation in mouse cortex measured using the inDrop protocol (Extended Data Fig. 5), and of the intestinal epithelium (Extended Data Fig. 6), oligodendrocyte differentiation (Extended Data Fig. 7) and hippocampus development (see below), measured using 10x Genomics Chromium⁷. Estimates of RNA velocity were robust to variations in the model parameters, and gene and cell subsampling, with the most sensitive parameter being the size of the neighbourhood used in the visualization of velocity in pre-defined embeddings (Supplementary Note 2 Sections 10, 11). Most genes showed a positive correlation between velocity estimates and empirically observed expression derivatives (Extended Data Fig. 8), confirming that velocity vectors are informative. Failures in specific cases had several apparent causes, including genes observed exclusively far from equilibrium, uneven contribution of non-coding transcripts, and alternative splicing leading to multiple rates of γ across the measured populations (Supplementary Note 2 Section 4).

We next applied RNA velocity to the branching lineage of the developing mouse hippocampus¹⁴. After removing vascular and immune cells, and GABAergic (γ -aminobutyric-acid-releasing) and Cajal-Retzius neurons (which originate from outside the hippocampus), *t*-SNE plot revealed a complex manifold with multiple branches (Fig. 3a). We used known markers to identify the tips of the

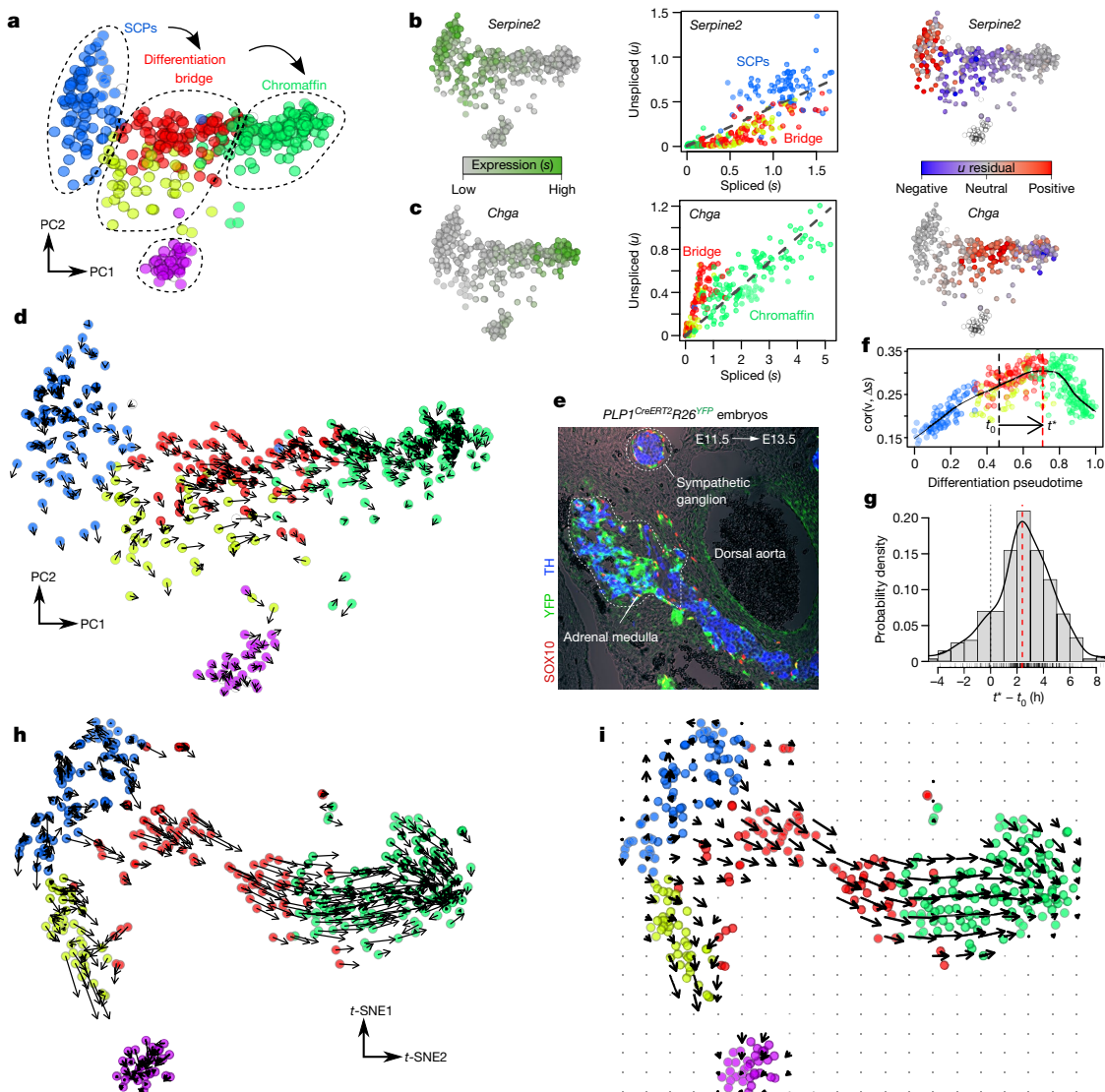


Fig. 2 | RNA velocity recapitulates dynamics of chromaffin cell differentiation. **a**, PCA projection showing major subpopulations of Schwann cell precursors (SCPs) differentiating into chromaffin cells in embryonic day (E)12.5 mice ($n = 385$ cells). **b, c**, Expression pattern (left), unspliced–spliced phase portraits (centre, cells coloured according to a), and u residuals (right) are shown for the repressed *Serpine2 (b) and induced *Chga* (c) genes. Read counts were pooled across the five nearest cell neighbours. **d**, The observed and the extrapolated future states (arrows) are shown on the first two PCs. RNA velocity was estimated without cell or gene pooling. **e**, SCP-to-chromaffin cell transition as evidenced by lineage tracing with SCP-specific *PLP1-CreERT2* line. A cross-section through the developing adrenal medulla is shown. Note the high proportion of TH^+YFP^+ cells in the developing medulla and the absence of such double-positive cells in the sympathetic ganglion*

($n = 3$ replicates). YFP labels Htr3a^+ bridge cells; TH marks chromaffin cells; TH^+YFP^+ marks chromaffin cells that are freshly differentiated from the bridge population. **f**, Extrapolation distance along the chromaffin differentiation trajectory is estimated for a single cell at pseudotime t_0 , on the basis of the correlation (y axis) between the velocity v and cell expression difference. The red line shows optimal extrapolation time (t^*) (see Supplementary Note 2 Section 6). **g**, Distribution of optimal extrapolation times ($t^* - t_0$) for the chromaffin differentiation time course. The red line marks the distribution mode (2.1 h). **h**, The velocities are visualized on the pre-defined t-SNE plot from the original publication¹³. Velocity estimates based on nearest-cell pooling ($k = 5$) were used. **i**, Same velocity field as h, visualized using Gaussian smoothing on a regular grid.

branches that corresponded to astrocytes, oligodendrocyte precursors (OPCs), dentate gyrus granule neurons and pyramidal neurons of the five fields of the hippocampus: the subiculum, CA1, CA2, CA3 and hilus (Extended Data Fig. 9). Phase portraits of individual genes showed specific induction and repression of gene expression along the manifold (Fig. 3b and Extended Data Fig. 10). For example, *Pdgfra* (a marker of OPCs) was induced in pre-OPCs and maintained in OPCs; it showed corresponding positive velocity in the pre-OPC state, but was neutral in the OPCs. Similarly, *Igfbpl1* was expressed specifically in neuroblasts and showed positive velocity from radial glia to neuroblasts, but negative velocity going from neuroblasts to the two main neuronal branches.

RNA velocity showed a strong directional flow towards each of the main branches (Fig. 3c and Extended Data Fig. 10), originating in a small group of cells arranged in a band (Fig. 3c, inset, dashed line). We identified these cells as radial glia on the basis of the expression of markers, including the Notch target *Hes1* and the homeobox transcription factor *Hoxp* (Extended Data Fig. 9). Indeed, fate mapping has previously shown radial glia to be the true origin of the lineage tree of the hippocampus¹⁵. Using a Markov random-walk model on the velocity field, the terminal and root states could be automatically identified (Fig. 3c), demonstrating the power of RNA velocity to orient the lineage tree without prior knowledge about the developmental process. On one side, velocity pointed towards astrocytes (expressing *Aqp4*) without

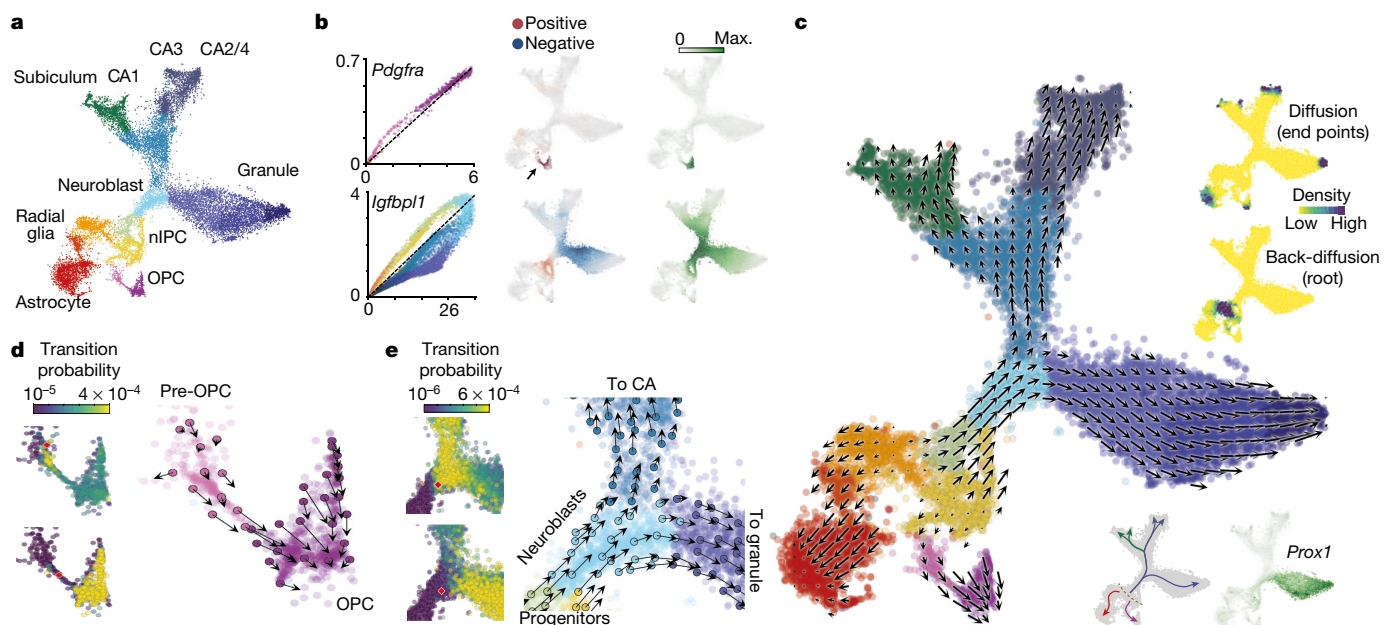


Fig. 3 | RNA velocity field describes fate decisions of major neural lineages in the hippocampus. **a**, t-SNE plot of the developing mouse hippocampus cells ($n = 18,213$ cells), showing major transient and mature subpopulations. **b**, Phase portraits (left, coloured as in **a**), unspliced residuals (middle) and spliced expression (right) are shown for two regulated genes. k -nearest neighbour (k NN) cell pooling was used. **c**, Velocity field projected onto the t-SNE plot. Arrows show the local average velocity evaluated on a regular grid. Top right inset, differentiation endpoints as high density regions on the manifold after forward Markov process with velocity-based transition probabilities; the root

intervening cell division, or alternatively to a pre-OPC state, leading through a narrow passage to proliferating OPCs. We speculated that the narrow passage represented the moment of commitment to the oligodendrocyte lineage. At this microstate level, fate choice is likely to be a non-deterministic process involving the tilting of gene expression in favour of one or the other fate, followed by a lock-in of the final fate once transcription-factor feedback loops are established¹⁶. Comparing the probability distribution of future states for a cell starting among the pre-OPCs, with one starting in the narrow passage leading to OPCs revealed a clear difference—the latter cell was overwhelmingly likely to end up as a fully formed OPC whereas the former was as likely to remain in the pre-OPC state (Fig. 3d).

Some cycling progenitor cells (Extended Data Fig. 9b) expressed neurogenic transcription factors (for example, *Neurod2*, *Neurod4*, *Eomes*), and those cells showed velocity towards the immature neuroblast state, leading towards the three main neuronal branches in the upper part of the manifold. Granule neurons of the dentate gyrus first split from the hippocampus proper, and a second split divided the hippocampal cells into subiculum/CA1 and CA2–4, respectively (Extended Data Figs. 9, 10), in agreement with the major functional and anatomical subdivisions of the hippocampus. The detailed, single-cell view of a branching lineage allowed us to interrogate fate choice. Examining two adjacent neuroblasts just at the entrance to the branching point between CA and granule fates (Fig. 3e), we found that although their current states were neighbours (in gene-expression space), their futures were already tilted towards different fates, distinguished by activation of *Prox1* (Fig. 3c, inset). Consistent with these findings, it has been shown that *Prox1* is required for the formation of granule neurons and that, when *Prox1* is deleted, neuroblasts instead adopt a pyramidal neuron fate¹⁷.

To demonstrate that RNA velocity is detectable in the human embryo, we performed droplet-based single-cell mRNA-seq of the developing human forebrain at ten weeks post-conception, focusing on the glutamatergic neuronal lineage (Fig. 4a). We found a strong

of the branching tree is identified simulating the process in the reverse direction. Bottom right inset, summary schematic of the RNA velocity field, and expression of the transcription factor *Prox1*. **d**, Commitment to oligodendrocyte fate. Left, visualization of single-step transition probabilities from two starting cells (red) to neighbouring cells. Right, velocities of a sampled subset of cells shown on the t-SNE plot in **c**. **e**, Fate decision of neuroblasts. Left, visualization of single-step transition probabilities from two starting cells (red) to neighbouring cells. Right, velocities of a sampled subset of cells shown on the t-SNE plot in **c**.

velocity pattern originating from a proliferating progenitor state (radial glia), and proceeding through a sequence of intermediate neuroblast stages to a more mature differentiated glutamatergic neuron expressing *SLC17A7* (the vesicular glutamate transporter (which is also known as *VGLUT1*) used in forebrain excitatory neurons). We validated the expression of known and novel markers of cortical neuron development by multiplexed in situ hybridization (Fig. 4b, c), confirming the predicted expression of *CLU* and *FBXO32* in the ventricular zone (radial glia; marked by *SOX2*), *UNC5D* in the intermediate zone (neuroblasts; marked by *EOMES*) and *SEZ6* and *RBFOX1* in the cortical plate (neurons; marked by *SLC17A7*). The layered expression of these genes in the tissue (Fig. 4c) corresponded closely to the pseudotemporal distribution of their expression in the single-cell RNA-seq data (Fig. 4b).

We used principal curve analysis to order the cells according to a differentiation pseudotime, and examined the temporal progression of transcription in human primary cells. We confirmed that unspliced mRNAs consistently preceded spliced mRNAs during both up- and downregulation (Fig. 4d). We observed both fast and slow kinetics. For example, *RNASEH2B* exhibited fast kinetics, with little difference between unspliced and spliced RNAs. By contrast, genes such as *DCX*, *ELAVL4* and *STMN2* showed evidence of an initial burst of rapid transcription, followed by sustained transcription at a reduced level (as evidenced by the shape of the unspliced RNA curve, Fig. 4d), with spliced transcripts following a noticeably delayed trajectory. Such dynamic induction with overshooting has been proposed to help to quickly induce genes with slow degradation kinetics², but this has not been possible to study in human embryos.

As RNA velocity is grounded in real transcription kinetics, this approach promises to bring a more solid quantitative foundation to our understanding of the dynamics of cells in gene-expression space during differentiation. We envision future manifold learning algorithms that simultaneously fit a manifold and the kinetics on that manifold, on the basis of RNA velocity. RNA velocity has already enabled the detailed

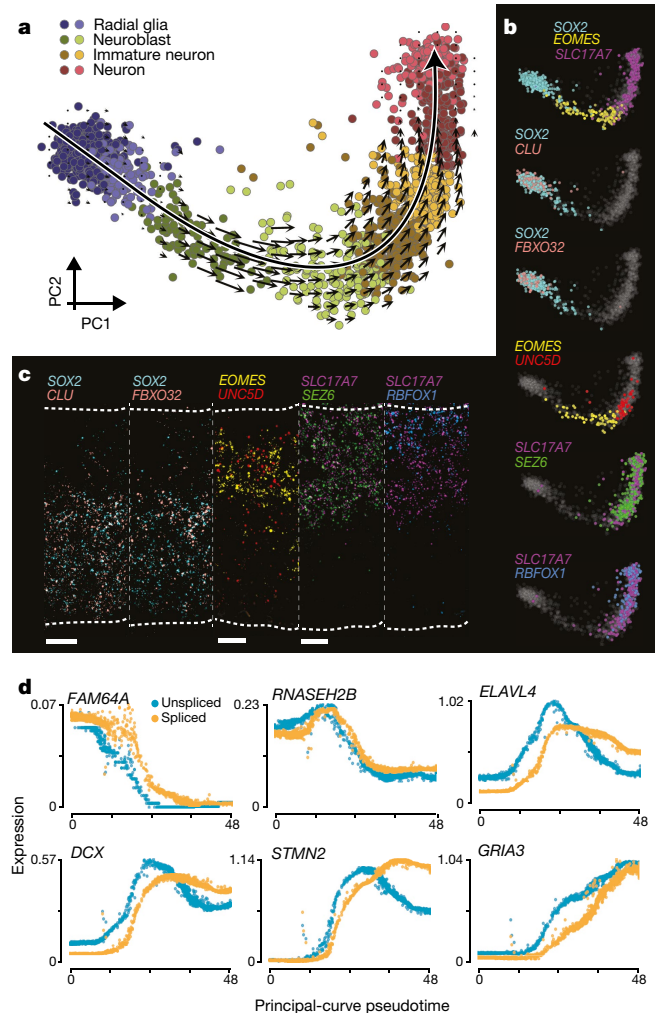


Fig. 4 | Kinetics of transcription during human embryonic glutamatergic neurogenesis. **a**, PCA projection of human glutamatergic neuron differentiation ($n = 1,720$ cells) at post-conception week 10, shown with velocity field. Colours indicate cell types and intermediate states. A corresponding principal curve is shown in bold. **b**, Gene expression of known markers of radial glia (SOX2), neuroblasts (EOMES) and neurons (SLC17A7), and of novel markers is visualized on the PCA projection for the indicated genes in pseudocolour. **c**, Fluorescent in situ hybridization (RNAscope) for the same genes as in **b** on a cross-section of human developing cortex, oriented with the ventricular zone towards the bottom and the cortical surface towards the top ($n = 1$). Scale bars, 25 μm . **d**, Pseudotime expression profiles during glutamatergic neuron maturation for six example genes. Spliced abundance was multiplied by γ to match the scale of unspliced abundance.

study of dynamic processes in whole organisms¹⁸, and will greatly facilitate lineage analysis particularly in the human embryo.

Online content

Any Methods, including any statements of data availability and Nature Research reporting summaries, along with any additional references and Source Data files, are available in the online version of the paper at <https://doi.org/10.1038/s41586-018-0414-6>.

Received: 13 December 2017; Accepted: 3 July 2018;
Published online 8 August 2018.

- Linnarsson, S. & Teichmann, S. A. Single-cell genomics: coming of age. *Genome Biol.* **17**, 97 (2016).
- Zeisel, A. et al. Coupled pre-mRNA and mRNA dynamics unveil operational strategies underlying transcriptional responses to stimuli. *Mol. Syst. Biol.* **7**, 529 (2011).

- Gray, J. M. et al. SnapShot-Seq: a method for extracting genome-wide, in vivo mRNA dynamics from a single total RNA sample. *PLoS ONE* **9**, e89673 (2014).
- Gaidatzis, D., Burger, L., Florescu, M. & Stadler, M. B. Analysis of intronic and exonic reads in RNA-seq data characterizes transcriptional and post-transcriptional regulation. *Nat. Biotechnol.* **33**, 722–729 (2015).
- Picelli, S. et al. Smart-seq2 for sensitive full-length transcriptome profiling in single cells. *Nat. Methods* **10**, 1096–1098 (2013).
- Islam, S. et al. Quantitative single-cell RNA-seq with unique molecular identifiers. *Nat. Methods* **11**, 163–166 (2013).
- Klein, A. M. M. et al. Droplet barcoding for single-cell transcriptomics applied to embryonic stem cells. *Cell* **161**, 1187–1201 (2015).
- Zheng, G. X. Y. et al. Massively parallel digital transcriptional profiling of single cells. *Nat. Commun.* **8**, 14049 (2017).
- Schwalb, B. et al. TT-seq maps the human transient transcriptome. *Science* **352**, 1225–1228 (2017).
- Islam, S. et al. Characterization of the single-cell transcriptional landscape by highly multiplex RNA-seq. *Genome Res.* **21**, 1160–1167 (2011).
- The Tabula Muris Consortium, Quake, S. R., Wyss-Coray, T. & Darmanis, S. Single-cell transcriptomic characterization of 20 organs and tissues from individual mice creates a Tabula Muris. Preprint at <https://biorxiv.org/content/early/2018/03/29/237446> (2018).
- Vollmers, C. et al. Circadian oscillations of protein-coding and regulatory RNAs in a highly dynamic mammalian liver epigenome. *Cell Metab.* **16**, 833–845 (2012).
- Furlan, A. et al. Multipotent peripheral glial cells generate neuroendocrine cells of the adrenal medulla. *Science* **357**, eaal3753 (2017).
- Kriegstein, A. & Alvarez-Buylla, A. The glial nature of embryonic and adult neural stem cells. *Annu. Rev. Neurosci.* **32**, 149–184 (2009).
- Malatesta, P. et al. Neuronal or glial progeny: regional differences in radial glia fate. *Neuron* **37**, 751–764 (2003).
- Johnston, R. J. & Desplan, C. Stochastic mechanisms of cell fate specification that yield random or robust outcomes. *Annu. Rev. Cell Dev. Biol.* **26**, 689–719 (2010).
- Iwano, T., Masuda, A., Kiyonari, H., Enomoto, H. & Matsuzaki, F. Prox1 postmitotically defines dentate gyrus cells by specifying granule cell identity over CA3 pyramidal cell fate in the hippocampus. *Development* **139**, 3051–3062 (2012).
- Plass, M. et al. Prox1 postmitotically defines dentate gyrus cells by specifying granule cell identity over CA3 pyramidal cell fate in the hippocampus. *Science* **360**, eaao1723 (2018).

Acknowledgements The work reported here was supported by the Swedish Foundation for Strategic Research (RIF14-0057 and SB16-0065), the Knut and Alice Wallenberg Foundation (2015.0041), the Erling Persson Foundation (HumDevCellAtlas) and the Wellcome Trust (108726/Z/15/Z) to S.L.; Center for Innovative Medicine (CIMED) to K.L. and P.C.; Swedish Research Council, Marie Curie Integration Grant EPIOPC, 333713, European Research Council EPISCOPE, 681893, Swedish Brain Foundation, Ming Wai Lau Centre for Reparative Medicine, Cancerfonden and Karolinska Institutet to G.C.-B. P.V.K. was supported by NIH R01HL131768 from NHLBI and CAREER (NSF-14-532) award from NSF.

Reviewer information *Nature* thanks A. Klein, R. Satija, M. Stadler and the other anonymous reviewer(s) for their contribution to the peer review of this work.

Author contributions S.L. conceived the concept of RNA velocity and P.V.K. showed that RNA velocity could be detected through analysis of unspliced transcripts in single cells. P.V.K. and S.L. designed and supervised the study. P.V.K., S.L., G.L.M. and R.S. developed the analytical framework, analysed data, made figures and drafted the manuscript, with contributions from all co-authors. P.V.K., G.L.M., R.S. and P.L. implemented the software, with assistance from V.P. and J.F.Z.L. examined RNA degradation signals. A.Z. and H.H. performed the mouse hippocampus experiment. P.C. supervised and K.L. and H.H. performed metabolic labelling. M.E.K. and I.A. performed validations of chromaffin differentiation rate. E.B. and L.E.B. performed and analysed the fluorescent in situ hybridization experiment on tissue dissected by X.H. E.S. and R.B. provided human embryonic brain tissue. D.v.B. performed the human forebrain single-cell RNA-seq experiment under supervision of G.C.-B. J.G. assisted with measurement and interpretation of mouse bone marrow. The paper was read and approved by all co-authors.

Competing interests The authors declare no competing interests.

Additional information

Extended data is available for this paper at <https://doi.org/10.1038/s41586-018-0414-6>.

Supplementary information is available for this paper at <https://doi.org/10.1038/s41586-018-0414-6>.

Reprints and permissions information is available at <http://www.nature.com/reprints>.

Correspondence and requests for materials should be addressed to S.L. and P.V.K.

Publisher's note: Springer Nature remains neutral with regard to jurisdictional claims in published maps and institutional affiliations.

METHODS

No statistical methods were used to predetermine sample size. The experiments were not randomized. The investigators were not blinded to allocation during experiments and outcome assessment.

Theoretical description of RNA velocity. On the basis of the model of transcription shown in Fig. 1, we developed a computational framework for robust inference of RNA velocity. A detailed description of the theory and computational methods is available as Supplementary Note 1.

Analysis pipeline, parameters and implementations. We implemented the procedures above as two complete pipelines, one in R and one in Python, called *velocyto.R* and *velocyto.py*, respectively. These were used to generate all of the analyses in the paper, with detailed settings as described in the following sections.

Annotation of spliced and unspliced reads. Read annotation for all protocols was performed using *velocyto.py* command-line tools. The *velocyto.py* annotation starts with BAM file(s). For the 10x genomics platform datasets, the BAM file was processed using the default parameters of the Cellranger software (10x Genomics). For the inDrop dataset, the reads were demultiplexed using *dropEst* pipeline¹⁹, using ‘-F -L eiEIBA’ options to produce an annotated BAM file analogous to Cellranger output. For SMART-seq2 data, demultiplexed cell-specific BAM files were fed into *velocyto.py* directly. The genome annotations GRCm38.84 and GRCh37.82 from the Cellranger pre-built packages were used to count molecules while separating them into three categories: ‘spliced’, ‘unspliced’ or ‘ambiguous’.

The annotation process considered only reads that could be mapped uniquely. Reads with multiple mappings and reads mapped inside repeat-masked (based on the UCSC genome browser repeat masker output) regions were discarded. For UMI-based protocols, the counting was performed at the level of molecules, taking the annotation (such as spliced, unspliced, etc.) of all reads associated with that molecule (supporting read sets) into consideration. The supporting read sets for each molecule were determined by a combination of cell barcode and UMI sequence. For inDrops datasets, where UMI barcode does not have sufficient complexity to uniquely identify a molecule in the dataset, the reads were grouped based on the cell barcode, UMI and the region of the genome where it mapped (chromosomes, binned in 10-Mb regions). For each molecule, all annotated transcripts that were compatible with the given set of read mappings were considered, and cases where the set of reads associated with a given molecule was not compatible with any annotated transcript model were discarded. Cases where a set of supporting read mappings was compatible with transcript models of two or more different genes were also discarded.

The following set of rules was applied to annotate a set of reads supporting a given molecule as spliced, unspliced or ambiguous:

1. A molecule was annotated as spliced if all of the reads in the set supporting a given molecule map only to the exonic regions of the compatible transcripts.
2. A molecule was annotated as unspliced if all of the compatible transcript models had at least one read among the supporting set of reads for this molecule mapping that (i) spanned exon-intron boundary, or (ii) mapped to the intron of that transcript.

Molecules for which some of the compatible transcript models had exonic-only mappings, while others included intronic mappings, were annotated as ambiguous and not used in the downstream analyses.

A similar logic was applied when annotating and counting reads for the SMART-seq2 dataset, with the following notable differences: (1) as reads lacked UMIs, each read was considered to be an independent molecule; (2) as the protocol does not distinguish strands, transcript annotations on both strands were considered when annotating each read.

Chromaffin dataset processing. Data analysis for Fig. 2. Chromaffin datasets of mice aged embryonic day (E)12.5 and E13.5 were processed using the *velocyto.R* pipeline. The γ coefficients and velocity estimates were calculated for genes meeting a number of filtering criteria: $\gamma \geq 0.1$; Spearman rank correlation between s and $u \geq 1$; average s counts for a gene ≥ 5 for at least one cell subpopulation (cluster); average u counts for a gene ≥ 1 for at least one cell subpopulation; for the datasets where spanning reads were annotated (E12.5, E13.5), average spanning read counts were required to be ≥ 5 in at least one subpopulation. For SMART-seq2 datasets, the abundance of reads spanning intron and exon boundaries is sufficiently high to enable estimation of the unspliced offset σ . The offset was estimated using linear regression.

Mouse hippocampus dataset analysis. Data analysis for Fig. 3. A total of 18,213 cells were analysed (postnatal day (P)0: 8,113 cells; postnatal day (P)5: 10,100 cells). The embedding was computed on the correlation similarity matrix using *pagoda2* (<https://github.com/hms-dbmi/pagoda2>). In brief, gene variance normalization was performed by fitting a generalized additive model of variance on expression magnitude, and rescaling the gene variance by matching the tail probabilities of log residuals from the *F* distribution to the χ^2 distribution with the degrees of freedom corresponding to the total number of cells. Cell distances were determined as $1 - r_{ij}$, where r_{ij} is Pearson linear correlation of the cell i and j scores on the first 100 principal components of the top 3,000 variable genes in the dataset. Clustering was performed using the Louvain community detection algorithm on the nearest neighbour cell graph ($k = 30$, *pagoda2* implementation).

For the velocity analysis lowly expressed (spliced) genes were excluded (requiring 40 minimum expressed counts and detected over 30 cells) and the top 3,000 high variable genes were selected on the basis of a non-parametric fit of the coefficient of variation (CV) using the mean as predictor (using support vector regression). Only 1,706 genes that had unspliced molecule counts above a detection threshold (25 minimum expressed counts and detected over 20 cells) were kept for the analysis. To normalize for the cell size, the counts were divided by the total number of molecules in each cell, and multiplied by the mean number of molecules across all cells. Spliced and unspliced counts were normalized separately. To reduce dimensionality, PCA was performed and the top 19 variable components were kept on the basis of the explained variance ratio profile. Euclidean distance in this reduced PCA space was used to construct a *kNN* graph ($k = 500$), using a greedy balanced *kNN* algorithm that limits each node to a maximum of $4k$ incoming edges. This graph was used to perform *kNN* pooling. Velocity-based extrapolation was performed using model I assumptions.

Human glutamatergic neurogenesis analysis. Data analysis for Fig. 4. Pseudotime analysis was performed by fitting principal curve in the space of the top four principal components (using the R package *princurve*). The cell positions were projected onto the curve and the length of the arc between projections was used as pseudotime coordinates. The direction of the pseudotime was determined using the velocity field. Clusters were determined using Louvain community detection algorithm on the nearest neighbour graph in the same subspace. For the velocity analysis lowly expressed (spliced) genes were excluded (requiring 30 minimum expressed counts and detected over 20 cells). The top 2,000 most variable genes were selected on the basis of a non-parametric fit of CV versus mean (using support vector regression). A total of 987 genes that had unspliced molecules above a detection threshold (requiring 25 minimum expressed counts and detected over 20 cells; average spliced counts for a gene 0.06 in a subpopulation and average unspliced counts for a gene 0.007 in a subpopulation) were kept for the analysis. To normalize for the cell size, the counts were divided by the total number of molecules in each cell and multiplied by the median number of molecules across all cells. For cell *kNN* pooling, a *k*-nearest neighbour graph ($k = 550$) was constructed based on Euclidean distance in the space of the top six principal components, as described above. The γ coefficients were fit using the extreme quantile fit with diagonal quantiles, as described above.

For the visualizations in Fig. 4b, the following maximum-projection procedure was used to colour the cells according to expression of the pre-defined gene set. First, the (cell-size normalized) expression of each gene included in the set was rescaled, dividing it by the 98th percentile magnitude. After rescaling, each cell was coloured with the colour corresponding to the gene that was expressed at highest level compared to other genes, and the saturation of the colour was chosen to be proportional to the level of expression in the cell. The rescaled expression of the gene was required to exceed 0.45 in order for the cell to be coloured.

Genes whose expression peaks at different stages of neurogenesis were selected using a heuristic gene enrichment score: where μ indicates the average molecule count of a gene and f is the fraction of cells in which the gene is detected. Figure 4d shows a selection of top-enriched genes, spliced and unspliced molecules were brought to a comparable scale by multiplying spliced molecular counts by the estimated γ .

Analysis of mouse oligodendrocytes lineage. Data analysis for Extended Data Fig. 7. We analysed a dataset of oligodendrocyte differentiation from mouse pons extracted from a recently published cellular atlas²⁰. We restricted the analysis to the trajectory of differentiation from OPCs to mature oligodendrocytes by selecting cells that were labelled in the atlas as OPCs, committed oligodendrocyte precursor cells, newly formed oligodendrocytes and myelin-forming oligodendrocytes, for a total of 6,307 cells.

As an initial step, for Extended Data Fig. 7d-f, we performed a straightforward feature selection, first removing genes for which fewer than 15 spliced molecules were expressed, or fewer than 8 unspliced molecules, requiring a minimal average spliced expression of 0.075 and minimal unspliced expression of 0.03 in the highest expressing cluster. A CV-mean fit was used to select the 606 most variable genes.

As the simple procedure above retained significant sex-driven batch effect (shown in Extended Data Fig. 7e), we then used a different approach aimed at minimizing batch effects by focusing on the genes that were uniquely relevant to the observed oligodendrocytes. Specifically, a list of genes enriched in the oligodendrocyte lineage when compared to all other cell types was used to analyse the dataset. For each cell cluster we used the top 190 genes as sorted by enrichment (differential upregulation) scores, calculated as described²⁰. The resulting set of genes was subjected to further filtering where lowly detected genes were excluded, requiring at least 5 spliced and 3 unspliced mRNA molecules detected in the whole dataset, resulting in 606 genes. We then normalized the cell total molecule counts using the initial molecule count as a normalization factor. For cell *kNN* pooling we built a *k*-nearest neighbour graph ($k = 90$) based on Euclidean distance in the top nine principal components. Data were clustered using a Louvain community

detection algorithm on the nearest neighbour graph and coloured according to a pseudotime computed by a principal curve. Finally, we calculated gammas, velocity and extrapolation as described above; transition probabilities were computed using $n_sight = 300$ and log transform.

Analysis of visual cortex response to light simulation. Data analysis for Extended Data Fig. 5. For the pre-processing of the inDrops light-stimulated mouse visual cortex dataset²¹ we used the dropEst pipeline (<https://github.com/hms-dbmi/dropEst>). First the droptag command was run on each FASTQ file using 10 as the minimum quality parameter. Then, mapping was performed using the STAR aligner. Finally, the dropEst command was run to perform UMI and cell barcode correction, and the following flags were passed ‘-m -V -b -L eiEIBA’ to produce a Cellranger-like BAM file. The velocyto.py ‘run_dropes’ command was used to annotate and count molecules.

Cell annotations from the original publication²¹ were used to extract ExcL23_1 (the largest and most homogeneous cell population described as responsive to stimulus in the original publication). We excluded cells whose total spliced RNA abundance was below the 15th percentile (as low-quality cells) and above the 99.5th percentile (as possible doublets). The dataset was further balanced by equalizing the number of cells representing each stimulation condition (unstimulated, 1-h stimulation, 4-h stimulation), randomly down-sampling subpopulations to match the number of cells in the less abundant condition. Genes whose total spliced molecule count was less than 250, or the number of expressing cells was less than 150 were removed. Similarly, we removed genes whose total unspliced molecule count was less than 18, or the number of expressing cells was less than 15. To focus our analysis on the stimulation process and to avoid capturing orthogonal variation, we performed a model-based feature selection. In brief, we considered a negative binomial generalized linear model with predictors: size (as estimated by the total number of molecules), the stimulation time (categorical and interaction with size) and no offset (that is, correspondent to the R formula: expression \approx size + size: stimulation – 1). We then performed a likelihood ratio test comparing our model against the alternative model that does not take the stimulation predictor into account. Only statistically significant genes ($P < 0.001$ for spliced and $P < 0.03$ for unspliced molecules) were considered for downstream analysis. After this step, we further eliminated the cells ranking in bottom 10% of total molecular counts over all of the selected genes. For the cell kNN pooling, we built a k -nearest neighbour graph ($k = 70$) based on the Euclidean distance. Importantly, in this case, we reasoned that it was not correct to average across different independent stimulation conditions (for example, non-stimulated and 1-h stimulation), therefore pooling was only allowed between cells of the same stimulation condition. Model 2 was used for velocity-based extrapolation, with t set to 15. For the transition probability calculation, the n_sight parameter was set to 200, and square root was used as a variance stabilizing transformation. Early and late response genes illustrated in Extended Data Fig. 6 were extracted from the supplementary table 3 of the original publication, containing a list of significantly induced genes in different cell types²¹.

Analysis of gammas over different cell types using Tabula Muris. Data analysis for Extended Data Fig. 3. The Tabula Muris dataset (including only the samples generated using droplet-based 10x Genomics Chromium protocol) was analysed using velocyto.py, using the BAM files and the valid barcodes list provided by the authors¹¹. All of the experiments were merged into a single dataset. The average of spliced and unspliced raw molecule counts over the different annotated cell types were calculated, and Pearson’s correlation coefficient was computed. To reduce bias associated with variation in cell coverage, we removed from the analysis the clusters with less than 120 cells as well as several outlier clusters that had more than 3,000 cells. Erythrocytes were also excluded, as they lack nuclei. To avoid inflating our correlations with trivial cases where a gene is expressed by just one or two cell types we applied the following filters: a gene was taken into consideration only if its expression levels met all of the following conditions: (1) at least 5 cell types with an average of at least 0.04 spliced molecules; (2) at least 4 cell types with an average of at least 0.02 unspliced molecules; (3) the highest expressing cell type expressed the gene at an average of at least 0.15 spliced molecules; (4) at least 2 other cell types express the gene at least 15% the level of the maximum expressing cell type. Furthermore, to avoid the inflation of correlation estimates by zeros, the correlation of each gene was calculated considering only the cell types that expressed the gene at minimum 10^{-5} spliced and 5×10^{-6} unspliced levels. The estimates of gammas provided in Extended Data Fig. 3 were obtained as the slope of RANSAC regression without intercept. Double gammas were estimated using a mixture of generalized linear regression models fitted by expectation maximization, as implemented in the R package flexmix. The fraction of genes that are better explained by two or more values of gammas than by a single gamma was estimated by comparing the double gamma model fit with a single-gamma generalized linear model fit. Specifically, a log-likelihood ratio test was used with the difference in degrees of freedom between the single- and double-gamma models taken to be the number of cell types + 1. Bonferroni correction was applied, and genes with $P < 0.05$ were reported as being significantly better explained by two gammas.

Analysis of the intestinal epithelium. Data analysis for Extended Data Fig. 6. velocyto.py was run on the BAM files and the valid barcode list provided by the authors. Cells with low levels of spliced (<2,000 molecules) and unspliced (<300 molecules) genes were filtered out. Cell cycle genes, as defined by gene ontology annotation (using Goatools) were removed from the analysis. Genes with at least 30 spliced molecules and 20 unspliced molecules in the dataset were used in the downstream analysis. No clustering was performed, instead, the cell type annotation from the original publication²² was used. Feature selection was performed using these clusters. Specifically, the top 110 differentially upregulated genes in each cluster were selected. Genes for which minimum average expression in the highest expressing cluster was low were removed (unspliced <0.008 , and spliced <0.08). PCA was performed on the cell-size-normalized data, and the first nine principal components were retained and used to calculate the t-SNE plot (cytograph implementation, Euclidean distance). We calculated cell kNN pooling using the 70 nearest neighbours, as determined by the Euclidean distance in the same nine dimensional PCA space. Gammas were fitted, velocities computed using default parameters, and extrapolation carried on using model II with $t = 4$. Transition probability was computed using n_sight of 30, using square root variance stabilizing transformation.

Human tissue and single-cell RNA sequencing. Data analysis for Fig. 4. Human first trimester forebrain tissue was obtained from elective routine abortions (10 weeks post-conception) with the written informed consent of the pregnant woman and in accordance with the ethical permit given by the Regional Ethics Vetting Board (Stockholm, Sweden, reference no. 2007/1477-31/3; for scRNA-seq), as well as from Addenbrooke’s Hospital, Cambridge, UK with approval by the National Research Ethics Service Committee East of England - Cambridge Central (Local Research Ethics Committee, reference no. 96/085; for in situ hybridizations). Human fetal forebrain tissue was collected and stored in hibernation media with the addition of GlutaMAX and B-27 supplements according to the manufacturer’s instructions (overnight, 4°C, Hibernate-A, Thermo-Fisher). The tissue was then cut into small cubic pieces of approximately 1–2 mm length. Tissue was dissociated using a dissociation kit (Miltenyi, Neural Tissue Dissociation Kit (P)) according to the manufacturer’s instructions. In brief, tissue was prepared in the kit buffer containing 0.067 mM β-mercaptoethanol. After addition of enzyme mix 1 and 2, the tissue was mechanically dissociated using three increasingly smaller gauges of fire-polished Pasteur pipettes, pipetted 20, 15 and 10 times up and down, respectively. Finally, collected cells were stored on ice in PBS containing 1% BSA and immediately prepared for single-cell library preparation. Single-cell RNA sequencing was performed using the 10x Genomics Chromium V2 kit, following the manufacturer’s protocol, and sequenced on an Illumina HiSeq 2500.

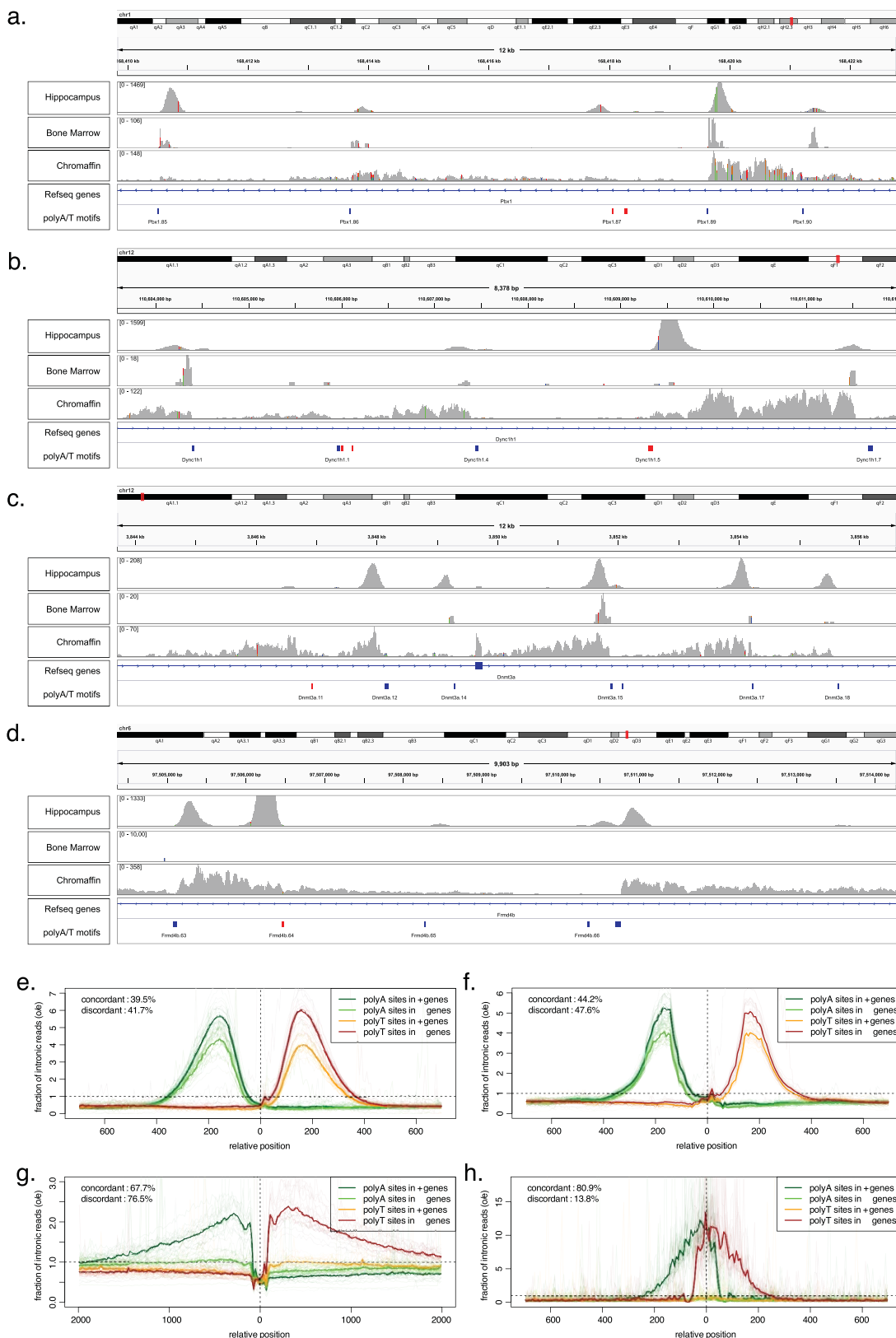
Ethical compliance for animal experiments. All experimental procedures followed the guidelines and recommendations of Swedish animal protection legislation and were approved by the local ethical committee for experiments on laboratory animals (N68/14, Stockholms Norra Djurförsöketiska nämnd, Sweden).

Reporting summary. Further information on experimental design is available in the Nature Research Reporting Summary linked to this paper.

Code availability. The software described in this paper, in the form of a pipeline called Velocyto (from velox, quick and κύτος, cell) is available at <http://velocyto.org>. This includes complete analysis libraries in R and Python, as well as R and Python notebooks.

Data availability. The data from mouse P0 and P5 hippocampus was extracted from dataset C²³, available from the Gene Expression Omnibus (GEO) under accession GSE104323. The oligodendrocyte differentiation dataset was obtained from a recent survey of the mouse nervous system²⁰ (Sequence Read Archive (SRA) accession SRP135960). The bulk mouse liver circadian variation RNA-seq data¹² is available at SRA accession SRA025656. The SMART-seq2 data on chromaffin cell differentiation¹³ is available at GEO accession GSE99933. The mouse bone marrow dataset¹⁹ is available at GEO accession GSE109989. The visual cortex inDrop dataset²¹ is available at GEO accession GSE102827. The intestinal epithelium dataset²² is available at GEO accession GSE92332. We have deposited the human week 10 fetal forebrain dataset in the SRA under accession code SRP129388 and the metabolic labelling data in the GEO under accession code GSE115813. All other data are available from the corresponding authors upon reasonable request.

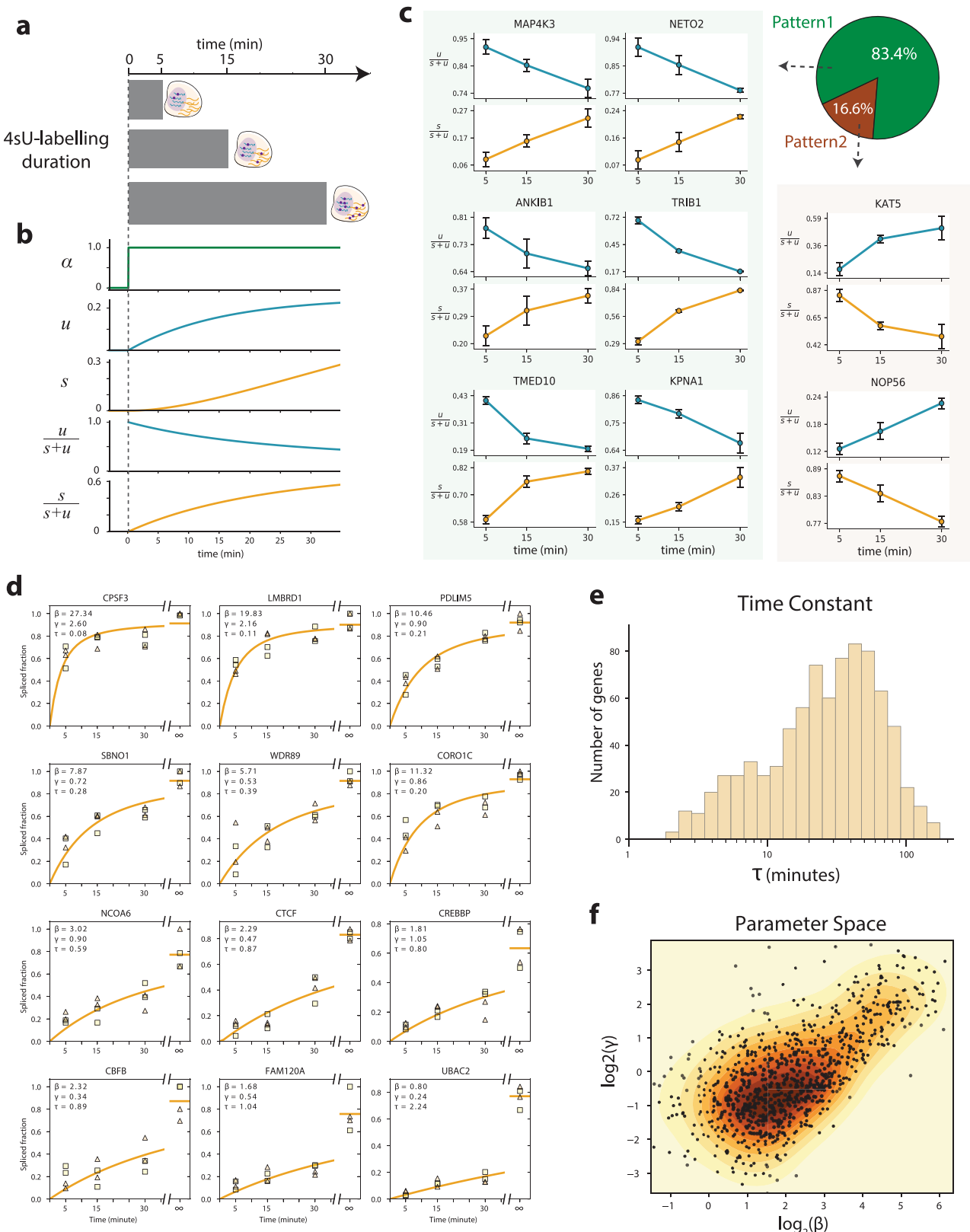
19. Petukhov, V. et al. dropEst: pipeline for accurate estimation of molecular counts in droplet-based single-cell RNA-seq experiments. *Genome Biol.* **19**, 78 (2018).
20. Zeisel, A. et al. Molecular architecture of the mouse nervous system. Preprint at <https://bioRxiv.org/content/early/2018/04/06/294918> (2018).
21. Hrvatin, S. et al. Single-cell analysis of experience-dependent transcriptomic states in the mouse visual cortex. *Nat. Neurosci.* **21**, 120–129 (2018).
22. Haber, A. L. et al. A single-cell survey of the small intestinal epithelium. *Nature* **551**, 333–339 (2017).
23. Hochgerner, H., Zeisel, A., Lönnérberg, P. & Linnarsson, S. Conserved properties of dentate gyrus neurogenesis across postnatal development revealed by single-cell RNA sequencing. *Nat. Neurosci.* **21**, 290–299 (2018).
24. Lein, E. S. et al. Genome-wide atlas of gene expression in the adult mouse brain. *Nature* **445**, 168–176 (2007).



Extended Data Fig. 1 | See next page for caption.

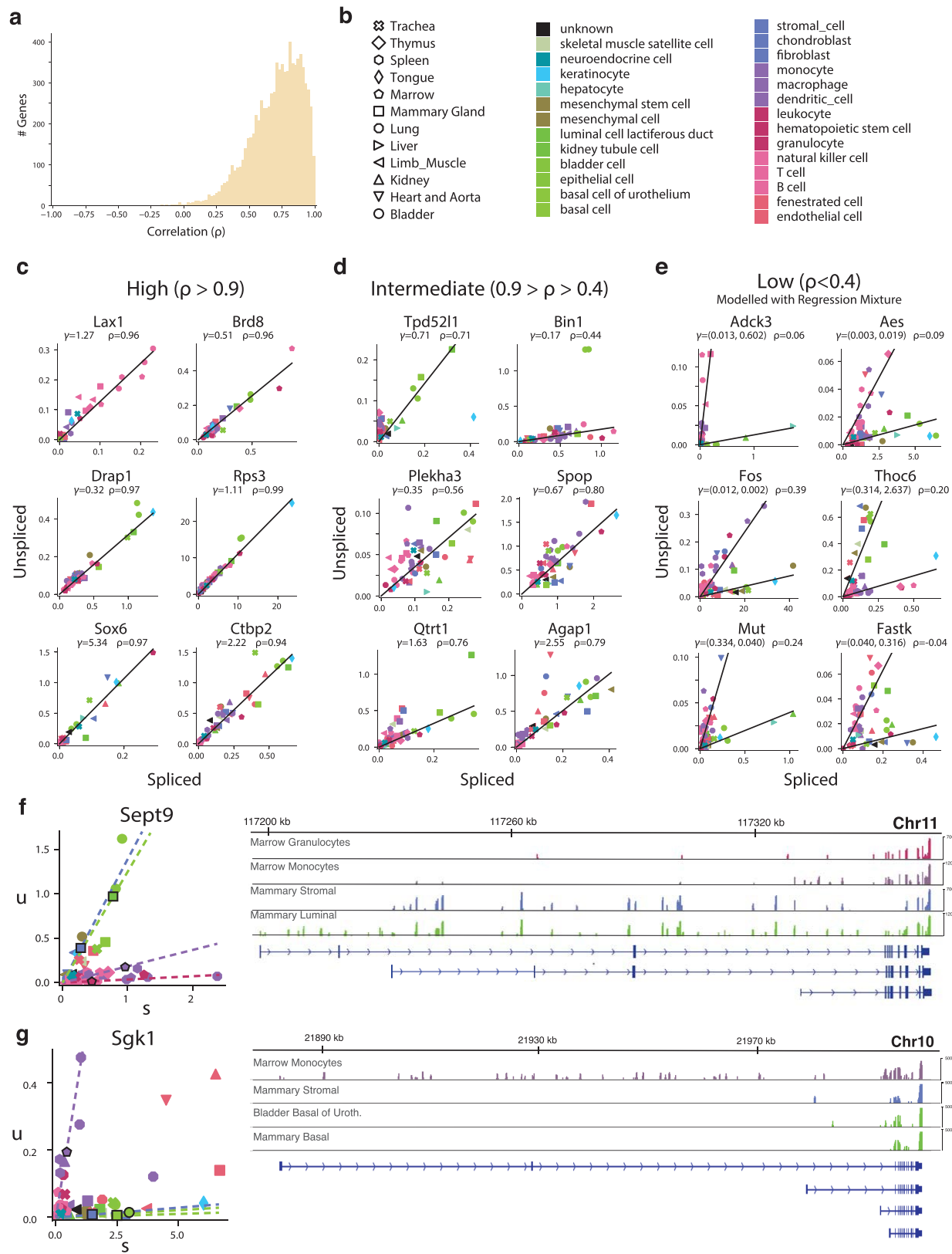
Extended Data Fig. 1 | Most of the intronic reads arise due to internal priming from stable positions. **a–d**, Examples of read density around intronic polyA and polyT sequences. The browser screenshots show the density of reads from the 10x Chromium mouse hippocampus dataset (top track of each panel), mouse bone marrow inDrop dataset (second track from the top), and chromaffin differentiation assessed using SMART-seq2 (third track). The bottom two tracks show gene annotation, and positions of polyA or polyT sequences with a length of at least 15 bp with one allowed mismatch. The polyA/polyT boxes are coloured blue if the stretch is in a concordant orientation to the transcription of the underlying gene (that is, would result in a polyA sequence in the nascent RNA molecule being transcribed), or red if they are oriented in the discordant position (that is, would result in a polyT sequence in the RNA). The 3'-end-based 10x Chromium and inDrop protocols show discrete peaks downstream of the polyA priming sites, with the 10x dataset also showing peaks upstream of the polyT sites. The SMART-seq2 protocol shows much more diffused peaks, expected from the full-length purification procedure used by the protocol. **e–h**, Average read density profiles around concordant and discordant internal priming sites. The

plots show observed/expected intronic read density around (A)₁₅ or (T)₁₅ sequences (with 1 allowed mismatch) within the intronic regions. The x axis shows position relative to the motif position (in basepairs), in a genomic reference orientation. The bold lines show genome-wide average (trimmed of two extreme values among chromosomes for each position). The averages of individual chromosomes are shown as semi-transparent lines. **e**, Profiles of mouse hippocampus 10x Chromium dataset ($n = 18,213$). **f**, Profile for human forebrain 10x data ($n = 1,720$). **g**, Profile for the chromaffin differentiation data measured using SMART-seq2 ($n = 385$). **h**, Profile for the mouse bone marrow data measured using inDrop ($n = 3,018$). The top left corner of each plot shows the number of all intronic reads (that is, falling within the gene, but not touching an exon) that falls within the 250 bp around internal priming sites (1,500 bp was used for the SMART-seq2 dataset). In 10x data, while concordant internal priming sites produce stronger signal, their frequency within the genome is lower than those of discordant sites, so that overall discordant sites account for slightly higher fraction of intronic signals. By contrast, the inDrop dataset appears to have very limited discordant priming.



Extended Data Fig. 2 | Estimation of the characteristic time of RNA metabolism in human cells. **a**, Design of the metabolic labelling experiment in human cells. HEK293 cells were exposed to 4-thiouridine (4sU) for 5, 15 or 30 min, and the labelled fraction was isolated and analysed. A no pull-down control was also analysed, and represents the equilibrium state (indicated by ∞). **b**, Expected profiles of the abundance and fraction of labelled spliced and unspliced RNA molecules. **c**, The observed dynamic profiles of genes were clustered, yielding two groups:

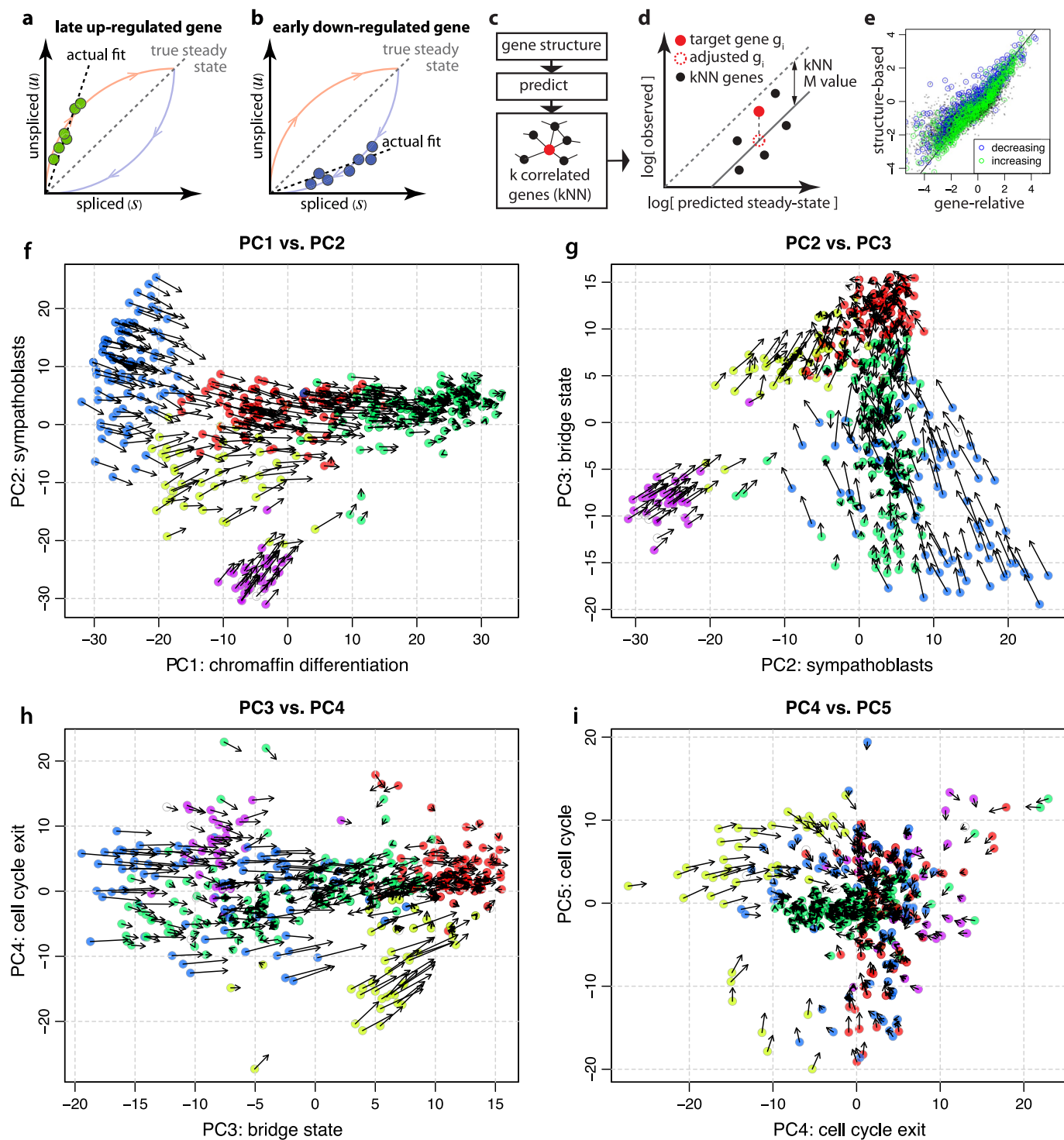
the majority (83.4%) were concordant with the expectation of increasing labelling; and a smaller fraction (16.6%) of discordant genes. Bars indicate s.e.m. $n_{\text{genes}} = 998$, $n_{\text{technical}} = 2$, $n_{\text{biological}} = 2$. **d**, Curves showing maximum likelihood fit to the data, based on the analytical solution for a step increase in the transcription rate. The fit yields values of β and γ , and of the characteristic time constant τ , defined as the time required to reach $1 - 1/e \approx 63.2\%$ of the asymptotic value. **e**, The distribution of τ values. **f**, The joint distribution of the fit β and γ parameters ($n = 832$).



Extended Data Fig. 3 | Degradation rates are conserved over a wide range of terminally differentiated cell types. Conservation of the RNA degradation rate over a wide range of different cell types in the adult mouse (Tabula Muris dataset). **a**, The distribution over the genes of the correlation of spliced and unspliced molecule counts across all the cell types ($n_{\text{genes}} = 8,385$). **b**, Legend enumerating the tissues and cell classes annotated by the Tabula Muris consortium ($n = 48$). Functionally, developmentally or phenotypically related classes are coloured with

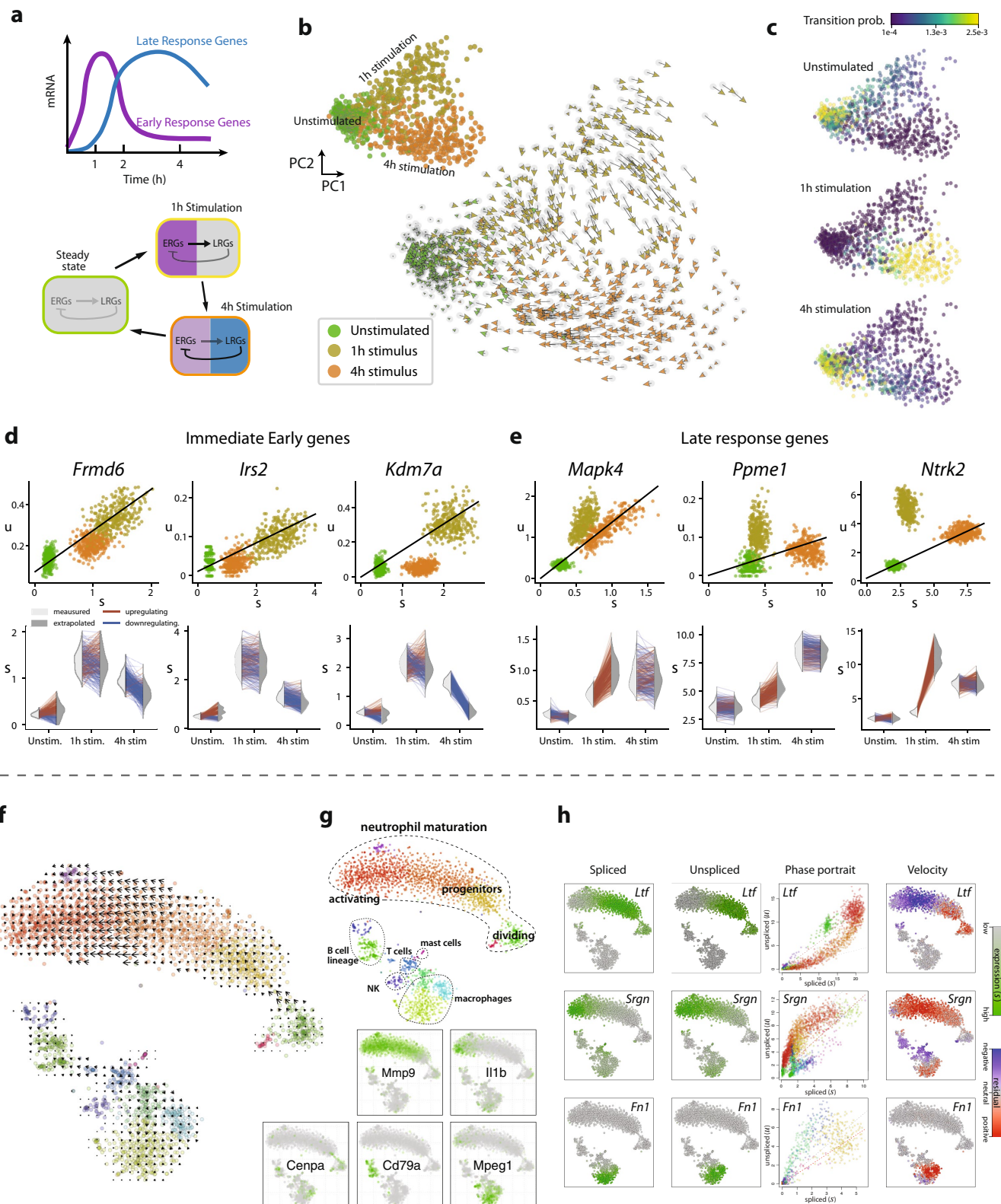
similar colours to aid the interpretation of the plots below.

c, d, A representative selection of genes with high correlation ($\rho > 0.9$) (**c**) and typical correlation ($0.9 > \rho > 0.4$) (**d**). γ was estimated by robust linear regression (RANSAC). **e**, Plots show a selection of genes displaying two clearly distinct degradation rates (such genes with double γ amounted to 10.8% of the total). The values of the two different γ were estimated by regression mixture modelling. **f, g**, Two examples of genes where multiple values of γ are explained by alternative splicing in different cell types.



Extended Data Fig. 4 | Structure-based velocity estimation. **a, b**, For genes that are observed only outside of the steady state, such as genes upregulated late in the chromaffin differentiation (**a**) or downregulated early in the Schwann cell precursors (**b**), gene-relative γ fit is likely to deviate from its steady-state value. **c, d**, To correct for such effects, a structure-based γ fit will first predict γ for every gene based on its structural parameters, and then use the k most correlated genes in the dataset to adjust M value ($M = \log_2(u_o/u_{ss})$, where u_{ss} is the unspliced

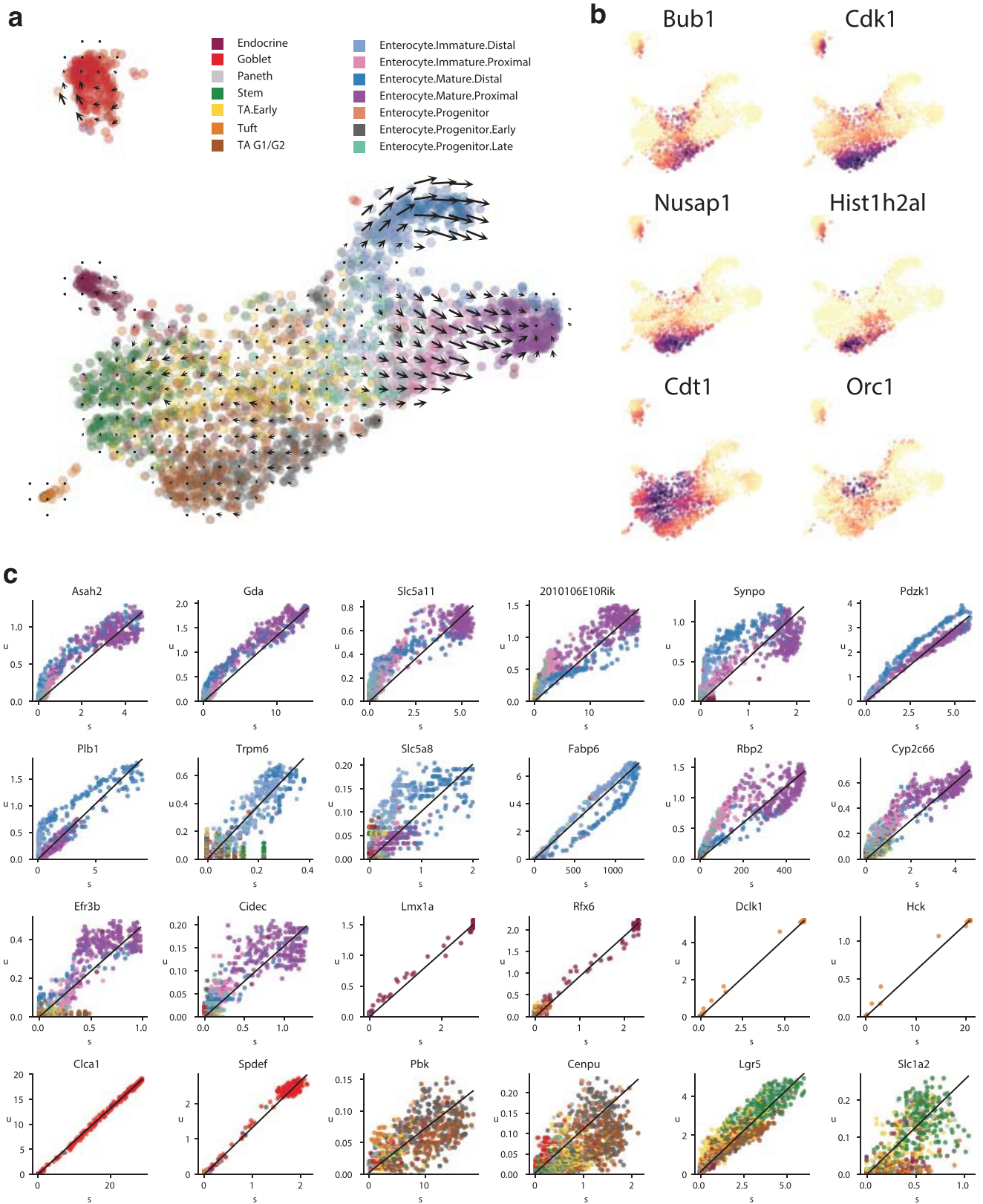
counts predicted from spliced counts under steady-state, and u_o is the observed unspliced count) using robust mean, and re-estimate γ . **e**, Scatter plot comparing gene-relative and structure-based γ estimates, with coloured circles highlighting γ adjustments for genes downregulated early in SCPs (blue) and upregulated late in chromaffin cells (green). The values are shown on a natural log scale. **f-i**, Cell expression velocity in the chromaffin E12.5 dataset, based on the structure-based γ estimates, shown on the first five PCs.



Extended Data Fig. 5 | See next page for caption.

Extended Data Fig. 5 | RNA velocity analysis of inDrop datasets: visual stimulus response of cortical pyramidal neurons and neutrophil differentiation. **a**, Simplified illustration of a model of activation of pyramidal neurons of the visual cortex after exposure to a light stimulus. **b**, Velocity estimates projected onto a two-dimensional PCA plot of the dataset ($n = 952$). **c**, Average transition probability of unstimulated cells (top), cells stimulated for 1 h (middle) and cell stimulated for 4 h (bottom). The unstimulated cells mostly were stationary and only few cells show the tendency of activating early response genes (probably as a result of the dissociation procedure). Cells stimulated for 1 h were characterized by expressing immediate early genes and high velocity in late response genes, and they were, therefore, transitioning to a state more similar to the one observed for the 4-h activation time point. After 4 h of stimulations cells appeared to be reverting to a state comparable to the unstimulated sample (bottom). **d, e**, Top panels, phase portraits of early (**d**) and late (**e**) response genes. Bottom panels, violin plots show expression distribution over the cell population at each time point (left half of the violin) and extrapolation to the future using velocity (right half of the violin). In the plot, transitions

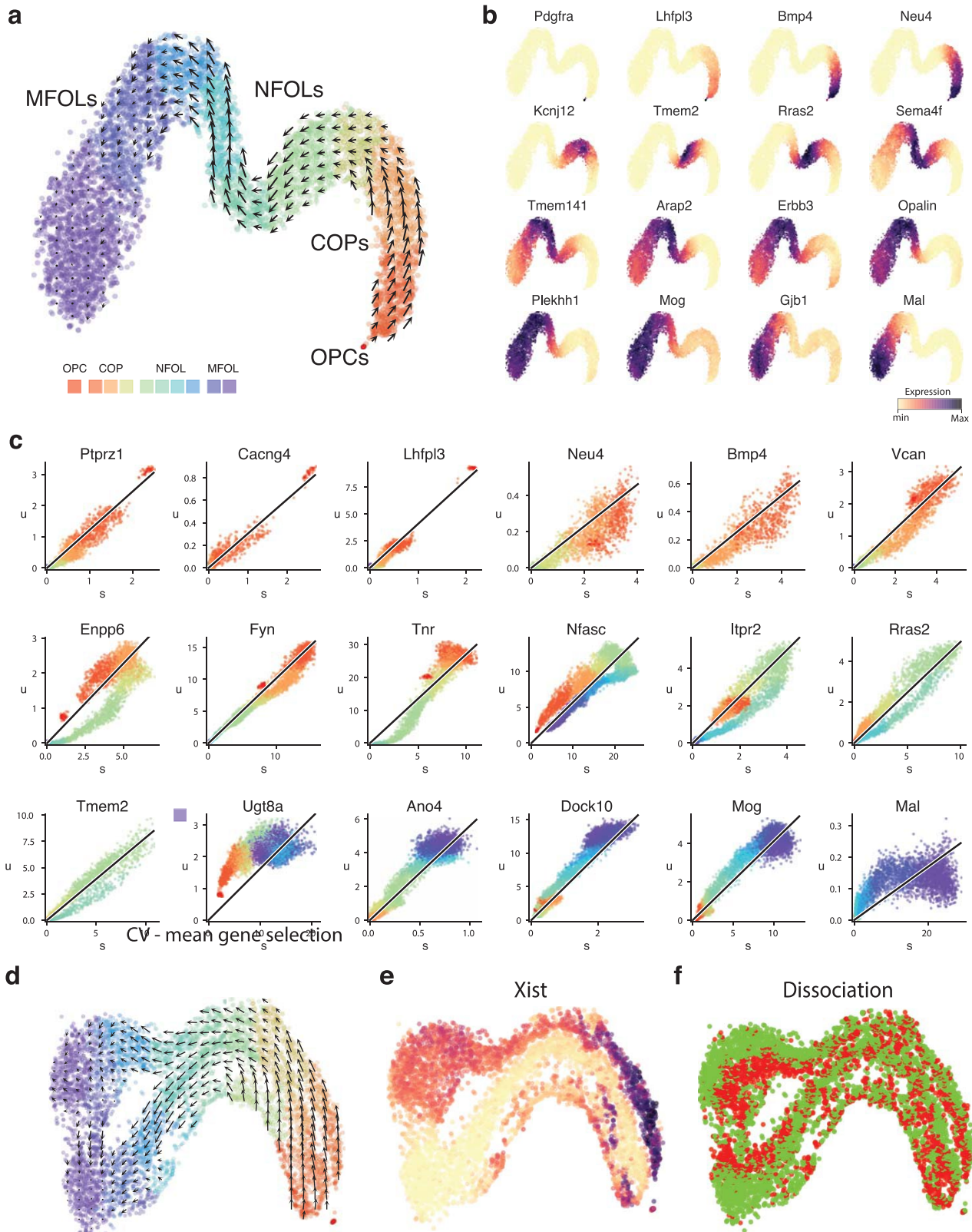
of single cells are indicated by lines connecting the two halves of the violins and coloured by the sign of the velocity of each gene. **f**, Grid visualization shows cell expression velocity estimates for the inDrop mouse bone marrow dataset on a t-SNE plot ($n = 3,018$). **g**, Major cell populations are labelled based on manual annotation. The velocity flow in **a** captures neutrophil maturation, starting from the dividing cells on the right, all the way to *Il1b* activation on the left. Expression profiles for five marker genes are shown below. **h**, The plots illustrate gene-relative model fits for several example genes. For each gene, the first column shows spliced molecular counts in different cells. The second column shows unspliced molecular counts. The third column shows phase portrait of a gene (unspliced versus spliced dependency) and the resulting γ fit (dashed red line), as determined using extreme quantile method. Each point corresponds to a cell, coloured according to cluster labels shown in **g**. The last column shows unspliced count signal residual based on the estimated γ fit, with positive residuals indicating expected upregulation, and negative residuals indicating expected downregulation of a gene.



Extended Data Fig. 6 | See next page for caption.

Extended Data Fig. 6 | Dynamics of maturation of enterocytes during intestinal homeostasis. **a**, Velocity field projected on a 2D t-SNE plot. The clusters are labelled and coloured as in the original publication¹¹ to facilitate comparison ($n = 2,683$). Velocity analysis revealed a transition related to the maturation of distal and proximal enterocytes. No consistent velocity was observed in the part of the manifold occupied by stem cells and transit amplifying (TA) cells, suggesting that stem cell dynamics are more difficult to capture either for their slower rate or a more stochastic nature. The small velocities of transit amplifying cells were likely to be driven by the cell cycle. **b**, A selection of the cell cycle genes that were

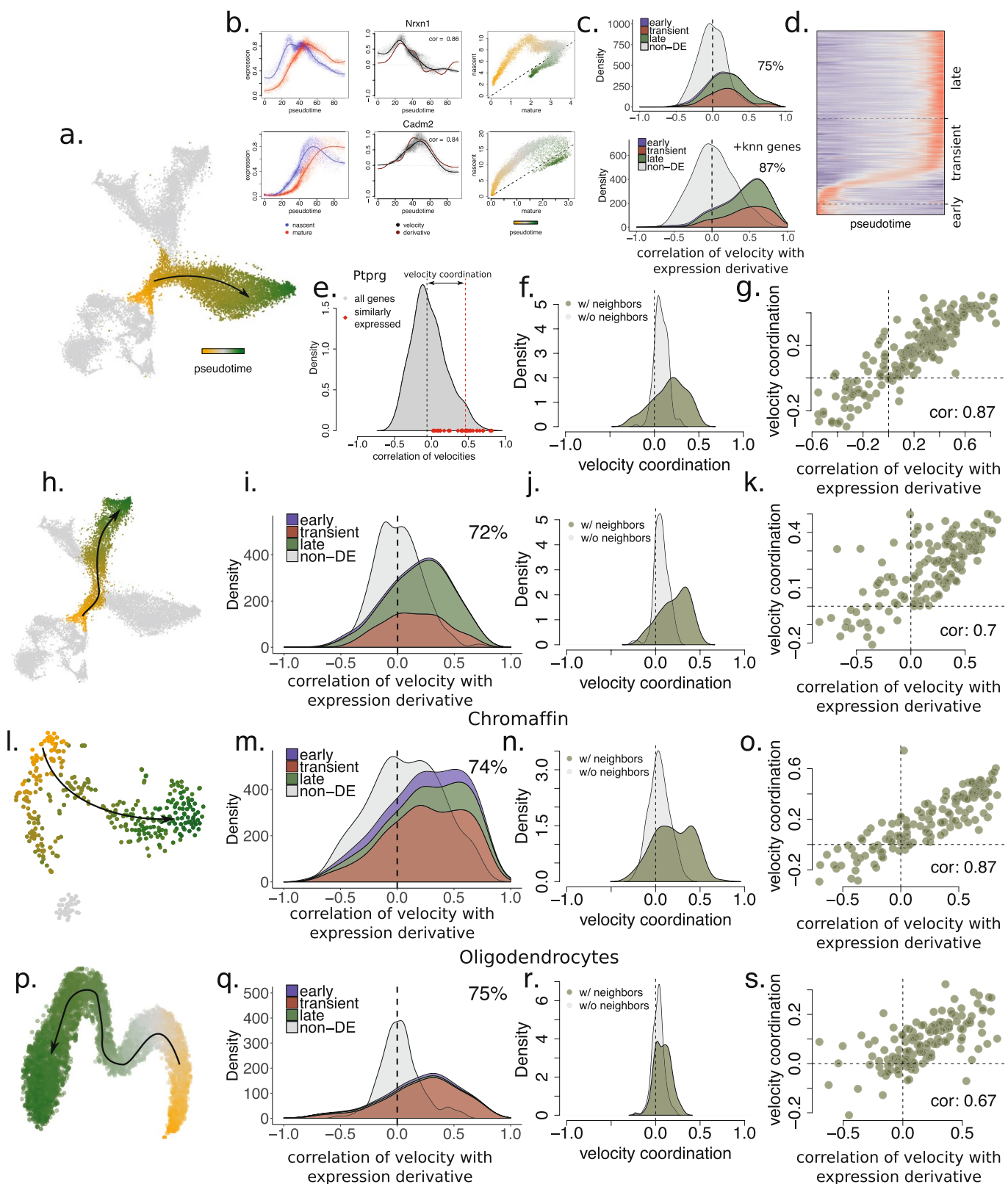
removed from the analysis is plotted on the t-SNE. Despite the removal of the genes annotated as cell cycle genes, we still observed important segregation by cell cycle, illustrating the difficulty of disentangling cell cycle phase from the cell state. **c**, A selection of phase portraits that show genes underlying the observed velocity field. Markers of endocrine, goblet and tuft cells displayed no detectable velocity. Velocity towards and from stem cell states was detectable for a limited set of genes (such as the stem cell marker *Lgr5*), however, on the genome-wide level, the exact dynamics of this process was probably confounded by the high correlation with cell cycle.



Extended Data Fig. 7 | See next page for caption.

Extended Data Fig. 7 | RNA velocity unveils the dynamics of differentiation and myelination of oligodendrocytes. **a**, *t*-SNE projection shows the landscape of oligodendrocyte lineage differentiation and myelination process in the hindbrain (pons) of adolescent (P20) mice ($n = 6,307$). The velocity field reflects the dynamics of expression of both the initial differentiation wave and the following expression changes associated with the myelination process. The cell clusters are coloured by pseudotime as in **c** to facilitate interpretation. **b**, Expression patterns of landmark genes of the differentiation process. *Pdgfra* is the canonical marker of oligodendrocyte precursors (OPCs), *Neu4* marks committed oligodendrocyte precursors (COPs), *Tmem2* is enriched in newly formed oligodendrocytes (NFOLs) and the expression of *Mog* is upregulated at the

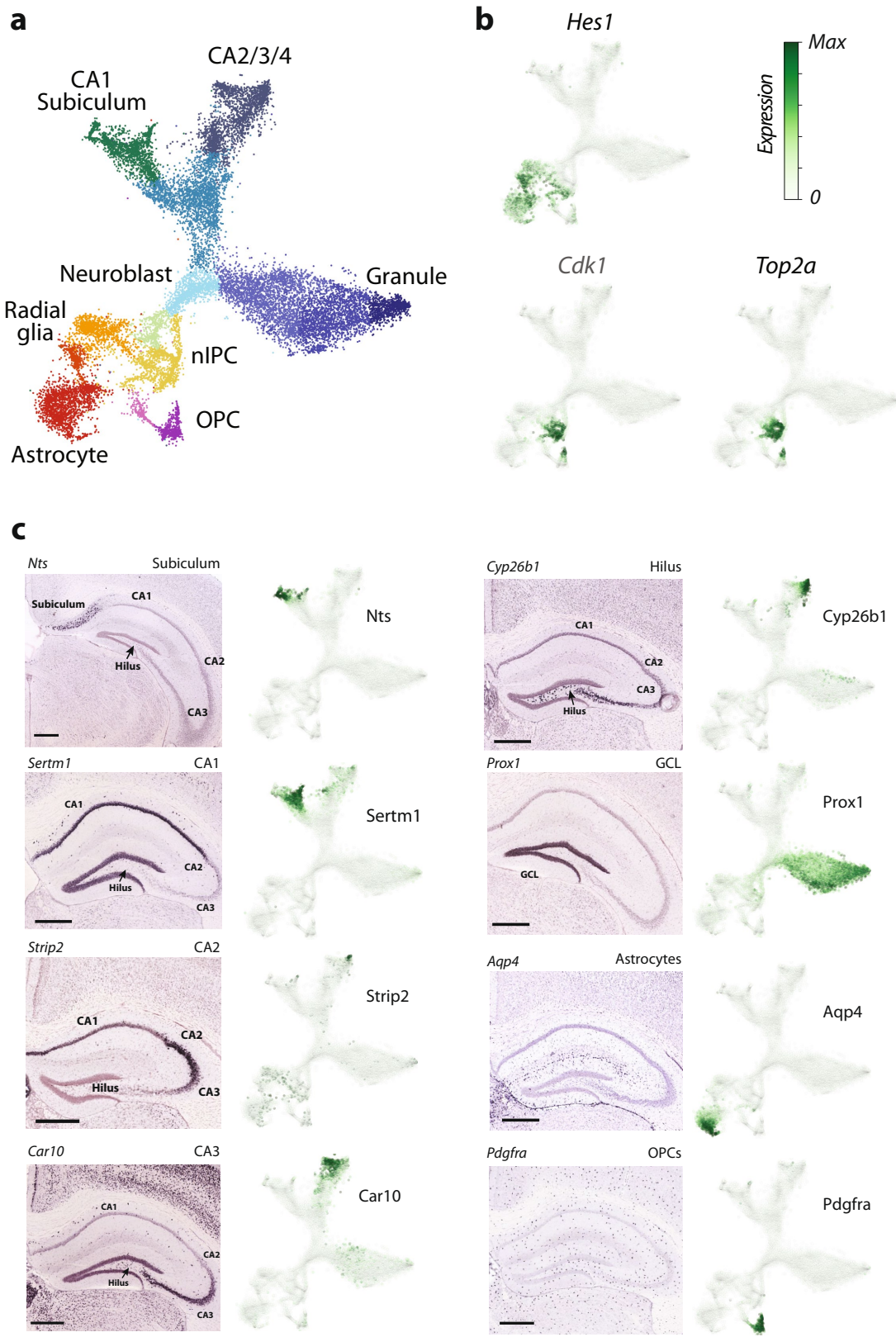
beginning of the myelination process in myelin-forming oligodendrocytes (MFOLs). **c**, A selection of phase portraits underlying the velocity field shown in **a**. **d**, *t*-SNE projections and velocity vector field of the same dataset, but analysed using a more naive feature selection that has retained other axes of variation on top of the oligodendrocyte maturation (sex and day of dissection). Notice that despite the separation of populations into *Xist*⁺ and *Xist*⁻ tracks, the velocity field correctly captures progression from progenitors to newly formed oligodendrocytes in the two parallel tracks. **e**, Level of expression of *Xist* showing that most of the extra variation is driven by the sex of the animal. **f**, Cells coloured by the day on which the experiment was performed.



Extended Data Fig. 8 | See next page for caption.

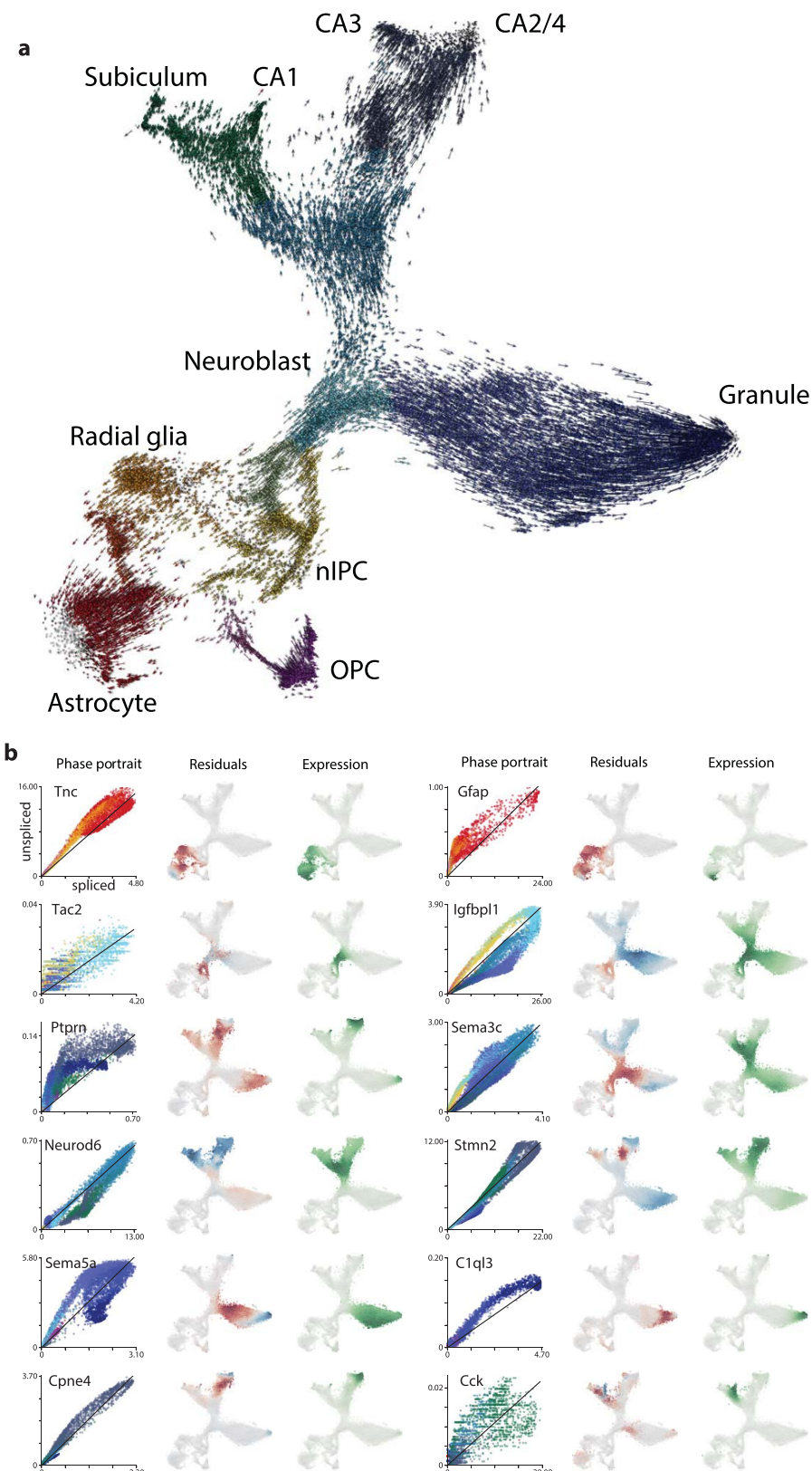
Extended Data Fig. 8 | Agreement of velocity predictions with the observed expression derivatives. **a**, Maturation progression of granule neurons in the mouse hippocampus dataset is approximated by pseudotime (estimated with a principal curve). **b**, For a pair of example genes (rows), the plots show unspliced and spliced gene expression profiles along the pseudotime (left panels), empirically estimated smoothed pseudotime derivative of the observed gene expression and the estimated RNA velocity (middle panels), as well as the relationship between spliced and unspliced expression (right panel). The velocity estimates for the two chosen genes are highly correlated with the empirically observed derivative, indicating accurate velocity estimation. **c**, The majority (75%) of the genes that were differentially regulated along the pseudotime trajectory showed a positive correlation with the empirical expression derivative. The distribution of such genes is split according to three classes of trajectory-associated genes as shown in **d**. By contrast, velocity estimates for genes that were not differentially expressed along the pseudotime trajectory did not show such correlation (grey). Incorporating information about co-regulated genes into velocity estimation using gene *k*NN clustering (see Supplementary Note 1) can significantly boost the accuracy of the velocity predictions (lower panel). **d**, Trajectory-associated genes were classified as early, transient and late, according to their peak expression time. *x* axis, cells ordered by pseudotime; *y* axis, genes ordered by their peak expression time. **e**, The genes that were well-correlated in terms of their spliced expression patterns with *Ptprg*, also showed a high

correlation of their velocity estimates with *Ptprg*. To assess the degree of consistency of the velocities of co-regulated genes, we introduced a measure of velocity coordination for a given gene, as a difference between the mean correlations of the velocity estimates of the co-regulated genes and the velocity estimates of all genes. The two quantities being compared are shown for *Ptprg* with dotted vertical lines: grey, mean velocity correlation with all genes; red, mean velocity correlation with top co-regulated genes. Velocity coordination provides an unbiased measure of quality for velocity estimates. **f**, Velocities of co-regulated genes were correlated. Distribution of gene velocity coordination values is shown for genes that had co-regulated genes (that is, the genes that had well-correlated gene neighbours in terms of their spliced expression pattern, green), as well as for the genes that did not have enough co-regulated genes (without neighbours, grey). **g**, Co-regulated genes that had high velocity coordination tended to have high correlation with the empirical derivatives. Spearman correlation coefficient is shown. **h–k**, Velocity performance during maturation of pyramidal neurons (**h**). Genes differentially expressed during maturation had high correlation of velocity with empirical derivative (**i**), co-regulated genes tended to have correlated velocity estimates (**j**) and the degree of velocity coordination was associated with its correlation with empirical derivative (**k**). **l, m**, Velocity performance during chromaffin differentiation. **p–s**, Velocity performance during maturation of oligodendrocytes. Number of top co-regulated genes analysed for velocity correlation: 200 (**g**), 150 (**k, o, s**).



Extended Data Fig. 9 | Branching developmental trajectories of developing hippocampus. **a**, t-SNE plot of the developmental dentate gyrus dataset. Cells are coloured by cluster identities, with labels shown for the major cell types. **b**, Expression of radial glia (and astrocyte) marker *Hes1*, and cell cycle genes *Top2a* and *Cdk1* shown on the t-SNE

plot. **c**, Marker genes of different regions of the hippocampus (in situ hybridization images from Allen Mouse Brain Atlas²⁴) show prominent expression signals at different extremities of the branching plot. Scale bars, 0.5 mm.



Extended Data Fig. 10 | Single-cell velocity estimates for individual cells in the embryonic hippocampus dataset. **a**, Arrows indicate the extrapolated state projected onto the t-SNE plot of the manifold. **b**, Selected phase portraits and fits of the equilibrium slope (γ) for the developing cells in the embryonic hippocampus dataset. For each gene, the first column shows spliced–unspliced phase portrait. The dashed

line shows the γ fit. The second column illustrates the magnitude of the residuals (that is, the difference between observed and expected unspliced abundance, which closely tracks with velocity) for several genes involved in the development of different neural lineages. The third column shows the observed expression profile for spliced molecules.

Suppression of insulin feedback enhances the efficacy of PI3K inhibitors

Benjamin D. Hopkins¹, Chantal Pauli^{2,3}, Du Xing⁴, Diana G. Wang^{1,5}, Xiang Li⁶, David Wu¹, Solomon C. Amadiume¹, Marcus D. Goncalves^{1,7}, Cindy Hodakoski¹, Mark R. Lundquist¹, Rohan Bareja^{1,3,8}, Yan Ma⁴, Emily M. Harris⁴, Andrea Sboner^{1,3,8,9}, Himisha Beltran^{1,3,10}, Mark A. Rubin^{3,11}, Siddhartha Mukherjee^{4*} & Lewis C. Cantley^{1,*}

Mutations in PIK3CA, which encodes the p110 α subunit of the insulin-activated phosphatidylinositol-3 kinase (PI3K), and loss of function mutations in PTEN, which encodes a phosphatase that degrades the phosphoinositide lipids generated by PI3K, are among the most frequent events in human cancers^{1,2}. However, pharmacological inhibition of PI3K has resulted in variable clinical responses, raising the possibility of an inherent mechanism of resistance to treatment. As p110 α mediates virtually all cellular responses to insulin, targeted inhibition of this enzyme disrupts glucose metabolism in multiple tissues. For example, blocking insulin signalling promotes glycogen breakdown in the liver and prevents glucose uptake in the skeletal muscle and adipose tissue, resulting in transient hyperglycaemia within a few hours of PI3K inhibition. The effect is usually transient because compensatory insulin release from the pancreas (insulin feedback) restores normal glucose homeostasis³. However, the hyperglycaemia may be exacerbated or prolonged in patients with any degree of insulin resistance and, in these cases, necessitates discontinuation of therapy^{3–6}. We hypothesized that insulin feedback induced by PI3K inhibitors may reactivate the PI3K-mTOR signalling axis in tumours, thereby compromising treatment effectiveness^{7,8}. Here we show, in several model tumours in mice, that systemic glucose-insulin feedback caused by targeted inhibition of this pathway is sufficient to activate PI3K signalling, even in the presence of PI3K inhibitors. This insulin feedback can be prevented using dietary or pharmaceutical approaches, which greatly enhance the efficacy/toxicity ratios of PI3K inhibitors. These findings have direct clinical implications for the multiple p110 α inhibitors that are in clinical trials and provide a way to increase treatment efficacy for patients with many types of tumour.

The relationship between PI3K inhibitors and the disruption of systemic glucose homeostasis has been evident from the beginning of their use in clinical trials³. However, hyperglycaemia has largely been approached as a treatment-related complication that requires management in only a subset of patients for whom it becomes persistent. Owing to the body's normal glycaemic regulation, patients treated with these agents experience some degree of systemic hyperinsulinaemia as the pancreas attempts to normalize serum glucose levels. Because insulin is a potent stimulator of PI3K signalling in tumours and can have profound effects on cancer progression^{9–11}, we hypothesized that the treatment-induced hyperinsulinaemia might limit the therapeutic potential of agents that target the PI3K pathway. To test this theory, we treated wild-type mice with therapeutic doses of compounds targeting a variety of kinases in the insulin receptor-PI3K-mTOR pathway, including inhibitors of IRS1 and IGFR, PI3K, AKT, and mTOR, and

monitored their blood glucose levels over time after treatment (Fig. 1a, Extended Data Fig. 1a, b). As expected, many of these agents caused substantial increases in blood glucose levels. Notably, the hyperglycaemia resolved after only a few hours without additional intervention, suggesting that PI3K signalling had been reactivated in muscle and liver despite the presence of the drug. For each of the agents that caused an increase in blood glucose, there was also an increase in the amount of insulin released into the serum as measured by enzyme-linked immunosorbent assays (ELISAs) for insulin over time (Fig. 1b) and c-peptide, which is clinically used as a surrogate for insulin over time^{12–14} (Fig. 1c, Extended Data Fig. 1c, d). To assess whether these PI3K inhibitor-induced spikes in glucose and insulin affected tumours, we performed fluorodeoxyglucose positron emission tomography (FDG-PET) on mice bearing orthotopic Kras-Tp53-Pdx-Cre (KPC) tumour allografts in the pancreas¹⁵. We observed an increase in glucose uptake in these tumours 90 min after PI3K inhibition as compared to vehicle-treated mice, indicating that the spikes in insulin could be causing transient increases in glucose uptake in these tumours (Fig. 1d).

To test whether these spikes in insulin were stimulating PI3K signalling in the context of PI3K inhibition, we treated KPC cells in vitro with PI3K inhibitors in the presence or absence of 10 ng ml⁻¹ insulin (the amount observed in the mice within 15–30 min of drug administration; Fig. 1d). This level of insulin was sufficient to partially rescue PI3K signalling in the continued presence of PI3K inhibitors, as indicated by partial re-activation of phosphorylated AKT (pAKT) and almost complete reactivation of phosphorylated S6 (pS6), a reporter of growth signalling through the mTORC1 complex (Fig. 2a, Supplementary Fig. 1). In addition, this enhanced signalling correlated with a partial recovery of cellular proliferation (Fig. 2b, c). Insulin also stimulated proliferation in the presence of a PI3K inhibitor in a variety of other tumour cell lines and patient-derived organoids¹⁶ (Extended Data Fig. 2a–g). The amount of stimulation was not uniform across all cell lines, as would be expected in tumours with variable expression of the insulin receptor and differential dependence on PI3K signalling for growth. These observations support the conclusions that insulin is a potent activator of PI3K signalling in certain tumours, and that elevation of serum insulin following administration of a PI3K inhibitor can reactivate PI3K signalling and potentially other PI3K-independent responses to insulin in both normal tissues and tumours.

Research into diabetes and treatment of patients with diabetes have resulted in the development of numerous approaches to manage blood glucose and insulin levels. Using these tools, we sought to identify ways to augment PI3K inhibitor therapies by circumventing the acute glucose-insulin feedback. We chose to evaluate metformin and inhibitors of sodium-glucose co-transporter 2 (SGLT2), both of which are

¹Meyer Cancer Center, Weill Cornell Medicine, New York, NY, USA. ²Institute of Pathology and Molecular Pathology, University Hospital Zurich, Zurich, Switzerland. ³Englander Institute for Precision Medicine, Weill Cornell Medicine-New York Presbyterian Hospital, New York, NY, USA. ⁴Department of Medicine, Division of Hematology and Oncology, Columbia University Medical Center and New York Presbyterian Hospital, New York, NY, USA. ⁵Weill Cornell Medicine/Rockefeller University/Sloan Kettering Tri-Institutional MD-PhD Program, New York, NY, USA. ⁶Weill Cornell Graduate School of Medical Sciences, New York, NY, USA. ⁷Division of Endocrinology, Department of Medicine, Weill Cornell Medicine, New York, NY, USA. ⁸Institute for Computational Biomedicine, Weill Cornell Medicine, New York, NY, USA. ⁹Department of Pathology, Weill Cornell Medicine, New York, NY, USA. ¹⁰Department of Medicine, Division of Hematology and Medical Oncology, Weill Cornell Medicine, New York, NY, USA. ¹¹Department of Biomedical Research and the Center for Precision Medicine, University of Bern and the Inselspital, Bern, Switzerland.
*e-mail: sm3252@cumc.columbia.edu; lcantley@med.cornell.edu

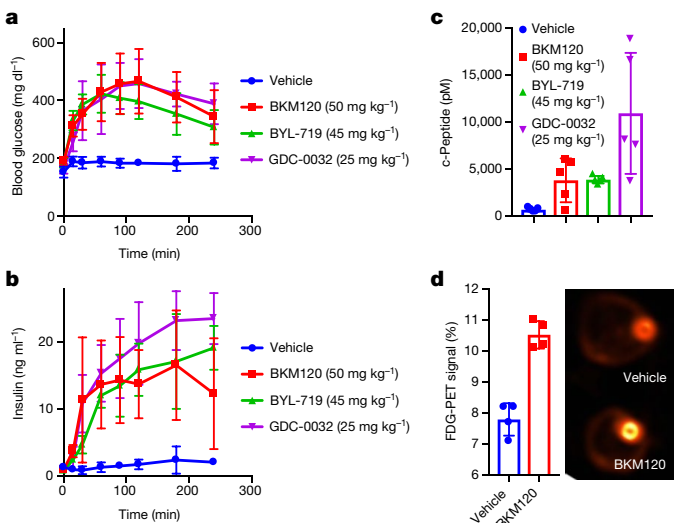


Fig. 1 | Treatment with PI3K inhibitors causes systemic feedback that results in increases in blood glucose and insulin. a, b, Mean (\pm s.d.) blood glucose (a) and insulin (b) levels in mice treated with the indicated PI3K inhibitor compounds ($n = 5$ per arm, $P < 0.0001$ by two-way ANOVA for all curves as compared to vehicle). c, Mean (\pm s.d.) of c-peptide levels assessed at 240 min (P values comparing vehicle to BKM120, BYL-719, and GDC-0032 by two-sided t -test were 0.017, <0.0001 and 0.007 respectively). d, Mean per cent (\pm s.d.) of FDG-PET signal (left) of orthotopically implanted KPC tumours imaged (right) 90 min after a single treatment with BKM120 ($n = 4$ per arm, $P = 0.0002$, by two-sided t -test).

extensively used to treat diabetes^{17–20}, as well as a ketogenic diet in our mouse models of cancer. Metformin was chosen because it has an extremely low toxicity profile and is commonly used in patients with diabetes or pre-diabetes to increase their insulin sensitivity, which reduces hyperglycaemia and insulin levels²⁰. Metformin is also commonly used in trials of PI3K inhibitors to manage patients who become chronically hyperglycaemic^{21–23}. SGLT2 inhibitors are also generally well tolerated and work by inhibiting the glucose transporters that are responsible for the reabsorption of glucose in the kidney. The rationale for using a ketogenic diet was to deplete hepatic glycogen stores and thereby limit the acute release of glucose from the liver that occurs following PI3K inhibition. Ketogenic diets have been used to treat patients with epilepsy since the 1970s and have been shown to reduce blood glucose levels and increase insulin sensitivity as compared to normal western diets^{7,24}.

To test whether these approaches could limit acute glucose–insulin feedback and alter signalling in tumours, treatment-naïve mice bearing KPC tumour allografts were placed on a ketogenic diet or treated with metformin for 10 days before a single treatment with the PI3K inhibitor BKM120. During this treatment, blood glucose was monitored and, after 3 h, c-peptide (a surrogate for blood insulin) was measured (Fig. 3a, b). In some mice, tumours were removed after 90 min and stained for pS6, a reporter of mTORC1 activity (Fig. 3c, d). These results demonstrated that pretreatment with metformin had only a minimal effect on the PI3K inhibitor-induced elevation in blood glucose and insulin levels or on growth signalling through mTORC1. By contrast, both the SGLT2 inhibitor and the ketogenic diet decreased hyperglycaemia and reduced the release of insulin in response to BKM120 treatment, and these effects correlated with reduced signalling through mTORC1 in the tumour. Similar effects were seen in mice treated with the p110 α -specific inhibitor BYL-719, in which the response of KPC allografts to BYL-719 was enhanced in a manner concordant with the relative ability of each treatment to reduce serum insulin levels (Fig. 3e–g, Extended Data Fig. 3a–d).

Various hormones and metabolites can reactivate growth in the setting of PI3K inhibition. To test whether the enhancement in tumour

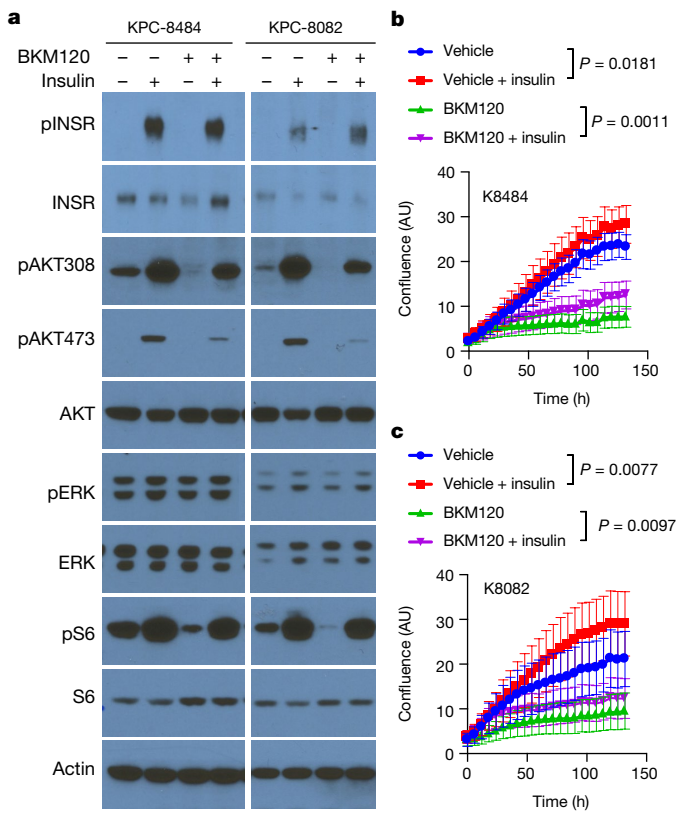


Fig. 2 | Effect of feedback levels of insulin on cellular proliferation, signalling and survival. a, Western blot analysis of KPC cell lines K8484 and K8082 treated with or without PI3K inhibitor BKM120 (1 μ M) in the presence or absence of physiological feedback levels of insulin (10 ng ml⁻¹). Similar results were observed in three independent experiments. b, c, Mean (\pm s.d.) confluence of KPC cell lines K8484 and K8082 over time grown in the presence or absence of insulin (10 ng ml⁻¹) and BKM120 (1 μ M). P values determined by ANOVA comparing conditions with or without insulin are shown; $n = 16$ biologically independent samples per group. AU, arbitrary units.

signalling and growth was mediated directly by insulin, we generated a doxycycline-inducible short hairpin RNA (shRNA) to target the insulin receptor in KPC tumours (Extended Data Fig. 4a, Supplementary Fig. 2). Induction of this hairpin in the absence of a PI3K inhibitor had little effect on tumour growth. However, induction of the hairpin at the initiation of BYL719 treatment resulted in tumour shrinkage and was almost as effective as the ketogenic diet (Fig. 4a). This result supports a model in which the insulin receptor does not have a major role in tumour growth until supra-physiological amounts of insulin are released following treatment with a PI3K inhibitor. The specificity of this effect was further corroborated by combining the PI3K inhibitor BKM120 with OSI-906, which inhibits the insulin receptor and the IGF1 receptor. This had a great effect on the growth of KPC allografts than either drug alone (Extended Data Fig. 4b–g). Notably, feeding a ketogenic diet to mice bearing tumours with insulin receptor knock-down (Fig. 4a) or to mice treated with OSI-906 (Extended Data Fig. 4b) in the absence of a PI3K inhibitor provided little or no enhancement of therapeutic response.

To further test whether the improved response to PI3K inhibitors while on a ketogenic diet is a consequence of lowering blood insulin levels, we attempted to ‘rescue’ the PI3K reactivation using exogenous insulin. A cohort of mice bearing *Pik3ca* mutant breast tumour allografts were treated with a combination of a ketogenic diet and BYL-719, and then given 0.4 mU of insulin 15 min after each dose of PI3K inhibitor (Fig. 4b). The addition of insulin markedly reduced the therapeutic benefit of supplementing PI3K inhibitor therapy with a ketogenic diet, and also rescued tumour growth in allografted KPC tumours (Extended

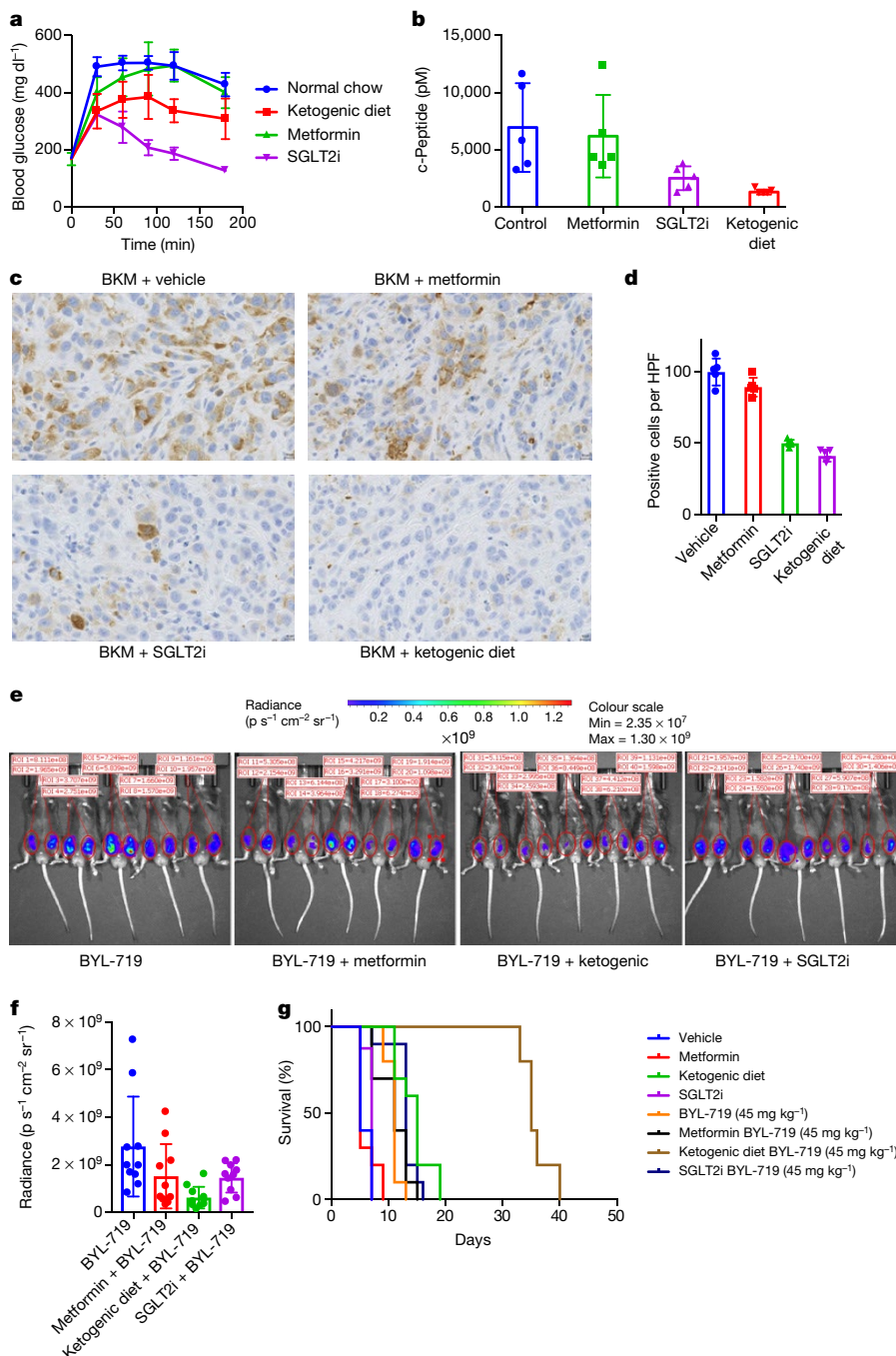


Fig. 3 | Targeting PI3K-inhibitor-induced glucose/insulin feedback in vivo. **a**, Mean (\pm s.d.) blood glucose levels over time of wild-type c57/bl6 mice bearing syngeneic K8484 KPC allografted tumours and pretreated with metformin, SGLT2-inhibitor (SGLT2i), or a ketogenic diet, after treatment with a single dose of BKM120 ($n = 5$ mice). P values calculated by two-way repeated measures ANOVA for metformin, SGLT2i, and the ketogenic diet were 0.2136 (not significant), <0.0001 , and 0.007, respectively. **b**, Mean (\pm s.d.) blood levels of c-peptide of the same mice ($n = 5$) taken 180 min after treatment with BKM120. P values calculated by unpaired two-sided t -test for metformin, SGLT2i, and ketogenic diet were 0.7566 (not significant), 0.0386, and 0.0117, respectively. **c**, Immunohistochemical staining for pS6 (ser-235) to observe the level

of active PI3K signalling in these tumours. **d**, Quantification of staining shown as mean (\pm s.d.) number of positive cells per high power field (HPF) ($n = 5$ mice per group). P values comparing pS6-positive cells in tumours treated with BKM120 alone compared to those treated with BKM120 in combination with metformin, SGLT2i, or the ketogenic diet using two-sided t -tests were 0.6186, <0.0001 and <0.0001 , respectively. **e**, IVIS images of luciferase reporter luminescence in mice with KPC K8484 tumours after 12 days of treatment with the PI3K α -specific inhibitor BYL-719 alone or in combination with metformin, ketogenic diet, or SGLT2i ($n = 10$ tumours per arm). **f**, Mean (\pm s.d.) luminescence from images of these tumours. **g**, Survival analysis of these mice. $P = 0.0019$ and 0.0001 , respectively, as determined by log-rank (Mantel–Cox) test.

Data Fig. 4h). It should be noted that the combination of the ketogenic diet, insulin, and BYL-719 was not well-tolerated in young mice, so ethical endpoints were reached in this cohort. Together these data strongly support a model in which a ketogenic diet improves responses to PI3K inhibitors by reducing blood insulin and the consequent ability of insulin to activate the insulin receptor in tumours.

In this study, we evaluated the ability of a ketogenic diet to improve responses to PI3K inhibitors in tumours with a wide range of genetic aberrations. Therapeutic benefit was observed in patient-derived xenograft models of advanced endometrial adenocarcinoma (harbouring a PTEN deletion and PIK3CA mutation) and bladder cancer (FGFR-amplified) as well as in syngeneic allograft models of *Pik3ca* mutant

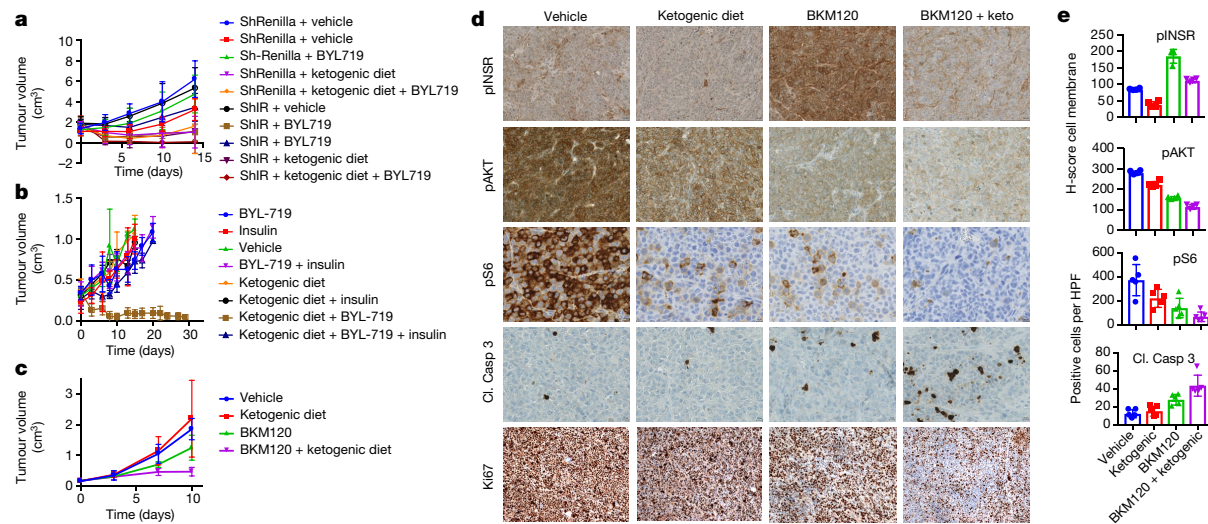


Fig. 4 | Effect of circumventing the on target glucose–insulin feedback of PI3K inhibitors upon tumour growth. **a**, Graph of mean (\pm s.d.) tumour volumes of K8484 KPC with doxycycline-inducible shRNA targeting Renilla (shRenilla) or insulin receptor (shIR), treated with doxycycline and as indicated with the PI3K inhibitor BYL-719 and/or co-administration of a ketogenic diet ($n = 8, 9, 8, 10$, for shRenilla tumours treated with vehicle, BYL719, ketogenic diet, and BYL + ketogenic diet, respectively, and $n = 8, 8, 10, 8$ for shIR tumours treated with vehicle, BYL719, ketogenic diet, and BYL + ketogenic diet, respectively). **b**, Mean (\pm s.d.) volumes of ES272 Pika3ca mutant breast cancer allograft tumours treated with BYL719 and/or insulin along with the ketogenic diet (keto) as indicated. $n = 3, 3, 5, 5, 5, 3, 4, 4$ for vehicle, insulin, BYL, BYL + insulin, ketogenic diet, ketogenic + insulin, ketogenic + BYL, and

ketogenic + BYL + insulin, respectively. **c**, Mean (\pm s.d.) tumour volume of endometrial PDXs treated with BKM120 and/or a ketogenic diet ($n = 5$ per arm, $P = 0.0028$ by ANOVA comparison between BKM120 alone and BKM120 + ketogenic diet). **d, e**, Histology and quantification of phospho-insulin receptor (pINSR), pAKT, pS6, cleaved caspase 3 (Cl. Casp 3), and ki67 of the tumours from **d** taken 4 h after the last treatment with vehicle, ketogenic diet, BKM120, or the combination of the ketogenic diet with BKM120 (BKM120 + keto). Quantification is depicted as score per HPF, four images were taken for each of the $n = 5$ mice. P values from two-sided *t*-tests comparing the blinded scoring in BKM120-treated tumours with those treated with BKM120 + ketogenic diet were 0.005, 0.005, 0.017 and 0.028 for pINSR, pAKT, pS6 and Cl. Casp 3, respectively. H-score denotes intensity and percent of cells with staining at the cell membrane.

breast cancer and *MLL-AF9* driven acute myeloid leukaemia (AML) (Fig. 4c, Extended Data Figs. 5–7).

The addition of the ketogenic diet improved drug efficacy with an array of agents that target the PI3K pathway in addition to BKM120 and BYL719, including the pan-PI3K inhibitor GDC-0941, the PI3K- β -sparing compound GDC-0032, the mTOR/PI3K dual inhibitor GDC-0980, and the recently approved PI3K- α/δ inhibitor Copanlisib (Extended Data Fig. 5). It is important to note that treatment with the ketogenic diet alone had variable effects in different tumour models, indicating that the dietary changes themselves were insufficient to cause the tumour responses observed across the mouse models. In some instances, such as the AML model, the ketogenic diet alone accelerated disease progression, suggesting that this diet may be detrimental for some patients with cancer when used in isolation.

Our data suggest that insulin feedback limits the efficacy of PI3K inhibition in several tumour models. By reducing the systemic insulin response, the addition of a ketogenic diet to BKM120 reduced immunohistochemical markers of insulin signalling in *PTEN/PIK3CA* mutant endometrial patient-derived xenograft (PDX) tumours, compared to tumours from mice treated with BKM120 alone. In these tumours, the ketogenic diet enhanced the ability of BKM120 to reduce levels of phosphorylated insulin receptor, phosphorylated AKT and phosphorylated S6 and this reduction in signalling correlated with decreased levels of proliferation as shown by Ki67 staining, and increased levels of apoptosis as indicated by cleaved caspase 3 staining (Fig. 4d, e).

While these data do not exclude insulin-independent effects of combining PI3K inhibition with anti-glycaemic therapy, they demonstrate that using this approach has the potential to substantially increase the therapeutic efficacy of these compounds. In light of these results, it may also be important to think about how common clinical practices such as intravenous glucose administration, glucocorticoid use, or providing patients with glucose-laden nutritional supplements may impact therapeutic responses. As therapeutic agents that target this critical oncogenic pathway are brought through clinical trials, they should be

paired with strategies such as SGLT2 inhibition or the ketogenic diet to limit this self-defeating systemic feedback.

Online content

Any Methods, including any statements of data availability and Nature Research reporting summaries, along with any additional references and Source Data files, are available in the online version of the paper at <https://doi.org/10.1038/s41586-018-0343-4>

Received: 25 July 2017; Accepted: 26 June 2018;

Published online 4 July 2018.

- Kandoth, C. et al. Mutational landscape and significance across 12 major cancer types. *Nature* **502**, 333–339 (2013).
- Millis, S. Z., Ikeda, S., Reddy, S., Gatalica, Z. & Kurzrock, R. Landscape of phosphatidylinositol-3-kinase pathway alterations across 19784 diverse solid tumors. *JAMA Oncol.* **2**, 1565–1573 (2016).
- Bendell, J. C. et al. Phase I, dose-escalation study of BKM120, an oral pan-class I PI3K inhibitor, in patients with advanced solid tumors. *J. Clin. Oncol.* **30**, 282–290 (2012).
- Juric, D. et al. Phase I dose-escalation study of taselisib, an oral PI3K inhibitor, in patients with advanced solid tumors. *Cancer Discov.* **7**, 704–715 (2017).
- Patnaik, A. et al. First-in-human phase I study of copanlisib (BAY 80-6946), an intravenous pan-class I phosphatidylinositol 3-kinase inhibitor, in patients with advanced solid tumors and non-Hodgkin's lymphomas. *Ann. Oncol.* **27**, 1928–1940 (2016).
- Mayer, I. A. et al. A Phase Ib study of alpelisib (BYL719), a PI3K α -specific inhibitor, with letrozole in ER $^{+}$ /HER2 $^{-}$ metastatic breast cancer. *Clin. Cancer Res.* **23**, 26–34 (2017).
- Hopkins, B. D., Goncalves, M. D. & Cantley, L. C. Obesity and cancer mechanisms: cancer metabolism. *J. Clin. Oncol.* **34**, 4277–4283 (2016).
- Fruman, D. A. et al. The PI3K pathway in human disease. *Cell* **170**, 605–635 (2017).
- Belardi, V., Gallagher, E. J., Novosyadlyy, R. & LeRoith, D. Insulin and IGFs in obesity-related breast cancer. *J. Mammary Gland Biol. Neoplasia* **18**, 277–289 (2013).
- Gallagher, E. J. & LeRoith, D. Minireview: IGF, insulin, and cancer. *Endocrinology* **152**, 2546–2551 (2011).
- Kiln-Drori, A. J., Azoulay, L. & Pollak, M. N. Cancer, obesity, diabetes, and antidiabetic drugs: is the fog clearing? *Nat. Rev. Clin. Oncol.* **14**, 85–99 (2017).

12. Ma, J. et al. A prospective study of plasma c-peptide and colorectal cancer risk in men. *J. Natl. Cancer Inst.* **96**, 546–553 (2004).
13. Xu, J. et al. Association between markers of glucose metabolism and risk of colorectal cancer. *BMJ Open* **6**, e011430 (2016).
14. Ma, J. et al. Prediagnostic body-mass index, plasma c-peptide concentration, and prostate cancer-specific mortality in men with prostate cancer: a long-term survival analysis. *Lancet Oncol.* **9**, 1039–1047 (2008).
15. Olive, K.P. et al. Inhibition of Hedgehog signaling enhances delivery of chemotherapy in a mouse model of pancreatic cancer. *Science* **324**, 1457–1461 (2009).
16. Pauli, C. et al. Personalized in vitro and in vivo cancer models to guide precision medicine. *Cancer Discov.* **7**, 462–477 (2017).
17. Komoroski, B. et al. Dapagliflozin, a novel, selective SGLT2 inhibitor, improved glycemic control over 2 weeks in patients with type 2 diabetes mellitus. *Clin. Pharmacol. Ther.* **85**, 513–519 (2009).
18. Demin, O., Jr, Yakovleva, T., Kolobkov, D. & Demin, O. Analysis of the efficacy of SGLT2 inhibitors using semi-mechanistic model. *Front. Pharmacol.* **5**, 218 (2014).
19. Pollak, M. Metformin and other biguanides in oncology: advancing the research agenda. *Cancer Prev. Res. (Phila.)* **3**, 1060–1065 (2010).
20. Pollak, M. Potential applications for biguanides in oncology. *J. Clin. Invest.* **123**, 3693–3700 (2013).
21. Saura, C. et al. Phase I b study of buparlisib plus trastuzumab in patients with HER2-positive advanced or metastatic breast cancer that has progressed on trastuzumab-based therapy. *Clin. Cancer Res.* **20**, 1935–1945 (2014).
22. Juvekar, A. et al. Combining a PI3K inhibitor with a PARP inhibitor provides an effective therapy for BRCA1-related breast. *1158/2159–8290.CD-11-0336*
23. Puchalska, P. & Crawford, P.A. Multi-dimensional roles of ketone bodies in fuel metabolism, signaling, and therapeutics. *Cell Metab.* **25**, 262–284 (2017).
24. Sampaio, L. P. Ketogenic diet for epilepsy treatment. *Arq. Neuropsiquiatr.* **74**, 842–848 (2016).

Acknowledgements This work was supported by NIH grant R35 CA197588 (L.C.C.), R01 GM041890 (L.C.C.), U54 U54CA210184 (L.C.C.), Breast Cancer Research Foundation (L.C.C.) and the Jon and Mindy Gray Foundation (L.C.C.). The content is solely the responsibility of the authors and does not necessarily

represent the official views of the National Institutes of Health. We appreciate the help of the small animal imaging core at MSKCC for assistance with FDG-PET imaging and the Columbia Irving Cancer Center Flow Core Facility, funded in part through Center Grant P30CA013696.

Reviewer information *Nature* thanks V. Longo, M. Pollak, C. Rask-Madsen and the other anonymous reviewer(s) for their contribution to the peer review of this work.

Author contributions B.D.H., S.M. and L.C.C. conceived of the project. B.D.H., C.P., D.X., Y.M. and D.W. performed the mouse experiments. S.C.A., C.P., B.D.H., E.M.H. and X.L. did the culture assays. S.C.A. performed immunoblotting. B.D.H., C.H. and M.D.G. assessed the impact of treatments on cellular and systemic metabolism. D.G.W. and S.C.A. cloned and validated the IR knockdowns. M.R.L. and R.B. performed the data analysis. C.P., A.S., H.B., M.A.R., L.C.C., S.M., B.D.H. and R.B. assisted with implementation of patient-derived models. All authors assisted with data interpretation and contributed to the writing and editing of the manuscript.

Competing interests L.C.C. is a founder and member of the board of directors of Agios Pharmaceuticals and is a founder and receives research support from Petra Pharmaceuticals. S.M. is a founder and on the board of Vor Pharmaceuticals. These companies are developing novel therapies for cancer. All other authors declare no competing interests.

Additional information

Extended data is available for this paper at <https://doi.org/10.1038/s41586-018-0343-4>.

Supplementary information is available for this paper at <https://doi.org/10.1038/s41586-018-0343-4>.

Reprints and permissions information is available at <http://www.nature.com/reprints>.

Correspondence and requests for materials should be addressed to S.M. or L.C.C.

Publisher's note: Springer Nature remains neutral with regard to jurisdictional claims in published maps and institutional affiliations.

METHODS

Mice procurement and treatment. All animal studies were conducted following IACUC approved animal protocols (#2013-0116) at Weill Cornell Medicine and (AC-AAQ5405) at Columbia University. Ethical requirements for the treatment of animals were followed for all of the animal studies as per institutional guidelines. Mice were maintained in temperature- and humidity-controlled specific pathogen-free conditions on a 12-h light/dark cycle and received a normal chow diet (PicoLab Rodent 20 5053 laboratory Diet St. Louis, MO) or ketogenic diet (Thermo-Fisher AIN-76A) with free access to drinking water. Diets were composed as indicated in Supplementary Table 1. Owing to the nature of the diets used, blinding was not possible. No statistical methods were used to predetermine sample size.

For solid tumour studies Nude (genotype) and C57/BL6 mice were purchased at 8 weeks of age from Jackson laboratories (Bar Harbour, ME). They were injected with $0.5\text{--}1 \times 10^6$ cells in a 1:1 mix of growth media and matrigel (Trevigen, # 3433-005-R1) and tumours were allowed to grow to a minimum diameter of 0.6cm before the initiation of treatment. Tumours that did not meet this criterion at the time of treatment initiation were not used for experimentation.

For AML studies 10-12 weeks old male C57BL/6J mice were used for MLL-AF9 Ds-Red AML study (Approved protocol AC-AAQ5405). For pre-treatment study with MLL-AF9 Ds-Red cells, keto and Keto/BKM group mice were given a ketogenic diet for 10 days before injection with MLL-AF9 Ds-Red cells (2×10^5 per mouse in 200 μl) via lateral tail vein. The day after iv injection, the mice were given 0.5% carboxymethyl cellulose (CMC) as vehicle control or BKM120 (37.5 mg/kg) by oral gavage for two weeks (5 out of 7 days). The mice were euthanized after two-week treatment to check the bone marrow for AML progress. The mice were euthanized and one femur and tibia were removed from each mouse. The bone marrow cells were flushed with PBS (2% FBS). The red blood cells were lysed with ACK lysis buffer (Invitrogen). DAPI was used to exclude dead cells. The DS-red AML cells from the BM were analysed with BD LSRII. The tumour progress was also monitored via IVIS spectrum machine. For co-current treatment study with MLL-AF9 Ds-Red cells, the mice were injected with MLL-AF9 Ds-Red cells (2×10^5 per mouse in 200 μl) via lateral tail vein. The day after iv injection, the mice were given vehicle or BKM120 (37.5 mg/kg) by oral gavage for two weeks. The Keto or Keto/BKM group were changed to a ketogenic diet on the same day. The mice were euthanized after two-week treatment to check the bone marrow for AML progress.

To check whether Keto/BKM treatment affects the AML engraftment, Keto and Keto/BKM group mice were given a ketogenic diet for 10 days, then treated with vehicle or BKM120 by oral gavage for two weeks. The mice were then injected with MLL-AF9 Ds-Red cells (2×10^5 per mouse in 200 μl) via lateral tail vein. Two weeks after the iv injection, the mice were euthanized to check the bone marrow for AML burden.

The survival study, pre-treatment study, and co-current treatment were conducted at the same time. The mice were treated with vehicle or BKM120 (5 out of 7 days) until spontaneous death, or mice were euthanized when they appeared to be very sick (reduced spontaneous activity, unkempt coat, and dehydrated appearance), achieved body weight loss over 20%, or demonstrated signs of limb paralysis. **Compounds.** GDC-0032, MK2206, BEZ235, BKM-120, GDC-0941, GDC-0980, and Canagliflozin were all procured from Medchem Express (Monmouth Junction, NJ) and given via oral gavage in 100 μl . Metformin was procured from Sigma Aldrich (St. Louis, MO). BAY-80 6946 and OSI-906 came from Selleckchem catalogue #S2802 and #S1091 respectively. The targeting information for these compounds is displayed in Supplementary Table 3. IC₅₀ data was obtained from the Selleckchem website (Selleckchem.com). The canagliflozin was administered 60 min before the PI3K pathway inhibitors so that its optimal efficacy lined up with the peak glucose levels. Mice treated with metformin were pretreated for 10 days before BKM120 treatment. Ketogenic diet was initiated at the time of initial PI3K inhibitor treatment unless otherwise stated. Doxycycline was procured from Sigma (St. Louis, Missouri) catalogue number D3072-1ML and administered via intraperitoneal injection once daily at a dose of 3mg/kg.

Culture. Murine pancreas cell lines were a gift from K. Olive, Columbia University¹⁵. Murine breast lines were a gift from R. Parsons, Mount Sinai School of Medicine. PDX models were derived by the Englehardt Institute of Precision Medicine in accordance with an IRB approved protocol as described^{16,25}. Cell lines HEK293, HCC-38, MDA-MB-468, PC-3, BT-549 were purchased from ATCC and grown in DMEM supplemented with 10% FBS and 1% Pen/Strep. HCT-116 and DLD-1 isogenic lines with and without PTEN deletion were kindly provided by the Laboratory of Todd Waldman²⁶. A chart of cells/organoids is in Supplementary Table 2, with known oncogenic alterations as described in publications cited above or as available from the ATCC (https://www.atcc.org/~media/PDFs/Culture%20Guides/Cell_Lines_by_Gene_Mutation.ashx). Authentication was not required for the cells that came directly from ATCC. Key genetic alterations of mouse lines

were confirmed via genotyping for transgenes. Mutant HCT-116 and DLD-1 lines from the Waldman lab were validated by western blot analysis to demonstrate PTEN deletion.

For signalling assays, cells were washed 1x in PBS and placed in starvation media (-FBS) for 6–18 h depending upon cell line, and treated 1 h before harvesting with PI3K inhibitors as indicated alone or in combination with insulin 10 min before harvesting. Three dimensional culture and dose response experiments of patient derived organoids were run as previously described¹⁶. In brief, ~1,000 cells were plated in 10 μl of 1:1 matrigel to culture media in 96 well angiogenesis plates and allowed to solidify for 30 min at 37 degrees before 70 μl of culture media was added. Organoids were then treated in triplicate in a log scale dose response and CellTiter-Glo assay (Promega) was run at 96 h to determine the IC₅₀ values.

Knockdown of insulin receptor was achieved using a doxycycline-inducible shRNA strategy. For generation of miR-E shRNAs, 97-mer oligonucleotides were purchased (IDT Ultramers) coding for predicted shRNAs using an siRNA prediction tool Splash RNA, <http://splashrna.mskcc.org>²⁷. Oligonucleotides were PCR amplified using the primers miRE-Xho-fw (5'-TGAAGTCGAGAAAGGTATATTGCTGTTGACAGTGAGCG-3') and miRE-Eco-rev (5'-TGAAGTCGAGAAAGGTATATTGCTGTTGACAGTGAGCG-3'). PCR products were purified and both PCR product and LT3GEPIR²⁸ vectors were double digested with EcoRI-HF and XhoHI. PCR product and vector backbone were ligated and transformed in Stbl3 competent cells and grown at 32 °C overnight. Colonies were screened using the primer miRE-fwd (5'-TGTTGAATGAGGCTTCAGTAC-3'). Renilla, TGCTGTTGACAGTGAGC-GCAGGAATTATAATGCTTATCTATAGTAAGGCCACAGAT

GTATAGATAAGCATTATAATTCTATGCCTACTGCCTCGGA; INSR4, TGCTGTTGACAGTGAGCGGGGTTCATGCTGTTCTACAATAGTGAAG CCACAGATGTATTGAGAACAGCATGAACCCATGCCTACTGCCTCGGA.

Immunoblotting. Cell lysates were prepared in 1x CST Cell Lysis Buffer #9803, (Danvers MA). Total protein concentration was evaluated with the BCA kit (Pierce) 23227. The lysates were run out on 4–20% Tris-Glycine Gels (ThermoFisher, Carlsbad CA). Primary antibodies against pAKT473, pAKT308, pS6, pTYR, AKT, and S6 were procured from Cell Signaling (Danvers, MA), and were used overnight at 1:1,000 in 5% bovine serum albumin. Actin and tubulin antibodies came from Sigma Aldrich and were used at 1:5,000 in 5% milk. All these antibodies were visualized with HRP conjugated secondary antibodies from Jackson Immuno at 1:5,000 in 5% milk.

Immunohistochemistry. Tumour sections (3 μm) were antigen retrieved with 10 mmol/L citrate acid, 0.05% Tween 20, pH6.0, and incubated with antibodies as indicated (Ki67 (Abcam, ab16667) 1:500; cleaved caspase-3 (Asp175; 5A1E; Cell Signaling Technology, 9664) 1:200; phospho-INSR (Tyr 1162; Thermo Fisher #AHR0271) 1:100; phospho-AKT (Ser473; Cell Signaling Technology, 8101) 1:20; and phospho-S6 ribosomal protein (Ser235/236; Cell Signaling Technology, 2211) 1:300).

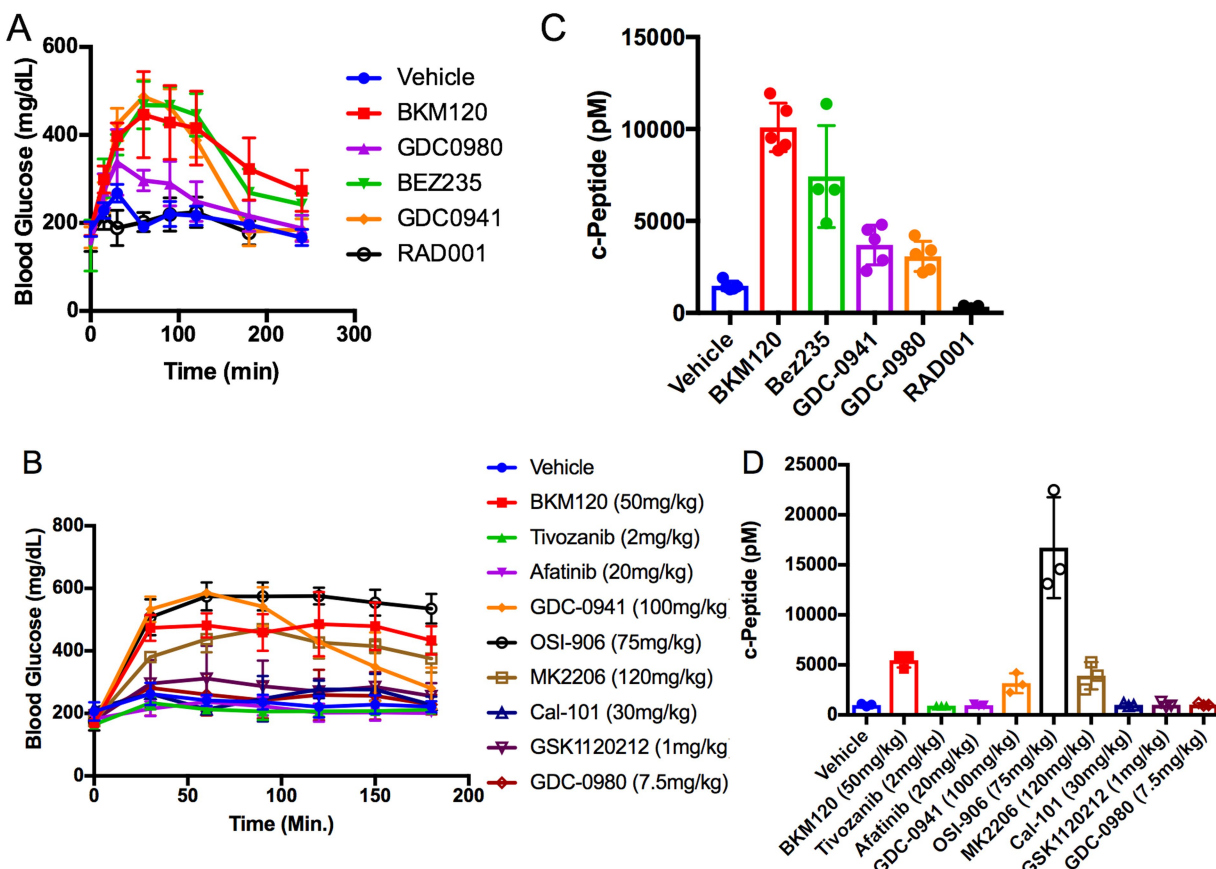
Blood measurements. For assessment of blood glucose, 10 μl of blood was taken from the tail of mice before treatment (time 0) and then again at the indicated time points (15, 30, 60, 90, 120, 180 min) using a OneTouch Ultra Glucometer. At end point >100 μl of blood was drawn from the mice into EDTA tubes (Sarstedt #16.444). Blood was centrifuged (10,000g for 10 min at 4 °C), and plasma was stored at –20 °C. Plasma β -hydroxybutyrate, triglyceride (Stabio Laboratory, Boerne, TX), serum insulin, and c-peptide (APLCO Diagnostics, Salem, NH) levels were quantified by ELISA.

FDG-PET. Male c57/bl6 mice ($n=4/\text{arm}$) bearing orthotopic pancreatic adenocarcinoma allografts were injected with 200–250 μCi [⁸⁹Zr]liposomes (3–4 μmol lipid) in 200–250 μL PBS solution into the tail vein. At the time of peak blood insulin feedback 90 min post BKM120 injection animals were anaesthetized and scans were then performed using an Inveon PET/CT scanner (Siemens Healthcare Global). Whole body PET scans were performed recording a minimum of 50 million coincident events, with a duration of 10 min. The energy and coincidence timing windows were 350–750 keV and 6 ns. The data were normalized to correct for non-uniformity of response of the PET, dead-time count losses, positron branching ratio, and physical decay to the time of injection. The counting rates in the reconstructed images were converted to activity concentrations (percentage injected dose [%ID] per gram of tissue) by use of a system calibration factor derived from the imaging of a phantom containing ⁸⁹Zr. Images were analysed using ASIPro VMTM software (Concorde Micro-systems). Quantification of activity concentration was done by averaging the maximum values in at least 5 ROIs drawn on adjacent slices of the pancreatic tumours.

Reporting summary. Further information on experimental design is available in the Nature Research Reporting Summary linked to this paper.

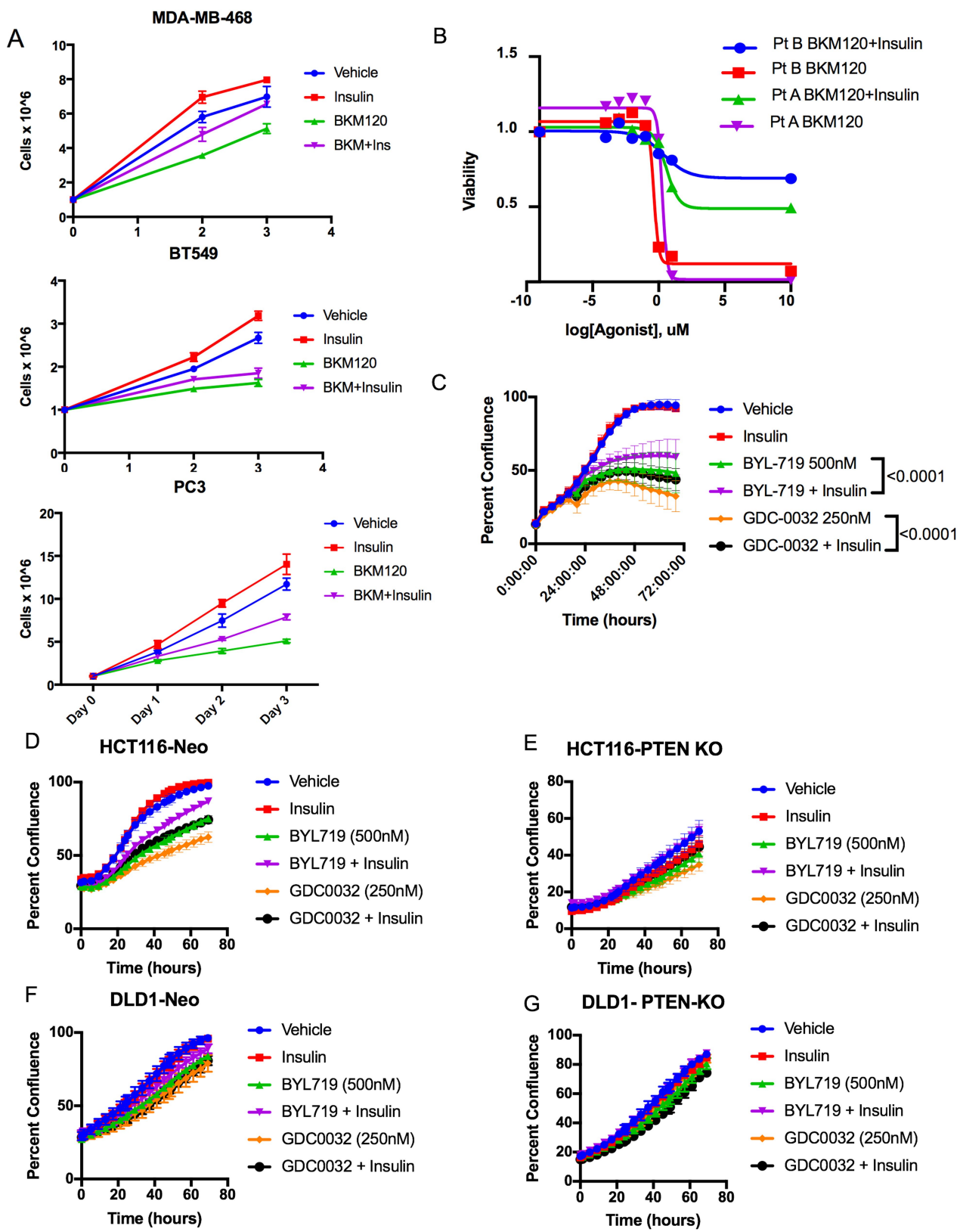
Data availability. Source data for Figs. 1, 3 and 4 and Extended Data Figs. 1–7 are provided in the online version of the paper. All other data are available from the corresponding author upon reasonable request.

25. Pauli, C. et al. An emerging role for cytopathology in precision oncology. *Cancer Cytopathol.* **124**, 167–173 (2016).
26. Lee, C., Kim, J. S. & Waldman, T. PTEN gene targeting reveals a radiation-induced size checkpoint in human cancer cells. *Cancer Res.* **64**, 6906–6914 (2004).
27. Pelosof, R. et al. Prediction of potent shRNAs with a sequential classification algorithm. *Nat. Biotechnol.* **35**, 350–353 (2017).
28. Fellmann, C. et al. An optimized microRNA backbone for effective single-copy RNAi. *Cell Reports* **5**, 1704–1713 (2013).
29. Douris, N. et al. Adaptive changes in amino acid metabolism permit normal longevity in mice consuming a low-carbohydrate ketogenic diet. *Biochim. Biophys. Acta* **1852**, 2056–2065 (2015).



Extended Data Fig. 1 | Blood glucose and c-peptide levels after treatment with agents that target the PI3K pathway. **a, b,** Mean \pm s.d. blood glucose levels over time where time 0 is the time of treatment with the indicated inhibitor. $n = 5$ and 3 mice per arm for **a** and **b**, respectively. **c, d,** Mean \pm s.d. c-peptide levels from mice in **a** and **b** taken 240 and 180 min after treatment with indicated inhibitors. **c**, $n = 5$ for vehicle,

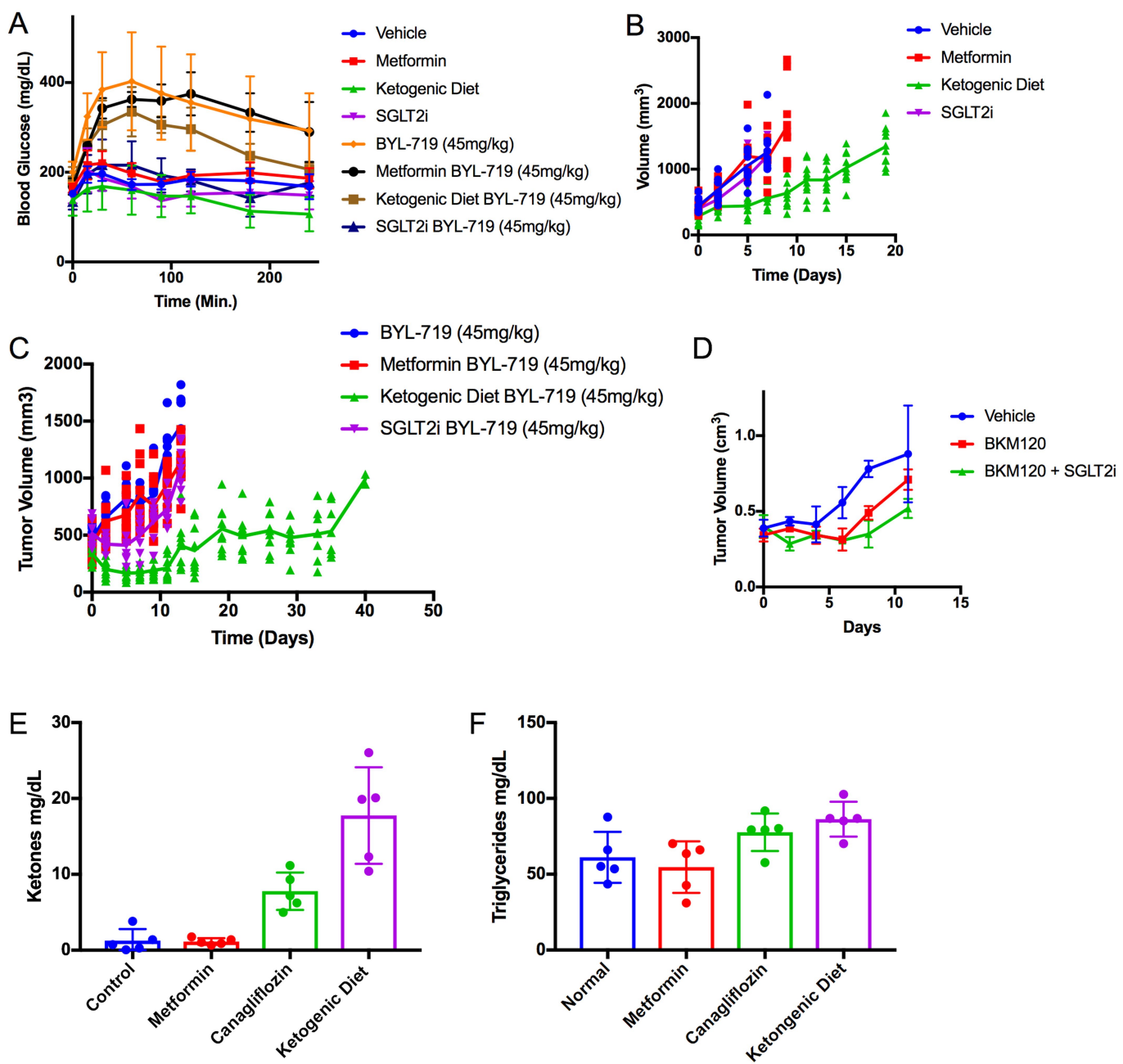
BKM120, GDC-0941, and GDC-0980; $n = 4$ for BEZ235; $n = 3$ for RAD001. **D**, $n = 3$ mice per arm. As a surrogate for total insulin release, c-peptide levels show that the PI3K and IGFR/INSR inhibitors markedly increase insulin release. In all cases, compounds that caused acute increases in blood glucose also increased serum insulin.



Extended Data Fig. 2 | See next page for caption.

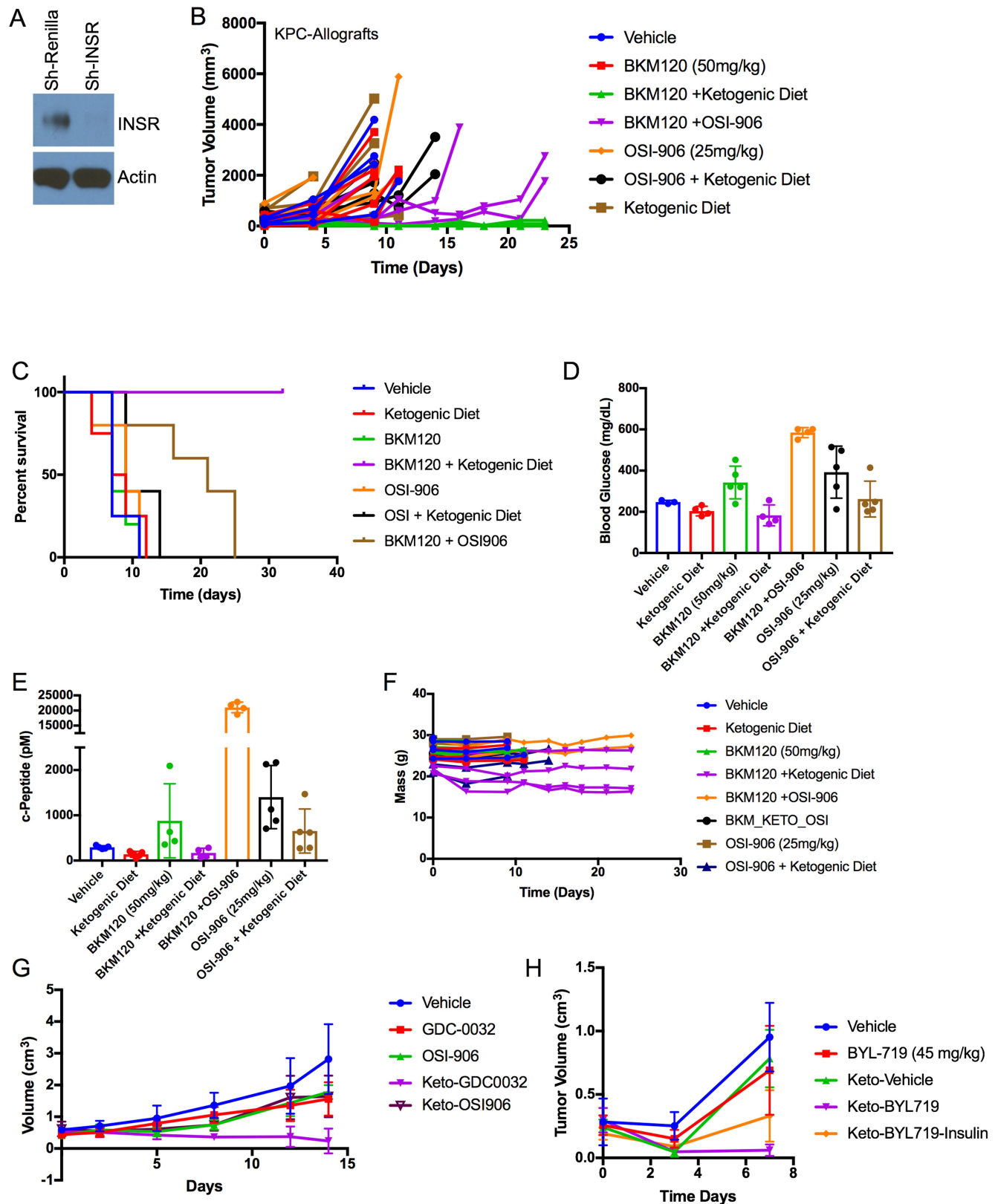
Extended Data Fig. 2 | Effect of feedback levels of insulin observed in Fig. 1 on BKM120 efficacy in vitro. **a**, Proliferation in minimal growth medium of cells whose growth is partially rescued by the addition of the observed feedback levels of insulin (10 ng ml^{-1}) induced by BKM120 in mice. $n = 3$ biologically independent samples per arm, mean \pm s.d. number of cells. **b**, Cell viability assay demonstrating the effects of feedback levels of insulin on two patient-derived organoid cultures (PtA and PtB) being treated in a dose response with BKM120 as measured by cell titre-glo at 96 h. $n = 3$ biologically independent samples per treatment. **c**, Proliferation in minimal growth medium of mouse TNBC cells treated with PI3K inhibitors partially rescued by the addition of the observed feedback levels of insulin induced by BKM120 in mice (Fig. 1). $n = 6$ biologically independent samples per treatment, mean \pm s.d. **d, e**, Proliferation of

HCT116-neo cells (**d**) and HCT116 PTEN knockout (KO) cells (**e**) with and without treatment with physiologically observed levels of insulin (10 ng ml^{-1}) and treatment with the clinically relevant PI3K inhibitors GDC-0032 and BYL-719. $n = 4$ biologically independent samples per treatment, mean \pm s.d. confluence. **f, g**, Proliferation of DLD1-Neo cells (**f**) and DLD-1 PTEN knockout cells (**g**) under the same treatment conditions as in **d** and **e**. Of note, the loss of PTEN in these isogenic sets of colon cancer lines does not uniformly alter the response to insulin in the setting of PI3K inhibition. In the context of PTEN loss, physiological levels of insulin can restore normal proliferation in HCT116 cells despite the presence of PI3K inhibitors. $n = 4$ biologically independent samples per treatment, mean \pm s.d. confluence.



Extended Data Fig. 3 | KPC K8484 allografts treated with PI3K inhibitors with or without supplementary approaches to target systemic insulin feedback. **a**, Mean \pm s.d. blood glucose of mice from Fig. 3e–g treated with control diet, ketogenic diet, metformin (250 mg kg^{-1}), or canagliflozin (SGLT2i; 6 mg kg^{-1}), after the first dose of BYL-719 (45 mg kg^{-1}). $n = 5$ animals per arm. **b**, Volumes of tumours shown in Fig. 3 without PI3K inhibitors. $n = 10$ tumours per arm for vehicle, metformin, and ketogenic diet; $n = 8$ tumours per arm for SGLT2i. **c**, Mean tumour volumes (lines) with scatter (points) for each of these treatment cohorts. $n = 10$ tumours per arm for

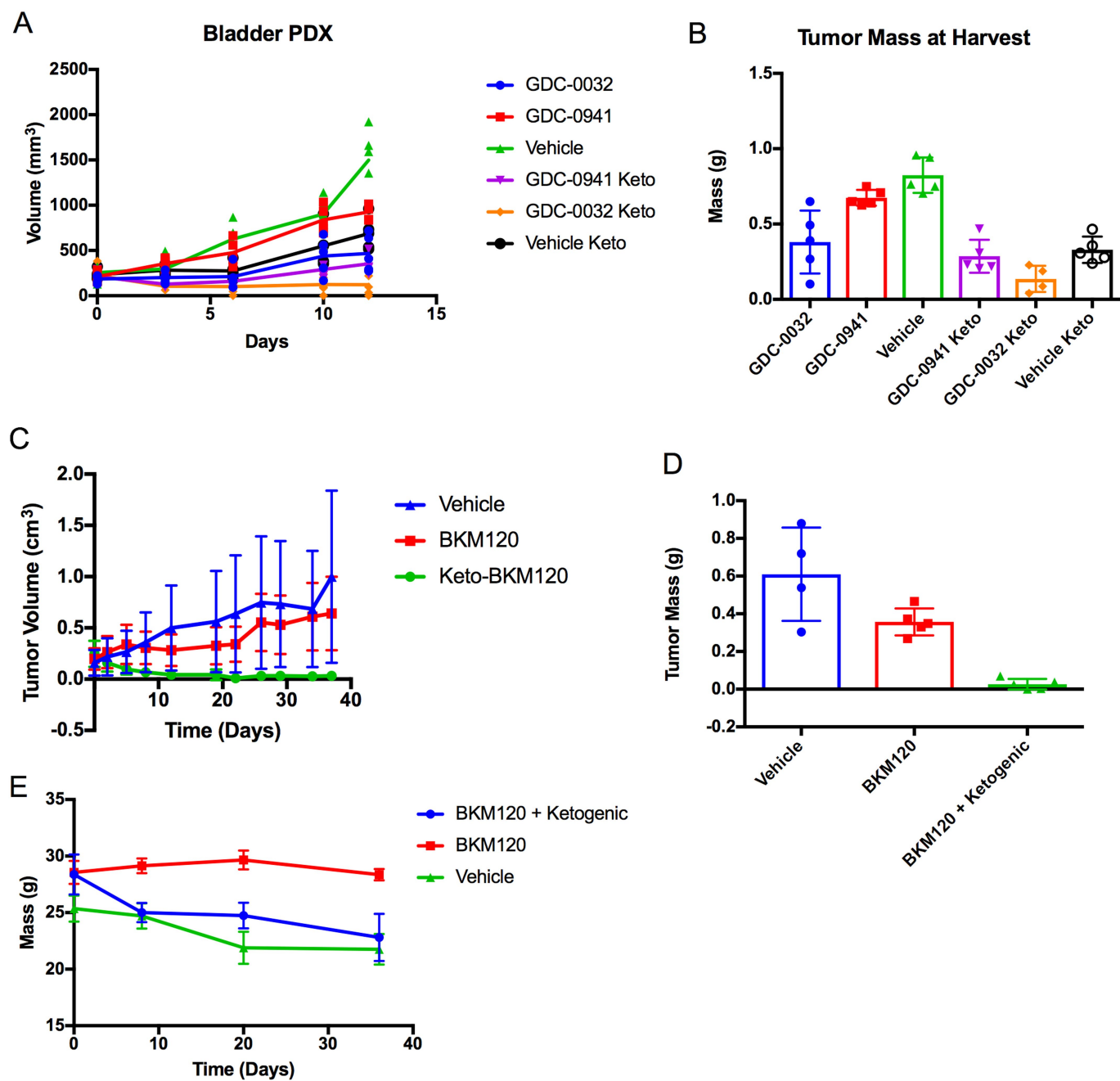
BYL-719, BYL-719 + metformin, and BYL-719 + ketogenic diet; $n = 9$ tumours for BYL-719 + SGLT2i. **d**, Mean \pm s.d. tumour volumes from an independent experiment with mice ($n = 4$ mice per arm) treated daily with BKM120 with or without 6 mg kg^{-1} canagliflozin administered 60 min before PI3K treatment, so that peak SGLT2 inhibition is aligned with peak blood glucose levels after PI3K inhibitor treatment. **e, f**, Mean \pm s.d. blood ketones (e) and triglycerides (f) as determined by calorimetric assay of mice shown in Fig. 3a–d after a single treatment with BKM120 with or without pretreatment with metformin, canagliflozin, or the ketogenic diet. $n = 5$ mice per arm.



Extended Data Fig. 4 | See next page for caption.

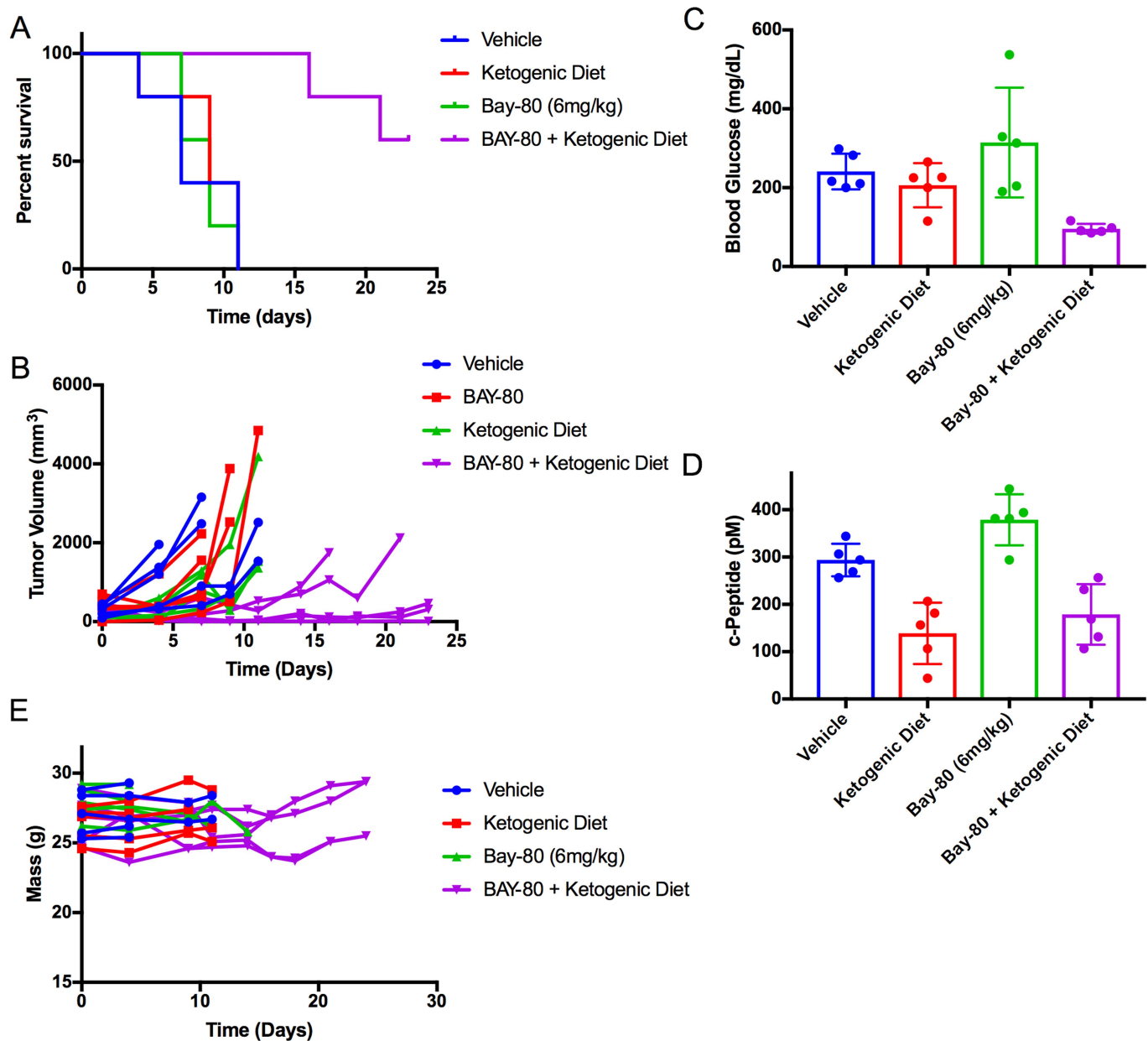
Extended Data Fig. 4 | Role of insulin receptor inhibition in the observed changes in tumour response. **a**, Western blot of cell lysates from K8484 cells used to generate xenografts in Fig. 4a after 36 treatments with doxycycline to induce the shRenilla and shIR hairpins as indicated. Similar results were observed in two independent experiments. **b**, Tumour volumes of individual mice allografted with KPC-K8484 tumours as measured by calipers over time. $n = 4, 5, 4, 4, 5, 5$ and 5 for vehicle, BKM120, BKM120 + ketogenic diet, BKM120 + OSI-906, OSI-906, OSI-906 + ketogenic diet, and ketogenic diet, respectively. **c**, Survival curves of mice in **b**. **d**, **e**, Mean \pm s.d. blood glucose (**d**) and c-peptide (**e**) from these mice 240 min after respective treatments. Two of the glucose measurements in the OSI-906 and BKM120 were beyond the range of the detector ($>600 \text{ mg dl}^{-1}$). **f**, Masses of individual mice over the course of treatment. As has been previously published, mice lose 10–20% of

their mass upon initiation of a ketogenic diet²⁹. **g**, Similar to the data for the tumours in **a**, both OSI-906, a INSR/IGFR inhibitor, and GDC-0032 showed greater anti-tumour efficacy in PIK3CA + MYC mutant mouse breast tumour allografts, ES-278, grown in wild-type *c57/bl6* mice fed a ketogenic diet. $n = 5$ tumours per arm. Points depict mean \pm s.d. tumour volume. **h**, Mean \pm s.d. tumour volumes of wild-type *c57/bl6* mice bearing KPC allografted tumours as measured by calipers over time. Mice were treated as indicated with combinations of BYL-719, the ketogenic diet, or insulin as in Fig. 4b. Mice in the ketogenic + BYL719 + insulin cohort lost $>20\%$ of their body mass over the 1 week of treatment so the experiment was terminated at day 7. $n = 6, 4, 4, 6, 6$ for vehicle, BYL-719, ketogenic diet, BYL-719 + ketogenic diet, and BYL-719 + ketogenic diet + insulin, respectively.



Extended Data Fig. 5 | Effect of PI3K inhibitor treatments on PDX model of bladder cancer and syngeneic allograft models of PIK3CA mutant breast cancer. **a**, Graph of tumour growth over time of a PDX from a patient with bladder cancer (Patient C) treated with the pan-PI3K inhibitor GDC-0941 or the β -sparing inhibitor GDC-0032, alone or with a ketogenic diet. Lines indicate mean tumour volume of each treatment group, points indicate individual tumour volumes over time. $n=5$

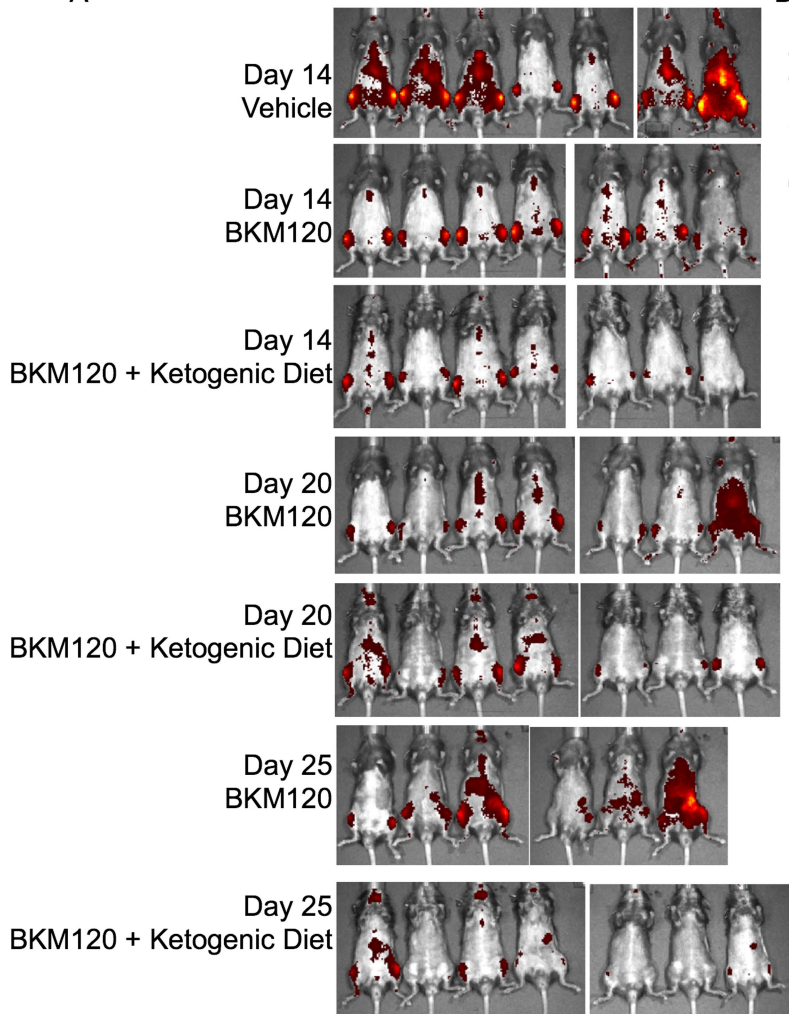
tumours per arm. **b**, Mean \pm s.d. tumour mass at the time of removal on day 12. **c, d**, Mean \pm s.d. tumour growth over time (**c**) and tumour mass at time of removal (**d**) from mice with orthotopic allografts of a PIK3CA (H1047R) mutant mouse breast cancer, ES272, treated as indicated with BKM120 alone or in combination with a ketogenic diet. $n=4, 5, 5$ tumours per arm for vehicle, BKM120 and BKM120 + ketogenic diet, respectively. **e**, Mean \pm s.d. mass of mice over time.



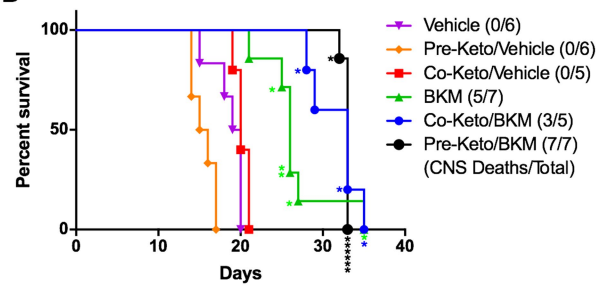
Extended Data Fig. 6 | Effect of copanilisib with or without ketogenic diet on growth of KPC tumour model K8082 grown in the flank of wild-type *c57/bl6* mice. **a**, Survival curves for mice with KPC K8082 allografts grown in the flank and treated as indicated with BAY 80-6946 alone or combined with pretreatment with a ketogenic diet as indicated (*P* value comparing BAY 80-6946 with the combination of BAY 80-6946 with ketogenic diet was 0.0019 by Mantel–Cox log-rank test). *n* = 5 mice

per arm for vehicle, BAY 80-6946, and BAY 80-6946 + ketogenic diet; *n* = 4 for ketogenic diet alone. **b**, Volume of each tumour in this cohort plotted individually. **c, d**, Mean \pm s.d. blood glucose (c) and c-peptide (d) in mice in **b, c**, 240 min after treatment. **e**, Mass of these mice over time on treatment. Tumours were allowed to grow until their diameters were >0.6 cm before the initiation of treatment.

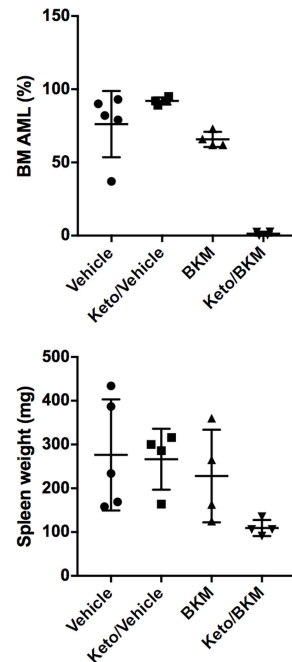
A



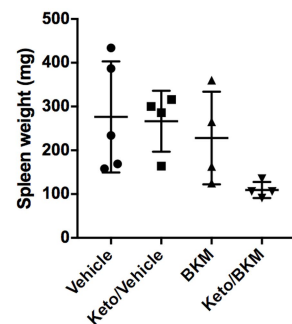
B



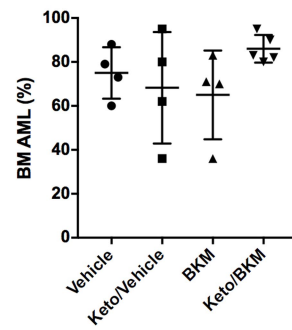
C



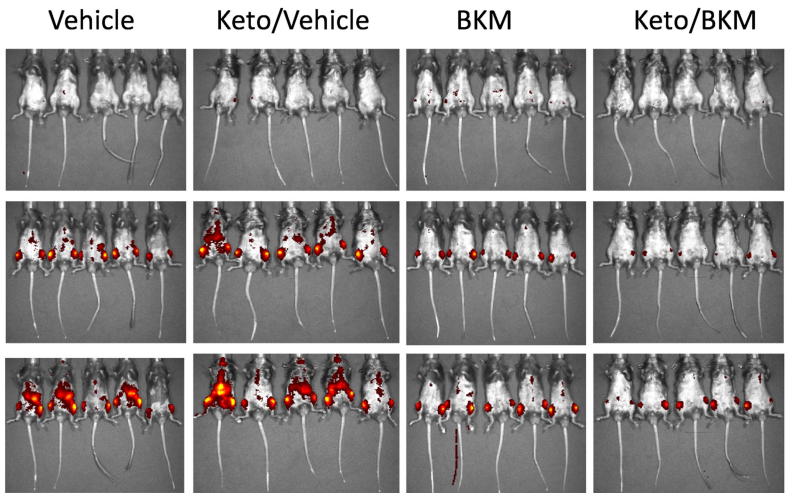
D



E



F



Extended Data Fig. 7 | See next page for caption.

Extended Data Fig. 7 | Effect of BKM120 + ketogenic diet on a syngeneic model of AML. **a**, IVIS images of AML burden (as reported by DS-red) in over time. The group labelled BKM120 plus ketogenic diet were pre-treated with a ketogenic diet. $n = 7$ mice per arm. **b**, Survival curves of mice from a with additional mice to evaluate pre-treatment versus co-treatment with the ketogenic diet in the syngeneic model of AML treated with BKM120 alone or in combination with a ketogenic diet. Individual lines are shown for initiation of ketogenic diet before (pre) or at the same time as the initiation of BKM120 treatment (co); in both cases, BKM120 efficacy is significantly enhanced by the addition of the ketogenic diet ($P = 0.0142$ and 0.0316 by Gehan–Breslow Wilcoxon test for pre and co compared to BKM alone, respectively). *Mice that were euthanized owing to paralysis resulting from AML infiltrating the CNS, rather than deaths typically seen in these mice due to tumour burden. Of note, the mice in the BKM + ketogenic diet group were frequently euthanized due to paralysis, but this was not frequently a cause of mortality in the other treatment

groups. $n = 6, 6, 5, 7, 5, 7$ mice per arm for vehicle, pre-ketogenic diet, co-ketogenic diet, BKM120, co-ketogenic diet + BKM120, and pre-ketogenic diet + BKM120, respectively. **c, d**, Disease burden of AML as measured by per cent DS-red positive AML cells in bone marrow (c) and spleen weight across the treatment groups (**D**) (pre-treated with ketogenic diet). Data are mean \pm s.d. $n = 5, 4, 4, 4$ mice per arm for vehicle, pre-ketogenic diet, BKM120, and pre-ketogenic diet + BKM120, respectively. **e**, Measurement of AML burden in mice that were pretreated with BKM120 and/or a ketogenic diet to demonstrate that the effects observed in the AML studies are not the result of implantation issues related to the pretreatment. Data are mean \pm s.d. $n = 4, 4, 4, 5$ mice per arm for vehicle, pre-ketogenic diet, BKM120, and pre-ketogenic diet + BKM120, respectively. **f**, Images of mice treated as indicated with BKM120 and ketogenic diet where the diet and BKM120 therapy were initiated on the same day (co-treatment). $n = 5$ mice per arm.

Automethylation-induced conformational switch in Clr4 (Suv39h) maintains epigenetic stability

Nahid Iglesias^{1,2,3}, Mark A. Currie^{1,2,3}, Gloria Jih^{1,2}, Joao A. Paulo¹, Nertila Siuti^{1,2}, Marian Kalocsay¹, Steven P. Gygi¹ & Danesh Moazed^{1,2*}

Histone H3 lysine 9 methylation (H3K9me) mediates heterochromatic gene silencing and is important for genome stability and the regulation of gene expression^{1–4}. The establishment and epigenetic maintenance of heterochromatin involve the recruitment of H3K9 methyltransferases to specific sites on DNA, followed by the recognition of pre-existing H3K9me by the methyltransferase and methylation of proximal histone H3^{5–11}. This positive feedback loop must be tightly regulated to prevent deleterious epigenetic gene silencing. Extrinsic anti-silencing mechanisms involving histone demethylation or boundary elements help to limit the spread of inappropriate H3K9me^{12–15}. However, how H3K9 methyltransferase activity is locally restricted or prevented from initiating random H3K9me—which would lead to aberrant gene silencing and epigenetic instability—is not fully understood. Here we reveal an autoinhibited conformation in the conserved H3K9 methyltransferase Clr4 (also known as Suv39h) of the fission yeast *Schizosaccharomyces pombe* that has a critical role in preventing aberrant heterochromatin formation. Biochemical and X-ray crystallographic data show that an internal loop in Clr4 inhibits the catalytic activity of this enzyme by blocking the histone H3K9 substrate-binding pocket, and that automethylation of specific lysines in this loop promotes a conformational switch that enhances the H3K9me activity of Clr4. Mutations that are predicted to disrupt this regulation lead to aberrant H3K9me, loss of heterochromatin domains and inhibition of growth, demonstrating the importance of the intrinsic inhibition and auto-activation of Clr4 in regulating the deposition of H3K9me and in preventing epigenetic instability. Conservation of the Clr4 autoregulatory loop in other H3K9 methyltransferases and the automethylation of a corresponding lysine in the human SUV39H2 homologue¹⁶ suggest that the mechanism described here is broadly conserved.

While examining the *in vitro* methyltransferase activity of Clr4 (Extended Data Fig. 1a), we noticed that Clr4 methylated itself in the presence or absence of its canonical histone H3^{1–20} substrate (Fig. 1a, Extended Data Fig. 1b). Whereas wild-type Clr4 readily methylated itself, it was unable to methylate a catalytically inactive Clr4 N-terminally tagged with glutathione S-transferase (GST–Clr4^{dead}) *in trans*, which suggests that Clr4 undergoes intramolecular automethylation (Fig. 1b, Extended Data Fig. 1b). Moreover, Clr4 automethylation produced a more-active enzyme—as shown by the fact that pre-incubation of Clr4 with non-radioactive S-adenosyl-L-methionine (SAM) to enable automethylation, before performing methylation reactions with ³H-SAM and histone H3^{1–20}, increased the activity of Clr4 on H3^{1–20} (Fig. 1c, Extended Data Fig. 1c, d).

To identify the automethylated lysine(s) in Clr4, we incubated Clr4 with non-radioactive SAM for various periods of time and then performed liquid chromatography with tandem mass spectrometry (LC–MS/MS) analysis. A purified catalytically dead Clr4 protein was also analysed by quantitative mass spectrometry to rule out lysines that may have been methylated by *Escherichia coli* enzymes. We consistently

identified methylation of Clr4 K127 (monomethylation (me1) and trimethylation (me3)) and K455 (me1, dimethylation (me2) and me3) in wild-type relative to catalytically dead Clr4, K127 (me2) in both wild-type and catalytically dead Clr4, and K464 (me1) in some preparations (Fig. 1d, Extended Data Fig. 1e, Extended Data Fig. 2). Among these lysines, only the substitution of K455 with arginine (K455R)—a lysine mimic that cannot be methylated by SET-domain methyltransferases such as Clr4—greatly diminished Clr4 automethylation, and combining K455R with a K464R substitution did not further decrease Clr4 automethylation (Fig. 1e, Extended Data Fig. 1f, g). Clr4 K455 was also the only lysine that showed increased time-dependent methylation upon the incubation of Clr4 with SAM (Extended Data Fig. 2d). Furthermore, in contrast to wild-type Clr4, pre-incubation of Clr4(K455R) with non-radioactive SAM did not stimulate its ability to methylate H3^{1–20} (Fig. 1f). Thus, K455 of Clr4 is a primary target of automethylation and its substitution with arginine inhibits Clr4 autoactivation.

To gain insight into the conformation of the catalytic domain of Clr4, we solved the crystal structure of Clr4 (Clr4^{192–490}) in complex with the methyl-donor analogue S-adenosyl-L-homocysteine (SAH) (Fig. 1d). The 2.4 Å resolution Clr4^{192–490} structure displayed a similar overall conformation to the previously described Clr4^{192–490} structure¹⁷, but, unlike the previous structure, contained density that enabled us to model the post-SET domain and SAH (Fig. 1g, Extended Data Fig. 3a). The catalytic pocket of Clr4^{192–490} was occluded by K455, whether or not our crystallization conditions included the histone H3 peptide (Fig. 1h, Extended Data Fig. 3b). Clr4 K455 is located in a loop (amino acids 453–472) that connects the SET and post-SET domains, hereafter referred to as the autoregulatory loop (Fig. 1d, highlighted in red). The alignment of our Clr4^{192–490} structure with the published structure of DIM-5 in complex with a histone H3 peptide¹⁸ showed that the histone H3 peptide and the backbone of the Clr4 autoregulatory loop occupied similar positions (root-mean-square deviation = 0.761 Å) but were stabilized through distinct contacts with the respective catalytic pockets (Extended Data Fig. 3c–e). More importantly, Clr4 K455 occupied a similar position (near the sulfur of SAH) to that of K9 of the histone H3 substrate in DIM-5, and interacted in an almost identical manner with the residues of the catalytic site (Fig. 1h, i, Extended Data Fig. 3f). Thus—consistent with the biochemical and mass spectrometry identification of Clr4 K455 as a target of automethylation—this lysine is located in the Clr4 active site, where it can block access to the histone substrate and could itself act as a methyl-group acceptor. To directly test this hypothesis, we substituted Clr4 K455 with arginine—a lysine mimic that cannot be methylated by Clr4—or with alanine, a small non-polar side chain that cannot interact with the active site and which should disfavour the autoinhibited conformation (Extended Data Fig. 3g–i). Consistent with our hypothesis, whereas Clr4(K455R) displayed reduced Clr4 activity on the H3 substrate relative to wild-type Clr4, Clr4(K455A) increased histone H3^{1–20} methylation (Fig. 1j).

¹Department of Cell Biology, Harvard Medical School, Boston, MA, USA. ²Howard Hughes Medical Institute, Boston, MA, USA. ³These authors contributed equally: Nahid Iglesias, Mark A. Currie.
*e-mail: danesh@hms.harvard.edu

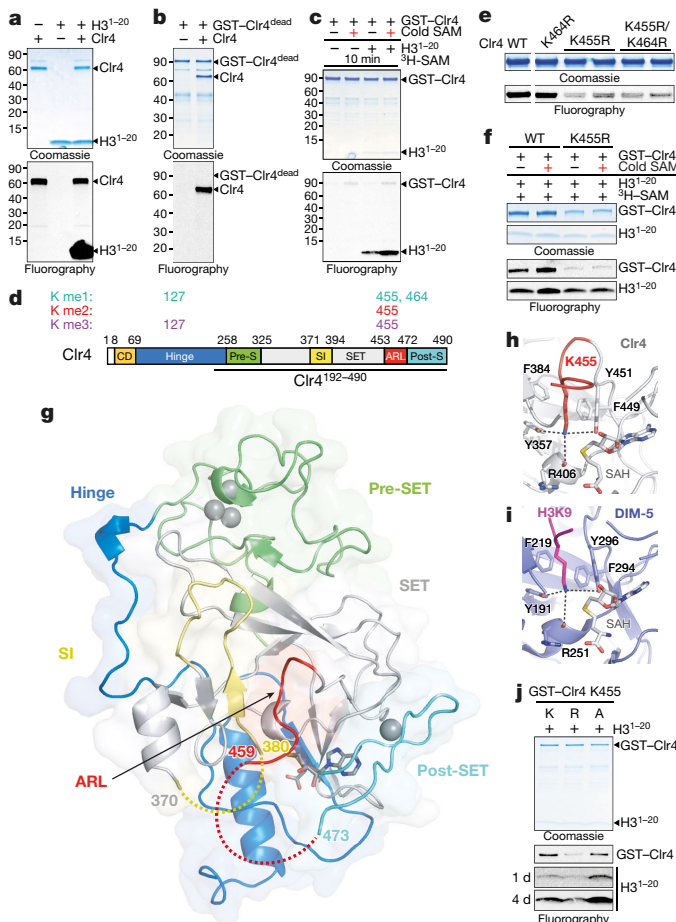


Fig. 1 | Clr4 automethylation and the structural basis of its autoinhibition. **a**, Clr4 undergoes automethylation in the absence (−) or presence (+) of histone H3^{1–20} peptide. Coomassie-stained gel (top) and fluorography (bottom). Experiment repeated more than ten times with similar results. **b**, Purified GST–Clr4^{dead} mutant (Clr4(Y451N)) is not methylated *in trans* by the purified Clr4 wild-type protein. The GST tag was left on the Clr4^{dead} mutant, which enabled us to distinguish the slower-migrating GST–Clr4^{dead} from wild-type Clr4. Experiment repeated twice with similar results. **c**, Clr4 automethylation increases its methyltransferase activity. Experiment repeated five times with similar results. **d**, Domain organization of *S. pombe* Clr4 protein (bottom) and the position of methylated lysines (K) identified by LC–MS/MS (top). Mono- (me1), di- (me2) and trimethylated (me3) states are indicated. Bold line indicates the Clr4 protein (Clr4^{192–490}) used for crystallization. ARL, autoregulatory loop; CD, chromodomain; pre-S, pre-SET; post-S, post-SET; SI, SET insertion domain. **e**, In vitro methyltransferase assay showing that the substitution of Clr4 K455 with arginine (K455R) decreased automethylation, whereas substitution of Clr4 K464 with arginine (K464R) alone—or in combination with K455R—did not further decrease automethylation. Experiment repeated three times with similar results. WT, wild type. **f**, Unlike wild-type Clr4, the methyltransferase activity of the Clr4(K455R) mutant is not stimulated after automethylation (red +). Experiment repeated twice with similar results. **g**, Structure of *S. pombe* Clr4^{192–490} autoinhibited conformation with the SET (methyltransferase domain) and other domains presented in the indicated colours. Clr4^{192–490}, SAH and zinc cations are shown in cartoon representation, sticks and grey spheres, respectively. **h**, **i**, K455 is located in the Clr4 catalytic pocket in proximity to the sulfur atom of SAH (**h**), in a similar position to K9 of histone H3 substrate (H3K9) bound to DIM-5 (RCSB Protein Data Bank code (PDB ID) 1PEG, purple) (**i**) (see Extended Data Fig. 3f for overlay). **j**, Clr4(K455R) and Clr4(K455A) mutant proteins have decreased and increased methyltransferase activity, respectively, towards the H3^{1–20} peptide substrate. Exposure times are indicated. Experiment repeated twice (Clr4(K455R)) or four times (Clr4(K455A)) with similar results. See Supplementary Fig. 1 for the uncropped gels.

To evaluate the consequences of automethylation on Clr4 conformation, we solved the crystal structure of automethylated Clr4^{192–490}. The 2.8 Å structure revealed a marked conformational rearrangement in Clr4 (Fig. 2a). In contrast to the autoinhibited conformation (Fig. 2b, left), K455 and C-terminal amino acids in the automethylated Clr4 were disordered and therefore no longer occluded the catalytic pocket (Fig. 2b, right, Extended Data Fig. 4a–e). Conversely, the C-terminal residues in the autoregulatory loop (residues 468 to 472)—which were disordered in the autoinhibited structure (Fig. 2b, left)—formed a helix that interacted with and stabilized the SET insertion domain (residues 371 to 379) (Fig. 2b, right), which was also partially disordered in the autoinhibited structure (Fig. 2b, left). The SET insertion domain has previously been proposed to have a conserved role in substrate recognition and cofactor binding, and its conformation is also modulated by protein–protein interactions in other SET-domain methyltransferases^{19,20}. Clr4 therefore exists in an inhibited conformation, which is reversed by an automethylation-induced conformational switch.

Similar to wild-type Clr4, we detected stimulation of Clr4(K455A) methyltransferase activity on histone H3^{1–20} after pre-incubation with non-radioactive SAM (Fig. 1c, Fig. 3a). This observation suggested that, in addition to K455, methylation of at least one other lysine contributed to the relief of Clr4 autoinhibition. In addition to K455, the Clr4 autoregulatory loop contains lysines at positions 464, which we had already ruled out as a major target of automethylation (Fig. 1e), and 472. In vitro methyltransferase assays showed that Clr4(K472A) led to increased methylation of the H3 peptide, which was greatly enhanced in combination with K455A (Fig. 3b). By contrast, Clr4(K472R) had slightly reduced automethylation activity and reduced H3 peptide substrate methylation activity, which was further reduced in combination with K455R (Fig. 3b). The addition of the K472R mutation to the hyperactive Clr4(K455A) protein also greatly reduced both Clr4(K455A) automethylation and methyltransferase activity towards H3^{1–20} (Extended Data Fig. 5a). Together, these findings suggest that the full activation of Clr4 requires the methylation of both K455 and K472. Consistently, Clr4(K472R) methylation activity on histone H3^{1–20} was not stimulated after pre-incubation with non-radioactive SAM (Extended Data Fig. 5b). Kinetic analysis indicated that, relative to wild-type Clr4, alanine (Clr4(K455A), Clr4(K472A) or Clr4(K455A/K472A)) and arginine (Clr4(K455R), Clr4(K472R) or Clr4(K455R/K472R)) substitutions resulted in faster and slower rates of histone H3^{1–20} methylation, respectively, with the double mutants showing stronger effects than the single mutants (Fig. 3c). Analysis of auto-methylated Clr4 by LC-MS/MS (Fig. 1d, Extended Data Figs 1, 2) did not uncover Clr4 K472 methylation, probably because trypsin or LysC digestion generated K472 peptides that were not readily detectable by LC-MS/MS. However, in human SUV39H2, K392—the lysine that corresponds to Clr4 K472—was recently reported¹⁶ to be automethylated, which together with our findings supports an evolutionarily conserved role for this automethylation event. We note that in contrast to our findings, which reveal an activating role for the automethylation of Clr4 K472, automethylation of the corresponding human SUV39H2 K392 was proposed to inhibit its methyltransferase activity¹⁶. This apparent contradiction is likely due to dilution of ³H-SAM by excess non-radioactive SAM, which was not removed before histone peptide methylation assays with SUV39H2¹⁶.

To investigate the effect of Clr4 autoregulation on heterochromatin formation and silencing, we constructed *S. pombe* cells that express endogenous Clr4 mutant proteins with single or double substitutions at K455 and K472 (Extended Data Fig. 5c). We predicted that silencing would be weakened in cells that express hypoactive Clr4 with lysine-to-arginine substitutions and strengthened in cells that express hyperactive Clr4 with lysine-to-alanine substitutions (Fig. 3c, Extended Data Fig. 5d) or with lysine substituted with tryptophan, which is too bulky to fit into the active site and should destabilize the autoinhibited conformation. Gene silencing was examined using an *ade6⁺* reporter transgene inserted within the heterochromatic *mat* locus (*mat2P::ade6⁺*; Fig. 3d, left). Silencing of *ade6⁺* depends on

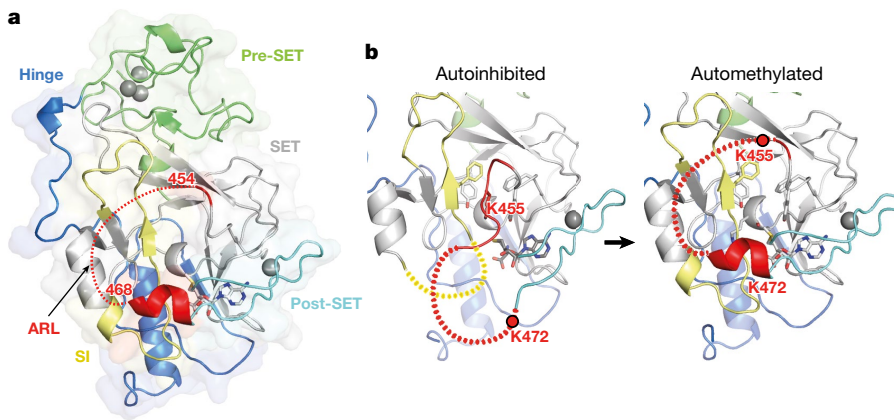


Fig. 2 | Crystal structure of automethylated Cln4^{192–490} reveals a conformational switch. **a**, Crystal structure of automethylated Cln4^{192–490} with bound SAM. See Fig. 1d, g legend for abbreviations. **b**, Expanded view of the active site showing that automethylation (right) results

heterochromatin spreading from surrounding regions and results in growth of red colonies on medium with limiting adenine. The lysine-to-arginine *clr4* mutant cells displayed partial or complete loss of *mat2P::ade6⁺* silencing relative to *clr4⁺* cells, as shown by the fact that they formed a greater percentage of white colonies, with the strongest effect observed in the double mutant *clr4^{K455R/K472R}* cells (Fig. 3d, middle). Conversely, substitutions of one or both of the lysines with alanine—or of K455 with tryptophan—resulted in increased *mat2P::ade6⁺* silencing, as indicated by growth of a higher percentage of red colonies (Fig. 3d, right). Cln4 autoinhibition therefore has a critical role in heterochromatin-dependent transgene silencing.

To gain insight into possible genome-wide changes in H3K9me in the Cln4-activity mutants, we performed chromatin immunoprecipitation combined with high throughput sequencing (ChIP-seq). Consistent with the silencing data, ChIP-seq analysis in hypoactive *clr4^{K455R}* and *clr4^{K472R}* mutant cells showed reduction or loss of H3K9me levels at ribosomal DNA, and subtelomeric and pericentromeric DNA repeats (Fig. 3e, Extended Data Fig. 5e, f). More notably, several clones that express hyperactive Cln4 enzymes with lysine-to-alanine or lysine-to-tryptophan substitutions showed a variable increase in H3K9me levels as well as spreading beyond the restricted H3K9me domains of wild-type cells. In some clones, this occurred at all heterochromatin regions, with marked increases in spreading at *tel2R* that spanned over 100 kb in some clones. A subset of these clones gained H3K9me3 at all meiotic genes and other euchromatic genes (Fig. 3e, f, Extended Data Fig. 5e, f, Supplementary Tables 1, 2), whereas other clones showed a loss of centromeric reporter gene silencing and severely diminished (or loss of) H3K9me3 levels, particularly at the *mat* locus (Extended Data Fig. 6a, b). In addition, the hyperactive *clr4* mutant cells grew slower than *clr4⁺* or *clr4Δ* cells, which suggests that inappropriate heterochromatin formation in the hyperactive mutant cells inactivates genes that are required for growth (Extended Data Fig. 7a). Thus, disruption of Cln4 autoregulation results in illegitimate spreading of heterochromatin beyond its normal boundaries, ectopic gain of H3K9me at euchromatic loci and growth inhibition.

We next asked whether Cln4 intrinsic autoinhibition acts in parallel with other anti-silencing pathways. We first tested whether a limitation in the cellular concentration of Cln4 contributes to anti-silencing by increasing the dosage of wild-type or mutant Cln4 enzymes. Cells carrying two copies of *clr4⁺* displayed stronger *mat2P::ade6⁺* silencing than cells carrying only one copy, which indicates that the dosage of *clr4⁺* influenced the strength of silencing at the *mat* locus (Extended Data Fig. 7b, first two rows). Moreover, an increased dosage of hypoactive *clr4* single and double mutants partially suppressed their *mat2P::ade6⁺* silencing defect (Extended Data Fig. 7b). By contrast, when we increased the dosage of hyperactive *clr4^{K455A}* or *clr4^{K455A/K472A}*

in a conformational switch that creates an open catalytic pocket and stabilization of SET insertion domain (residues 371–379), which are disordered in the autoinhibited conformation (left). See Extended Data Fig. 4a, b for surface presentations.

mutants we observed variable and decreased silencing as indicated by the appearance of pink and white colonies (Fig. 4a). Consistent with the hypothesis that a balance between Cln4 levels and activation potential regulates silencing in vivo, ChIP-seq analysis of H3K9me indicated that two independent clones carrying an extra copy of *clr4⁺* displayed increased H3K9me spreading (for example, at *tel2R*) and gained de novo domains of H3K9me (Fig. 4b, Extended Data Fig. 7c, d, Supplementary Table 1). Furthermore, an increased dosage of the hyperactive *clr4* mutants exacerbated their growth defect, increased H3K9me spreading at ribosomal and subtelomeric and pericentromeric DNA repeats, and resulted in the appearance of several de novo peaks of H3K9me—including at *clr4⁺*, *rik1⁺* and *rpb1⁺*, which encodes the largest subunit of RNA polymerase I (Fig. 4b, c, Extended Data Fig. 7c–e, Supplementary Table 1). *clr4⁺* and *rik1⁺* encode subunits of the Cln4 methyltransferase complex, which suggests that epigenetic adaptation—previously observed in other mutant backgrounds that promote deleterious heterochromatin spreading²¹—may enable cells to overcome the toxicity of unchecked Cln4 hyperactivity.

We next investigated whether Cln4 intrinsic autoinhibition acts in parallel with Epe1, a putative H3K9 demethylase that limits heterochromatin spreading^{13–15}. Consistent with previous studies, genome-wide analysis of H3K9me in *epe1Δ* cells revealed variations in levels of H3K9me at native heterochromatic loci, increased H3K9me spreading at some heterochromatic loci and higher levels of H3K9me at meiotic genes^{14,15} (Extended Data Fig. 8a, b, Supplementary Table 2). In addition, we observed ectopic peaks of H3K9me at several non-meiotic genes in *epe1Δ* cells (Extended Data Fig. 8b, Supplementary Table 2). These ectopic H3K9me peaks became more prevalent in *epe1Δ ago1Δ* double mutant cells, and some clones also displayed signatures of epigenetic adaptation such as gaining H3K9me at *clr4⁺* itself (Extended Data Fig. 8c, d)—similar to hyperactive Cln4 mutants at an increased dosage (Fig. 4c). The enhancement of the phenotype associated with *epe1* deletion in *epe1Δ ago1Δ* double mutant cells is probably the result of an increase in free Cln4 concentration owing to its release from pericentromeric and telomeric DNA repeats, where heterochromatin formation is dependent on Ago1²². To more directly test the relationship between Cln4 autoinhibition and anti-silencing mediated by Epe1, we deleted *epe1⁺* in hyperactive *clr4* mutant cells. In contrast to *epe1Δ* *clr4⁺* cells, hyperactive *epe1Δ* *clr4* mutant cells reduced rather than increased the silencing of *mat2P::ade6⁺*, which was more marked in some *epe1Δ* *clr4^{K455A/K472A}* mutant clones (Fig. 4d, Extended Data Fig. 8e). ChIP-seq analysis of different clones with variable silencing defects showed that loss of *mat2P::ade6⁺* silencing in a representative *epe1Δ* *clr4^{K455A/K472A}* clone was accompanied by loss of H3K9me at *ade6⁺* and the *mat* locus (clone #5; Fig. 4d, e, Extended Data Fig. 8f). The loss or reduced silencing in hyperactive *epe1Δ* *clr4* double mutants

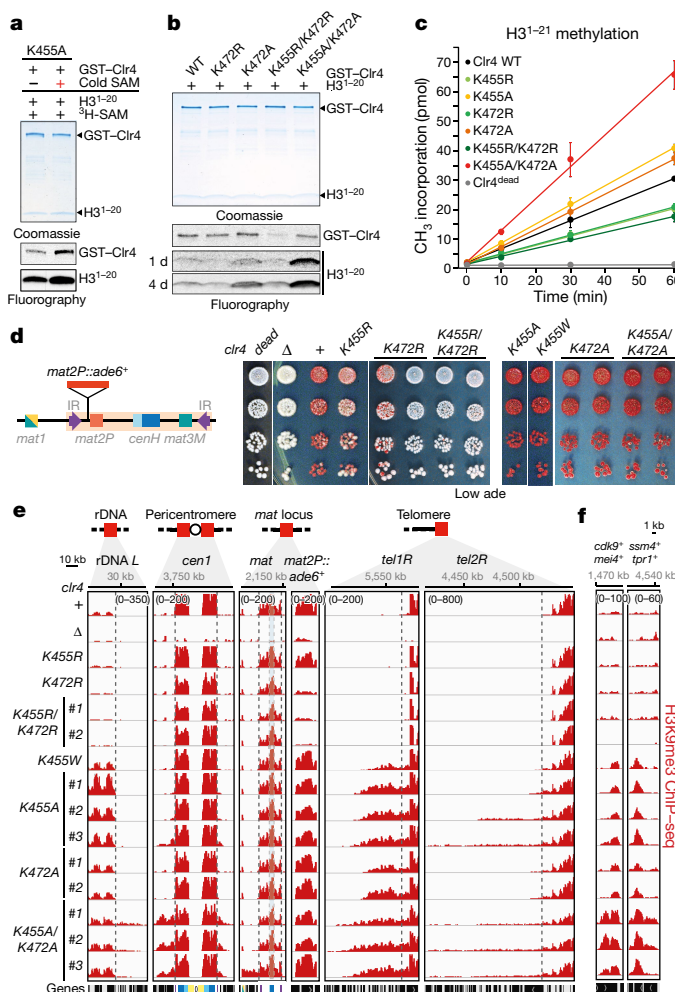


Fig. 3 | Autoregulatory loop lysines regulate Clr4 histone H3K9 methylation in vitro and heterochromatin formation in vivo. **a**, In vitro methyltransferase assay showing that methyltransferase activity of the Clr4(K455A) mutant can be stimulated after autometylation (red +). Experiment repeated twice with similar results. **b**, Compared to Clr4 wild-type protein, Clr4(K472R) and Clr4(K472A) mutants have decreased and increased methyltransferase activity, respectively, towards the H3^{1–21} peptide. Exposure times are indicated. Experiment repeated twice with similar results. **c**, Time course of methyltransferase activity of Clr4 wild-type and autoregulatory-loop-mutant proteins towards H3^{1–21} peptide substrate, measured by scintillation counts of ³H-SAM incorporation. Data are mean ± s.d. from three biological replicates. **d**, Left, map of the *mat2P::ade6⁺* locus. IR, inverted repeat. Right, silencing assays of *mat2P::ade6⁺* on low-adenine medium (Low ade) to assess *ade6⁺* silencing in the indicated genotypes. Experiment repeated at least three times with two or three independent clones with similar results. **e**, **f**, Examples of H3K9me3 ChIP-seq reads mapped to representative heterochromatin regions (e) or euchromatic genes (f) in the indicated genotypes are presented as reads per million (number in parentheses in the first row of each set of ChIP-seq data). Sequencing performed once with three to four independent clones. See Supplementary Fig. 1 for the uncropped gels.

was often accompanied by the gain of de novo peaks of H3K9me at genes that encode heterochromatin proteins, such as *clr4⁺* itself, *rik1⁺* or *sir2⁺* (Fig. 4f, Extended Data Fig. 8f, right, Supplementary Table 2).

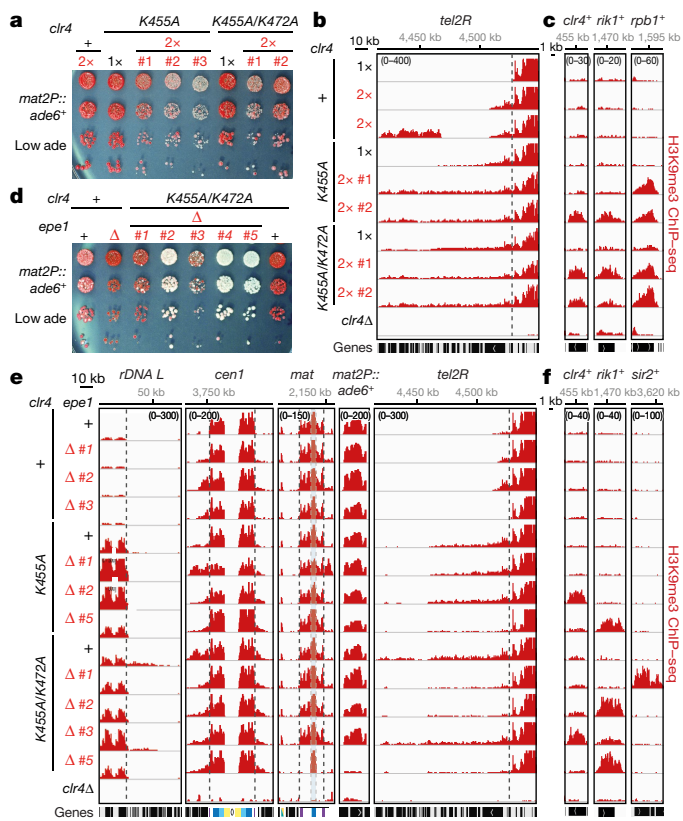


Fig. 4 | Disruption of Clr4 autoinhibition results in growth defects and epigenetic instability. **a**, Silencing assay of *mat2P::ade6⁺* on low-adenine medium with one (1x) or two (2x) copies of Clr4 wild-type or mutant genes. # indicates an independent clone. Experiment performed once with two to three independent clones. **b**, **c**, H3K9me3 ChIP-seq reads mapped to representative heterochromatin regions (b) or euchromatic genes (c) in the indicated genotypes are presented as reads per million (number in parentheses in the first row of each set of ChIP-seq data). Sequencing performed once with two independent clones. **d**, Silencing assay of *mat2P::ade6⁺* on low-adenine medium, showing that the combination of *epe1^Δ* deletion (Δ) with hyperactive Clr4 mutant results in clone-to-clone variegation of the *ade6⁺* silencing defect. Experiment performed once with five independent clones as shown. **e**, **f**, H3K9me3 ChIP-seq reads mapped to representative heterochromatin regions (e) or euchromatic genes (f) in the indicated genotypes are presented as reads per million (number in parentheses in the first row of each set of ChIP-seq data). Sequencing performed once with three to four independent clones.

This suggests that the survival of cells that lack both intrinsic Clr4 autoinhibition and extrinsic H3K9me demethylation depends on epigenetic downregulation of factors required for heterochromatin formation. Thus, Clr4 intrinsic autoinhibition acts in parallel with extrinsic anti-silencing mechanisms (that is, Clr4 levels and Epe1-promoted demethylation) to maintain accurate H3K9me domains and epigenetic stability. Our results also raise the possibility that Clr4 is a target of Epe1-mediated demethylation. However, as combining *epe1^Δ* with hyperactive *clr4* mutants resulted in more severe growth and silencing phenotypes than those of the hyperactive mutants alone (Fig. 4), Epe1 is likely to have substrates beyond Clr4 K455 or K472.

Finally, combining mutations in the chromodomain of Clr4 (W31G/W41G)—which disrupt its ability to recognize H3K9me—with hyperactive Clr4 mutants (K455A/K472A) suppressed the illegitimate heterochromatin formation phenotype of the hyperactive mutants (Extended Data Fig. 9a, b). This indicates that autoregulation counteracts the Clr4 positive feedback loop, preventing it from mediating aberrant H3K9 methylation and heterochromatin formation (Extended Data Fig. 9c).

The intrinsic enzyme inhibition mechanism described here represents a previously unknown layer of control that complements the extrinsic anti-silencing mechanisms that involve Epe1-promoted

H3K9 demethylation, boundary elements and appropriate Clr4 levels (Extended Data Fig. 10a). Previous structural analyses of SET-domain methyltransferases suggests that intrinsic inhibition is broadly conserved^{19,20,23,24}. The autoregulatory loop described here appears to be conserved in the mammalian Clr4 homologues²³, although its physiological importance in mammals has not been addressed. In the crystal structure of human SUV39H2, K375—which corresponds to Clr4 K455 (Extended Data Fig. 10b)—is located between the SET and post-SET domains, in a similar position to Clr4 K455. But unlike Clr4 K455, SUV39H2 K375 is inserted only halfway into the catalytic pocket²³ (Extended Data Fig. 10c). This lysine is also conserved in mouse Suv39h2, and mouse and human versions of both SUV39H1 and SUV39H2 contain a lysine—recently reported to be automethylated in human SUV39H2¹⁶—in a position that may be analogous with Clr4 K472, the second inhibitory lysine in the Clr4 autoregulatory loop (Extended Data Fig. 10b). The fission yeast Clr4 and mammalian SUV39H are components of positive feedback loops that can mediate sequence-independent spreading and epigenetic inheritance of histone modifications^{8,9,25,26}. We propose that intrinsic enzyme inhibition, which was first described for cyclin-dependent kinases²⁷, has a critical role in preventing chromatin-modifying enzymes coupled to positive feedback loops from initiating illegitimate epigenetic inactivation of the genome.

Online content

Any Methods, including any statements of data availability and Nature Research reporting summaries, along with any additional references and Source Data files, are available in the online version of the paper at <https://doi.org/10.1038/s41586-018-0398-2>.

Received: 22 November 2017; Accepted: 13 July 2018;

Published online 23 July 2018.

- Rea, S. et al. Regulation of chromatin structure by site-specific histone H3 methyltransferases. *Nature* **406**, 593–599 (2000).
- Lachner, M., O'Carroll, D., Rea, S., Mechtler, K. & Jenuwein, T. Methylation of histone H3 lysine 9 creates a binding site for HP1 proteins. *Nature* **410**, 116–120 (2001).
- Bannister, A. J. et al. Selective recognition of methylated lysine 9 on histone H3 by the HP1 chromo domain. *Nature* **410**, 120–124 (2001).
- Nakayama, J., Rice, J. C., Strahl, B. D., Allis, C. D. & Grewal, S. I. Role of histone H3 lysine 9 methylation in epigenetic control of heterochromatin assembly. *Science* **292**, 110–113 (2001).
- Moazed, D. Mechanisms for the inheritance of chromatin states. *Cell* **146**, 510–518 (2011).
- Zhang, K., Mosch, K., Fischle, W. & Grewal, S. I. Roles of the Clr4 methyltransferase complex in nucleation, spreading and maintenance of heterochromatin. *Nat. Struct. Mol. Biol.* **15**, 381–388 (2008).
- Al-Sady, B., Madhani, H. D. & Narlikar, G. J. Division of labor between the chromodomains of HP1 and Suv39 methylase enables coordination of heterochromatin spread. *Mol. Cell* **51**, 80–91 (2013).
- Ragunathan, K., Jih, G. & Moazed, D. Epigenetic inheritance uncoupled from sequence-specific recruitment. *Science* **348**, 1258699 (2015).
- Audergon, P. N. et al. Restricted epigenetic inheritance of H3K9 methylation. *Science* **348**, 132–135 (2015).
- Wang, X. & Moazed, D. DNA sequence-dependent epigenetic inheritance of gene silencing and histone H3K9 methylation. *Science* **356**, 88–91 (2017).
- Jih, G. et al. Unique roles for histone H3K9me states in RNAi and heritable silencing of transcription. *Nature* **547**, 463–467 (2017).
- Thon, G., Bjerling, P., Bünnner, C. M. & Verhein-Hansen, J. Expression-state boundaries in the mating-type region of fission yeast. *Genetics* **161**, 611–622 (2002).

- Treich, S. C., Minc, E., Antonelli, R., Urano, T. & Allshire, R. C. The JmjC domain protein Epe1 prevents unregulated assembly and disassembly of heterochromatin. *EMBO J.* **26**, 4670–4682 (2007).
- Wang, J. et al. Epe1 recruits BET family bromodomain protein Bdf2 to establish heterochromatin boundaries. *Genes Dev.* **27**, 1886–1902 (2013).
- Zofall, M. & Grewal, S. I. Swi6/HP1 recruits a JmjC domain protein to facilitate transcription of heterochromatic repeats. *Mol. Cell* **22**, 681–692 (2006).
- Piao, L. et al. Automethylation of SUV39H2, an oncogenic histone lysine methyltransferase, regulates its binding affinity to substrate proteins. *Oncotarget* **7**, 22846–22856 (2016).
- Min, J., Zhang, X., Cheng, X., Grewal, S. I. & Xu, R. M. Structure of the SET domain histone lysine methyltransferase Clr4. *Nat. Struct. Biol.* **9**, 828–832 (2002).
- Zhang, X. et al. Structural basis for the product specificity of histone lysine methyltransferases. *Mol. Cell* **12**, 177–185 (2003).
- Li, Y. et al. Structural basis for activity regulation of MLL family methyltransferases. *Nature* **530**, 447–452 (2016).
- Moritz, L. E. & Trievel, R. C. Structure, mechanism, and regulation of polycomb repressive complex 2. *J. Biol. Chem.* <https://doi.org/10.1074/jbc.R117.800367> (2017).
- Wang, J., Reddy, B. D. & Jia, S. Rapid epigenetic adaptation to uncontrolled heterochromatin spreading. *eLife* **4**, (2015).
- Volpe, T. A. et al. Regulation of heterochromatic silencing and histone H3 lysine-9 methylation by RNAi. *Science* **297**, 1833–1837 (2002).
- Wu, H. et al. Structural biology of human H3K9 methyltransferases. *PLoS ONE* **5**, e8570 (2010).
- Southall, S. M., Wong, P. S., Odho, Z., Roe, S. M. & Wilson, J. R. Structural basis for the requirement of additional factors for MLL1 SET domain activity and recognition of epigenetic marks. *Mol. Cell* **33**, 181–191 (2009).
- Bintu, L. et al. Dynamics of epigenetic regulation at the single-cell level. *Science* **351**, 720–724 (2016).
- Hathaway, N. A. et al. Dynamics and memory of heterochromatin in living cells. *Cell* **149**, 1447–1460 (2012).
- Morgan, D. O. Principles of CDK regulation. *Nature* **374**, 131–134 (1995).

Acknowledgements We are grateful for assistance from the staff at NE-CAT at Argonne National Laboratory, the SBGrid consortium at Harvard Medical School, and S. Jenni for useful discussions, H. Yoon for help with the scintillation counter, Z. Moqtaderi and R. Yu for Python scripts, G. Shipkovenska, A. Tatarakis, X. Wang, A. Yuan and H. Zhou for comments on the manuscript, and members of the Moazed laboratory for discussion. This work used NE-CAT beamlines (GM103403), a Pilatus detector (RR029205), an Eiger detector (OD021527) and APS Synchrotron source (DE-AC02-06CH11357). This work was supported by an EMBO long-term fellowship and a Swiss National Science Foundation postdoctoral fellowship (N.I.), K01 DK098285 (J.A.P.), NIH P50 GM107618 (M.K., S.P.G.) and NIH RO1 GM072805 (D.M.). D.M. is a Howard Hughes Medical Institute Investigator.

Author contributions N.I., M.A.C. and D.M. designed experiments. N.I. prepared recombinant proteins for methyltransferase assays, performed methylation, mutagenesis, strain construction, ChIP-seq, western blot, silencing and growth assays. G.J. performed strain construction and ChIP-seq for Extended Data Fig. 8a–d. N.I. analysed all other sequencing libraries. M.A.C. prepared and crystallized Clr4^{192–490} proteins, collected X-ray diffraction data, solved structures and performed molecular modelling and structural analysis. J.A.P., N.S. and M.K. performed mass spectrometry. S.P.G. and D.M. supervised research. N.I., M.A.C. and D.M. wrote and edited the paper.

Competing interests : The authors declare no competing interests.

Additional information

Extended data is available for this paper at <https://doi.org/10.1038/s41586-018-0398-2>.

Supplementary information is available for this paper at <https://doi.org/10.1038/s41586-018-0398-2>.

Reprints and permissions information is available at <http://www.nature.com/reprints>.

Correspondence and requests for materials should be addressed to D.M.

Publisher's note: Springer Nature remains neutral with regard to jurisdictional claims in published maps and institutional affiliations.

METHODS

No statistical methods were used to predetermine sample size. The experiments were not randomized and the investigators were not blinded to allocation during experiments and outcome assessment.

Strains and plasmids construction. *S. pombe* strains used in this study and their genotypes are listed in Supplementary Table 3. Plasmids are listed in Supplementary Table 4. To generate pGEX-6P-1-Clr4 (pDM2113) and pGEX-6P-1-Clr4 192–490 (pDM1906), the coding sequence of full-length Clr4 (amino acids 1–490) and the Clr4 sequence encoding amino acids 192–490 were amplified from *S. pombe* genomic DNA and cloned into an *EcoRI*/*XbaI* or *BamHI*/*XbaI* digested pGEX-6P-1 plasmid backbone (GE Healthcare), respectively. pGEX-6P-1-Clr4-Y451N (GST-C^{dead} Clr4, pDM2142) contains the Y451N amino acid substitution in the catalytic SET domain²⁸. Mutagenesis was performed by partial overlap PCR and plasmids sequences were verified by DNA sequencing.

All strains except SPY7249–SPY7260 were constructed by transformation using a PCR-based targeting method and lithium acetate protocol²⁹ and selected on yeast extract plus adenine (YEA) plates that contained appropriate antibiotic. SPY7249–SPY7260 strains (*ago1Δ epe1Δ* strains #4–14 in Extended Data Fig. 8d) were constructed by crossing SPY2352 and SPY3216 followed by random spore analysis. Integrations were confirmed by colony PCR and *clr4*⁺ and mutant sequences were verified by DNA sequencing. All Flag-tagged Clr4 or mutant genes were expressed under the control of their endogenous promoters and terminators. SPY8363–SPY8365 strains were constructed by integrating the open reading frames of full-length *3 × Flag-clr4*^{W31G/W41G/K455A/K472A} mutants in place of *3 × Flag-clr4*^{K455A/K472A} in SPY7361. SPY7363, SPY7364, SPY7366–SPY7369, SPY7371, SPY7372, SPY7374–SPY7376, SPY7384 and SPY7385 strains were constructed by integrating the open reading frames of full-length *clr4*⁺ or mutants, and the endogenous *clr4*⁺ promoter and terminator sequences, about 450-bp upstream of the *trp1*⁺ gene in the SPY3 strain.

Silencing assays. Cells were grown at 30 °C overnight in 5 ml of YEA medium. 1×10^7 cells were collected, washed once with sterile water, suspended in 200 µl of sterile water, and then serially diluted tenfold. Three microlitres of each dilution was spotted on the appropriate growth medium (YE, YEA, EMM-Ura, YEA + FOA, containing 1 mg/ml of FOA). Silencing of the *ade6*⁺ reporter gene was assessed by growth on yeast extract plates at 32 °C for 3–5 days followed by incubation at 4 °C for 1–2 days to enhance the red pigmentation before imaging. *ura4*⁺ reporter gene silencing was assessed by growth on the drug 5-fluoro-orotic acid (FOA), which is toxic to cells expressing Ura4.

Protein purification and methyltransferase assay. BL21(DE3) strains that express GST-Clr4 and mutant proteins were grown at 37 °C to an optical density at 600 nm (OD₆₀₀) of between 0.6–0.8. Protein expression was induced for 16 h at 18 °C with 0.2 mM of IPTG. GST-Clr4 and mutant fusion proteins were then purified on glutathione-Sepharose 4B beads (GE Healthcare) in the presence of 0.2% Triton X-100 as previously described³⁰. GST fusion proteins were eluted either by addition of 15 mM glutathione or by addition of PreScission Protease.

Methyltransferase activity on Clr4 wild-type and mutant proteins was typically carried out with approximately 1.8 µM Clr4 with or without 18 µM H3^{1–20} peptide (Anaspec) in HMT buffer (50 mM Tris-HCl, pH 8, 20 mM KCl, 10 mM MgCl₂, 1 mM DTT, 0.02% Triton, 5% glycerol, 1 mM PMSF) in the presence of 0.42 µM ³H-S-adenosyl methionine (³H-SAM, Perkin Elmer) and 70 µM cold SAM for 1 h at 30 °C with mild agitation. Samples were boiled for 5 min, separated in two halves and loaded on 4–20% gradient SDS-PAGE (Bio-Rad). Gels were either stained with Coomassie blue to visualize protein or were transferred onto a PVDF membrane (Immobilon-P^{SO}, Millipore), sprayed with EN³HANCE spray (Perkin Elmer) and exposed on Hyperfilm (Amersham) at –80 °C for between 1 and several days for analysis of ³H incorporation. Kinetic analysis of the methyltransferase activity of Clr4 (Fig. 3c) was performed as described above, except that 10.8 µM of biotinylated histone H3^{1–21} peptide (Anaspec, #61702) was used instead of H3^{1–20} peptide. Samples were taken at different time intervals and the reaction was stopped by the addition of 1 × sample buffer. Samples were then spotted on a streptavidin matrix (SAM2 biotin capture membrane; Promega, #V2861), which was washed three times with 1 M NaCl and then two times with deionized water. After the membrane was fully dried, each membrane square was placed in a scintillation vial containing Ultima Gold scintillation cocktail (Perkin Elmer) and scintillation counting was performed on a Tri-Carb 2910 TR scintillation counter (Perkin Elmer).

In vitro methyltransferase assays with unmethylated and automethylated Clr4 were performed by first incubating GST-Clr4 immobilized on beads in HMT buffer in the absence or presence, respectively, of 250 µM cold SAM for 1 h at 30 °C with mild agitation. Unmethylated and automethylated GST-Clr4 beads were then washed three times in HMT buffer and used for methyltransferase assays with histone H3^{1–20} peptide as described above, except that reactions were incubated for 10 min. Kinetic analysis of the methyltransferase activity of Clr4 after auto-methylation (Extended Data Fig. 1d) was performed as described above, except that unmethylated and automethylated GST-Clr4 beads were used for methyl-

transferase assays with 10.8 µM biotinylated histone H3^{1–21} peptide (Anaspec, #61702) in the presence of 70 µM cold SAM and 0.42 µM ³H-SAM. Samples were taken at different time intervals and the reaction was stopped by the addition of 1 × sample buffer. Samples were then spotted on a streptavidin matrix (SAM2 biotin capture membrane; Promega, #V2861), which was washed three times with 1 M NaCl followed by two washes with deionized water. After the membrane was fully dried, each membrane square was placed in a scintillation vial containing Ultima Gold scintillation cocktail (Perkin Elmer) and scintillation counting was performed on a Tri-Carb 2910 TR scintillation counter (Perkin Elmer).

Mass spectrometry analysis for identification of Clr4 methylated lysines. For mass spectrometry analysis of Clr4 methylated lysines, a methyltransferase assay was performed as described above, except that 2.4 µM recombinant Clr4 was incubated with 250 µM cold SAM for 4 h followed by trichloroacetic acid precipitation and protein digestion. In brief, 100% trichloroacetic acid was added to each designated sample to achieve a final concentration of 12.5%. The sample was vortexed, incubated on ice for 1 h and centrifuged at 20,000 rpm for 30 min at 4 °C. The supernatant was aspirated and the sample was washed once with 1 ml of acetone. The sample was centrifuged at 20,000 rpm for 10 min at 4 °C. The supernatant was aspirated and the sample was washed once with 1 ml of methanol and allowed to air-dry.

Samples were digested with either trypsin or LysC at a 100:1 protein-to-protease ratio overnight at 37 °C. Samples were subsequently vacuum-centrifuged to near dryness, acidified to 1% formic acid, desalted via StageTip and dried via vacuum centrifugation. The desalted peptides were reconstituted in 5% acetonitrile, 5% formic acid for LC-MS/MS processing. Mass spectrometry data were collected using an Orbitrap Fusion Lumos mass spectrometer (Thermo Fisher Scientific) coupled to a Proxeon EASY-nLC 1200 LC pump (Thermo Fisher Scientific). Peptides were separated on a 100-µm inner diameter microcapillary column packed with 35 cm of Accucore C18 resin (2.6 µm, 150 Å, Thermo Fisher). For each analysis, we loaded ~2 µg desalted peptides onto the column. Separation was in-line with the mass spectrometer and was performed using a 3-h gradient of 5 to 22% acetonitrile in 0.125% formic acid at a flow rate of ~450 nL/min. Each analysis used an SPS-MS3-based tandem mass tag method^{31,32}, which has been shown to reduce ion interference compared to MS2 quantification³³. The scan sequence began with an MS1 spectrum (Orbitrap analysis; resolution 120,000; mass range 400–1400 m/z; automatic gain control target 5×10^5 ; maximum injection time 100 ms). Precursors for MS2 and MS3 analysis were selected using a Top20 method. MS2 analysis consisted of collision-induced dissociation; automatic gain control 2.0×10^4 ; normalized collision energy 35; maximum injection time 120 ms; and isolation window of 1.2 Da. Mass spectra were processed using a SEQUEST-based in-house software pipeline³⁴. Spectra were converted to mzXML using a modified version of ReAdW.

Database searching included only the Clr4 protein and the sequence coverage was up to 86%. This database was concatenated with one composed of all protein sequences in the reversed order. Searches were performed using a 50-ppm precursor ion tolerance for total protein level analysis. The product ion tolerance was set to 0.9 Da. These wide mass tolerance windows were chosen to maximize sensitivity in conjunction with Sequest searches and linear discriminant analysis^{34,35}. We searched for the following modifications: oxidized methionine (+15.9949), mono-methylated lysine (+14.0157), dimethylated lysine (+28.0313) and trimethylated lysine (+42.0470). Candidate peptides were manually triaged with mass errors limited to greater than –10 and less than 10 ppm, XCORR values > 2, and with the requirement of trypsin specificity.

For quantitative mass spectrometry analysis of the kinetics of Clr4 lysine methylation (Extended Data Fig. 2d), methyltransferase assays were performed twice in triplicate as described above, except that 150 µg of recombinant Clr4 at a concentration of 6 µM was incubated with 640 µM cold SAM for 0, 20, 40 and 240 min followed by trichloroacetic acid precipitation and protein digestion as described above. For quantitative mass spectrometry analysis of methylated lysines in wild-type versus catalytically dead Clr4 (Extended Data Fig. 1e), the experiment was performed twice in triplicate using 150 µg of *E. coli*-purified recombinant wild-type and catalytically dead Clr4, which was precipitated using trichloroacetic acid followed by protein digestion as described above. Tandem mass tag reagents (0.8 mg) were dissolved in anhydrous acetonitrile (40 µl) of which 10 µl was added to the peptides (100 µg) with 30 µl of acetonitrile to achieve a final acetonitrile concentration of approximately 30% (v/v). Following incubation at room temperature for 1 h, the reaction was quenched with hydroxylamine to a final concentration of 0.3% (v/v). The tandem mass tag-labelled samples were pooled across all samples. The pooled sample was vacuum centrifuged to near dryness and subjected to C18 solid-phase extraction (Sep-Pak, Waters).

All samples were analysed on an Orbitrap Fusion mass spectrometer (Thermo Fisher Scientific) coupled to a Proxeon EASY-nLC 1000 LC pump (Thermo Fisher Scientific). Peptides were separated on a 100-µm inner diameter microcapillary column packed with 35 cm of Accucore C18 resin (2.6 µm, 150 Å, Thermo Fisher). For each analysis, we loaded approximately 2 µg onto the column. Peptides were separated using a 150-min gradient of 3 to 25% acetonitrile in 0.125% formic

acid with a flow rate of 450 nl/min. Each analysis used an MS3-based tandem mass tag method³¹, which has been shown to reduce ion interference compared to MS2 quantification³⁶. Before starting the analysis, we performed two injections of trifluoroethanol to elute any peptides that may have been bound to the analytical column from previous injections, to limit carry over. The scan sequence began with an MS1 spectrum (Orbitrap analysis, resolution 120,000, 350–1,400 Th, automatic gain control target 5×10^5 , maximum injection time 100 ms). The top ten precursors were then selected for MS2 and MS3 analysis. MS2 analysis consisted of: collision-induced dissociation, quadrupole ion trap analysis, automatic gain control 2×10^4 , normalized collision energy 35, *q*-value 0.25, maximum injection time 120 ms and isolation window at 0.7. Following the acquisition of each MS2 spectrum, we collected an MS3 spectrum in which multiple MS2 fragment ions are captured in the MS3 precursor population using isolation waveforms with multiple frequency notches. MS3 precursors were fragmented by higher-energy collisional dissociation and analysed using the Orbitrap (normalized collision energy 65, automatic gain control 1.5×10^5 , maximum injection time 150 ms, resolution was 50,000 at 400 Th). For MS3 analysis, we used charge-state-dependent isolation windows: For charge state $z=2$, the isolation window was set at 1.3 Th, for $z=3$ at 1 Th, for $z=4$ at 0.8 Th and for $z=5$ at 0.7 Th. Mass spectra were processed using a Sequest-based pipeline³⁴. Spectra were converted to mzXML using a modified version of ReAdW. Database searching included only the Clr4 protein. This database was concatenated with one composed of the protein sequence in the reversed order. Searches were performed using a 3-Da precursor ion tolerance for total protein level analysis. The product ion tolerance was set to 0.9 Da. Tandem mass tags (TMTs) on lysine residues and peptide N termini (+229.163 Da) and carbamidomethylation of cysteine residues (+57.021 Da) were set as static modifications, and oxidation of methionine residues (+15.995 Da) was set as a variable modification. Candidate peptides were manually triaged with mass errors limited to greater than –10 and less than 10 ppm, XCorr values > 2, and with the requirement of trypsin specificity.

ChIP-seq. ChIP was performed essentially as described¹¹. In brief, 50 ml of logarithmically growing cells was fixed with 1% formaldehyde for 15 min at room temperature, quenched with 130 mM glycine for 5 min, collected and washed twice with 1 × TBS (50 mM Tris-HCl, pH 7.5, 150 mM NaCl). Cells were resuspended in 500 µl lysis buffer (50 mM HEPES-KOH, pH 7.5, 500 mM NaCl, 1 mM EDTA, 1% Triton X-100, 0.1% SDS and protease inhibitors) in 2-ml screw-cap tubes and lysed by bead beating with 1 ml acid-washed 0.5-mm glass beads with 6 cycles of 30 s at 5,000 rpm on a MagNA Lyser Instrument (Roche). Extracts were sonicated for 3 × 20 s at 50% amplitude using a sonicator (Branson Digital Sonifier). For H3K9me2 ChIP, 2 µg of anti-H3K9me2 antibody (Abcam, ab1220) coupled to 30 µl Dynabeads protein A (Invitrogen) was used for each immunoprecipitation. For H3K9me3 ChIP, 1 µg of anti-H3K9me3 antibody (Diagenode, C15500003) was first incubated with 30 µl Dynabeads M-280 streptavidin beads (Invitrogen), followed by blocking with 5 µM biotin, according to the manufacturer's instructions, before using for each immunoprecipitation. Half (250 µl) of the sheared chromatin lysate was added to the antibody-bead mixture and incubated for 2 h at 4 °C on a rotating device.

After reversing cross-links and DNA clean-up, libraries for Illumina sequencing were constructed as previously described¹¹ following the manufacturer's protocols, starting with 1 to 10 ng of immunoprecipitated DNA fragments. In brief, each library was generated with custom-made adaptors carrying unique barcode sequences at the ligating end³⁷. Barcoded libraries were pooled and sequenced with Illumina HiSeq2000. Raw reads were separated according to their barcodes and mapped to the *S. pombe* genome using Bowtie's default parameters. Reads that mapped to repeated regions were randomly assigned to the *dg* and *dh* repeats of each chromosome and therefore the reads at *cenH* in the *mat* locus are shared with those at the pericentromeric *dg* and *dh* repeats (with which *cenH* shares 98% sequence identity). Mapped reads were normalized to reads per million, tiled with igvtools and visualized in IGV (<http://www.broad.mit.edu/igv/>). The raw and processed ChIP-seq data are publicly available at the NCBI Gene Expression Omnibus under accession number GSE102905.

Expression and purification of Clr4 SET domain for crystallization. The GST-Clr4 fusion protein containing amino acids 192 to 490 (Clr4^{192–490}) was expressed in BL21-CodonPlus (Agilent Technologies) cells. One-litre cultures of Luria Burtani medium supplemented with 100 µg/ml ampicillin were inoculated with overnight cultures and shaken at 37 °C until they reached an OD₆₀₀ of 0.6–1.0. Cultures were then cooled to 16 °C and ethanol, ZnSO₄ and IPTG were added to a final concentration of 2%, 20 µM and 0.2 mM, respectively. Cultures were shaken at 16 °C for an additional 16 h and then collected by centrifugation. Cell pellets were resuspended in buffer A (50 mM Tris-HCl, pH 8.0, and 500 mM NaCl) and 1 mg/ml DNase, 1 mg/ml lysozyme, and 1 mM MgCl₂ and incubated at 4 °C with mixing for 1 h. The suspension was subsequently sonicated and centrifuged at 32,000g for 20 min. The supernatant was nubated with glutathione-Sepharose 4B resin that had been preequilibrated in buffer A for 1 h at 4 °C. The resin was washed with buffer A and eluted with buffer A containing 10 mM reduced glutathione. The

eluted protein was dialysed overnight, with PreScission Protease (GE Healthcare) to cleave the GST tag, into buffer B (5 mM Tris-HCl, pH 8.0, 200 mM NaCl, 1 mM DTT). The protein was again incubated with glutathione-Sepharose 4B resin equilibrated in buffer B. The unbound fraction was further purified using a HiTrap Q (GE Healthcare) column and a High Load 16/60 Sephadex 200 pg column (GE Healthcare) equilibrated in buffer B. Fractions containing Clr4^{192–490} were concentrated to 10 mg/ml for crystallization.

Crystallization. Clr4^{192–490} crystals were produced by the sitting-drop vapour diffusion method at 25 °C. Clr4^{192–490} at a concentration of 10 mg/ml was preincubated with a threefold molar excess of SAH for 15 min on ice and mixed in an equal volume of reservoir solution containing 200 mM calcium acetate, 100 mM imidazole, pH 7.5, 15% PEG 8,000. Clr4-SAH complex crystals were cryoprotected in reservoir solution containing 20% glycerol. Automethylated Clr4^{192–490} was prepared for crystallization by incubating the protein at a concentration of 0.5 µM with 80 µM SAM at 25 °C. The buffer was exchanged extensively three times and replenished with fresh SAM after 8, 24 and 32 h. The protein was then concentrated to 10 mg/ml, supplemented with stoichiometric excess of SAM and mixed with an equal volume of reservoir solution containing 0.1 M magnesium formate dihydrate and 20% PEG 3,350. Crystals of the automethylated Clr4 were cryoprotected in reservoir solution containing 30% PEG 3,350. Another crystal was isolated from the same drop as the one used for data collection, washed three times in water, digested with trypsin and LysC, and subjected to mass spectrometry analysis as described above (Supplementary Table 5).

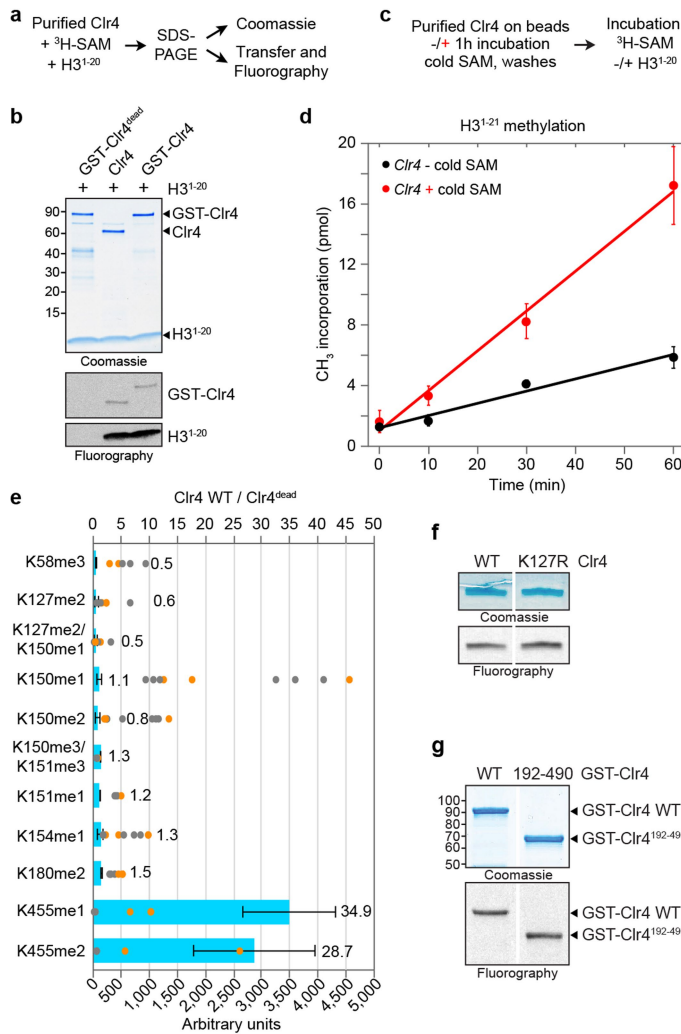
Crystallographic data collection and structure determination. X-ray diffraction data were collected at The Northeastern Collaborative Access Team (NE-CAT) beamline 24-ID-E at The Advanced Photon Source (APS) at Argonne National Laboratory, at a wavelength of 0.97918 Å³⁸. All structural biology software was accessed through the SBGrid consortium. Data were processed using XDS³⁹ and the CCP4 suite⁴⁰. The data for the automethylated form of Clr4 were corrected for anisotropy using the Staraniso server (<http://staraniso.globalphasing.org>) developed by Global Phasing. Molecular replacement was performed with Phaser⁴¹ and coordinates from PDB ID 1MVH. Phenix was used for refinement and generating omit maps⁴² and model building was carried out using COOT⁴³. Ramachandran statistics for the autoinhibited and automethylated Clr4 structures were 95.98% favoured, 3.82% allowed and 0.19% outliers and 90.86% favoured, 8.96% allowed and 0.19% outliers, respectively. All structure alignments and figures were generated using PyMOL Molecular Graphics System, version 1.8.0.3. Crystallographic data collection and refinement statistics are presented in Supplementary Table 6.

Reporting summary. Further information on experimental design is available in the Nature Research Reporting Summary linked to this paper.

Code availability. The Python script used in this study is available upon request.

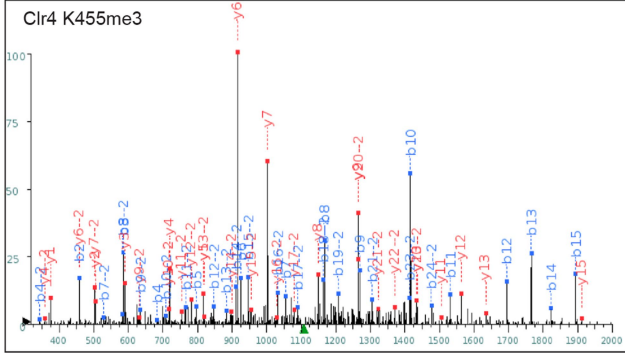
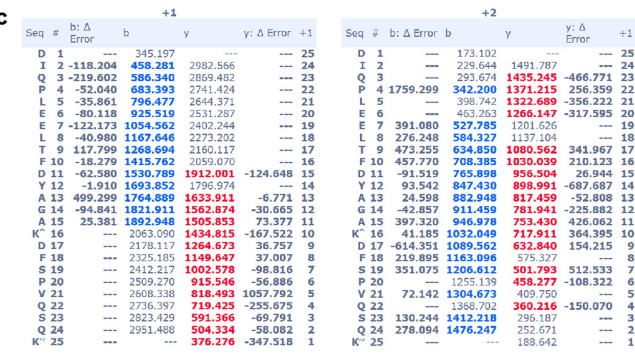
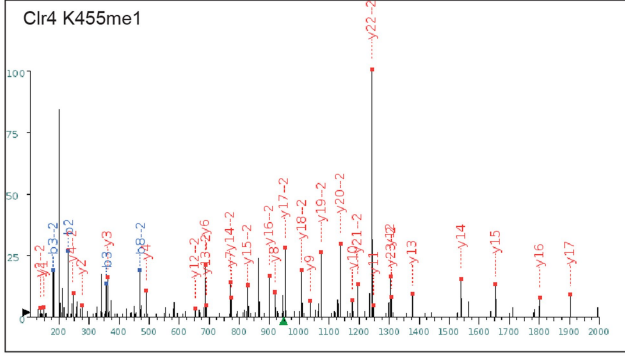
Data availability. Genome-wide datasets are deposited in the Gene Expression Omnibus (GEO) under the accession number GSE102905. Structure coordinates are deposited in the RCSB Protein Data Bank (PDB ID 6BOX and 6BP4).

28. Shan, C. M. et al. A histone H3K9M mutation traps histone methyltransferase Clr4 to prevent heterochromatin spreading. *eLife* **5**, e17903 (2016).
29. Bähler, J. et al. Heterologous modules for efficient and versatile PCR-based gene targeting in *Schizosaccharomyces pombe*. *Yeast* **14**, 943–951 (1998).
30. Iglesias, N. et al. Ubiquitin-mediated mRNP dynamics and surveillance prior to budding yeast mRNA export. *Genes Dev.* **24**, 1927–1938 (2010).
31. Ting, L., Rad, R., Gygi, S. P. & Haas, W. MS3 eliminates ratio distortion in isobaric multiplexed quantitative proteomics. *Nat. Methods* **8**, 937–940 (2011).
32. McAlister, G. C. et al. MultiNotch MS3 enables accurate, sensitive, and multiplexed detection of differential expression across cancer cell line proteomes. *Anal. Chem.* **86**, 7150–7158 (2014).
33. Paulo, J. A., O'Connell, J. D. & Gygi, S. P. A triple knockout (TKO) proteomics standard for diagnosing ion interference in isobaric labeling experiments. *J. Am. Soc. Mass Spectrom.* **27**, 1620–1625 (2016).
34. Huttlin, E. L. et al. A tissue-specific atlas of mouse protein phosphorylation and expression. *Cell* **143**, 1174–1189 (2010).
35. Beausoleil, S. A., Villén, J., Gerber, S. A., Rush, J. & Gygi, S. P. A probability-based approach for high-throughput protein phosphorylation analysis and site localization. *Nat. Biotechnol.* **24**, 1285–1292 (2006).
36. Paulo, J. A., O'Connell, J. D., Gaun, A. & Gygi, S. P. Proteome-wide quantitative multiplexed profiling of protein expression: carbon-source dependency in *Saccharomyces cerevisiae*. *Mol. Biol. Cell* **26**, 4063–4074 (2015).
37. Wong, K. H., Jin, Y. & Moqtaderi, Z. Multiplex Illumina sequencing using DNA barcoding. *Curr. Protoc. Mol. Biol.* **101**, 7.11.1–7.11.11 (2013).
38. Morin, A. et al. Collaboration gets the most out of software. *eLife* **2**, e01456 (2013).
39. Kabsch, W. Xds. *Acta Crystallogr. D* **66**, 125–132 (2010).
40. Winn, M. D. et al. Overview of the CCP4 suite and current developments. *Acta Crystallogr. D* **67**, 235–242 (2011).
41. McCoy, A. J. et al. Phaser crystallographic software. *J. Appl. Crystallogr.* **40**, 658–674 (2007).
42. Adams, P. D. et al. PHENIX: a comprehensive Python-based system for macromolecular structure solution. *Acta Crystallogr. D* **66**, 213–221 (2010).
43. Emsley, P., Lohkamp, B., Scott, W. G. & Cowtan, K. Features and development of Coot. *Acta Crystallogr. D* **66**, 486–501 (2010).

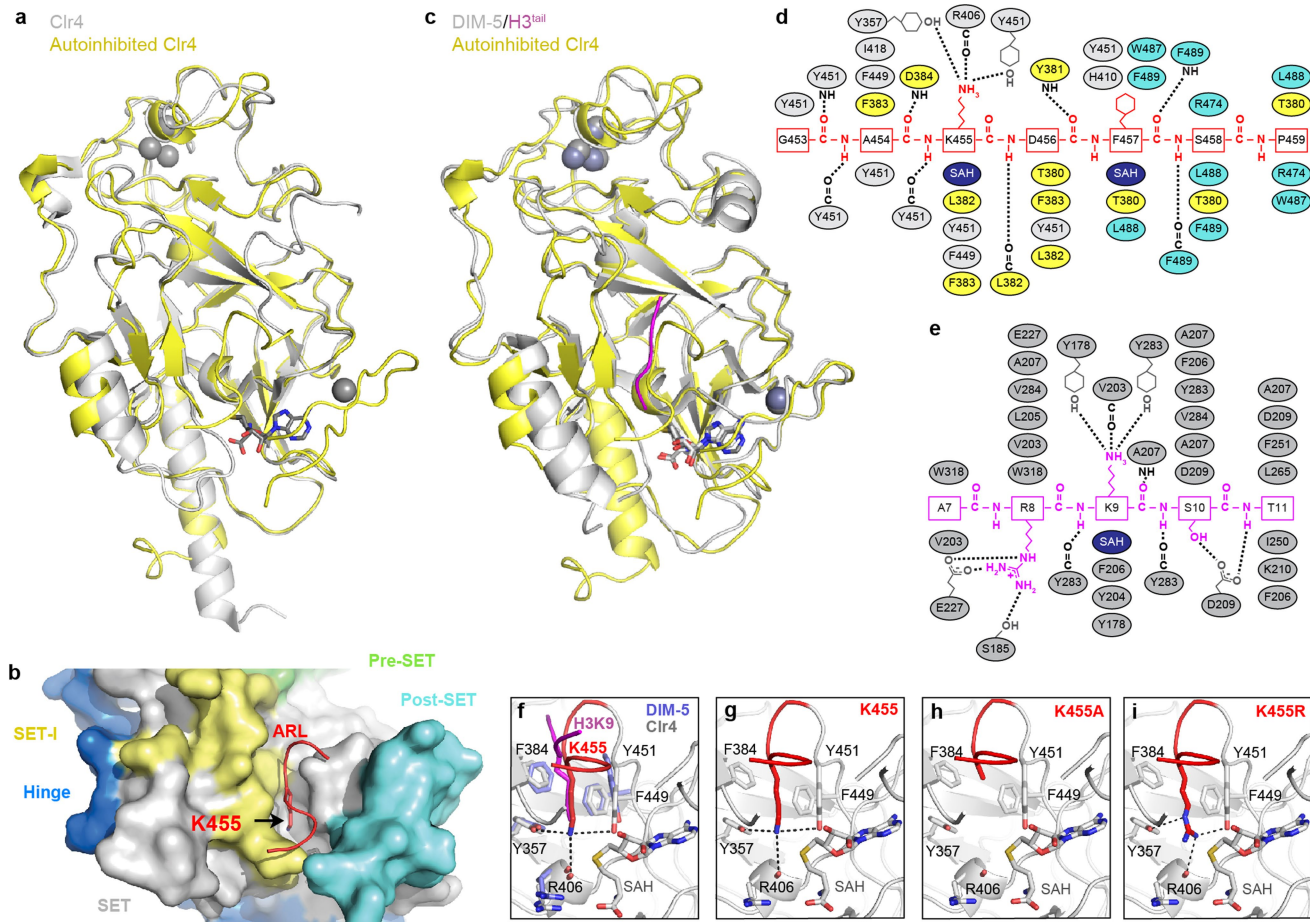


Extended Data Fig. 1 | Analysis of Clr4 automethylation. **a**, Outline of the in vitro methyltransferase activity assays. **b**, In vitro methyltransferase assay showing that Clr4^{dead} (Clr4(Y451N)) has no methyltransferase activity towards itself or histone H3¹⁻²⁰ peptide and that wild-type Clr4 with or without an N-terminal GST tag displays similar methyltransferase activities. Experiment repeated twice with similar results. **c**, Outline of the in vitro methyltransferase assay with unmethylated or automethylated Clr4. **d**, Time course of methyltransferase activity of GST-Clr4 towards H3¹⁻²¹ peptide substrate (10.8 μM) after a 1-h incubation of GST-Clr4 with 512 μM cold SAM (+) or without SAM (-), showing that the automethylation of Clr4 increases its methyltransferase activity on the H3¹⁻²¹ substrate. Incorporation of ^3H -SAM on H3¹⁻²¹ peptide was assessed by scintillation counting. Data are mean \pm s.d. from three biological replicates. **e**, Quantitative mass spectrometry analysis of *E. coli*-purified GST-Clr4 wild type and GST-Clr4^{dead}, showing that Clr4 K455 is the sole target of automethylation detected in our experiments and that the remaining sites were methylated by *E. coli* enzymes. Data are mean \pm s.e.m. from three (wild type, orange circles) or six (Clr4^{dead}, grey circles) biological replicates. Data are presented as a ratio (upper axis) of values for each peptide (lower axis) of Clr4 wild type versus GST-Clr4^{dead} containing the indicated methylated lysine. **f**, **g**, In vitro methyltransferase assays showing that Clr4 K127 is not a major target of automethylation, as substitution of K127 with arginine (K127R) (**f**) or deletion of a part of the hinge and the chromodomain (Clr4¹⁹²⁻⁴⁹⁰) that contains K127 (**g**) did not affect the level of Clr4 automethylation. Experiment performed once (**f**) and more than three times with similar results (**g**). See Supplementary Fig. 1 for the uncropped gels.

Seq #	b: Δ Error	+1		+2		Seq #	b: Δ Error	+1		+2		Seq #	b: Δ Error	+1		+2									
		b	y	y: Δ Error	+1			b	y	y: Δ Error	+1			b	y	y: Δ Error	+1								
D 1	---	116.094	---	25	D 1	---	58.521	---	25	D 1	---	116.094	---	25	K 1	---	58.521	---	25						
I 2	-1.518	229.118	2725.272	---	I 2	---	115.063	1363.190	---	I 2	---	115.063	1370.197	---	I 2	---	115.063	1370.197	---						
Q 3	-1.826	357.177	2612.288	---	Q 3	-4061.318	179.092	1306.648	27.284	23	Q 3	-1.826	357.177	2612.288	---	Q 3	-4048.004	179.092	1313.655	---					
P 4	---	454.230	2484.229	---	P 4	---	227.618	1242.618	401.232	22	P 4	-3.516	454.230	2498.245	---	E 6	696.356	2288.108	20	E 6	227.618	1242.618	398.095	22	
L 5	---	567.314	2387.177	---	L 5	---	284.160	1194.092	416.624	21	L 5	---	567.314	2401.192	---	E 7	696.356	2288.108	20	E 7	---	284.160	1194.092	414.996	
E 6	696.356	2274.092	---	20	E 6	---	348.682	1137.550	-1.240	20	E 7	696.356	2288.108	19	E 7	---	348.682	1137.550	425.843						
E 7	696.356	2251.550	---	19	E 7	696.356	1013.029	-2.930	19	E 7	696.356	2288.108	19	E 7	696.356	1013.029	425.843								
L 8	---	1016.007	18	L 8	-1101.654	469.459	1000.007	-1.650	18	L 8	-626.589	1016.007	401.232	18	T 9	1039.531	1916.939	17	T 9	1039.531	1916.939	2.471			
T 9	1039.531	1902.923	0.641	18	T 9	520.269	951.965	-2.220	17	F 10	1186.599	1815.891	2.243	16	F 10	520.269	951.965	-2.220	17						
F 10	1186.599	1801.876	-2.604	16	F 10	593.803	901.441	-3.040	16	D 11	1301.626	1668.823	4.960	15	D 11	593.803	908.449	-2.166	16						
D 11	1301.626	1654.807	-1.327	15	D 11	651.317	827.907	1012.537	15	Y 12	1464.689	1533.796	3.027	14	Y 12	732.848	777.402	-0.399	14						
Y 12	1464.689	1539.780	-1.527	14	Y 12	732.848	770.394	-2.287	14	A 13	1535.726	1390.733	-0.675	13	A 13	768.367	695.870	---	A 13	1535.726	1390.733	-0.675			
A 13	1535.726	1376.717	-2.614	13	A 13	768.367	688.862	-2.841	13	G 14	1653.785	1245.659	-1.584	12	G 14	793.398	686.351	---	G 14	1653.785	1245.659	-1.584			
A 14	1653.785	1248.659	-3.579	11	A 15	632.396	694.833	1.111	11	K ⁰ 16	1819.911	1191.637	-3.768	10	K ⁰ 16	910.459	596.322	---	K ⁰ 16	1819.911	1191.637	-3.768			
K ⁰ 16	1805.898	1177.621	1.288	10	K ⁰ 16	304.451	589.534	10	D 17	1920.923	1035.511	-4.531	9	D 17	967.973	518.259	---	D 17	1920.923	1035.511	-4.531				
D 17	1920.923	1035.511	-0.876	9	D 17	960.965	518.259	9	F 18	2067.993	920.484	-2.482	8	F 18	1041.507	460.745	---	F 18	2067.993	920.484	-2.482				
F 18	2067.993	920.484	-2.482	8	S 19	1024.499	480.745	8	S 19	1078.015	387.211	7	P 20	2286.033	663.383	-1.937	6	P 20	1085.023	367.211	7	P 20	2286.033	663.383	-1.937
S 19	1024.499	773.415	-0.200	7	S 19	1078.015	387.211	7	V 21	2286.160	589.100	5	V 21	1133.549	343.695	1336.670	6	V 21	2286.160	589.100	5	V 21	1133.549	343.695	1336.670
P 20	2286.033	663.383	-2.116	5	P 20	1126.592	343.896	6	Q 22	2493.218	490.362	-2.666	4	Q 22	1247.113	245.625	2070.493	4	Q 22	2493.218	490.362	-2.666	4		
V 21	2286.160	589.100	5	V 21	1240.105	245.625	2070.554	4	S 23	1823.621	181.605	3	S 23	1290.629	181.605	3	S 23	1823.621	181.605	3	S 23	1290.629	181.605	3	
Q 22	2716.397	719.425	-255.675	4	Q 22	130.244	1412.218	296.187	3	Q 24	2823.429	591.366	-69.791	3	Q 24	278.094	147.113	242.789	2	Q 24	278.094	147.113	242.789	2	
S 23	2823.429	591.366	-69.791	3	K ⁰ 25	2951.488	504.334	-58.082	2	K ⁰ 25	2708.309	275.171	-2.257	1	K ⁰ 25	2708.309	275.171	-2.257	1	K ⁰ 25	2708.309	275.171	-2.257	1	

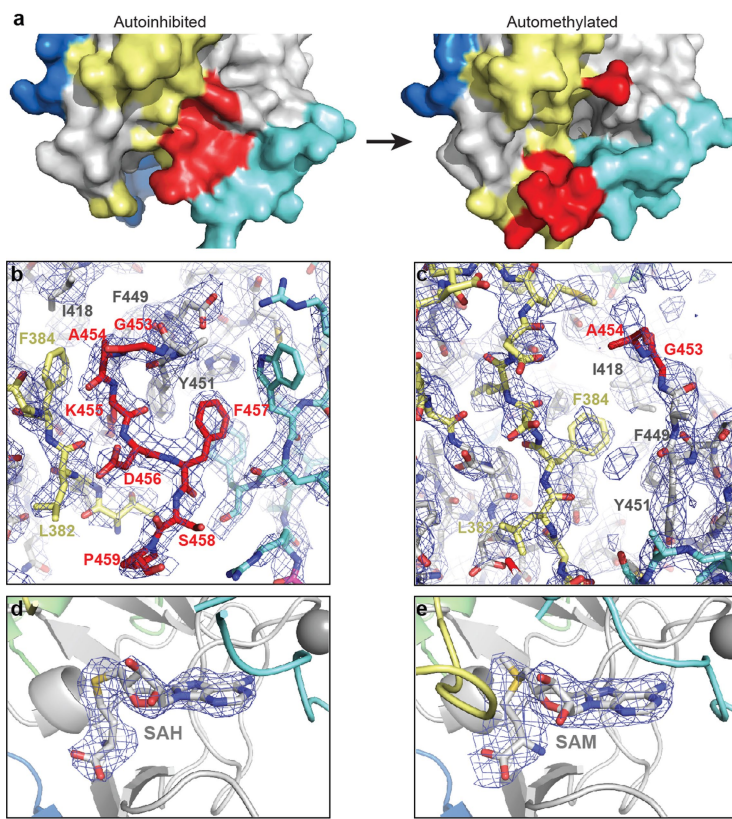


Seq #	b: Δ Error	+1		+2		Seq #	b: Δ Error	+1		+2		Seq #	b: Δ Error	+1		+2									
		b	y	y: Δ Error	+1			b	y	y: Δ Error	+1			b	y	y: Δ Error	+1								
D 1	---	116.094	---	25	I 2	---	58.521	---	25	I 2	---	116.094	---	25	I 2	---	58.521	---	25						
I 2	-1.518	229.118	2725.272	---	I 2	---	115.063	1363.190	---	I 2	---	115.063	1370.197	---	I 2	---	115.063	1370.197	---						
Q 3	-1.826	357.177	2612.288	---	Q 3	-4061.318	179.092	1306.648	27.284	23	Q 3	-1.826	357.177	2612.288	---	Q 3	-4048.004	179.092	1313.655	---					
P 4	---	454.230	2484.229	---	P 4	---	227.618	1242.618	401.232	22	P 4	-3.516	454.230	2498.245	---	E 6	696.356	2288.108	20	E 6	227.618	1242.618	425.843		
L 5	---	567.314	2387.177	---	L 5	---	284.160	1194.092	416.624	21	L 5	---	567.314	2401.192	---	E 7	696.356	2288.108	20	E 7	---	284.160	1194.092	425.843	
E 6	696.356	2274.092	---	20	E 6	---	348.682	1137.550	-1.240	20	E 7	696.356	2288.108	19	E 7	696.356	2288.108	19	E 7	696.356	2288.108	19			
E 7	696.356	2251.550	---	19	E 7	696.356	1013.029	-2.930	19	E 7	696.356	2288.108	19	E 7	696.356	1013.029	425.843	E 7	696.356	2288.108	19				
T 9	1039.531	1902.923	0.641	18	T 9	520.269	951.965	-2.220	17	F 10	1186.599	1815.891	2.243	16	F 10	520.269	951.965	-2.220	17						
F 10	1186.599	1801.876	-2.604	16	F 10	593.803	901.441	-3.040	16	D 11	1301.626	1668.823	4.960	15	D 11	593.803	908.449	-2.166	16						
D 11	1301.626	1654.807	-1.327	15	D 11	651.317	827.907	1012.537	15	Y 12	1464.689	1533.796	3.027	14	Y 12	732.848	777.402	-0.399	14						
Y 12	1464.689	1539.780	-1.527	14	Y 12	732.848	770.394	-2.287	14	A 13	1535.726	1390.733	-0.675	13	A 13	768.367	695.870	---	A 13	1535.726	1390.733	-0.675			
A 13	1535.726	1376.717	-2.614	13	A 13	768.367	688.862	-2.841	13	G 14	1653.785	1245.659	-1.584	12	G 14	793.398	686.351	---	G 14	1653.785	1245.659	-1.584			
G 14	1653.785	1248.659	-3.579	11	G 14	793.398	688.862	-1.584	11	K ⁰ 16	1819.911	1191.637	-3.768	10	K ⁰ 16	910.459	596.322	---	K ⁰ 16	1819.911	1191.637	-3.768			
K ⁰ 16	1805.898	1177.621	1.288	10	K ⁰ 16	304.451	589.534	10	D 17	1920.923	1035.511	-4.531	9	D 17	967.973	518.259	---	D 17	1920.923	1035.511	-4.531				
D 17	1920.923	1035.511	-0.876	9	D 17	960.965	518.259	9	F 18	2067.993	920.484	-2.482	8	F 18	1041.507	460.745	---	F 18	2067.993	920.484	-2.482				
F 18	2067.993	920.484	-2.482	8	S 19	1024.499	480.745	8	S 19	1078.015	387.211	7	P 20	2286.033	663.383	-1.937	6	P 20	1085.023	367.211	7	P 20	2286.033	663.383	-1.937
S 19	1024.499	773.415	-0.200	7	S 19	1078.015	387.211	7	V 21	2286.160	589.100	5	V 21	1247.113	245.625	2070.									



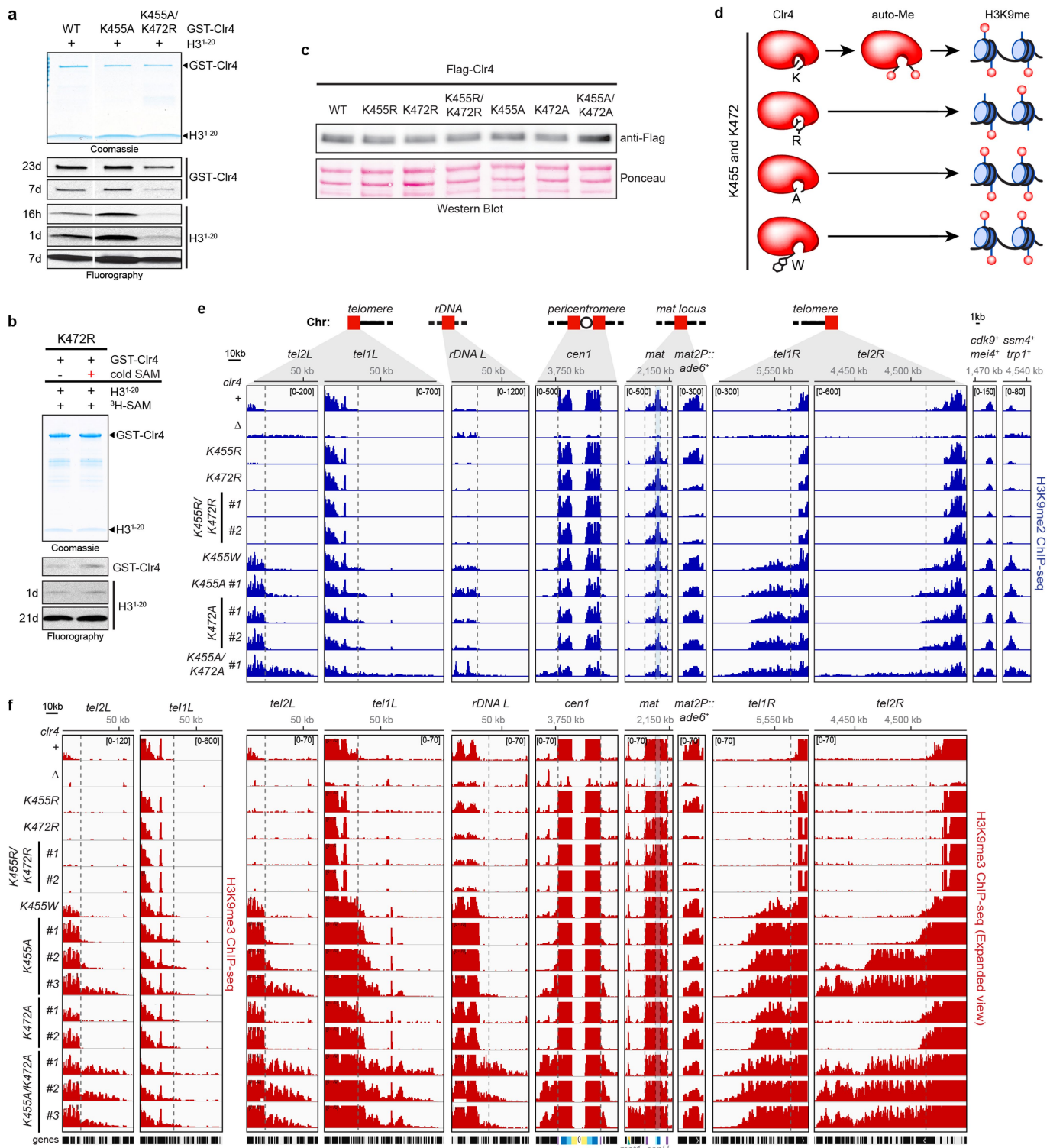
Extended Data Fig. 3 | Comparison of Clr4 structure with other SUV39H methyltransferases. **a**, Alignment of the autoinhibited Clr4^{192–490} (yellow) and the previously determined Clr4^{192–490} structure that lacks post-SET domain and cofactor (grey) (PDB ID: 1MVH). **b**, Close-up view of *S. pombe* Clr4^{192–490} autoinhibited conformation (surface) showing that K455 (red stick) in the autoregulatory loop (red) is located within the active site pocket. **c**, Alignment of autoinhibited Clr4^{192–490} (yellow) and DIM-5 (grey) in complex with histone H3 peptide (magenta) and SAH (dark blue) (PDB ID: 1PEG). **d, e**, Schematic of residues that engage in interactions between Clr4 (grey, yellow and cyan) and Clr4 autoregulatory loop (red) (**d**) and DIM-5 (grey) and histone H3 (magenta) (**e**). Hydrogen

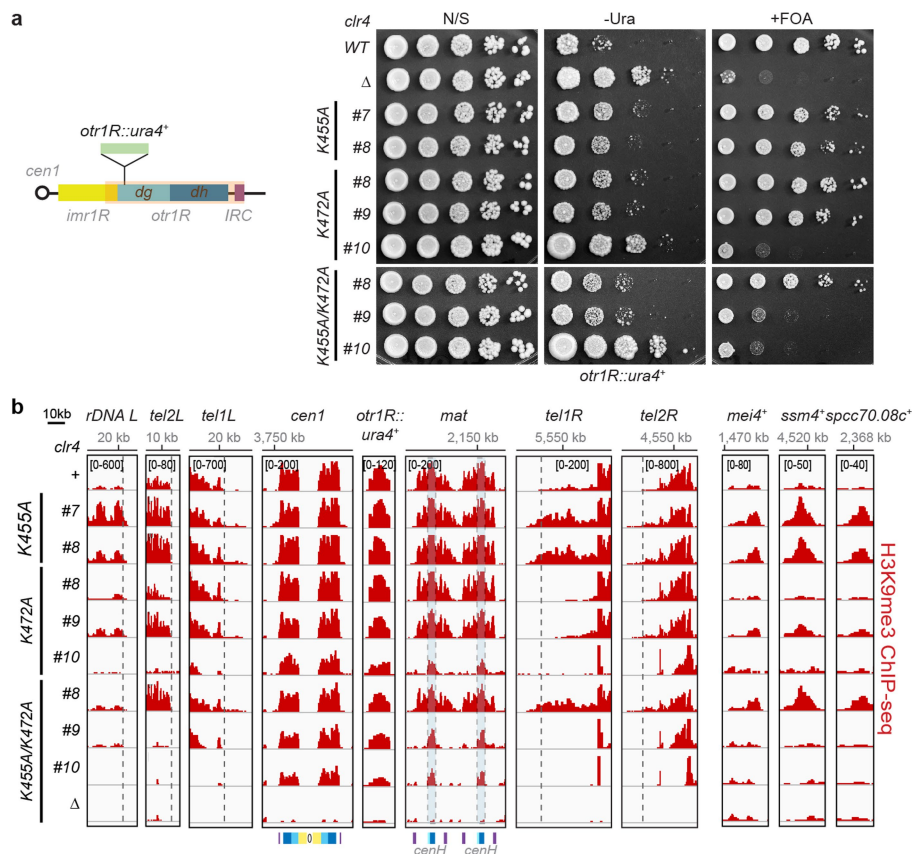
bonds and salt bridge interactions are shown as dashed lines. Colour assignments are as in Fig. 1d; residues in the SET insertion domain, SET and post-SET domain are shown in yellow, grey and cyan, respectively. SAH is shown in dark blue. **f**, Alignment of the catalytic pockets of Clr4^{192–490} and DIM-5 (PDB ID: 1PEG) showing that Clr4 K455 (red) and K9 of the histone H3 substrate (magenta) occupy similar positions. **g–i**, Close-up view of the autoinhibited conformation of Clr4 active site (**g**, as in Fig. 1h, shown here for comparison) and modelling the K455A (**h**) and K455R (**i**) mutants in the active site. Possible bonding interactions are shown as dashed lines.



Extended Data Fig. 4 | Conformational change in Clr4 induced by automethylation. **a**, Surface representation of the active-site area of Clr4 in autoinhibited Clr4 (left) and automethylated Clr4 (right), showing the opening of the catalytic pocket induced by automethylation; the methyl group of SAM is visible in the active-site tunnel. **b**, Simulated annealing composite omit map for the autoregulatory-loop-occupied active site

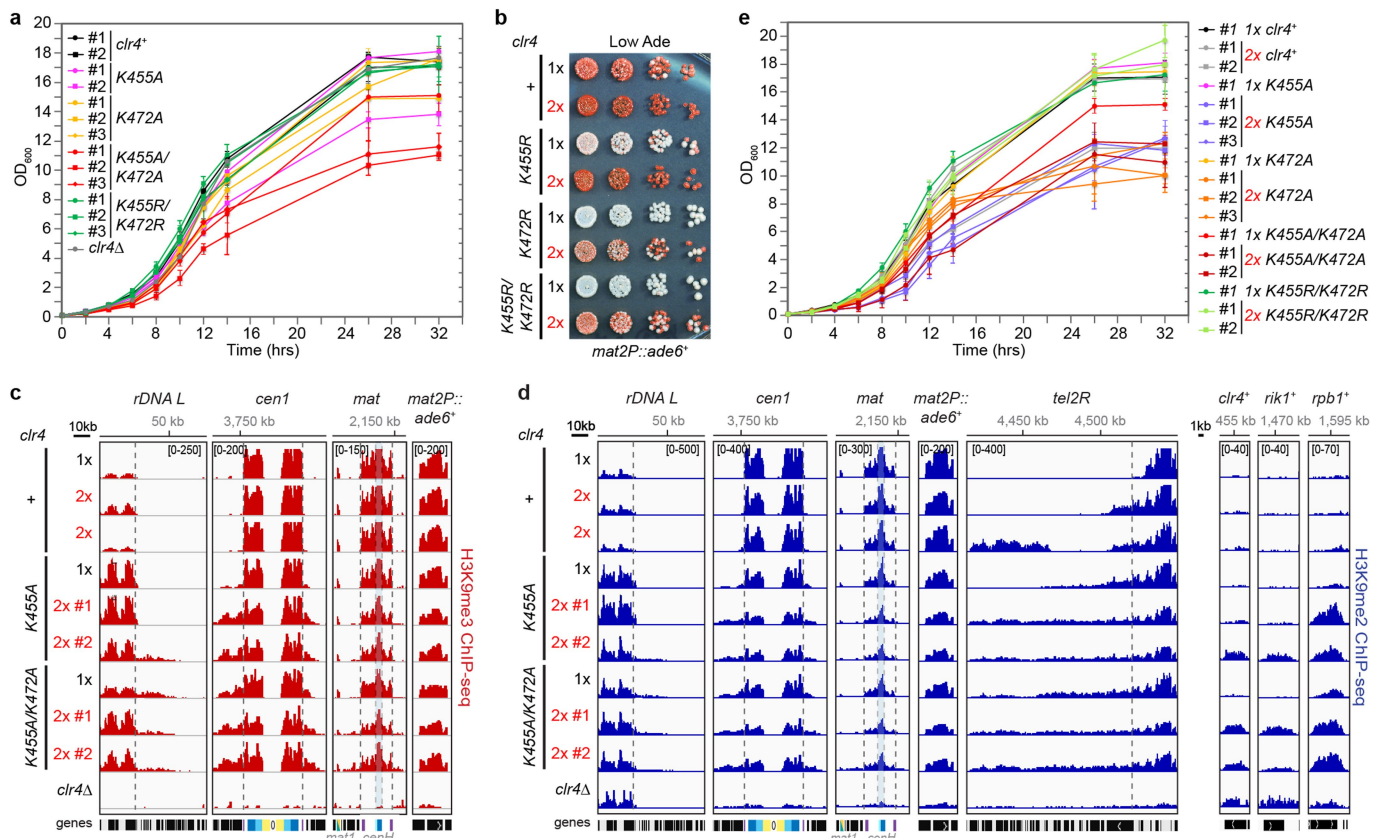
of Clr4 contoured at 1.0σ . The protein is coloured as in Fig. 1d and the electron density is shown in blue. **c**, The simulated annealing composite omit map of the same region in the automethylated Clr4 crystal structure, contoured at 1.0σ , lacks density for autoregulatory loop residues. **d, e**, Polder omit map for the bound cofactors of the autoinhibited (**d**) and automethylated (**e**) crystal structures contoured at 3.5σ .





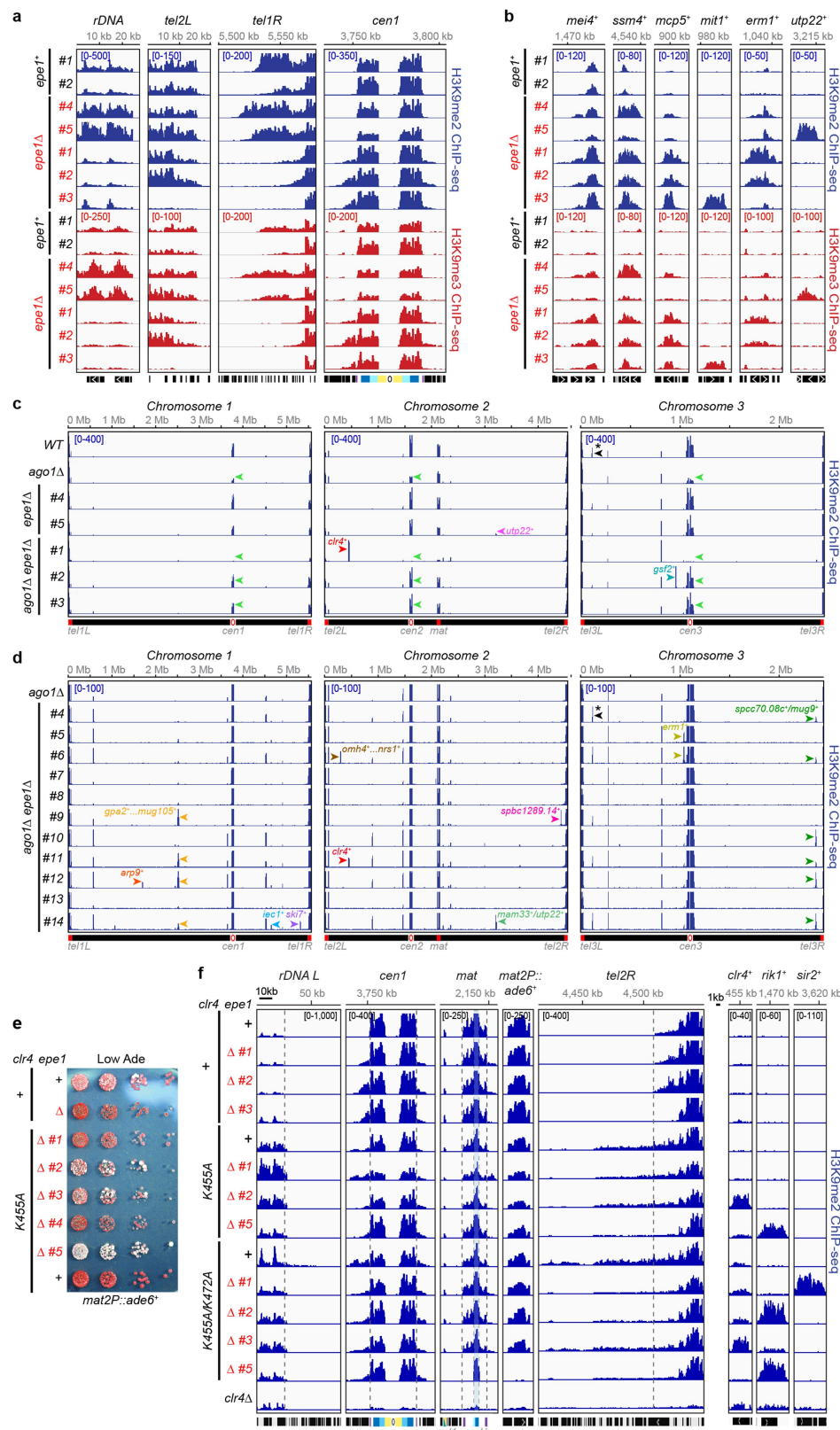
Extended Data Fig. 6 | Hyperactive Clr4 mutants promote epigenetic instability. **a**, Left, map of the right arm of centromere 1 (*cen1*) with the insertion of the *ura4⁺* reporter gene at the pericentromeric *otr1R* repeat (*otr1R::ura4⁺*). Right, *otr1R::ura4⁺* silencing assay in the indicated genotypes, showing clone-to-clone variation of *ura4⁺* silencing in hyperactive *clr4* mutants. N/S, nonselective medium; -Ura, medium without uracil; +FOA, medium containing 5-FOA. # indicates an independent clone. Experiment performed twice with similar results with two to three independent clones, as shown. **b**, H3K9me3 ChIP-seq

reads mapped to different heterochromatin regions (left) or euchromatic genes (right) in the indicated genotypes are presented as reads per million (number in brackets in the first row of each set of ChIP-seq data) and highlight increased or decreased spreading of H3K9me2 or me3 in Clr4 K455 mutants. *S. pombe* *h⁺* cells used for the ChIP-seq experiments have a duplicated *mat* locus. Top, chromosome coordinates. See legend of Fig. 3 for abbreviations. Sequencing performed once with two to three independent clones as shown.



Extended Data Fig. 7 | Disruption of Clr4 autoinhibition results in growth defects, inappropriate H3K9me spreading and formation of new H3K9me domains. **a**, Growth assays showing that cells that express the indicated hyperactive Clr4 mutants have growth defects. # indicates an independent clone. Data are mean \pm s.d. from three biological replicates. **b**, Silencing assay of *mat2P::ade6*⁺ on low-adenine medium with one (1 \times) or two (2 \times) copies of *clr4*⁺ or mutant *clr4* genes. See main text for details. Experiment performed twice with at least two independent clones with similar results. **c, d**, H3K9me3 (**c**) or H3K9me2 (**d**) ChIP-seq reads

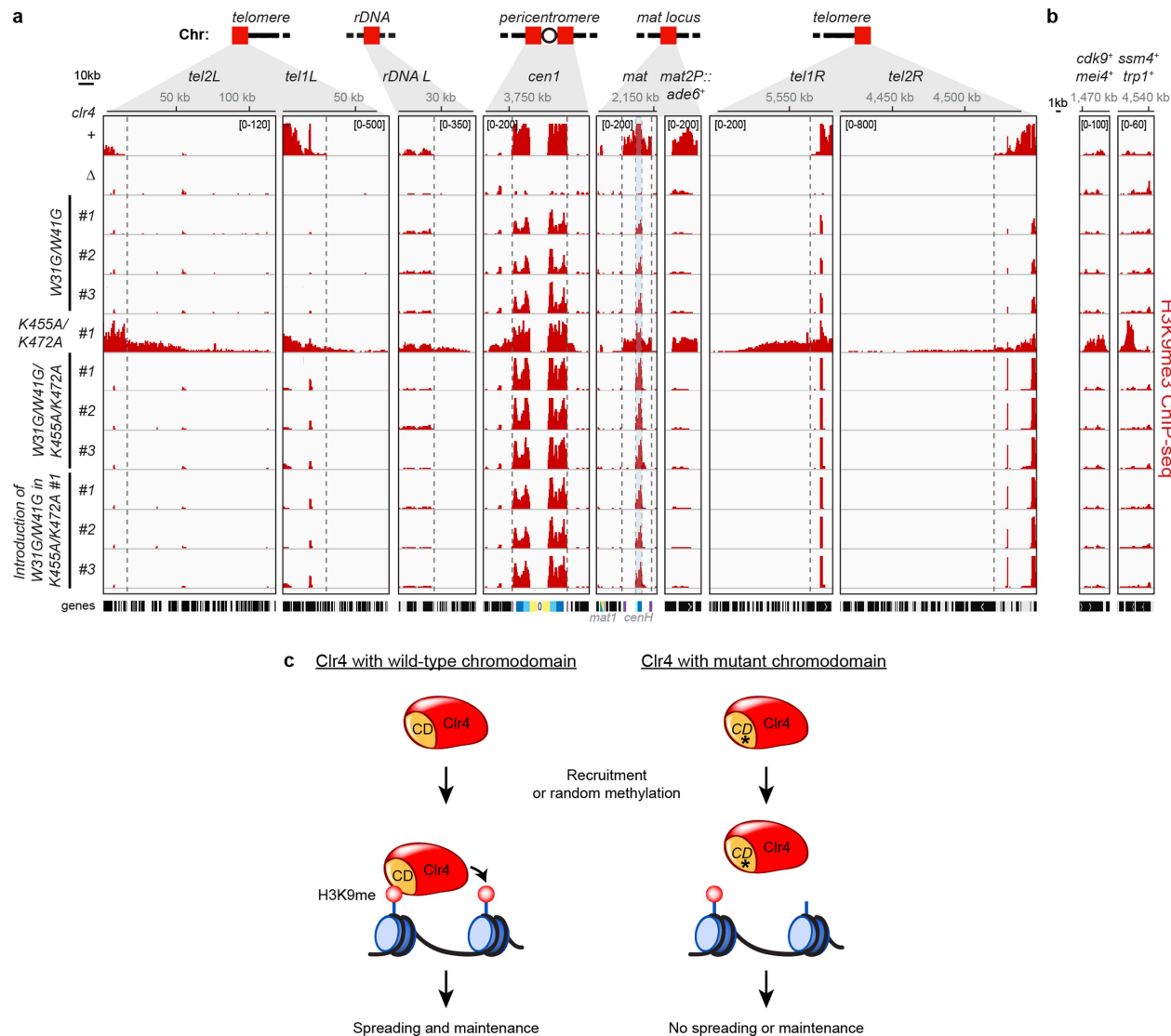
mapped to different heterochromatin regions (left) or euchromatic genes (right) in the indicated genotypes are presented as reads per million (number in brackets in the first row of each set of ChIP-seq data). Top, chromosome coordinates. See legend of Fig. 3 for abbreviations. Sequencing performed once with two independent clones, as shown. **e**, Growth assays showing that the addition of a second copy (2 \times) of the *clr4* gene that encodes hyperactive Clr4 mutants exacerbates growth defects. # indicates an independent clone. Data are mean \pm s.d. from three biological replicates.



Extended Data Fig. 8 | See next page for caption.

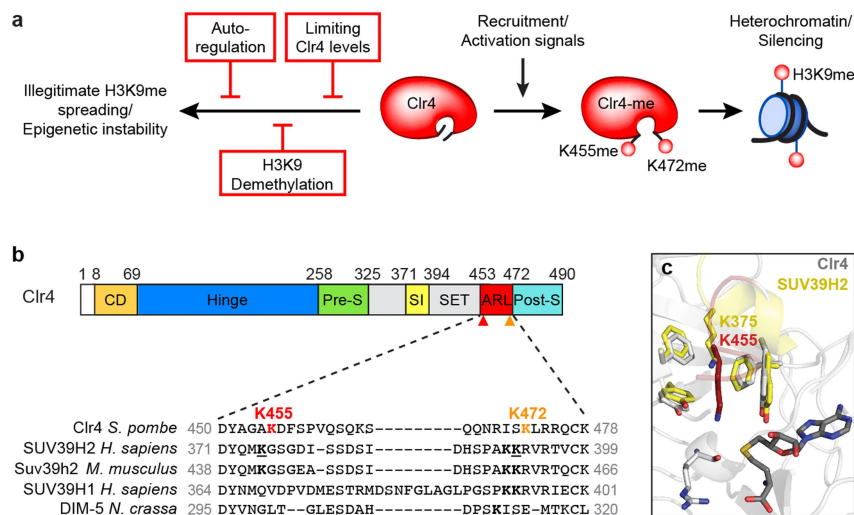
Extended Data Fig. 8 | Deletion of the Epe1 anti-silencing pathway leads to epigenetic instability. **a, b**, H3K9me2 (top, blue) and H3K9me3 (bottom, red) ChIP-seq reads mapped to different heterochromatin regions (**a**) or euchromatic genes (**b**) in the indicated genotypes are presented as reads per million (number in brackets in the first row of each set of ChIP-seq data). Top, chromosome coordinates. *mit1*⁺ encodes a Clr3 HDAC-associated factor required for efficient heterochromatic silencing; *erm1*⁺ encodes an endoplasmic reticulum peptidase; and *utp22*⁺ encodes a ribosomal RNA processing factor. Note that *epe1*⁺ #1, *epe1*^Δ #4 and *epe1*^Δ #5 clones were constructed in the SPY137 background (which has an insertion of *ura4*⁺ at the pericentromeric region of chromosome 1) and *epe1*⁺ #2 and *epe1*^Δ #1–*epe1*^Δ #3 clones were constructed in the SPY3 background (which has an insertion of *ade6*⁺ at the *mat* locus, see Supplementary Table 3 for detailed genotypes). Sequencing performed once with the indicated independent clones (#) for each genotype. **c, d**, H3K9me2 ChIP-seq in the indicated genotypes showing clone-to-clone variation in the appearance of H3K9me2 peaks throughout the *S. pombe* genome (coloured arrowheads). H3K9me2 ChIP-seq reads mapped to all three *S. pombe* chromosomes in the indicated genotypes

are presented as reads per million (number in brackets in the first row of each set of ChIP-seq data). Top, chromosome coordinates. Black arrowhead with asterisk indicates the location of the *ura4*⁺ gene. Strains were constructed by crossing cells with and without a *ura4*⁺ insertion at pericentromeric repeats. Therefore, not all progeny of the cross show H3K9me2 mapping to *ura4*⁺ (highlighted with asterisk on the left arm of chromosome 3). See Supplementary Table 2 for a list of H3K9me peaks. Sequencing performed once with the indicated independent clones (#) for each genotype. **e**, Silencing assay of *mat2P::ade6*⁺ on low-adenine medium, showing that the combination of *epe1*⁺ deletion (Δ) and a hyperactive *clr4* mutant results in clone-to-clone variegation of the *ade6*⁺ silencing defect. Experiment performed once with five independent clones as shown. **f**, H3K9me2 ChIP-seq reads mapped to different heterochromatin regions (left) or euchromatic genes (right) in the indicated genotypes are presented as reads per million (number in brackets in the first row of each set of ChIP-seq data). Top, chromosome coordinates. See legend of Fig. 3 for abbreviations. Sequencing performed once with three to four independent clones. # indicates an independent clone.



Extended Data Fig. 9 | Cln4 autoregulation prevents illegitimate heterochromatin formation mediated by the Cln4 read-write positive feedback mechanism. a, b, H3K9me3 ChIP-seq reads mapped to different heterochromatin regions (a) or euchromatic genes (b) in the indicated genotypes are presented as reads per million (number in brackets in the first row of each set of ChIP-seq data). Top, chromosome coordinates. See legend of Fig. 3 for abbreviations. Sequencing performed once with the indicated independent clones (#) for each genotype. c, Schematic showing Cln4 chromodomain (CD)-dependent spreading and maintenance of histone H3K9me. The CD-dependent positive feedback loop is critical even with hyperactive Cln4.

legend of Fig. 3 for abbreviations. Sequencing performed once with the indicated independent clones (#) for each genotype. c, Schematic showing Cln4 chromodomain (CD)-dependent spreading and maintenance of histone H3K9me. The CD-dependent positive feedback loop is critical even with hyperactive Cln4.



Extended Data Fig. 10 | Clr4 automethylation-dependent heterochromatin regulation and evidence for its evolutionary conservation. **a**, Schematic of the role of lysine automethylation in the autoregulatory loop, in preventing illegitimate heterochromatin formation and epigenetic instability (left). Intrinsic regulation of Clr4 by automethylation (of K455 and probably of K472) acts in parallel with other anti-silencing mechanisms that involve that regulation of Clr4 levels and H3K9 demethylation (red boxes). See main text for additional discussion. **b**, Top, diagram illustrating the domain organization of the *S. pombe* Clr4 protein and the location of Clr4 K455 (red arrowhead)

and K472 (orange arrowhead). Bottom, sequence alignment of the Clr4 autoregulatory loop that contains K455 (red) and K472 (orange) in the indicated methyltransferases. SUV39H2 K375 and SUV39H2 K392 are indicated in underlined bold. *H. sapiens*, *Homo sapiens*; *M. musculus*, *Mus musculus*; *N. crassa*, *Neurospora crassa*. **c**, Overlay of *S. pombe* Clr4 in grey (this study, PDB ID: 6BOX) and human SUV39H2 in yellow (PDB ID: 2R3A), showing that *S. pombe* Clr4 K455 (shown as red stick) and human SUV39H2 K375 (shown as yellow stick) occupy partially overlapping positions inside the catalytic pocket.

Inositol phosphates are assembly co-factors for HIV-1

Robert A. Dick^{1*}, Kaneil K. Zadrozny², Chaoyi Xu³, Florian K. M. Schur^{4,5}, Terri D. Lyddon⁶, Clifton L. Ricana⁶, Jonathan M. Wagner², Juan R. Perilla³, Barbie K. Ganser-Pornillos², Marc C. Johnson⁶, Owen Pornillos^{2*} & Volker M. Vogt¹

A short, 14-amino-acid segment called SP1, located in the Gag structural protein¹, has a critical role during the formation of the HIV-1 virus particle. During virus assembly, the SP1 peptide and seven preceding residues fold into a six-helix bundle, which holds together the Gag hexamer and facilitates the formation of a curved immature hexagonal lattice underneath the viral membrane^{2,3}. Upon completion of assembly and budding, proteolytic cleavage of Gag leads to virus maturation, in which the immature lattice is broken down; the liberated CA domain of Gag then re-assembles into the mature conical capsid that encloses the viral genome and associated enzymes. Folding and proteolysis of the six-helix bundle are crucial rate-limiting steps of both Gag assembly and disassembly, and the six-helix bundle is an established target of HIV-1 inhibitors^{4,5}. Here, using a combination of structural and functional analyses, we show that inositol hexakisphosphate (InsP₆, also known as IP₆) facilitates the formation of the six-helix bundle and assembly of the immature HIV-1 Gag lattice. IP₆ makes ionic contacts with two rings of lysine

residues at the centre of the Gag hexamer. Proteolytic cleavage then unmasks an alternative binding site, where IP₆ interaction promotes the assembly of the mature capsid lattice. These studies identify IP₆ as a naturally occurring small molecule that promotes both assembly and maturation of HIV-1.

IP₆ is a highly negatively charged compound that is present in all mammalian cells at concentrations of 10–40 μM⁶. Inositol phosphates stimulate in vitro assembly of HIV-1 Gag into immature virus-like particles (VLPs), with previous data suggesting that IP₆ interacts with both the MA and NC domains of Gag^{7–9}. To understand how IP₆ affects HIV-1 assembly, we used an HIV-1 Gag construct spanning the CA to NC domains and having one extra amino acid residue, Ser, preceding the normal N-terminal Pro at the start of the CA domain (*s*-CANC; Fig. 1a), because this should disfavour formation of the N-terminal β-hairpin that promotes mature assembly¹⁰. Longer N-terminal extensions of CANC constructs have been shown to assemble inefficiently into immature VLPs at pH 8, but into mature VLPs at pH 6^{1,10}.

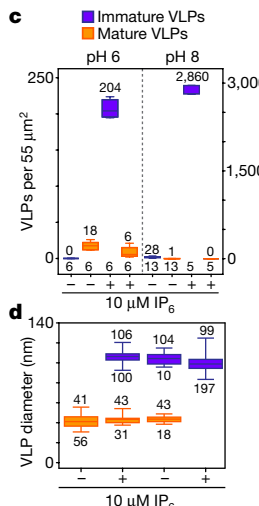
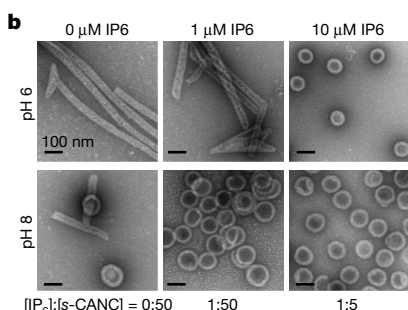
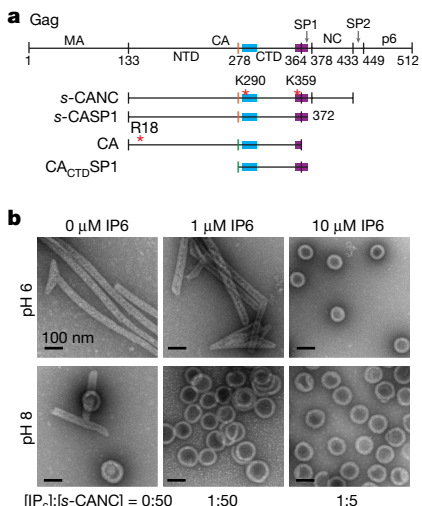
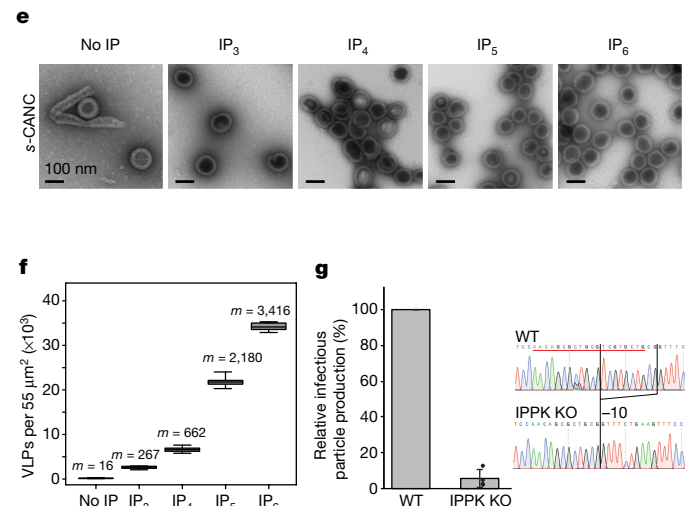


Fig. 1 | IP₆ induces assembly of HIV-1 Gag in vitro. **a**, Map of the HIV-1 Gag protein, indicating the MA, CA, NC and p6 domains, and spacer peptides SP1 and SP2. Gag-derived constructs used in this study are shown underneath. Blue bar, major homology region; purple bar, SP1 helix; NTD and CTD, N-terminal and C-terminal domains of CA; R18, K290 and K359, locations of mutations; N372, C-terminal residue of the *s*-CASP1 and CA_{CTD}SP1 constructs. **b**, Negative-stain electron microscopy images of mature and immature VLPs formed by *s*-CANC (50 μM) at pH 6 and pH 8 in the absence or presence of the indicated molar ratios of IP₆ (0–10 μM). Scale bars, 100 nm. **c**, Number of VLPs per 55 μm² without (−) and with (+) 10 μM IP₆ at pH 6 and pH 8; *n* shown below and mean above box plots. The experiment was repeated three times with similar results. **d**, Diameters of immature and mature VLPs; *n* shown below and mean



above box plots. **e**, Representative images of *s*-CANC VLPs assembled at pH 8 in the absence and presence of IP₃, IP₄, IP₅ and IP₆. Scale bars, 100 nm. The experiment was repeated twice with similar results. **f**, Number of VLPs per 55 μm² without and with 10 μM IP₃–IP₆; *n* = 5, mean shown above box plots. **g**, Parallel transfections of 293FT wild-type (WT) and IPPK knockout (KO) cells were performed with a VSV-G-pseudotyped HIV-1 provirus containing GFP, and infectivity was measured on WT 293T cells. Graphs show mean ± s.d. of four independent experiments; dots show individual data points. Right panels show sequences of total PCR products of the guide RNA target sites from WT and KO cells; guide RNA sequence is underlined in red. **c**, **d**, **f**, Centre lines show medians; box limits indicate 25th and 75th percentiles as determined by R software²⁴; whiskers extend to minimum and maximum values.

¹Department of Molecular Biology and Genetics, Cornell University, Ithaca, NY, USA. ²Department of Molecular Physiology and Biological Physics, University of Virginia, Charlottesville, VA, USA.

³Department of Chemistry and Biochemistry, University of Delaware, Newark, DE, USA. ⁴Structural and Computational Biology Unit, EMBL, Heidelberg, Germany. ⁵Institute of Science and Technology Austria, Klosterneuburg, Austria. ⁶Department of Molecular Microbiology and Immunology, University of Missouri, Columbia, MO, USA. *e-mail: rad82@cornell.edu;

opornillos@virginia.edu

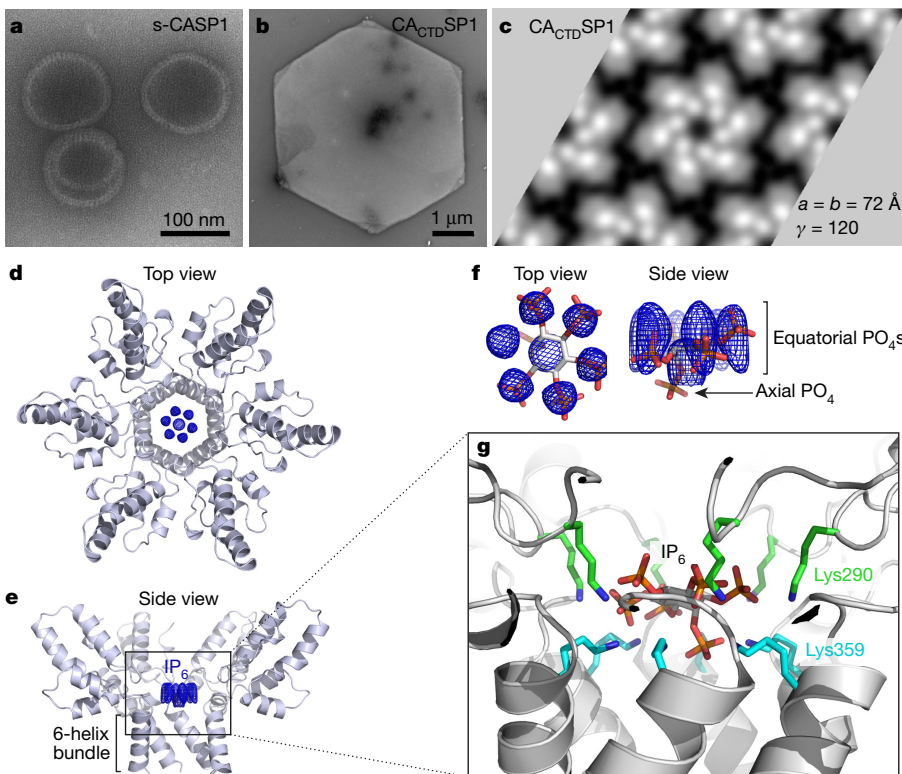


Fig. 2 | IP₆ interacts with Lys290 and Lys359 in the immature HIV-1 Gag hexamer.

a, IP₆-induced assembly of s-CASP1 into immature VLPs. The experiment was repeated four times with similar results. **b**, IP₆-induced assembly of CA_{CTD}SP1 into flat micro-crystals. The experiment was repeated six times with similar results. **c**, Two-dimensional cryo-EM projection map of a micro-crystal. Images of multiple crystals were collected during two rounds of data collection from separate assembly reactions and all crystals had similar unit cells. Two individual crystals had single layer regions and could be further processed. These crystals generated similar maps. **d, e**, Top view (**d**) and side view (**e**) of the CA_{CTD}SP1 hexamer X-ray crystal structure showing the protein in grey ribbons and unbiased mF₀-DF_c difference density in blue mesh, contoured at 2σ . **f**, Top and side views of IP₆ in its *myo* configuration, docked into the difference density as a rigid body in one of six rotationally equivalent orientations. All six binding modes are shown in Extended Data Fig. 4a. **g**, Side view of the two rings of Lys290 (green) and Lys359 (cyan) with bound IP₆ in the middle. Densities were omitted for clarity, and are shown in Extended Data Fig. 4b.

However, we found that s-CANC still formed mature-like particles at both pH values (Fig. 1b). Notably, the presence of IP₆ induced a marked switch to the formation of spherical, immature VLPs (Fig. 1b, d). At pH 8, even a substoichiometric 1:50 molar ratio of IP₆ to protein resulted in an approximately 100-fold increase in immature VLPs (Fig. 1b, c). At pH 6, the effect of IP₆ was less strong, requiring at least a 1:10 ratio to induce immature assembly (Fig. 1b). We conclude that

IP₆ imposes an *in vitro* immature assembly phenotype, even under conditions that favour the mature lattice (pH 6).

Other inositol derivatives also promoted s-CANC assembly, but to a lesser extent, in the order IP₃ < IP₄ < IP₅ < IP₆ (Fig. 1e, f), with efficacy correlating with the number of phosphate groups. Other negatively charged compounds did not promote or only marginally promoted assembly (Extended Data Fig. 1). Overall, these results indicate that

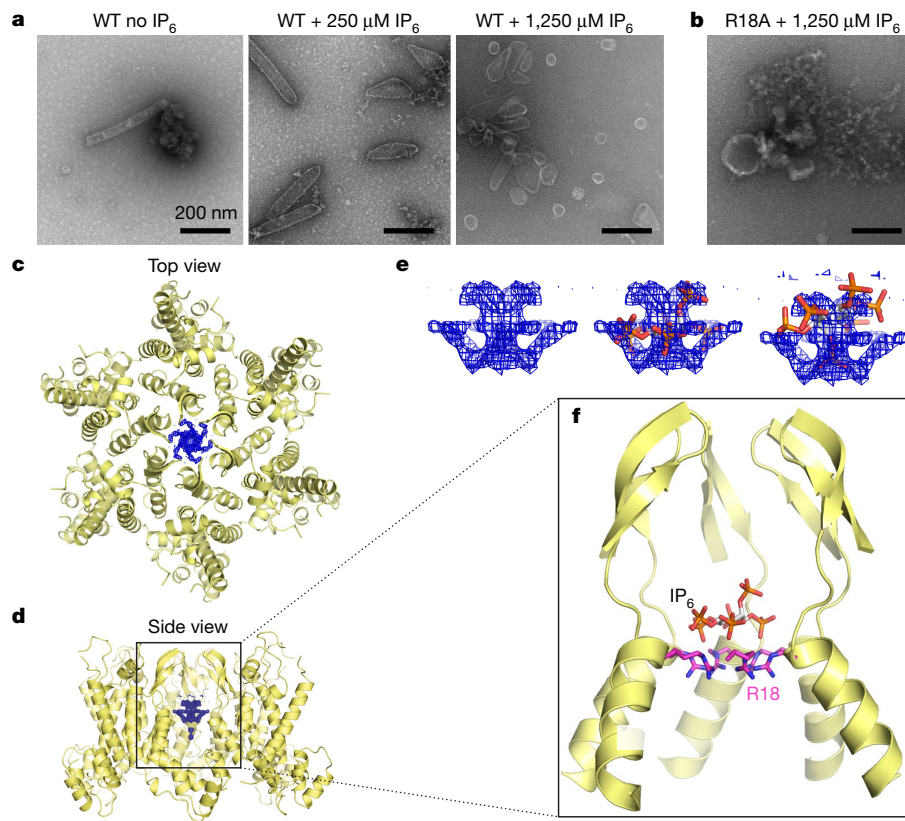


Fig. 3 | IP₆ induces mature CA assembly by interacting with Arg18.

a, Representative negative stain images of mature CA assemblies at pH 6 and 100 mM NaCl with increasing IP₆ concentrations (0–1,250 μM). The experiment was repeated five times with similar results. **b**, Representative image of failed CA R18A assembly even in the presence of 1,250 μM IP₆. The experiment was repeated three times with similar results. **c, d**, Top view (**c**) and side view (**d**) of a CA hexamer crystal structure showing the protein in yellow ribbons and unbiased mF₀-DF_c difference density in blue mesh, contoured at 2.2σ . **e**, Side views of *myo*-IP₆ docked into the difference density in two possible binding modes. **f**, Illustration of a single IP₆ molecule bound within a chamber enclosed by the N-terminal β -hairpins and the Arg18 ring (magenta). In a second crystal form, IP₆ densities were observed both above and below the Arg18 ring (Extended Data Fig. 8).

charge neutralization is a fundamental aspect of IP₆-mediated HIV-1 Gag assembly, and that the details of coordination geometry and/or local stereochemistry are also important.

To address the biological importance of IP₆ in HIV-1 replication, we generated a knockout cell line in which the gene encoding inositol pentakisphosphate 2-kinase (IPPK), the enzyme responsible for the final step in IP₆ synthesis, was ablated (Fig. 1g). Infectious HIV-1 particle production from these knockout cells was reduced by between 10- and 20-fold (Fig. 1g). We interpret this result as implying that IP₆ has a critical role in assembly of immature and/or mature HIV-1.

As the s-CANC construct lacks the MA domain, the effect of IP₆ cannot depend on this domain, as previously suggested^{7–9}. The NC domain also cannot be essential, because IP₆ still promoted assembly in the absence of nucleic acid (Extended Data Fig. 2a, d). Furthermore, IP₆ also promoted the formation of abundant immature VLPs from the smaller protein s-CASP1, which lacks the NC domain altogether (Fig. 2a and Extended Data Fig. 2b, d). However, deletion of the SP1 domain abrogated the effect of IP₆, as IP₆ failed to induce assembly of s-CA into immature VLPs (Extended Data Fig. 2c).

Both the CA domain of Gag and the mature CA protein are composed of two separately folded sub-domains, CA_{NTD} and CA_{CTD}. To further define the site of action of IP₆, we removed the N-terminal CA_{NTD} sub-domain to create CA_{CTD}SP1, which makes up the minimal Gag hexagonal lattice^{3,11}. In the presence but not the absence of IP₆, and at physiological pH and ionic strength, CA_{CTD}SP1 formed flat hexagonal crystals, as shown by negative-stain electron microscopy (Fig. 2b). These crystals had the characteristic immature lattice spacing (Fig. 2c). That s-CASP1 formed a spherical lattice while CA_{CTD}SP1 formed a flat lattice suggests that CA_{NTD} provides the contacts necessary for enforcing lattice curvature.

We next determined the X-ray crystal structure of CA_{CTD}SP1 crystallized in the presence of IP₆ (Fig. 2d, e and Extended Data Table 1). This revealed a single, six-fold symmetric density in the middle of the hexameric ring (blue mesh in Fig. 2d–f), indicating that one IP₆ molecule binds one CA_{CTD}SP1 hexamer. Notably, this density coincides precisely with an unknown density feature observed in cryo-electron microscopy (cryo-EM) maps of the HIV-1 Gag hexamer derived from authentic immature virions² (Extended Data Fig. 3). This further supports the idea that IP₆ is a cofactor of Gag assembly in cells and is a structural component of the HIV-1 particle.

IP₆ is an asymmetric molecule with multiple stereoisomers, the most abundant of which is the *myo* form, with a chair configuration of one axial and five equatorial phosphate groups¹²; this is the most commonly observed stereoisomer in structures of various IP₆-binding proteins^{13–15}. In our CA_{CTD}SP1 structure, the IP₆ density is also consistent with the *myo* form, with the axial phosphate pointing towards the six-helix bundle (6HB) (Fig. 2f). The bound ligand can adopt six energetically equivalent orientations, and the six-fold symmetric density is therefore the sum of these equivalent positions (Extended Data Fig. 4a). More importantly, the bound IP₆ is surrounded by two rings of lysine sidechains—Lys290 from the major homology region loop and Lys359 from the 6HB (Fig. 2g). In our previous crystal structure of the CA_{CTD}SP1 hexamer in the absence of IP₆, sidechain densities for these lysines were not visible, implying that these residues were highly flexible³. In the current structure, these sidechains are better ordered, and in direct ionic contact through their primary ε-amines with the IP₆ phosphate groups (Fig. 2g and Extended Data Fig. 4b).

Consistent with the structure, we found that s-CANC mutant proteins in which Lys290 or Lys359 were replaced with alanine (K290A and K359A) were 100-fold less responsive to added IP₆ (Extended Data Fig. 5a–d). These results further indicate that both lysine rings are required for productive IP₆ binding. K290R and K359R mutants had less pronounced defects but still did not respond to IP₆ as well as wild-type s-CANC, consistent with the high degree of lysine conservation in these positions (99.94% for K290 and 99.84% for K359; <http://www.hiv.lanl.gov>). Furthermore, the K290A and K359A mutations abolished infectivity (Extended Data Fig. 5e). Thus, optimal HIV-1

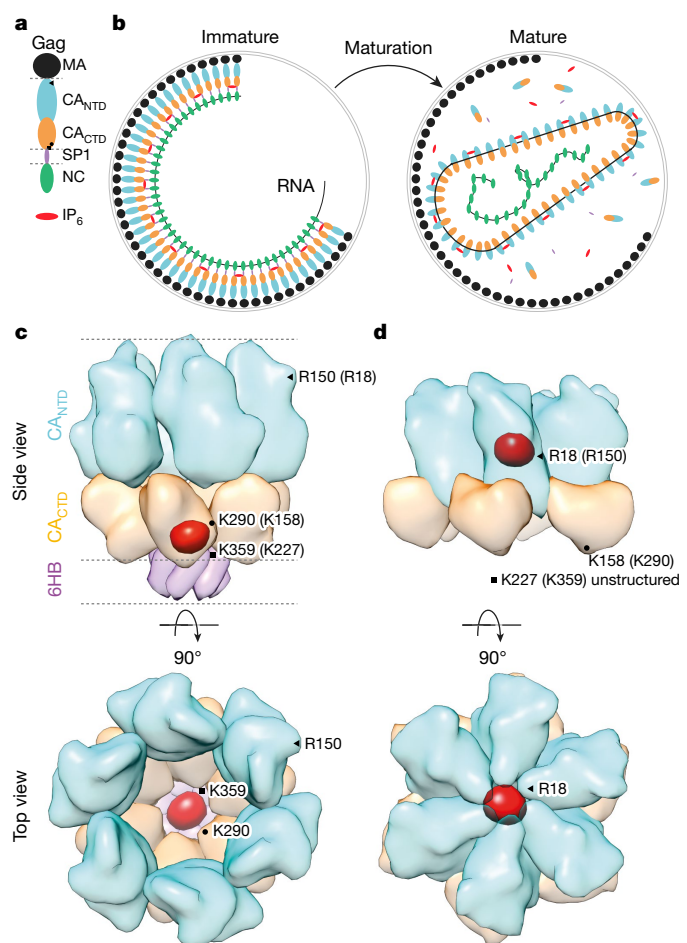


Fig. 4 | Model. **a**, Diagram of HIV-1 Gag, with the indicated positions of R150 (triangle; R18 in mature CA), K290 (circle; K158 in mature CA), K359 (square; K227 in mature CA). Dotted lines indicate protease cleavage sites. **b**, Diagram of Gag organization in immature virions (left). Following cleavage of Gag by protease (that is, maturation), CA re-organizes to form a mature core around viral RNA (right). **c, d**, Surface representations of the CASP1 and CA hexamers in the immature (**c**) and mature virus (**d**), with IP₆ shown in its binding sites. The marked rearrangement of CA upon maturation is evident, as is the change in IP₆ binding site between immature and mature viruses. CA_{NTD}, blue; CA_{CTD}, orange; 6HB, purple; IP₆, red.

assembly in cells appears to require lysines at both positions. The results of previous studies that examined the effects of the above mutations on virus budding from cells and on virus infectivity are consistent with our findings^{16–19}.

The above data suggest that IP₆ acts by stabilizing the 6HB and promoting the formation of the immature Gag hexamer. To test this notion, we examined the dynamic behaviour of the CA_{CTD}SP1 hexamer by using all-atom molecular dynamics simulations. In the absence of IP₆, the six-fold symmetry of the CA_{CTD}SP1 hexamer collapsed after 200 ns and did not recover during the 2 μs of simulation (Extended Data Fig. 6 and Supplementary Video 1). By contrast, six-fold symmetry in the presence of IP₆ was maintained, particularly at the top of the 6HB, proximal to the IP₆-binding site. Other inositol derivatives and mellitic acid (hexacarboxybenzene) also stabilized the 6HB in our simulations, consistent with their ability to also support immature s-CANC assembly *in vitro* (Extended Data Fig. 6b, c).

We also examined the effect of IP₆ on mature capsid assembly, which is mediated by the CA protein that is generated upon Gag proteolysis. We found that IP₆ promoted assembly of HIV-1 CA into mature-like structures^{1,10,20} (Fig. 3a and Extended Data Fig. 7b, d). Compared to immature s-CANC assembly, however, higher amounts of IP₆ were

required (Extended Data Fig. 7b, d). Mellitic acid (Extended Data Fig. 7c, e) and IP₅, but not IP₄ or IP₃ (Extended Data Fig. 7f, g), stimulated mature CA assembly, although less potently than IP₆.

The mature HIV-1 CA hexamer also contains a positively charged ring, made up of Arg18 sidechains (Arg150 in Gag numbering)^{21,22}. This ring was previously shown to mediate transport of nucleoside triphosphates, which facilitates reverse transcription of the encapsulated genome²³. We therefore tested whether IP₆ would promote assembly of the HIV-1 CA R18A mutant, and found that it did not (Fig. 3b). HIV-1 virions containing this mutation were also non-infectious^{17,23} (Extended Data Fig. 5e). We next crystallized the mature CA hexamer in the presence of IP₆ (Extended Data Table 1). Although IP₆ can bind both above and below the ring (Extended Data Fig. 8), densities were most pronounced in the upper binding site, inside a chamber surrounded by the N-terminal β-hairpins of CA (Fig. 3c–f). Thus, IP₆ also binds and promotes assembly of the mature HIV-1 CA lattice.

Our results lead to the following model (Fig. 4). IP₆ facilitates the formation of the six-helix CA-SP1 bundle by binding to two rings of primary amines at Lys290 and Lys359, thereby neutralizing otherwise repulsive charges at the centre of the HIV-1 Gag hexamer (Fig. 4c). Although other negatively charged molecules can also bind this pocket, our data suggest that IP₆ is the most potent in promoting assembly, probably because it has the most optimal binding geometry. Some 300–400 molecules of IP₆—one per hexamer—are incorporated into the virus particle as a structural component of the immature Gag shell (Fig. 4c). During virus maturation, proteolysis of Gag disrupts the 6HB, thus releasing IP₆ and at the same time unmasking the Arg18 binding site in mature CA. IP₆ then binds to this newly exposed site in CA (Fig. 4d), promoting the formation of CA hexamers and in turn the mature CA lattice. This involvement of a small molecule in two distinct steps in virus assembly, by binding to highly conserved sites, suggests strategies for possible therapeutic intervention in HIV-1 replication.

Online content

Any Methods, including any statements of data availability and Nature Research reporting summaries, along with any additional references and Source Data files, are available in the online version of the paper at <https://doi.org/10.1038/s41586-018-0396-4>.

Received: 1 December 2017; Accepted: 10 July 2018;

Published online 1 August 2018.

- Gross, I. et al. A conformational switch controlling HIV-1 morphogenesis. *EMBO J.* **19**, 103–113 (2000).
- Schur, F. K. et al. An atomic model of HIV-1 capsid-SP1 reveals structures regulating assembly and maturation. *Science* **353**, 506–508 (2016).
- Wagner, J. M. et al. Crystal structure of an HIV assembly and maturation switch. *eLife* **5**, e17063 (2016).
- Keller, P. W., Adamson, C. S., Heymann, J. B., Freed, E. O. & Steven, A. C. HIV-1 maturation inhibitor bevirimut stabilizes the immature Gag lattice. *J. Virol.* **85**, 1420–1428 (2011).
- Wang, M. et al. Quenching protein dynamics interferes with HIV capsid maturation. *Nat. Commun.* **8**, 1779 (2017).
- Letcher, A. J., Schell, M. J. & Irvine, R. F. Do mammals make all their own inositol hexakisphosphate? *Biochem. J.* **416**, 263–270 (2008).
- Campbell, S. et al. Modulation of HIV-like particle assembly *in vitro* by inositol phosphates. *Proc. Natl Acad. Sci. USA* **98**, 10875–10879 (2001).
- Datta, S. A. K. et al. Interactions between HIV-1 Gag molecules in solution: an inositol phosphate-mediated switch. *J. Mol. Biol.* **365**, 799–811 (2007).
- Munro, J. B. et al. A conformational transition observed in single HIV-1 Gag molecules during *in vitro* assembly of virus-like particles. *J. Virol.* **88**, 3577–3585 (2014).
- von Schwedler, U. K. et al. Proteolytic refolding of the HIV-1 capsid protein amino-terminus facilitates viral core assembly. *EMBO J.* **17**, 1555–1568 (1998).

- Accola, M. A., Strack, B. & Göttlinger, H. G. Efficient particle production by minimal Gag constructs which retain the carboxy-terminal domain of human immunodeficiency virus type 1 capsid-p2 and a late assembly domain. *J. Virol.* **74**, 5395–5402 (2000).
- Loewus, F. A. & Murthy, P. P. N. Myo-inositol metabolism in plants. *Plant Sci.* **150**, 1–19 (2000).
- van Galen, J. et al. Interaction of GAPR-1 with lipid bilayers is regulated by alternative homodimerization. *Biochim. Biophys. Acta* **1818**, 2175–2183 (2012).
- Ouyang, Z., Zheng, G., Tomchick, D. R., Luo, X. & Yu, H. Structural basis and IP6 requirement for Pds5-dependent cohesin dynamics. *Mol. Cell* **62**, 248–259 (2016).
- Macbeth, M. R. et al. Inositol hexakisphosphate is bound in the ADAR2 core and required for RNA editing. *Science* **309**, 1534–1539 (2005).
- Chang, Y. F., Wang, S. M., Huang, K. J. & Wang, C. T. Mutations in capsid major homology region affect assembly and membrane affinity of HIV-1 Gag. *J. Mol. Biol.* **370**, 585–597 (2007).
- von Schwedler, U. K., Stray, K. M., Garrus, J. E. & Sundquist, W. I. Functional surfaces of the human immunodeficiency virus type 1 capsid protein. *J. Virol.* **77**, 5439–5450 (2003).
- Melamed, D. et al. The conserved carboxy terminus of the capsid domain of human immunodeficiency virus type 1 gag protein is important for virion assembly and release. *J. Virol.* **78**, 9675–9688 (2004).
- Rihm, S. J. et al. Extreme genetic fragility of the HIV-1 capsid. *PLoS Pathog.* **9**, e1003461 (2013).
- Ganser-Pornillos, B. K., von Schwedler, U. K., Stray, K. M., Aiken, C. & Sundquist, W. I. Assembly properties of the human immunodeficiency virus type 1 CA protein. *J. Virol.* **78**, 2545–2552 (2004).
- Ganser-Pornillos, B. K., Cheng, A. & Yeager, M. Structure of full-length HIV-1 CA: a model for the mature capsid lattice. *Cell* **131**, 70–79 (2007).
- Pornillos, O., Ganser-Pornillos, B. K. & Yeager, M. Atomic-level modelling of the HIV capsid. *Nature* **469**, 424–427 (2011).
- Jacques, D. A. et al. HIV-1 uses dynamic capsid pores to import nucleotides and fuel encapsidated DNA synthesis. *Nature* **536**, 349–353 (2016).
- R Core Team. *R: A Language and Environment for Statistical Computing* (R Foundation for Statistical Computing, Vienna, 2013).

Acknowledgements We thank J. Briggs for discussions and reading of the manuscript. This work was supported by the National Institutes of Health (NIH) grants R01-GM107013 (V.M.V.), R01-GM105684 (G. W. Feigenson), P30-GM110758 and P50-GM082251 (J.R.P.), R01-AI129678 (O.P. and B.K.G.-P.), U54-GM103297 (O.P.) and R01-GM110776 (M.C.J.). F.K.M.S. was supported by Deutsche Forschungsgemeinschaft grant BR 3635/2-1 awarded to J. A. G. Briggs. J.M.W. was supported by NIH postdoctoral fellowship grant F32-GM115007. Anton computer time was provided by the Pittsburgh Supercomputing Center (PSC) through NIH grant R01-GM116961. The Anton machine at PSC was generously made available by D. E. Shaw Research. This work used the Extreme Science and Engineering Discovery Environment (XSEDE), which is supported by National Science Foundation (NSF) grant number OCI-1053575. Specifically, it used the Bridges system, which is supported at PSC by NSF award number ACI-1445606. Some of The EM work was conducted at the Molecular Electron Microscopy Core facility at the University of Virginia.

Reviewer information *Nature* thanks E. Freed and the other anonymous reviewer(s) for their contribution to the peer review of this work.

Author contributions R.A.D. performed protein purification and *in vitro* assembly. F.K.M.S. did comparative analyses of cryo-EM and crystal structure data. K.K.Z., J.M.W., B.K.G.-P. and O.P. carried out crystallization trials and structure determination. B.K.G.-P. performed 2D cryo-EM. J.R.P. and C.X. performed all-atom MD simulations. T.D.L., C.L.R. and M.C.J., performed cell biology and virology. The manuscript was written primarily by R.A.D., J.R.P., B.K.G.-P., O.P. and V.M.V. The project was originally conceived by R.A.D., with input from all authors throughout experimentation and manuscript preparation.

Competing interests The authors declare no competing interests.

Additional information

Extended data is available for this paper at <https://doi.org/10.1038/s41586-018-0396-4>.

Supplementary information is available for this paper at <https://doi.org/10.1038/s41586-018-0396-4>.

Reprints and permissions information is available at <http://www.nature.com/reprints>.

Correspondence and requests for materials should be addressed to R.A.D. or O.P.

Publisher's note: Springer Nature remains neutral with regard to jurisdictional claims in published maps and institutional affiliations.

METHODS

No statistical methods were used to predetermine sample size. The experiments were not randomized and investigators were not blinded to allocation during experiments and outcome assessment.

Protein purification. DNA coding for HIV-1 Gag proteins were cloned into a His₆-SUMO vector²⁵. The proteins were expressed in *Escherichia coli* and purified using standard Ni²⁺ affinity chromatography followed by cleavage of the SUMO moiety by ULP1 protease. In brief, bacterial pellets were resuspended in buffer and lysed by sonication and cellular debris removed by centrifugation. The supernatant was filtered through a 0.2-μm filter, applied to a Ni²⁺ affinity resin, and eluted with imidazole. The eluted protein was dialysed overnight in the presence of ULP1 protease, and subjected to Ni²⁺ chromatography a second time to remove the SUMO tag and ULP1 protease.

All proteins containing the NC domain were purified with additional steps for more stringent removal of nucleic acid. Following bacterial lysis and centrifugation, nucleic acid was precipitated by addition of 0.03% (v/v) polyethyleneimine followed by centrifugation. Ammonium sulfate to 20% saturation was added to the resulting supernatant, and the precipitate was resuspended in buffer (20 mM Tris-HCl, pH 8, 100 mM NaCl, 2 mM TCEP (tris(2-carboxyethyl)phosphine), 5 μM ZnCl₂). The protein was then purified by anion exchange and Ni²⁺ chromatography as above. All purification steps were performed at 4 °C or on ice. All of the final purified proteins, at concentrations of 2–5 mg/ml and having A₂₆₀/A₂₈₀ ratios of <0.6, were flash-frozen in liquid nitrogen and stored at -80 °C.

In vitro assembly. Assembly of s-CANC VLPs was performed by dialysing 50 μM protein against buffer (50 mM MES, pH 6 or 50 mM Tris-HCl, pH 8, 100 mM NaCl, 5 μM ZnCl₂, 2 mM TCEP) with a single-stranded 50-mer oligonucleotide (GT₂₅) at a 1:5 molar ratio of oligonucleotide to protein for 4 h at 4 °C. All reactions were adjusted to a final volume of 100 μl with buffer following dialysis. Working stocks of 10 mM inositol phosphates were made fresh (IP₆, TCI cat# P0409; IP₃-IP₅, Cayman Chemical cat #s IP₃-60960, IP₄-60980, and IP₅-10009851) with the pH adjusted to 6.0 with NaOH, and added both to the assembly reaction and dialysis buffer. Both s-CASP1 and CA_{CTD}SP1 assembly reactions were performed as described for s-CANC but with 500 μM protein and 500 μM IP₆. Mature CA assembly was performed by dilution into buffer (50 mM MES, pH 6, 100 mM NaCl) to 250 μM final concentration in the presence of increasing amounts of IP₆. Note that under these low-salt conditions, HIV-1 CA does not spontaneously assemble efficiently. The mature reactions were diluted 1:10 before spotting on EM grids. All VLP assemblies were visualized by EM negative staining with uranyl acetate. Quantification was performed by counting particles on at least five images from at least two different assembly reactions. Box plot; centre lines show the medians; box limits indicate the 25th and 75th percentiles as determined by R software²⁴; whiskers extend to minimum and maximum values.

CRISPR knockout. The lentiCRISPR v2 vector was a gift from F. Zhang (Addgene plasmid # 52961)²⁶. The VSV-G expression vector²⁷ was obtained through the NIH AIDS Research and Reference Reagent Program. HEK293FT cells were purchased from Invitrogen. Cell lines were tested for, and showed no mycoplasma contamination. The plasmid v906 is an HIV-1 NL4-3 derived provirus lacking Vpr, Vif, Env, and containing CMV GFP in place of Nef. The construct has several silent restriction sites added to the CA domain of Gag for cloning purposes. The IPPK-targeted guide RNA (5'-AACAGCGCTGCGTGTGCTG-3') was cloned into lentiCRISPR v2, which was then used to transduce 293FT cells, followed by selection with puromycin at 1 μg/ml. Clonal isolates of the stably transduced cells were obtained by limiting dilution. To confirm the knockout, genomic DNA was isolated from clonal isolates using the DNeasy blood and tissue kit (Qiagen) following the manufacturer's protocol. The guide RNA target sequence was amplified from genomic DNA using primers 5'-GAAATGTGTGCCACTGTGTTTA-3' and 5'-ATGATGGACACACCACTTCT-3'. The PCR product was directly sequenced.

Infectivity assays. Equivalent numbers of 293FT WT or IPPK KO cells were plated in 35-mm dishes and transfected with 900 ng of v906 and 100 ng of VSV-G. Medium was collected two days post-transfection and frozen at -80 °C to lyse cells in the supernatant. Thawed supernatants were centrifuged at 1,500g for 5 min to remove cellular debris. Infections were performed in fresh 293FT cells. Cells were collected two days later, fixed with 4% paraformaldehyde, and analysed for GFP expression using an Accuri C6 flow cytometer.

Two-dimensional crystallography. CA_{CTD}SP1 2D crystals were produced by incubating 0.8 mM protein with 0.8 mM IP₆ at room temperature for 30 min. Samples were placed on a carbon-coated grid, washed with 0.1 M KCl, blotted to near dryness and flash frozen by plunging in liquid ethane. Low-dose images were collected on a Tecnai F20 equipped with 4k × 4k Ultrascan CCD camera (Gatan) under low electron-dose conditions (~20 e⁻/Å²). Images were converted to MRC format and manual indexing, unbending, and corrections for CTF were performed with 2dx²⁸.

X-ray crystallography. Purified CA_{CTD}SP1 protein (stock = 4.5 mg/ml) was mixed with equal volume of IP₆ (stock = 1.4 mM) and incubated briefly at room temperature. Crystals were formed by the vapour diffusion method in sitting drops containing

a 1:1 ratio of the protein/IP₆ mix and precipitant (0.2 M NaCl, 20% PEG 3,350, 0.1 M Bis-Tris, pH 5.35). Hexagonal plate crystals grew after 2 days of incubation at 17 °C. Crystals were cryoprotected in 25% ethylene glycol and flash-frozen in liquid nitrogen. Diffraction data were collected at the Advanced Photon Source beamline 22-ID and were indexed and scaled with HKL2000²⁹. The structure was solved by molecular replacement using as search model one monomer of the previously reported CA_{CTD}SP1 hexamer structure (PDB 5I4T)³, with Lys290 and Lys359 sidechains truncated at Cα. Refinement and model building was performed using the PHENIX suite of programs³⁰ and Coot³¹. Refinement of the protein was first completed before modelling the IP₆ and Lys290/Lys359 sidechain densities. The IP₆ density was unambiguously identified from mF_o - DF_c difference maps, and the interpretation that the density was due to bound IP₆ was further supported by comparison with difference maps from our previously reported CA_{CTD}SP1 structure in the absence of IP₆³. Given the resolution of the data and crystallographic averaging of the ligand density, we assumed that the bound IP₆ was in the *myo* conformation and refined the ligand as a rigid body with 1/6 occupancy. Only weak residual difference densities were observed after this treatment, suggesting that the modelled IP₆ conformation was a reasonable interpretation of the data.

Disulfide-stabilized CA A14C/E45C/W184A/M185A was prepared as previously described^{32,33}. IP₆-containing samples were prepared for crystallization as described for CA_{CTD}SP1, except that the protein stock concentration in this case was 10 mg/ml. P6 crystals were obtained in precipitant containing 2% Tacsimate, 14% PEG 8,000, 0.1 M Tris, pH 8.4, whereas P212121 crystals were obtained in 8% PEG 8,000, 0.1 M Tris, pH 8.2. Data were collected at Advanced Photon Source beamline 22-BM (P6 form) or 22-ID (P212121 form) and processed with HKL2000²⁹. The crystals were isomorphous with previously deposited structures solved in the absence of IP₆ (PDB 3H47 and 3H4E)³², and so initial refinement was through rigid body placement of the deposited coordinates (with Arg150 sidechains and waters removed). Refinement of protein-only models were first completed before modelling the IP₆ and Arg150 sidechain densities. As with the immature hexamer, IP₆ densities were unambiguously identified by mF_o - DF_c difference maps and by difference density comparisons of CA hexamers crystallized with and without IP₆. The IP₆ densities in the mature hexamers were modelled as follows. For the P6 crystal form, a single well-defined IP₆ density was found inside the β-hairpin chamber (Fig. 3c-e). As in the case of the immature hexamer, the ligand density was also six-fold symmetric due to crystallographic averaging, but in this case indicated at least two binding modes, one with the axial phosphate pointing away from the Arg18 ring and a second pointing towards the ring. Two IP₆ molecules were therefore docked into the density, again in the *myo* form and refined as rigid bodies with 1/12 occupancy (Fig. 3e). Again, only weak residual difference densities were observed after this treatment, suggesting that the modelled IP₆ conformations were reasonable interpretations of the data. For the P212121 form, IP₆ densities were observed on both sides of the Arg18 ring (there were 2 hexamers in the asymmetric unit and so we observed 4 density features) (Extended Data Fig. 8). These were modelled by docking *myo*-IP₆ in one or two configurations that appeared most consistent with the local density distribution, and then refined as rigid bodies with appropriate occupancy. In this case, significant residual difference densities were observed at the ligand positions after refinement, indicating that additional binding modes were possible. However, we did not attempt to model these multiple overlapping binding modes. The P6 form crystallized in the presence of Tacsimate (Hampton Scientific), which is a mixture of organic carboxylic acids. The excess of negatively charged precipitant therefore appears to have inhibited binding of IP₆ below the Arg18 ring; this can be reasonably interpreted to mean that IP₆ has greater affinity for the site enclosed by the β-hairpins. The P212121 form crystallized in the absence of Tacsimate, allowing IP₆ binding on both sides of the Arg18 ring.

Statistics for all three crystal structures are reported in Extended Data Table 1. Structure visualizations and images were made by using PyMol (Schrödinger Scientific).

Molecular dynamics simulations. The structure of the IP₆-bound CA_{CTD}SP1 hexamer was used to derive bound and unbound CA_{CTD}SP1 models. The IPs and mellitic acid molecules were placed in the central pore of the hexamer between K290 and K359 rings in the corresponding models by aligning the carbons present in the central cyclic ring. All models were then solvated with TIP3P water³⁴ and the salt concentration was set to 150 mM NaCl. Sixteen chloride molecules and twenty-three sodium ions were placed near the hexamer using the CIONIZE plugin in VMD³⁵ to minimize the electrostatic potential. The resulting CA_{CTD}SP1 models each contained a total of 30,000 atoms.

After model building, the systems were initially subjected to minimization in two stages, both using the conjugated gradient algorithm³⁶ with linear searching³⁷. Each stage consisted of 10,000 steps of energy minimization. During the first stage, only water molecules and ions were free to move, while the protein and IP molecules, if any, were fixed. In the second stage, the backbone atoms of the protein were restrained with a force constant of 10.0 Kcal mol⁻¹ Å⁻². Convergence of the

minimizations were confirmed once the variances of gradients were not greater than 1 Kcal mol⁻¹ Å⁻¹. During thermalization the systems were heated from 50 K to 310 K in 20 K increments over 1 ns. Subsequently, the systems were equilibrated, while the backbone atoms of CA_{CTD}SP1 were restrained. The positional restraints were gradually released at a rate of 1.0 Kcal mol⁻¹ Å⁻² per 400 ps from 10.0 to 0.0 Kcal mol⁻¹ Å⁻². NAMD 2.12³⁸ was employed during minimization/thermalization and equilibration steps.

Simulations of IP₆-bound and unbound CA_{CTD}SP1 were then performed on the special purpose computer Anton²³⁹ in the Pittsburgh supercomputing centre for 2 μs. The CHARMM 36m⁴⁰ force-field was used for all simulations. Parameters for IP₆ were derived by analogy following the CGENIFF protocol⁴¹. During the simulation, the temperature (310 K) and pressure (1 atm) were maintained by using the Multigrator integrator⁴² and the simulation time-step was set to 2.5 fs/step, with short-range forces evaluated at every time step, and long-range electrostatics evaluated at every second time step. Short-range non-bonded interactions were cut off at 17 Å; long range electrostatics were calculated using the k-Gaussian Split Ewald method⁴³.

Simulations of CA_{CTD}SP1 bound to IP₃, IP₄, and IP₅ were performed for 2 μs on TACC Stampede 2 using NAMD 2.12³⁸. The molecular simulations were conducted under isothermal (310 K) and isobaric (1 atm) conditions, regulated by the Langevin thermostat⁴⁴ and the Nosé–Hoover Langevin piston^{45,46}, respectively. All bonds to hydrogen atoms were constrained with the SHAKE algorithm⁴⁷. A time step of 2 fs was used for all simulations. Long-range electrostatics were calculated using the Particle-Mesh-Ewald method, as implemented in NAMD³⁸, with a cutoff of 1.2 nm. Full electrostatic interactions were calculated every two time steps while nonbonded interactions were performed every time step.

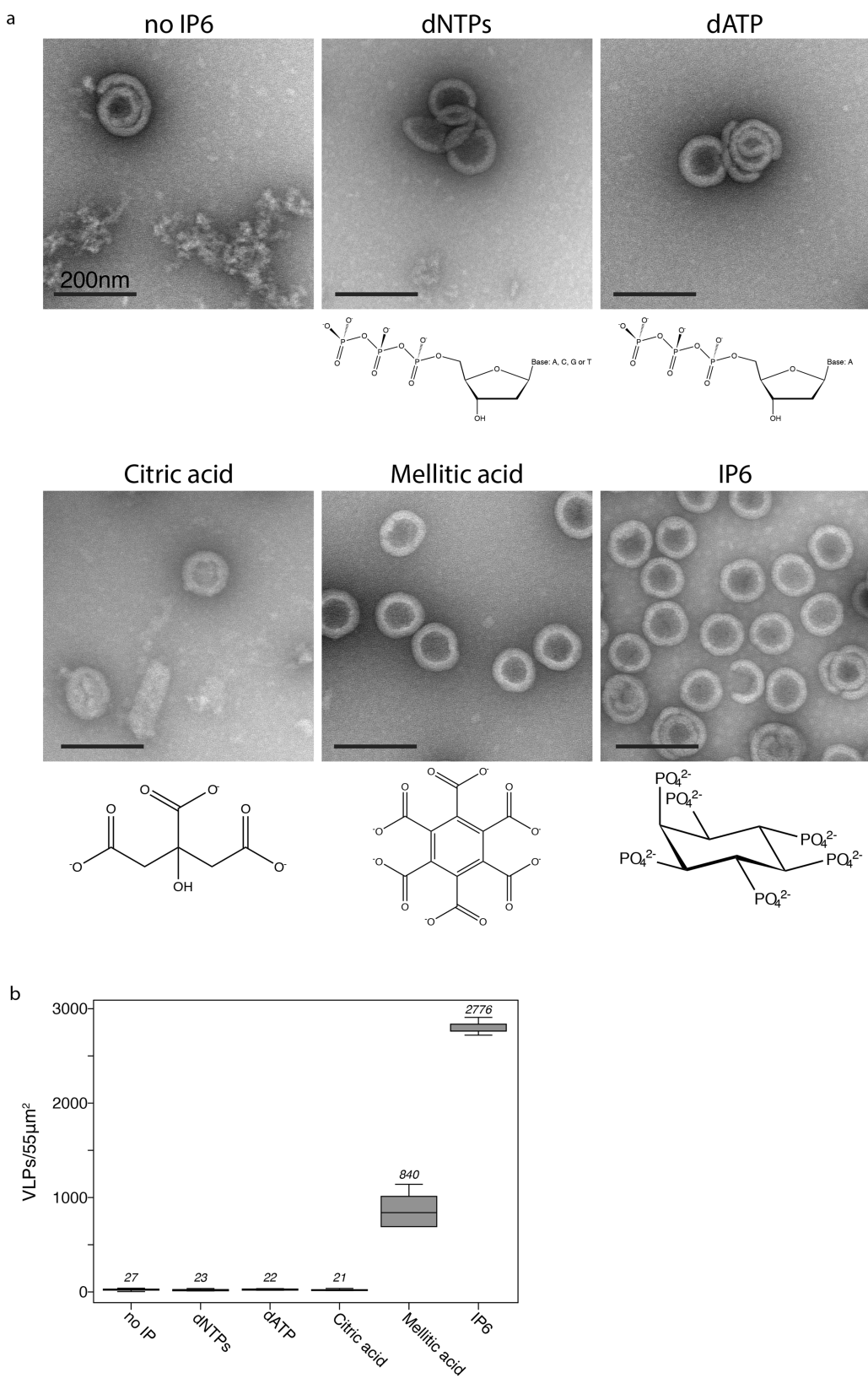
Analysis of MD simulations. Root-mean-square deviations (RMSDs) and root mean square fluctuations (RMSFs) of the Cα of the CA_{CTD}SP1 hexamers were computed using the measure command in VMD³⁵. Before RMSD and RMSF calculations, the structure of the hexamer was aligned to a common reference. RMSFs of each monomer in a central hexamer were calculated to obtain RMSF standard deviations of an entire hexamer.

Reporting summary. Further information on experimental design is available in the Nature Research Reporting Summary linked to this paper.

Data availability. Coordinates and structure factors have been deposited at the RCSB Protein Bank Bank (PDB) database, under accession numbers 6BH5, 6BHT, and 6BHS. All other data are available from the authors on request; see author contributions for specific datasets.

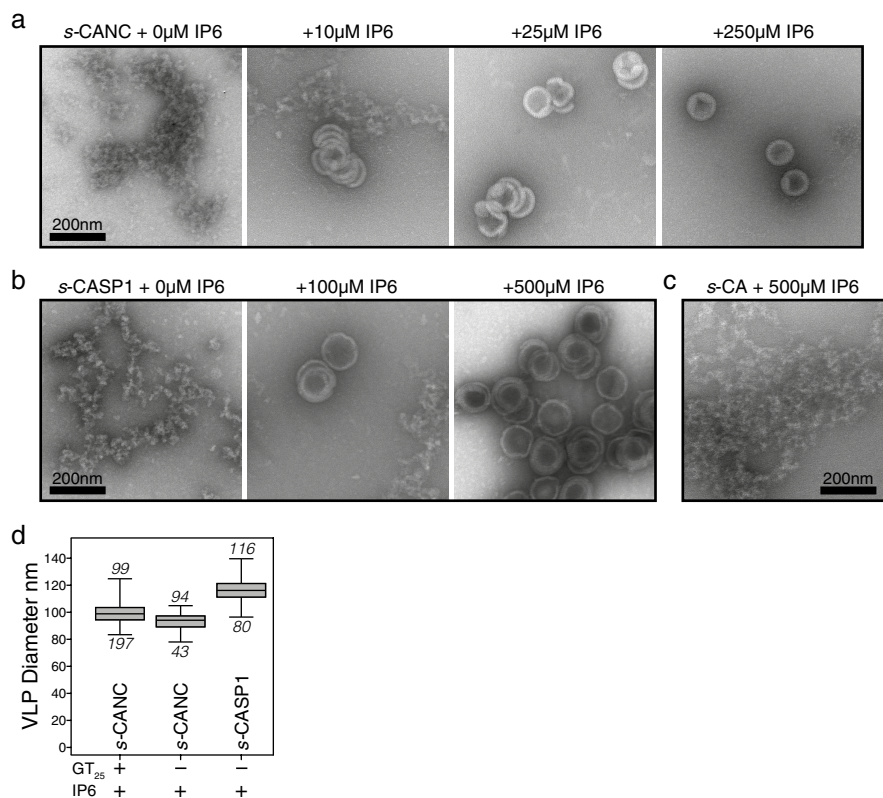
- 25. Malakhov, M. P. et al. SUMO fusions and SUMO-specific protease for efficient expression and purification of proteins. *J. Struct. Funct. Genomics* **5**, 75–86 (2004).
- 26. Sanjana, N. E., Shalem, O. & Zhang, F. Improved vectors and genome-wide libraries for CRISPR screening. *Nat. Methods* **11**, 783–784 (2014).

- 27. Chang, L. J., Urlacher, V., Iwakuma, T., Cui, Y. & Zucali, J. Efficacy and safety analyses of a recombinant human immunodeficiency virus type 1 derived vector system. *Gene Ther.* **6**, 715–728 (1999).
- 28. Gipson, B., Zeng, X., Zhang, Z. Y. & Stahlberg, H. 2dx-user-friendly image processing for 2D crystals. *J. Struct. Biol.* **157**, 64–72 (2007).
- 29. Otwinowski, Z. & Minor, W. Processing of X-ray diffraction data collected in oscillation mode. *Methods Enzymol.* **276**, 307–326 (1997).
- 30. Adams, P. D. et al. PHENIX: a comprehensive Python-based system for macromolecular structure solution. *Acta Crystallogr. D* **66**, 213–221 (2010).
- 31. Emsley, P., Lohkamp, B., Scott, W. G. & Cowtan, K. Features and development of Coot. *Acta Crystallogr. D* **66**, 486–501 (2010).
- 32. Pornillos, O. et al. X-ray structures of the hexameric building block of the HIV capsid. *Cell* **137**, 1282–1292 (2009).
- 33. Pornillos, O., Ganser-Pornillos, B. K., Banumathi, S., Hua, Y. & Yeager, M. Disulfide bond stabilization of the hexameric capsomer of human immunodeficiency virus. *J. Mol. Biol.* **401**, 985–995 (2010).
- 34. Jorgensen, W. L. & Jenson, C. Temperature dependence of TIP3P, SPC, and TIP4P water from NPT Monte Carlo simulations: seeking temperatures of maximum density. *J. Comput. Chem.* **19**, 1179–1186 (1998).
- 35. Humphrey, W., Dalke, A. & Schulten, K. VMD: visual molecular dynamics. *J. Mol. Graph.* **14**, 33–38, 27–28 (1996).
- 36. Fletcher, R. & Reeves, C. M. Function minimization by conjugate gradients. *Comput. J.* **7**, 149–154 (1964).
- 37. Sun, W. & Yuan, Y.-X. *Optimization Theory and Methods: Nonlinear Programming* (Springer US, 2006)
- 38. Phillips, J. C. et al. Scalable molecular dynamics with NAMD. *J. Comput. Chem.* **26**, 1781–1802 (2005).
- 39. Shaw, D. E. et al. In *Proc. Intl Conf. High Performance Computing, Networking, Storage and Analysis* 41–53 (IEEE Press, New Orleans, 2014).
- 40. Best, R. B. et al. Optimization of the additive CHARMM all-atom protein force field targeting improved sampling of the backbone φ , ψ and side-chain $\chi(1)$ and $\chi(2)$ dihedral angles. *J. Chem. Theory Comput.* **8**, 3257–3273 (2012).
- 41. Vanommeslaeghe, K. et al. CHARMM general force field: A force field for drug-like molecules compatible with the CHARMM all-atom additive biological force fields. *J. Comput. Chem.* **31**, 671–690 (2010).
- 42. Lippert, R. A. et al. Accurate and efficient integration for molecular dynamics simulations at constant temperature and pressure. *J. Chem. Phys.* **139**, 164106 (2013).
- 43. Shan, Y., Klepeis, J. L., Eastwood, M. P., Dror, R. O. & Shaw, D. E. Gaussian split Ewald: A fast Ewald mesh method for molecular simulation. *J. Chem. Phys.* **122**, 54101 (2005).
- 44. Berendsen, H. J. C., Postma, J. P. M., Vangunsteren, W. F., Dinola, A. & Haak, J. R. Molecular dynamics with coupling to an external bath. *J. Chem. Phys.* **81**, 3684–3690 (1984).
- 45. Martyna, G. J., Tobias, D. J. & Klein, M. L. Constant pressure molecular dynamics algorithms. *J. Chem. Phys.* **101**, 4177–4189 (1994).
- 46. Feller, S. E., Zhang, Y. H., Pastor, R. W. & Brooks, B. R. Constant pressure molecular dynamics simulation—the Langevin Piston Method. *J. Chem. Phys.* **103**, 4613–4621 (1995).
- 47. Ryckaert, J.-P., Ciccotti, G. & Berendsen, H. J. Numerical integration of the cartesian equations of motion of a system with constraints: molecular dynamics of *n*-alkanes. *J. Comput. Phys.* **23**, 327–341 (1977).



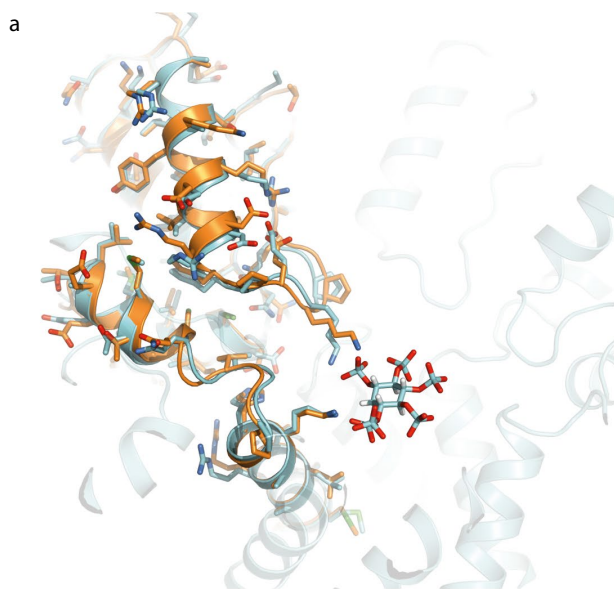
Extended Data Fig. 1 | Effect of acidic molecules on immature s-CANC assembly. **a,** Representative negative-stain electron microscopy images. Scale bars, 200 nm. The experiment was repeated twice with similar results. **b,** Number of immature VLPs per $55\mu\text{m}^2$. $n=5$, mean shown

above box plots; centre lines show medians; box limits indicate 25th and 75th percentiles as determined by R software; whiskers extend to minimum and maximum values.



Extended Data Fig. 2 | s-CANC and s-CASP1 VLPs. **a–c**, Representative negative-stain electron microscopy images of s-CANC (a), s-CASP1 (b) and s-CA (c) proteins assembled in the absence of GT₂₅ and in the presence of the indicated IP₆ concentrations. Scale bars, 200 nm.

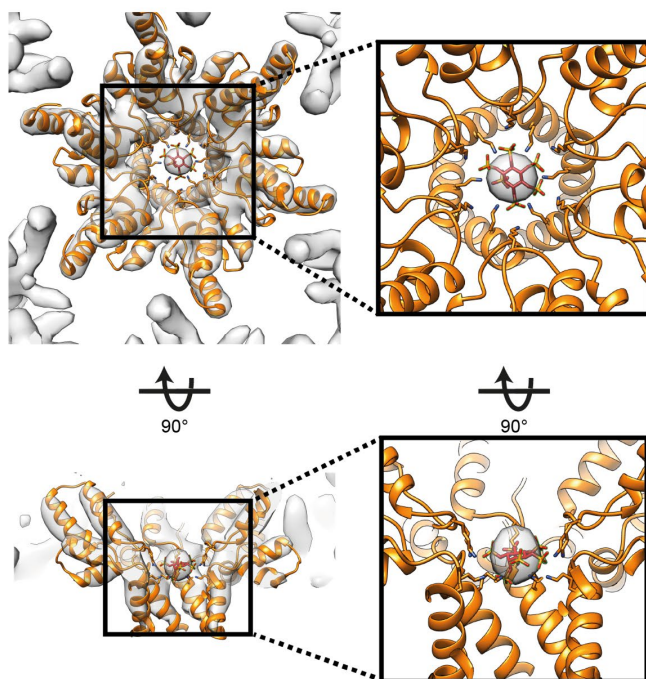
d, Diameters of immature VLPs; mean diameter above plot; n below plot. Centre lines show medians; box limits indicate 25th and 75th percentiles as determined by R software; whiskers extend to minimum and maximum values.



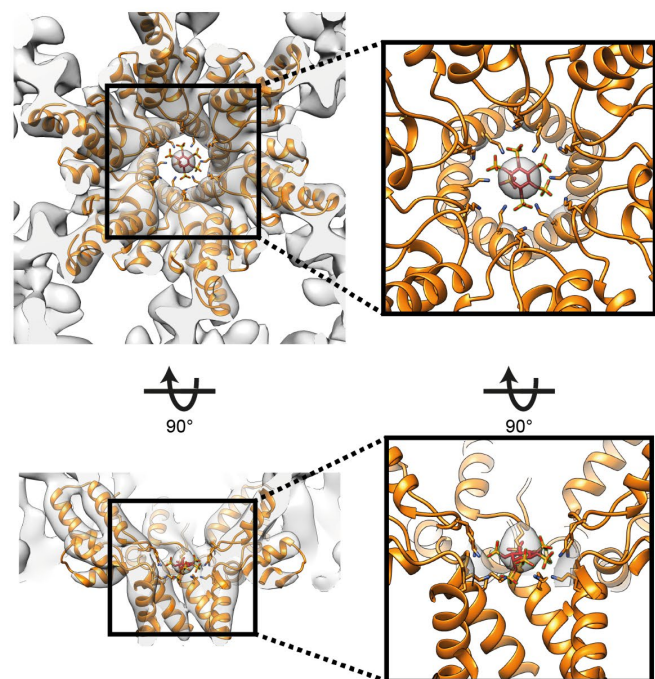
b

Selection	RMSD (Å)
full chain (624 atom pairs)	1.391
Cα (backbone, 89 atom pairs)	0.763
CA-SP1 (92 atom pairs)	1.397
K290& K359 (18 atom pairs)	1.299

EMD-2706
immature HIV-1 (+APV)

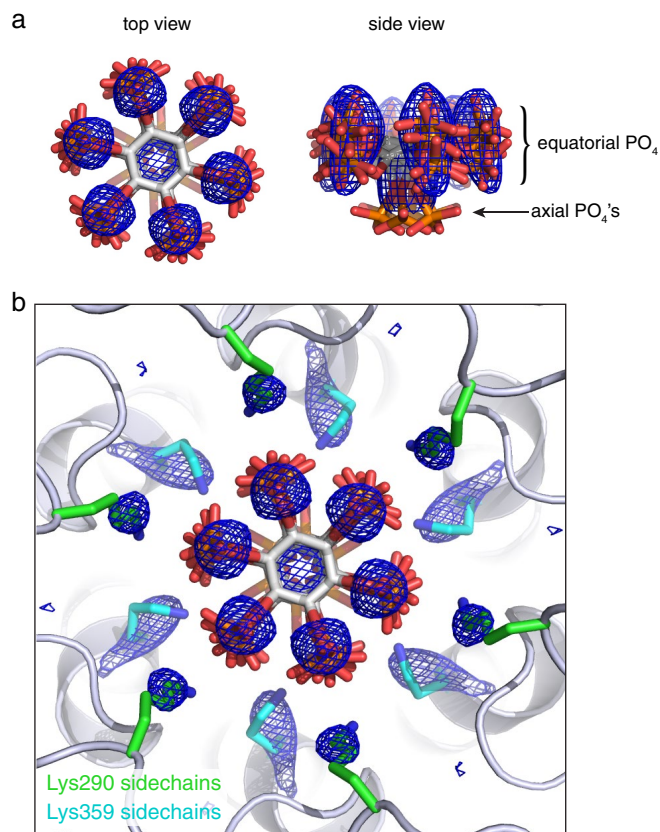


EMD-4017
immature HIV-1
(protease defective D25A)

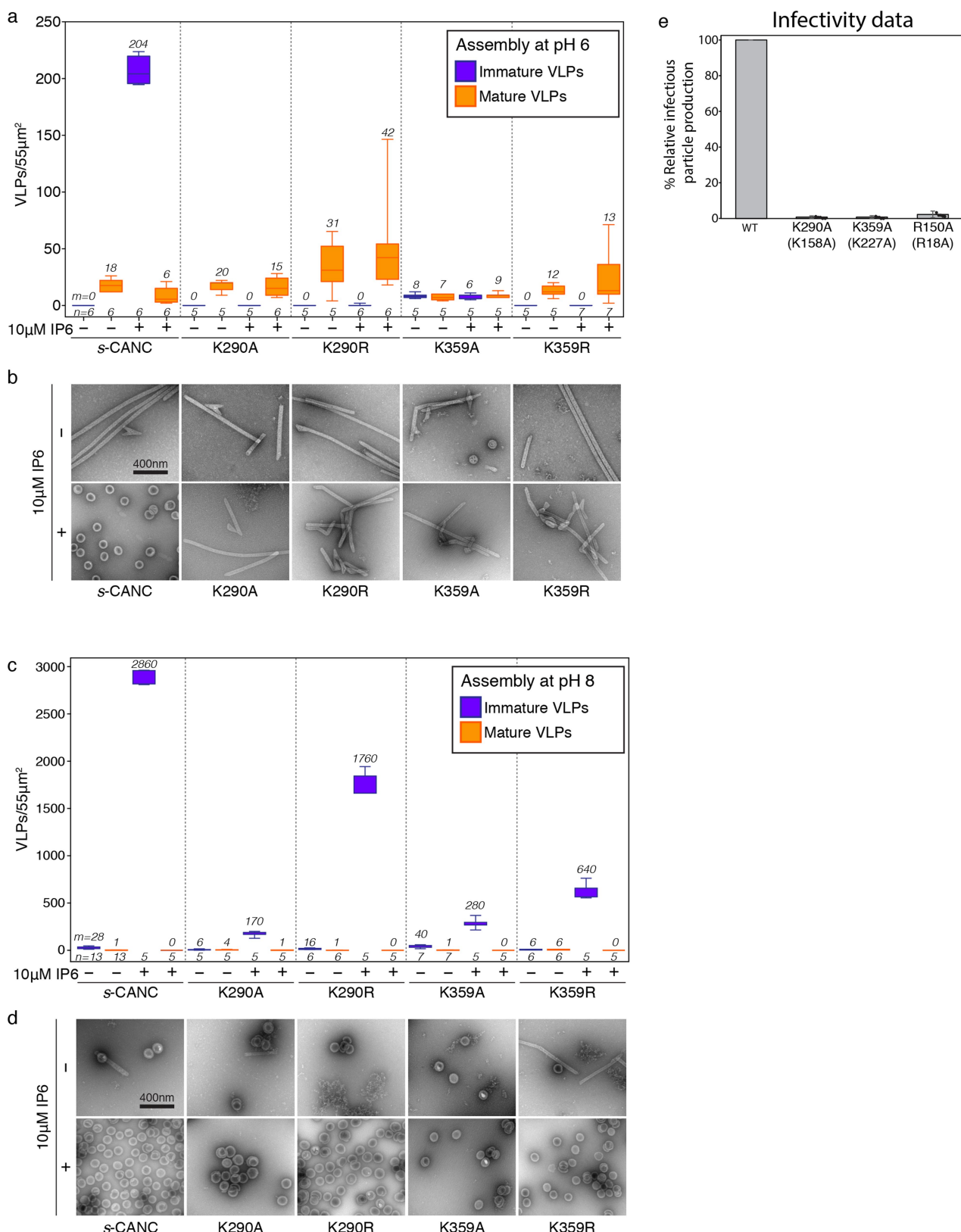


Extended Data Fig. 3 | Comparison of the HIV-1 Gag cryo-EM structure with the CA_{CTD}SP1-IP₆ crystal structure. a, The crystal structure of CA_{CTD}SP1 bound to IP₆ (cyan) was superimposed on a previously described model of the CA-SP1 segment build into cryo-EM densities of immature HIV-1 particles (PDB 5L93, orange²). Note the close correspondence in K359 rotamers, which were modelled independently in the two structures. For visualization purposes, only one of the six possible IP₆ conformations is displayed. b, RMSD calculations of the crystal structure and PDB 5L93. For full-length (residues 149–237) and CA-SP1 (residues 223–237), the RMSDs were calculated only for the atoms that

were modelled in both maps. If a sidechain was not modelled, the entire residue was omitted from the calculation. The overall agreement of the models is very high, indicating that the crystal structure corresponds well with conformations found in the virus. c, The CA_{CTD}SP1 bound to IP₆ (orange and red, respectively) was fitted into two previously published cryo-EM densities² from VLPs collected from cells (EMD-2706 and EMD-4017). Both maps are shown at 8.8 Å, which is the resolution of the lower resolved map, EMD-2706. In the zoomed insets, only the density corresponding to IP₆ is shown. Matching of models and maps and RMSD calculations were performed in Chimera.

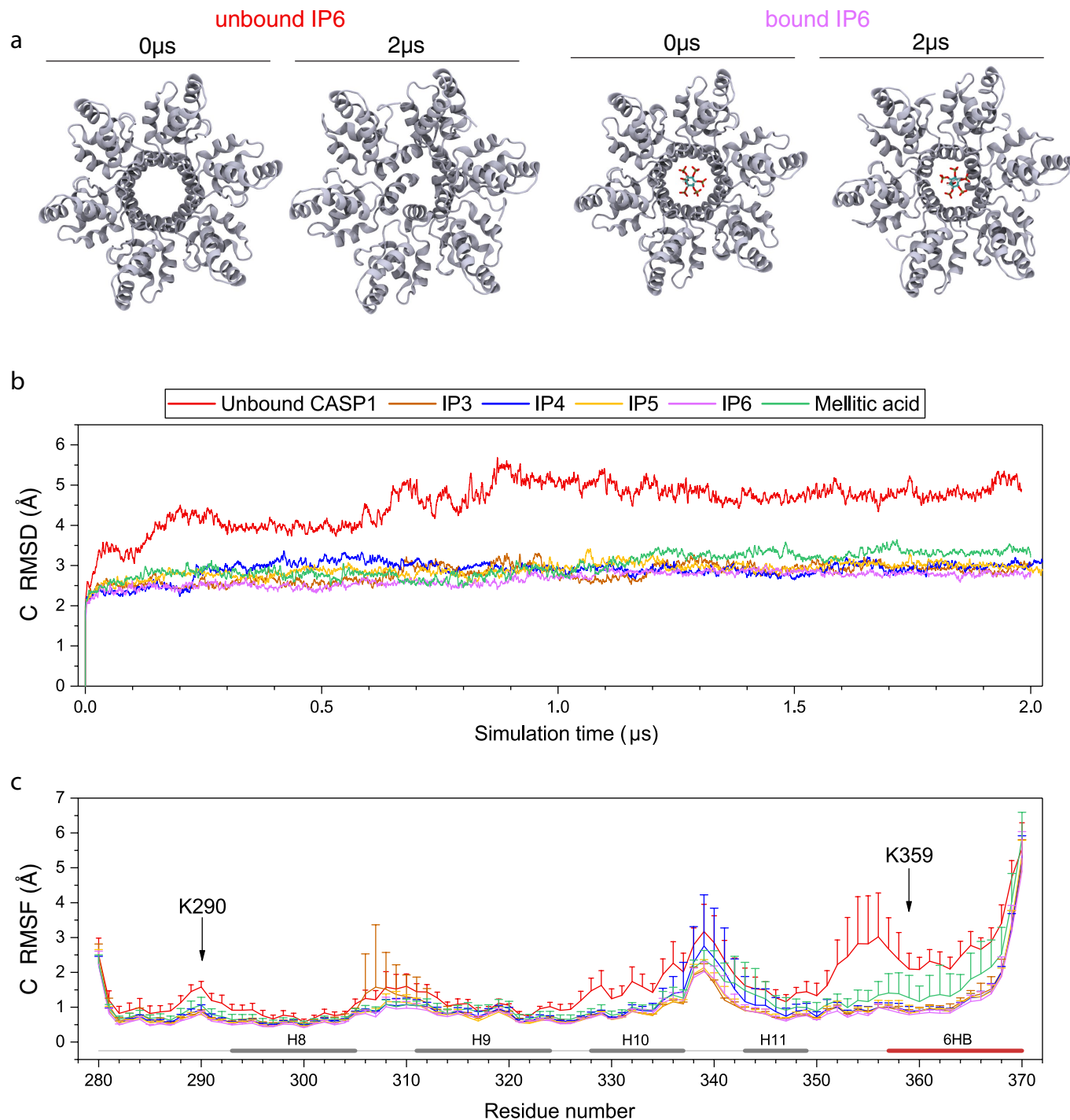


Extended Data Fig. 4 | Interpretation of the IP_6 density in the immature $\text{CA}_{\text{CTD}}\text{SP1}$ hexamer structure. **a**, Top and side views of the unbaised $\text{mF}_o\text{-}DF_c$ difference density (blue mesh, 2σ) ascribed to the bound IP_6 . Shown are six IP_6 molecules docked in six rotationally equivalent positions, consistent with the six-fold rotational symmetric density. **b**, Top view of the docked IP_6 molecules within the $\text{CA}_{\text{CTD}}\text{SP1}$ hexamer. Unbiased $\text{mF}_o\text{-}DF_c$ difference densities (blue mesh) are also shown for both the bound IP_6 and sidechains of Lys290 (green) and Lys359 (cyan). Density for Lys359 is more pronounced, which we interpret to mean that this residue adopts a more restricted range of rotamers for binding IP_6 .



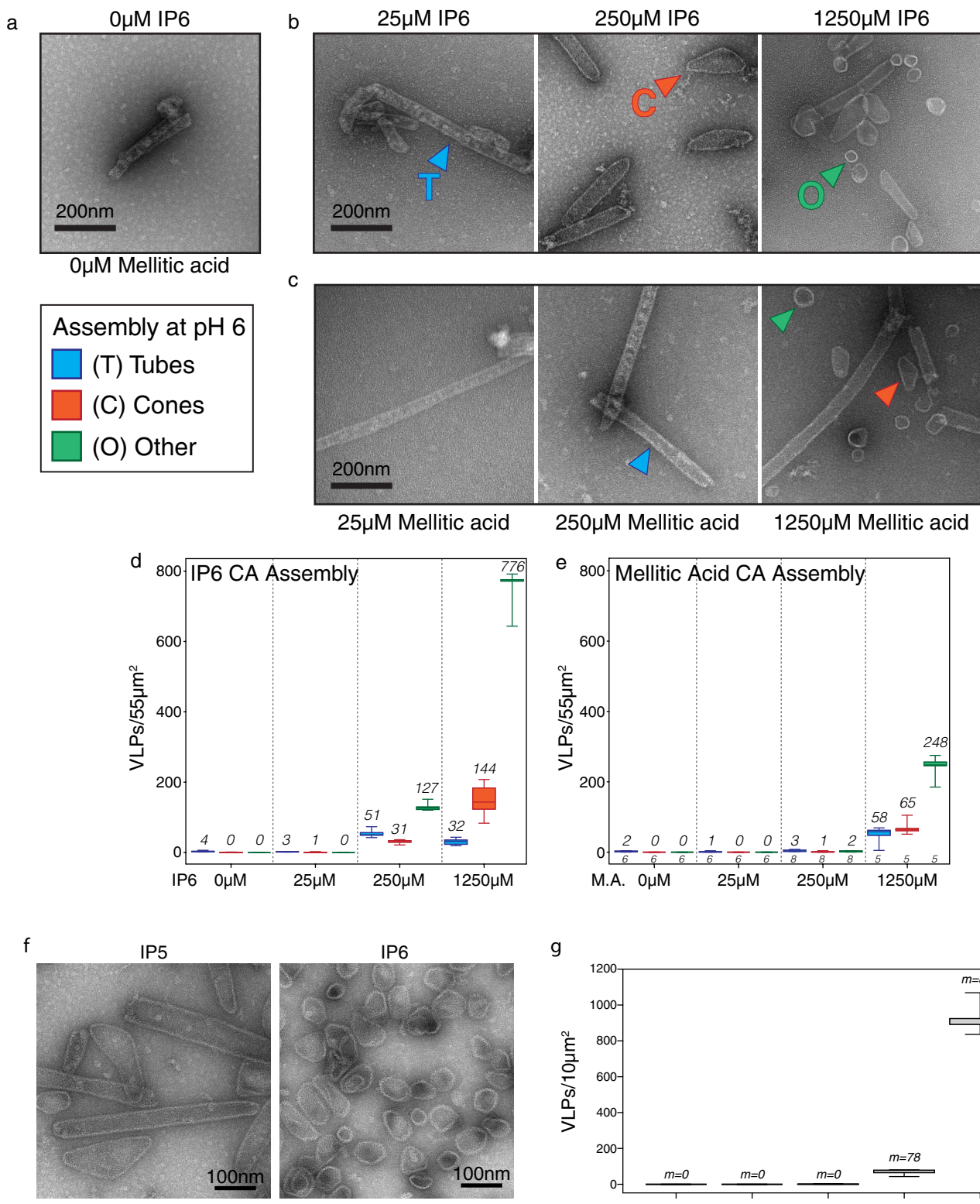
Extended Data Fig. 5 | Quantification of wild-type and mutant HIV s-CANC assembly at pH 6 and pH 8. **a, c**, Number of immature (purple) and mature (orange) VLPs per $55\text{ }\mu\text{m}^2$ without (–) and with (+) $10\text{ }\mu\text{M}$ IP₆ at pH 6 and pH 8. Mean above and n below box plots. Centre lines show medians; box limits indicate 25th and 75th percentiles as determined by R software; whiskers extend to minimum and maximum values. **b, d**, Representative negative stain electron microscopy images of wild-

type and mutant s-CANC assembly in the absence (–) and presence (+) of $10\text{ }\mu\text{M}$ IP₆ at pH 6 and pH 8. Scale bar, 400 nm. Repeated three times with similar results. **e**, Infectivity relative to wild-type virus of IP₆ binding residues mutated to alanine and CA residue numbering in parenthesis. Error bars represent s.d., individual data points represented as dots; from four independent experiments.

**Extended Data Fig. 6 | IP₆ modulates the stability of the 6HB.**

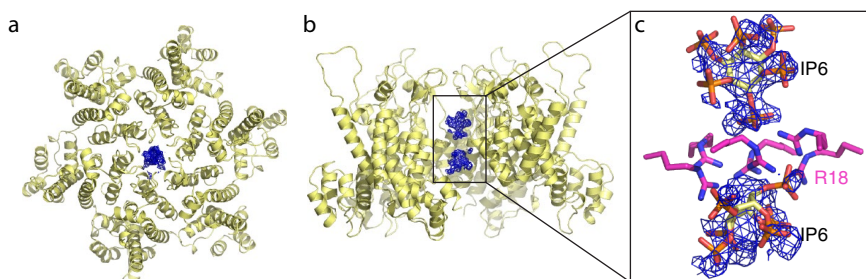
a, Structural changes observed after 2 μs of molecular dynamics simulations of CA_{CTD}SP1 with and without bound IP₆. **b**, RMSDs of the

ligand-bound and unbound forms of the CA_{CTD}SP1 hexamer. **c**, RMSFs of the central hexamer during the simulation. The RMSF was averaged over the six central monomers; dashed line shows the s.d. for each residue.



Extended Data Fig. 7 | Quantification of mature HIV-1 CA assembly and VLP diameter at pH 6. **a**, Example of CA assembly in the absence of IP₆ or mellitic acid. **b, c**, Representative negative-stain electron microscopy images of assemblies induced by IP₆ (**b**) and mellitic acid (**c**). Scale bars, 200 nm. Tubes (T), cones (C), and other (O) morphologies are marked by coloured arrowheads. **a–c**, Repeated four times with similar results. **d**, Number of assembled CA tubes (blue), cones (orange) and other (green) per 55 μm^2 at increasing IP₆ concentrations. Mean shown above plots, $n = 5$. **e**, Number of assembled tubes (blue), cones (orange) and other

(green) per 55 μm^2 at increasing mellitic acid concentrations. Mean shown above and n below box plots. **f**, Representative images of mature VLPs assembled with IP₅ and IP₆ at 50 mM NaCl. Scale bars, 100 nm. Repeated three times with similar results. **g**, Number of CA VLPs per 10 μm^2 without and with IP₃, IP₄, IP₅, and IP₆. Mean shown above, $n = 5$. **d, e, g**, Centre lines show medians; box limits indicate 25th and 75th percentiles as determined by R software; whiskers extend to minimum and maximum values.



Extended Data Fig. 8 | Crystal structure of IP_6 bound to the mature CA hexamer. **a, b,** Top view (**a**) and side view (**b**) of a second CA hexamer crystal structure (*P212121* space group) showing the protein in yellow

ribbons and unbiased $mF_o - DF_c$ difference density in blue mesh, contoured at 2.5σ . **c,** Close-up view showing IP_6 densities both above and below the ring of Arg18 residues (magenta).

Extended Data Table 1 | Crystallographic statistics

	CA _{CTD} SP1+IP6	CA ^{CC1} +IP6	CA ^{CC1} +IP6
Data collection			
Space group	P6	P6	P212121
Cell dimensions			
a, b, c (Å)	70.9,70.9,42.0	90.6,90.6,56.6	135.6,137.8,209.9
α, β, γ (°)	90,90,120	90,90,120	90,90,90
Resolution (Å)	50-2.90 (2.95-2.90)	50-1.98 (2.03-1.98)	50-2.69 (2.74-2.69)
R_{merge}	0.16 (0.94)	0.16 (1.69)	0.06 (0.79)
$I/\sigma I$	10.3 (1.1)	15.2 (1.2)	13.1 (1.1)
Completeness (%)	96.3 (87.8)	100 (100)	99.3 (98.8)
Redundancy	8.1 (4.3)	11.0 (8.8)	3.8 (3.6)
Refinement			
Resolution (Å)	35.47-2.91	39.25-1.98 (2.12-1.98)	39.90-2.69 (2.97-2.69)
No. reflections	1,986	18,196 (2,660)	95,906 (2,545)
$R_{\text{work}}/R_{\text{free}}$	21.5/26.5	23.6/28.4 (28.0/32.4)	22.7/25.4 (30.3/35.5)
No. atoms			
Protein	668	1,641	19,621
IP6	36	72	144
Water	0	145	173
B -factors (Å ²)			
Protein	33.0	35.4	57.0
IP6	39.2	39.6	157.5
Water	n/a	35.9	31.0
R.m.s. deviations			
Bond lengths (Å)	0.005	0.005	0.003
Bond angles (°)	1.093	1.091	0.630

Values in parentheses are for highest-resolution shell. Each structure was solved from data collected with 1 crystal.

Values in parentheses are for highest-resolution shell. Each structure was solved from data collected with one crystal.

TECHNOLOGY FEATURE

A TOOLKIT FOR DATA TRANSPARENCY

A simple software toolset can help to ease the pain of reproducing computational analyses.

MEHAU KULYK/SPL/GETTY



BY JEFFREY M. PERKEL

Julia Stewart Lowndes studied metre-long Humboldt squid (*Dosidicus gigas*), tagging them to track their dives, as a graduate student at Stanford University in California in 2011. When she wrote up her dissertation, she had data on five animals. Then, two months before the project was due, another tag was located in Hawaii.

"I got a sixth of my data within months of finishing," Lowndes says — a lucky break. But luck favours the prepared. Each data set contained hundreds of thousands of points; Lowndes was able to use the new one easily because she had conducted her analyses with an eye on reproducibility. Computational reproducibility is the ability to repeat an analysis of a particular data set and obtain the same or similar results, says Victoria Stodden, who studies reproducibility at the University of Illinois at Urbana-Champaign. In practice, it

means that researchers who publish scientific findings based on computational analyses should release 'digital artefacts,' including data and code, so that others can test their findings.

That hasn't always been the case. Figures have long been published with no way of viewing the underlying data, and algorithms have been described in plain English. But there are many ways to implement an algorithm, and many 'knobs and dials' that can be tweaked to produce subtly different results. Without the actual code, parameters and data used, it is impossible for other researchers to be certain whether the published implementation is correct, or whether their own data are consistent with the published results.

Reproducibility doesn't necessarily mean that the results are scientifically accurate, Stodden emphasizes. "It just says we have this level of computational transparency that permits verification, so that we know that those computational steps, combined with all the

workflow information, including the data and any input parameters, actually did produce the results in the article."

That transparency comes from a handful of key tools, especially version control, scripting and programming. Similar to many researchers, Lowndes — now a marine data scientist at the US National Center for Ecological Analysis and Synthesis at the University of California, Santa Barbara — was trained to work with point-and-click graphical applications such as Microsoft Excel.

But precisely documenting one's analytical steps in such software is difficult, which complicates reproducibility. When Lowndes's first data sets arrived, she discovered that they were too large to open in Excel, so she had to learn to crunch her numbers in the programming language MATLAB. It wasn't easy. But by the time that sixth tag washed up on a beach in Maui, she could update her entire analysis by running her code again. ▶

► Computational reproducibility, Lowndes says, is about “thinking ahead”. She adds: “It’s not thinking, ‘This is easiest for myself right now.’ It’s thinking, ‘When I’m working on this next week, next month, right before I graduate — how do I set myself up so that it’s easier later?’”

SHARING KNOWLEDGE

David Donoho, a statistician at Stanford, co-authored a 1995 paper describing a library of signal-processing functions called WaveLab, in which he explained the history of computational reproducibility so far (J. B. Buckheit and D. L. Donoho *Wavelets Statist.* **103**, 55–81; 1995). Paraphrasing Stanford geologist Jon Claerbout, a leader in the reproducibility field, Donoho wrote: “An article about computational science in a scientific publication is not the scholarship itself, it is merely advertising of the scholarship. The actual scholarship is the complete software development environment and the complete set of instructions which generated the figures.”

Put simply, this means that researchers should make their computational workflow and data available for others to view. They should include the code used to generate published figures and omit only data that cannot be released for privacy or legal reasons. Lorena Barba, an aerospace engineer at George Washington University in Washington DC, for instance, creates ‘reproducibility packs’ — including the code, data and final image — for every figure she publishes. She archives those packages on digital-repository sites such as Figshare, and includes the digital object identifiers (DOIs) in the papers themselves.

But reproducibility is incredibly complex, because neither software nor data are static.

“When you write a program to analyse a piece of biological data, for example, you’re sitting on the pinnacle of a huge pile of software, the top bit of which you wrote, and underneath it is this enormous pile of stuff which other people have written,” says Les Hatton, a mathematician at Kingston University in London, who has been studying computational reproducibility since the 1970s (and who also releases reproducibility packages for his publications).

In this era of open-source, community-developed software, the data and software are constantly in flux. Seemingly simple code optimizations can alter output values. But even the same code can fail to produce the same outcome if it is run on different hardware or compiled using different settings, or because it makes assumptions about the user’s file-directory structure.

“The sum total of all of this is that unquantifiable errors are extremely simple to introduce into the results,” Hatton says.

SOFTWARE STRUGGLES

Take Chris Baldassano, for instance. Baldassano was a postdoctoral fellow doing memory research at Princeton University in New Jersey

Getting reproducible

There’s no one-size-fits-all solution for computational reproducibility. But these practices can help.

● **Use code.** Instead of pointing and clicking, use programming languages to download, filter, process and output your data, and command-line scripts to document how those tools are executed.

● **Go open-source.** Code transparency is key to reproducibility, so use open-source tools whenever possible. “If you give me a black box with no source code and it just gives me numbers, as far as I am concerned, it’s a random-number generator,” says mathematician Les Hatton of Kingston University in London.

● **Track your versions.** Using version-control software such as Git and GitHub, researchers can document and share the precise version of the tools that they use, and retrieve specific versions as necessary.

● **Document your analyses.** Use computational notebooks such as Jupyter to interleave code, results and explanatory text in a single file.

● **Archive your data.** Freeze data sets at key points — when submitting an article for publication, for example — with archiving services such as Zenodo, Figshare or the Open Science Framework.

● **Replicate your environment.** Software ‘containers’, such as Docker, bundle code, data and a computing environment into a single package; by unboxing it, users can recreate the developer’s system. ReproZip, developed in the lab of New York University computer scientist Juliana Freire, simplifies container creation by watching program execution to identify its requirements. The commercial service Code Ocean and an open-source alternative, Binder, enable researchers to create and share executable Docker containers that users can explore in a web browser.

● **Automate.** Automation provides reproducibility without users really having to think about it, says bioinformatician Casey Greene at the University of Pennsylvania in Philadelphia. Continuous integration services such as Travis CI can automate quality-control checks, for instance, and the Galaxy biocomputing environment automatically logs details of the jobs it runs.

● **Get help.** Resources abound for interested researchers; see practicereproducibleresearch.org, for instance, or find a Software Carpentry workshop near you to learn basic computing skills.

when he developed MATLAB code to analyse brain-activity data. Now at Columbia University in New York City, he shared that code with his collaborator, who was using a different version of MATLAB and so got errors instead of results. “There was something about how the underlying system dealt with large numbers that was slightly different on my software and theirs,” he says. Baldassano circumvented the problem by encapsulating his code on Code Ocean, a cloud-based service that allowed him to share his computational environment and code in a web browser, where people could also execute the scripts. (On 1 August, *Nature Methods*, *Nature Biotechnology* and *Nature Machine Intelligence* announced a pilot programme that allows authors “to share fully-functional and executable code accompanying their articles and to facilitate peer review of code by the reviewers” using Code Ocean. See go.nature.com/2akz52b for details.)

“Users often find themselves struggling to replicate other scientists’ research – and even their own.”

Data sets can also evolve over time. Morgan Ernest, an ecologist at the University of Florida in Gainesville, leads a research project that has been documenting biodiversity in the Arizona

desert for more than 40 years. “It’s ‘living data’ because it’s still changing,” she says. In such cases, pinpointing and documenting the precise state of the data at the time the analyses are run becomes crucial, because the data set might well have evolved by the time researchers want to revisit it. Ernest published a strategy for handling such data using GitHub and continuous integration — a form of automated code checking — in June (see go.nature.com/2o2lsza).

The upshot of all these layers is that users often find themselves struggling to replicate other scientists’ research — and even their own. As part of his postdoc, Casey Greene, a bioinformatician at the University of Pennsylvania in Philadelphia, ran a computational analysis of gene-expression data. He documented every aspect of his work, except the specific version of a key database. Four years later, those findings were irreproducible, at least in the fine details. “That was troubling,” he says.

Today, journals increasingly consider reproducibility when evaluating and publishing manuscripts. The *Journal of the American Statistical Association* has appointed editors specifically to assess computational reproducibility. At the *American Journal of Political Science*, a recent emphasis on reproducibility

extended average publication times by more than seven weeks, requiring (on average) two resubmissions of author materials and eight hours of employee time per manuscript “to replicate the analyses and curate the materials for public release”, according to a 2017 analysis published in *Inside Higher Ed* (see go.nature.com/2vhvv3x). Thu-Mai Christian, a data archivist at the H. W. Odum Institute for Research in Social Science at the University of North Carolina at Chapel Hill, which performs the journal’s reproducibility assessments, says the biggest issue with submitted material is poor documentation.

All articles published in Nature Research journals, and in *Nature* itself, require a statement indicating where the data can be found, and those with custom code require a code-availability statement. Code is reviewed on a case-by-case basis. At the moment, reviewers must install the software themselves to test it, and hiccups are not infrequent, says *Nature Methods* chief editor Natalie de Souza. “It’s not 1–5%” of cases, she says. “It is more common.”

TOOLKIT TEST

Reproducibility advocates are converging around a tool set to minimize these problems. The list includes version control, scripting, computational notebooks and containerization — tools that allow researchers to document their data, the

steps they follow to manipulate it, and the computing environment in which they work (see ‘Getting reproducible’).

Without these pieces, says Ben Marwick, an archaeologist at the University of Wollongong in Australia, tantalizing connections lie abandoned because they’re impossible to explore. “It’s like we’re a roomful of hungry people handing around tins of canned food, and nobody has a can opener. And then we’re asking each other, why doesn’t anyone eat anything?”

Reproducibility can be a tough sell. Researchers aren’t software engineers, and learning to work that way is an intimidating prospect, says Lowndes. Reproducibility work can also be time-consuming, and there’s little incentive to pursue it, adds Rich FitzJohn, a research software engineer at Imperial College London. “If researchers are spending all of their time stressing about how long something is going to stay working for them, that’s just time they’re not spending doing the thing that they’re good at, which is solving science problems.”

Academia in many ways disincentivizes reproducibility, as most institutions reward high-profile publications, and making code and data freely available could expose researchers to criticism and the possibility of getting scooped, Stodden says. Speaking of how much academics can realistically achieve, she adds: “Whatever people feel like they can fit in their regular day-to-day job of

being a researcher, I think that’s enough for right now”. Even if researchers cannot build executable containers, for instance, making code available on GitHub or Zenodo repositories allows others to see what they did. (Stodden, Barba and Donoho are members of a US National Academies panel on reproducibility and replicability in science. The panel’s final report is anticipated by early 2019.)

Such approaches might be most useful for researchers themselves. Computational ecologist Christie Bahls ran a course at Michigan State University in East Lansing that taught graduate students in ecology to work with data. One year, her students submitted a paper describing a model of firefly activity, including their code. A reviewer actually tested the code and pointed out that the team was basing its conclusions on an assumption; if they changed that assumption, they might draw a different conclusion.

“He was able to make this insightful comment because of the higher level of reproducibility of the paper,” says Bahls, who is now at Kent State University in Ohio. The team expanded the article’s discussion to elaborate.

“This is how science is supposed to work, isn’t it?” she says. “Because of reproducibility, people were able to critique the work at a deeper level.” ■

Jeffrey M. Perkel is technology editor at *Nature*.

Q&A Harriet Alexander Software training in Antarctica

Harriet Alexander is a postdoctoral fellow in oceanography bioinformatics at the University of California, Davis. In January, she travelled to McMurdo Station in Antarctica to take part in this year’s Antarctic Biology Training Program, a month-long course sponsored by the US National Science Foundation. When bad weather delayed her flight home, she was able to host a workshop for the non-profit training organization Software Carpentry, its first in Antarctica.

What is Software Carpentry?

Software Carpentry is one branch of The Carpentries, a project based in San Francisco, California, that trains researchers in data science and software. For US\$2,500, plus travel and accommodation, volunteer instructors present a 2-day workshop at your location, on topics such as the command line, programming, and how to work with data. Lessons can be tailored to specific fields, and are constantly being improved in line with best practices.



I have led two workshops, and I really love the format. That sort of intensive, full-day immersion in the technology, with lots of hands-on material, is a really great model.

How did the workshop go?

We had about 20 students. The first day, I taught the Unix command-line introduction and it went really well. The second day was Python, which we typically teach

by introducing some packages using the Conda packaging system. Anaconda is about 300 megabytes. That doesn’t sound like much — but when you’re in Antarctica, where the Internet is very slow, it’s huge. I ended up downloading Miniconda, a stripped-down version of 35 megabytes, and it took me probably 2.5 days. But I forgot that Miniconda has to download other stuff, so there was no way it was going to work.

Bottom line: if you’re going to be teaching somewhere remote, download what you need before you get there.

How was Antarctica?

It’s a completely different world — very stark, yet absolutely gorgeous. McMurdo is like a mining town plopped down in the middle of this barren ice. So it’s like moving to a small town for a month and living in a dorm. It was a wonderful experience. ■

INTERVIEW BY JEFFREY M. PERKEL

This interview has been edited for length and clarity.

grateful to have landed his job as a research associate at the New Zealand Institute for Plant & Food Research, a government institute in Nelson funded partially by industry. He earned a master's in biology in 2005 from the University of Basel, Switzerland, but despite his focus on marine science and several internships, he could not find work in ecology. He took a job in a cancer-research lab at the University of Otago in Dunedin, New Zealand, where he gained experience in molecular-biology techniques. These skills helped him to land his current position in 2015, where he genotypes fish for a breeding project. He also spends days at sea, testing net systems, which he helps to design, for their effects on fish.

Research technicians in industry often have more-varied advancement opportunities than do their counterparts in academia or government. Technicians at Roche Innovation Center in Basel, for example, can explore a new pursuit by spending half of their time in business units such as competitive intelligence, supply-chain management, or technology transfer, says Benjamin Hall, a principal scientist at the centre.

Paula Soteropoulos, chief executive of the pharmaceutical company Akcea Therapeutics in Cambridge, Massachusetts, says biotechnology managers are on the look-out for technicians who will add long-term value to their company, for instance, advancing into jobs in regulatory affairs or other areas. Soteropoulos says he has hired clinical-trials-management specialists whose previous experience included work at the bench as technicians.

Whether a candidate wants to carry on in a tech position or pursue a PhD, it is vital that they keep on top of relevant research developments. "Nothing stays stagnant in industry or academia. You need to constantly keep yourself updated," says Anil Koul, director of the Institute of Microbial Technology in Chandigarh, India, and a former senior director at Johnson & Johnson in Beerse, Belgium. Master's degrees are also the norm in the pharmaceutical industry and salaries are generally higher than in academia, he adds. "A job in pharma is extremely competitive," he says, "even at the entry technical level."

Assessing the scientific-enterprise landscape and deciding which direction to pursue can be tough for an aspiring scientist. Soteropoulos says that "regardless of bachelor's, master's or PhD, my advice to any young person is to take risks on new opportunities", adding that it is important to have the confidence to try new things. Speaking of one's career arc, she adds: "It does not have to be on the straight ladder." ■

Charlotte Schubert is a freelance writer in Seattle, Washington.

UDO RINGEISEN/EMBL PHOTOLAB

BACK STORY

Depression tracker

Sociologist Katia Levecque had studied mental health and social inequality in diverse populations before joining the Centre for Research & Development Monitoring (ECOOM) at Ghent University in Flanders, Belgium, in 2012. Her report on graduate-student mental-health concerns (K. Levecque et al. Res. Policy 46, 868–879; 2017) went viral, becoming the second-most-discussed article on social media for 2017, according to research-metrics tracker Altmetric.

What did your study find?

Our survey of 12,000 PhD students from 5 universities in Belgium found that one-third of the 3,659 students who responded had or were at risk of developing a common mental-health disorder, mainly depression or general anxiety. When we compared our data with a survey of highly educated people in Flanders, we saw that PhD students had a risk of mental-health issues that was 1.8–2.8 times higher than for comparable groups.

What responses did you get?

The reactions fell largely into two camps: "This is nothing new, we have known it for years"; or "We are surprised — this is not what we have expected". Some professors admitted that they felt powerless and ill-equipped to do anything. Others acknowledged that they, too, experience the stigmas and taboos that make it a difficult topic to talk about.

The report was retweeted more than 7,000 times. What was that like?

In every presentation I give, when people are 'allowed' to talk or when they feel safe enough, we get to a catharsis moment and they all start sharing their experiences. I continue to get e-mail and phone calls. PhD students send heartbreaking testimonies. Supervisors ask what they can do to spot mental-health concerns, or to better support students. Research organizations have asked for advice on high-level policy programmes to tackle these issues.

How long was this report in the making?

When I joined ECOOM, they were finalizing a survey to be sent to all junior researchers, including PhD students. I asked why they were not covering mental health or well-being. We added those questions at the last minute. I started analysing the data in 2014, but the study wasn't published until last year.

Why the delay?

With results like these, we realized the study could have significant impact. First, our team



checked and rechecked the data to confirm that the methodology was sound and the conclusions were robust. We then informed funders and policymakers about our findings and the possible media attention. We waited to make the results public until we were published in a reputable journal, but our study was discussed in the Flemish parliament before publication.

Has this study affected your research plans?

We are organizing a follow-on survey in Flanders for deeper insights into well-being and social support. I'm also working with the United Kingdom, the Netherlands and other countries to do comparative analyses.

Do you have concerns about future surveys?

Yes. Although the boost in recognition of mental-health issues is good, and a lot of departments or universities are setting up surveys, I worry some may get data that are not comparable. For example, if institutions use survey measures that are not valid and reliable, it might not be clear what is being measured. The concern is that we could have a growth of data, but those might not be the best data to base policies on.

What do you think of the attention your study has attracted?

Having this kind of impact is something you can only dream of as a researcher. The barriers that students have encountered when they experience problems and can't talk about them are the same ones we experienced when we tried to publish our findings. But some of those barriers have been broken down by the fact that this paper has been so well received. ■

INTERVIEW BY VIRGINIA GEWIN

This interview has been edited for clarity and length.

BREAKTHROUGH

An error of judgement?

BY JOHN GILBEY

After years of fairly pointed silence, it was a surprise to get an e-mail from my old institute. When I retired, everyone told me to keep in touch — “don’t be a stranger” — but sadly the invitations to research seminars quickly dried up. The message turned out to be from one of my old students, who I was glad to see had now risen to the lofty heights of research director.

One of her postdocs was running some data-mining operations on the huge catalogue of archived material from the early life of the accelerator and had run across some problems. Would I be able to help out? If so, a flight and hotel would be booked and I’d be picked up on Monday. Sure enough, a car — and a human driver, no less — turned up on cue.

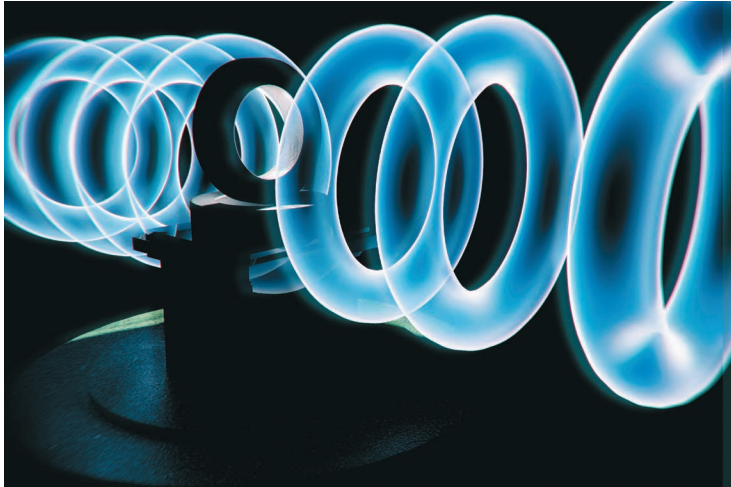
“I was only expecting a shuttle,” I pointed out as Becca met me at security. She laughed.

“I wasn’t sure how old and vague you’d got — I figured it’d be safer to make sure you caught the flight ...”

Her genial banter flowed over me like a warm bath — it was good to be back. The seminar room was much slicker than the last time I’d seen it, and the coffee was infinitely better. Jeff, the postdoc, was already there with a raft of paperwork and screens spread across the table.

Jeff was jovial, keen and very excited — and a degree of arm-waving illustrated his background talk. His problem was interesting, and showed how much had changed since I retired. For the first time in its history, thanks to a generational shift in quantum devices, the computing capacity of the institute exceeded the rate at which the vast fire-hose of raw data gushed from the detector arrays. This freed up some resources for folk, like Jeff, to go back over old, archived material to see what had been missed.

Looking into the immersive display, even my unpractised eye could see the anomaly that was exciting them. The cloud of data points was from an early test run, part of the engineering tests where we had fought hard to drive some of the gremlins from the system. As Jeff scrolled the time-line back and forth, he pointed out the curious banding that had first attracted his attention. In the saturated false colour of the visualization, it



looked oddly like the moving ring patterns you get in the glow discharge of an old fluorescent tube — something Jeff was too young to have seen.

When Jeff spun the image into three dimensions, the full glory of what he’d found was revealed — and I swore, loudly and repeatedly. “That looks like ...”

“Structure,” Becca interrupted with a grin. “Unexplained, repeated structure ...” I thought for a long moment, trying not to let the old madness flood back in. They had clearly excluded the obvious answers or they wouldn’t have called me, but what could give results like these? Equally importantly, had they been sustained? Was there more?

“Nope. Sadly, this is the only test in which the patterns appear.” Jeff began shuffling through the papers in front of him. “The tests were stopped immediately after this run, and the system was offline for over a year.” He slid a set of meeting minutes towards me. “It seems the decision was yours ...”

I looked at the document, and the bland reporting of the meeting secretary triggered a series of panic responses as I recalled something I’d blanked out for years — the story of C57a.

“C57a? What’s that?” asked Becca. Wiping the sweat from my palms, I related the tale of my first cosmically massive mess-up as construction director. I maintain it wasn’t my fault, but it happened on my watch, so it was mine to resolve. For some reason, the contractor who built the coils for dipole C57a

delivered a mirror image of the winding pattern that was specified. Nobody noticed at installation, but the

commissioning tests exposed the error as an anomaly in the external magnetic field. Testing stopped abruptly and the contractor slunk off to build another one.

Becca and Jeff exchanged glances. “I think we can say that it’s a great pity we didn’t know about the data patterns at the time,” said Becca. “We’ve talked to some of the theoretical folk and they got really excited... Like, tap-dancing excited... One even suggested... No, it’s ridiculous...”

I pressed her to explain. Becca sighed deeply and looked at me. “One even suggested that the patterns might be crosstalk,” she paused. “Crosstalk — *from somewhere else...*” That brought me up short. Nobody was even going to say the word — but she was talking multiverses. The potential, and the consequences, awed me into silence. Something that doesn’t happen often.

In the quiet that ensued, Jeff muttered: “If only we had the old dipole we might be able to recreate the conditions. The paperwork just says the original was decommissioned and when we checked, the contractors didn’t have any record. We wondered if you might know, as you were there at the time?”

I said I’d have to think about it and suggested lunch, to give myself some breathing space — I needed to be sure. When I asked if the cafe on site was still open they said yes, but wouldn’t I prefer to go out somewhere? “No thanks, the cafe will do fine.”

The grilled swiss-cheese sandwich was as good as I remembered. Looking out through the long glass wall across the sculpture garden, mostly arty representations of fundamental particles, I saw that the trees had grown up but little else had changed.

“So,” said Becca, “has lunch given you any ideas?” I smiled, and pointed across the lawn. On a granite plinth labelled ‘Chirality’, half hidden by shrubs and still in its impervious Kevlar casing, the huge double doughnut of the rejected C57a dipole magnet stood in the summer sunshine, patiently waiting for its moment of glory to arrive. ■

John Gilbey writes from the academic seclusion of the University of Rural England, where he has managed many infrastructure projects with varying degrees of success. He tweets as @John_Gilbey.

ILLUSTRATION BY JACEY